UNIVERSIDAD AUTÓNOMA DEL ESTADO DE MORELOS

INSTITUTO DE INVESTIGACIÓN EN CIENCIAS BÁSICAS Y APLICADAS

CENTRO DE INVESTIGACIONES QUÍMICAS (CIQ)

Desracemización de Viedma: Un Modelo Integral de la Ruptura Espontánea de la Simetría Quiral en un Sistema de Clorato de Sodio

TESIS

QUE PARA OBTENER EL GRADO DE

DOCTOR EN CIENCIAS

PRESENTA

MARÍA EUGENIA NOBLE TERÁN

DIRECTOR DE TESIS

Dr. THOMAS BUHSE

CUERNAVACA, MORELOS   JUNIO, 2023

UNIVERSIDAD AUTÓNOMA DEL ESTADO DE MORELOS

Agradecimientos

En primer lugar, me gustaría agradecer al Dr. Thomas Buhse por darme la oportunidad de crecer académicamente dentro de su grupo de investigación y por la confianza brindada a lo largo de estos años, permitiendo formarme como investigadora.

Así mismo, agradecerles a los doctores José Manuel Cruz Martínez y Jean-Claude Micheau por sus contribuciones a este proyecto de investigación, sin duda su apoyo fue fundamental para el desarrollo del mismo.

A cada uno de los miembros del comité revisor de tesis, muchas gracias por su tiempo, dedicación, comentarios y disposición para la culminación de este proyecto.

Un agradecimiento especial a mis compañeros del grupo de investigación de Cinética y Dinámica Compleja por su apoyo a lo largo de estos años.

A mi esposo, familia y amigos, muchas gracias por ser parte de los pilares que me sostuvieron en el proceso.

Y finalmente, gracias a mí por un cumplir con uno más de mis sueños.

Para Copito ❄ y Arturo...

Índice general

Resumen

El rompimiento de la simetría quiral ocurre cuando un proceso físico o químico que no tiene preferencia sobre un enantiómero es capaz de conducir de manera espontánea a un resultado en el cual uno de los dos enantiómeros (D o L) es producido en exceso. En la naturaleza este fenómeno se manifiesta por medio de los bloques esenciales para la vida, siendo las biomoléculas homoquirales. El surgimiento de sistemas químicos capaces de manifestar asimetría quiral resultan atractivos para el entendimiento de esta característica de la biosfera. En este sentido, la desracemización de Viedma de cristales de clorato de sodio ($NaClO_3$) es un ejemplo fascinante de estos sistemas. Este proceso basado en la cristalización puede convertir una fase sólida racémica en una enantioméricamente pura. A pesar de la abundancia de investigaciones, todos los detalles fundamentales no han sido clarificados explícitamente. En el presente trabajo, se llevó a cabo el análisis de un modelo cinético integral basado en las relaciones de energía libre de la teoría clásica de la nucleación, crecimiento y maduración de Ostwald. Utilizando un enfoque de tipo Becker-Döring totalmente micro reversible e incluyendo una solubilidad dependiente del tamaño de acuerdo a la regla de Gibbs-Thomson. Para la validación del modelo, se utilizaron datos cinéticos reportados de un experimento real de desracemización de $NaClO_3$. Posterior a la parametrización, y bajo condiciones de molienda el modelo muestra rompimiento espontáneo de la simetría quiral. Así como una ventana de bifurcación dependiente de la intensidad de molienda. El modelo revela que los procesos de ruptura espontánea de la simetría quiral son consecuencia de múltiples procesos autocatalíticos implícitos ocultos. Además, el modelo es capaz de imitar algunas de las características de la precipitación/disolución. Finalmente, se debe agregar que además proveer nuevas perspectivas a la síntesis de moléculas quirales, nuestros descubrimientos pueden contribuir a la discusión sobre el origen de la homoquiralidad biológica.

Abstract

Mirror image symmetry breaking occurs when a physical or chemical process that has no preference over one enantiomer is able to spontaneously lead to a result in which one of the two enantiomers (D or L) is produced in excess. In nature, this phenomenon is manifested by the essential building blocks for life, being homochiral biomolecules. The emergence of chemical systems capable of manifesting chiral asymmetry is attractive for the understanding of this biosphere feature. In this regard, the Viedma deracemization of sodium chlorate ($NaClO_3$) crystals is a fascinating example of such systems. This crystallization-based process can convert a racemic solid phase into an enantiomerically pure one. Despite the abundance of research, all the fundamental details have not been explicitly clarified. In the present work, an analysis of a comprehensive kinetic model based on the free energy relationships of the classical nucleation theory, Ostwald ripening and growth is presented. Using a fully micro-reversible Becker-Döring type approach and including a size-dependent solubility according to the Gibbs-Thomson rule. For model validation, kinetic data reported from a real $NaClO_3$ deracemization experiment were used. After the parameterization, and under grinding conditions, the model shows a mirror image symmetry breaking. As well a bifurcation window dependent on the grinding intensity. The model reveals that mirror image symmetry breaking is the consequence of multiple hidden implicit autocatalytic processes. Furthermore, the model is able to mimic some of the features of precipitation/dissolution. It should be added that besides providing new perspectives for the synthesis of chiral molecules, our discoveries may contribute to the discussion on the origin of biological homochirality.

Índice de figuras

Índice de tablas

Capítulo 1.

Introducción

1.1 Enantiómeros

Se dice que dos objetos son quirales si sus estructuras comparten los mismos elementos, pero difieren únicamente en la manera en la cual están dispuestos espacialmente. De tal modo que uno es la imagen especular del otro, tal cual ocurre con nuestras manos. Si colocamos nuestra mano derecha frente a un espejo podremos ver en éste reflejada nuestra mano izquierda y viceversa (Figura 1), a estas formas quirales se les conoce como enantiómeros.
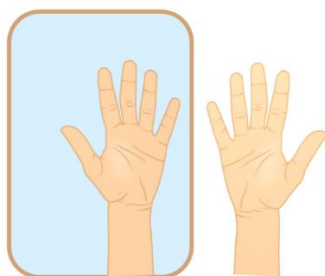
Figura 1. La imagen en el espejo de nuestra mano derecha corresponde a la mano izquierda. Debido a que ambas no son superponibles son un ejemplo didáctico de quiralidad. Los objetos que son superponibles entre sí, se dice que son aquirales.

La quiralidad también se manifiesta a un nivel molecular. En moléculas orgánicas lo hace a través de un centro quiral, es decir, de un átomo unido a cuatro sustituyentes distintos entre sí en una disposición tetraédrica (C_{1234}) (Figura 2).
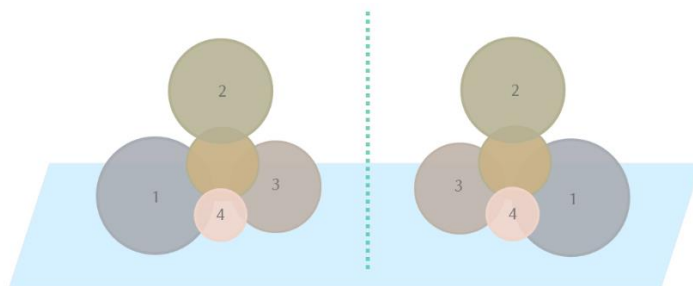
Figura 2. Diagrama general de dos moléculas con una disposición tetraédrica que son imágenes especulares entre sí.

[1]

Las imágenes especulares tienen propiedades físicas y químicas idénticas, sin embargo, su actividad óptica es distinta. Los enantiómeros (o isómeros ópticos) presentan actividad óptica debido a que desvían la luz polarizada que los atraviesa. Pudiendo rotar el plano de la luz polarizada en sentidos opuestos, pero de igual magnitud. Si la molécula rota la luz polarizada en sentido de las manecillas del reloj se le denomina dextrógiro *(d)* o (+). En caso contrario, se le conoce como levógiro *(l)* o (-).

Debido a que el signo de la rotación óptica no determina la estructura espacial del enantiómero, éstos se pueden identificar en función de las configuraciones relativa o absoluta. La nomenclatura L-D corresponde a la descripción de una configuración relativa, la cual se basa en la comparación de un compuesto estándar (enantiómeros del gliceraldehído) con la estructura de los isómeros en cuestión. Pudiéndose determinar si se trata de un enantiómero L o D.[1,2]

La disposición espacial también se puede determinar sin tener que relacionar la molécula con ninguna otra. Utilizando las reglas de Cahn-Ingold-Prelog se asigna la configuración absoluta con las etiquetas S (*sinister*) o R (*rectus*).[3,4]

Cuando sustancias quirales son sintetizadas a partir de reactivos aquirales, usualmente se obtiene una mezcla de moléculas zurdas y diestras[*]en una proporción 50:50 denominada como mezcla racémica o racemato. Si una mezcla posee una mayor cantidad de un enantiómero que del otro se utiliza el concepto de exceso enantiomérico (*ee*). El *ee* determina la enantioselectividad de una reacción o la pureza enantiomérica de un producto, pudiéndose expresar como:

$$ee^{\dagger} \; = \; \frac{(n_d - n_l)}{(n_d + n_l)}$$

El exceso enantiomérico puede oscilar entre -1 y +1. Si el *ee* = 0 se trata de una mezcla racémica. Si el |*ee*| = 1, significa que sólo está presente uno de los enantiómeros, el signo que acompaña al valor del *ee* corresponde a la lateralidad del enantiómero en cuestión. Usando un signo positivo para referirse al enantiómero +*d* y uno negativo para el enantiómero −*l*.

---

[*] Término didáctico utilizado para referirse a moléculas levógiras (zurdas) y dextrógiras (diestras).

[†] n_d y n_l pueden estar en términos de mol o masa.

1.2 Homoquiralidad biológica

A diferencia de la síntesis de moléculas quirales en el laboratorio, la naturaleza es completamente selectiva, siendo los bloques esenciales para la vida *homoquirales*. Es decir, están construidos de unidades quirales de la misma lateralidad, existiendo casi exclusivamente L-aminoácidos y D-azúcares como constituyentes de las proteínas y ácidos nucleicos respectivamente (Figura 3).
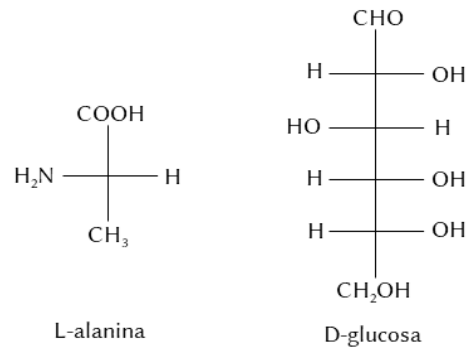
Figura 3. Ejemplo de un L-aminoácido y un D-azúcar en una proyección de tipo Fischer.

Debido a que las biomoléculas se presentan en una sola forma enantiomérica, la quiralidad desempeña un papel de gran importancia dentro de la industria farmacéutica. Ya que la interacción entre los receptores biológicos del cuerpo humano y, las moléculas zurdas y diestras de una sustancia quiral es distinta. Ocasionando que los procesos bioquímicos en el organismo se vean afectados, siendo uno de los enantiómeros farmacológicamente activo, mientras que el otro puede permanecer inactivo o ser tóxico. La talidomida es un ejemplo trágico de las consecuencias de estas interacciones (Figura 4). En 1956, este fármaco fue prescrito como auxiliar en el tratamiento de las náuseas matutinas en mujeres embarazadas. Años más tarde se descubrió que este medicamento causó deformidades en las extremidades de los recién nacidos de las madres a las que se les administró dicho fármaco. Revelándose que la (S)-talidomida aumenta considerablemente la incidencia de malformaciones congénitas, mientras que su enantiómero presenta un efecto antiemético. Concluyéndose que los fármacos quirales deben ser comercializados en su forma pura más no en su forma racémica.
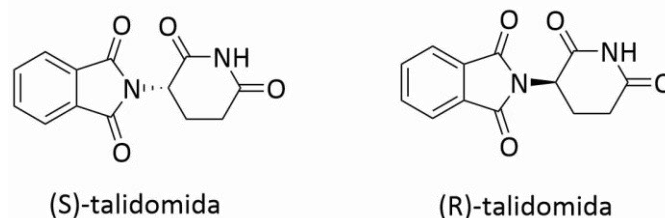
Figura 4. Enantiómeros de la talidomida. La (S)-talidomida es una molécula teratogénica, mientras que la (R)-talidomida tiene un efecto terapéutico.

En virtud de que las biomoléculas están presentes en una sola forma enantiomérica, el origen de esta asimetría y cómo ésta se ha propagado para conducirnos a una biósfera de una "sola mano" ha sido un tema de gran fascinación dentro de la comunidad científica.[5-18] Ya que posiblemente la homoquiralidad biológica es uno de los eventos más notables de la ruptura de la simetría.

1.3 Fuerzas físicas quirales

De manera química, los enantiómeros pueden ser distinguidos por la interacción que presentan con otras especies quirales, a esta característica se le conoce como reconocimiento quiral. Mediante el reconocimiento quiral, las fuerzas físicas pueden influenciar la formación espontánea de productos enantioméricamente enriquecidos a partir de precursores aquirales. La Tabla 1 muestra algunas de las fuerzas quirales que han sido reportadas como inductores asimétricos.

Tabla 1. Descripción de fuerzas físicas que pueden inducir polarizaciones asimétricas.

Fuerza física	Comentario
Dicroísmo magneto-quiral	Campo magnético orientado de manera paralela a la dirección de propagación de un haz de luz genera un pequeño *ee*.[19]
Quiralidad inducida por selectividad de espín	Diferencia entre las velocidades de adsorción de los enantiómeros en una superficie ferromagnética provocada por una polarización enantioespecífica del espín.[20]
Radiación beta (β) polarizada	Radiación beta (β) producido en el fenómeno de decaimiento beta (β) puede conducir a una fotólisis asimétrica de moléculas quirales.[21]

Violación de paridad	Los enantiómeros muestran una pequeña diferencia de energía debido a la violación de paridad.[22]
Luz circularmente polarizada	Interacción de la luz linealmente polarizada zurda o diestra en sistemas químicos genera un imbalance enantiomérico.[10,11,23]
Movimiento de vórtice	Una muestra que es sometida a agitación en sentido y contra-sentido de las manecillas del reloj forma un vórtice que a su vez genera un efecto de corte que da lugar a la ruptura de la simetría.[24]

1.4 Concepto de racemato

De acuerdo a las reglas de nomenclatura de la IUPAC[25] se define como racemato a una mezcla equimolar de un par de enantiómeros. Este concepto abarca en su definición a los conglomerados, cristales racémicos, líquidos y soluciones. La definición de racemato como sustantivo y no como adjetivo de mezcla no es un error, por el contrario, es necesaria para referirse al comportamiento de conjuntos largos de moléculas. En ausencia de un efecto de reconocimiento quiral ejercido por una fuerza física quiral, ambientes quirales, especies quirales o, interacciones homo o heteroquirales, los enantiómeros son especies termodinámicamente indistinguibles. Sin el reconocimiento quiral, los racematos son termodinámicamente más estables con respecto a cualquier mezcla escalémica[‡] de sus enantiómeros, manteniéndose en un estado de equilibrio.[§]

[‡] Mezcla de enantiómeros en una proporción distinta a 50:50.

[§] Estado en el que no hay cambios netos en las propiedades termodinámicas de un sistema a lo largo del tiempo. En un sistema en equilibrio termodinámico, todas las reacciones químicas y las transformaciones físicas que ocurren dentro del sistema están equilibradas. Lo que quiere decir que la velocidad de las reacciones directas es la misma que la velocidad de las reacciones inversas, y las concentraciones de los distintos componentes se mantienen constantes con el tiempo.

1.5 Ruptura espontánea de la simetría quiral (RESQ)

De acuerdo a la definición de K. Mislow,[26] la síntesis asimétrica absoluta corresponde a la formación de productos enantioméricamente enriquecidos a partir de precursores aquirales y sin la intervención de reactivos o catalizadores químicos quirales. La síntesis asimétrica absoluta es de gran interés por su posible contribución a la discusión sobre el surgimiento de la homoquiralidad biológica. Además, se utiliza como un término análogo para la ruptura espontánea de la simetría quiral (RESQ).[27] La ruptura espontánea de la simetría quiral consiste en la producción espontánea y no preferencial de una forma enantiomérica durante el transcurso de un proceso químico que parte de condiciones aquirales o cuasi-racémicas.[28–33] Al contrario de una síntesis simétrica en donde el racemato es la composición más estable, la RESQ es una consecuencia de la biestabilidad y bifurcación del sistema. En un sistema dinámico la biestabilidad consiste en la existencia de dos estados de equilibrio estables. En términos de la ruptura de la simetría quiral, un racemato se encuentra en un estado energético mayor y puede transitar entre los dos estados de equilibrio coexistentes, estos estados de mínima energía corresponden a los estados escalémicos (Figura 5). Cuando el racemato inestable es dirigido hacía uno de estos estados es que ocurre la bifurcación del sistema. En ausencia de una fuerza física quiral, la RESQ da como resultado un producto cuya lateralidad está dada de manera aleatoria. En una serie de procesos repetidos ambas formas enantioméricas tienen la misma probabilidad de formarse. Sin embargo, presentan una alta sensibilidad a pequeñas perturbaciones inducidas por la presencia de dichas fuerzas, convirtiendo un escenario aleatorio en uno determinista.
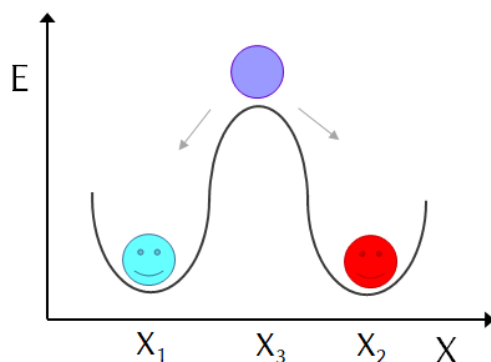
Figura 5. Gráfico que representa de manera general la energía potencial de un sistema dinámico biestable que manifiesta ruptura espontánea de la simetría quiral. La circunferencia morada localizada en el punto X_3 representa

al racemato inestable, la menor perturbación puede provocar que el sistema se mueva hacía uno de los dos estados de equilibrio localizados en los puntos X_1 y X_2 que representan a los estados escalémicos.

Para que un escenario de RESQ ocurra se deben cumplir con ciertas restricciones como, condiciones fuera del equilibrio[**]con una alta producción de entropía y la presencia de un mecanismo de retroalimentación cinética como una autocatálisis enantioselectiva.[34–37]

1.5.1 Autocatálisis enantioselectiva

La autocatálisis se refiere a un proceso en el cual el producto generado actúa como un catalizador para favorecer su propia producción. Este proceso no sólo implica la auto aceleración del producto sino también una actividad enantioselectiva en el producto final (promoviendo la formación de un enantiómero en mayor cantidad que el otro), se le conoce como autocatálisis enantioselectiva. Un ejemplo experimental bien documentado de este tipo de autocatálisis es la reacción de Soai.[38]

La reacción de Soai (Figura 6) consiste en la alquilación de ciertos aldehídos de pirimidinilo con diisopropil zinc, en donde el alcanol de pirimidina quiral acelera su propia formación y promueve la prevalencia de su configuración, dando como resultado la auto multiplicación del compuesto quiral, manifestando el acoplamiento entre cinéticas no lineales y una termodinámica fuera del equilibrio en un sistema abierto.[31] Esta peculiar reacción resulta atractiva por su alta sensibilidad a una gran variedad de aditivos quirales y criptoquirales,[††] su capacidad para producir RESQ a partir de condiciones aquirales y esencialmente su relación con posibles vías que pudieran explicar el origen de la homoquiralidad biológica. Recientemente, la reacción de Soai ha sido explorada en términos de la elucidación de los aspectos estructurales, cinéticos y termodinámicos de su mecanismo de reacción.[39–41]

[**] El sistema experimenta procesos irreversibles, flujos de energía y materia, así como cambios en las propiedades del sistema. Estos cambios pueden ser impulsados por gradientes de temperatura, presión, concentración u otros factores que desequilibren al sistema. Desde reacciones químicas que se llevan a cabo en sistemas abiertos en donde hay un flujo constante de reactivos y productos, hasta organismos vivos que están en un continuo intercambio de materia y energía con su entorno, son ejemplos de sistemas que se encuentran lejos del equilibrio termodinámico.

[††] Compuestos quirales ópticamente activos que se encuentran por debajo del nivel de detección experimental.
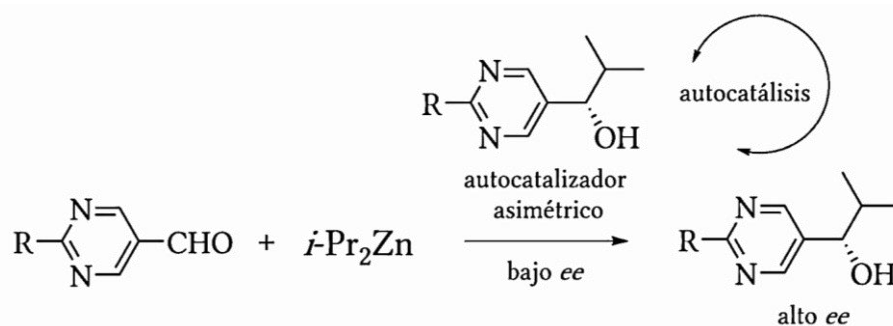
Figura 6. Principio de la autocatálisis quiral en la reacción de Soai.

Para que la RESQ ocurra es necesaria una producción de entropía por arriba de un valor crítico que desestabilice el racemato y dé lugar a los estados escalémicos. La transición entre dichos estados estacionarios es la consecuencia de un potencial físico que surge del balance entre los flujos de entropía con los alrededores y la producción de entropía de la red de reacciones químicas. La autocatálisis enantioselectiva es un proceso capaz de acceder las altas tasas de producción de entropía que dan lugar a un escenario de RESQ, presentando dependencias cinéticas altamente no lineales en las concentraciones de los enantiómeros. De manera teórica, la expresión más sencilla de un proceso autocatalítico es:

$$A + nL \rightarrow (n+1)L$$
$$A + nD \rightarrow (n+1)D$$
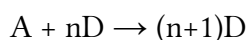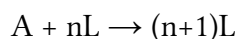
En donde A es un compuesto aquiral, L y D son los enantiómeros, y n indica el orden de la autocatálisis.

Para que un proceso autocatalítico presente un escenario de RESQ, es necesario el acoplamiento de diversas redes cinéticas que consideren efectos no lineales,[‡‡] de tal manera que el orden de la autocatálisis sea mayor a 1. Existen dos posibles escenarios mediante los cuales la autocatálisis enantioselectiva puede generar productos escalémicos en ausencia de una polarización quiral.

[1]. Mediante el control cinético en sistemas cerrados altamente exergónicos y con procesos irreversibles. En los que la autocatálisis progresa rápidamente sobre el enantiómero que presenta un exceso inicial generado por una perturbación estocástica. Las altas

---

[‡‡] Los efectos no lineales en síntesis asimétrica están definidos por la relación no lineal entre el exceso enantiomérico del producto versus el exceso enantiomérico del catalizador quiral.[154]

[8]

velocidades de reacción y las bajas concentraciones enantioméricas iniciales aumentan la probabilidad de generar mezclas escalémicas, aunque de igual manera racematos o mezclas cuasi-racémicas también pueden ser obtenidas.

[2]. Cuando el producto resultante de la reacción correspondiente al racemato es inestable y de manera espontánea desracemiza estocásticamente hacia uno de los dos estados estables escalémicos enantioméricos. Con el fin de que este escenario ocurra, es necesaria una red de reacción de autocatálisis enantioselectiva con un grado alto de efectos no lineales y trabajando en un sistema abierto.

1.5.2.1 Modelo de Frank

En el año de 1953, F. C. Frank[42] propuso un mecanismo cinético para explicar la autocatálisis enantioselectiva que da lugar a un escenario de RESQ. El mecanismo involucra dos procesos acoplados (Figura 7), la autocatálisis selectiva [2] y la inhibición mutua entre los enantiómeros [3] L y D. La formación directa [1] transforma a un reactivo aquiral A en los productos quirales L y D, el flujo constante de entrada del reactivo aquiral mantiene al sistema fuera del equilibrio.

$$A \xrightarrow{k_1} L \qquad\qquad A \xrightarrow{k_1} D \qquad [1]$$

$$A + L \xrightarrow{k_2} 2L \qquad A + D \xrightarrow{k_2} 2D \qquad [2]$$

$$L + D \xrightarrow{k_3} LD \qquad [3]$$
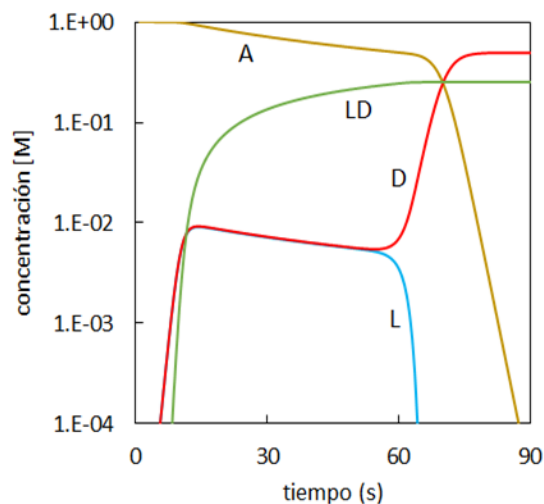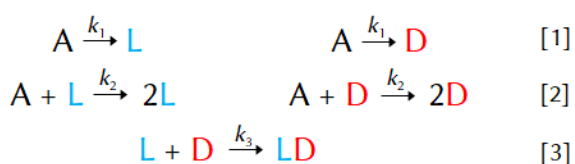
Figura 7. Modelo de Frank representado en términos de reacciones químicas. Cuando es trasladado a ecuaciones diferenciales ordinarias es posible obtener la evolución en tiempo de cada una de las especies, pudiéndose observar la bifurcación de los enantiómeros. $[A]_0 = 1$ M, $[L]_0 = [D]_0 = 0$ (la bifurcación tiene lugar por el ruido numérico presente en la simulación); $k_1 = 1e\text{-}6$ s^{-1}, $k_2 = 1$ M^{-1}·s^{-1}, $k_3 = 100$ M^{-1}·s^{-1}.

Un pequeño sesgo en el racemato puede amplificarse gracias a la inhibición mutua [3] por medio de la eliminación de complejos heteroquirales que no presentan poder autocatalítico (Figura 8). La pérdida de masa resultante es compensada por la reproducción homoquiral de cada enantiómero.
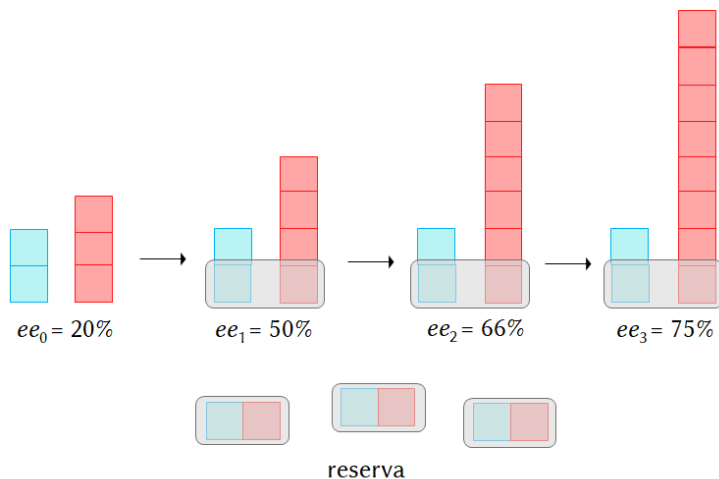
Figura 8. Representación del proceso de inhibición mutua que da lugar a la amplificación del *ee* en el modelo de Frank.

Sin la inhibición mutua la amplificación del *ee* no sería posible, exhibiéndose un escenario de autocatálisis simple en el que la proporción de enantiómeros permanece constante a lo largo del proceso.
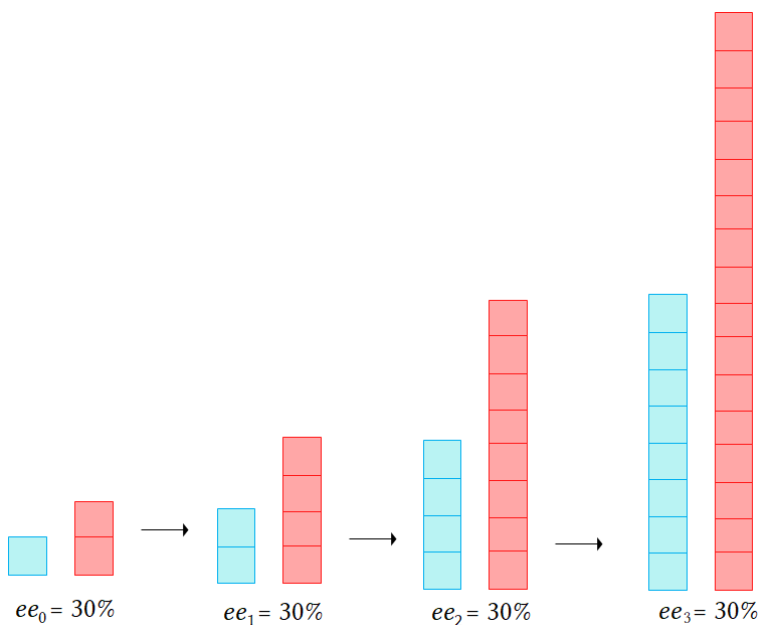
Figura 9. Representación de un proceso autocatalítico simple en el que la inhibición mutua no está presente, generando que el *ee* permanezca constante a lo largo del proceso.

[10]

1.6 Homoquiralidad de cristales

Al igual que la reacción de Soai, la cristalización quiral es un ejemplo relevante dentro de la síntesis asimétrica absoluta. Ya que existen numerosos fármacos capaces de formar cristales quirales,[§§] la separación de sus formas enantioméricas puede ser esencial para garantizar la eficacia y seguridad terapéutica adecuada. Existen tres maneras mediante las cuales un compuesto quiral puede cristalizar[43] (Figura 10), la más común es la formación de un compuesto racémico (i). El 90-95% de los compuestos quirales producen un cristal racémico el cual está compuesto por una proporción 1:1 de cristales L y D dentro de él. Los conglomerados (ii) corresponden a una mezcla de cristales enantiopuros sin una interacción directa entre las formas L y D, del 5-10% de las moléculas quirales cristalizan de esta manera. Finalmente, los compuestos pseudo racémicos (iii) son la forma menos común de cristalización (<1%). En su composición se incluye a los enantiómeros L y D, pero en una proporción distinta al cristal racémico.

La manera en la que el compuesto cristaliza influye en el método de separación de las moléculas quirales. Siendo los conglomerados los únicos que pueden ser separados de manera mecánica.
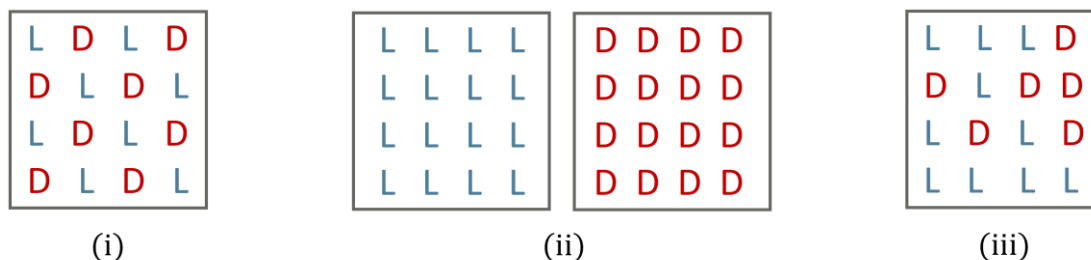
Figura 10. Tipos de cristalización quiral. (i) Racémicos,[***] (ii) Conglomerados,[†††] (iii) Pseudo racémicos.[‡‡‡]

[§§] Fármacos antiinflamatorios no esteroideos (AINE) como el naproxeno y el ibuprofeno, warfarina y propanolol.

[***] Aminoácidos como la valina, alanina y leucina pueden cristalizar como racematos.

[†††] Por ejemplo, el ácido tartárico.

[‡‡‡] Las sustancias que cristalizan como pseudo racematos son aquellas que bajo ciertas condiciones de cristalización pueden formar cristales con una mezcla desigual de enantiómeros dentro del cristal. Debido a la dependencia que se tiene con las condiciones exactas de cristalización, no hay una lista específica de sustancias que siempre cristalicen como pseudo racematos.

1.6.1 Sistemas cristalinos

En cristalografía los sistemas cristalinos, los grupos espaciales y los grupos puntuales son conceptos fundamentales para la descripción de la simetría y estructura de los cristales.

Los sistemas cristalinos son una clasificación utilizada para describir la simetría tridimensional de un cristal en términos de la forma geométrica que adopta su red tridimensional y las relaciones que existen entre las longitudes y los ángulos de sus ejes. Bajo estas consideraciones existen 7 sistemas cristalinos: triclínico, monoclínico, ortorrómbico, tetragonal, trigonal, hexagonal y cúbico. Cada uno de éstos tiene un conjunto característico de grupos espaciales asociados a él.

Los grupos espaciales describen la simetría tridimensional y la disposición ordenada de átomos, iones o moléculas en un cristal. Cada grupo espacial está compuesto por una serie de operaciones de simetría (como traslaciones, rotaciones y reflexiones) que preservan la estructura cristalina en todo el espacio de tres dimensiones.

1.6.1.1 Grupos espaciales de Sohncke

De un total de 230 grupos espaciales, 65 corresponden a grupos no centro simétricos (Tabla 2).[44] Es decir, sólo presentan operaciones de simetría como rotaciones, reflexiones y traslaciones, pero no incluyen la operación de inversión. En la literatura, los también denominados grupos de Sohncke han sido catalogados erróneamente como grupos quirales. Ya que representan la posible simetría de los objetos quirales, pero por sí mismos no son necesariamente quirales. En su lugar, un subconjunto de 22 tipos de grupos espaciales son quirales y forman 11 pares enantioméricos. Los 43 grupos restantes no presentan su contraparte enantiomérica por lo que no son quirales.[45]

Tabla 2. Lista de los 65 tipos de grupos de Sohncke. Los grupos espaciales resaltados corresponden a los grupos quirales.

Sistema cristalino	Grupo puntual	Grupo espacial
Triclínico	1	$P1$
Monoclínico	2	$P2$, $P2_1$, $C2$
Ortorrómbico	222	$P222$, $P222_1$,
		$P2_12_12$, $P2_12_12_1$, $C222_1$, $C222$

		$F222$, $I222$, $I2_12_12_1$
Tetragonal	4	$P4$, $\mathbf{P4_1}$-$\mathbf{P4_3}$, $P4_2$,
		$I4$, $I4_1$
	422	$P422$, $P42_12$, $\mathbf{P4_122}$-$\mathbf{P4_322}$
		$\mathbf{P4_12_12}$-$\mathbf{P4_32_12}$, $P4_222$, $P4_22_12$,
		$I422$, $I4_122$
Trigonal	3	$P3$, $\mathbf{P3_1}$-$\mathbf{P3_2}$
	32	$P312$, $P321$, $\mathbf{P3_112}$-$\mathbf{P3_212}$, $\mathbf{P3_121}$-$\mathbf{P3_221}$
Hexagonal	6	$P6$, $\mathbf{P6_1}$-$\mathbf{P6_5}$, $\mathbf{P6_2}$-$\mathbf{P6_4}$, $P6_3$
	622	$P622$, $\mathbf{P6_122}$-$\mathbf{P6_522}$, $\mathbf{P6_222}$-$\mathbf{P6_422}$, $P6_322$
Cúbico	23	$P23$, $F23$, $I23$, $P2_13$, $I2_13$
	432	$P432$, $P4_232$, $F432$, $\mathbf{F4_132}$-$\mathbf{F4_332}$, $I432$, $P4_132$,
		$I4_132$

Dentro de los 65 grupos de Sohncke se pueden encontrar compuestos tanto quirales como aquirales. Los enantiómeros puros sólo pueden cristalizar como cristales quirales (por ejemplo, el ácido aspártico, el monohidrato de asparagina, la treonina, clorhidrato de ácido glutámico).[46] La mayoría de las veces las moléculas aquirales producen cristales aquirales, pero alrededor del 10% de los cristales quirales son formados a partir de moléculas aquirales.[47–49] Esto se logra a través de su disposición helicoidal cuyo giro determina la lateralidad del cristal. Algunos ejemplos de este tipo de compuestos son: el dióxido de silicio o cuarzo (SiO_2) que a bajas temperaturas cristaliza en un sistema trigonal (α-cuarzo) en el grupo espacial P3$_1$21 o P3$_2$21 dependiendo de su quiralidad y a altas temperaturas cristaliza en un sistema hexagonal (β-cuarzo) en los grupos espaciales P6$_2$22 o P6$_4$22,[50] el sulfato de litio (Li_2SO_4) en el grupo espacial Pn2$_1$/a, y el bromato de sodio ($NaBrO_3$) en el grupo P2$_1$3.

1.7 Cristalización de clorato de sodio (NaClO₃)

Otro ejemplo representativo de las transformaciones aquirales-quirales es la sal de clorato de sodio ($NaClO_3$). En solución, los iones Na^+ y ClO_3^- se encuentran disociados sin una quiralidad definida. Cuando esta sal cristaliza produce cristales cúbicos en el grupo espacial $P2_13$.[51] Dentro de la celda

unitaria se albergan cuatro moléculas cuyo arreglo helicoidal le confiere actividad óptica al cristal (Figura 11).
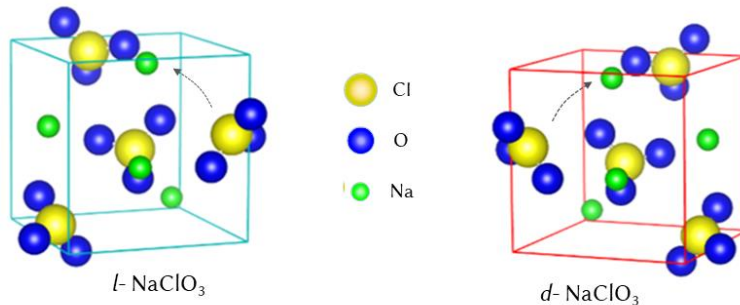
Figura 11. Celda unitaria del clorato de sodio. La disposición espacial de sus iones produce un arreglo helicoidal que de acuerdo al sentido de su giro se puede determinar la lateralidad del cristal.

La lateralidad de los cristales individuales (*d*- o *l*-) de $NaClO_3$ puede ser identificada experimentalmente de una manera muy sencilla. Mediante el uso de placas polarizadoras los cristales pueden ser distinguidos como claros u oscuros, la Figura 12 ilustra este proceso.
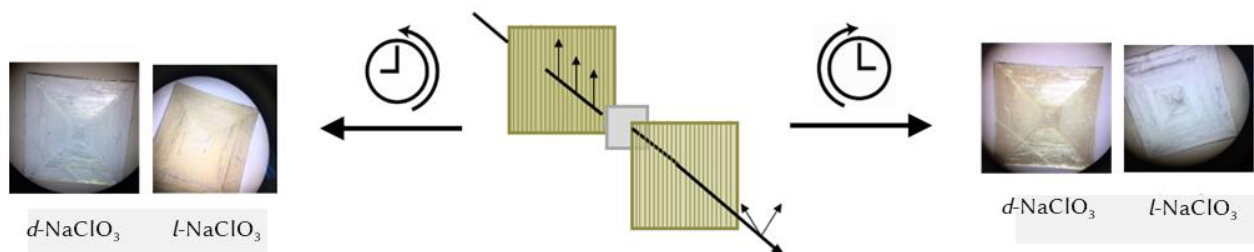
Figura 12. Procedimiento experimental para la identificación de *l*- y *d*-cristales de clorato de sodio.[50] Cuando un cristal es colocado en medio de dos placas polarizadoras, el giro de la placa superior en sentido de las manecillas del reloj desvía la luz linealmente polarizada en ese sentido, tornándose los cristales *d*-$NaClO_3$ en un color café amarillento. Por el contrario, si en lugar de rotar la placa superior a favor de las manecillas lo hacemos en contra, los cristales *l*-$NaClO_3$ son los que van a adquirir esta coloración.

1.7.1 Cristalización de $NaClO_3$ en reposo

La manera más común de cristalizar una sustancia es mediante la cristalización en reposo. En ésta, el soluto es disuelto para formar una solución saturada, la cual es mantenida en reposo mientras el disolvente se evapora lentamente. En 1898, Kipping y Pope[52] llevaron a cabo una serie de experimentos de cristalización de $NaClO_3$ en condiciones de reposo. En los que, en ausencia de una

[14]

influencia quiral los procesos de nucleación y crecimiento de los cristales guiaron la cristalización. Los experimentos fueron repetidos de manera sistemática, encontrando que en la mayoría de los casos se obtiene una distribución enantiomérica final simétrica con 50% de *l*-cristales y 50% de *d*-cristales (Figura 13).

Figura 13. Esquema que ilustra la cristalización en reposo. Posterior a la evaporación del disolvente de una solución saturada de NaClO₃, una distribución racémica en la población de los cristales es obtenida.

A diferencia del comportamiento típico de la cristalización en reposo, Cruz *et al.*[53] reportaron un sesgo estadístico significativo hacía los *d*-cristales en la mayoría de sus experimentos. Planteando una hipótesis relacionada a la presencia de biocontaminantes como responsables de sus resultados. Así mismo, la tendencia hacía una determinada forma enantiomérica podría estar relacionada con la violación de paridad.[54] Esto implica que una pequeña diferencia de energía posiciona a una molécula quiral en un estado de energía más bajo con respecto a su enantiómero.[55–59] En este sentido, la selección de la lateralidad resultante sería una consecuencia de pequeñas diferencias en la velocidad de una reacción o diferencias en la energía del enlace entre las dos formas enantioméricas.[60]

1.7.2 Cristalización de NaClO₃ en agitación

Para que un sistema químico exhiba ruptura de la simetría quiral, generalmente se requiere una competencia entre ambos enantiómeros, así como una autocatálisis quiral (como en el modelo de Frank). La cristalización de NaClO₃ en agitación cumple con ambos procesos. Si la solución saturada es sometida a agitación durante el periodo de cristalización, el resultado final será una población de *l*- o *d*-cristales (Figura 14). En cada repetición del proceso la lateralidad de la población cristalina resultante se da de manera aleatoria.[61]

En estas condiciones, la ruptura espontánea de la simetría quiral involucra dos procesos de nucleación. La nucleación primaria consiste en el surgimiento de un primer núcleo en la solución

sobresaturada, el cual puede adquirir de manera indistinta la configuración –*l* o -*d*. A su vez, la formación de esta entidad denominada como "cristal madre" implica el decremento de la concentración del soluto, y con ello disminuye la probabilidad de que un nuevo núcleo de lateralidad opuesta surja. La agitación promueve el desgaste de la superficie del cristal madre, produciendo el desprendimiento de pequeñas piezas del material cristalino. La nucleación secundaria sucede cuando se crean nuevos sitios potenciales de nucleación con la misma morfología del cristal de origen. La supresión de la formación de un núcleo de morfología opuesta a la del cristal madre provocada por la nucleación primaria y el carácter autocatalítico de la nucleación secundaria son esenciales para el rompimiento de la simetría quiral en este sistema.
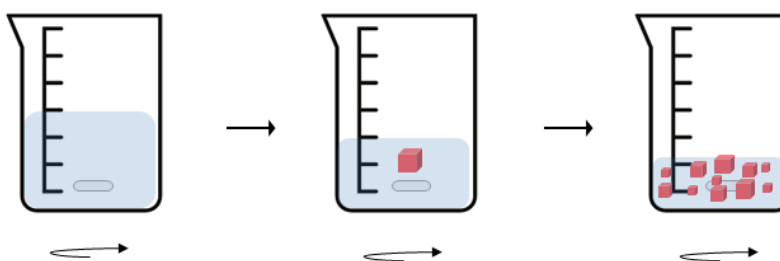
Figura 14. Ilustración del proceso de cristalización bajo condiciones de agitación. Cuando una solución sobresaturada de $NaClO_3$ es sometida a agitación da como resultado una población final homoquiral cuya lateralidad está dada de manera aleatoria. Siendo los procesos de nucleación primaria y secundaria los responsables de la ruptura espontánea de la simetría quiral. La lateralidad final obtenida es independiente de la dirección de la agitación.

1.8 Desracemización de Viedma

Un caso muy especial de autocatálisis asimétrica absoluta es la desracemización de mezclas de cristales enantiopuros racémicos reportada por primera vez por C. Viedma.[62] En donde la ruptura de la simetría fue conseguida mediante la agitación y molienda de una suspensión acuosa de conglomerados de $NaClO_3$ en presencia de esferas de vidrio (Figura 15). Bajo estas condiciones las dos poblaciones de los cristales zurdos y diestros no pueden coexistir en la misma suspensión, es decir, una de las poblaciones se extingue en beneficio de la otra. La formación de una sola forma enantiomérica cuya lateralidad cristalina está dada de manera aleatoria en cada experimento individual parece ser un resultado ineludible en la desracemización de Viedma.
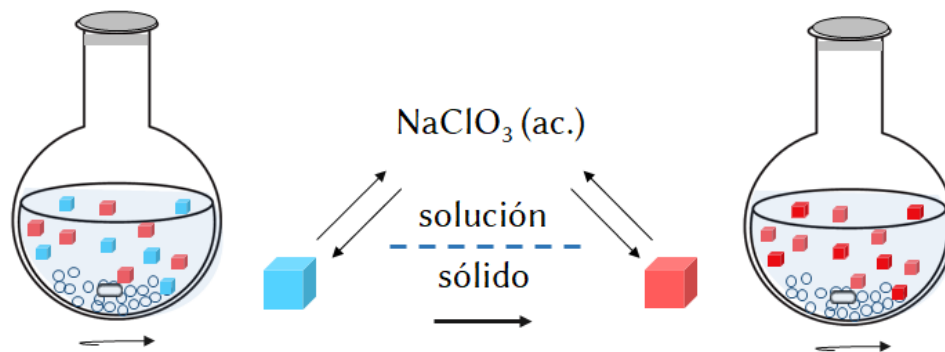
Figura 15. Diagrama que ilustra el experimento de desracemización de Viedma. La agitación de una suspensión sobresaturada que contiene cristales racémicos de NaClO3 y en presencia de esferas de vidrio da lugar al rompimiento de la simetría quiral.

La desracemización de Viedma representa un tipo de ruptura espontánea de la simetría quiral, en la cual se presenta el surgimiento de estados ópticamente activos partiendo de condiciones racémicas o cuasi-racémicas sin la influencia de una fuerza quiral externa o aditivos. Tal cual ocurre en todos los procesos de nucleación, la formación y crecimiento cristalino conllevan un cambio en la energía libre de Gibbs (Figura 16). Para la formación de los primeros núcleos, la energía relacionada al volumen es liberada por la transformación líquido/sólido. No obstante, es requerida una ganancia energética asociada a la formación de las nuevas superficies sólidas. Debido a que el aspecto superficial es dominado en los cristales pequeños y el volumétrico en los cristales más grandes, es que existe un tamaño crítico.[63] Más allá de éste tamaño los cristales crecen, mientras que por debajo los cristales se disuelven (regla de Gibbs-Thomson).[64-67]
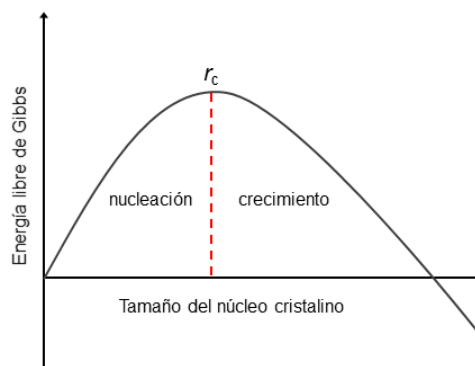
Figura 16. Perfil de energía libre de Gibbs en la teoría clásica de la nucleación. La línea punteada indica la formación de un cristal con un tamaño crítico. Por debajo de éste, los núcleos son inestables y tenderán a disolverse. Y por encima del valor crítico los núcleos son inestables y tenderán a disolverse. Por encima del valor crítico lo núcleos han ganado estabilidad y procederán a crecer.

A causa de la molienda abrasiva, los cristales de $NaClO_3$ se rompen en piezas más pequeñas. Cuando éstas son disueltas se transforman en un soluto aquiral y experimentan un efecto de "amnesia quiral".[68] La disolución de los cristales está sujeta a la regla de Gibbs-Thomson, siendo los núcleos quirales más pequeños los que tienden a disolverse con mayor facilidad. Cuando un determinado umbral en el tamaño del cristal es excedido, la sobresaturación promueve la nucleación primaria, produciendo la formación de la misma cantidad de cristales L y D.[69,70]

El crecimiento de los cristales es promovido por la maduración de Ostwald.[71] Este proceso espontáneo ocurre debido a que los cristales grandes son más favorecidos energéticamente que los cristales pequeños. Éstos al poseer una relación superficie-volumen superior a la de los cristales grandes presentan un mayor número de sitios de interacción con otras sustancias (como los solventes), haciéndolos más susceptibles a la disolución. En consecuencia, las partículas en solución pueden depositarse en la superficie de los cristales más grandes (Figura 17). Así mismo, los cristales pequeños pueden aglomerarse con cristales de mayor tamaño y de la misma lateralidad. Bajo estas condiciones, los núcleos quirales pequeños pueden disolverse o favorecer la nucleación secundaria de cristales con la misma lateralidad.
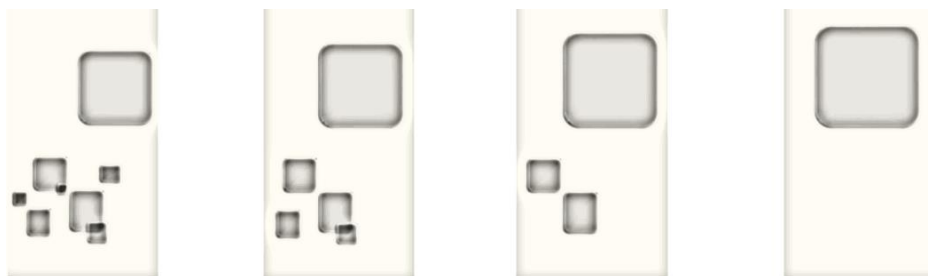
Figura 17. Representación del crecimiento cristalino por medio de la maduración de Ostwald, en la cual los cristales grandes crecen a expensas de la disolución de los más pequeños.

El proceso continuo de disolución-recristalización da como resultado el surgimiento autocatalítico de una sola fase quiral mediante la conversión de un enantiomorfo sólido en otro.[72] En términos del exceso enantiomérico cristalino ($Cee = n_d - n_l / n_d + n_l$), el sistema se transforma de un $Cee \approx 0$ a un casi 100% sin la influencia de una fuerza quiral asimétrica. En donde el signo de la quiralidad del enantiómero predominante varía de manera aleatoria en una serie de experimentos repetidos, pudiéndose obtener de manera individual L o D cristales de $NaClO_3$. De acuerdo a la evidencia

[18]

experimental,[73] la desracemización de Viedma exhibe un claro carácter autocatalítico (Figura 18), produciéndose cinéticas sigmoidales en las que el C*ee* máximo producido puede alcanzar un valor del 100%. A diferencia del modelo de Frank en el que se presentan interacciones heteroquirales entre los enantiómeros para aumentar el orden de la autocatálisis enantioselectiva, en la desracemización de Viedma las interacciones homoquirales son las que dan lugar a un orden mayor de la dinámica autocatalítica.
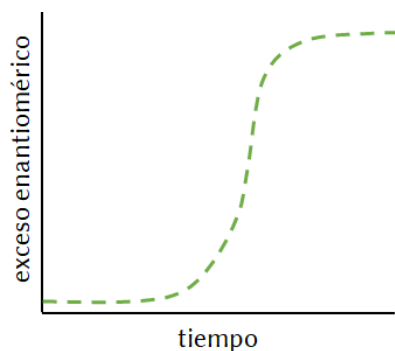
Figura 18. Representación de la evolución cinética del ee en un experimento de tipo Viedma, mostrando el crecimiento sigmoidal como una característica representativa de la autocatálisis.

A pesar de que el sistema de Viedma es considerado como un sistema cerrado en el que no hay intercambio de materia, el sistema es alejado del equilibrio mediante el suministro de energía que le proporciona la molienda.[74–82] Además de esta fuente de energía mecánica, los gradientes y ciclados de temperatura,[83–88] ultrasonido[89] y catálisis fotoquímica[90] son capaces de mantener al sistema lejos del equilibrio y dar lugar a la ruptura de la simetría.

La desracemización de compuestos aquirales se ha expandido a diversos compuestos distintos al $NaClO_3$, considerando que (i) el compuesto tiene que cristalizar como conglomerados y (ii) necesita ser racemizado eficientemente en solución. Ya que a través de la disolución se pierde la información quiral (amnesia quiral)[91] y las moléculas son susceptibles a interconvertirse en su otro enantiómero. El bromato de sodio ($NaBrO_3$),[92] el sulfato de etilendiamonio ($C_8H_{24}N_2O_4S$)[93,94] y numerosos compuestos orgánicos aquirales que forman conglomerados han sido evaluados bajo las condiciones de molienda de Viedma, dando lugar al proceso de desracemización.

1.8.1 Modelos de la Desracemización de Viedma

La comprensión teórica de la desracemización de Viedma continúa abierta a discusión. Diversos modelos teóricos han sido propuestos para poder explicar completamente este fenómeno, no obstante, no existe un mecanismo conclusivo para este sistema. Para el modelado de la desracemización de Viedma se han utilizado técnicas como las simulaciones Monte Carlo, modelos de balance de población y ecuaciones cinéticas de velocidad. Estos enfoques convergen en la solubilidad dependiente del tamaño de los cristales, el desgaste por molienda y el crecimiento enantioselectivo de los cristales.

1.8.1.1 Modelos Monte Carlo

Los modelos Monte Carlo[95–99] se basan en la generación de múltiples muestras aleatorias para obtener estimaciones estadísticas y, comprender la variabilidad y el rango de resultados probables. Para modelar la desracemización de Viedma se describen los cambios en la distribución de tamaño del cristal de manera discreta. Por ejemplo, cada movimiento de Monte Carlo representa un intervalo de tiempo durante el cual un cristal elegido al azar crece a costa de otros más pequeños o, se divide en pedazos más pequeños con una probabilidad aleatoria determinada.

1.8.1.2 Modelos basados en agentes

En un modelo basado en agentes se representan a los agentes individuales y su comportamiento en un entorno simulado. Los agentes son entidades autónomas que pueden presentar distintas características, habilidades, reglas de comportamiento y objetivo. Los cambios en su comportamiento o en las condiciones de su entorno pueden afectar al sistema en su conjunto. En la desracemización de Viedma las dinámicas microscópicas de la cristalización son incorporadas como las reglas de comportamiento de los cristales individuales (o agentes).[100]

1.8.1.3 Modelos de balance poblacional

Los modelos de balance poblacional están basados en la idea de que las poblaciones están influenciadas por los procesos de natalidad, mortalidad, migración y crecimiento. La interacción de estos procesos entre sí afecta la estructura y el tamaño de una población a lo largo del tiempo. Los modelos de balance poblacional propuestos[66,67,101–103] para explicar la desracemización de los cristales de clorato de sodio están fundamentados en la termodinámica de Gibbs y describen el

cambio en las longitudes características de las partículas en función de su tamaño, temperatura y sobresaturación de acuerdo a la teoría clásica de la nucleación. Considerando que el nacimiento y la muerte de un gran número de partículas de distintos tamaños se debe a la nucleación, crecimiento, disolución, racemización en solución, aglomeración y fractura mecánica. Además de obedecer el balance de masa para tener en cuenta la continuidad de fase.[104]

1.8.1.4 Modelos de cinética química

Las ecuaciones cinéticas de velocidad describen cuantitativamente la relación que existe entre la velocidad de reacción y las concentraciones de los reactivos. Los modelos de cinética química[72,73,99,105–113] propuestos se fundamentan en el supuesto de campo medio, es decir, la descripción de un sistema con múltiples especies que interactúan entre sí es simplificada. La idea es que cada especie en el sistema se ve afectada únicamente por un "campo medio" promedio generado por todas las demás especies, en lugar de considerar de manera individual las interacciones entre cada par.

Al igual que en los modelos de balance de población el efecto de Gibbs-Thomson[114] también es considerado, clasificando la disolución del cristal en términos del tamaño crítico. Si se está por debajo del tamaño crítico la especie será más propensa a la disolución. Entonces, las relaciones correspondientes de energía libre§§§ son trasladadas a ecuaciones diferenciales de velocidad reversibles (o irreversibles) para respetar (o no) el principio de microrreversibilidad.****[115,116]

Las simulaciones son llevadas a cabo mediante la integración numérica del sistema de ecuaciones diferenciales que describen a la red cinética propuesta.

---

§§§ El cambio en la energía libre de Gibbs de una reacción (ΔG) está relacionada a la constante de equilibrio (K) a través de la ecuación: $\Delta G = -RT\ln(K)$. En donde R es la constante de los gases y T es la temperatura. Un $\Delta G < 0$ indica un proceso espontáneo con una K > 1, un $\Delta G > 0$ y una K < 1 corresponde a un proceso no espontáneo y finalmente, un $\Delta G = 0$ indica que la reacción está en equilibrio y por lo tanto su K = 1.

**** El equilibrio termodinámico en un sistema químico es alcanzado cuando las tasas de reacción en ambos sentidos son iguales, es decir, las reacciones directas e inversas ocurren a la misma velocidad. El principio de microrreversibilidad es fundamental para la descripción de sistemas químicos en equilibrio termodinámico. Estableciendo que los procesos químicos al equilibrio pueden revertirse microscópicamente, esto quiere decir que, si se invierten las velocidades y las trayectorias de las moléculas, las leyes de la termodinámica seguirán siendo válidas y el sistema evolucionará de manera reversible.

Capítulo 2.

Objetivos

2.1 Generales

El objetivo de la presente tesis es dilucidar el mecanismo de la desracemización de Viedma, mostrando un modelo basado en ecuaciones cinéticas que pueda contribuir a la comprensión de la desracemización de $NaClO_3$ en un sistema de tipo Viedma. Considerando que únicamente la interacción de los procesos de nucleación primaria (produciendo la misma cantidad de cristales L y D), agregación selectiva paso a paso, molienda (generando cristales secundarios de la misma lateralidad que el cristal del que provienen) y disolución no-selectiva de los cristales L y D son suficientes para el surgimiento de una cinética autocatalítica y enantioselectiva que describa la evolución en tiempo del *Cee* observado en ajustes experimentales. Así mismo, la reproducción del efecto de ruptura espontánea de la simetría quiral.

2.2 Particulares

- Desarrollar un modelo integral que considere dentro de su estructura a los cuatro elementos principales contenidos en las desracemizaciones de tipo Viedma. Es decir, nucleación primaria, crecimiento cristalino, disolución y molienda.

- Incorporar por primera vez la fase aquiral de $NaClO_3$ y la transformación martensítica[††††] mediante la cual el sistema desracemiza hacía las formas quirales L y D.

- Todas las transformaciones reversibles involucradas deben cumplir con el principio de micro reversibilidad, a excepción de la molienda que es el único proceso irreversible.

- Obtener un conjunto único de valores de parámetros cinéticos por medio de un análisis de ajuste de curvas de experimentos reales de desracemización de $NaClO_3$ que muestran el *Cee* a distintos valores iniciales.

[††††] Fenómeno que implica un cambio en la estructura cristalina mediante el reordenamiento de sus átomos.

- Con los valores de los parámetros cinéticos obtenidos en el punto anterior reproducir las características básicas de los procesos de nucleación.

- Identificar los tiempos característicos de la nucleación, crecimiento cristalino, maduración de Ostwald y equilibrio.

- Reproducir la ruptura espontánea de la simetría quiral a partir de un exceso enantiomérico cristalino inicial (Cee_0) igual a cero.

- Reproducir observaciones experimentales tales como el impacto de la intensidad de molienda en la desracemización y el tiempo de bifurcación.

Capítulo 3.

Metodología

3.1 Presentación del modelo

Con el fin de contribuir en el entendimiento de la desracemización de Viedma en un sistema de NaClO$_3$,[64,92,117] se ha desarrollado un modelo que pretende imitar los distintos mecanismos presentes en este sistema, es decir: nucleación primaria, agregación selectiva, disolución y molienda. El modelo cinético se basa en un enfoque Becker-Döring[‡‡‡‡] que describe la nucleación y la maduración con base en la adsorción y desorción enantioselectiva de unidades monoméricas en clústeres quirales de distintos tamaños.[104,110,111,118–122] En adición, el modelo es considerado como simétrico debido a que todos los procesos que operan sobre una forma enantiomérica lo hacen de la misma manera con su opuesto, compartiendo las mismas constantes de velocidad (Figura 19).

[‡‡‡‡] Propuesto en 1930 por John W. Becker y Wilhelm Döring, el enfoque Becker-Döring es utilizado para describir el crecimiento y evolución de clústeres en procesos de nucleación y crecimiento cristalino. El modelo establece que los clústeres pertenecen a un "solvente" en una proporción mucho menor y se asume que se encuentran homogéneamente distribuidos en el espacio. A lo largo de su movimiento, los clústeres dan lugar a dos tipos de reacciones conocidas como las *reglas de Becker-Döring*: (1) un clúster de tamaño 1, también llamado monómero o partícula elemental, puede aglomerarse a un clúster de tamaño $i \geq 1$, dando lugar a un clúster de tamaño $i + 1$; (2) un clúster de tamaño $i \geq 2$ puede liberar de manera espontánea a un monómero y formar a un clúster de tamaño i -1 y a un clúster de tamaño 1. De manera general, el conjunto de reacciones cinéticas para cada clúster $i \geq 1$ se expresa como: $C_1 + C_i \rightleftharpoons C_{i+1}$.[155]
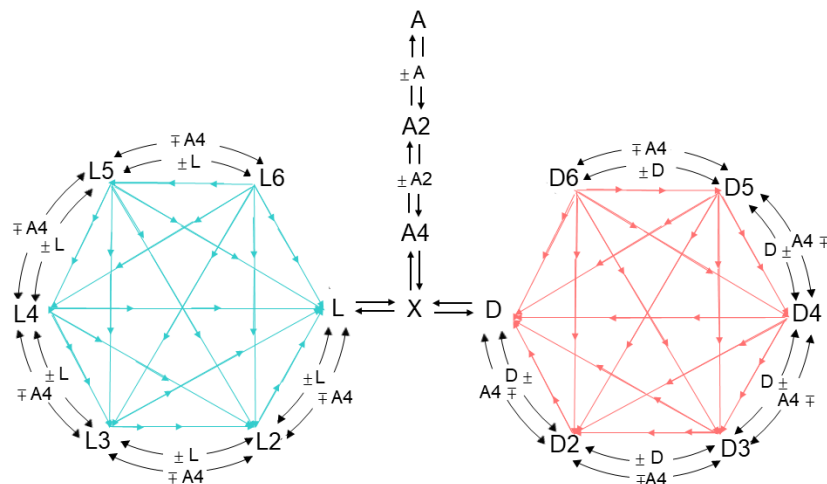
Figura 19. Esquema general del modelo cinético de ecuaciones de velocidad propuesto para llevar a cabo las simulaciones numéricas de la desracemización inducida por la molienda de los cristales de $NaClO_3$.

El modelo está compuesto por un total de 16 especies aquirales y quirales (A, A2, A4, X, L, L2, L3, L4, L5, L6, D, D2, D3, D4 D5, D6), 3 procesos aquirales (nucleación primaria) y 44 procesos quirales distribuidos entre los lados L y D en perfecta simetría (transformación martensítica: 2 procesos, crecimiento cristalino: 12 procesos, disolución: 12 procesos, molienda: 18 procesos). De acuerdo a la Figura 19, la especie A corresponde al soluto libre, A2 y A4 a la formación de un líquido denso; X representa la fase aquiral que desracemiza hacia la fase quiral L o D por medio de una transformación martensítica.[123] Los múltiples equilibrios que van de L a L6 pretenden imitar los procesos de crecimiento cristalino y la disolución de cristales a líquido denso; por ejemplo, el crecimiento reversible de un cristal como Ln + L ⇌ Ln+1 (o Ln+1 – L ⇌ Ln). Mientras que la nucleación /disolución secundaria reversible es representada por Ln + A4 ⇌ Ln+1 (o Ln+1 – A4 ⇌ Ln). La serie de pasos irreversibles (flechas delgadas) hacen referencia a la fragmentación cristalina ocurrida en condiciones de molienda. Las moléculas de solvente no se expresan pues se consideran como inertes.

A continuación, se muestra una descripción detallada de cada uno de los procesos involucrados en el modelo bajo las condiciones de equilibrio y molienda.

3.1.1 Nucleación primaria

Niinomi *et al.*[124] reportaron una variedad de fenómenos de cristalización obtenidos por la manipulación plasmónica§§§§ de la cristalización quiral del $NaClO_3$. Encontrando una fase monoclínica aquiral ($P2_1/a$) como intermediaria en el proceso de la formación de la fase cúbica quiral ($P2_13$) del $NaClO_3$. Así mismo, observaron una región líquida de alta densidad como precursora de la fase sólida cristalina. De acuerdo a sus observaciones, se consideró que en el modelo la vía de transformación entre las fases aquiral-quiral es transitada en dos pasos. El primero hace referencia a la formación de una región local de alta concentración (Figura 20) y el segundo al desarrollo del núcleo cristalino en dicha región (Figura 21).

En el modelo se asume que, en una solución sobresaturada, el soluto (moléculas o pares iónicos) forma embriones transitorios de vida corta a través de las adiciones bimoleculares como se muestra en los procesos K_{A2} y K_{A4} en la Tabla 3. La especie A representa a las especies aniónicas y catiónicas solvatadas, A2 es un dímero parcialmente desolvatado y A4 hace referencia a la fase líquida de alta densidad observada durante la cristalización de $NaClO_3$ (Figura 20). Los pasos de dimerización han sido truncados hasta K_{A4} para enfatizar que hay 4 moléculas de $NaClO_3$ contenidas en una celda unitaria cúbica del cristal quiral.[125]
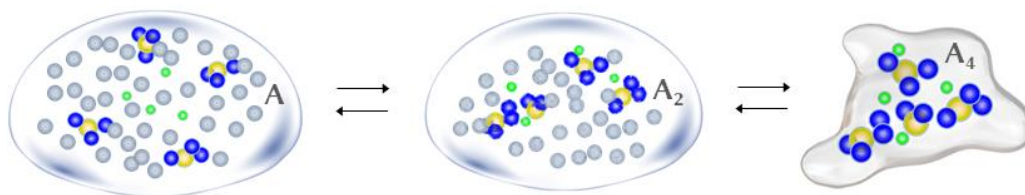
Figura 20. Representación del primer paso de nucleación que corresponde al surgimiento de una región de alta densidad precursora de la fase sólida. A: iones solvatados; A2: dímero parcialmente solvatado; A4: líquido de alta densidad. (amarillo) átomo de cloro; (azul oscuro) átomo de oxígeno; (verde) átomo de sodio; (azul claro) moléculas de agua.

---

§§§§ En la cristalización se refiere a la utilización de campos electromagnéticos generados por oscilaciones colectivas de electrones (plasmones) para influir sobre la orientación y dirección de crecimiento cristalino, control de nucleación, modificación de la velocidad de crecimiento y manipulación de las propiedades cristalinas.

Experimentalmente el líquido de alta densidad es un medio termodinámicamente lábil,[*****] por lo que es transformado rápidamente a la fase cristalina. La fase sólida resultante pertenece al cristal monoclínico aquiral X,[126] este proceso ha sido modelado por el paso K_X en la Tabla 3. Posteriormente esta especie intermediaria es transformada a la forma cúbica quiral ($P2_13$)[123] por medio de un reacomodo de sus átomos (transformación martensítica), indicando que la fase monoclínica es menos estable que la fase cúbica y por lo tanto, el cristal aquiral es una fase metaestable. En la conversión aquiral-quiral, los dos cristales enantioméricos L o D tienen la misma probabilidad de surgir[123,127] (Figura 21). La evolución polimórfica[†††††] ha sido modelada por el paso K_C en la Tabla 1, en donde L (o D, no se muestra) representa el núcleo mínimo quiral que se puede formar. Los cuatro procesos K_{A2}, K_{A4}, K_X y K_C emulan la dependencia de la nucleación primaria con la concentración del soluto.[128] El modelo predice que a valores bajos de sobresaturación, la nucleación es insignificante. Por el contrario, una alta sobresaturación origina la nucleación.[67,129]Además como todos los pasos involucrados son reversibles, los monómeros quirales (L o D) pueden perder su quiralidad.[69]
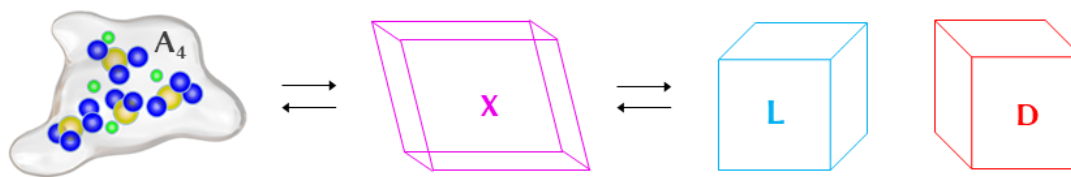
Figura 21. Representación del segundo paso de nucleación que, a través de un proceso reversible el líquido de alta densidad da lugar al primer sólido cristalino, siendo éste un polimorfo metaestable aquiral. Y mediante una transformación martensítica da lugar a la fase cúbica quiral. A4: líquido de alta densidad; X: polimorfo metaestable aquiral; L, D: cristales quirales.

3.1.2 Crecimiento cristalino

Tan pronto como emergen los monómeros quirales comienza la incorporación de unidades elementales a los cristales existentes (Figura 22). Los cristales que se encuentran en exceso catalizan su propia producción, aumentando su tamaño mediante la captura de elementos de la

---

[*****] Sistema o sustancia que es inestable desde un punto de vista termodinámico y que tiende a cambiar o descomponerse en condiciones normales debido a la naturaleza de sus componentes o a las interacciones presentes.

[†††††] Evolución entre distintas estructuras sólidas con la misma composición química, pero con disposiciones espaciales distintas de las moléculas que los componen.

misma quiralidad. Esto a su vez agota la sobresaturación, favoreciéndose la disolución de los cristales de menor tamaño (maduración de Ostwald). Para describir la adición/disociación enantioespecífica de un determinado cristal de la misma quiralidad el modelo utiliza un enfoque Becker-Döring.[118] Es decir, una serie de procesos de la forma: $L + L_n \rightleftharpoons L_{n+1}$ (igual para D) (ver Tabla 3, procesos K_2 a K_6). Por lo tanto, los cristales pueden crecer o fragmentarse por la ganancia o pérdida de una unidad monomérica, reproduciendo el cambio de la distribución en el tamaño de los cristales y el flujo de masa entre ellos.[121] Para que el modelo sea manejable, se ha truncado a 6 el tamaño máximo que un cristal puede alcanzar. A pesar de que este tamaño es minúsculo comparado con el tamaño que puede adquirir un cristal de $NaClO_3$ ($\approx 10^{22}$ unidades), se ha demostrado que un modelo de esta magnitud es suficiente para poder exhibir la ruptura de la simetría quiral.[111,130]Además, se mantiene el balance de masas y también único estado de equilibrio al tomar en cuenta la condición de balance detallado para todos los procesos elementales reversibles.[121] Finalmente, se asume que la distribución de tamaño de los cristales está clasificada en tres categorías, cristales pequeños (n = 1, 2), medianos (n = 3, 4) y grandes (n = 5, 6).[107] Más adelante se demostrará que esta distribución general contiene suficiente información sobre el número y tamaño de los cristales para simular escenarios en los que un cristal de tamaño grande o bien, un mayor número de cristales pueden determinar la lateralidad resultante.[131]
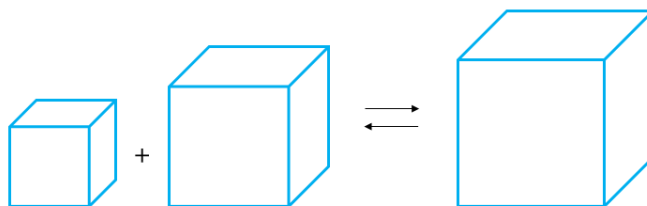
Figura 22. Representación de la adición enantioselectiva de monómeros a los cristales existentes, resultando en un crecimiento cristalino en donde el tamaño máximo que puede alcanzar un cristal es igual a 6.

3.1.3 Disolución

Un ciclo continuo de recristalización-disolución ocurre sobre la superficie de un cristal en un equilibrio sólido-líquido[132] en el que se asume que los cristales pequeños son más propensos a disolverse.[67,133] En el modelo, la disolución de un cristal involucra la pérdida de una unidad quiral, la cual regresará de manera no discriminativa a formar parte de la solución (Figura 23). Como se puede observar en la Tabla 3, la quiralidad de la fase sólida del $NaClO_3$ no se conserva durante este

proceso. Como resultado los compuestos aquirales generados por la disolución son reciclables, por lo que existe la posibilidad de recristalizarse en cualquiera de las dos formas enantioméricas.[64] Cabe destacar que todos los procesos involucrados en esta etapa son totalmente reversibles.[73]
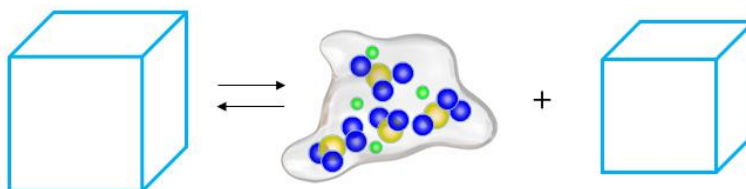
Figura 23. Representación de la disolución de un cristal. El regreso de un monómero a la solución implica la pérdida de su quiralidad, abriendo la posibilidad de recristalizarse en forma de L o D con la misma probabilidad.

En la Tabla 3 se recopila una lista de especies y procesos que se han considerado para la construcción de la nucleación, crecimiento cristalino y disolución en el modelo propuesto.

Tabla 3. Lista de procesos y constantes que describen el modelo propuesto para la nucleación, crecimiento y disolución del clorato de sodio en condiciones de equilibrio. Para simplificar, sólo se muestra la parte de L. A es una representación esquemática del $NaClO_3$. K_{A2} y K_{A4} son dos constantes de equilibrio semi empíricas para la formación de los agregados A2 y A4. En A4 $\rightleftharpoons$ X, la constante de equilibrio K_X hace referencia al fortalecimiento de los enlaces iónicos que dan lugar a la fase metaestable aquiral X. En X $\rightleftharpoons$ L, la transformación martensítica (quiralización de X a L) ha sido descrita por la constante de velocidad k_c y la constante de equilibrio K_C. Para mantener la sencillez, todos los pasos correspondientes a la agregación de L2 a L6 han sido descritos sólo por un factor de frecuencia de encuentro (k) mientras las distintas contantes de equilibrio (K_2 a K_6) obedecen la variación de entalpía libre de acuerdo a la regla de Gibbs-Thomson. La constante de velocidad k_d ha sido utilizada para describir las cinéticas de disolución mientras que las correspondientes constantes de equilibrio han sido calculadas de acuerdo a los requerimientos del balance detallado.

Especies y procesos	Constantes de velocidad de "ida"	Constantes de equilibrio	Velocidades	Comentarios
A + A $\rightleftharpoons$ A2	$k_a \cdot K_{A2}$	K_{A2}	$k_a(K_{A2}[A]^2 - [A2])$	dimerización del líquido denso
A2 + A2 $\rightleftharpoons$ A4	$k_a \cdot K_{A4}$	K_{A4}	$k_a(K_{A4}[A2]^2 - [A4])$	tetramerización del líquido denso
A4 $\rightleftharpoons$ X	$k_a \cdot K_X$	K_X	$k_a(K_X[A4] - [X])$	nucleación de la fase aquiral
X $\rightleftharpoons$ L	$k_c \cdot K_C$	K_C	$k_c(K_C[X] - [L])$	transformación martensítica

$L + L \rightleftharpoons L2$	$k.K_2$	K_2	$k(K_2[L]^2 - [L2])$	dimerización de unidades quirales
$L2 + L \rightleftharpoons L3$	$k \cdot K_3$	K_3	$k(K_3[L][L2] - [L3])$	trimerización de unidades quirales
$L3 + L \rightleftharpoons L4$	$k \cdot K_4$	K_4	$k(K_4[L][L3] - [L4])$	tetramerización de unidades quirales
$L4 + L \rightleftharpoons L5$	$k \cdot K_5$	K_5	$k(K_5[L][L4] - [L5])$	pentamerización de unidades quirales
$L5 + L \rightleftharpoons L6$	$k \cdot K_6$	K_6	$k(K_6[L][L5] - [L6])$	hexamerización de unidades quirales
$L6 \rightleftharpoons L5 + A4$	k_d	$1/(K_X.K_C.K_6)$	$k_d([L6] - (K_X.K_C.K_6)[L5][A4])$	disolución de hexámero
$L5 \rightleftharpoons L4 + A4$	k_d	$1/(K_X.K_C.K_5)$	$k_d([L5] - (K_X.K_C.K_5)[L4][A4])$	disolución de pentámero
$L4 \rightleftharpoons L3 + A4$	k_d	$1/(K_X.K_C.K_4)$	$k_d([L4] - (K_X.K_C.K_4)[L3][A4])$	disolución de tetrámero
$L3 \rightleftharpoons L2 + A4$	k_d	$1/(K_X.K_C.K_3)$	$k_d([L3] - (K_X.K_C.K_3)[L2][A4])$	disolución de trímero
$L2 \rightleftharpoons L + A4$	k_d	$1/(K_X.K_C.K_2)$	$k_d([L2] - (K_X.K_C.K_2)[L][A4])$	disolución de dímero

3.1.4 Molienda

En presencia de esferas de vidrio, los cristales van a colisionar y se van a fragmentar, generando pequeños cristales de la misma lateralidad.[107,108,127,134–136]. Una molienda abrasiva continua imprime energía mecánica al sistema y por consecuencia lo aleja del equilibrio. Por el contrario, si la molienda es detenida, tras un lapso de tiempo largo el sistema regresa a un estado racémico. Por otro lado, la molienda es promotora tanto de la disolución (las pequeñas piezas cristalinas tienden a disolverse con mayor rapidez)[133] como de la tasa de recristalización[65] (las colisiones generan núcleos secundarios que podrían ser futuras semillas).[137,138] En nuestro modelo, la fragmentación de los cristales está descrita por una serie de pasos irreversibles que considera todas las posibles combinatorias de fragmentación que un agregado puede presentar.[139,140] La fractura de los cristales es efectiva en tamaños superiores al tamaño mínimo, por lo que la molienda actúa en agregados que van de L2 a L6 (o D2 a D6). De acuerdo al tamaño de los fragmentos liberados, la molienda se

[30]

clasifica en piezas: grandes + finas o medianas + medianas tal y como se describe en la Figura 24 y Tabla 4. Cabe mencionar que la intensidad de la molienda está relacionada con la frecuencia de rotación del agitador y el número de esferas de vidrio presentes.

molienda fina

molienda media
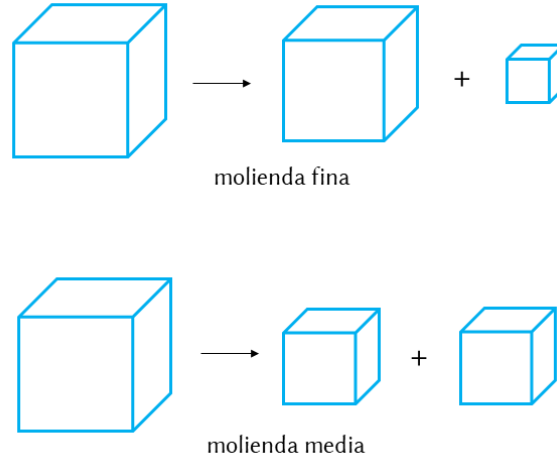
Figura 24. Esquema que ilustra de manera general los dos tipos de molienda a los que están sujetos los cristales del modelo.

La Tabla 4 muestra la lista de las especies y procesos que constituyen a la molienda en el modelo propuesto.

Tabla 4. Lista de procesos y constantes de velocidad que describen el desgaste de los cristales de clorato de sodio bajo una molienda producida por la presencia de esferas de vidrio en el modelo propuesto. Para simplificar, sólo el lado L es mostrado. K_g representa la intensidad de molienda; de h_6 a h_2 denota la sensibilidad a la molienda que tiene cada tamaño cristalino (L6 a L2), mientras que j_1 y j_2 caracterizan la fragmentación por abrasión o fractura.

Especies y procesos	Constantes de velocidad de "ida"	Velocidades	Comentarios
L6 → L5 + L	$k_g.h_6.j_1$	$k_g.h_6.j_1$ [L6]	molienda fina
L6 → L4 + L2	$k_g.h_6.j_2$	$k_g.h_6.j_2$ [L6]	molienda media
L6 → L3 + L3	$k_g.h_6.j_2$	$k_g.h_6.j_2$ [L6]	molienda media
L5 → L4 + L	$k_g.h_5.j_1$	$k_g.h_5.j_1$ [L5]	molienda fina
L5 → L3 + L2	$k_g.h_5.j_2$	$k_g.h_5.j_2$ [L5]	molienda media
L4 → L3 + L	$k_g.h_4.j_1$	$k_g.h_4.j_1$ [L4]	molienda fina
L4 → L2 + L2	$k_g.h_4.j_2$	$k_g.h_4.j_2$ [L4]	molienda media

L3 → L2 + L	$k_g.h_3.j_1$	$k_g.h_3.j_1$ [L3]	molienda fina
L2 → L + L	$k_g.h_2.j_1$	$k_g.h_2.j_1$ [L3]	molienda fina

Tomando en cuenta todos los procesos descritos en las Tablas 3 y 4, se propone un modelo simple y simétrico basado en un enfoque cinético. En donde, las etapas inscritas en la Tabla 3 correspondientes a la nucleación, agregación y disolución comprenden una serie de procesos reversibles definidos por una constante de equilibrio y una constante de relajación. En los que la constante de velocidad directa ha sido escrita como el producto de la constante de velocidad inversa por la constante de equilibrio, por ejemplo, en A + A $\rightleftharpoons$ A2, $K_{A2} = (k_a \cdot K_{A2}) / k_a$, donde $(k_a \cdot K_{A2})$ es una constante directa de primer orden que describe el proceso de nucleación primaria. De esta manera, la constante de velocidad inversa se desempeña como una constante de relajación que determina la velocidad a la cual el equilibrio es alcanzado, además de obedecer de manera estricta el principio de balance detallado.‡‡‡‡‡ De la misma manera, la Tabla 4 describe los procesos irreversibles de abrasión ocurridos durante la molienda en una situación fuera del equilibrio.

Para analizar al sistema dentro y fuera del equilibrio, el modelo ha sido trasladado a un conjunto de 16 ecuaciones diferenciales ordinarias (EDO´s). Que posteriormente fueron sometidas a un cuidadoso análisis de ajuste de curvas basado en un experimento real, permitiendo la obtención de un conjunto de valores realistas de los parámetros del modelo.

3.2 Software, integradores y algoritmos de optimización

Para llevar a cabo el análisis de ajuste de curvas que proporciona un conjunto de valores realistas de los parámetros se utilizaron los programas cinéticos COPASI[141] y Sa.[142]

3.2.1 COPASI

COPASI (COmplex PAthway Simulator) es un software libre creado para el análisis de redes bioquímicas y su dinámica. Para el análisis de ajuste de curvas se emplearon los métodos de

---

‡‡‡‡‡ Principio de la cinética química que relaciona las velocidades de una reacción directa e inversa a un nivel molecular. En el cual la proporción entre las constantes de velocidad debe ser igual a la proporción de las concentraciones de los reactivos y productos al equilibrio: $k_{directa}/ k_{inversa}$ = [A]eq [B]eq / [C]eq [D]eq. En otras palabras, las rutas que siguen las moléculas de los reactivos en la reacción directa son las mismas que siguen las moléculas del producto en la reacción inversa.

optimización de búsqueda aleatoria y Hooke & Jeeves. El primero fue utilizado al inicio del análisis para realizar una búsqueda general sobre "la superficie del paisaje" y posicionarnos en un valle o pozo. Es decir, una función objetivo es evaluada con una serie de combinatorias de valores aleatorios de los parámetros ajustables hasta encontrar el mínimo error residual. Para un número infinito de iteraciones este método garantiza encontrar el óptimo global de la función objetivo. Dado que el número de iteraciones en nuestro análisis es finito, la capacidad de búsqueda es limitada. Por consiguiente, se implementó el método de Hooke & Jeeves partiendo del conjunto de valores obtenidos (posible mínimo local) en la búsqueda aleatoria. Realizando una búsqueda directa del mínimo de una función no lineal sin calcular sus derivadas. En su lugar, éste algoritmo se basa en una heurística que sugiere una dirección descendente utilizando los valores de la función calculada en un número previo de iteraciones. A diferencia de la búsqueda aleatoria éste va llevando un seguimiento de la dirección a medida que el proceso se mueve de un punto a otro, en lugar de empezar desde cero en cada nuevo punto.

3.2.2 Sa

Una vez obtenido el conjunto de valores realistas de nuestro modelo, se procedió al análisis del sistema en el equilibrio y fuera de él. Para ello, se utilizó el programa cinético Sa. Éste es un software libre escrito por D. Lavabre del Laboratoire des Interactions Moléculaires et Réactivité Chimique et Photochimique, Université Paul Sabatier, Francia. El algoritmo general para la integración numérica de las ecuaciones diferenciales está basado en el método Runge-Kutta de cuarto orden. Un efecto notable es que el tamaño del paso de integración automático introduce redondeo aritmético que da lugar a ruido numérico. Para valores específicos de parámetros este ruido numérico es suficiente para llevar a cabo el rompimiento espontáneo de la simetría quiral, es decir, introducir pequeñas fluctuaciones asimétricas que se amplifican por la dinámica autocatalítica.

Capítulo 4.

Resultados

4.1 Parametrización del modelo

Para la parametrización del modelo se seleccionaron los datos reportados por Xiouras *et al.,*[143] ya que muestran la evolución del exceso enantiomérico cristalino del $NaClO_3$ a distintos excesos enantioméricos iniciales (20%, 30%, 40% y 50%) en un sistema de tipo Viedma. Las cuatro curvas fueron sometidas a un ajuste simultáneo, obteniéndose un solo conjunto de parámetros para las distintas condiciones iniciales. Para evitar la sobreparametrización[§§§§§] y cumplir con los requerimientos termodinámicos del crecimiento cristalino y la solubilidad, asumimos que las constantes de equilibrio que van de K_X a K_6 adquieren valores tales que dan forma a un patrón de energía libre que satisface el efecto de Gibbs-Thomson [63] (Tabla 5).

Tabla 5. Valores empíricos de energía libre resultantes de las constantes de equilibrio (K_X a K_6) que fueron mantenidas fijas durante el ajuste de curvas. Los valores negativos corresponden a los pasos endergónicos de la primera nucleación y agregación.

$\dfrac{-\mathbf{G}(K_{A2})}{RT}$	$\dfrac{-\mathbf{G}(K_{A4})}{RT}$	$\dfrac{-\mathbf{G}(K_{X})}{RT}$	$\dfrac{-\mathbf{G}(K_{C})}{RT}$	$\dfrac{-\mathbf{G}(K_{2})}{RT}$	$\dfrac{-\mathbf{G}(K_{3})}{RT}$	$\dfrac{-\mathbf{G}(K_{4})}{RT}$	$\dfrac{-\mathbf{G}(K_{5})}{RT}$	$\dfrac{-\mathbf{G}(K_{6})}{RT}$
-42	90	270	100	-42	800	1800	5000	7000

La teoría clásica de la nucleación considera dos etapas para la formación de un núcleo cristalino: (1) la agrupación de un conjunto de átomos, moléculas o iones que constituyen a un núcleo crítico, y posteriormente (2) el crecimiento de éste núcleo hasta convertirse en un cristal. La nucleación (1) es un proceso endergónico, es decir, requiere de una entrada de energía adicional para formar un

---

[§§§§§] Término utilizado en el contexto de modelado y estadística para referirse a la situación en la que un modelo tiene un número excesivo de parámetros en comparación con los datos disponibles para el ajuste del modelo. Ocasionando que el modelo se adapta en gran medida a los datos disponibles, siendo capaz de reproducir el ruido o fluctuaciones aleatorias presentes en los mismos. Dando como resultado un modelo que no puede generalizar y hacer predicciones precisas con un nuevo conjunto de datos.

núcleo. Ya que la energía liberada por la formación de enlaces dentro de éste es menor con respecto a la energía necesaria para superar la barrera energética impuesta para la formación de nuevos enlaces y la reorganización de las moléculas o iones en solución. Por lo que la energía libre del sistema aumenta durante de esta etapa. Por otro lado, el crecimiento del núcleo crítico (2) es un proceso exergónico. Esto quiere decir que la energía liberada por la formación de enlaces en el núcleo es mayor que la requerida para superar la barrera energética. Causando que, durante este proceso la energía libre del sistema disminuya, lo que indica que el proceso de crecimiento es favorable en términos energéticos. En el modelo, se considera que la especie L2 (o D2) es el tamaño crítico que dará paso a la transición entre los procesos de agregación endergónicos y exergónicos. [144,145] En la Figura 25 se puede observar la curva de energía libre *vs* el tamaño del clúster, sólo los clústeres más grandes que el tamaño crítico tienen la probabilidad de crecer, mientras que los de tamaño menor al crítico presentan una tendencia a la disolución (maduración de Ostwald). [100,109,128,146]
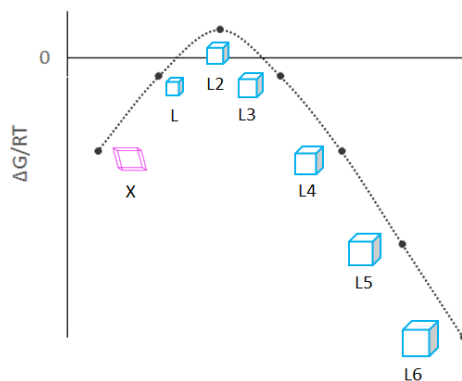
Figura 25. Curva de nucleación clásica que muestra la variación de la energía libre entre el volumen y la superficie vs el tamaño de un clúster en crecimiento, donde, $K_{(X \, a \, 6)}$ = exp (-$\Delta G_{(X \, a \, 6)}$ / RT). L2 representa el tamaño crítico.

Al igual que la constante de equilibrio K_X que hace referencia al fortalecimiento de los enlaces iónicos que dan lugar a la fase metaestable aquiral y las constantes de equilibrio de agregación (K_2-K_6), los valores de las constantes K_{A2}, K_{A4} y K_C que corresponden a la formación de los agregados A2 y A4, y a la quiralización de la fase metaestable aquiral se les asignó un valor fijo. Esto para satisfacer la dependencia que tiene la solubilidad de $NaClO_3$ con la temperatura, lo que significa que la solubilidad de esta sal aumenta significativamente a medida que la temperatura aumenta. De igual

manera, estas condiciones cumplen con la metaestabilidad de la fase líquida de alta densidad (A4) con respecto a la solución diluida.[147]

La Tabla 6 muestra a las constantes de equilibrio cuyos valores fueron mantenidos fijos durante la parametrización con base en datos experimentales.

Tabla 6. Valores de las constantes de equilibrio que permanecieron fijas durante el análisis de ajuste de curvas para poder satisfacer las condiciones de energía libre, solubilidad y metaestabilidad.

K_{A2}	K_{A4}	K_X	K_C	K_2	K_3	K_4	K_5	K_6
0.87	1.35	2.46	1.40	0.87	21	400	1.7e+7	1.2e+10

Para llevar a cabo el ajuste de curvas, se consideró que al inicio el único material presente corresponde al clorato de sodio solubilizado (A_0) y a una mezcla de cristales L6 y D6 con su respectivo exceso enantiomérico (Tabla 7). Siendo la cantidad inicial de cada especie calculada con base en el protocolo experimental de Xiouras.[143]

Tabla 7. Condiciones iniciales utilizadas para el análisis de ajuste de curvas. $[A]_0 = 13$.

Experimento	*Cee* inicial (%)	L6	D6
1	20	7.62e-2	1.16e-1
2	30	6.77e-2	1.23e-1
3	40	5.98e-2	1.49e-1
4	50	4.95e-2	1.52e-1

Una vez establecidas las condiciones iniciales, los valores de los parámetros k_a, k_c, k, k_d, k_g, j_1 y j_2 fueron sometidos al ajuste de curvas, permitiendo que sus valores fluctuaran en cada una de las ejecuciones del análisis. El resultado final se ve reflejado en la Figura 26 y la Tabla 8.
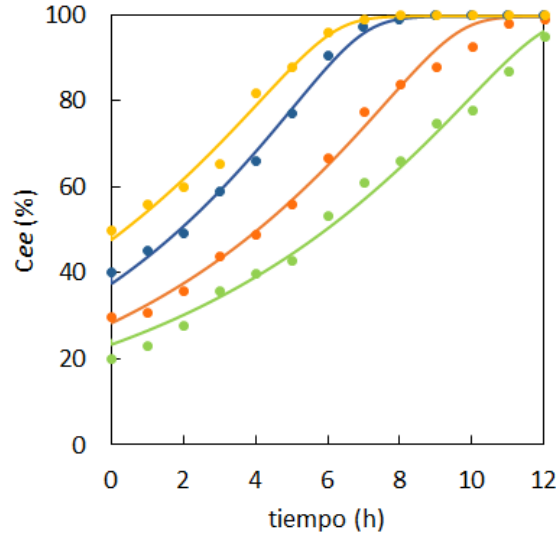
Figura 26. Modelado cinético que muestra la evolución del exceso enantiomérico cristalino en una serie de experimentos de desracemización de $NaClO_3$ iniciando de distintos excesos enantioméricos cristalinos iniciales (líneas sólidas). Datos experimentales extraídos de la ref. 142. Líneas sólidas: simulación numérica del modelo. Curva verde $Cee_0 = 20\%$, curva naranja $Cee_0 = 30\%$, curva azul $Cee_0 = 40\%$ y curva amarilla $Cee_0 = 50\%$.

Tabla 8. Conjunto de parámetros obtenidos mediante el análisis de ajuste de curvas que mostraron un menor error residual.

k_a	k_c	k	k_d	k_g	j_1	j_2
8.6e-2	25.8	0.24	1.24e-3	1.54e-2	0.96	0.78

Puesto que algunos de los parámetros son empíricos, ninguno de los presentes en la Tabla 8 puede ser discutido de manera independiente. Para explorar las principales características del modelo y evaluar su habilidad para reproducir el comportamiento general de una suspensión de clorato de sodio en reposo y bajo condiciones de desracemización se llevó a cabo un análisis dinámico tanto en condiciones de equilibrio (sin agitación) como fuera de éste (con agitación). Asumiendo que los 6 tamaños de clústeres (de L-L6 o D-D6) considerados en el modelo representan una distribución real de los tamaños de los cristales.

[37]

4.2 Análisis dinámico del modelo

4.2.1 Simulaciones en condiciones de equilibrio

El conjunto de 16 EDO´s que componen al modelo fue integrado con una molienda igual a cero hasta que el sistema alcanzó una situación de equilibrio. La saturación del medio se reprodujo mediante la variación de la cantidad inicial de clústeres grandes ($[L6]_0$ y $[D6]_0$) presentes en agua pura. La Figura 27a pone en evidencia que, si la cantidad de clústeres es muy baja, éstos se disuelven en su totalidad. Caso contrario, cuando la cantidad de clústeres $[L6]_0$ y $[D6]_0$ aumenta hay un punto de inflexión en donde la cantidad de $[A]$ es suficiente para saturar, manifestándose la solubilidad máxima del soluto. Sin embargo, este punto de inflexión no es completamente plano ya que la región de saturación aumenta ligeramente. Es posible que este resultado se deba al número limitado de clústeres considerados en el modelo. La Figura 27b muestra que a medida que la sobresaturación aumenta, los clústeres subcríticos (tamaño n = 1, L o D) se van transformando progresivamente a clústeres supercríticos (tamaño = 6, L6 o D6).
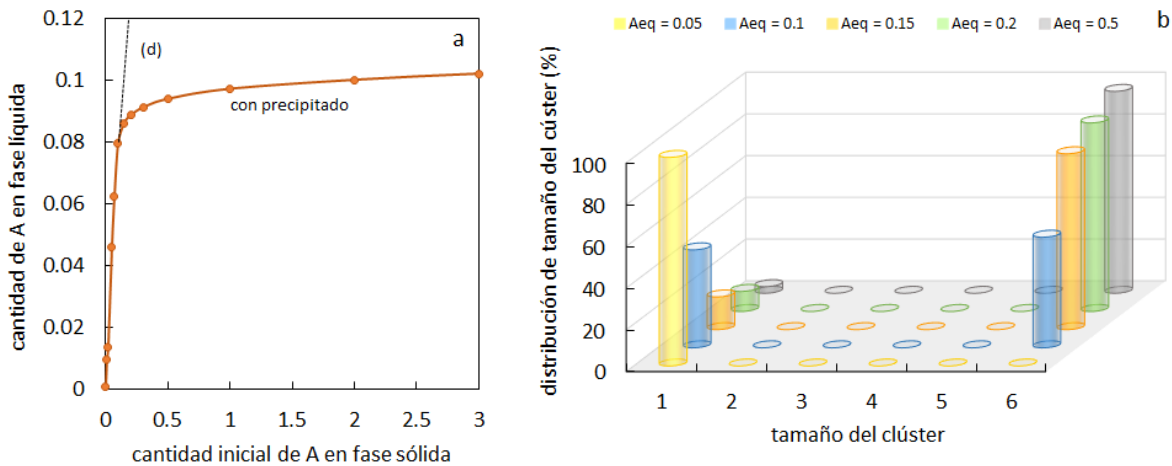
Figura 27. a: Variación de la cantidad de A en fase líquida (Aeq) vs la cantidad inicial de A en fase sólida. La diagonal (d) indica la región en la cual toda la fase sólida está solubilizada; la "solubilidad" del soluto se encuentra entre 0.5 y 0.05 unidades arbitrarias. Más allá de este punto, la fase sólida se presenta como precipitado. **b:** Distribución relativa del tamaño del clúster alrededor del punto de inflexión, mostrando el intercambio que se presenta en función del incremento de la cantidad inicial de A en fase sólida entre los clústeres subcríticos (L o D) y los supercríticos (L6 y D6). Los valores de los parámetros utilizados en estas simulaciones son los mismos de la Figura 26, a excepción de k_g (la intensidad de la molienda) que es igual a cero.

El modelo es capaz de representar un equilibrio sólido-líquido. La cantidad de soluto en solución no depende de la historia del sistema, siempre y cuando las condiciones iniciales y la temperatura se mantengan. En la Figura 28a se considera que en una solución saturada caliente de $NaClO_3$ que es enfriada rápidamente a una temperatura de 30°C hasta alcanzar la precipitación, es posible identificar la nucleación (N), el crecimiento de los cristales pequeños L y D (CG), la disolución de las especies cristalinas de menor tamaño a expensas del crecimiento de los cristales más grandes L6 y D6 (maduración de Ostwald (OR)) y el equilibrio (EQ). La Figura 28b exhibe una situación inversa, o sea, la disolución parcial de la misma cantidad de $NaClO_3$ en forma de los cristales L6 y D6 en el mismo volumen de agua pura a 30°C. En ambos escenarios se alcanzan los mismos valores al equilibrio.
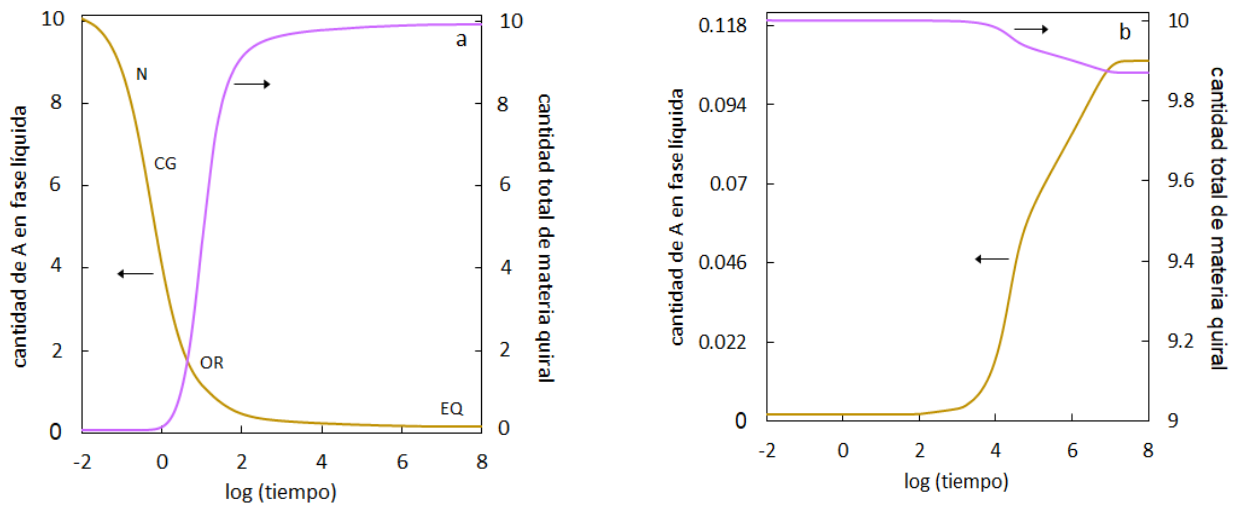
Figura 28. a: Simulación de la precipitación después de haber enfriado la solución. $[A]_0$ = 10 (curva verde); cantidad de materia quiral = 0 (curva violeta). **b:** Disolución de los cristales en agua pura. $[A]_0$ = 0 (curva verde): $[L6]_0$ = $[D6]_0$ = 10/48 (en unidades de A); el resto Ln = Dn = 0. Los valores al equilibrio de $[A]_{eq}$ = 0.11; $[L6 + D6]_{eq}$ = 9.87 son iguales en ambos escenarios. Las flechas pequeñas indican la escala a la cual pertenece la variable. Los valores utilizados para efectuar estas simulaciones son los mismos de la Figura 26, a excepción de k_g = 0.

Cabe destacar que en la Figura 28a la evolución de toda la materia quiral tiene una forma sigmoidal. Lo cual es congruente con los perfiles de tipo autocatalíticos observados en distintas situaciones de crecimiento de cristales.[148,149] Estos resultados demuestran que el modelo es capaz de imitar satisfactoriamente el comportamiento de cristalización y disolución del soluto en solución.

4.2.2 Simulaciones en condiciones fuera del equilibrio (Desracemización de Viedma)

4.2.2.1 Efecto del Cee_0 en la evolución del Cee.

Bajo condiciones de molienda el modelo da como resultado la ruptura de la simetría. Lo que quiere decir que en ausencia de una fuerza quiral externa la proporción "simétrica" de los cristales enantioméricos evoluciona a un estado enantioméricamente puro, en donde una de las dos formas enantioméricas desaparece de manera aleatoria. En la desracemización de Viedma el sistema se encuentra alejado del equilibrio, por lo que un racemato se considera inestable y evoluciona hacia uno de los estados quirales energéticamente idénticos. En el que la lateralidad resultante es consecuencia de un pequeño imbalance estocástico ocasionado por fluctuaciones estadísticas. Esta ruptura de la simetría es una clara manifestación de la teoría de bifurcación, la cual establece que un cambio en la estabilidad del punto de equilibrio existente (en este caso el racemato) conduce a un cambio drástico en el comportamiento del sistema. La trayectoria que sigue el sistema se ilustra mediante un diagrama de fase, la ruptura espontánea de la simetría quiral está descrita por un diagrama de fase de tipo *pitchfork* (Figura 29).
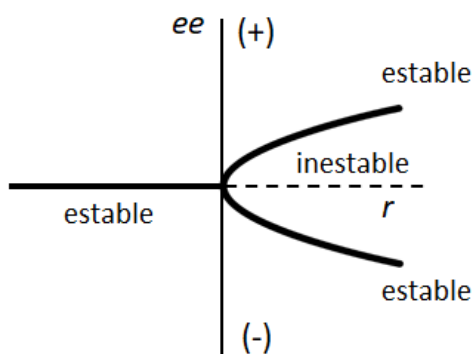
Figura 29. Diagrama de bifurcación de tipo pitchfork que inicia en un estado estable (racemato) y se dirige hacia las ramas que conducen a los dos estados estables (L o D) en ausencia de un sesgo quiral. *r*: distancia del equilibrio.

La Figura 30 muestra la evolución del Cee de una suspensión de $NaClO_3$ bajo condiciones de molienda para distintos y muy bajos Cee_0. Como se puede observar entre más alto es el Cee_0, más rápida es la desracemización.[103] Por ejemplo, un incremento exponencial del Cee_0 (de 1e-5 a 1e-2) conduce a un decremento lineal del tiempo de desracemización.[102] Por otro lado, el comportamiento estocástico con un Cee_0 = 0 se debe al ruido numérico generado por el redondeo del integrador semi

implícito Runge-Kutta de 4° orden empleado. Este resultado nos recuerda a la alta sensibilidad de las condiciones iniciales que han sido reportadas en algunos experimentos.[89,150]
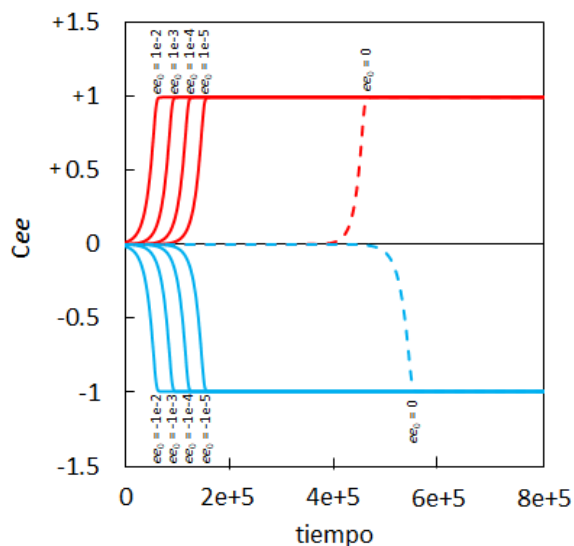
Figura 30. Efecto del exceso enantiomérico cristalino inicial (*Cee₀*) en la evolución del *Cee* en una serie de simulaciones de desracemización de $NaClO_3$. Para el *Cee₀* = 0 se aprecia la ruptura espontánea de la simetría y el comportamiento estocástico con respecto al tiempo de desracemización y la lateralidad final. Los valores de los parámetros son los mismos de la Figura 18, excepto: $[L6]_0$ = 7e-2 − ε y $[D6]_0$ = 7e-2 + con ε = ± 6.86e-2 para el *Cee₀* = ± 1e-2, ε = ± 6.986e-2 para el *Cee₀* = ± 1e-3, ε = ±6.999e-2 para el *Cee₀* = ±1e-4, ε = 6.99986e-2 para el *Cee₀* = ±1e-5 y ε = 0 para *Cee₀* = 0.

Un aspecto destacable del modelo es que con los mismos parámetros con los que se reproduce el experimento real es posible obtener ruptura de la simetría a partir de condiciones racémicas. Tal situación es completamente distinta a los modelos publicados anteriormente, ya que éstos utilizan parámetros seleccionados con ese propósito. Cuando el *Cee₀* = 0, la desracemización ocurre de manera sistémica, no obstante, tal y como se observa en la Figura 30 la lateralidad resultante no puede ser predicha.

4.2.2.2 Efecto de la intensidad de molienda.

El modelo exhibe cierta sensibilidad a la intensidad de molienda de los cristales, siendo un factor determinante para que la desracemización sea exitosa. La Figura 31 muestra una ventana con los valores de la intensidad de molienda que son efectivos para obtener la ruptura de la simetría.
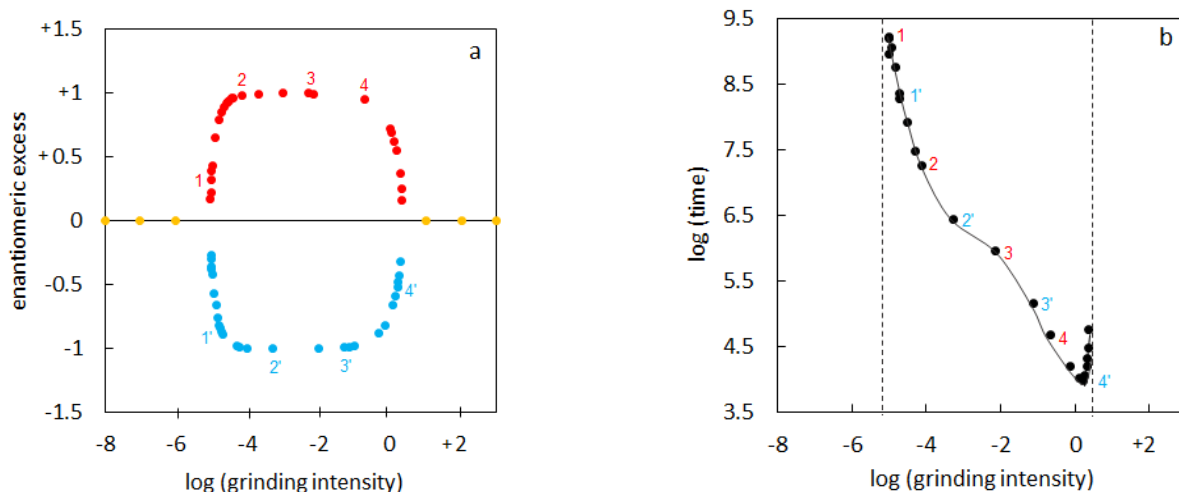
Figura 31. a: Simulación numérica de la ruptura espontánea de la simetría en la desracemización de cristales de NaClO$_3$ bajo diversas intensidades de molienda (Cee_0 = 0). **b:** Tiempo necesario para alcanzar un exceso enantiomérico cristalino del 90% en función de la intensidad de molienda. Los valores de los parámetros son los mismos que los utilizados en la Figura 26, a excepción de [A]$_0$ =10, [L6]$_0$ = [D6]$_0$ = 7e-2.

De acuerdo a Saito *et al.*[151] la maduración de Ostwald sin molienda es extremadamente lenta para seleccionar la quiralidad (si es que es posible). En el modelo la racemización en solución previene la desracemización. Esta situación claramente está retratada en la región izquierda de la Figura 31a, en donde la intensidad de la molienda es baja y la desracemización no va a ocurrir. Por el contrario, si la intensidad de molienda es suficiente o moderada, la desracemización va a tener lugar. La Figura 31b muestra que el tiempo de desracemización disminuye al incrementarse la intensidad de la molienda,[146] existiendo un valor óptimo después del cual no hay más ganancias. Al aplicar una intensidad de molienda alta se produce una fractura de los cristales muy rápida, lo que conduce a una reducción significativa del tamaño medio de los cristales ya que la abrasión destruye a los de mayor tamaño. Mientras la distribución del tamaño de los cristales se vuelve más estrecha, los gradientes de solubilidad inducidos por el tamaño se desvanecen, de tal manera que el sistema permanece racémico. Estos resultados pueden interpretarse desde un punto de vista experimental con referencia en los sistemas que son sometidos a una molienda por ultrasonido. En éstos, el aumento del exceso enantiomérico se ve obstaculizado después de tiempos prolongados de ultrasonificación.[77,135,140]Además, los resultados obtenidos coinciden con los obtenidos por Mazzotti *et al.* al utilizar ecuaciones de balance poblacional. Mediante las tendencias observadas se puede predecir que la aplicación de una agitación fuerte puede ser perjudicial en términos del rendimiento

del proceso.[152] Finalmente, el modelo predice la existencia de un escenario de bifurcación con dos intensidades de molienda críticas dentro de las cuales se produce la desracemización.

4.2.2.3 Efecto de la intensidad de molienda sobre la distribución del tamaño de los cristales.

A pesar de que el modelo considera una distribución total de seis tamaños distintos de agregados, las simulaciones muestran el efecto que tiene la intensidad de la molienda sobre la cantidad de agregados pequeños y grandes presentes durante la desracemización.

Con una intensidad baja de molienda, el sistema se encuentra cerca del equilibrio y por lo tanto en un estado racémico, y los enantiomorfos están presentes en la forma L6/D6 (ver Figura 32a y b, fila 1e-6 y 1.2e-5). A medida que la intensidad de la molienda aumenta la desracemización ocurre por un fenómeno de ruptura de la simetría quiral, en el cual el enantiomorfo que se encuentra en una mayor proporción está en la forma n = 6, 3 y 2 (ver Figura 32a, fila 7e-3). Por su parte los clústeres L o D más pequeños dominan la población del enantiómero minoritario (ver Figura 32b, fila 7e-3). Si de nueva cuenta la intensidad de la molienda es aumentada, los clústeres más grandes se van a fracturar en pequeñas piezas, dando lugar a la ampliación de la distribución de los tamaños del enantiomorfo mayoritario (ver Figura 32a, fila 2.1). Un incremento aún mayor de la intensidad de la molienda va a provocar que las distribuciones de tamaño sean idénticas en ambas poblaciones, presentándose en clústeres pequeños L o D. En este punto la desracemización se pierde y el sistema regresa a un estado racémico (ver Figura 32a y b, fila 10). La pérdida de la desracemización a intensidades altas de molienda es originada por la presencia de cristales pequeños de tamaños similares que dan lugar a gradientes de solubilidad muy pequeños. Estos resultados coinciden con lo reportado por Ahn *et al.* quienes encontraron que el tamaño del cristal del enantiómero minoritario decrece bajo un flujo suficientemente turbulento.[78]
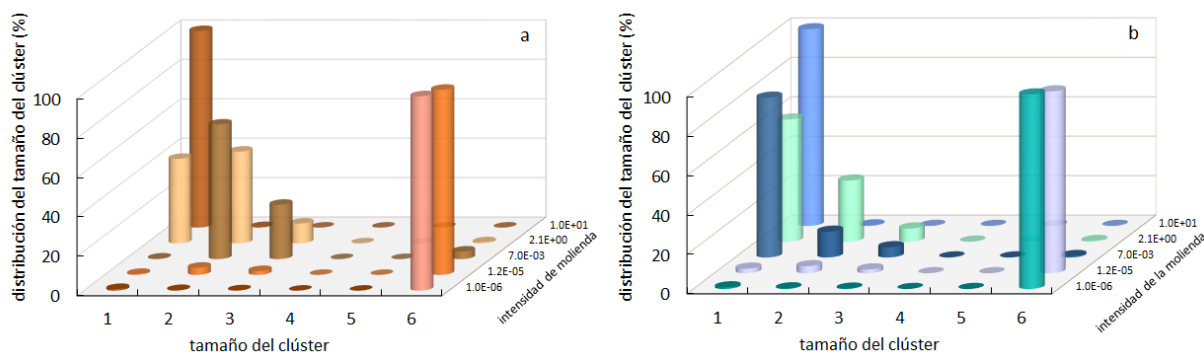
Figura 32. Efecto de la intensidad de molienda en la distribución del tamaño del cristal. a: enantiómero mayoritario; b: enantiómero minoritario.

4.2.2.4 Efecto de la cantidad inicial de cristales enantioméricos sobre la lateralidad final.

Otra característica importante a mencionar es la influencia que tiene la cantidad inicial de materia quiral sobre la bifurcación. Mostrando que los cristales de mayor tamaño son los que imponen la dirección de la evolución del sistema. La Figura 33 expone la competencia que existe entre los cristales pequeños (L2) y los cristales grandes (D4).
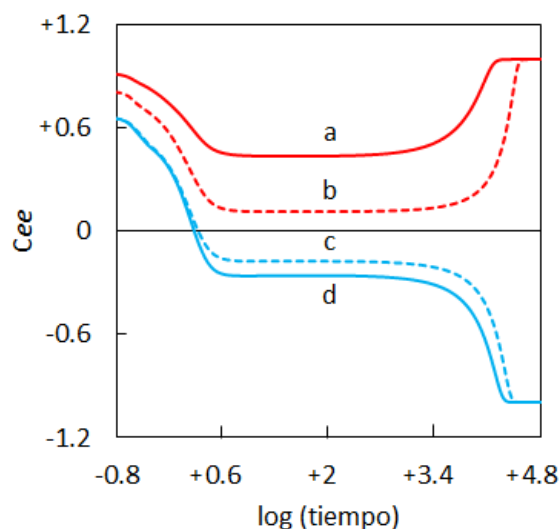
Figura 33. Simulación de la competencia entre los cristales más grandes y más pequeños como aditivos iniciales. Los valores de los parámetros son los mismos de la Figura 18, con excepción de $[A]_0 = 10$ y **a:** $[D2]_0 = 0.5$, $[L4]_0 = 0.01$; **b:** $[D2]_0 = 0.4$, $[L4]_0 = 0.02$; **c:** $[D2]_0 = 0.3$, $[L4]_0 = 0.03$; **d:** $[D2]_0 = 0.2$, $[L4]_0 = 0.02$, el resto de los cristales a 0.

En las curvas c y d el efecto que existe entre la competencia de cristales grandes (L4) *vs* los cristales pequeños (D2) es tan fuerte que la evolución hacía la forma L ocurre a pesar de que la cantidad de L4 es menos de 10 veces la cantidad de D2. Para contrarrestar el efecto que tiene L4, es decir, para dirigir al sistema hacía la forma D, es necesario aumentar D2 hasta una proporción cercana a 20 veces la cantidad de L4 (curvas a y b). Este efecto es el resultado de dos procesos antagonistas: la solubilidad y la fractura. La combinación de ambos procesos determina la lateralidad resultante. Pese a que las simulaciones únicamente consideran a los cristales L2 y D4, los resultados obtenidos son consistentes con la desracemización de un derivado de imina que fue llevada a cabo utilizando mezclas R y S con distintas distribuciones del tamaño del cristal.[131] El enantiómero minoritario gana si su tamaño es mayor. De la misma manera, el cristal más pequeño gana si es el enantiómero mayoritario. Recapitulando, en las simulaciones el enantiómero minoritario L4 gana porque tiene el tamaño más grande (curvas c y d) e igualmente el cristal D2 cuyo tamaño es menor gana si se encuentra en cantidad suficientemente alta (curvas a y b).

4.3 Dilucidando la desracemización

La continua molienda que actúa sobre el sistema de Viedma lo mantiene en un estado fuera del equilibrio termodinámico, generando la competencia entre los dos enantiomorfos que concluirá en la extinción de una las dos poblaciones. Durante este proceso, el principio de microrreversibilidad es violado por la existencia de un flujo neto dentro de los ciclos. La presencia de estos flujos unidireccionales desencadena los efectos de una autocatálisis de orden superior que se encuentra escondida en la red cinética. Cuando la molienda está activa, las especies monoméricas L/D son producidas por distintas vías junto con cristales de mayor tamaño (n= 2 a 5). La gran cantidad de monómeros L/D desplaza a los procesos de agregación reversibles hacía el curso directo de agregación. Por ejemplo, al considerar la primera fila de la Tabla 9, se tiene que los procesos unidireccionales que están ocurriendo son: $L + L5 \rightarrow L6$ con $L + L \rightarrow L2$, luego $L + L2 \rightarrow L3$, luego $L + L3 \rightarrow L4$, luego $L + L4 \rightarrow L5$, luego $L + L5 \rightarrow L6$ cuyo balance de masa global incluye a la agregación ($L + L5 \rightarrow L6$) y a la molienda ($L6 \rightarrow L5 + L$) se expresa como $L6 + 6L \rightarrow 2L6$, resultando en una autocatálisis de orden 6 en L. De manera general, los efectos derivados del acoplamiento de la agregación y la molienda, dan lugar a una autocatálisis de orden ≥ 2 de la forma $Ln + nL \rightarrow 2Ln$ (n = 2 a 6) que sostiene la amplificación asimétrica sin el requisito de interacciones heteroquirales

como, por ejemplo, la inhibición mutua presente en el modelo de Frank. La completa desracemización está asegurada por el crecimiento continuo del enantiómero mayoritario (aquí L) a expensas del enantiómero minoritario (aquí D) a través del puente de comunicación de racemización, $L \leftrightharpoons X \leftrightharpoons D$, que ocurre dentro de la solución (Figura 19). El enantiómero que es más capaz de producir una mayor cantidad de monómeros bajo condiciones de molienda, será más eficiente y resultará como ganador. Si las distribuciones de tamaño son parecidas entre sí, el ganador será aquél que al inicio esté presente en una mayor cantidad. Pero si las distribuciones son distintas, el ganador será aquél que produzca una mayor cantidad de monómeros. Puede ser el enantiómero minoritario si su distribución de tamaños es lo suficientemente grande, ya que lo haría más sensible a la molienda como en la Figura 33. Cabe recordar que estos flujos netos responsables de los efectos autocatalíticos no existen en una situación de equilibrio cuando el principio de microrreversibilidad es respetado sin ningún flujo unidireccional.

Tabla 9. La fractura de los cristales por molienda y el flujo de agregación de monómeros L a las especies que van de L a L5 en condiciones fuera del equilibrio, revelan diversos balances globales con una autocatálisis de orden mayor. Esta misma situación ocurre para el enantiómero D.

Molienda	Agregación de la adición de L (flujo neto)		Balance global
L6 → L5 + L	L + L5 → L6	L + L → L2	L6 + 6L → 2L6
		L + L2 → L3	
		L + L3 → L4	
		L + L4 → L5	
		L + L5 → L6	
L6 → L4 + L2	L + L4 → L5	L + L2 → L3	L6 + 6L → 2L6
	L + L5 → L6	L + L3 → L4	
		L + L4 → L5	
		L + L5 → L6	
L6 → L3 + L3	L + L3 → L4	L + L3 → L4	L6 + 6L → 2L6
	L + L4 → L5	L + L4 → L5	
	L + L5 → L6	L + L5 → L6	
L5 → L3 + L2	L + L3 → L4	L + L2 → L3	L5 + 5L → 2L5
	L + L4 → L5	L + L3 → L4	

		$L + L4 \rightarrow L5$	
$L5 \rightarrow L4 + L$	$L + L4 \rightarrow L5$	$L + L \rightarrow L2$ $L + L2 \rightarrow L3$ $L + L3 \rightarrow L4$ $L + L4 \rightarrow L5$	$L5 + 5L \rightarrow 2L5$
$L4 \rightarrow L2 + L2$	$L + L2 \rightarrow L3$ $L + L3 \rightarrow L4$	$L + L2 \rightarrow L3$ $L + L3 \rightarrow L4$	$L4 + 4L \rightarrow 2L4$
$L4 \rightarrow L3 + L$	$L + L3 \rightarrow L4$	$L + L \rightarrow L2$ $L + L2 \rightarrow L3$ $L + L3 \rightarrow L4$	$L4 + 4L \rightarrow 2L4$
$L3 \rightarrow L2 + L$	$L + L2 \rightarrow L3$	$L + L \rightarrow L2$ $L + L2 \rightarrow L3$	$L3 + 3L \rightarrow 2L3$
$L2 \rightarrow L + L$	$L + L \rightarrow L2$	$L + L \rightarrow L2$	$L2 + 2L \rightarrow 2L2$

Capítulo 5.

Conclusiones

El proyecto desarrollado durante el doctorado consistió en la propuesta de un modelo capaz de describir el mecanismo mediante el cual opera la desracemización de cristales de clorato de sodio propuesta por C. Viedma. Este sistema fue abordado mediante una visión cinética en el que se utilizó un enfoque Becker-Döring microreversible truncado (es decir, una serie de procesos de la forma L + L$_n$ $\rightleftharpoons$ L$_n$+1, con un $n_{máx.}$ = 5). El modelo está compuesto por cuatro etapas, nucleación, agregación, disolución y molienda, a excepción de la molienda que es un proceso irreversible, el resto de las etapas son reversibles. La fase sólida aquiral del NaClO$_3$ está representada por la especie X que por medio de una transformación martensítica racemiza a las formas cúbicas quirales L y D. La nucleación secundaria fue incorporada, asumiendo que los clústeres amorfos de alta densidad denominados como A4 cristalizan por contacto cristalino. La solubilidad es dependiente del tamaño cristalino y está basada en la regla de Gibbs-Thomson.

Para la parametrización del modelo, se tomó en consideración una serie de experimentos de desracemización con el que se pudo efectuar un ajuste de curvas de la evolución en tiempo del *Cee* con resultados muy precisos. En una situación de equilibrio, es decir, sin la molienda activa, es posible obtener las distribuciones finales de los tamaños de los cristales en función del grado de saturación de la solución. Así mismo, el modelo es capaz de imitar el equilibrio sólido-líquido a través de la simulación de situaciones de precipitación y disolución, encontrándose que en ambas se alcanza el equilibrio con los mismos valores. Durante el proceso fue posible identificar a la nucleación, crecimiento de los cristales, maduración de Ostwald y el equilibrio.

Utilizando el mismo conjunto de parámetros, y con la molienda activa, el modelo exhibe una ruptura espontánea de la simetría quiral. En la que la lateralidad resultante en cada una de las simulaciones con un *Cee$_0$* = 0 fue obtenida de manera aleatoria, sin embargo, el sistema se torna determinista con la inclusión de C*ee$_0$* muy pequeño. Al igual que la lateralidad final, en condiciones racémicas

perfectas, el tiempo de desracemización es aleatorio. Por el contrario, se observa una tendencia cuando se incluye un ee_0, siendo el tiempo de desracemización dependiente de su magnitud. Esto quiere decir que el aumento del Cee_0 va a repercutir en una disminución del tiempo de desracemización.

Una característica original del modelo es que con el mismo conjunto de parámetros puede manifestar ruptura de la simetría quiral y reproducir un experimento real de desracemización. Otro hallazgo original es la presencia de una ventana de bifurcación que está dada en términos de la intensidad de la molienda. Si la molienda es demasiado baja o alta, la desracemización no va a ocurrir pues la diferencia en la forma de la distribución de tamaño cristalino desaparece y la ruptura de la simetría ya no es sostenible. Por lo que, una ventana de intensidad moderada, delimitada por dos intensidades críticas, es adecuada para que el sistema pueda desracemizar. Al iniciar con distintos Cee_0 se encontró un umbral que separa las condiciones en las que la desracemización evoluciona hacía los cristales L o D dependiendo de su respectiva cantidad y distribución de tamaño.

El modelo propuesto puede servir como una guía útil para el químico experimental porque ayuda a entender que la ruptura espontánea de la simetría quiral es el resultado de una autocatálisis culta de orden superior que es revelada bajo condiciones fuera del equilibrio. Así mismo, se han identificado más de 1800 especies quirales capaces de cristalizar en conglomerados,[153] por lo que se puede concluir que hay una abundante cantidad de situaciones en las que la desracemización de Viedma pudiera ser una forma viable hacia nuevos auxiliares quirales. Finalmente, el presente estudio contribuye a la discusión sobre el mecanismo que opera en la desracemización de Viedma. Destacándose su sencillez y manejabilidad comparada con los modelos teóricos previamente reportados. Ya que presenta el mismo enfoque cinético para imitar situaciones dentro y fuera del equilibrio.

Bibliografía

(1)   Fischer, E. Synthese Der Mannose Und Lävulose. *Berichte der Dtsch. Chem. Gesellschaft* **1890**, *23* (1), 370–394. https://doi.org/10.1002/cber.18900230162.

(2)   Fischer, E. Über Die Bezeichnung von Optischen Antipoden Durch Die Buchstaben d Und L. *Chem.Ber.* **1907**, *40*, 102–106.

(3)   Cahn, R. S.; Ingold, C. K. 131. Specification of Configuration about Quadricovalent Asymmetric Atoms. *J. Chem. Soc.* **1951**, 612. https://doi.org/10.1039/jr9510000612.

(4)   Cahn, R. S.; Ingold, C. K.; Prelog, V. The Specification of Asymmetric Configuration in Organic Chemistry. *Experientia* **1956**, *12* (3), 81–94. https://doi.org/10.1007/BF02157171.

(5)   Meierhenrich, U. *Amino Acids and the Asymmetry of Life Advances in Astrobiology and Biogeophysics*; 2008.

(6)   Pavlov, V.; Klabunovskii, E. Homochirality Origin in Nature: Possible Versions. *Curr. Org. Chem.* **2013**, *18* (1), 93–114. https://doi.org/10.2174/13852728113179990033.

(7)   Gol'danskiĭ, V. I.; Kuz'min, V. V. Spontaneous Breaking of Mirror Symmetry in Nature and the Origin of Life. *Sov. Phys. - Uspekhi* **1989**, *32* (1), 1–29. https://doi.org/10.1070/PU1989v032n01ABEH002674.

(8)   Podlech, J. Origin of Organic Molecules and Biomolecular Homochirality. *Cell. Mol. Life Sci.* **2001**, *58* (1), 44–60. https://doi.org/10.1007/PL00000777.

(9)   Cronin, J.; Reisse, J. Chirality and the Origin of Homochirality. **2005**, No. i, 473–515. https://doi.org/10.1007/10913406_14.

(10)   Takahashi, J.; Kobayashi, K. Origin of Terrestrial Bioorganic Homochirality and Symmetry Breaking in the Universe. *Symmetry (Basel).* **2019**, *11* (7), 919. https://doi.org/10.3390/sym11070919.

(11)   Evans, A. C.; Meinert, C.; Giri, C.; Goesmann, F.; Meierhenrich, U. J. Chirality, Photochemistry and the Detection of Amino Acids in Interstellar Ice Analogues and Comets. *Chem. Soc. Rev.* **2012**, *41* (16), 5447–5458. https://doi.org/10.1039/c2cs35051c.

(12)   Pizzarello, S.; Cronin, J. R. Alanine Enantiomers in the Murchison Meteorite [7]. *Nature* **1998**, *394* (6690), 236. https://doi.org/10.1038/28306.

(13)   Bonner, W. A. Terrestrial and Extraterrestrial Sources of Molecular Homochirality. *Orig. Life Evol. Biosph.* **1991**, *21* (5–6), 407–420. https://doi.org/10.1007/BF01808311.

(14)   Guijarro, A.; Yus, M. *The Origin of Chirality in the Molecules of Life*; Royal Society of Chemistry: Cambridge, 2008. https://doi.org/10.1039/9781847558756.

(15)   Siegel, J. S. Homochiral Imperative of Molecular Evolution. *Chirality* **1998**, *10* (1–2), 24–27. https://doi.org/10.1002/chir.5.

(16)   Sallembien, Q.; Bouteiller, L.; Crassous, J.; Raynal, M. Possible Chemical and Physical Scenarios towards Biological Homochirality. *Chem. Soc. Rev.* **2022**, *51* (9), 3436–3476. https://doi.org/10.1039/D1CS01179K.

(17)   Keszthelyi, L. Origin of the Homochirality of Biomolecules. *Q. Rev. Biophys.* **1995**, *28* (4), 473–507. https://doi.org/10.1017/S0033583500003309.

(18)   Breslow, R. The Origin of Homochirality in Amino Acids and Sugars on Prebiotic Earth. *Tetrahedron Lett.* **2011**, *52* (32), 4228–4232. https://doi.org/10.1016/j.tetlet.2011.06.002.

(19)   Rikken, G. L. J. A.; Raupach, E. Enantiosleective Magnetochiral Photochemistry. *Nature* **2000**, *405*, 932–935.

(20)   Banerjee-Ghosh, K.; Ben Dor, O.; Tassinari, F.; Capua, E.; Yochelis, S.; Capua, A.; Yang, S.-H.; Parkin, S. S. P.; Sarkar, S.; Kronik, L.; Baczewski, L. T.; Naaman, R.; Paltiel, Y. Separation of Enantiomers by Their Enantiospecific Interaction with Achiral Magnetic Substrates. *Science (80-.).* **2018**, *360* (6395), 1331–1334. https://doi.org/10.1126/science.aar4265.

(21)   Ulbricht, T. L. V.; Vester, F. Attempts to Induce Optical Activity with Polarized β-Radiation. *Tetrahedron* **1962**, *18* (5), 629–637. https://doi.org/10.1016/S0040-4020(01)92714-0.

(22)   Wu, C. S.; Ambler, E.; Hayward, R. W.; Hoppes, D. D.; Hudson, R. P. Experimental Test of Parity Conservation in Beta Decay. *Phys. Rev.* **1957**, *105* (4), 1413–1415. https://doi.org/10.1103/PhysRev.105.1413.

(23)   Meinert, C.; Filippi, J.-J.; Nahon, L.; Hoffmann, S. V.; D'Hendecourt, L.; De Marcellus, P.; Bredehöft, J. H.; Thiemann, W. H.-P.; Meierhenrich, U. J. Photochirogenesis: Photochemical Models on the Origin of Biomolecular Homochirality. *Symmetry (Basel).* **2010**, *2* (2), 1055–1080. https://doi.org/10.3390/sym2021055.

(24)   Ribó, J. M.; Crusats, J.; Sagués, F.; Claret, J.; Rubires, R. Chiral Sign Induction by Vortices during the Formation of Mesophases in Stirred Solutions. *Science (80-.).* **2001**, *292* (5524), 2063–2066. https://doi.org/10.1126/science.1060835.

(25)   *The IUPAC Compendium of Chemical Terminology*; Gold, V., Ed.; International Union of Pure and Applied Chemistry (IUPAC): Research Triangle Park, NC, 2019. https://doi.org/10.1351/goldbook.

(26)   Mislow, K. Absolute Asymmetric Synthesis: A Commentary. *Collect. Czechoslov. Chem. Commun.* **2003**, *68* (5), 849–864. https://doi.org/10.1135/cccc20030849.

(27)   Ribó, J. M.; Blanco, C.; Crusats, J.; El-Hachemi, Z.; Hochberg, D.; Moyano, A. Absolute Asymmetric Synthesis in Enantioselective Autocatalytic Reaction Networks: Theoretical Games, Speculations on Chemical Evolution and Perhaps a Synthetic Option. *Chem. - A Eur. J.* **2014**, *20* (52), 17250–17271. https://doi.org/10.1002/chem.201404534.

(28)   Kondepudi, D. K.; Nelson, G. W. Weak Neutral Currents and the Origin of Biomolecular Chirality. *Nature* **1985**, *314* (6010), 438–441. https://doi.org/10.1038/314438a0.

(29)   Kondepudi, D. K.; Nelson, G. W. Chiral Symmetry Breaking in Nonequilibrium Systems. *Phys. Rev. Lett.* **1983**, *50* (14), 1023–1026. https://doi.org/10.1103/PhysRevLett.50.1023.

(30)   Ribó, J. M.; Hochberg, D. Spontaneous Mirror Symmetry Breaking: An Entropy Production Survey of the Racemate Instability and the Emergence of Stable Scalemic Stationary States. *Phys. Chem. Chem. Phys.* **2020**, *22* (25), 14013–14025. https://doi.org/10.1039/D0CP02280B.

(31)   Buhse, T.; Cruz, J.-M.; Noble-Teran, M. E.; Hochberg, D.; Ribó, J. M.; Crusats, J.; Micheau, J. C. Spontaneous Deracemizations. *Chem. Rev.* **2021**, *121* (4), 2147–2229. https://doi.org/10.1021/acs.chemrev.0c00819.

(32)   Amabilino, D. B.; Kellogg, R. M. Spontaneous Deracemization. *Isr. J. Chem.* **2011**, *51* (10), 1034–1040. https://doi.org/10.1002/ijch.201100051.

(33)   Ribó, J. M.; Hochberg, D.; Crusats, J.; El-Hachemi, Z.; Moyano, A. Spontaneous Mirror Symmetry Breaking and Origin of Biological Homochirality. *J. R. Soc. Interface* **2017**, *14* (137). https://doi.org/10.1098/rsif.2017.0699.

(34)   Blackmond, D. G. An Examination of the Role of Autocatalytic Cycles in the Chemistry of Proposed Primordial Reactions. *Angew. Chemie Int. Ed.* **2009**, *48* (2), 386–390. https://doi.org/10.1002/anie.200804565.

(35)   Plasson, R.; Brandenburg, A.; Jullien, L.; Bersini, H. Autocatalyses. *J. Phys. Chem. A* **2011**, *115* (28), 8073–8085. https://doi.org/10.1021/jp110079p.

(36)   Schuster, P. What Is Special about Autocatalysis? *Monatshefte für Chemie - Chem. Mon.* **2019**, *150* (5), 763–775. https://doi.org/10.1007/s00706-019-02437-z.

(37)   Hordijk, W. Autocatalytic Confusion Clarified. *J. Theor. Biol.* **2017**, *435*, 22–28. https://doi.org/10.1016/j.jtbi.2017.09.003.

(38)   Soai, K.; Hayase, T.; Takai, K. Catalytic Chirally Self-Replicating Molecule. Asymmetric Autocatalytic Reaction of a Zinc Alkoxide of Chiral 1-Ferrocenyl-2-Methylpropan-1-Ol. *Tetrahedron: Asymmetry* **1995**, *6* (3), 637–638. https://doi.org/10.1016/0957-4166(95)00047-S.

(39)   Buhse, T.; Noble-Terán, M. E.; Cruz, J. M.; Micheau, J. C.; Coudret, C. *Kinetic and Structural Aspects of Mirror-Image Symmetry Breaking in the Soai Reaction*; 2017. https://doi.org/10.1016/B978-0-12-812824-4.00004-6.

(40)   Noble-Terán, M. E.; Cruz, J. M.; Micheau, J. C.; Buhse, T. A Quantification of the Soai Reaction. *ChemCatChem* **2018**, *10* (3), 642–648. https://doi.org/10.1002/cctc.201701554.

(41)   Buhse, T.; Noble-Terán, M. E.; Hochberg, D.; Ribó, J. M.; Micheau, J. Spontaneous Emergence of Chirality in Autocatalytic Cycle Models of the Soai Reaction. In *Asymmetric Autocatalysis: The Soai Reaction.*; Kawasaki, T., Matsumoto, A., Soai, K., Eds.; The Royal Society of Chemistry, 2023; pp 129–155.

(42)   Frank, F. C. On Spontaneous Asymmetric Synthesis. *Biochim. Biophys. Acta* **1953**, *11*, 459–463. https://doi.org/10.1016/0006-3002(53)90082-1.

(43)   Roozeboom, H. W. B. Löslichkeit Und Schmelzpunkt Als Kriterien Für Racemische Verbindungen, Pseudoracemische Mischkrystalle Und Inaktive Konglomerate. *Zeitschrift für Phys. Chemie* **1899**, *28U* (1), 494–517. https://doi.org/10.1515/zpch-1899-2832.

(44)   Sohncke, L. *Entwickelung Einer Theorie Der Krystallstruktur*; B.G. Teubner: Leipzig, 1879.

(45)   Nespolo, M.; Aroyo, M. I.; Souvignier, B. Crystallographic Shelves: Space-Group Hierarchy Explained. *J. Appl. Crystallogr.* **2018**, *51* (5), 1481–1491. https://doi.org/10.1107/S1600576718012724.

(46)   Addadi, L.; Weinstein, S.; Gati, E.; Weissbuch, I.; Lahav, M. Resolution of Conglomerates with the Assistance of Tailor-Made Impurities. Generality and Mechanistic Aspects of the "Rule of Reversal". A New Method for Assignment of Absolute Configuration. *J. Am. Chem. Soc.* **1982**, *104* (17), 4610–4617. https://doi.org/10.1021/ja00381a018.

(47)   Matsuura, T.; Koshima, H. Introduction to Chiral Crystallization of Achiral Organic Compounds: Spontaneous Generation of Chirality. *J. Photochem. Photobiol. C Photochem. Rev.* **2005**, *6* (1), 7–24.

https://doi.org/10.1016/j.jphotochemrev.2005.02.002.

(48)   Pidcock, E. Achiral Molecules in Non-Centrosymmetric Space Groups. *Chem. Commun.* **2005**, No. 27, 3457. https://doi.org/10.1039/b505236j.

(49)   Dryzun, C.; Avnir, D. On the Abundance of Chiral Crystals. *Chem. Commun.* **2012**, *48* (47), 5874. https://doi.org/10.1039/c2cc17727g.

(50)   Yogev-Einot, D.; Avnir, D. Quantitative Symmetry and Chirality of the Molecular Building Blocks of Quartz. *Chem. Mater.* **2003**, *15* (2), 464−472. https://doi.org/10.1021/cm0207806.

(51)   Abrahams, S. C.; Bernstein, J. L. Remeasurement of Optically Active NaClO 3 and NaBrO 3. *Acta Crystallogr. Sect. B Struct. Crystallogr. Cryst. Chem.* **1977**, *33* (11), 3601−3604. https://doi.org/10.1107/S0567740877011637.

(52)   Kipping, F. S.; Pope, W. J. LXIII.—Enantiomorphism. *J. Chem. Soc., Trans.* **1898**, *73*, 606−617. https://doi.org/10.1039/CT8987300606.

(53)   Cruz, J.; Hernández-Lechuga, K.; Domínguez-Valle, I.; Fuentes-Beltrán, A.; Sánchez-Morales, J. U.; Ocampo-Espindola, J. L.; Polanco, C.; Micheau, J.; Buhse, T. Non-stochastic Behavior in Sodium Chlorate Crystallization. *Chirality* **2020**, *32* (1), 120−134. https://doi.org/10.1002/chir.23154.

(54)   Viedma, C. Selective Chiral Symmetry Breaking during Crystallization: Parity Violation or Cryptochiral Environment in Control? *Cryst. Growth Des.* **2007**, *7* (3), 553−556. https://doi.org/10.1021/cg060698d.

(55)   Hegstrom, R. A. Parity Violation and Chiral Symmetry Breaking of a Racemic Mixture. *Biosystems* **1987**, *20* (1), 49−56. https://doi.org/10.1016/0303-2647(87)90019-0.

(56)   Mason, S. F.; Tranter, G. E. The Parity-Violating Energy Difference between Enantiomeric Molecules. *Chem. Phys. Lett.* **1983**, *94* (1), 34−37. https://doi.org/10.1016/0009-2614(83)87205-4.

(57)   Quack, M. How Important Is Parity Violation for Molecular and Biomolecular Chirality? *Angew. Chemie Int. Ed.* **2002**, *41* (24), 4618−4630. https://doi.org/10.1002/anie.200290005.

(58)   Lahamer, A. S.; Mahurin, S. M.; Compton, R. N.; House, D.; Laerdahl, J. K.; Lein, M.; Schwerdtfeger, P. Search for a Parity-Violating Energy Difference between Enantiomers of a Chiral Iron Complex. *Phys. Rev. Lett.* **2000**, *85* (21), 4470−4473. https://doi.org/10.1103/PhysRevLett.85.4470.

(59)   Macdermott, A. J. Chiroptical Signatures of Life and Fundamental Physics. *Chirality* **2012**, *24* (9), 764−769. https://doi.org/10.1002/chir.22076.

(60)   Yamagata, Y. A Hypothesis for the Asymmetric Appearance of Biomolecules on Earth. *J. Theor. Biol.* **1966**, *11* (3), 495−498. https://doi.org/10.1016/0022-5193(66)90110-X.

(61)   Kondepudi, D. K.; Kaufman, R. J.; Singh, N. Chiral Symmetry Breaking in Sodium Chlorate Crystallizaton. *Science (80-.).* **1990**, *250* (4983), 975−976. https://doi.org/10.1126/science.250.4983.975.

(62)   Viedma, C. Chiral Symmetry Breaking during Crystallization: Complete Chiral Purity Induced by Nonlinear Autocatalysis and Recycling. *Phys. Rev. Lett.* **2005**, *94* (6), 3−6. https://doi.org/10.1103/PhysRevLett.94.065504.

(63)   Perez, M. Gibbs-Thomson Effects in Phase Transformations. *Scr. Mater.* **2005**, *52* (8), 709−712. https://doi.org/10.1016/j.scriptamat.2004.12.026.

(64)   Viedma, C. Chiral Symmetry Breaking during Crystallization: Complete Chiral Purity Induced by Nonlinear Autocatalysis and Recycling. *Phys. Rev. Lett.* **2005**, *94* (6), 065504. https://doi.org/10.1103/PhysRevLett.94.065504.

(65)   Levilain, G.; Rougeot, C.; Guillen, F.; Plaquevent, J.-C.; Coquerel, G. Attrition-Enhanced Preferential Crystallization Combined with Racemization Leading to Redissolution of the Antipode Nuclei. *Tetrahedron: Asymmetry* **2009**, *20* (24), 2769–2771. https://doi.org/10.1016/j.tetasy.2009.11.015.

(66)   Iggland, M.; Mazzotti, M. A Population Balance Model for Chiral Resolution via Viedma Ripening. *Cryst. Growth Des.* **2011**, *11* (10), 4611–4622. https://doi.org/10.1021/cg2008599.

(67)   Iggland, M.; Mazzotti, M. Population Balance Modeling with Size-Dependent Solubility: Ostwald Ripening. *Cryst. Growth Des.* **2012**, *12* (3), 1489–1500. https://doi.org/10.1021/cg201571n.

(68)   Blackmond, D. G. "Chiral Amnesia" as a Driving Force for Solid-Phase Homochirality. *Chem. - A Eur. J.* **2007**, *13* (12), 3290–3295. https://doi.org/10.1002/chem.200601463.

(69)   Saito, Y.; Hyuga, H. Colloquium: Homochirality: Symmetry Breaking in Systems Driven Far from Equilibrium. *Rev. Mod. Phys.* **2013**, *85* (2), 603–621. https://doi.org/10.1103/RevModPhys.85.603.

(70)   Sögütoglu, L.-C.; Steendam, R. R. E.; Meekes, H.; Vlieg, E.; Rutjes, F. P. J. T. Viedma Ripening: A Reliable Crystallisation Method to Reach Single Chirality. *Chem. Soc. Rev.* **2015**, *44* (19), 6723–6732. https://doi.org/10.1039/C5CS00196J.

(71)   Noorduin, W. L.; Vlieg, E.; Kellogg, R. M.; Kaptein, B. From Ostwald Ripening to Single Chirality. *Angew. Chemie - Int. Ed.* **2009**, *48* (51), 9600–9606. https://doi.org/10.1002/anie.200905215.

(72)   Blanco, C.; Crusats, J.; El-Hachemi, Z.; Moyano, A.; Veintemillas-Verdaguer, S.; Hochberg, D.; Ribó, J. M. The Viedma Deracemization of Racemic Conglomerate Mixtures as a Paradigm of Spontaneous Mirror Symmetry Breaking in Aggregation and Polymerization. *ChemPhysChem* **2013**, *14* (17), 3982–3993. https://doi.org/10.1002/cphc.201300699.

(73)   Steendam, R. R. E.; Dickhout, J.; van Enckevort, W. J. P.; Meekes, H.; Raap, J.; Rutjes, F. P. J. T.; Vlieg, E. Linear Deracemization Kinetics during Viedma Ripening: Autocatalysis Overruled by Chiral Additives. *Cryst. Growth Des.* **2015**, *15* (4), 1975–1982. https://doi.org/10.1021/acs.cgd.5b00127.

(74)   Osuna-Esteban, S.; Zorzano, M.-P.; Menor-Salván, C.; Ruiz-Bermejo, M.; Veintemillas-Verdaguer, S. Asymmetric Chiral Growth of Micron-Size $NaClO_3$ Crystals in Water Aerosols. *Phys. Rev. Lett.* **2008**, *100* (14), 146102. https://doi.org/10.1103/PhysRevLett.100.146102.

(75)   Cintas, P. On Cavitation and Chirality: A Further Assessment. *Cryst. Growth Des.* **2008**, *8* (8), 2626–2627. https://doi.org/10.1021/cg800491f.

(76)   Iggland, M.; Fernández-Ronco, M. P.; Senn, R.; Kluge, J.; Mazzotti, M. Complete Solid State Deracemization by High Pressure Homogenization. *Chem. Eng. Sci.* **2014**, *111*, 106–111. https://doi.org/https://doi.org/10.1016/j.ces.2014.02.034.

(77)   Xiouras, C.; Van Aeken, J.; Panis, J.; Ter Horst, J. H.; Van Gerven, T.; Stefanidis, G. D. Attrition-Enhanced Deracemization of NaClO3: Comparison between Ultrasonic and Abrasive Grinding. *Cryst. Growth Des.* **2015**, *15* (11), 5476–5484. https://doi.org/10.1021/acs.cgd.5b01108.

(78)   Ahn, J.; Kim, D. H.; Coquerel, G.; Kim, W.-S. Chiral Symmetry Breaking and Deracemization of Sodium Chlorate in Turbulent Flow. *Cryst. Growth Des.* **2018**, *18* (1), 297–306. https://doi.org/10.1021/acs.cgd.7b01247.

(79)   Guijarro, A. *The Origin of Chirality in the Molecules of Life*; Royal Society of Chemistry: Cambridge, 2022. https://doi.org/10.1039/9781839163685.

(80)   Song, Y.; Chen, W.; Chen, X. Ultrasonic Field Induced Chiral Symmetry Breaking of NaClO 3 Crystallization. *Cryst. Growth Des.* 2008, *8* (5), 1448–1450. https://doi.org/10.1021/cg701072r.

(81)   Ward, M. R.; Copeland, G. W.; Alexander, A. J. Enantiomorphic Symmetry Breaking in Crystallization of Molten Sodium Chlorate. *Chem. Commun.* **2010**, *46* (40), 7634. https://doi.org/10.1039/c0cc02563a.

(82)   Song, Y.; Chen, W.; Chen, X. Crystal Chiral Symmetry Breaking: A Self-Seed Inducing Effect Controlled by Kinetics. *Cryst. Growth Des.* **2012**, *12* (1), 8–11. https://doi.org/10.1021/cg200339r.

(83)   El-Hachemi, Z.; Crusats, J.; Ribo, J. M.; Veintemillas-Verdaguer, S. Spontaneous Transition toward Chirality in the NaClO3 Crystallization in Boiling Solutions. *Cryst. Growth Des.* **2009**, *9* (11), 4802–4806. https://doi.org/10.1021/cg900638h.

(84)   El-Hachemi, Z.; Crusats, J.; Ribó, J. M.; McBride, J. M.; Veintemillas-Verdaguer, S. Metastability in Supersaturated Solution and Transition towards Chirality in the Crystallization of NaClO3. *Angew. Chemie - Int. Ed.* **2011**, *50* (10), 2359–2363. https://doi.org/10.1002/anie.201007209.

(85)   Viedma, C.; Cintas, P. Homochirality beyond Grinding: Deracemizing Chiral Crystals by Temperature Gradient under Boiling. *Chem. Commun.* **2011**, *47* (48), 12786–12788. https://doi.org/10.1039/c1cc14857e.

(86)   Suwannasang, K.; Flood, A. E.; Coquerel, G. A Novel Design Approach To Scale Up the Temperature Cycle Enhanced Deracemization Process: Coupled Mixed-Suspension Vessels. *Cryst. Growth Des.* **2016**, *16* (11), 6461–6467. https://doi.org/10.1021/acs.cgd.6b01139.

(87)   Suwannasang, K.; Flood, A. E.; Rougeot, C.; Coquerel, G. Use of Programmed Damped Temperature Cycles for the Deracemization of a Racemic Suspension of a Conglomerate Forming System. *Org. Process Res. Dev.* **2017**, *21* (4), 623–630. https://doi.org/10.1021/acs.oprd.7b00028.

(88)   Breveglieri, F.; Maggioni, G. M.; Mazzotti, M. Deracemization of NMPA via Temperature Cycles. *Cryst. Growth Des.* **2018**, *18* (3), 1873–1881. https://doi.org/10.1021/acs.cgd.7b01746.

(89)   Rougeot, C.; Guillen, F.; Plaquevent, J. C.; Coquerel, G. Ultrasound-Enhanced Deracemization: Toward the Existence of Agonist Effects in the Interpretation of Spontaneous Symmetry Breaking. *Cryst. Growth Des.* **2015**, *15* (5), 2151–2155. https://doi.org/10.1021/cg501765g.

(90)   Plaza, M.; Jandl, C.; Bach, T. Photochemical Deracemization of Allenes and Subsequent Chirality Transfer. *Angew. Chemie Int. Ed.* **2020**, *59* (31), 12785–12788. https://doi.org/10.1002/anie.202004797.

(91)   Blackmond, D. G. "Chiral Amnesia" as a Driving Force for Solid-Phase Homochirality. *Chem. - A Eur. J.* **2007**, *13* (12), 3290–3295. https://doi.org/10.1002/chem.200601463.

(92)   Viedma, C. Selective Chiral Symmetry Breaking during Crystallization: Parity Violation or Cryptochiral Environment in Control? *Cryst. Growth Des.* **2007**, *7* (3), 553–556. https://doi.org/10.1021/cg060698d.

(93)   Cheung, P. S. M.; Gagnon, J.; Surprenant, J.; Tao, Y.; Xu, H.; Cuccia, L. A. Complete Asymmetric Amplification of Ethylenediammonium Sulfate Using an Abrasion/Grinding Technique. *Chem. Commun.* **2008**, No. 8, 987. https://doi.org/10.1039/b716977a.

(94)   Nguyen, T. P. T.; Cheung, P. S. M.; Werber, L.; Gagnon, J.; Sivakumar, R.; Lennox, C.; Sossin, A.;

Mastai, Y.; Cuccia, L. A. Directing the Viedma Ripening of Ethylenediammonium Sulfate Using "Tailor-Made" Chiral Additives. *Chem. Commun.* **2016**, *52* (85), 12626–12629. https://doi.org/10.1039/C6CC06534A.

(95)   Katsuno, H.; Uwaha, M. Monte Carlo Simulation of a Cluster Model for the Chirality Conversion of Crystals with Grinding. *J. Cryst. Growth* **2009**, *311* (17), 4265–4269. https://doi.org/10.1016/j.jcrysgro.2009.07.005.

(96)   Saito, Y.; Hyuga, H. Crystal Chirality Selected by Mutual Antagonism. *J. Phys. Soc. Japan* **2010**, *79* (8), 083002. https://doi.org/10.1143/JPSJ.79.083002.

(97)   Ricci, F.; Stillinger, F. H.; Debenedetti, P. G. A Computational Investigation of Attrition-Enhanced Chiral Symmetry Breaking in Conglomerate Crystals. *J. Chem. Phys.* **2013**, *139* (17), 174503. https://doi.org/10.1063/1.4827478.

(98)   Katsuno, H.; Uwaha, M. Effect of Impurities on Chirality Conversion by Grinding. *Phys. Rev. E* **2017**, *95* (6), 062804. https://doi.org/10.1103/PhysRevE.95.062804.

(99)   Saito, Y.; Hyuga, H. Grinding-Induced Homochirality in Crystal Growth. *J. Cryst. Growth* **2011**, *318* (1), 93–98. https://doi.org/10.1016/j.jcrysgro.2010.10.099.

(100)   Cartwright, J. H. E.; Piro, O.; Tuval, I. Ostwald Ripening, Chiral Crystallization, and the Common-Ancestor Effect. *Phys. Rev. Lett.* **2007**, *98* (16), 165501. https://doi.org/10.1103/PhysRevLett.98.165501.

(101)   Suwannasang, K.; Coquerel, G.; Rougeot, C.; Flood, A. E. Mathematical Modeling of Chiral Symmetry Breaking Due to Differences in Crystal Growth Kinetics. *Chem. Eng. Technol.* **2014**, *37* (8), 1329–1339. https://doi.org/10.1002/ceat.201400056.

(102)   Iggland, M.; Müller, R.; Mazzotti, M. On the Effect of Initial Conditions in Viedma Ripening. *Cryst. Growth Des.* **2014**, *14* (5), 2488–2493. https://doi.org/10.1021/cg500196m.

(103)   Bodák, B.; Maggioni, G. M.; Mazzotti, M. Population-Based Mathematical Model of Solid-State Deracemization via Temperature Cycles. *Cryst. Growth Des.* **2018**, *18* (11), 7122–7131. https://doi.org/10.1021/acs.cgd.8b01292.

(104)   Blanco, C.; Ribó, J. M.; Hochberg, D. Modeling Spontaneous Chiral Symmetry Breaking and Deracemization Phenomena: Discrete versus Continuum Approaches. *Phys. Rev. E* **2015**, *91* (2), 022801. https://doi.org/10.1103/PhysRevE.91.022801.

(105)   Katsuno, H.; Uwaha, M. Appearance of a Homochiral State of Crystals Induced by Random Fluctuation in Grinding. *Phys. Rev. E - Stat. Nonlinear, Soft Matter Phys.* **2012**, *86* (5). https://doi.org/10.1103/PhysRevE.86.051608.

(106)   Katsuno, H.; Uwaha, M. Effect of Nucleation on Chirality Conversion Induced by Random Fluctuation. *J. Cryst. Growth* **2014**, *401*, 59–62. https://doi.org/10.1016/j.jcrysgro.2013.10.063.

(107)   Noorduin, W. L.; van Enckevort, W. J. P.; Meekes, H.; Kaptein, B.; Kellogg, R. M.; Tully, J. C.; McBride, J. M.; Vlieg, E. The Driving Mechanism Behind Attrition-Enhanced Deracemization. *Angew. Chemie* **2010**, *122* (45), 8613–8616. https://doi.org/10.1002/ange.201002036.

(108)   Uwaha, M. Simple Models for Chirality Conversion of Crystals and Molecules by Grinding. *J. Phys. Soc. Japan* **2008**, *77* (8), 083802. https://doi.org/10.1143/JPSJ.77.083802.

(109)   Uwaha, M.; Katsuno, H. Mechanism of Chirality Conversion by Grinding Crystals: Ostwald Ripening

vs Crystallization of Chiral Clusters. *J. Phys. Soc. Japan* **2009**, *78* (2), 023601. https://doi.org/10.1143/JPSJ.78.023601.

(110) Uwaha, M. Steady Chirality Conversion by Grinding Crystals—Supercritical and Subcritical Bifurcations. *J. Cryst. Growth* **2011**, *318* (1), 89–92. https://doi.org/10.1016/j.jcrysgro.2010.10.078.

(111) Wattis, J. A. D. Mathematical Models of the Homochiralisation of Crystals by Grinding. *Orig. Life Evol. Biosph.* **2011**, *41* (2), 133–173. https://doi.org/10.1007/s11084-010-9221-2.

(112) Xiouras, C.; Ter Horst, J. H.; Van Gerven, T.; Stefanidis, G. D. Coupling Viedma Ripening with Racemic Crystal Transformations: Mechanism of Deracemization. *Cryst. Growth Des.* **2017**, *17* (9), 4965–4976. https://doi.org/10.1021/acs.cgd.7b00908.

(113) Uwaha, M. A Model for Complete Chiral Crystallization. *J. Phys. Soc. Japan* **2004**, *73* (10), 2601–2603. https://doi.org/10.1143/JPSJ.73.2601.

(114) Perez, M. Gibbs-Thomson Effects in Phase Transformations. *Scr. Mater.* **2005**, *52* (8), 709–712. https://doi.org/10.1016/j.scriptamat.2004.12.026.

(115) Wegscheider, R. Über Simultane Gleichgewichte Und Die Beziehungen Zwischen Thermodynamik Und Reactionskinetik Homogener Systeme. *Monatshefte für Chemie* **1911**, *32* (8), 849–906. https://doi.org/10.1007/BF01517735.

(116) Blackmond, D. G. "If Pigs Could Fly" Chemistry: A Tutorial on the Principle of Microscopic Reversibility. *Angew. Chemie - Int. Ed.* **2009**, *48* (15), 2648–2654. https://doi.org/10.1002/anie.200804566.

(117) Viedma, C. Chiral Symmetry Breaking and Complete Chiral Purity by Thermodynamic-Kinetic Feedback Near Equilibrium: Implications for the Origin of Biochirality. *Astrobiology* **2007**, *7* (2), 312–319. https://doi.org/10.1089/ast.2006.0099.

(118) Wattis, J. A. D. A Becker-Döring Model of Competitive Nucleation. *J. Phys. A. Math. Gen.* **1999**, *32* (49), 8755–8784. https://doi.org/10.1088/0305-4470/32/49/315.

(119) Sandars, P. G. H. A Toy Model for the Generation of Homochirality during Polymerization. *Orig. Life Evol. Biosph.* **2003**, *33* (6), 575–587. https://doi.org/10.1023/A:1025705401769.

(120) Wattis, J. A. D.; Coveney, P. V. Symmetry-Breaking in Chiral Polymerisation. *Orig. Life Evol. Biosph.* **2005**, *35* (3), 243–273. https://doi.org/10.1007/s11084-005-0658-7.

(121) Katsuno, H.; Uwaha, M. Mechanism of Chirality Conversion by Periodic Change of Temperature: Role of Chiral Clusters. *Phys. Rev. E* **2016**, *93* (1). https://doi.org/10.1103/PhysRevE.93.013002.

(122) Katsuno, H.; Uwaha, M. Anomalous Size Distribution of Chiral Crystals during Deracemization by Grinding. *Cryst. Growth Des.* **2019**, *19* (4), 2428–2433. https://doi.org/10.1021/acs.cgd.9b00095.

(123) Niinomi, H.; Miura, H.; Kimura, Y.; Uwaha, M.; Katsuno, H.; Harada, S.; Ujihara, T.; Tsukamoto, K. Emergence and Amplification of Chirality via Achiral-Chiral Polymorphic Transformation in Sodium Chlorate Solution Growth. *Cryst. Growth Des.* **2014**, *14* (7), 3596–3602. https://doi.org/10.1021/cg500527t.

(124) Niinomi, H.; Sugiyama, T.; Tagawa, M.; Ujihara, T.; Omatsu, T.; Miyamoto, K.; Yoshikawa, H. Y.; Kawamura, R.; Nozawa, J.; Okada, J. T.; Uda, S. Plasmonic Manipulation of Sodium Chlorate Chiral Crystallization: Directed Chirality Transfer via Contact-Induced Polymorphic Transformation and Formation of Liquid Precursor. *Cryst. Growth Des.* **2020**, *20* (8), 5493–5507.

https://doi.org/10.1021/acs.cgd.0c00693.

(125) Crusats, J.; Veintemillas-Verdaguer, S.; Ribó, J. M. Homochirality as a Consequence of Thermodynamic Equilibrium? *Chem. - A Eur. J.* **2006**, *12* (30), 7776–7781. https://doi.org/10.1002/chem.200600580.

(126) Kimura, Y.; Niinomi, H.; Tsukamoto, K.; García-Ruiz, J. M. In Situ Live Observation of Nucleation and Dissolution of Sodium Chlorate Nanoparticles by Transmission Electron Microscopy. *J. Am. Chem. Soc.* **2014**, *136* (5), 1762–1765. https://doi.org/10.1021/ja412111f.

(127) Niinomi, H.; Yamazaki, T.; Harada, S.; Ujihara, T.; Miura, H.; Kimura, Y.; Kuribayashi, T.; Uwaha, M.; Tsukamoto, K. Achiral Metastable Crystals of Sodium Chlorate Forming Prior to Chiral Crystals in Solution Growth. *Cryst. Growth Des.* **2013**, *13* (12), 5188–5192. https://doi.org/10.1021/cg401324f.

(128) Vetter, T.; Iggland, M.; Ochsenbein, D. R.; Hänseler, F. S.; Mazzotti, M. Modeling Nucleation, Growth, and Ostwald Ripening in Crystallization Processes: A Comparison between Population Balance and Kinetic Rate Equation. *Cryst. Growth Des.* **2013**, *13* (11), 4890–4905. https://doi.org/10.1021/cg4010714.

(129) Iggland, M.; Mazzotti, M. Solid State Deracemisation through Growth, Dissolution and Solution-Phase Racemisation. *CrystEngComm* **2013**, *15* (12), 2319–2328. https://doi.org/10.1039/c3ce26620f.

(130) Saito, Y.; Hyuga, H. Chirality Selection in Crystallization. *J. Phys. Soc. Japan* **2005**, *74* (2), 535–537. https://doi.org/10.1143/JPSJ.74.535.

(131) Hein, J. E.; Gherase, D.; Blackmond, D. G. Chemical and Physical Models for the Emergence of Biological Homochirality; 2012; pp 83–108. https://doi.org/10.1007/128_2012_397.

(132) Malivuk, D. A.; Žekić, A. A.; Mitrović, M. M.; Misailović, B. M. Dissolution of Sodium Chlorate Crystals in Supersaturated Solutions. *J. Cryst. Growth* **2013**, *377*, 164–169. https://doi.org/10.1016/j.jcrysgro.2013.05.018.

(133) Suwannasang, K.; Flood, A. E.; Rougeot, C.; Coquerel, G. Using Programmed Heating-Cooling Cycles with Racemization in Solution for Complete Symmetry Breaking of a Conglomerate Forming System. *Cryst. Growth Des.* **2013**, *13* (8), 3498–3504. https://doi.org/10.1021/cg400436r.

(134) Kondepudi, D. K.; Sabanayagam, C. Secondary Nucleation That Leads to Chiral Symmetry Breaking in Stirred Crystallization. *Chem. Phys. Lett.* **1994**, *217* (4), 364–368. https://doi.org/10.1016/0009-2614(93)E1392-T.

(135) Noorduin, W. L.; Van Der Asdonk, P.; Bode, A. A. C.; Meekes, H.; Van Enckevort, W. J. P.; Vlieg, E.; Kaptein, B.; Van Der Meijden, M. W.; Kellogg, R. M.; Deroover, G. Scaling Up Attrition-Enhanced Deracemization by Use of an Industrial Bead Mill in a Route to Clopidogrel (Plavix). *Org. Process Res. Dev.* **2010**, *14* (4), 908–911. https://doi.org/10.1021/op1001116.

(136) Steendam, R. R. E.; Frawley, P. J. Secondary Nucleation of Sodium Chlorate: The Role of Initial Breeding. *Cryst. Growth Des.* **2019**, *19* (6), 3453–3460. https://doi.org/10.1021/acs.cgd.9b00317.

(137) Cartwright, J. H. E.; García-Ruiz, J. M.; Piro, O.; Sainz-Díaz, C. I.; Tuval, I. Chiral Symmetry Breaking during Crystallization: An Advection-Mediated Nonlinear Autocatalytic Process. *Phys. Rev. Lett.* **2004**, *93* (3). https://doi.org/10.1103/PhysRevLett.93.035502.

(138) Buhse, T.; Durand, D.; Kondepudi, D.; Laudadio, J.; Spilker, S. Chiral Symmetry Breaking in Crystallization: The Role of Convection. *Phys. Rev. Lett.* **2000**, *84* (19), 4405–4408. https://doi.org/10.1103/PhysRevLett.84.4405.

(139) Noorduin, W. L.; Meekes, H.; Bode, A. A. C.; Van Enckevort, W. J. P.; Kaptein, B.; Kellogg, R. M.; Vlieg, E. Explanation for the Emergence of a Single Chiral Solid State during Attrition-Enhanced Ostwald Ripening: Survival of the Fittest. *Cryst. Growth Des.* **2008**, *8* (5), 1675–1681. https://doi.org/10.1021/cg701211a.

(140) Xiouras, C.; Fytopoulos, A. A.; Ter Horst, J. H.; Boudouvis, A. G.; Van Gerven, T.; Stefanidis, G. D. Particle Breakage Kinetics and Mechanisms in Attrition-Enhanced Deracemization. *Cryst. Growth Des.* **2018**, *18* (5), 3051–3061. https://doi.org/10.1021/acs.cgd.8b00201.

(141) Hoops, S.; Gauges, R.; Lee, C.; Pahle, J.; Simus, N.; Singhal, M.; Xu, L.; Mendes, P.; Kummer, U. COPASI - A COmplex PAthway SImulator. *Bioinformatics* **2006**, *22* (24), 3067–3074. https://doi.org/10.1093/bioinformatics/btl485.

(142) Quaranta, M.; Gehring, T.; Odell, B.; Brown, J. M.; Blackmond, D. G. Unusual Inverse Temperature Dependence on Reaction Rate in the Asymmetric Autocatalytic Alkylation of Pyrimidyl Aldehydes. *J. Am. Chem. Soc.* **2010**, *132* (43), 15104–15107. https://doi.org/10.1021/ja103204w.

(143) Xiouras, C.; Van Aeken, J.; Panis, J.; Ter Horst, J. H.; Van Gerven, T.; Stefanidis, G. D. Attrition-Enhanced Deracemization of NaClO3: Comparison between Ultrasonic and Abrasive Grinding. *Cryst. Growth Des.* **2015**, *15* (11), 5476–5484. https://doi.org/10.1021/acs.cgd.5b01108.

(144) Blanco, C.; Crusats, J.; El-Hachemi, Z.; Moyano, A.; Veintemillas-Verdaguer, S.; Hochberg, D.; Ribõ, J. M. The Viedma Deracemization of Racemic Conglomerate Mixtures as a Paradigm of Spontaneous Mirror Symmetry Breaking in Aggregation and Polymerization. *ChemPhysChem* **2013**, *14* (17), 3982–3993. https://doi.org/10.1002/cphc.201300699.

(145) Blanco, C.; Ribó, J. M.; Hochberg, D. Modeling Spontaneous Chiral Symmetry Breaking and Deracemization Phenomena: Discrete versus Continuum Approaches. *Phys. Rev. E - Stat. Nonlinear, Soft Matter Phys.* **2015**, *91* (2), 1–13. https://doi.org/10.1103/PhysRevE.91.022801.

(146) Noorduin, W. L.; Meekes, H.; Van Enckevort, W. J. P.; Millemaggi, A.; Leeman, M.; Kaptein, B.; Kellogg, R. M.; Vlieg, E. Complete Deracemization by Attrition-Enhanced Ostwald Ripening Elucidated. *Angew. Chemie - Int. Ed.* **2008**, *47* (34), 6445–6447. https://doi.org/10.1002/anie.200801846.

(147) Vekilov, P. G. The Two-Step Mechanism of Nucleation of Crystals in Solution. *Nanoscale* **2010**, *2* (11), 2346–2357. https://doi.org/10.1039/c0nr00628a.

(148) Bentea, L.; Watzky, M. A.; Finke, R. G. Sigmoidal Nucleation and Growth Curves Across Nature Fit by the Finke-Watzky Model of Slow Continuous Nucleation and Autocatalytic Growth: Explicit Formulas for the Lag and Growth Times Plus Other Key Insights. *J. Phys. Chem. C* **2017**, *121* (9), 5302–5312. https://doi.org/10.1021/acs.jpcc.6b12021.

(149) Schwartz, G.; Hananel, U.; Avram, L.; Goldbourt, A.; Markovich, G. A Kinetic Isotope Effect in the Formation of Lanthanide Phosphate Nanocrystals. *J. Am. Chem. Soc.* **2022**, *144* (21), 9451–9457. https://doi.org/10.1021/jacs.2c02424.

(150) Hein, J. E.; Huynh Cao, B.; Viedma, C.; Kellogg, R. M.; Blackmond, D. G. Pasteur's Tweezers Revisited: On the Mechanism of Attrition-Enhanced Deracemization and Resolution of Chiral Conglomerate Solids. *J. Am. Chem. Soc.* **2012**, *134* (30), 12629–12636. https://doi.org/10.1021/ja303566g.

(151) Saito, Y.; Hyuga, H. Chiral Crystal Growth under Grinding. *J. Phys. Soc. Japan* **2008**, *77* (11), 113001. https://doi.org/10.1143/JPSJ.77.113001.

(152) Bodák, B.; Maggioni, G. M.; Mazzotti, M. Effect of Initial Conditions on Solid-State Deracemization via Temperature Cycles: A Model-Based Study. *Cryst. Growth Des.* **2019**, *19* (11), 6552–6559. https://doi.org/10.1021/acs.cgd.9b00988.

(153) Walsh, M. P.; Barclay, J. A.; Begg, C. S.; Xuan, J.; Johnson, N. T.; Cole, J. C.; Kitching, M. O. Identifying a Hidden Conglomerate Chiral Pool in the CSD. *J. Am. Chem. Soc.* **2022**, *2* (10), 2235–2250. https://doi.org/10.1021/jacsau.2c00394.

(154) Noble-Terán, M. E.; Buhse, T.; Cruz, J. M.; Coudret, C.; Micheau, J. C. Nonlinear Effects in Asymmetric Synthesis: A Practical Tool for the Discrimination between Monomer and Dimer Catalysis. *ChemCatChem* **2016**, *8* (10), 1836–1845. https://doi.org/10.1002/cctc.201600216.

(155) Hingant, E.; Yvinec, R. Deterministic and Stochastic Becker-Döring Equations: Past and Recent Mathematical Developments. In *Stochastic Processes, Multiscale Modeling, and Numerical Methods for Computational Cellular Biology*; Editions Springer, 2016; pp 175–204.

Apéndice A

Ecuaciones diferenciales del modelo que fueron introducidas en el programa cinético Sa que opera en el lenguaje de programación C++. Este software se puede descargar de forma gratuita desde: http://cinet.chim.pagesperso-orange.fr/tele_sa/install_Sa_Eng.html

```cpp
// VX10.cpp

// automatically written by modan

//-----------------------------------------------------------
#include "global.h"
//-----------------------------------------------------------
void Identification(Modele& modele)
{
   modele.Fichier = String(__FILE__);
   modele.Version = String(__DATE__) + String() + String(__TIME__);
   modele.Auteur = "JCM";
   nom_syst = "VX10b";
   n_diff = 16;
   first_var = 0;
   nv_mod = 22;
   nexp = 4;
}
//-----------------------------------------------------------
// Special declarations:

//-----------------------------------------------------------
void eqdiff(Sa_data x, Sa_data *y, Sa_data *dy)
{
   Sa_data      v0,v1,v2,v3,v4,v5,v6,v7,v8,v9,v10,v11,v12,v13,v14,v15,v16,v17,v18,v19,v20,v21,v22,v23,v24,v25,
v26,v27,v28,v29,v30,v31,v32,v33,v34,v35,v36,v37,v38,v39,v40,v41,v42,v43,v44,v45,v46,v47,v48,v49,v50,v51,v52,v53,
v54,v55,v56,v57,v58,v59,v60,v61,v62,v63,v64,v65,v66,v67;

// Dense-liquid

   v0 = p[0]*exp(-p[1]*p[18])*y[0]*y[0];            // A + A <-> A2,    p[1]=-ΔG($K_{A2}$)/R y p[18]=1/T
   v1 = p[0]*y[1];                                  // inverse
   v2 = p[0]*exp(p[2]*p[18])*y[1]*y[1];             // A2 + A2 <-> A4,  p[2]=-ΔG($K_{A4}$)/R
   v3 = p[0]*y[2];                                  // inverse

// Achiral
   v4 = p[0]*exp(p[3]*p[18])*y[2];                  //  A4 <-> X,          p[3]=-ΔG($K_X$)/R
   v5 = p[0]*y[3];                                  //  inverse

// Chiral -L
   v6 = p[4]*exp(p[5]*p[18])*y[3];                  // X <-> L,            p[5]=-ΔG($K_c$)/R
   v7 = p[4]*y[4];                                  // inverse

// Aggregation - L

   v8 = p[6]*exp(-p[13]*p[18])*exp(p[7])*y[4]*y[4];      // L + L <-> L2       p[13]=-ΔG($K2$)/R
   v9 = p[6]*y[5];                                       // inverse
   v10 = p[6]*exp(p[7]*2)*exp(p[14]*p[18])*y[4]*y[5];    // L + L2 <-> L3      p[14]=-ΔG($K_3$)/R
   v11 = p[6]*y[6];                                      // inverse
```

```
v12 = p[6]*exp(p[7]*3)*exp(p[15]*p[18])*y[4]*y[6];          // L + L3 <-> L4      p[15]=-ΔG(K₄)/R
v13 = p[6]*y[7];                                            // inverse
v14 = p[6]*exp(p[7]*4)*exp(p[16]*p[18])*y[4]*y[7];          // L + L4 <-> L5      p[16]=-ΔG(K₅)/R
v15 = p[6]*y[8];                                            // inverse
v16 = p[6]*exp(p[7]*5)*exp(p[17]*p[18])*y[4]*y[8];          // L + L5 <-> L6      p[17]=-ΔG(K₆)/R
v17 = p[6]*y[9];                                            // inverse

// Dissolution -L

v18 = p[8]*y[5];                                                                           // L2 <-> L + A4
v19 = p[8]*exp(p[3]*p[18])*exp(p[5]*p[18])*exp(-p[13]*p[18])*exp(p[7])*y[2]*y[4];           // inverse
v20 = p[8]*y[6];                                                                           // L3 <-> L2 + A4
v21 = p[8]*exp(p[3]*p[18])*exp(p[5]*p[18])*exp(p[7]*2)*exp(p[14]*p[18])*y[2]*y[5];          // inverse
v22 = p[8]*y[7];                                                                           // L4 <-> L3 + A4
v23 = p[8]*exp(p[3]*p[18])*exp(p[5]*p[18])*exp(p[7]*3)*exp(p[15]*p[18])*y[2]*y[6];          // inverse
v24 = p[8]*y[8];                                                                           // L5 <-> L4 + A4
v25 = p[8]*exp(p[3]*p[18])*exp(p[5]*p[18])*exp(p[7]*4)*exp(p[16]*p[18])*y[2]*y[7];          // inverse
v26 = p[8]*y[9];                                                                           // L6 <-> L5 + A4
v27 = p[8]*exp(p[3]*p[18])*exp(p[5]*p[18])*exp(p[7]*5)*exp(p[17]*p[18])*y[2]*y[8];          // inverse

// Chiral -D

v28 = p[4]*exp(p[5]*p[18])*y[3];                            // X <-> D
v29 = p[4]*y[10];                                           // inverse

// Aggregation -D

v30 = p[6]*exp(-p[13]*p[18])*exp(p[7])*y[10]*y[10];         // D + D <-> D2
v31 = p[6]*y[11];                                           // inverse
v32 = p[6]*exp(p[7]*2)*exp(p[14]*p[18])*y[10]*y[11];        // D + D2 <-> D3
v33 = p[6]*y[12];                                           // inverse
v34 = p[6]*exp(p[7]*3)*exp(p[15]*p[18])*y[10]*y[12];        // D + D3 <-> D4
v35 = p[6]*y[13];                                           // inverse
v36 = p[6]*exp(p[7]*4)*exp(p[16]*p[18])*y[10]*y[13];        // D + D4 <-> D5
v37 = p[6]*y[14];                                           // inverse
v38 = p[6]*exp(p[7]*5)*exp(p[17]*p[18])*y[10]*y[14];        // D + D5 <-> D6
v39 = p[6]*y[15];                                           // inverse

// Dissolution -D

v40 = p[8]*y[11];                                                                          // D2 <-> D + A4
v41 = p[8]*exp(p[3]*p[18])*exp(p[5]*p[18])*exp(-p[13]*p[18])*exp(p[7])*y[2]*y[10];          // inverse
v42 = p[8]*y[12];                                                                          // D3 <-> D2 + A4
v43 = p[8]*exp(p[3]*p[18])*exp(p[5]*p[18])*exp(p[7]*2)*exp(p[14]*p[18])*y[2]*y[11];         // inverse
v44 = p[8]*y[13];                                                                          // D4 <-> D3 + A4
v45 = p[8]*exp(p[3]*p[18])*exp(p[5]*p[18])*exp(p[7]*3)*exp(p[15]*p[18])*y[2]*y[12];         // inverse
v46 = p[8]*y[14];                                                                          // D5 <-> D4 + A4
v47 = p[8]*exp(p[3]*p[18])*exp(p[5]*p[18])*exp(p[7]*4)*exp(p[16]*p[18])*y[2]*y[13];         // inverse
v48 = p[8]*y[15];                                                                          // D6 <-> D5 + A4
```

```
    v49 = p[8]*exp(p[3]*p[18])*exp(p[5]*p[18])*exp(p[7]*5)*exp(p[17]*p[18])*y[2]*y[14];      // inverse

// Grinding -L

  v50 = p[9]*exp(p[12]*6)*p[10]*y[9];                          // L6 -> L5 + L
  v51 = p[9]*exp(p[12]*6)*p[11]*y[9];                          // L6 -> L4 + L2
  v52 = p[9]*exp(p[12]*6)*p[11]*y[9];                          // L6 -> L3 + L3
  v53 = p[9]*exp(p[12]*5)*p[10]*y[8];                          // L5 -> L4 + L
  v54 = p[9]*exp(p[12]*5)*p[11]*y[8];                          // L5 -> L3 + L2
  v55 = p[9]*exp(p[12]*4)*p[10]*y[7];                          // L4 -> L3 + L
  v56 = p[9]*exp(p[12]*4)*p[11]*y[7];                          // L4 -> L2 + L2
  v57 = p[9]*exp(p[12]*3)*p[10]*y[6];                          // L3 -> L2 + L
  v58 = p[9]*exp(p[12]*2)*p[10]*y[5];                          // L2 -> L + L

// Grinding -D

  v59 = p[9]*exp(p[12]*6)*p[10]*y[15];                         // D6 -> D5 + D
  v60 = p[9]*exp(p[12]*6)*p[11]*y[15];                         // D6 -> D4 + D2
  v61 = p[9]*exp(p[12]*6)*p[11]*y[15];                         // D6 -> D3 + D3
  v62 = p[9]*exp(p[12]*5)*p[10]*y[14];                         // D5 -> D4 + D
  v63 = p[9]*exp(p[12]*5)*p[11]*y[14];                         // D5 -> D3 + D2
  v64 = p[9]*exp(p[12]*4)*p[10]*y[13];                         // D4 -> D3 + D
  v65 = p[9]*exp(p[12]*4)*p[11]*y[13];                         // D4 -> D2 + D2
  v66 = p[9]*exp(p[12]*3)*p[10]*y[12];                         // D3 -> D2 + D
  v67 = p[9]*exp(p[12]*2)*p[10]*y[11];                         // D2 -> D + D

  dy[0] = -2*v0 +2*v1;      // d[A]/dt
  dy[1] = v0 - v1 -2*v2 +2*v3;         // d[A2]/dt
  dy[2] = v2 - v3 - v4 + v5 + v18 - v19 + v20 - v21 + v22 - v23 + v24 - v25 + v26 - v27 + v40 - v41 + v42 - v43 + v44 -
v45 + v46 - v47 + v48 - v49;          // d[A4]/dt
  dy[3] = v4 - v5 - v6 + v7 - v28 + v29;         // d[X]/dt
  dy[4] = v6 - v7 -2*v8 +2*v9 - v10 + v11 - v12 + v13 - v14 + v15 - v16 + v17 + v18 - v19 + v50 + v53 + v55 + v57 +2*v58;
         // d[L]/dt
  dy[5] = v8 - v9 - v10 + v11 - v18 + v19 + v20 - v21 + v51 + v54 +2*v56 + v57 - v58;        // d[L2]/dt
  dy[6] = v10 - v11 - v12 + v13 - v20 + v21 + v22 - v23 +2*v52 + v54 + v55 - v57;            // d[L3]/dt
  dy[7] = v12 - v13 - v14 + v15 - v22 + v23 + v24 - v25 + v51 + v53 - v55 - v56;  // d[L4]/dt
  dy[8] = v14 - v15 - v16 + v17 - v24 + v25 + v26 - v27 + v50 - v53 - v54;           // d[L5]/dt
  dy[9] = v16 - v17 - v26 + v27 - v50 - v51 - v52;       // d[L6]/dt
  dy[10] = v28 - v29 -2*v30 +2*v31 - v32 + v33 - v34 + v35 - v36 + v37 - v38 + v39 + v40 - v41 + v59 + v62 + v64 + v66
+2*v67; // d[D]/dt
  dy[11] = v30 - v31 - v32 + v33 - v40 + v41 + v42 - v43 + v60 + v63 +2*v65 + v66 - v67; // d[D2]/dt
  dy[12] = v32 - v33 - v34 + v35 - v42 + v43 + v44 - v45 +2*v61 + v63 + v64 - v66;          // d[D3]/dt
  dy[13] = v34 - v35 - v36 + v37 - v44 + v45 + v46 - v47 + v60 + v62 - v64 - v65; // d[D4]/dt
  dy[14] = v36 - v37 - v38 + v39 - v46 + v47 + v48 - v49 + v59 - v62 - v63;          // d[D5]/dt
  dy[15] = v38 - v39 - v48 + v49 - v59 - v60 - v61;      // d[D6]/dt
}
//------------------------------------------------------------
void fappel()
{
```

```
  // suppress or modify this loop, if needed:
  for (int i = 0; i < np; i++)
    p[i] = fabs(p[i]);

  for (int k = 0; k < nexp; k++)
  {
    first_var = k*nv_mod;
    srkvi(n_diff, &ca[first_var], ind, npt, h0, tol, iset, jacob, h_compt, c_min);

    // non integrated variables:
    for (int i = 0; i < npt; i++)
    {
// Total mass calculation (TM)

  Ca(k,16,i) = 4*Ca(k,4,i) + 8*Ca(k,5,i) + 12*Ca(k,6,i) + 16*Ca(k,7,i) + 20*Ca(k,8,i) + 24*Ca(k,9,i); //[L]tot

  Ca(k,17,i) = 4*Ca(k,10,i) + 8*Ca(k,11,i) + 12*Ca(k,12,i) + 16*Ca(k,13,i) + 20*Ca(k,14,i) + 24*Ca(k,15,i); // [D]tot

  Ca(k,18,i) = Ca(k,0,i) + 2*Ca(k,1,i)+ 4*Ca(k,2,i) +4*Ca(k,3,i) + Ca(k,16,i) + Ca(k,17,i); // TM

// ee

  Ca(k,19,i) = Ca(k,16,i) - Ca(k,17,i); // TOR in Ltot and Dtot

  Ca(k,20,i) = Ca(k,16,i) + Ca(k,17,i); // TCM

  if (Ca(k,20,i) !=0)
    Ca(k,21,i) = fabs(Ca(k,19,i)/Ca(k,20,i)); // ee(absolute)
    else ca[21][i] = 0;

    }
  }
}
```

Apéndice B

Spontaneous Deracemizations

Thomas Buhse, José-Manuel Cruz, María E. Noble-Terán, David Hochberg, Josep M. Ribó, Joaquim Crusats, and Jean-Claude Micheau, *Chemical Reviews* **2021** *121* (4), 2147-2229

CHEMICAL REVIEWS

Spontaneous Deracemizations

Thomas Buhse,* José-Manuel Cruz, María E. Noble-Terán, David Hochberg, Josep M. Ribó, Joaquim Crusats, and Jean-Claude Micheau

Read Online

ACCESS | Metrics & More | Article Recommendations

ABSTRACT: Spontaneous deracemizations is a challenging, multidisciplinary subject in current chirality research. In the absence of any chiral inductors, an achiral substance or a racemic composition is driven into an enantioenriched or even homochiral state through a selective energy input, e.g., chemical potential, photoirradiation, mechanical grinding, ultrasound waves, thermal gradients, etc. The most prominent examples of such transformations are the Soai reaction and the Viedma deracemization. In this review, we track the most recent developments in this topic and recall that many other deracemizations have been reported for solutions from mesophases to conglomerate crystallizations. A compiled set of simply available achiral organic, inorganic, organometallic, and MOF compounds, yielding conglomerate crystals, should give the impetus to realize new experiments on spontaneous deracemizations. Taking into account thermodynamic constraints, modeling efforts have shown that structural features alone are not sufficient to describe spontaneous deracemizations. As a guideline of this review, particular attention is paid to the physicochemical origin and symmetry requirements of such processes.
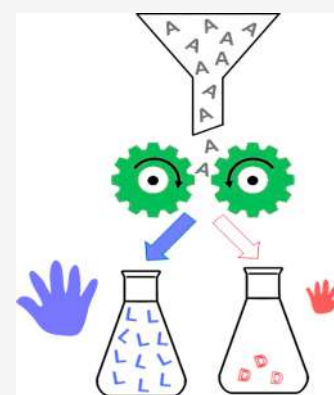
CONTENTS

1. INTRODUCTION

Chirality, or handedness, is a fundamental physical attribute, which spans the length scales ranging from the elementary particles to the asymmetry of galaxies.[1,2] The way that chirality in chemistry, or molecular handedness, arose in a primitive terrestrial environment and how it can be triggered, amplified, and transferred by chemists, are challenging problems with clear scientific and technological potentials for science and society.[3] Chirality constitutes a unifying feature of the living world and is a prime driving force for molecular selection and genetic evolution.[4,5]

The importance for studying the role of chirality in nonlinear chemical networks has been convincingly demonstrated.[6] Spontaneous mirror symmetry breaking (SMSB) can occur in enantioselective autocatalytic processes and in reactions of enantiomeric discrimination on surfaces or in crystals. SMSB takes place in thermodynamic scenarios and is highly sensitive to physical chiral polarizations; thus, weak natural chiral fields can transform stochastic chiral outcomes of SMSB into deterministic outcomes of a fixed chiral sign.[7] The underlying mechanisms and constraints have only begun to be understood recently within the framework of nonlinear nonequilibrium

thermodynamics. The fundamental question about SMSB leading to biological homochirality has flourished into a topic of intense interdisciplinary research, which has spurred experimental and theoretical efforts enabling dissymmetric molecular phenomena to be mapped at all length scales and at all levels of complexity.[8]

A fundamental point is whether the emergence of chirality is merely a simple consequence of symmetry breaking, or is, in fact, the triggering factor for the emergence of complex abiotic chemical networks. This distinguishes biological homochirality as being much more than merely an advantageous mechanism for the exchange of information between biological compartments and systems. According to this it is a reasonable speculation to consider chirality a necessary element to drive chemical evolution toward the emergence of complex chemical systems working cooperatively and in a complementary fashion,[9,10] i.e., the primordial factor that allows the transition from abiotic chemical evolution to systems with the capacity for Darwinian evolution.[11,12] The topic of chemical evolution provides a vast arena where the search for SMSB reactions can be developed. This is the case, for example, of the topics of bistability, oscillatory phenomena and the origin of life,[13,14] in relation to biological homochirality.[15,16] The emergence of nonequilibrium stationary states (NESS), distinct from those of the thermodynamic branch, appear naturally in the case of enantioselective autocatalysis. This topic is not only related to fundamental research but is also directed toward research on the preparation of compartmentalized biological active systems and so-called artificial cells. There is potential interest in the study of the emergence of instructed polymers from nucleotide synthesis and their polymerization by template mechanisms toward nucleic acids[17,18] and from the replicator peptide synthesis[19] in compartmentalized open systems.

The spontaneous emergence of enantiomeric biases in achiral-to-chiral transformations is of growing importance in the fields of supramolecular chemistry, nanoscience, pharmacology, asymmetric synthesis, solid-state chemistry and in the search for the origins of biomolecular homochirality.[20] Among the vast number of chemists working on the topic of chirality, only relatively few researchers are aware of the recent advances made or have access to the broad expertise that allows for developing the challenging methodologies required for the study of chirality in complex chemical systems. The concept of spontaneous deracemization has been coined by Gol'danskii and Kuz'min[21] and has been reviewed by Amabilino and Kellogg[22] in 2011 on the basis of being a kinetically controlled process, since that time it has not been given the survey and wider interpretation it deserves. This is a genuinely multidisciplinary field of inquiry which represents both a major scientific challenge as well as a prime opportunity for technological exploitation and that requires interaction between synthetic and physical experimentalists and theoreticians.

This review will be of particular interest for the communities of organic, inorganic, and physical chemists who are interested in achiral-to-chiral transformations and for all researchers acquainted with conglomerates, spontaneous asymmetric synthesis, cryptochirality, chiral fields and forces, chirality at the nanoscale, mirror-symmetry breaking processes, nonstochastic behavior, autocatalysis, nonlinear chemical dynamics, and the origin of biological homochirality.

We embrace some generally disconnected scientific domains ranging from the distinguishability in particle physics to the enantiomerism phenomenon in molecular chemistry, emphasiz-

ing both the experimental and the kinetic modeling aspects. This review deals with how racemic biases in chemical transformations arise by the action of physical forces, or even in the absence of any chiral polarization by the homo and heterochiral interactions between the enantiomeric reaction products (enantioselective autocatalysis). We give a critical survey of these spontaneous achiral-to-chiral transformations, mainly related to conglomerate crystallization, Viedma deracemization, supramolecular aggregation of achiral units, and the Soai reaction. In order to promote all avenues of investigation in this rich domain, a list of easily accessible achiral organic or inorganic compounds giving rise to conglomerate crystals that could be used to illustrate these transformations is provided from databases.

This review therefore summarizes recent efforts made toward understanding how chirality originates and operates on and modifies the properties of large molecular systems and complex networks that mimic biological responses and life-like transformations. We aim to make some of the more relevant advances available to the reader.

2. CHIRAL POLARIZATION FORCES

2.1. Physical Forces

Enantiomers are chemical species whose structures show parity breaking due to the set of symmetry elements that determine their molecular architectures. Therefore, and because of fundamental symmetry arguments, they can be chemically recognized only through the interaction with other chiral species, referred to as chiral recognition. Physical forces giving rise to parity breaking can interact differently with the enantiomers, which may lead to enantiomer resolutions and/or, when acting upon a chemical reaction paths, to kinetic enantiomer resolutions as well as asymmetric synthesis.

The question of the possible influence of chiral physical forces and fields on the spontaneous formation of enantiomerically enriched products from achiral precursors, i.e., the feasibility of an absolute asymmetric synthesis,[23,24] has been a founding cornerstone in the search for the origins of biological homochirality.[25,26]

2.1.1. True and False Chirality: Probing the Influence of Magnetic Fields. Early suppositions by Pasteur that static magnetic fields, which actually can induce optical rotation in achiral materials through the Faraday effect, could also provoke enantiomeric imbalances in chemical equilibrium systems were refuted by Barron's concept of *true and false chirality*.[27−31] According to these fundamental symmetry arguments, false chirality is exhibited by a system that changes the chiral sign under space inversion (P) but also under time reversal (T), i.e., by motion reversal combined with spatial rotation (R_π). On the other hand, true chirality is given by systems that exist in two distinct enantiomeric states that are interconverted by space inversion but not by time reversal (combined with any proper spatial rotation). The concept of false vs true chirality can be illustrated by a spinning cone (Figure 1).

It is apparent that chiral polarization at thermodynamic equilibrium, i.e., the change of the free energy degeneracy between enantiomers, can only be induced by true chiral forces, for instance by certain combinations of magnetic and electric fields, for example, a magnetic field that is orientated parallel to the propagation direction of a light beam. Barron's considerations have been experimentally corroborated by the pioneering work of Rikken and Raupach[32] demonstrating enantiose-
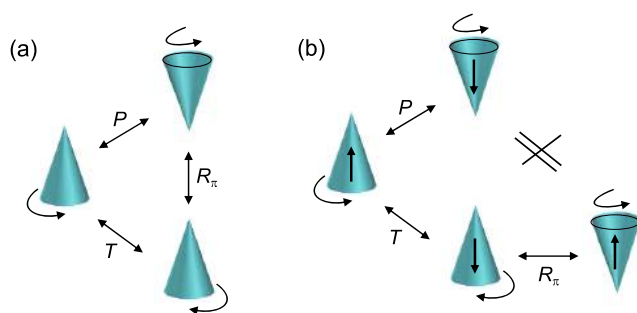
Figure 1. (a) False chirality: breaks both P and T, i.e., space inversion (P) or time reversal (T) of a *stationary* spinning cone results in the enantiomer of the starting cone. (b) True chirality: breaks parity P but not T, i.e., space inversion (P) of a *translating* spinning cone results in a different system as does time reversal (T). The vertical arrows denote the translations of the spinning cones. Adapted from ref 27. Copyright 1986 American Chemical Society.

lective magnetochiral anisotropy in a photochemical reaction using a chiral Cr(III)tris-oxalato system. In fact, an unpolarized laser beam propagating parallel to a static magnetic field generated a small enantiomeric excess (*ee*) of about 10^{-2} % of one Cr(III) tris-oxalato enantiomer over the other, depending on the strength of the magnetic field and *vice versa* of its optical antipode, by reversing the magnetic field direction, while the system was shown to be racemic in the absence of any magnetic field.

However, it is worth noting that the Rikken's experiment corresponds to a final photostationary state, i.e., a stable NESS that is clearly far from equilibrium conditions. It is mostly emphasized that the symmetry arguments of true chiral physical forces strictly apply only for systems of reversible reactions at thermodynamic equilibrium, but in fact they also apply to the NESS of the so-called thermodynamic branch. The thermodynamic branch is composed by those stable stationary states arising when the system is taken far from equilibrium before the entropy currents of the system lead to its destabilization (see also section 9).

Some turmoil was spread in 1994 by the report of absolute asymmetric synthesis triggered by a static magnetic field alone during in the synthesis of chiral aryl ethanols starting from prochiral ketones. However, as soon after it was revealed,[33] this report turned out to be clear scientific fraud. Interestingly, and according to Barron,[34] a magnetic field alone, i.e., a falsely chiral influence, as also recently discussed for extremely large magnetic fields in an astrophysical setting,[35] may indeed induce enantiomeric imbalances, even if the prochiral reactant molecules are randomly oriented. However, an influence of false chirality is only possible for kinetically controlled reaction outputs, because under falsely chiral influences the enantiomers remain strictly degenerate and only the breakdown of the reaction path microreversibility occurs.[34] Furthermore, such chemical reactions must comply with some subtle constraints such as the alignment of a particular prochiral species with the magnetic field at the very beginning of the reaction process, i.e., falsely chiral influences, which may show a breakdown of microscopic reversibility at the reaction path and because of this will yield very low *ee* values. Kinetically controlled absolute asymmetric synthesis would only be achieved through the coupling with an appropriate amplification process such as enantiospecific autocatalysis.

The former proposal, i.e., the possible influence of false chirality in kinetically controlled processes, was experimentally addressed by the Scolaro group[36] in the formation of chiral J-aggregate particles of the achiral 5-phenyl-10,15,20-tris(4-sulfonatophenyl)porphyrin (TPPS₃). During the nucleation phase, the nanoassemblies are oriented in a magnetic field (magnetic levitation inside a 16 or 25 T electromagnet) in a rotating sample (15 Hz). The combination of the magnetic field with rotation is a false chirality influence and the amplification of the kinetically obtained *ee* through the breakdown of micro-reversibility is then amplified by the autocatalytic growth of the particles.[29] It was shown that the chiral flow alone due to the rotation of the samples was not sufficient to direct the supramolecular chirality but that the alignment of the aggregates by the magnetic field was an essential requisite. It was also observed that the direction of the magnetic field did not influence the chiral sign of the aggregates. On the other hand, clockwise or counterclockwise rotation of the samples resulted in the opposite chirality signs of the growing aggregates. However, the results of this experiment may be also explained by the influence of a shear effect by the vortex originating in the rotating sample. The vortex is a true chiral force and the chiral induction of such hydrodynamic shear forces has been already reported, see below. This effect could appear as unlikely for a chemist, because it is an up-to-down chiral polarization exerted by the simple hydrodynamic shear of stirring. However, it may occur when the supramolecular particles are oriented and aligned in flow at the nucleation stage of their formation, and clearly the first effect of the magnetic field is to produce such an orientation. Therefore, the result can be either explained by the effect of false or true chirality.

Banerjee-Ghosh et al.[37] demonstrated that the interaction of *L*- or *D*-polyalanine based oligomers with a perpendicularly orientated ferromagnetic cobalt film covered with 5 nm of gold behaves enantioselectively. The authors found that in one magnetization direction, the *L*-polyalanine adsorption rate for the *L*-enantiomers was around eight times faster than for the *D*-enantiomers, while after switching the magnetization direction, the adsorption rate for the *D*-enantiomers was around 4 times faster than for their antipodes. The differences in the adsorption kinetics were attributed to different purification levels of the enantiomers. The authors rationalize their observations in terms of a chirality-induced spin selectivity since the charge redistribution in chiral molecules goes along with an enantiospecific spin polarization with spin up or down that finally results in the differently observed adsorption rates for the *L*- and *D*-enantiomers on the ferromagnetic surface. In accordance to the former suppositions, this effect was transitory and only persisted as long as the system remained under kinetic control, i.e., it vanished as the system was approaching equilibrium, which supports the kinetic effect of false chirality to break down the microreversibility.

An intriguing case, where the enantiomeric imbalance was retained due to stabilizing noncovalent interactions, was reported by Tassinari et al.[38] (Figure 2). Again, using a ferromagnetic substrate surface (Ni(120 nm)/Au(10 nm)), the authors observed the enantioselective crystallization of initially racemic mixtures of asparagine, glutamic acid, and threonine that are known to crystallize as conglomerates. The racemic mixtures were crystallized from aqueous solution on the ferromagnetic surfaces in the presence of two magnets, one pointing north and the other south, located at different sites of the surface. A clear enantioselective effect has been recorded in
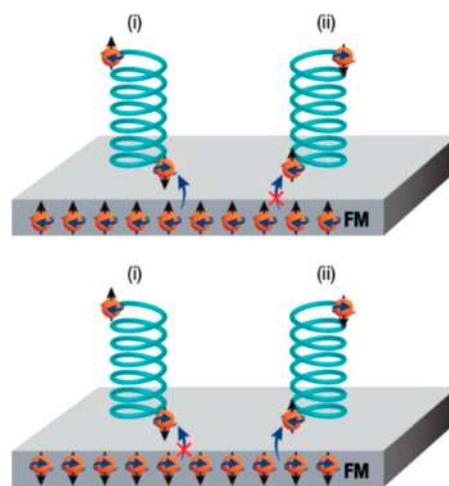
Figure 2. Enantioseparation by crystallization using magnetic substrates by chirality-induced spin selectivity (CISS). Spin-polarized ferromagnet interacts favorably with enantiomers that have antiparallel spin. Consequently, the longer residence time of one amino acid enantiomer on the surface, owing to its stronger interaction, increases its probability of crystallization. The left and right green helices indicate the handedness of each process. Reproduced from ref 38. Copyright 2019 The Royal Society of Chemistry under Creative Commons Attribution 3.0 Unported License https://creativecommons.org/licenses/by/3.0/.

the formation of an excess of *d*- or *l*-crystals, depending on the direction of the magnetization orientation. The authors emphasize that the reported results cannot arise by a chiral effect of the magnetic field but rather because of the so-called chiral induced spin selectivity (CISS) (see below) that aligns spins within the ferromagnets and that the findings may provide a novel method for resolving enantiomers by crystallization.

2.1.2. Natural Chiral Physical Forces and Fields: From Parity Violation to Vortex Motion. Nature's dissymmetry became clear with the universal charge-parity symmetry violation discovered in 1957 during the *β*-decay,[39] where the generation of primarily left-spinning over right-spinning electrons has been observed. Symmetry violation of time-reversal (T) and of charge parity (CP) is recovered in the CPT symmetry, i.e., in the "space-inverted anti-world made of antimatter".[30] Although time symmetry violation distinguishes between true and false chirality, there is another effect, more appealing for chemists, namely, that perfect degeneracy between enantiomers exists when it is compared with the corresponding antimatter structure composed by the negative nucleus and positrons. In fact, enantiomers show a very tiny energy difference due to CP violation, called parity violating energy difference (PVED). Parity violation and the resulting PVED between enantiomers is still playing a prominent role in the proposal of abiotic models for the emergence of biomolecular homochirality.[40,41] However, being of high interest from a physical point of view for the emergence of chirality itself, probably it does not play any role in the output of racemic biases in chemical reactions (see sections 2.2.1 and 7.1). The tiny PVED is predicted to be roughly in the range of $10^{-15}-10^{-11}$ J/mol between matter/matter enantiomers as existing in our world,[40] while theoretically true enantiomers with exactly the same energies would be composed of matter/antimatter pairs.[30] Although extremely small, this chiral influence is universal and acting consistently in the same direction everywhere and continuously[42] but is too tiny to expect any effect either in a

change of the equilibrium constant or in the asymmetric induction of racemization. However, Kondepudi and Nelson[7] demonstrated by computer simulations that such a difference could be sufficient, when added to the fluctuations, to drive deterministically the stochastic chiral sign bifurcation toward scalemic (near to homochiral) NESS's that may appear in enantioselective autocatalytic reaction networks in open systems (see section 9). Moreover, the natural enantiomer found in terrestrial biochemistry was shown, in many PVED calculations, to be more stable than its unnatural optical antipode.[43]

Vester and Ulbricht proposed the hypothesis that circularly polarized Bremsstrahlung (a truly chiral force) generated by chiral asymmetric β-radiation produced in the β-decay phenomenon could lead to an asymmetric photolysis of chiral molecules.[44] Many experiments have been undertaken to corroborate this hypothesis, reviewed by Bonner,[45−47] with sometimes disputed results. Furthermore, β-decay experiments yield polarized electrons that can interact with a chiral substrate through chiral recognition. Aqueous sodium chlorate evaporating solutions when subjected to left-handed electrons from a ^{90}Sr source led to an asymmetric crystal distribution favoring D-crystals being obtained. Conversely, exposure to energetic right-handed positrons from a ^{22}Na source yielded mainly L-crystals. It was concluded that the spin polarized energetic particles are able to produce chiral nucleating sites and that the chirality of the radiation was correlated with the chirality of the forming crystals.[48,49]

Electrons and neutrons showing an angular moment are chiral helicoidal elementary particles, and therefore they represent a true chiral force.[25,26] However, only reports on polarized electrons are chemically significant. The first report, but of low significance for applied chemistry, is the kinetically controlled enantioselective decomposition of the leucine enantiomers.[50] Dreiling and Gay[51] reported chiral sensitivity in the molecular breakup of chiral bromocamphor molecules during the irradiation with low-energy longitudinally spin-polarized electrons. The authors claimed that their findings stand for a demonstration of the viability of the hypothesis of Vester and Ulbricht. On the other hand, Rosenberg[52] recently stated that still no conclusive evidence has been found to support either the Vester−Ulbricht hypothesis or the direct interaction of high-energy spin-polarized electrons, with respect to inducing stereoselective degradation or absolute asymmetric synthesis that could be relevant to induce enantiomeric imbalances in, for instance, prebiotic scenarios. However, the significant point is that in the interaction of oriented chiral compounds with polarized electrons, the chiral recognition effect is manifested upon the electron: the chiral compound acts as a spin filter (CISS) and the moving electrons which have been injected into the substance show a preferred spin.[53−55] This depends in addition to the handedness of the compound on the direction of injection. The effect can be considered to show no chemical interest and not to be related to the origin of life topic. However, it could be of paramount importance to explain the efficiency of electron transport in metalloproteins acting in biological redox processes.

With respect to experimental approaches to detect parity-violating energy differences, efforts and an experimental outline by the use of high-resolution laser spectroscopy have been reported by a consortium of research groups proposing measurements on enantiomers of CHClFI.[56] Analyzing energy shifts in Mössbauer spectra, rather high energy differences of about 10^{-5} J/mol have been reported for L- and D-enantiomers

of the $Fe(phen)_3Sb_2(C_4H_2O_6)_2 \cdot 8H_2O$ complexes.[57] These elevated values arise in the order of magnitude of the theoretical Z^6 scaling law for the PVED, predicting that it increases in proportion to the sixth power of the atomic number Z of the element near the asymmetric center. However, as emphasized by Quack and Stohner,[58] these results do not represent a specific demonstration of molecular parity violation.

Basically, a direct impact on a chemical reaction generating a determinate ee due to parity violation appears to be out of reach so far and may perhaps never be realized. This is mainly due to inherent stochastic fluctuations that greatly overshadow any supposed PVED influence in a chemical process. Hawbaker and Blackmond[41] have recently evaluated a potential PVED effect on the autocatalytic and asymmetry amplifying Soai reaction[59,60] (see section 7). Based on experimental sensitivity measurements and subsequent theoretical calculations, the authors concluded that the energy difference between enantiomers needed to drive the highly sensitive Soai reaction into a specific direction would have to lie at minimum in the range of $10^{-8}-10^{-7}$ kJ/mol, hence several orders of magnitude higher than best predictions for the expected PVED values in the range of $10^{-18}-10^{-14}$ kJ/mol.[40]

A clear case scenario for the generation of directed enantiomeric imbalances by physical effects is given by the influence of circularly polarized light (CPL) as a truly chiral force.[2,61,62] Since the observation of strong infrared circular polarization in star-formation regions by Bailey and co-workers,[63] the influence of asymmetry induction by CPL has fueled the debate about the origins of biomolecular homochirality and its possible extra-terrestrial foundations.[64,65] The impact of left- or right-handed CPL on a chemical system can be manifold: by preferential photolysis, by asymmetric isomerization, or by preferential photosynthesis, exhaustively reviewed in the past.[46,66,67]

After the generation of amino acids by ultraviolet irradiation of interstellar ice analogues had been experimentally revealed,[68] Marcellus et al. reported the ee generation of up to 1.34% for (^{13}C)-alanine during the irradiation of artificial interstellar ice samples with ultraviolet CPL from a synchrotron source.[69] The authors considered their results as comparable with some L excesses of amino acids measured in meteorites,[70,71] stressing the role of possible asymmetric astrophysical forces at the origin of biomolecular homochirality. Recently, the possible impact of magnetic circular dichroism (MCD) of UV sunlight resulting in circular polarization anisotropy has been calculated to yield an ee of around 10^{-13} for glyceraldehyde,[72] i.e., a chiral molecule of prebiotic interest that has been shown before as relevant for extraterrestrial scenarios of sugar formation.[73−75] Without any doubt, the substantial gap between these rather small ee values and the high enantiopurity observed in Earth's biosphere trigger the search for new chemical scenarios leading to high racemic biases as for instance given by enantioselective autocatalysis in open systems (see sections 7 and 9).

Experimental examples of such new absolute asymmetric synthesis scenarios, and of the chiral selection effect exerted by true chiral forces, are the following: Kawasaki et al.[76] showed that the Soai reaction is sufficiently sensitive to amplify the impact of CPL, by the photolysis of a racemic pyrimidyl alkanol subjected to enantioselective autocatalysis yielding R- or as S-pyrimidyl alkanols with ee > 99%, according to the handedness of the CPL irradiation. Noorduin et al.[77] demonstrated another possible pathway of asymmetric amplification upon CPL irradiation combined with abrasive grinding, i.e., based on the so-called Viedma deracemization[78,79] (see section 2.2.4). The

authors showed that left- or right-handed CPL irradiation of 70 h of a racemic solid−liquid mixture of N-(2-methylbenzylidene)-phenylglycine amide and subsequent abrasive grinding during 5 days led to the generation of completely single-handed S- or R- conglomerate crystals of this amino acid derivate, respectively. In the absence of CPL irradiation, the authors noted the unexpected formation of exclusively R-N-(2-methylbenzylidene)-phenylglycine amide crystals, which was attributed to the presence of chiral impurities[80] (see section 2.2.3).

Yeom et al.[81] reported the generation of ee values higher than 30% through the direct CPL irradiation of racemic cadmium telluride nanoparticle dispersions yielding right- or left-handed twisted nanoribbons according to the handedness of the CPL, while the irradiation of linearly polarized light, or dark conditions, resulted in straight nanoribbons. The chirality induction and modulation of polymers by CPL has been reviewed recently.[82] In further regards to self-assembled structures, lately homochiral supramolecular structures were obtained from achiral triarylamine derivatives,[83] achiral porphyrin derivatives through irradiation with CPL (Figure 3),[84] as well as the irradiation of gold salt solutions that result in
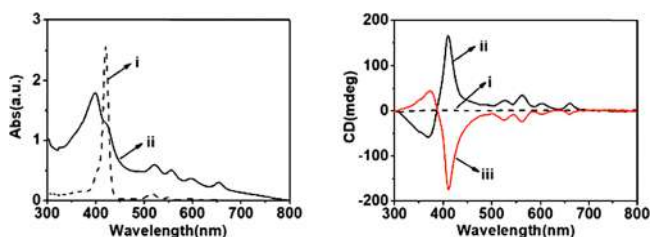
Figure 3. Supramolecular self-assembly of an achiral porphyrin precursor (TPPDA) triggered by left- or right handed CPL. Left: UV spectra of solution (i) and gel (ii). Right: CD spectra after light irradiation, (i) nonpolarized, (ii) right-CPL, and (iii) left-CPL. The light irradiation is directed to the initial stage of self-assembly, while the chiral transfer and the gelation process generating a helical packing of the TTPDA is occurring in the absence of CPL. Reproduced with permission from ref 84. Copyright 2019 The Royal Society of Chemistry.

the formation of gold nanoparticles and their assembly into chiral nanostructures.[85] Furthermore, significant chiral biases of around ee = 25% were observed in the static crystallization of sodium chlorate when the nucleation was induced by the optical

trapping of Ag nanoparticles during irradiation with right- or left-handed laser CPL.[86]

Mechanical shear in laminar flows, and vortices in particular, are true chiral forces. However, it was supposed that these do not have any influence on chemical processes, being unable to act upon chemical species. For this it would be necessary to break down the Brownian regime toward the orientation/alignment of the molecules, in order that they can detect the hydrodynamic shear forces. Therefore, similar effects were proposed and even experimentally observed by enantiomeric discrimination only for supersonic molecular jet scenarios.[87−89] Nevertheless, vortex motion was shown by Ribó et al.[90] to break chiral symmetry by clockwise or counterclockwise stirring during the formation of J-aggregates of achiral 5-phenyl-10,15,20-tris(4-sulfonatophenyl)-porphyrin (TPPS$_3$) as the starting material for a probability of around 85% (see also the reviews by Ribó and co-workers).[91,92] In unstirred solution, a stochastic distribution for left-handed and right-handed aggregates was found over a series of 23 experiments, where each individual experiment resulted with a clear preference for one or the other chirality sign. Later reports of the same group yielded similar results.[93,94] Skeptical reactions to these results have not taken into account that the size and shape of supramolecular objects, compared to molecules, do not exclude the possibility to be oriented in a laminar flow. However, these concerns were, in part, founded because of the difficulties to assess optical chirality in solutions showing linear anisotropies (see section 8). The issue is now settled because reports by other groups confirm the up-to-down chirality transfer of hydrodynamic shear forces as a true chiral influence. For example, as given by the effect of the fluid circle directions on the chiral sign in the preparation of Langmuir films (Figure 4), the competition between the chiral influence of the vortex motion (up-to-down effect) with that of a chiral dopant (down-to up effect) and recent reports using microvortices by Liu and Sun.[95,96] From all this, it may be stated that the conditions for the detection of this asymmetric effect of a chiral mechanical force are

(a) Systems showing enantioselective autocatalysis, such as the cooperative process that occurs in the formation of racemic conglomerates (crystals or mesophases) from achiral compounds at the first nucleation stages. Therefore, we are speaking of the effect of a chiral polarization at a bifurcation point,[7] otherwise the intensity of the chiral force is too weak for a typical asymmetric induction.

(b) The nuclei must be able to be aligned and oriented in the chiral laminar flow (velocity gradients in the 3D sections,
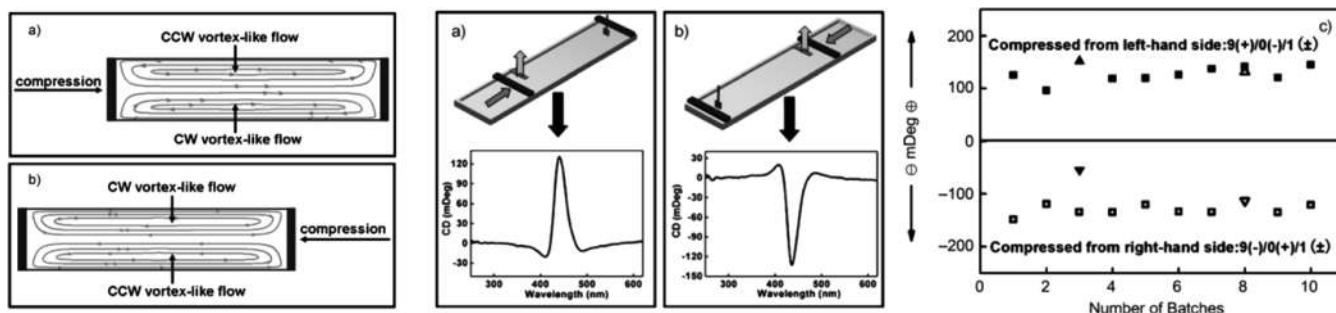
Figure 4. Formation of macroscopic chirality of interfacially organized achiral porphyrin assemblies. Vortex-like flows generated during unilateral compression determine the chiral sign (CD measurements) of the corresponding specific domains of the Langmuir layer. Samples formulated around the left-hand- and right-hand-side of the Langmuir barrier display opposite macroscopic chiralities. Reproduced with permission from ref 97. Copyright 2011 Wiley-VCH.
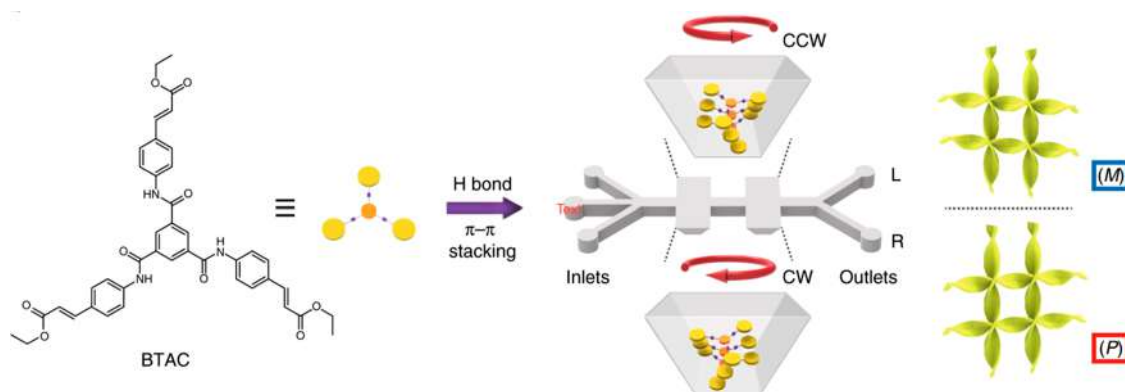
Figure 5. Chiral supramolecular gels of achiral BTAC are fastly generated within asymmetric microchambers in a microfluidic reactor.[69] The laminar chiral microvortices exert a viscous shear force leading to symmetry breaking and chiral selection in the self-assembled system. The chirality is correlated with the rotation sense of microvortices. Reproduced from ref 96. Copyright 2020 Springer Nature under Creative Commons Attribution 4.0 International License https://creativecommons.org/licenses/by/4.0/.

i.e., a true chiral force) otherwise the shear effect would be nonenantioselective.

(c) Orientation/alignment, i.e., the breakdown of the Brownian regime, depending on the size and shape of the particle and of the velocity gradients of the flow. However, the nucleation size at the bifurcation is determined by the nucleation process stage where autocatalysis occurs. Therefore, for very small particles, large hydrodynamic gradients are necessary, and these cannot be achieved before the formation of turbulent chaotic mixing which, as well the Brownian regime, can only lead to the racemate. Notice that in crystallizations from achiral compounds to racemic conglomerates, the round particle shapes of the nucleation clusters are not adequate for an orientation in the flow.

The recent reports of the Liu and Sun groups[95,96] not only support previous results in the topic but point toward further research directions in this field. Specifically, they point toward the study and design of the system hydrodynamics in open systems in order to achieve stronger chiral gradients (Figure 5) compared to the rough chiral hydrodynamics of the rotatory evaporator[98] used in the first publication in the topic.[90]

The effect of vortex motion on chiral self-assembly by the effect on the orientation in the flow of long shaped particles is twice. First, the orientation decreases rotational diffusion so that some growth paths become diffusion controlled leading to the selective growth of the particles. Second, the oriented particles may detect the shear forces leading to the selective growth of one enantiomorph. The speculations on this[92] where suggested by some experimental reports[99,100] and this double effect of vortices fits well in the justification of dramatic reports on the effect of stirring vortices.[101−103]

Hence the possible influences of physical forces to induce directed chiral polarizations in chemical systems are manifold. A number of the more recent developments reviewed here allow for a clearer view of what were formerly assessed as fact and fiction.[25] The physical forces presented here are resumed in Table 1 with respect to the symmetry arguments of true or false chirality.

In the view of the present review article, progress is noteworthy with respect to applied physical forces on processes under kinetic control. These are given by reported enantioselective behavior on ferromagnetic surfaces due to spin-polarization[37,38] as well as the vortex-induced chiral sign

Table 1. Compilation of Physical Forces That, Except for Static Magnetic Fields and Parity Violation, Were Reported to Induce Asymmetric Polarizations in Conclusive Experimental Settings and Their Respective Symmetry Arguments Regarding True or False Chirality

physical force	symmetry argument	ref (system)
static magnetic field	false	ref 27 (negative results in solution chemistry)
magneto-chiral dichroism	true	ref 32 (aligned magnetic field to light beam in solution chemistry)
chirality-induced spin selectivity	true	ref 53 (DNA material)
polarized β-radiation	true	refs 44 and 50 (enantioselective destruction of amino acid racemates)
parity violation	true	ref 43 (theoretical calculations only)
circularly polarized light	true	ref 104 (asymmetric synthesis)
vortex motion	true	ref 90 (self-assembly of porphyrin J-aggregates)

induction in open flow systems.[96] Along with these observations, reaction systems giving rise to asymmetric amplification processes have been shown to enhance the usually small *ee* values obtained through physical forces as for instance, during the CPL irradiation of the Soai reaction,[76] as well as during the Viedma deracemization[78] or the self-assembly of nanostructures.[83−85] Hence it became evident that from the coupling between chiral physical forces and appropriate amplification processes, such as enantiospecific autocatalysis, high *ee* values can be achieved, which could play a prominent role for possible scenarios in the abiotic origin of biomolecular homochirality. On the other hand, parity violation, as one prominent and frequently debated candidate for directed asymmetry induction in respect to such scenarios, has to be taken as with skepticism at the current state.[41]

2.2. Chiral Recognition and Chemical Enantioselective Transformations

2.2.1. Concept of Racemate.
Chirality in chemical curricula is studied as a part of stereochemistry,[105] and the teaching of chemical chirality is based on the description of molecular structures. However, molecular chirality is determined only by the breaking of the parity operation of structures that have an identical geometrical description. It is important to recall that the linkage between chirality and stereochemistry

arose from an historical accident when van't Hoff was studying the substitution of tetravalent C atoms: stereochemistry should be considered independently from optical activity and dissymmetry issues. Furthermore, structural chirality has macroscopic consequences depending on the enantiomeric ratio of the samples. The IUPAC rules of nomenclature already reflect this when defining a "*racemate*" as any equimolar mixture of a pair of enantiomers,[106] and discourage the usage of the term "*racemic mixture*". The "racemate" definition includes racemic conglomerates, racemic crystals,[107] liquids, and solutions. The definition of racemate as a noun, and not as an adjective of mixture, is not accidental because, in this way, the term refers to the behavior of sets of a large number of molecules. Racemates have a greater stability than any scalemic mixture of their enantiomers when there is a direct or indirect transformation path between them (racemization). This means that the racemate represents a trough of free energy in the racemization reaction. Despite the exceedingly small PVED (see section 2.1), enantiomers are energetically degenerate molecules in the absence of any chiral recognition between them. In this respect, the racemization reaction 1 is not different from reaction 2 in which the final achiral product B is obtained from A through two degenerate reaction paths. Only a Maxwell demon could distinguish which B molecules are coming from one path or the other:

$$D \rightleftharpoons A \rightleftharpoons L \qquad (1)$$

$$B \rightleftharpoons A \rightleftharpoons B \qquad (2)$$

The stability of the racemate, compared to those of scalemic and homochiral compositions, is a consequence of the indistinguishability of both enantiomers and the entropy derived from the law of large numbers.[108] As stated by Mills,[109] an exactly equal distribution of enantiomers will practically never occur. It is therefore of interest to know the average degree of chiral bias that can be expected for any given number of molecules. From a statistical point of view, it is expected that 50% of the racemic samples of n molecules will exhibit an *ee* higher than $0.6743/n^{1/2}$. For instance, one-half of a large set of 1 L femtomolar (10^{-15} M) racemic samples are expected to exhibit an *ee* > 0.0027%. As the number of molecules considered increases, the statistical *ee* becomes progressively negligible. Enantiomers, in the absence of any chiral recognition effect exerted either by a chiral physical force, a chiral surrounding, a chiral species, or through mutual recognition by homochiral or heterochiral interactions, are thermodynamically indistinguishable species. This implies that in the absence of any chiral polarization or any direct or indirect racemization path, any composition of a mixture of enantiomers showing ideal behavior, i.e., in the absence of mutual chiral recognition, is degenerate in energy. The paradox of the distinguishability/indistinguishability of enantiomers was already discussed by van't Hoff in the application of the Phase Rule for racemic conglomerates.[110] In agreement with the experimental results, the rule is only obeyed under the consideration that the enantiomorphs are thermodynamically identical species. In the transition from the liquid to the solid phase, solid-to-solid interactions are not present in the saturated solution at equilibrium or very near to equilibrium.[111,112] However, when there is mutual chiral recognition between enantiomorphs, as evidenced in binary melting diagrams or in the Viedma experiment, both enantiomorphs indeed become different thermodynamic phases. The role of chiral recognition as a necessary factor to reveal the existence of chirality is, in fact, a question older than modern chemistry, which has been

explicitly treated in metaphysics in the discussion of the nature of physical space.[113]

2.2.2. Asymmetric Induction vs Spontaneous Mirror Symmetry Breaking (SMSB): When the Racemate Becomes Unstable. The discovery of asymmetric catalysis has led to the development of asymmetric synthesis as perhaps the most important topic in the organic chemistry of the 20th century.[114,115] The strategy of asymmetric synthesis is based on the transformation of a prochiral substrate into a chiral product through a diastereomeric interaction with an enantiopure reagent or catalyst. For single chemical reactions, this can be readily rationalized using reaction coordinate diagrams within the formalism of the transition-state theory: the final *ee* depends on the energy differences between diastereoisomeric catalytic transition states. Under thermodynamic control, this corresponds to the free energy difference between reaction products, while under kinetic control the same is true for the difference between activation energies (Figure 6).[116] Whatever the
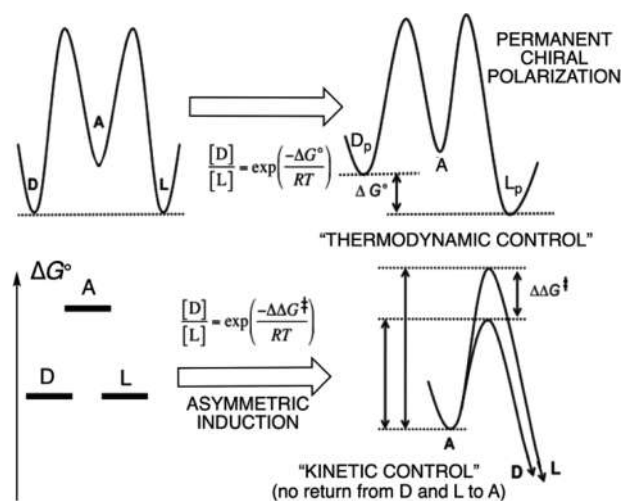
Figure 6. Asymmetric induction effects of a chiral polarization upon the relative stability of the enantiomers (thermodynamic control) or upon the enantiomeric activated complexes (kinetic control), see ref 116.

conditions, kinetic or thermodynamic control, the same difference in energies yields the same enantiomeric ratio. However, from a practical point of view, the strategy of acting on intermediate and activated complexes of the enantioselective transformation (i.e., kinetic control) is far more common in organic synthesis.[117]

The effect of a chiral physical natural force on an otherwise symmetric synthesis, so as to obtain a bias from the expected racemate composition, has been referred to as "absolute asymmetric synthesis".[23] The interest of absolute asymmetric synthesis lies in the question of how biological homochirality could emerge, despite the fact that chiral species should be available only as racemates. Recently, absolute asymmetric synthesis has been used as an analogous term for SMSB,[116] probably because the theoretical models of reaction networks able to lead to SMSB, even in absence of any chiral natural force, have been supported by a few but dramatic experimental reports.[78,118] Therefore, as we will see in what follows, reaction coordinate diagrams of equilibrium thermodynamics alone are not sufficient to explain absolute asymmetric synthesis or SMSB.

SMSB occurs when the racemate becomes unstable while scalemic mixtures are stable. Obviously, this can only occur in

systems which are unable to achieve thermodynamic equilibrium, i.e., in systems open to matter and/or energy exchange. Therefore, the final outcome corresponds to nonequilibrium stationary-states (NESS), and the whole system behavior can be explained within the framework of physicochemical dissipative systems, as first established by the Brussels school.[119,120] However, the high entropy production rates needed to achieve SMSB seem to be accessible only for enantioselective autocatalysis having highly nonlinear kinetic dependencies on the enantiomer concentrations.[121,122] From a synthetic point of view, reactions showing enantioselective autocatalysis are still very rare. Nonetheless, enantiospecificity and autocatalysis are implicit in the crucial chemical transformations implied in the functional biological polymers which allow the transfer of information between one generation and the next.

The simplest theoretical model of enantioselective autocatalysis can be written in the following way:

$$A + nD \rightarrow (n+1)D \quad A + nL \rightarrow (n+1)L \qquad (3)$$
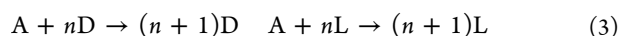
where A is an achiral compound and D and L are two enantiomers, and where n indicates the order of autocatalysis: $n = 1$ corresponds to first order (usually referred to as quadratic autocatalysis when thinking in terms of molecularity) and $n = 2$ to second order (cubic autocatalysis). Notice that enantioselective autocatalyis (3) corresponds, in fact, to a homochiral reproduction of each enantiomer. Owing to the exceptionality of reactions showing a molecular order higher than bimolecular, SMSB reaction systems can usually be obtained from the coupling of various kinetic networks including enantio- and diastereochiral reactions or other nonlinear effects, for example, precipitation of some species.[123] This may lead to nonlinear kinetic dynamics corresponding to autocatalysis of an apparent order higher than unity and even to noninteger values of n.

A pioneering theoretical kinetic mechanism for enantioselective autocatalysis had been proposed by F. C. Frank[124] already in 1953. The so-called Frank model comprises enantioselective quadratic autocatalysis ($n = 1$), equivalent to (3), coupled to the mutual inhibition between the enantiomers, D + L → P. Hence, an achiral reactant A is converted into the chiral products D and L, while the system is kept open by the continuous supply of A. The purpose of the mutual inhibition is to increase the ee by racemate elimination.[125] The loss of matter during the elimination is replenished by its own reproduction through the autocatalytic network. These conditions lead to the dominance of the enantiomer originally in slight excess and to the disappearance of its antipode, i.e., the difference between the enantiomer concentrations diverges exponentially during the evolution until a virtually homochiral stage is reached.

There are two possible scenarios where scalemic outcomes may arise from enantioselective autocatalysis in the absence of any chiral polarization: (a) by kinetic control, which is possible in closed systems for highly exergonic irreversible reactions, and (b) by stabilization of the whole system in the framework of out-of-equilibrium energy dissipative reversible systems. Both cases require the nonlinear kinetic dependences of (3). This means that they can occur only in reaction networks having either direct or indirect enantioselective autocatalysis.[121] Furthermore, the scenario (b) requires open systems with matter exchange or closed systems having inhomogeneous distributions of matter and energy.

Simulations of the first scenario (a) using stochastic kinetic methods have been reported.[126] The initial stochastic outputs of the very first transformations can differ in a significant way from the racemic composition and, because of the absence of backward reaction paths, autocatalysis progresses faster for the enantiomer in excess. High reaction rates and low initial enantiomer concentrations increase the probability of obtaining scalemic mixtures, but the racemate, or near to racemic compositions, can occur as well. The comparison among a large number of simulations shows different possibilities for the distribution of ee values: a Gaussian distribution centered at $ee = 0$ or, when the rate and the initial fluctuation are very high, even two symmetric distributions (bimodal) centered at $ee \pm 100\%$.[127] In the case of the crystallization of an achiral compound into chiral crystals, some stages of nucleation and crystal growth occurring in supersaturated solutions are autocatalytic, in contrast to the linear mechanisms between crystal and solution acting at the thermodynamic equilibrium of the final saturated solution. This approach may explain the experimental results which are based on the crystallization of a first (or few) Adam crystal(s), where autocatalytic growth transfers the initial handedness toward visible crystals.[128]

The method of enantiomer resolution through kinetically controlled growth of racemic conglomerates, such as in Havinga's seminal report,[129] is the basis of the so-called preferential crystallization method of enantiomer resolution.[105,107] Also, the addition of chiral additives, which inhibit the growth of a specific enantiomer, may lead to enantiomeric preferential crystallization (Scheme 1).[130,131]

Scheme 1. Rule of Reversal[a]
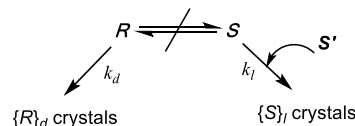
[a]S′ represents an impurity with preference for the surface of the S crystals; in the absence of S′, $k_d = k_l$, in the presence of S′, $k_d \gg k_l$.

The second scenario (b) is SMSB and occurs when the reaction output corresponding to the racemate is unstable and spontaneously deracemizes stochastically to one of the two enantiomeric stable scalemic states. This requires an enantioselective autocatalytic reaction network showing high nonlinearity and working in an open system. Notice that in a suitably intertwined reaction network of coupled reactions, even with an autocatalytic reaction of order $n = 1$, higher orders of autocatalysis in the whole system may be achieved. In this case, it is clear that the transition-state formalism, commonly used in traditional synthetic chemistry, does nothing to aid in discovering any mechanistic explanation of the origin of the SMSB, since the secret of SMSB does not lie in a specific step but within the coupling of several steps. Obviously, once they do couple, studying and identifying each single reaction of the coupled network is still of interest. Note also that there are different experimental ways to achieve the conditions of an open thermodynamic system leading to a "forced system" which will be kept out of equilibrium. For instance, by selectively giving energy to only one of the reactions of the coupled system either photochemically[132] or by chemical coupling with an external reaction.[122] The behavior of these systems belongs to the thermodynamic framework developed by the Brussels school for the description of chemical reactions in energy dissipative systems.[119,120] In such open systems at low levels of entropy production, determined by the affinity values and the absolute

reaction rates,[133,134] the NESS is the racemate. Racemic NESSs correspond to the so-called thermodynamic branch. Beyond a critical value of the entropy production, achieved by the increase in the affinity and the absolute rates, the thermodynamic branch becomes unstable and new NESSs may appear (Figure 7).[134]
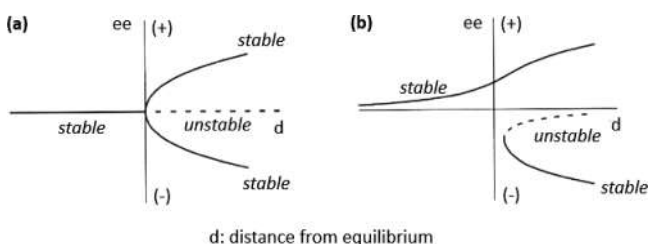
Figure 7. Pitchfork bifurcation from the thermodynamic branch to the flow branches (a) in the absence of any chiral bias, one or the other branch must be chosen stochastically and (b) deterministic output in the presence of a chiral polarization (e.g., cryptochirality, see section 2.2.3).

In the conditions in which the racemic NESS is destabilized, any statistical compositional fluctuation, such as those described by Mills in the previous section, will suffice to tip the system to one of the two enantiomeric scalemic NESS. Notice, however, that these fluctuations are not the driving force for the transition from racemic to scalemic but the cause that makes the instability of the racemic NESS evident. This irreversible move from the racemic NESS to the scalemic NESS is the consequence of a physical potential that stems from the balance between the entropy flows with the surroundings and the entropy production from the chemical reaction network. This physical potential is not directly derived from the thermodynamic state functions.[119,120,134,135] Note that this corresponds to the kinetic dynamic model of Pross,[136] which is a valuable factual and intuitive description of the stationary states of chemical networks in living systems. However, that model fails to explain the phenomenon from the point of view of modern thermodynamics and so maintains the conceptual gap, between synthetic chemistry and chemical physics, which must be bridged in order to understand the origin of SMSB.

In processes which show SMSB, the numerical simulations always lead to a scalemic output and the racemate does not occur. In well controlled experiments, a sharp bimodal distribution should be the signature of such a scenario, although depending on the experimental conditions, it may be occasionally difficult to obtain clear-cut results (Figure 8).

True SMSB is probably not yet significant in relation to applied synthesis, because it is limited to some enantioselective autocatalyses, but it is of paramount importance in order to understand the emergence of biological homochirality.

First order autocatalysis, as for example in (3) with $n = 1$, is not able to lead SMSB in the absence of any suitable coupled reaction network[121,116] or some nonlinear effect (e.g., selective precipitation).[123] However, it is able to move the system away from the racemate in a closed system involving only irreversible steps. Furthermore, reversible reaction networks are able to yield SMSB but in an open system. In closed systems, they may show a temporary scalemic window before reaching a racemate at thermodynamic equilibrium. The more exergonic (i.e., the less reversible) the enantioselective transformation is, the wider are these time windows showing racemic biases. Note that this is the case of the Soai reaction: this time window is large, because
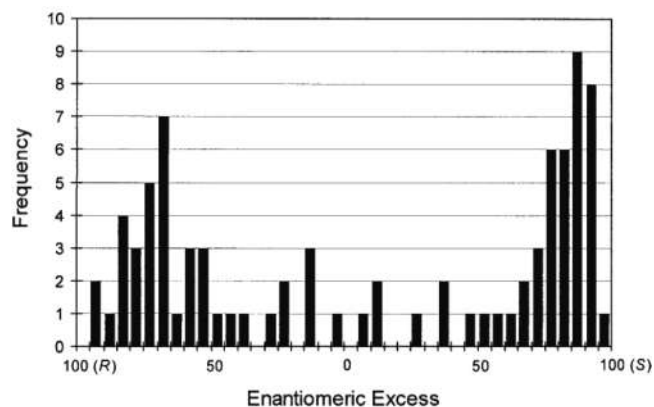
Figure 8. Histogram of the absolute configuration and the *ee* of pyrimidyl alkanol in the Soai reaction in the presence of achiral silica gel. Reproduced with permission from ref 137. Copyright 2006 John Wiley and Sons.

racemization in the closed system is extremely low. The reaction is quenched before any racemization.

2.2.3. Cryptochirality: Chiral Sign Selection vs Asymmetric Inductions. As shown in Figure 7a, in SMSB processes, the racemate becomes an unstable NESS beyond a critical point. The fluctuations, which are unavoidable in real systems,[138] tip the system toward one or the other stable scalemic NESS. The stochastic nature of fluctuations determines the stochastic distribution of chiral signs between experiments. Chiral polarizations acting on the unstable racemic NESS easily convert the stochastic fluctuations into deterministic ones; as a consequence, the evolution of the racemate becomes deterministic toward one (or the other) of the two stable-degenerate scalemic NESSs (Figure 7b). Note that this effect should be described as a chiral sign selection, and not as a chiral induction, because a nonracemic outcome is also obtained even in the absence of any chiral polarization. These chiral sign selections are achieved by chiral polarizations which are several orders of magnitude lower than those necessary for common asymmetric inductions.[139]

In our opinion, cryptochirality could be defined as a wider concept according to the following:

(a) Structural cryptochirality, as coined by Mislow,[140] is related to chiral compounds with optical activity well below the experimental detection level, as a consequence of a very small perturbation from a symmetric condition. The first experimental evidence of structural cryptochirality was reported in Soai's reaction through the chiral polarization exerted at the bifurcation of SMSB. The tested cryptochiral compounds in the Soai reaction have been chiral primary alcohols due to deuterium substitution,[141] chiral isotopomer arising from oxygen isotope substitution,[142] saturated quaternary and tertiary hydrocarbons,[143] or carbon (^{12}C/^{13}C) isotopomers.[144] These cryptochiral compounds are the result of sophisticated enantioselective synthesis, sometimes involving chiral HPLC racemic resolutions. With the exception of the saturated hydrocarbons, their *ee* values (often >95%) were determined by NMR analysis of diasteoisomeric derivatives.

(b) On the other hand, a second facet of the effect of very small amounts of optically active impurities has been related to cryptochirality by Hakansson,[145] Viedma,[146]

and then by Cuccia[147,148] in the context of symmetry breaking. The term "environmental cryptochirality" corresponds to solutions that contain optically active impurities, present in concentrations well below the level of detection. These chiral impurities are assumed to originate from the biological world.[149,150] The impact of such chiral contaminants has been recognized by several authors in the framework of chiral crystallizations[151−153] and chiral supramolecular porphyrin aggregation.[36,150] It has been shown that the effect of chiral impurities competes with the attrition intensity during Viedma deracemization of the N-(2-methylbenzylidine) phenyl-glycine amide.[154] Both enantiomers are harvested with equal probability when the attrition intensity becomes stronger and stronger. In fact, the impact of tiny but unknown chiral polarizations, on apparently unstable racemic NESS, has been observed in various reaction systems and a number of case studies are given in the later sections 4.2, 5.5, 5.6, 5.7.1, 6.1.2, and 7.1 of this review.

(c) Even a third facet is the statistical impossibility to achieve perfect ideal racemates. According to Mills' formula[109] (see section 2.2.1), a pure racemate always shows a tiny *ee*.[24,155] However, this effect is expected to be practically negligible, since a significant *ee* occurs only in very small samples which are not able to transform a SMSB from stochastic to deterministic.[151]

Whether "structural", i.e., related to molecular solutions (as in paragraph a) or "environmental", i.e., related to the material/sample (as in paragraph b), cryptochirality refers to minute perturbations of the symmetry which remain undetected in classical physical measurements or enantioselective reactions, but which are amplified in the bifurcation of these polarized SMSBs. Both aspects of cryptochirality remain within the framework of the Curie principle: "the symmetries of the causes are to be found in the effects".

2.2.4. Viedma Deracemization. In 2005, Viedma observed SMSB for a racemic population of NaClO₃ crystals, which is an achiral compound in solution and forms a conglomerate in the solid state. The deracemization was achieved by stirred grinding of the saturated aqueous crystal slurry in the presence of glass beads.[78] It turned out that under these conditions, the two populations of left-handed and right-handed crystals cannot coexist in the same suspension: one of the populations disappears to the benefit of the other. The formation of only one crystal enantiomeric form, which is random for (+) or (−) crystals in each individual experiment, seems to be an inescapable outcome in the Viedma deracemization. The method has been expanded to other compounds through two major requirements: (1) the compound has to crystallize as a conglomerate, and (2) it either needs to be efficiently racemized in the solution phase[156] or has to become achiral through redissolution (Figure 9).

The deracemization of NaClO₃ and other substances undergoing attrition induced deracemization presented the apparent paradox[111] of how could mechanical grinding of a racemic crystal population in saturated solution drive a system to crystal deracemization as the final and stable stationary state, while on the other hand the racemate should be expected to be the more stable mixture of enantiomers? The first clue to solving this paradox was given by the observation that the Viedma deracemization clearly exhibits autocatalytic character, as evidenced by the experimentally observed sigmoidal kinetic evolution as, for example, shown in Figure 10.
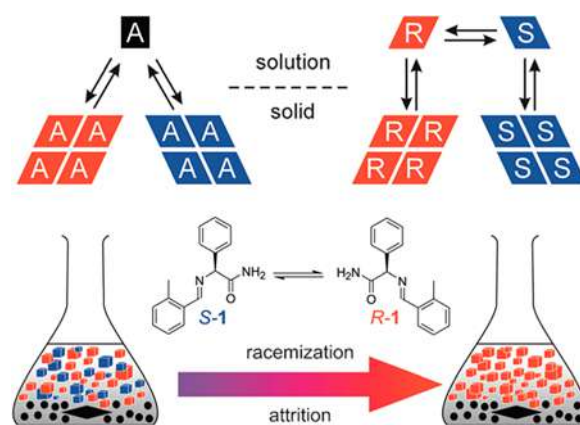
Figure 9. Viedma deracemization of a racemic conglomerate crystal mixture of an achiral (left top, e.g., case of NaClO₃) or racemizing compound in solution (right top). Bottom: the imine of 2-methyl-benzaldehyde and phenylglycinamide forms a conglomerate in the solid phase but racemizes rapidly in methanolic alkaline solution. Mechanical grinding or spatio/temporal temperature gradients of solutions of crystals in contact with their saturated solution may lead to homochiral crystal mixtures. Reproduced from ref 80 Copyright 2008 American Chemical Society.
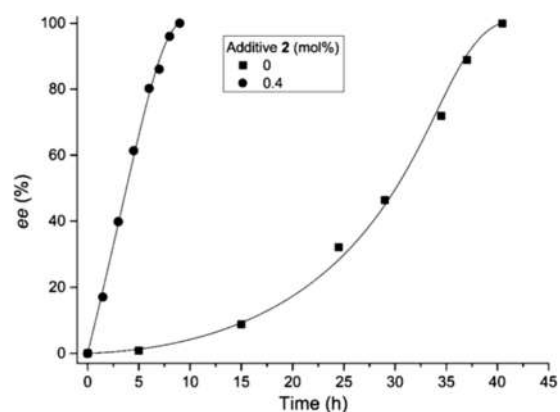
Figure 10. Kinetic evolution of the *ee* in a Viedma-type experiment on racemizing N-(2-methylbenzylidine) phenylglycine amide showing the sigmoidal exponential growth as a signature of autocatalysis and the accelerating effect through a chiral additive. Reproduced from ref 157. Copyright 2008 American Chemical Society.

As a consequence of this autocatalytic behavior, typical Viedma-like deracemizations yield around ±100% *ee*. However, kinetically controlled common crystallizations in stagnant solutions and at specific experimental conditions may also show similar results[158,159] due to the kinetically controlled growth of a first Adam crystal.[129,158,159] It was shown in earlier reports,[160−162] as well as for recent cases of commercial crystals,[112,163] that conglomerate crystallizations of achiral compounds often yield biases from the racemic composition. Small variance bimodal distributions should be expected for a SMSB process (section 9). However, some reports on Viedma-like experiments describe different frequency distributions (see Figure 11), which may be caused by an insufficient control of some experimental parameters. Hence a third peak around the racemic composition could be the signature of an experimentally limited Viedma approach.

Prior to the Viedma report[78] are the seminal works of Kondepudi on the achievement of practically homochiral outcomes under strong stirring conditions.[165−167] These results
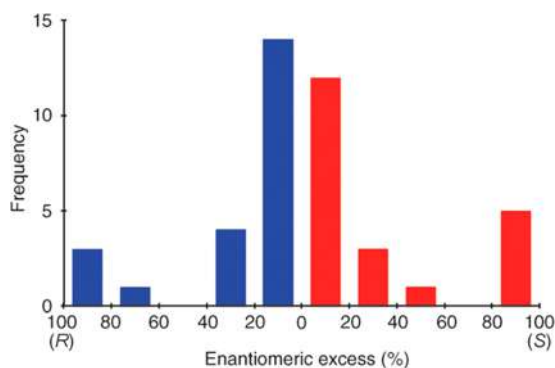
Figure 11. Histogram showing a trimodal frequency distribution of the *ee* in the *α*-imino nitrile Strecker synthesis coupled to the deracemization of the racemic conglomerate. The complex coupling of the synthetic reaction generating the deracemization in the solution and the cyclic crystallization explain the trimodal distribution instead of the expected bimodal one. This observation should be attributed to an insufficient experimental control of the system, which is composed of reaction, racemization in the solution, and deracemization of a racemic conglomerate. Reproduced with permission from ref 164 Copyright 2019 The Royal Society of Chemistry.

were first interpreted as an unprecedented way to increase the kinetic control of the first Adam crystal by secondary nucleation.[168−171] However, when improved by attrition, the birth of new crystals, in the presence of parent crystals by secondary nucleation, cannot lead to a differential growth between the enantiomers when the crystal growth is strictly from monomer to cluster. Only the acceleration toward the saturated solution condition will occur and, despite being autocatalytic,[172] is unable to select between enantiomers but can maintain the initial *ee* values of the primordial formation of the Adam crystals. Therefore, Ostwald ripening was proposed as an additional mechanism to increase the *ee* values.[169] Viedma deracemizations that show similar deracemization outputs cannot be described as a kinetically controlled process, because they show permanent recycling.[173] Grinding fragmentation or attrition of the big crystals cause this recycling, owing to the higher solubility of the newborn smaller crystals (Gibbs−Thomson effect).[174] The final outcome is a NESS. From this point of view, it can be considered

as analogous to the so-called "thermodynamically controlled" synthesis,[111] because the system is closed to matter but open to energy exchange. However, since it is autocatalytic, it gives rise to a scalemic output, while a nonautocatalytic one gives rise to a racemate.

Ostwald ripening arguments have been also proposed as part of Viedma mechanisms.[79,169,175] However, any ripening process is supported in a near to equilibrium framework, and Viedma deracemization clearly belongs to a very far from equilibrium scenario. Moreover, in Viedma procedures, grinding must act preferentially on the bigger crystals, while Ostwald ripening promotes the growth of bigger crystals at the expense of the smaller ones.[176] In this respect, a recent Viedma communication pointed out that, when the starting racemic mixture of crystals is composed by big crystals of one enantiomorph and small crystals of the other one, the final homochiral chiral sign corresponds to that of the initially smaller crystals,[177] which stands in contrast to any ripening or curing-like mechanism. We believe that the "ripening" term obscures the real character of the mechanisms acting in far from equilibrium irreversible scenarios, and therefore, the term "Viedma deracemization" is preferentially used in this review.

Nowadays, it is widely believed that the Viedma and Kondepudi experiments belong to the same type of scenario. However, the important question is about the mechanisms of crystal growth that yield the high-order autocatalytic dynamics leading to stable scalemic NESSs and which destabilize the racemic NESS.[8,178] In the search for nonclassical crystal growth mechanisms that could lead to autocatalysis, the existence of nanoparticles and microcrystals has been observed in supersaturated solutions before the formation of visible crystals. At this stage, the small cluster sizes could justify cluster-to-cluster growth that exhibits autocatalytic dynamics not present in classical crystallization theory.[179−181] It was experimentally shown for $NaClO_3$ at high supersaturation, very near to the point where the abrupt formation of crystals occurs, that the solution is already nonracemic as demonstrated by taking samples in different regions (see Figure 12).[182,183] This means that autocatalysis is occurring before the formation of visible crystals. Simulations and models on this are discussed in section 9.2.
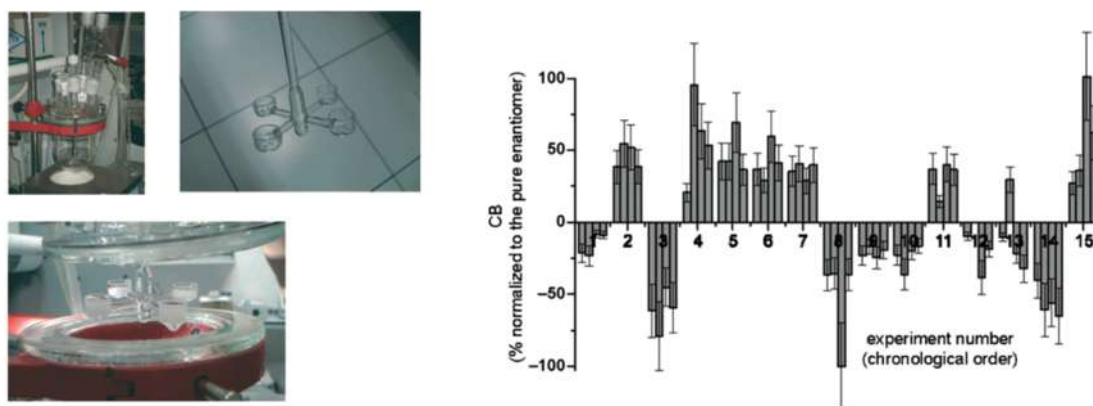
Figure 12. Left: (a) Reactor for the crystallization experiments in boiling solutions of $NaClO_3$. (b) Detail of the glass rod equipped with four cups, which allows simultaneous collection of four samples from the solution. (c) Cups with the crystallized solution. The boiling solution was slowly concentrated by water distillation. The cups were extracted from the solution at high supersaturation, before precipitation occurs. Right: the histogram on the right shows the circular birefringence values of the harvested crystals at the four cups (see section 8). Results show that SMSB has already occurred before the precipitation, an explosionlike process under these experimental conditions. Reproduced with permission from ref 183. Copyright 2011 Wiley-VCH.

The far from equilibrium scenario of selective energy leading to recycling from crystals to clusters can be achieved not only by mechanical grinding but also, for example, by temperature cycles/gradients or in photostationary states (see below). A further indication for SMSB, in an energy dissipative scenario, is the effect of small concentrations of chiral compounds or cryptochiral influences[80,146] able to convert the stochastic distribution of chiral signs between successive experiments into a deterministic sign (see sections 2.2.3 and 9). However, the chiral polarization must be effective at the bifurcation point, and this implies specific experimental conditions.

After the original Viedma publication appeared, the number of reports dealing with this deracemization has increased so fast that an in-depth exhaustive review is probably not an easy accomplishment, but previous mini-reviews on this topic have already been published.[79,184] While all experimental reports are sound, reliable, and reproducible, the interpretations of the underlying mechanisms, such as commented above, have not been (see section 9). The present review only aims to give a general perspective of the range of applications and scenarios of the Viedma phenomenon, together with a critical revision of the mechanisms proposed to explain it. The reports in relation to the Viedma phenomenon can be classified into following four categories:

(a) Deracemization of achiral compounds other than $NaClO_3$. Here the class of inorganic compounds is reduced to $NaBrO_3$,[146] that has only been barely studied because of its low solubility, compared to that of $NaClO_3$, which reduces the range of experimental conditions in which deracemization occurs.[185] Ethylenediammonium sulfate was the first compound other than $NaClO_3$ and $NaBrO_3$ for which the phenomenon was detected.[147,186] To the best of our knowledge, all commercial achiral organic compounds forming racemic conglomerates tested under Viedma grinding conditions have led to deracemization and no negative results have been reported. Viedma deracemization has also been reported to occur in the case of tetrahedral and octahedral chiral transition metals[187,188] and also in the self-assembly of supramolecular structures formed by achiral coordination ligands and metal cations.[189]

(b) Reports expanding the method to chiral compounds crystallizing as racemic conglomerates by the coupling with a deracemization of the chiral compounds in solution (Figure 9). The theoretical proposal that Viedma deracemization should also occur in the case of enantiomorphic phases of chiral compounds racemizing in solution,[111] by virtue of the equivalence in the number of compounds and phases with the case of $NaClO_3$, was soon experimentally reported.[80] The number of reports of this group on the topic is large and, being initially supported by a thesis work,[190] has then been expanded to the deracemization of chiral drugs[80,191−195] or their intermediates. BINOL is a case of particular interest to the asymmetric autocatalysis community.[196] Today, Viedma deracemization can be considered a practical method for the deracemization of some organic compounds.[197] Reports on the improvement of grinding equipment for this purpose have also been published.[198] Probably, if Viedma deracemization in applied chemistry is not found more frequently in the published reports, it is because the method may belong to industrial know-how processes,[199]

with no patent needed, substituting the classical preferential enantiomer crystallization followed by racemization of the remaining enantiomer and recycling.[200,201] However, the application of Viedma deracemization as a method for absolute asymmetric resolution needs considerable efforts. The success for expanding Viedma deracemization to chiral racemates crystallizing as racemic conglomerates hinges on the feasibility to racemize the solution monomer in addition to the compatibility of the racemization process with the deracemization of the crystals. Also the first step of the identification of the crystals belonging to one of the 65 Sohncke groups and despite the help that CBD offers[202] generally requires previous X-ray diffraction studies. In this respect, there is a lack of studies of phase diagrams for knowing the range of concentrations or type of solvent where the racemic conglomerate is the stable form: a recent report constitutes an example of this type of necessary preliminary work.[203] Most of the reported works are based on α-amino acid derivatives by converting them into imines,[204] which then by tautomerization racemize the H atom bearing a stereogenic center (example of Figure 9). However, other racemization procedures, through a redox reaction,[205] thermal sigmatropic rearrangement,[206] atropisomerism,[207] and photoisomerization[208,209] are being reported. The efficiency of the deracemization and its compatibility in the Viedma procedure have been used for direct absolute asymmetric synthesis and one-pot procedures.[164,210,211] In summary, Viedma deracemization is on the way to become part of retrosynthetic analysis for absolute asymmetric synthesis.[212,213]

(c) Experimental reports improving the mechanical crystal attrition[153,214−220] or using other types of selective energy, for example, temperature gradients and temperature cycles,[182,183,221−224] ultrasound,[225] and photochemical catalysis.[226] These reports indicate that supersaturation for the bigger crystals is a necessary condition to generate permanent recycling through the initial crystal growth stages. An interesting point, when comparing deracemization in solid crystals with that in liquids and solutions, is that when the grinding procedure is halted, racemization does not take place because there is no longer chiral recognition between the solid enantiomorphs. At saturation, fluctuations in the crystal solubilization/crystallization occur only between the solution monomers and the solid enantiomorphs, and this means that there are no chemical potential interactions between both enantiomorphs and therefore no chemical potential interactions. As a consequence, there is no thermodynamic difference between both enantiomorphs[111] in conditions of saturation and in the absence of any chiral force. A racemic conglomerate or any scalemic mixture of their enantiomorphs are thermodynamically indistinguishable in the absence of any additional chiral polarization.[227] When the grinding and stirring are halted, there is a time-lapse during which the crystals tend to achieve similar sizes (similar surface free energies) by Ostwald ripening,[228] but having deracemization already taken place, size changes due to ripening occur between homochiral crystals. It is worth noting that the solubility difference between crystal sizes (Gibbs−Thomson effect) is only significant between tiny,

just visible crystals.[229,230] In this respect, it is experimentally well-known that the signature of a successful Viedma experiment is when thorough grinding leads to tiny crystals, generally milkylike suspensions: gentle crystal fragmentation does not lead easily to deracemization.[176]

(d) Theoretical models and simulations in order to explain the deracemization process.[173,178,231−235] Many experimental reports have been published with the objective to prove or to rule out hypotheses concerning the mechanism of the deracemization (see section 9).[79,182,183,236−241] The discussion on the mechanisms of the Viedma deracemization may not be settled yet. However, any assumption should be made within the framework of a bifurcation scenario in an energy dissipative system, composed by a high-order autocatalytic network that may lead to stable scalemic or homochiral stationary states (see section 9).

Efforts to explain the Viedma deracemization exemplify how difficult it is to define the crucial points in interdisciplinary issues. In this respect, it is worth remarking:

(i) *Irreversible thermodynamics in energy dissipative scenarios.* The permanent recycling of monomeric achiral species through crystal growth stages, as a consequence of the mechanical energy of grinding, is taken selectively by only some species of the system. Under these conditions, the system does not involve a homogeneous energy distribution and belongs to a nonequilibrium system, therefore a final stationary state must be a stable NESS. Further, deracemization can be only explained in a bifurcation scenario generated by high-order autocatalytic dynamics.

(ii) *Chemical chirality is not only structural molecular dissymmetry.* Deracemizations, not only in the Viedma deracemization, concern the whole sample dissymmetry (see section 3.3). Structural chirality and enantiomorphic reaction coordinate hypersurfaces describe the set of internal reactions but do not take into account the coupling with the surroundings. Therefore, when changing interactions with the surroundings, the same reaction mechanism may lead either to a racemic NESS or to a scalemic NESS.

The interest to reach a scientific consensus on the Viedma deracemization is probably because it occurs in the self-assembly of achiral compounds in mesophases (section 6.3)[92] and may also be operative in polymerizations (section 9),[242] and is described by a reaction network quite different to that of the Frank model. The latter requires a heterochiral reaction between enantiomers in order to increase the effective order of the otherwise first-order enantioselective autocatalysis. However, in the Viedma deracemization, the mechanisms for increasing the order of autocatalytic dynamics are homochiral. This is surely an important distinction with respect to the emergence of functional and instructed polymers in chemical evolution,[18] where heterochiral interactions not only decrease synthetic efficiency but represent an inhibitory obstacle for the emergence of evolutionary capabilities.[243,244]

3. SPACE AND POINT GROUPS SUPPORTING CHEMICAL CHIRALITY

The chirality of the sample of a substance and, in consequence, the physical properties of a material arises from the symmetry

elements of this material, in relation to the symmetry elements of the interacting electromagnetic radiation (optical rotatory dispersion and circular dichroism).[245] Even chemical recognition and the enantioselectivity of chemical reactions may be analyzed by considering the symmetry of the physical interactions between the molecules.

As established by P. Curie,[245,246] asymmetric phenomena arise from the interaction of the symmetry of a physical force with the dissymmetry of matter or the contrary; it is dissymmetry that creates dissymmetry. Dissymmetry is defined by the absence of a specific set of symmetry elements. Chemical chirality is a specific case of Curie dissymmetry, first proposed by Pasteur,[247] as the absence of any S_n symmetry element (improper rotation) in the smaller unit retaining the symmetry characteristics of the material. This creates the structural phenomenon of enantiomerism.

The parity breaking of these structures can be revealed when the sample interacts with physical fields of a given symmetry or with other chemical structures which share the same dissymmetry. In other words, the handedness of a sample of a substance can only be unveiled from a chiral recognition, either physical, i.e., from an interacting electromagnetic radiation (optical rotatory dispersion and circular dichroism) or chemical, i.e., from the interaction of another chiral substance. In the case of isotropic homogeneous samples, chemists recognize chirality through the point group of the molecular structure once the dynamic transformations that the molecule shows in the liquid, solution, or gas phases are taken into account. The chirality in crystals, and the physical properties derived from this, can be correlated with the symmetry elements of the crystals as expressed by their point and space group classification.

3.1. Space Groups Supporting Chiral Crystals

There are three basic points to take into account with respect to the chirality of crystals:

(a) Pure enantiomers can crystallize only as chiral crystals.

(b) Achiral molecules, although mostly yielding achiral crystals, sometimes crystallize as chiral crystals. This is a consequence of the freezing to a defined static chiral structure that, when in solution, conformational and vibrational dynamics racemize.

(c) Racemate solutions of enantiomeric molecules give rise to two types of crystals, racemic crystals, where both enantiomers are present in the same crystal and racemic conglomerates, where the two enantiomers are separated into different chiral crystals. In this latter case, chiral resolution can occur through homochiral crystallization.[248]

The chirality in crystals, and the physical properties derived from this, can be correlated with their symmetry elements as expressed by their point and space group classification. In order to understand the differences between racemic and chiral crystals, it is essential that certain fundamental concepts related to symmetry transformations are defined.

All transformations under which a geometrical object is invariant are known as the symmetry group of this object. Symmetry operations of the first kind, such as rotations, translations, and screw rotations preserve the orientation of the object. On the contrary, if an operation of the first kind is followed by an improper rotation, the orientation of the object is reversed. For instance, reflections, glide reflections, inversions, and improper rotations are operations of the second kind.[249]

Table 2. Notations for the 32 Point Groups in Both Schoenflies (S) and Hermann−Mauguin (H−M) Systems[a]

notations/ crystal systems	triclinic		monoclinic		orthorhombic		tetragonal		trigonal		hexagonal		cubic	
S H−M	C_1	1	C_2	2	D_2	222	C_4	4	C_3	3	C_6	6	T	23
	$C_i = S_2$	−1	$C_s = S_i$	m	C_{2v}	2mm	S_4	−4	S_6	−3	C_{3h}	−6	T_h	m3
			C_{2h}	2/m	D_{2h}	mmm	C_{4h}	4/m	D_3	32	C_{6h}	6/m	O	432
							D_4	422	D_{3d}	−3m	D_6	622	T_d	−43m
							C_{4v}	4mm	T_h	m3	C_{6v}	6mm	O_h	m -3m
							D_{2d}	−42m			D_{3h}	−62m		
							D_{4h}	4/mmm			D_{6h}	6/mmm		
Bravais lattice	P		P, C		P, C, I, F		P, I		P, R		P		P, I, F	

[a]C_n (for cyclic) indicates the n-fold rotation axis, C_{nh} and C_{nv} add a reflection either perpendicular (horizontal) or containing the axis of rotation (vertical). S_{2n} (for Spiegel, German for mirror) contains a $2n$-fold rotation-reflection axis. D_n (for dihedral or two-sided) has an n-fold rotation axis plus n twofold axes perpendicular to that axis. D_{nh} and D_{nd} have in addition n vertical mirror planes either containing one or passing between two twofold axes. T (the chiral tetrahedral group) has the rotation axes of a tetrahedron (three 2-fold axes and four 3-fold axes). T_d and T_h include mirror planes, either diagonal or horizontal. O (the chiral octahedral group) has the rotation axes of an octahedron or cube (three 4-fold axes, four 3-fold axes, and six diagonal 2-fold axes), O_h includes horizontal mirror planes and, as a consequence, vertical mirror planes, inversion center, and improper rotation elements. In the Hermann−Mauguin system, a slash "/" indicates that a mirror plane is perpendicular to a n-fold symmetry axis; moreover, the various classes of mirror planes (m) must be distinguished as σ_v (vertical,) σ_h (horizontal). and σ_d (diagonal). The sign "−" indicates that there is an inversion center. Note that there are 11 point-group types (1, 2, 222, 4, 422, 3, 32, 6, 622, 23, and 432) that do not contain a mirror plane or inversion center.
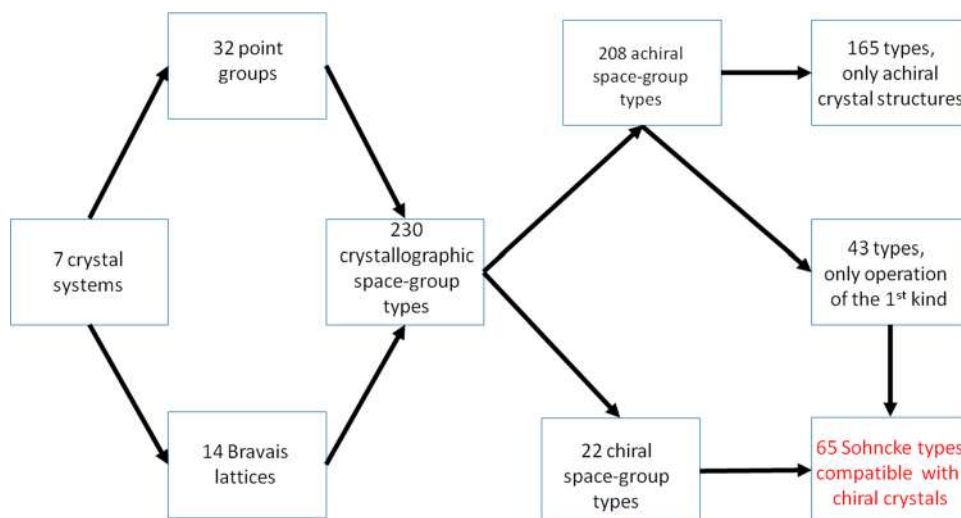
Figure 13. From crystal systems to Sohncke space group types.

3.1.1. Crystallographic Point Groups. A point group is a set of symmetry operations which leave at least one point fixed while the whole object is reoriented. The three symmetry elements, reflection plane, rotation axis, and roto-inversion axis can be combined in 32 crystallographic point groups (Table 2).

A crystal is made up of a periodic arrangement of one or more atoms repeated at each lattice point; therefore, in addition to the point groups, translation symmetry operations must also be taken into account. A crystal looks the same after being translated by one unit-cell. Considering the seven crystal systems (triclinic, monoclinic, orthorhombic, tetragonal, trigonal, hexagonal, and cubic and the different centering types of the lattice points in the unit cell), there are only 14 different ways, according to their translational repetition modes to describe all crystal classes (the Bravais lattices). Altogether, the symmetry operations of the point groups plus those of the Bravais lattices give rise to the whole set of possible crystallographic space groups. There are 448 ways to combine the 32 crystallographic point groups with the 14 Bravais lattices. Degeneracies reduces the total number of combinations to 230.

They form the so-called Sohncke group, which is compatible with the chiral crystal structure.[250] Figure 13 shows the various relationships between the crystal systems and the Sohncke space-group types.

3.1.2. Sohncke Space Groups. The 230 space group types are a rigorously complete set of descriptions of crystal symmetries in 3D space. Among them, there are 22 chiral space-group types (11 enantiomorphic pairs) and 43 which contain only symmetry operations of the first kind (i.e., no inversion or mirror symmetry). In the international Hermann−Mauguin notation, four symbols are used to specify the group properties of each of the 230 space groups. The first symbol is a single letter P, I, R, F, A, B, or C which refers to the Bravais lattice type; P = primitive, I = body-centered, R = rhombohedral, F = face-centered, A = base-centered (A-face only), B = base-centered (B-face only), C = base-centered (C-face only). The remaining symbols refer to the point group of the crystal to completely specify the symmetries along each crystal axis.[251] Subscripts indicate the degree of translation of rotary translation along screw axes. The angle of rotation ($360°/n$) is given by the

Table 3. List of the 65 Sohncke Space Group Types[a]

triclinic	monoclinic	orthorhombic	tetragonal	trigonal	hexagonal	cubic
$P1$	$P2$, $P2_1$	$P222$, $P222_1$, $P2_12_12$, $P2_12_12_1$	$P4$, $P4_2$, **$P4_1$-$P4_3$**, $P422$, $P42_12$, **$P4_122$-$P4_322$**, $P4_222$, $P4_22_12$, **$P4_12_12$-$P4_32_12$**	$P3$, **$P3_1$-$P3_2$**, $P312$, $P321$, **$P3_112$-$P3_212$**, **$P3_121$-P3_221$**	$P6$, $P6_3$, **$P6_1$-$P6_5$**, **$P6_2$-$P6_4$**, $P622$, $P6_322$, **$P6_122$-$P6_522$**, **$P6_222$-$P6_422$**	$P23$, $P2_13$, $P432$, $P4_232$, **$P4_132$-$P4_332$**
	C2	$C222$, $C222_1$				
		$F222$				$F23$, $F432$, $F4_132$
		$I222$, $I2_12_12_1$	$I4$, $I4_1$, $I422$, $I4_122$			$I23$, $I2_13$, $I432$, $I4_132$
				$R3$, $R32$		

[a]From top to bottom are primitive (P), base-centered (C-face), face-centered (F), body-centered (I), and rhombohedral (R).
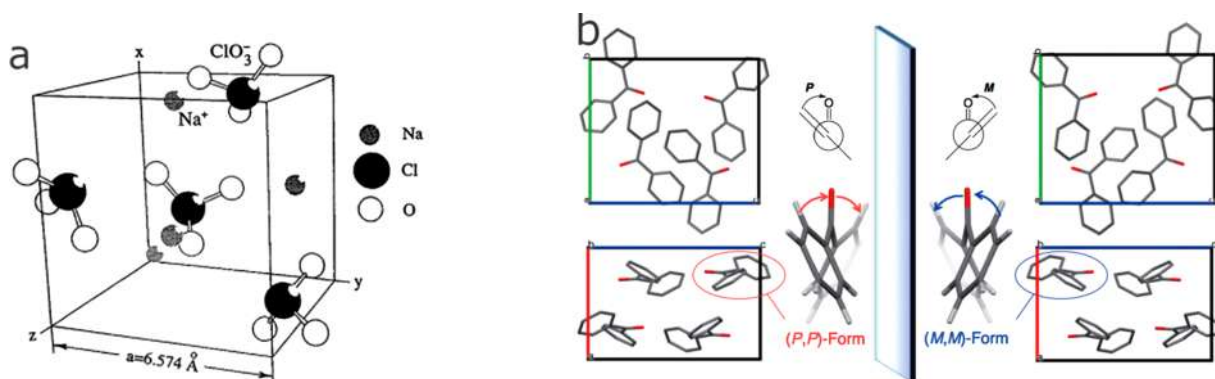
Figure 14. Examples of chiral unit cell from achiral compounds. (a) Unit cell of $NaClO_3$. The space group is $P2_13$ and there are four molecules per cubic unit cell. (b) Unit cell of benzophenone. The space group is $P2_12_12_1$. All the four molecules in the crystal exhibit chiral conformation with the same handedness. Reproduced with permissions from ref 259 and ref 258. Copyrights 2018 Springer Nature and 2016 The Chemical Society of Japan, respectively.

number n before the subscript. For instance, 3_1 is a 120° (360°/3) right-hand rotation followed by a translation of 1/3 of the lattice vector. Right-hand and left-hand screw operations generate different groups, hence the enantiomorphous pairs. These 11 group types (in **bold**) are truly chiral since they are transformed into another by inversion through a point. For instance, $P4_1$ transforms into $P4_3$ and vice versa. On the contrary, the remaining 43 space group types are intrinsically achiral. For instance, through point inversion $P1$ remains the same. However, all these 65 space group types contain only symmetry operations of the first kind, thus they give rise to chiral crystals. Table 3 gathers the list of the 65 Sohncke group types allowing chiral crystals.

Among the 65 Sohncke space group types, both chiral and achiral building blocks are encountered. Pure enantiomers can crystallize only as chiral crystals (for instance, glutamic acid hydrochloride, aspartic acid, threonine, asparagine monohydrate, sodium ammonium tartrate).[252] A total of 5−10% of all racemates crystallize as mixtures of enantiopure crystals (conglomerates). Achiral molecules mostly yield achiral crystals, but around 10% of chiral crystals are formed from achiral molecules.[253−255] This is a consequence of the freezing to a defined static chiral structure that, when in solution, conformational and vibrational dynamics racemize. For molecules having no chiral conformation, a helical arrangement is necessary. An example of helical arrangements is quartz (SiO_2) which crystallizes in the trigonal α-quartz system (low quartz), within the space group $P3_121$ or $P3_221$ depending on its chirality or in the hexagonal β-quartz system, within the space group $P6_222$ or $P6_422$.[256] Another well-known example is sodium chlorate (Figure 14a). Its achiral solution crystallizes into optically active cubic crystals. The space group is $P2_13$. The ClO_3^- anion is achiral, but there are four $NaClO_3$ per cubic unit cell. The planes

of the four O_3 groups are not parallel but have a peculiar helical configuration, and this gives rise to its optical activity.[257]

3.1.3. Examples of Chiral Crystals from Achiral Components. For conformationally flexible molecules, the generation of chirality can be obtained when a transient chiral conformation is locked into the crystal. An example of locked chiral conformation is benzophenone, which is one of the simplest achiral organic compounds that crystallizes in the chiral form (Figure 14b). While the benzene rings rotate freely in solution, they exhibit a fixed clockwise or anticlockwise torsion angle of the CC bond between the carbonyl group and the phenyl ring, thus generating enantiomorphous crystals belonging to the orthorhombic space group $P2_12_12_1$.[258]

It is rather difficult to discriminate between two enantiomorphous crystals which do not show hemiedral faces since they exhibit identical physicochemical properties. Observation with polarizers works fine for crystals of the cubic system due to the lack of polar point groups (all the axes equivalent).[260] Otherwise, solid-state circular dichroism (CD) on microcrystalline (i.e., nonoriented) samples or single-crystal X-ray diffraction can be used.

3.1.4. Determination of the Absolute Configuration of Chiral Crystals. As X-rays measure the interatomic distance that does not differ by inversion, they are expected to be unable to determine absolute configurations. However, a difference in the diffraction pattern of the right- and left-hand occurs in the phases of the inversion-related reflections, whereas their amplitudes are identical in the absence of any resonant effects. That is why the determination of the absolute configuration of a chiral crystal is based on the resonant scattering of X-rays. A phase-lag can be introduced into the primary scattering process by using a wavelength near the absorption edge of an atom in the molecule (the so-called anomalous X-ray scattering which

corresponds in fact to the response of a forced damped harmonic oscillator).[261] Some new X-ray radiation is generated from a partial ionization of the inner electron shells of the atoms. The new radiation interferes with the already scattered one, thus altering both amplitude and phase. Under these conditions there are small deviations from the Friedel's law[250,262] and the distinction between two possible absolute structures could be made based on the relative successive intensities of the diffraction spots with a fixed rotation sense of the crystal. The Bjivoet anomalous X-ray scattering method is not an *a priori* method to determine absolute configurations, because it requires a chiral recognition implicit in the direction of X-ray beam with respect to the crystallographic axes and then a "triage" between left and right, such as it is done for hemihedral crystals (pages 217−218 of ref 107) is made by the operator.

The absolute structure is found by determining the relative proportion of the inverted one (Flack parameter).[263] This parameter is usually between 0 and 1. If near 0, the assumed absolute structure is likely to be correct; on the contrary if it is near 1, then this is the inverted one. If the Flack parameter is around 0.5, the crystal may not be chiral.[250] However, with compounds containing only light atoms, a reliable determination is not guaranteed. On the contrary, if an organic molecule possesses a heavy atom such as sulfur, phosphorus, or halogen, the determination of the absolute configuration is expected to be more reliable.

The characterization of the optical activity coefficients in crystals is still an incomplete task that today is advancing thanks to new and more accurate polarimetric methods and instruments (see section 8).[264,265] The question with respect to chemical chirality in crystals refers to the resulting optical activity by the integration in all directions,[266] in the same way that single chiral molecules do in isotropic homogeneous solutions. This is because some achiral crystal symmetries, also some achiral molecular point groups, exhibit enantiomorphic pairs of optically active axes.[267]

3.2. Chirality at Surfaces: 2D and 1D Chirality?

In 2D, there are 17 plane groups, analogous to the 230 3D space groups. Those without mirror or glide lines are chiral. The topic is of archeological interest because of the development of wall repetitive patterns, starting in the Neolithic and then continuing through the relationship between different cultures until nowadays in the applied arts (the so-called wallpaper figures). It is even of interest for the history of science because it shows the achievements in Euclidian geometry in Islamic culture (Figure 15):[268] for example, all 2D point groups (12) and plane groups (17) have been found in Granada's Alhambra mosaics.[269,270]
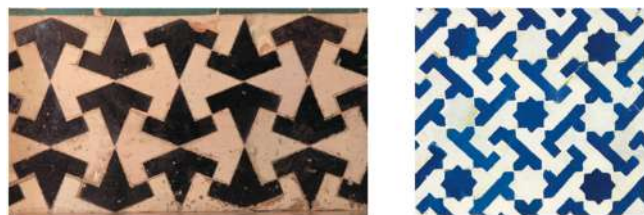
Figure 15. Example of achiral (left) and chiral (right) old Islamic tiles, whose design and further combination to complex mosaics was made with the mathematical knowledge of the 2D plane and point groups (refs 268−270). Adapted with permission from ref 269. Copyright 2015 Elsevier.

Despite the fascination of the regular patterns observed in planar nano- and microstructures as originated, for example, by epitaxial deposition, the discussion on the 2D symmetry of enantiomorphic chemical planar structures is inappropriate because any molecular structure always has a finite extension, admittedly small, in three-dimensional space and, obviously, that is also the case for molecular monolayers. Needless to say, no experiment has ever or will ever be carried out in 2D, as empasized by Ernst[271] when he notes that the term "2D chirality" can be misleading for real experimental systems as it remains a purely theoretical construct.

1D chirality (helicity in physics) would be that of an elementary particle moving linearly with angular momentum. The so-called 1D chirality in linear polymers and columnar structures[272,273] correspond to an unidirectional growth, but bend and folding make the tertiary resulting structure tridimensional thus leading to 3D chiral topologies.[274]

Asymmetric synthesis by chiral solids through heterogeous catalysts (surface catalysis) by chiral MOF[275] is a well-developed topic. Furthermore, the proof of concept that asymmetric synthesis can be also performed by chiral surfaces of achiral crystals (obtained by selective cleavage of achiral monocrystals)[276] has been thoroughly reported,[277] including asymmetric redox reactions on chiral surfaces of Pt or Au electrodes.[278] From an applied point of view, monocrystal surfaces offer a less active surface than mesoporous MOF. However, with respect to the origin of life topic, there are naturally abundant crystals that usually show chiral surfaces despite possessing achiral structures, such as calcite ($CaCO_3$) and gypsum ($CaSO_4 \cdot 2H_2O$) which allowed reasonable speculations on their role in chemical evolution.[26] Of special interest are natural abundant phylosilicates such as kaolinite $(Al_2(OH)_4Si_2O_5)_n$ which have been proposed as catalysts in abiotic evolution scenarios and which form chiral layered structures. In SMSB processes, the expected effect of these chiral surfaces, when they participate in any reaction network, is to select the chiral sign of the product,[279] i.e., to convert a stochastic distribution of chiral signs into a deterministic one. There are several reports showing this induction for the Soai reaction using either the heterogeneous effect of chiral crystals,[118] i.e., their chiral surfaces, or the effect of chiral surfaces of achiral crystal of gypsum.[280] Modeling studies[281] of abiotic evolution scenarios have shown the spontaneous emergence of chirality when racemic phylosilicates are acting as a part of an autocatalytic reaction network of limited enantioselectivity. Furthermore, a small imbalance from the racemic composition of the silicates should lead deterministically to one final chiral sign.

The question of the emergence of chirality during the formation of monolayers from achiral molecular building blocks is a topic of increasing interest.[271,282−284] Structured monolayers obtained by absorption or epitaxis on an ordered surface or at interfaces such as water/air have two different sides that helps to obtain chirality.[283] However, the formation of layers showing two equal interfaces, both having the same interaction with the surroundings, is also possible, such as is the case of some bilayers and monolayers which eventually lead to vesicles[285] and nanotubes[286,287] in a more advanced stage of their self-assembly process. The difference between ordered monolayers and crystals is that in the former, the self-assembly of the building blocks is not favored in the third dimension so that self-organization occurs only or very frequently, along the two orthogonal axes in a plane. Therefore, the formation of a chiral monolayer from achiral building blocks may also occur, such as
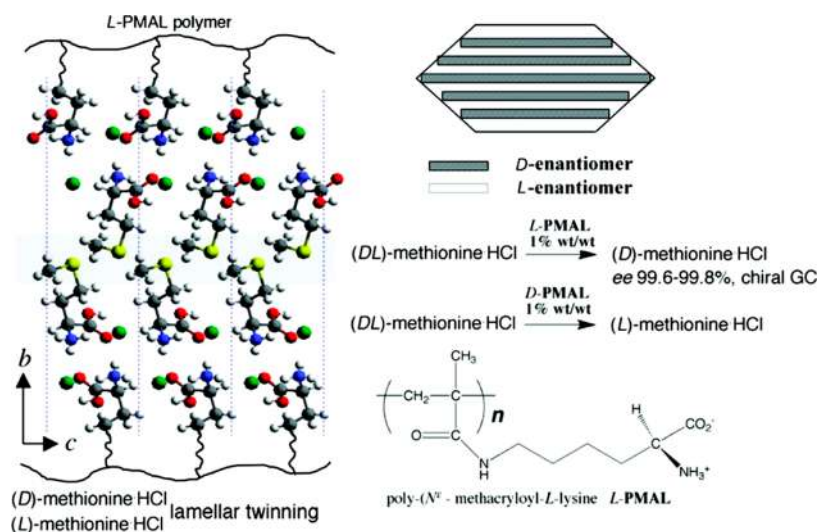
Figure 16. Example of how the manipulation of racemic crystals constituted by homochiral layers can yield the racemate resolution. Reproduced from ref 291. Copyright 2011 American Chemical Society.

in the case of crystals by the freezing of the dynamic interconversions between enantiomeric structures in solution or by a preferential homochiral interaction between these monomers when confined in a 2D dimensional space. The growth along the third orthogonal axis is frustrated. The symmetry breaking leading to chiral layers from achiral or racemic mixtures of building blocks is of high interest with respect to the topic of the origin of life. It is obviously related to the formation of chiral membranes where SMSB could take place. In this regard, it is worth noting that some racemic crystals are composed by alternating enantiomorphic layers: the growth along two space directions occurs by homochiral interactions but through heterochiral ones along the direction of the third orthogonal axis. The manipulation of this heterochiral constraint to the crystal growth may lead to the resolution of solution racemates (Figure 16).[288−291]

A mostly unanswered question is whether the formation of chiral monolayers on regular surfaces, when observed by atomic-force-microscopy or electron-diffraction, corresponds or not to a resolved racemic conglomerate (i.e., if a SMSB has occurred) because of the low number of domains that the technique allows one to observe.

The self-assembly of achiral compounds to layered or filamentlike structures stems from the frustrated growth in a third or a second space direction. However, these structures lead to secondary aggregation implying the transfer of chirality toward a larger size scale and, finally, to aggregations typical of colloidal chemistry. In the case of isotropic suspensions of monolayered particles, chirality may be detected through the measurement of optical polarization properties (see section 8). In the case of nanostructures supported on planar regular surfaces, which are not the subject of this review, plasmon resonance techniques and second harmonic generation analysis are the techniques of choice.[292,293]

3.3. Chirality in Suspensions of Nano- and Microparticles, Anisotropic Liquids, and Molecular Solutions

The dissymmetry of molecular solutions, anisotropic suspensions of small particles ordered by flows, and molecular anisotropies such as those arising in liquid crystals, are defined by the limiting point groups which describe the symmetry elements of the sample. There are seven Curie symmetry

limiting groups according to the Hermann−Maugin notation. Here, we will discuss them in the framework of Shubikov comments.[246] (see Figure 17). The reader can also find a pedagogical description of this topic on pages 22−28 of ref 245.
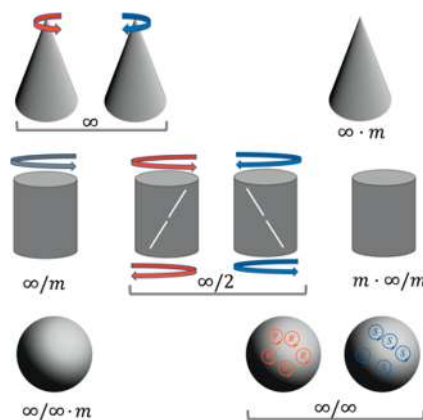
Figure 17. Curie limiting point groups (Hermann−Maugin notation) that allow the description of lower anisotropies than those of crystal structures. For example, the spherical groups differentiate between racemate solutions and scalemic and homochiral solutions. Adapted with permission from ref 246. Copyright 1988 Elsevier.

The conical group ∞ (see Figure 17) has no other symmetry elements except for an axis of infinite order: it is the group of a rotating cone. It admits the existence of enantiomorphous (right- and left-handed) forms: a cone rotating in one sense vs a cone rotating in the opposite sense, such as would be the case for the symmetry of a stirred solution of achiral long-shaped particles oriented in the vortex flow. The second conical group ∞ · m possesses, in addition to an axis of infinite order, an infinite number of longitudinal symmetry planes: it is the group of a cone at rest, which does not admit enantiomorphism.

The cylindrical groups, also able to be represented by double fused cones,[245] describe scenarios such as those resulting from liquid crystal anisotropies. ∞:m is the group of a cylinder showing an inversion center, a transverse symmetry plane, and a longitudinal axis of infinite order; it does not admit enantiomorphism. Group ∞:2 has only a symmetry axis of infinite order

and an infinite number of transverse 2-fold symmetry axes; it admits enantiomorphism (right-and left-handed screws). The group $m \cdot \infty : m$ has an axis of infinite order, an infinite number of longitudinal, and transverse symmetry planes, also an infinite number of transverse 2-fold axes and a center of symmetry; therefore, does not admit enantiomorphism (Figure 17 and Table 4).

Table 4. Examples of Experimental Situations Belonging to the Seven Curie Limiting Space Point Groups[245,246]

limiting point group	achiral	chiral
∞	∅	spherical particles moving along a vortex[294]
$\infty \cdot m$	case of some confined achiral smectic phases[295]	∅
$\infty : m$	smectic C. Rotating calamitic phase	∅
$\infty : 2$	∅	smectic C (cholesteric) phases. Nematic phases under shear stress orthogonal to the longitudinal axis[30]
$m \cdot \infty : m$	nematic calamitic phase	∅
$\infty / \infty : m$	achiral solutions or racemate molecular solutions (Brownian regime)	∅
∞ / ∞	∅	Scalemic and enantiopure molecular solutions (Brownian regime). Enantiomorphic liquids

Isotropic liquids and achiral or racemic molecular solutions belong to the spherical limiting group $\infty / \infty \cdot m$. It corresponds to a conventional sphere having an infinite number of axes of infinite order, an infinite number of symmetry planes and a center of symmetry. Obviously, it does not admit enantiomorphism, i.e., it cannot show chirality. Scalemic mixtures or homochiral solutions and isotropic enantiomorphic liquids belong to the group ∞ / ∞, which is the symmetry group of a sphere having no symmetry planes and no center of symmetry but possessing an infinite number of symmetry axes of infinite

order. The symbolic small circles rotating in opposite directions, representing the two enantiomers.

A classical asymmetric synthesis corresponds to the transfer of chirality from a chiral inductor to a chiral product, i.e., from ∞ / ∞ to ∞ / ∞. Without any chiral inductor, the same chemical transformation gives rise to a racemate that represents a transfer from achiral $\infty / \infty \cdot m$. to racemic $\infty / \infty \cdot m$. On the contrary, SMSB such as inferred in this review occurs thanks to an enantioselective autocatalytic network working in an open dissipative system in absence of any chiral inductor. It represents a transition from the achiral $\infty / \infty \cdot m$. limiting group to one of the right of left enantiomorphic (∞ / ∞) limiting groups.

Note that Curie dissymmetry differs from Pasteur (or Barron) dissymmetry, because in addition to parity breaking, time reversal must also be taken into account. For example, a simple rotating cone represents false chirality when stationary but true chirality when translating (see section 2.2.1).[25]

4. INORGANIC CONGLOMERATES

A compilation of the Inorganic Crystal Structure Database (ICSD from FIZ Karlsruhe-2020) which comprises more than 200 000 inorganic crystal structures shows that the number of compounds crystallizing within the 65 Sohncke space groups is limited to less than 8000 (<4%). The most frequently encountered are in decreasing order: $P6_3$, $P2_12_12_1$, $P2_13$, $P3_121$, and $P1$. Among them, the number of crystals belonging to the 22 chiral space groups is around only 1%.

4.1. Examples of Achiral Salts Giving Rise to Chiral Crystals

To illustrate how our compilation has been undertaken, we provide some examples of well-known flagship achiral compounds giving rise to inorganic chiral crystals. We have privileged water-soluble salts whose crystals can be easily grown by slow evaporation from supersaturated aqueous solution at room temperature or by slow cooling. This is because we believe that such crystals could be chosen to carry-out some easy-to-handle Viedma deracemization experiments.

Table 5. Examples of Easily Available Metallic Salts (Achiral) Giving Rise to Chiral Crystals

structure	name	space groups	crystal system	ref
$Na(HSO_4)(H_3PO_4)$	mixed sodium hydrogen sulfate phosphate	$P2_1$	monoclinic	296
$MgSO_4, 7H_2O$	magnesium sulfate heptahydrate	$P2_12_12_1$	orthorhombic	297, 298
$ZnSO_4, 7H_2O$	zinc sulfate heptahydrate	$P2_12_12_1$	orthorhombic	299
$NaH_2PO_4, 2H_2O$	sodium dihydrogen phosphate dihydrate	$P2_12_12_1$	orthorhombic	300
$Sr(HCOO)_2, 2H_2O$	strontium formate dihydrate	$P2_12_12_1$	orthorhombic	301,302
α-$Sr(HCOO)_2$	anhydrous strontium formate	$P2_12_12_1$	orthorhombic	303
$Ba(HCOO)_2$	anhydrous barium formate	$P2_12_12_1$	orthorhombic	303
$NiSO_4(H_2O)_6$	nickel sulfate hexahydrate	$P4_12_12$ and $P4_32_12$	tetragonal	304−307
$Cs(NO_3)$	cesium nitrate	$P3_1$ and $P3_2$	trigonal	308
$Rb(NO_3)$	rubidium nitrate	$P3_1$ and $P3_2$	trigonal	309, 310
$Sr(S_2O_6), 4H_2O$	strontium dithionate tetrahydrate	$P3_1$ and $P3_2$	trigonal	311, 312
$CaCl_2, 6H_2O$	calcium dichloride hexahydrate	$P321$	trigonal	313
$SrCl_2, 6H_2O$	strontium dichloride hexahydrate	$P321$	trigonal	313
$K_2(S_2O_6)$	potassium dithionate	$P321$	trigonal	314
$Ca(S_2O_6), 4H_2O$	calcium dithionate tetrahydrate	$P6_2$ and $P6_4$	hexagonal	315
$Ba(NO_2)_2, H_2O$	barium nitrite monohydrate	$P6_1$ and $P6_5$	hexagonal	316, 317
$Li(IO_3)$	lithium iodate	$P6_3$	hexagonal	318, 319
$LiKSO_4$	lithium potassium sulfate	$P6_3$	hexagonal	320−323
$NaClO_3$	sodium chlorate	$P2_13$	cubic	324
$NaBrO_3$	sodium bromate	$P2_13$	cubic	324

Table 6. Relative Occurrence of Achiral Inorganic Compounds Crystallizing within One of the 22 Chiral Space Groups (From the 2020 ICSD Database)

groups	$P3_1/P3_2$	$P3_112/P3_212$	$P3_121/P3_221$	$P4_1/P4_3$	$P4_122/P4_322$	$P4_12_12/P4_32_12$	$P6_1/P6_5$	$P6_2/P6_4$	$P6_122/P6_522$	$P6_222/P6_422$
counts	90/35	50/3	475/160	65/22	31/15	307/108	50/14	4/1	55/40	250/50
apparent $ee\%$	44	88.7	49.6	49.4	34.8	47.9	56.2	60	15.8	66.7

Table 5 gathers some examples of common salts within one of the 65 Sohncke space-group types. They are tabulated on the basis of their belonging to a specific crystal system.

Ordinary crystallization techniques may be employed to prepare chiral crystals from achiral compounds. However, it is essential to obtain single crystals suitable for X-ray crystallographic analysis, because the chirality of the crystal must be ultimately established by identifying its space group. For instance, it is likely that some enantiomeric twinning would have prevented the determination of the absolute configuration. A further influence on crystal growth in terms of shape and structure is that of the presence of impurities. Because nucleation and growth are quite often under kinetic control, crystals are affected by the adsorption of impurity molecules on particular faces with a consequent slowing-down in their growth rate and change in their morphology. Impurities adsorbed on the surface or trapped in the host crystal, especially those that are close in chemical structure to the bulk compound, may cause symmetry changes (the Shubnikov effect)[325] but also habit modification.[326] In these conditions, a single crystal may result from less stable but faster growing nuclei. The result is polymorphism which may prevent an accurate structural refinement (see section 5.7). The loss of water in crystal hydrates can lead to the destruction of crystals, so the thermal stability and the crystallization temperature are important parameters.

For instance, the common tetragonal $NiSO_4$ hexahydrate crystallizes from aqueous solution between 30.7 and 53.8 °C. Below these temperatures, the orthorhombic heptahydrate $NiSO_4 \cdot 7H_2O$ crystallizes, and above these temperatures an orthorhombic hexahydrate forms.[306]

4.2. Analysis of the Chirality of Some Inorganic Crystals

According to classical polarizability theory, there is a correlation between the sign of the optical rotation and the arrangement of the atoms in the crystal structure.[327] The highest polarizable atoms are the major contributors to the optical rotation and refractive indices in the crystals. The directions of highest polarizability are parallel to the directions of the shortest distances between polarizable atoms. The contribution to the optical rotation is largest for helices with short interatomic distances and low pitches. This is the orientation of the anisotropic polarizabilities of the polarizable atoms in the plane perpendicular to the helix axis which determines the sign of the optical rotation. The plane of polarization rotates either in the same or in the opposite sense to that of the helix according to the relative magnitude of the helix tangential vs radial components.

For instance, $NaClO_3$ and $NaBrO_3$ crystals (both cubic, $P2_13$) with identical chirality, exhibit opposite senses of optical rotation. For these isotropic crystals, the optical activity can be observed in any crystal orientation, (+)- and (−)-crystals can be discriminated by using polarizer sheets.

$NiSO_4 \cdot 6H_2O$ crystallizes in one of the enantiomorphic space groups $P4_12_12$ or $P4_32_12$. The two space groups correspond to the presence of structural helices of polarizable atoms, whose sense could be related to the sense of rotation of plane-polarized light. For instance, a crystal $P4_12_12$ is optically levo at 0.458 and

0.476 μm and dextro at 0.515 μm; this is the reverse for a crystal $P4_32_12$. Powdered crystals in Nujol[328] exhibit around the 390 nm region a negative CD if $P4_12_12$ while positive if $P4_32_12$. In such a case, the CD spectrum is an average of the CD spectra for every crystal plane. This technique could be useful to screen the chirality of crystals obtained from achiral compounds. Correlations between the chirality of the space group and the absolute configuration of the crystals have been pointed out in the case of $Sr(S_2O_6) \cdot 4H_2O$,[311] $Ca(S_2O_6) \cdot 4H_2O$,[315] and $Ba(NO_2)_2 \cdot H_2O$.[316]

In biaxial crystals like $MgSO_4 \cdot 7H_2O$[298] or strontium and barium formates and strontium formate dihydrate[329] (orthorhombic space group: $P2_12_12_1$), optical activity can be observed along optic axes, especially in conoscopic illumination. On the contrary, in uniaxial crystals (trigonal, tetragonal and hexagonal), optical activity can only be observed along one symmetry axis of the crystal. However, twinning, i.e., the occurrence of alternating layers of levo- and dextrorotatory-type crystals with opposite polarity along the optical axis,[320] is not detectable by optical analysis.[323]

In the literature, there are few examples where the chirality of the inorganic crystals was analyzed from a statistical point of view from repeated experiments. However, it is interesting to note that while the probability of crystallization of each of the two enantiomorphic crystals is completely identical, it appears that many times the final result departs from the mere random 1:1 expected result.[330] This may be due to the presence of trace chiral impurities in the various laboratories. The chiral trace behaves as a nucleating seed and preferentially favors the growth of one crystal over the other (see section 2.2.3).[331]

Another remarkable bias has been pointed-out by Urusov et al.[332] Among the 11 enantiomorphous space groups, there exists a clear dissymmetry between the occurrences of each enantiomorphous group. It appears that the space groups having a screw like 31, 41, 61, or 62, i.e., turning clockwise away from the viewer or anticlockwise toward the viewer are systematically more frequent than their mirror image, i.e., 32, 43, 64, 65, turning anticlockwise away from the viewer or clockwise toward the viewer.[327] Results of the compilation are gathered in Table 6.

Such an unexpected bias poses the problem of the correctness of these assignments. It seems that the first space group type is more often allocated than the second. Another assumption could be the manifestation of some "universal" cryptochiral effect. For instance, in the case of epsomite ($MgSO_4 \cdot 7H_2O$), Pocklington (1906) observed entirely left-handed crystals.[333] We will see in the next section that some nonstochastic chiral bias are also observed in the case of chiral crystals of organic achiral compounds.

5. ORGANIC CONGLOMERATES

The Cambridge Crystal Structure Database (CCSD) is the world's largest repository for small-molecule organic and metal−organic crystal structures. This database contains more than one million structures. Its survey shows that there are about one hundred thousand achiral molecules crystallized in a Sohncke space group, i.e., without inversion centers, mirror or glide

planes, or rotoinversion axes.[334,335,202,336] The most frequently encountered space groups are the $P2_12_12_1$ and the $P2_1$.[337]

5.1. Supramolecular Chirality

In order to understand the possible scenarios describing the crystallization of an achiral molecule with no chiral center in a Sohncke space group, it must be borne in mind that the four-point assembly serves as the simplest basis for chirality generation in 3D space. Right- or left-handedness of a four-point structure can be determined in a manner similar according to the well-known Cahn−Ingold−Prelog rule (Figure 18).
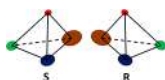
Figure 18. Handedness determination of four points with a sequence order in 3D.

There are two main ways to generate chirality from an achiral environment: the first one is the formation of a chiral conformation by bond rotation, and the second is the presence of a helical arrangement of molecules. A supramolecular assembly of molecules forming a columnar arrangement always plays an essential role in the chirality generation by either bond rotation, helical arrangement, or both. However, in many cases, the right-handed and left-handed molecules simultaneously exist in the same unit cell, canceling their chiralities and giving rise to an achiral crystal.[253,254] On the other hand, Miyata et al.[338] developed the idea that achiral molecules can create chiral 2_1 columns which are bundled via a chiral bottom-up process to yield chiral crystals. Some of these principles of supramolecular chirality generation are displayed in Figure 19.

Over 70% of the CSD involves the 2-fold helices. Although achiral molecules strongly prefer crystallization in centrosymmetric space groups, it is worth noting that in the case of achiral compounds yielding enantiopure crystals, such crystallizations can lead to spontaneous deracemization. In the next section, we will provide a list of a few readily available achiral compounds giving rise to organic chiral crystals. We have privileged crystals which can be easily grown by slow evaporation from supersaturated solutions at room temperature or by slow cooling. This is because we believe that such crystals could be used to shed light on polymorphism and to better understand the Viedma deracemization mechanism.

5.2. Two-Component Chiral Crystals

Although chiral crystallization of achiral molecules occurs statistically with a low probability, it appears that this probability can be increased by considering two-component crystals through cocrystal or salt formation of achiral ion-pairing molecules. For instance, the self-assembly of 3-indolepropionic acid and phenanthridine or the cocrystal of tryptamine and hydrocinnamic acid have been shown to belong to Sohncke space groups.[339,340]

5.2.1. Chiral Cocrystals. Some more recent, easily attainable two-component chiral crystals are gathered in Table 7 and their structures are shown in Figure 20 associated with Table 7. They have been tabulated according to their main chemical functions, phenols, benzoates, pyridinium, and miscellaneous.

When an acid is reacted with a base, the resulting product will be a salt or a cocrystal. The ΔpK can be used as a guideline to guess the nature of the crystalline solid, but it must be borne in mind that solvent and temperature also impact the packing forces between the molecules or ions in the crystal structure. Proton-transfers can be stabilized by a highly directional hydrogen-bonding network. N−H···O, O−H···N, and C−H···O hydrogen bonding and π−π stacking interactions play a crucial role in controlling the packing modes of molecular crystals.

Nitrophenols act not only as π-acceptors to form various π-stacking complexes with other aromatic molecules but also as acidic ligands to form salts through specific electrostatic or hydrogen-bonding interactions. Carboxylic acids also constitute suitable building blocks able to make a variety of supramolecular assemblies through hydrogen-bonding. The combination of strength and directionality of the hydrogen bond interactions is a master key in the crystal engineering field.

5.2.2. Chiral Organic/Inorganic Salts. Chiral cocrystals are also formed when an achiral organic base is reacted with an inorganic acid or when an achiral organic acid is reacted with an inorganic base. Some examples are gathered in Table 8, and they are tabulated according to their anions, halogenides, oxy-halogenides, phosphates, sulfates, and miscellaneous. The corresponding chemical structures are shown in Figure 21.

Compared to pure organic or inorganic materials, one of the most interesting aspects of organic−inorganic hybrids is that their properties are strongly dependent on the included inorganic anion groups. Short and multiple hydrogen-bonded
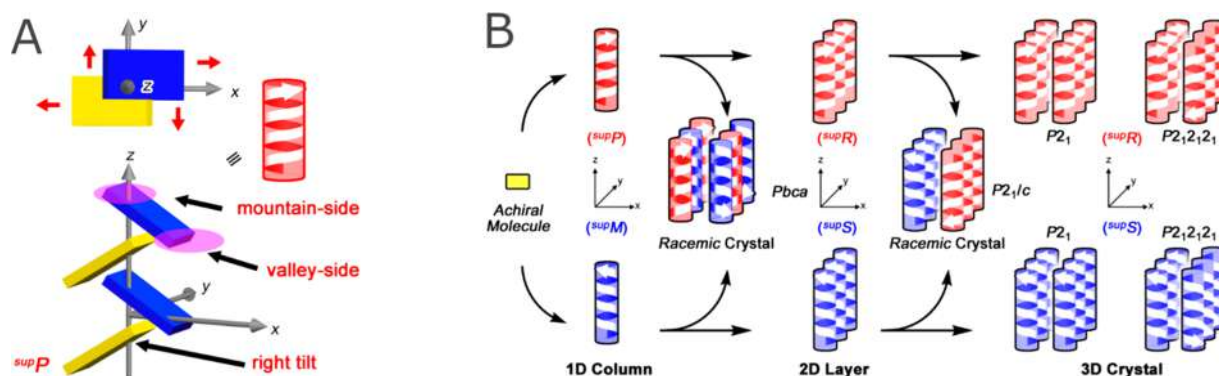
Figure 19. (A) Assembly of descending plates giving rise to a right-handed 2_1 helix with directionality owing to mountain- or valley-side deformations. (B) Processes of step-by-step crystallization of an achiral molecule to racemates (P_{bca} and $P2_1/c$) and conglomerates ($P2_1$ and $P2_12_12_1$) from supramolecular 2_1 helices assemblies. Reproduced from ref 338. Copyright 2015 MDPI (Basel, Switzerland) under Creative Commons Attribution 4.0 International License https://creativecommons.org/licenses/by/4.0/.

Table 7. Examples of Simple Achiral Molecules Crystallizing in Sohncke Space Groups with Some Achiral Organic Acids or Bases[a]

empirical formula	name or structure	T K	space group	crystal system	Flack parameter	ref
$C_6H_5NO_3$ /$C_{12}H_8N_2$ (**1**)	4-nitrophenol/1,10-phenanthroline, Z = 4	296	$P2_12_12_1$	orthorhombic		341
$C_6H_5NO_3$ /$C_5H_{11}N$ (**2**)	4-nitrophenol/piperidine, Z = 4	295	$P2_12_12_1$	orthorhombic		342
$C_6H_5NO_3$/$C_6H_4NO_3^-$/ $C_7H_{11}N_2^+$ (**3**)	4-nitrophenol/4-nitro- phenolate/dimethylaminopyridinium (1/1/1), Z = 4	120	$P2_12_12_1$	orthorhombic		343
$C_{16}H_{24}N_4O_8$ (**4**)	o-nitrophenol/piperazine 2:1, dihydrate cocrystal, Z = 2	295	$P2_1$	monoclinic		344
$C_4H_{10}NO$/$C_7H_5O_3$ (**5**)	morpholinium/2-hydroxybenzoate, Z = 2	200	$P2_1$	monoclinic	0.2(14)	345
$C_6H_9N_2^+$/$C_7H_6NO_2^-$ (**6**)	2-amino-4-methylpyridinium 4-amino-benzoate, Z = 4	295	$P2_12_12_1$	orthorhombic		346, 347
$CH_6N_3^+$/$C_7H_4NO_4^-$ (**7**)	guanidinium 3-nitrobenzoate, Z = 4	297	$P2_12_12_1$	orthorhombic		348
$C_7H_5NO_4$/C_9H_7N (**8**)	quinolinium/4-nitrobenzoate cocrystal, Z = 2		$P2_1$	monoclinic		346
$C_5H_6BrN_2^+$/$C_7H_4ClO_3^-$ (**9**)	2-amino-5-bromopyridinium 5-chloro-2-hydroxybenzoate, Z = 2	100	$P2_1$	monoclinic	0.037(11)	349
$C_{14}H_{14}N_2O_3$ (**10**)	4-acetylpyridine/4-amino benzoic acid adduct, Z = 4	296	$P2_12_12_1$	orthorhombic	2.2 (1.6)	350
$C_{24}H_{16}N_6O_{12}$ (**11**)	(3,5-dinitrobenzoic acid),(2,2′-bipyridine), Z = 2	293	$P2_1$	monoclinic		351
$C_{12}H_{11}N_3O_4$ (**12**)	(p-nitrobenzoic acid),(2-amino pyridine), Z = 2	293	$P2_1$	monoclinic		351
$C_5H_7N_2^+$/$C_4H_3O_4^-$ (**13**)	4-aminopyridinium hydrogen maleate, Z = 2	295	$P2_1$	monoclinic	0.4(9)	352
$C_6H_9N_2^+$ /$C_6H_4NO_2^-$/ 0.63H_2O (**14**)	2-amino-5-methylpyridinium pyridine-2-carboxylate, 0.63hydrate (picolinate), Z = 8	100	$P2_12_12_1$	orthorhombic		353
$C_{13}H_{13}NO_5$ (**15**)	8-hydroxyquinoline succinate, Z = 2	293	$P2_1$	monoclinic		354
$C_{22}H_{20}N_6O_4$ (**16**)	phthalic acid, 2-amino benzimidazole, Z = 4	293	$P2_12_12_1$	orthorhombic		351
$C_6H_{14}N$, $C_6H_7NO_3S$ (**17**)	cyclohexylammonium sulfanilate,		$P2_12_12_1$	orthorhombic		355
$C_9H_{20}N_4O_2$ (**18**)	piperazinium piperazine-4-carboxamide, Z = 4	100	$P2_12_12_1$	orthorhombic		356

[a]There is only one Flack parameter value (0.037(11)) ascertaining that a clearcut spontaneous resolution has arisen in the brominated product.
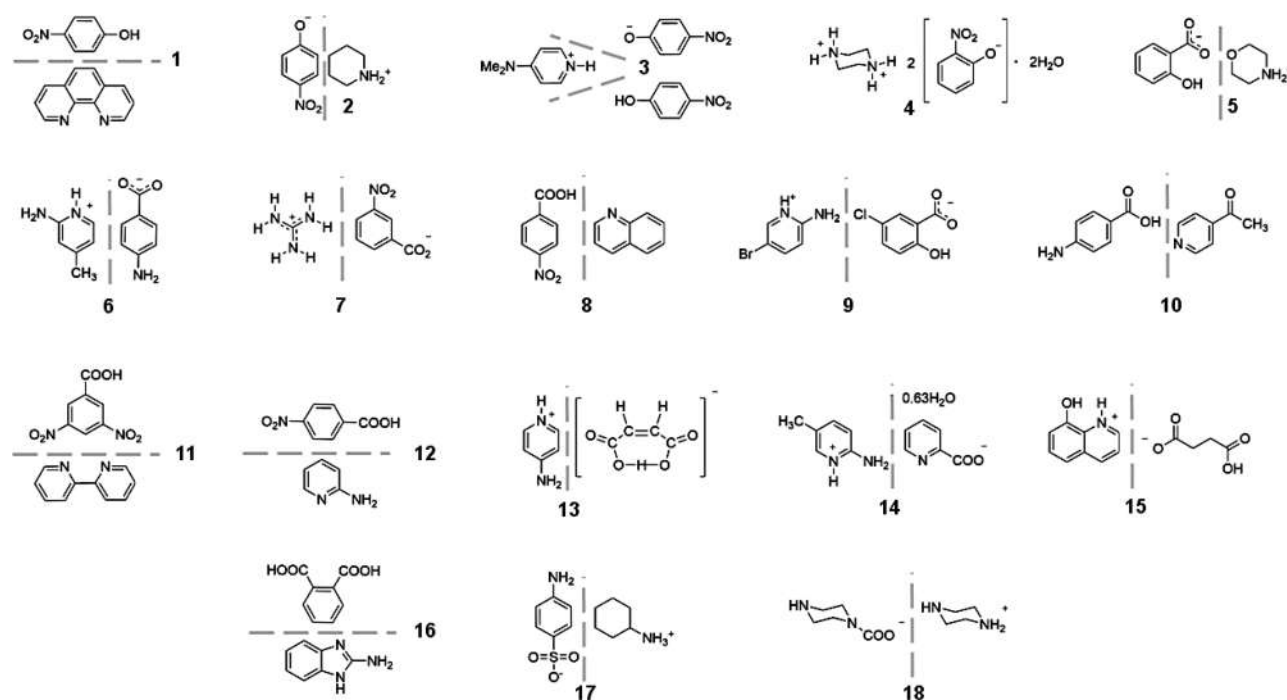
Figure 20. Chemical structures of the cocrystals listed in Table 7. Dashed bars illustrate the anion-cation interactions.

networks observed in all these organic−inorganic structures provide crystalline materials with improved thermal, chemical, and mechanical stabilities.

Co-crystallization is a supramolecular synthetic method to combine two different achiral molecules. It appears to provide a higher feasibility for chiral crystal architecture than a single-component approach. This is a powerful tool for designing absolute asymmetric syntheses and new functional solid materials. For instance, applications in optoelectronics, conductivity, and superconductivity, charge-transfer and mag-netism, nanoporous materials, and biomimetic materials could be expected from chiral crystals formed from achiral organic compounds. In the more specific field of aromatic and heterocyclic molecules, frozen rotamers or other conformers can be chiral, and it is possible that they crystallize within a Sohncke space group.

5.3. Aromatic Compounds

Table 9 gathers some easily available, low-cost achiral aromatic molecules giving rise to well- recognized chiral conglomerate

Table 8. Examples of Simple Achiral Molecules Crystallizing in Sohncke Space Groups with Some Inorganic Acids or Bases[a]

empirical formula	name or structure	T K	space group	crystal system	Flack parameter	ref
$C_5H_{10}NO^+$ Cl^- (19)	N-methyl-2-pyrrolidone hydrochloride, Z = 4	200	$P2_12_12_1$	orthorhombic	0.04(9)	357
$C_5H_7ClN_2O_2$ (20)	imidazole-4-acetic acid hydrochloride, Z = 4		$P2_12_12_1$	orthorhombic		358
$C_7H_9ClN_2O_2$ (2)1	2-methyl-4-nitroanilinium chloride (β-form), Z = 4		$P2_12_12_1$	orthorhombic	−0.01(7)	359
$C_7H_9N_2O_2^+$ Cl^- (2)2	4-amino-(1-carboxymethyl) pyridinium chloride, Z = 4	115	$P2_12_12_1$	orthorhombic	0.32(8)	360
$C_5H_6N_3O_2^+/Cl^-$ (23)	2-amino-5-nitropyridinium chloride, Z = 2	293	$P2_1$	monoclinic		361, 362
$C_5H_6ClN_3O_2$ (24)	2-amino-3-nitropyridinium chloride, Z = 2	293	$P2_1$	monoclinic		363
$C_5H_6IN_3O_2$ (25)	2-amino-3-nitropyridinium iodide, Z = 4	173	$P2_12_12_1$	orthorhombic		363
$C_6H_8NO.ClO_4$ (26)	3-aminophenol-$HClO_4$, Z = 2	295	$P2_1$	monoclinic	0.07(4)	364
$C_6H_8NO.ClO_4$ (27)	4-aminophenol-$HClO_4$, Z = 4	295	$P2_12_12_1$	orthorhombic	0.09(9)	364
$C_4H_{10}NO^+/ClO_4^-$ (28)	morpholinium perchlorate, Z = 12	100	$P2_12_12_1$	orthorhombic	0.42(3)	365
$C_6H_{10}NO_5P$ (29)	3-aminophenol-H_3PO_4, Z = 4	100	$P2_12_12_1$	orthorhombic	0.01(7)	366
$C_6H_{10}NO_5P$ (30)	4-aminophenol-H_3PO_4, Z = 4	100	$P2_12_12_1$	orthorhombic	0.04(7)	366
$C_5H_{10}NO^+/HSO_4^-$ (31)	5-hydroxy-1-methyl-3,4-dihydro-2H-pyrrolium hydrogensulfate, Z = 4	173	$P2_12_12_1$	orthorhombic	0.01(9)	367
$C_7H_{10}N_2O_3$ (32)	4-aminosalicylic acid ammonium salt (polymorphs I and II), Z = 4	293	$P2_12_12_1$	orthorhombic		368
$C_8H_{11}N_2O_3Na$ (33)	sodium 5,5-diethylbarbiturate, Z = 4		$P2_12_12_1$	orthorhombic		369

[a]In some cases, the presence of halogen, sulfur, or phosphorus atoms has allowed an accurate determination of the Flack parameter showing that a spontaneous resolution has occurred. On the contrary, in the case of the morpholinium perchlorate, the crystal studied was an inversion twin, as expected from a Flack parameter close to 0.5.
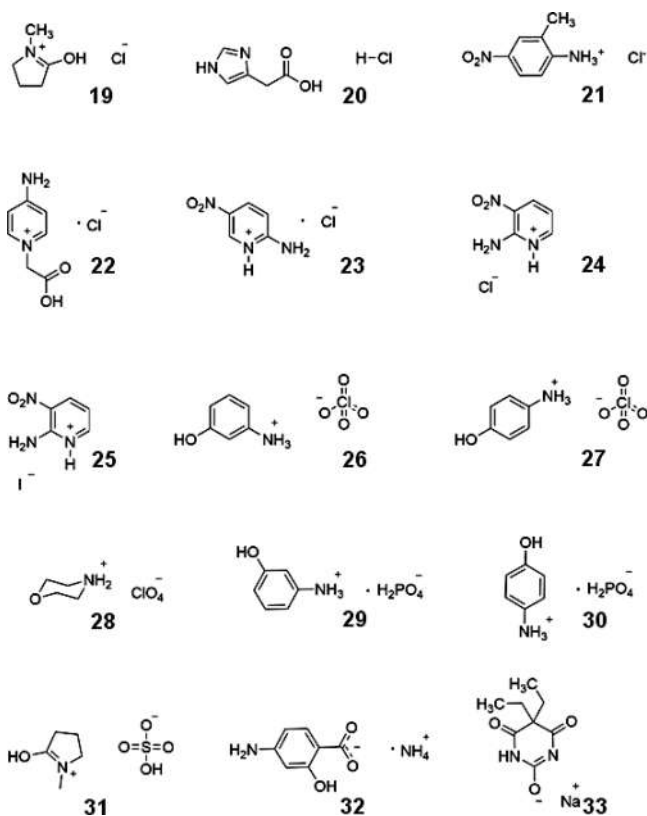
Figure 21. Structures of the chiral salts gathered on Table 8.

crystals at room temperature. They are tabulated according to their main substituents, chloro-derivatives, ethers, amides, phenols, aromatic amines, etc. Their structures are shown in Figure 22, which is associated with Table 9.

In chloro-compounds, the presence of the halogen makes the establishment of the Flack parameter possible. However, for chloro-acetamide and chloro-benzoate, the reported values are too high and not sufficiently accurate to allow a safe absolute structure determination. On the other hand, triclosan **36** crystallizes in the chiral space group $P3_1$ (and not to its

enantiomer $P3_2$). In spite of a Flack parameter close to zero, the possible presence of a small amount of the inverted structure cannot be excluded (twinning).

An interesting proportion of diarylethers crystallize in $P2_1$ or $P2_12_12_1$ space groups. This situation is understandable, since it is well-known that, if adequately substituted, they give rise to atropoisomerism, i.e., to stereoisomers whose stability is conferred by bond rotation inhibition.[385] Except for 1,3-dimethyl 2-phenoxybenzene **37**, which is planar but organized into helical chains, all of these compounds exhibit a chiral twisted conformation which is frozen in the solid state. The three phenylethers display nice solid-state CD spectra for both enantiomorphs. The lack of heavier atoms has not allowed any absolute structure determination. Intermolecular hydrogen bonds are formed between molecules that bring NH and/or OH groups. π−π stacking interactions can also be involved if the aromatic rings belonging to parallel chains are not too widely separated.

An example of cohesion ensured mainly by intermolecular S⋯H hydrogen bonds between semiparallel chains is given by the structure of the 4-methoxybenzenecarbothioamide **42** ortho-rhombic $P2_12_12_1$ crystal (Figure 23).

Other examples of mainly hydrogen-bonded structures with no or few π−π stacking interactions because the aromatic rings are too widely separated can be found in 2,4-di-tert-butyl-6-hydroxymethylphenol **45**,[380] 3-(aminophenyl)methanol **47**,[383] and sulfanilic acid hydrate **48**.[384] Even in the case of 4-nitrobenzyl chloride **43**,[377] short contacts between one of the H atoms of the methylene group and one of the O atoms of the nitro group form chains along the main crystal axis.

On the other hand, in the crystal of 5-amino-1-naphthol **46**,[381] molecules assemble into a two-dimensional hydrogen-bonded polymeric structure. Within this layer, molecules related by a translation along the crystal axis are arranged into slipped stacks via π−π stacking interactions (Figure 24).

m-Nitrophenol **44** occurs at room temperature in two solid modifications: monoclinic $P2_1/n$ (non-Sohncke) plates and orthorhombic $P2_12_12_1$ (Sohncke) elongated prisms grown preferably from nonpolar solvents.[378,379] In both polymorphs (see section 5.7), the hydroxyl group points toward the nitro

Table 9. Examples of Simple Aromatic Derivatives Crystallizing in Sohncke Space Groups

empirical formula	name or structure	T K	space group	system	Flack	ref
C_8H_8ClNO (34)	2-(4-chlorophenyl)acetamide, Z = 4	293	$P2_12_12_1$	orthorhombic	−0.12(8)	370
$C_8H_8ClNO_2$ (35)	methyl 2-amino-5-chlorobenzoate, Z = 2	293	$P2_1$	monoclinic	0.30(14)	371
$C_{12}H_6Cl_3O_2$ (36)	triclosan, Z = 3	293	$P3_1$	trigonal	0.014(13)	372
$C_{14}H_{14}O$ (37)	1,3-dimethyl 2-phenoxybenzene, Z = 4	100	$P2_12_12_1$	orthorhombic		373
$C_{12}H_{12}N_2O$ (38)	di(4-aminophenyl) ether, Z = 4	298	$P2_12_12_1$	orthorhombic		373
$C_{14}H_{14}O$ (39)	di(p-tolyl) ether, Z = 4	100	$P2_12_12_1$	orthorhombic		373
$C_8H_9NO_2$ (40)	2-methoxy-benzamide, Z = 4	298	$P2_12_12_1$	orthorhombic		374
C_7H_6ClNO (41)	2-chlorobenzamide (β-form)		$P2_12_12_1$	orthorhombic		375
C_8H_9NOS (42)	4-methoxybenzenecarbothioamide, Z = 8	173	$P2_12_12_1$	orthorhombic	0.03(7)	376
$C_7H_6ClNO_2$ (43)	4-nitrobenzyl chloride, Z = 4	200	$P2_12_12_1$	orthorhombic	−0.03(9)	377
$C_6H_5NO_3$ (44)	m-nitrophenol, Z = 4 (polymorphs)	100−340	$P2_12_12_1$	orthorhombic		378, 379
$C_{15}H_{24}O_2$ (45)	2,4-ditert-butyl-6-hydroxy methyl phenol, Z = 3	123	$P3_1$	trigonal		380
$C_{10}H_9NO$ (46)	5-amino-1-naphthol, Z = 4	130/295	$P2_12_12_1$	orthorhombic		381, 382
C_7H_9NO (47)	(3-aminophenyl)methanol, Z = 4	200	$P2_12_12_1$	orthorhombic		383
$C_6H_7NO_3S, H_2O$ (48)	sulfanilic acid monohydrate, Z = 4 (polymorphs)	150	$P2_12_12_1$	orthorhombic		384
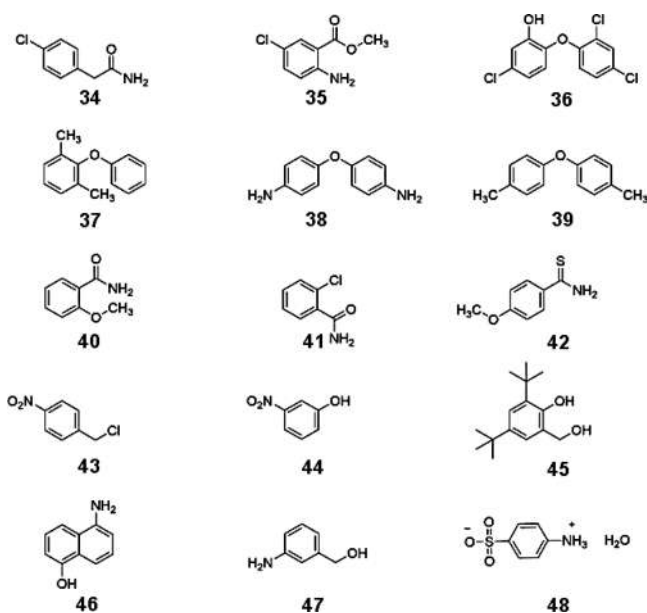
Figure 22. Structures of the aromatic compounds gathered in Table 9.
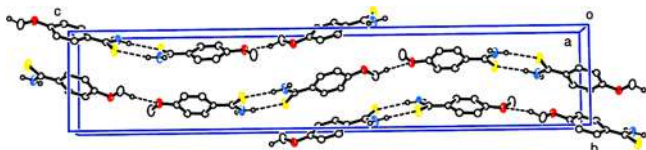
Figure 23. Structure of the 4-methoxybenzenecarbothioamide crystal containing hydrogen bonded dimers linked into elongated chains by hydrogen bonds between the methoxy groups. Reproduced from ref 376. Copyright 2010 International Union of Crystallography under Creative Commons Attribution 4.0 International License https://creativecommons.org/licenses/by/4.0/.

Figure 24. Crystal structure of 5-amino-1-naphthol 46, showing the intermolecular O−H···N hydrogen-bonded network. An intermolecular π−π interaction links the parallel aromatic rings. Reproduced from ref 381. Copyright 2009 International Union of Crystallography under Creative Commons Attribution 4.0 International License https://creativecommons.org/licenses/by/4.0/.
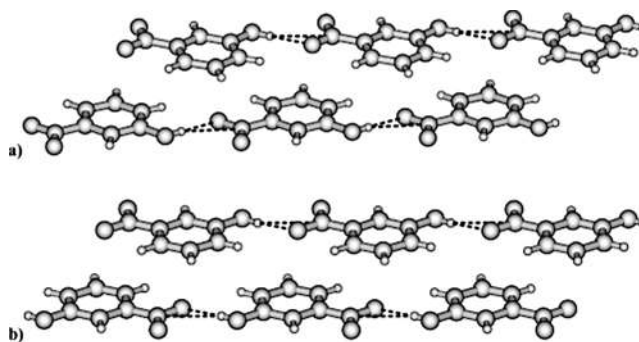
Figure 25. Molecular packing in adjacent molecular ribbons in orthorhombic (a) and monoclinic (b) m-nitrophenol 44 polymorphs. Reproduced from ref 379. Copyright 2006 American Chemical Society.

group of the adjacent molecule, thus forming an intermolecular OH···O hydrogen-bonded ribbon. The main difference between the two polymorphs is due to parallel and antiparallel orientation of the adjacent chains (Figure 25).

5.4. Heterocyclic Compounds

Because they favor hydrogen-bonding and π−π stacking, heterocyclic compounds are prompt to give rise to a rich supramolecular chemistry. Table 10 gathers some examples of simple heterocycles which have been found to crystallize in a Sohncke space group. They have been tabulated according to the presence of a benzene ring, a pyridine ring etc. Their structures are displayed in Figure 26, which is associated with Table 10.

The crystal structures are stabilized by intermolecular hydrogen bonds which lead to supramolecular chains. The chains are arranged edge-to-edge to form a layer. Moreover, when the ring orientations are favorable, π−π interactions are

Table 10. Examples of Simple Heterocyclic Derivatives Crystallizing in Sohncke Space Groups[a]

empirical formula	name or structure	T K	space group	system	Flack	ref
$C_8H_7NO_2$ (**49**)	5-amino-3H-isobenzofuran-1-one, (5-aminophthalide), Z = 4	173	$P2_12_12_1$	orthorhombic	4.2(15)	386
$C_9H_8N_2O_2$ (**50**)	1-oxoisoindoline-2-carboxamide, Z = 4	296	$P2_12_12_1$	orthorhombic		387
$C_{11}H_{11}NO_2$ (**51**)	1-propyl-1H-indole-2,3-dione, Z = 4	100	$P2_12_12_1$	orthorhombic	−0.5(5)	388
$C_8H_4N_2O_4$ (**52**)	4-nitrophthalimide, Z = 4	291	$P2_12_12_1$	orthorhombic		389
$C_{10}H_{12}N_2$ (**53**)	2-propyl-1H-benzimidazole, (polymorphs)		$P2_12_12_1$	orthorhombic		390, 391
$C_7H_4N_4O_4$ (**54**)	3,7-dinitro-1(2)H-indazole, Z = 4		$P2_12_12_1$	orthorhombic		392
$C_9H_9N_3O_2$ (**55**)	1-ethyl-5-nitro-1H-indazole, Z = 4	150	$P2_12_12_1$	orthorhombic	0.3(3)	393
$C_7H_5NO_2$ (**56**)	benzoxazoline-2 one, Z = 4		$P2_12_12_1$	orthorhombic		394
$C_{15}H_{14}N_2O$ (**57**)	2-benzylimino 3-methyl benzoxazoline, Z = 2		$P2_1$	monoclinic		394
C_7H_5NOS (**58**)	benzothiazoline-thione, Z = 2		$P2_1$	monoclinic		394
$C_9H_7NO_3S$ (**59**)	3-oxo-2,3-dihydro-1,2-benzothiazol-2-yl) acetic acid Z = 4	153	$P2_12_12_1$	orthorhombic	0.08(7)	395
$C_5H_4BrNO_2$ (**60**)	2-bromo-3-hydroxypyridine-N-oxide, Z = 4	298	$P2_12_12_1$	orthorhombic		396
$C_5H_5BrN_2$ (**61**)	2-Bromo-3-aminopyridine, Z = 8	100	$P2_1$	monoclinic		396
$C_7H_7NO_3$ (**62**)	4-hydroxy-pyridinioacetate, Z = 4	293	$P2_12_12_1$	orthorhombic		397
$C_7H_5NO_4$ (**63**)	3,4-dicarboxypyridine (cinchomeronic acid) (polymorphic form I), Z = 4	293	$P2_12_12_1$	orthorhombic		398
$C_{12}H_9NO$ (**64**)	phenyl 2-pyridyl ketone, Z = 4	150	$P2_12_12_1$	orthorhombic	−1(2)	399
$C_{10}H_8N_2O$ (**65**)	4,4′-oxybispyridine, Z = 4	291	$P2_12_12_1$	orthorhombic		400
$C_5H_5NO_2$ (**66**)	3-hydroxy-2-(1H)-pyridinon, Z = 4	213	$P2_12_12_1$	orthorhombic	0.1(4)	401
C_5H_5NO (**67**)	2-oxopyrimidine (α-pyridone),	123	$P2_12_12_1$	orthorhombic		402
$C_{17}H_{21}NO_2$ (**68**)	2,2,7,7-tetramethyl-1,2,3,4,5,6,7,8-octa-hydroacridine-1,8-dione, Z = 4	123	$P4_322$	tetragonal		403
$C_4H_5NO_3$ (**69**)	N-hydroxysuccinimide, Z = 4	133	$P2_12_12_1$	orthorhombic		404
$C_8H_{11}NO_2$ (**70**)	3,4-diethyl-2,5-dihydro-1H-pyrrole-2,5-dione, Z = 12	193	$P2_12_12_1$	orthorhombic		405

[a]In most cases, a Flack parameter cannot be determined due to the lack of adequate scattering. On the other hand, there are a few cases where it is clearly insignificant (4.2(15), −0.5(5), −1(2),) or ambiguous (0.1(4), 0.3(3)) while some spontaneous resolution is expected with 0.08(7).
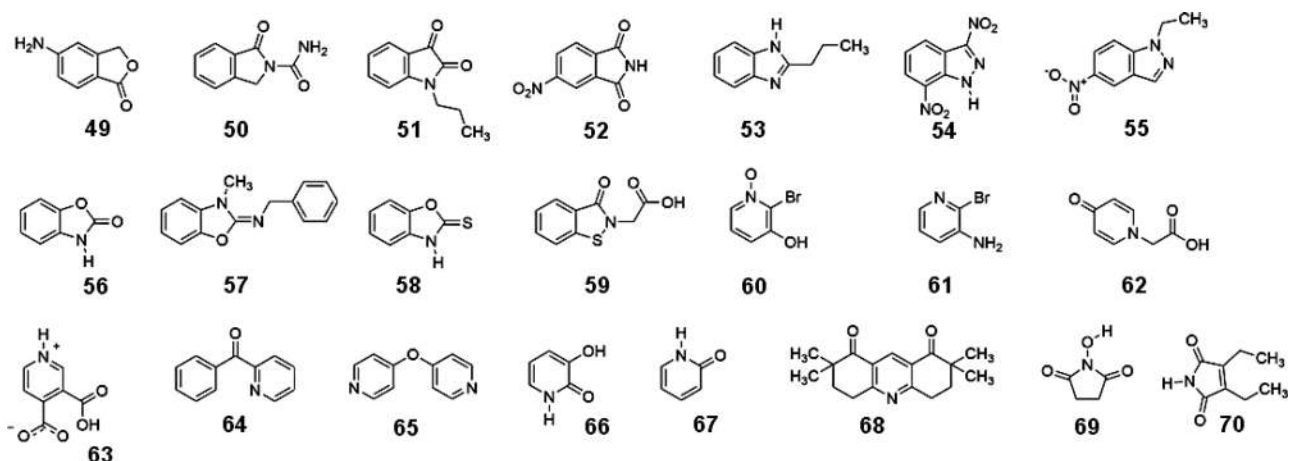
Figure 26. Structure of the heterocycles gathered on Table 10.

observed between the five- and six-membered rings of the neighboring molecules.

5.5. Curious Case of 2-Propyl-*1H*-benzimidazole in the Solid State

The case of 2-propyl-*1H*-benzimidazole (2PrBzIm)[390,391] is particularly interesting. In the absence of chiral additives, the compound is expected to crystallize as a 50/50 conglomerate, i.e., a polycrystalline powder sample of this compound must be without any chiral response. However, repeated VCD measurements always showed a clear-cut chiral signal no matter what synthesis or crystallization method was employed to produce the polycrystalline samples. While no chiral additives were present in any of the experiments, it appeared that either commercial, synthesized, or recrystallized samples always displayed identical chiral VCD responses (Figure 27).

Despite both enantiomeric crystals being energetically identical and despite the specific nature of the crystal structure (Figure 28), these findings show the influence of a hidden source of chirality, such as a cryptochiral environment that the authors have not been able to identify.

In pushing further their investigations, Elguero et al.[391] discovered a high-temperature solid−solid phase transition from a chiral to a new achiral form. Once the samples were heated above 380 K, the VCD signals that were typical of chiral form disappeared completely. This observation has resulted in the discovery of three new temperature phases (all belonging to non Sohncke space groups) which are related to the previously reported form by conformational polymorphism. These structural transformations involve significant changes in the crystal packing as well as a conformational variation from a linear to a twisted conformer around the propyl chain of the molecule.
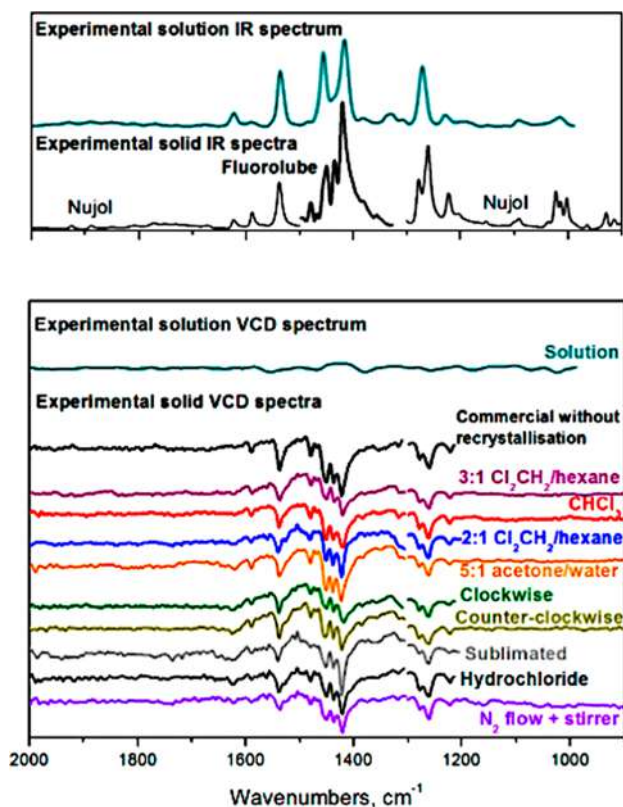
Figure 27. IR (upper) and VCD (lower) spectra for liquid (dark cyan) and solid samples of 2PrBzIm in fluorolube ($2000-1300$ cm^{-1} region) or nujol mulls ($2000-1500$ cm^{-1} and $1300-900$ cm^{-1} regions). Partial and total polycrystalline samples resulting from different recrystallization processes were taken for the preparation of the studied mulls. 3:1 Cl_2CH_2/hexane crystals obtained without any stirring; clockwise and counterclockwise, stirring direction during crystallization in CHCl$_3$; sublimated, noncrystalline samples condensed on a coldfinger (without any square planar crystals); hydrochloride, regenerated base from its salt. N$_2$ flow + stirrer, removing the acetone solvent using a magnetic stirrer and a N$_2$ flow. Reproduced from ref 390. Copyright 2017 American Chemical Society.
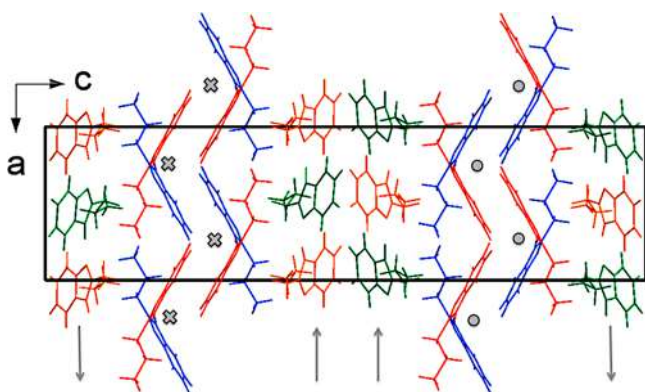
Figure 28. Crystal structure of 2PrBzIm. Note the conformational chirality of the molecules exhibiting syn configurations with deviations from planarity via rotation through the C_1-C_2 bond of about 45°. Four independent molecules (color-coded) form two perpendicular hydrogen-bonded chains. Finally, the chains are arranged within two interpenetrated perpendicular helical substructures. The arrows, dots (up), and crosses (down) indicate the polarity of the chains. Reproduced from ref 390. Copyright 2017 American Chemical Society.

In spite of this very detailed analysis of the crystal structures, polymorphism, and solid−solid phase transitions, the authors recognize that the same persistent chiral response in this material has not found until now any acknowledged explanation. Carefully looking at the literature, it appears that only a few authors have reported similar observations. Ethylenediammonium sulfate (space group $P4_1/P4_3$) crystallization exhibits a preference toward levorotatory crystals.[147] Spontaneous asymmetric generation of supramolecular chiral fibers was observed in the folding induced self-assembly of a lock-washer shaped pyridine/pyridazine foldamer. Solutions of this foldamer do not form the expected pseudoracemic mixtures but rather tend to amplify toward a preferential negative CD helical sense upon aging.[148] In 2014, Cuccia et al.[163] published a list of achiral small molecules giving rise to spontaneously enantio-enriched conglomerate mixtures, among them, benzophenone, hippuric acid, diphenyl disulfide, butylated hydroxytoluene (BHT), cytosine, and adeninium dinitrate ($P2_12_12_1$), benzil ($P3_121$/$P3_221$), ninhydrine ($P2_1$), and guanidinium carbonate ($P4_12_12$/$P4_32_12$). It was shown that, except for adeninium dinitrate, all these as-received commercial samples exhibited a significant *ee* (from 3% to >90%). Similar unexplained chiral bias has been reported during the low temperature crystallization of the LiCl complex of a dynamic combinatorial library of macrocyclic imines (space group $P2_12_12_1$).[335] Cu(II) coordination polymers with nitrogen heterocycles (space group $P2_12_12_1$) were always obtained in an optically active form and always the same enantiomer (see section 6.1).[373] A hidden source of optical activity or a "cryptochiral" environment is traditionally invoked to interpret these phenomena (see section 2.2.3).

5.6. Discrete Coordination Complexes

A final set of examples is related to some discrete transition metal coordination complexes giving rise to spontaneous resolution upon crystallization. They are gathered in Table 11 according to their coordination number starting from tetrahedral to seven-coordinate complexes. The structures of the corresponding ligands are displayed in Figure 29.

$[Ag(PS)_2]BF_4$ with PS = (2-(methylthio)ethyl)-diphenylphosphine) provides a rare example of a chiral metal complex undergoing attrition-enhanced deracemization to enantiopurity. Despite the repeated addition of the opposite enantiomer, a continual evolution toward the same CD amplitude has been witnessed. Moreover, it is reported that nine crystallizations from neat dichloromethane gave crystal batches with an average of 89% *ee* and quantitative yield.[187]

On the other hand, the pale-yellow needle-shaped crystals which have been harvested from a DMF solution by reacting the methyl-3-hydroxy-3-phenyl-2-propenedithioate (L) with Zn-(NO$_3$)$_2$·6H$_2$O in a water−methanol mixture behave more normally. Circular dichroism (CD) and single-crystal X-ray diffraction (SCXRD) studies of this discrete tetrahedral zinc(II) complex demonstrated the presence of a conglomerate product. Addition of small amount of chiral or racemic compounds has been carried-out. L-(+)-tartaric and L-(+)-mandelic acids induced mainly the Λ-enantiomer, while D-(−)-tartaric and mandelic acids, the Δ-one. No significant dichroic signals were recorded when using (±)-racemic acids.[406]

Generally, five-coordinate complexes undergo rapid inter-conversion in solution. However, when coupled with a conglomerate crystallization, this stereochemical lability can give rise to a spontaneous resolution. This is the case, for instance, in $[Zn(S_2CNEt_2)_2(vinim)]$ (vinim = 1-vinylimida-

Table 11. Examples of Discrete Transition Metal Complexes Crystallizing in Sohncke Space Groups

empirical formula	name or structure	T K	space group	system	Flack parameter	ref
$C_{30}H_{34}AgBF_4P_2S_2$	Δ-[Ag(PS)$_2$]BF$_4$	293	$P3_121$	trigonal	0.04(5)	187
$C_{20}H_{18}O_2S_4Zn$	Λ-[Zn(L)$_2$] and Δ-[Zn(L)$_2$]	150	$C2$	monoclinic	0.12(4)	406
$C_{15}H_{26}N_4S_4Zn$	Λ- and Δ-[Zn(S$_2$CNEt$_2$)$_2$(vinim)]	293	$P2_1$	monoclinic	0.002(6)	407
$C_{17}H_{29}CdN_4S_4$	Δ-[Cd(S$_2$CNEt$_2$)$_2$(lut)]	293	$P2_1$	monoclinic	−0.062(16)	407
$C_{34}H_{28}CuN_6O_8S_2$	[Cu(sac)(bipy)$_2$](sac)(H$_2$O)$_2$	289	$C222_1$	orthorhombic	0.004(11)	408
$C_{30}H_{24}Cl_2N_6O_8Ru$	Ru(bipy)$_3$(ClO4)$_2$	293	$P2_12_12_1$	orthorhombic		409
$C_{30}H_{24}CoF_{12}N_6P_2$	Δ- and Λ-[Co(bipy)$_3$](PF$_6$)$_2$	293	$P3_1$; $P3_2$	trigonal	−0.03(1); 0.010(18)	188, 410
$C_6H_{19}ClN_4NiO_6$	Δ-cis-[Ni(en)$_2$OAc][ClO$_4$]	173	$P4_32_12$	tetragonal	0.00(2)	411
$C_6H_{19}ClN_4NiO_6$	Λ-cis-[Ni(en)$_2$OAc][ClO$_4$]	293	$P4_12_12$	tetragonal	0.03(4)	411
$C_{12}Fe_2K_6O_{24}$	potassium tris(oxalato)ferrate(III)	293	$P4_132$	cubic	−0.07(6)	412
$C_{45}H_{35}O_7Ln$	[Ln(dbm)$_3$H$_2$O], Ln = Pr, Sm, Er	293	$R3$	trigonal	0.078(16); 0.018(12); 0.019(17)	260
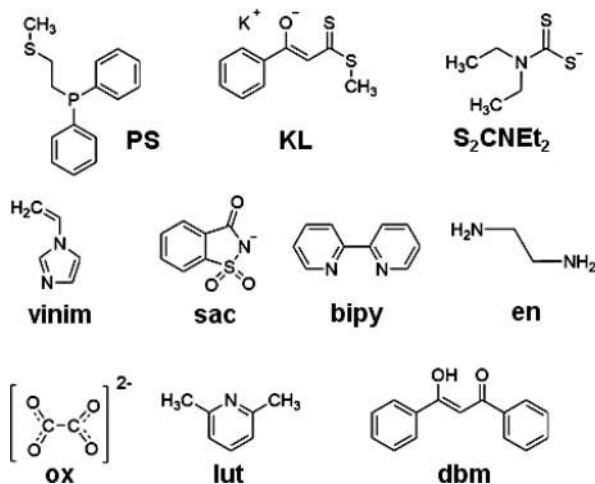
Figure 29. List of ligands corresponding to the complexes gathered in Table 11.

zole), [Cd(S$_2$CNEt$_2$)$_2$(lut)] (lut = 2,6-lutidine),[407] and [Cu-(sac)(bipy)$_2$](sac)(H$_2$O)$_2$, (sac = saccharinate, bipy = 2,2′-bipyridine).[408]

Werner metal complexes with octahedral coordination may exist as Δ and Λ enantiomers. In the crystalline state, such materials may exist as conglomerates. The chiral complex cis-[CoBr(NH$_3$)(en)$_2$]Br$_2$(en = ethylenediamine) was previously used to demonstrate its self-replication through secondary nucleation under stirring. Crystals of each enantiomer, when introduced into the reaction medium were shown to lead to the preferential production of the same enantiomer. The *ee* of the product increased with increasing the stirring rate. The random fluctuations of the final *ee* showed the stochastic nature of such autocatalytic processes.[413,414] However, from a more recent study,[415] it appears that a new racemic crystalline phase (belonging to the non-Sohncke space group $P2_1/n$) was consistently obtained. These observations could be an example of polymorphism (see section 5.7).

[Ru(bipy)$_3$]$^{2+}$ (bipy = 2,2′-bipyridine), which has been studied widely with regard to its photochemical properties, is also of considerable interest from the point of view of its chirality. A new anhydrous chiral phase of Ru(bipy)$_3$(ClO$_4$)$_2$ has been obtained from its chiral hydrate (space group $C2$) either by mechanical grinding and annealing or simply by solid-state dehydration at higher temperature.[409] However, this new anhydrous phase is a microcrystalline powder, thus reducing the possible collection of a single crystal for X-ray diffraction.

The reaction of [Co(NO$_3$)$_2$]·6H$_2$O with 2,2 bipyridine and NH$_4$PF$_6$ yields racemic solutions of [Co(bipy)$_3$]$^{2+}$. The two enantiomers are stereochemically labile. However, quantitative yield of enantiopure crystals batches of either handedness of [Co(bipy)$_3$]$^{2+}$ can be obtained by attrition-enhanced deracemization.[188] Next, the crystal chirality has been transferred to molecular chirality by bromine vapor oxidation of Co(II) to Co(III) giving rise to the stereochemically stable [Co(bipy)$_3$]$^{3+}$ complex.

When nickel acetate tetrahydrate was reacted in methanol with diaminoethane and an excess of sodium perchlorate, the two enantiomers Δ-cis-[Ni(en)$_2$OAc][ClO$_4$] and Λ-cis-[Ni-(en)$_2$OAc][ClO$_4$] were obtained (Figure 30).
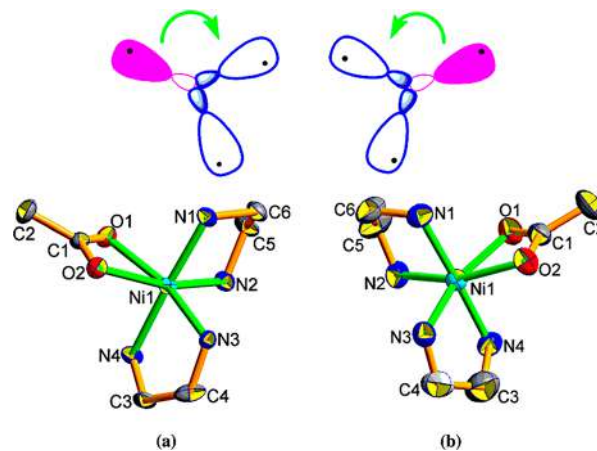
Figure 30. Both complexes Δ- (a) and Λ- (b) crystallize in the chiral space group $P4_32_12$ and $P4_12_12$. Their spontaneous resolution and absolute structure were confirmed by their significant Flack parameters. Reproduced with permission from ref 411. Copyright 2014 Springer Nature.

In the crystals, the monomers Δ- and Λ- are connected through N−H···O intermolecular hydrogen bonds between the carboxylate oxygen atom of an acetate and nitrogen atom of an adjacent diaminoethane. This interaction generates one-dimensional right- and left-handed homochiral helical chains, respectively. In contrast, when diaminoethane is replaced by 1,3-propanediamine, the reaction gave a different complex which crystallizes in the centrosymmetric space group $P2_1/n$. The monomers are connected through similar N−H···O hydrogen bonds forming a zigzag chain instead of a helical one.

The potassium tris(oxalato)ferrate(III) trihydrate belongs to the non Sohncke monoclinic system with a $P2_1/c$ space group.

However, by modifying the synthesis procedure, a chiral anhydrous form has been obtained. It crystallizes in cubic chiral space group $P4_132$. Figure 31 shows some collected crystals.

Figure 31. Anhydrous chiral potassium ferrioxalate crystals. Elemental analysis has confirmed the absence of hydrogen. Reproduced with permission from ref 412. Copyright 2012 Elsevier B.V.

While several crystals were harvested, there is neither a mention of the corresponding[411] enantiomeric space group $P4_332$ nor an estimation of the Flack parameter.

The resolution of complexes with coordination numbers higher than six remains a challenge due to the frequent lability of such complexes. However, total spontaneous resolution of seven-coordinates lanthanide complexes has been performed also by the Gothenburg group.[260] $[\text{Ln}(\text{dbm})_3\text{H}_2\text{O}]$ with Ln = Pr, Sm, and Er and dbm = dibenzoylmethane have been synthesized by reacting dibenzoylmethane and LnCl_3 hydrate in alkaline medium. They display seven-coordinate propeller-shaped molecules, which are chiral and crystallize as conglomerates in space group $R3$. These compounds form an essentially enantiopure microcrystalline reaction product. Numerous attempts to crystallize the Λ-Sm complex were unsuccessful, and only Δ-Sm crystals were harvested. Some cryptochiral effect was assumed, but seeding was useful to retrieve this missing enantiomer.

In this section, we have provided some examples of low cost discrete organo-metallic complexes, easily available from strictly achiral sources, but which crystallize as conglomerates since they belong to Sohncke space groups. As long as twinning-by-inversion can be avoided, the two enantiomers can be separated upon crystallization into left- and right handed crystals. While, we must be cautious to the possible presence of polymorphism (see section 5.7), it remains that a good proportion demonstrates an easily accessible spontaneous resolution. Such compounds could be used to analyze Viedma deracemization experiments and the possible influence of heterogeneous (at the nucleation level) and homogeneous (at the crystal growing level) chiral additives. Some other compounds also provide the opportunity to investigate polymorphic phase transitions.

5.7. Polymorphs

Polymorphism refers to the existence of more than one crystal structure for a particular molecule. It can be the result of a difference in crystal packing (packing polymorphism), the existence of different conformers (conformational polymorphism), or of the presence of different tautomers (tautomeric polymorphism). On the other hand, polymorphism can also be the result of the formation of hydrates or solvates. Polymorphs have different stabilities. In the case of organic molecules they only differ by a few kJ/mol in lattice energy. However, melting

points, solubility, dissolution rate, reactivity, and bioavailability are different and therefore polymorphism has ramifications for the pharmaceutical industry.[416] The appearance of concurrent polymorphs in solution results from an interplay between kinetic and thermodynamic factors, with the kinetic factor playing the dominant role. The main reason responsible for the development of different polymorphic forms lies in the variations of the crystallization processes. It was soon noted that fast evaporation or cooling can favor the growth of the less stable polymorph. The lower surface energy crystallizes first even the less stable in bulk. Ostwald stated that an unstable system would not necessarily convert to the most stable one but would rather progress in stages through forms that most closely resembled themselves.[417] Ostwald's rule is not a universal law but is only a possible trend. Seeding with one of the already obtained polymorphs is often the most successful way of preferentially producing it, rather than another.[418] On the other hand, unintentional seeding is often invoked as an explanation of the sudden emergence of a possibly undesired new crystal form.

From a statistical CSD standpoint, the odds are 50% to find polymorphs for any particular compound.[419] However, it is difficult, if not impossible, to find a link between a molecular property and polymorphism. However, it is the lack of molecular chirality which has been found to most significantly enhance a molecule's likelihood to polymorphism. Achiral molecules are considerably more likely to be polymorphic than chiral molecules. The absence of chiral centers in a molecule may increase the number of energetically identical ways to pack it. There are numerous reports of new polymorphic compounds or new structural characterization of already known polymorphic compounds.[420] Here, we report some examples of easily available achiral compounds giving rise to polymorphic crystals, some of them belonging to Sohncke space groups (chiral), while the others do not.

5.7.1. Azoles. Azoles provide examples of achiral monomers giving rise to supramolecular structures and spontaneous resolution.[390] For instance, achiral 1H-benzotriazole (BTA) crystallizes as two different polymorphs, one is chiral (α-BTA, $P2_1$) while the other is centrosymmetric (β-BTA, P-1) (Figure 32).[421]

Centrosymmetric achiral polymorph (β-BTA) involves both 1,2 and 1,3 hydrogen bonds in a 1:4 ratio (Figure 33a), while M-
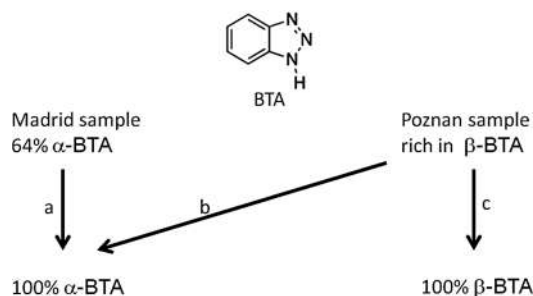
Figure 32. Pure chiral crystals (α-BTA) were obtained either from the Madrid or the Poznan samples by recrystallization from ethanol, 2-propanol, ethyl acetate, and xylene (crystallizations a and b). The centro-symmetric (achiral β-BTA) polymorph was only obtained by recrystallization of the Poznan sample from acetone, toluene, and benzene (crystallization c). It was assumed that the β-BTA was metastable since crystallization of the Madrid commercial sample (α-BTA rich) did not afford the β-BTA achiral polymorph regardless of the solvents they have used (inspired from ref 421).
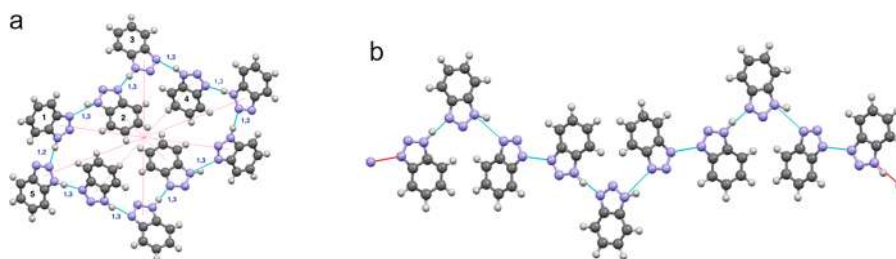
Figure 33. (a) Centrosymmetric β-BTA decamer showing the 1,3- and 1,2-hydrogen bonds and (b) helical chain fragment of 10 α-BTA molecules linked by 1,3- hydrogen bonds. The two polymorphs are 1H-tautomers. Reproduced with permission from ref 421. Copyright 2019 The Royal Society of Chemistry.

and P-helices generated by a 1,3 hydrogen bond are expected in the chiral α-BTA polymorph (Figure 33b).

A 50:50 mixture of the enantiomeric crystals was never obtained. All the VCD bands observed had the same positions and signs, indicating that of the two possible helices, i.e., M or P, only one was found in the crystals. The same enantiomer always predominated in each crystallization experiment. Such a chiral bias is assumed to originate from a cryptochirality effect thereafter amplified by a Viedma deracemization process related to the different sizes of the crystals (see section 2.2.4). In order to assign the absolute configuration of this catemer, i.e., if the helices are P or M, an analysis of the signs of the VCD bands has been performed with the aid of quantum chemical calculations. It was concluded that the absolute configuration of the helices of the chiral polymorph were left-handed, i.e., M helices.

An example of temperature-driven polymorphism is provided by the already mentioned 2-propyl benzimidazole (see section 5.5). Figure 34 shows that upon heating, an irreversible
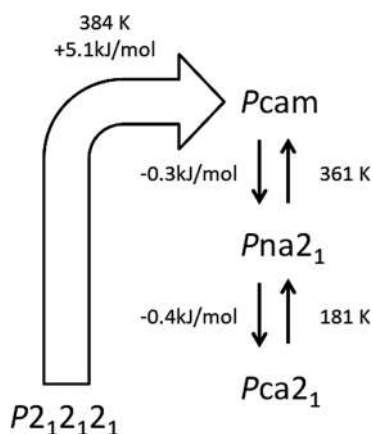
Figure 34. Temperature induced conversions between 2PrBzIm chiral and achiral polymorphs (inspired from ref 391).

polymorphic phase transition at $T = 384$ K from the chiral form ($P2_12_12_1$) to a new achiral form ($Pcam$), is observed. Then upon cooling, the high temperature ($Pcam$) form undergoes two further reversible phase transitions at 361 K ($Pna2_1$) and 181 K ($Pca2_1$), respectively. The chiral−achiral transition is endothermic and the chiral polymorph is the most stable form at low temperature. This is also the chiral form which is most often obtained by crystallization.

4-Benzoyl-1,2,3-dithiazol-5-one (Figure 35) provides another example of temperature induced polymorphism.[422] A racemic ($Pbca$) and a homochiral ($P2_12_12_1$) are regularly obtained by slow evaporation of chlorobenzene at 23 and 95 °C, respectively. When kept over several days at temperatures >70 °C, 4-benzoyl-1,2,3-dithiazol-5-one undergoes a solid-to-solid phase transition from the racemic low-temperature form to the high-temperature chiral form. Racemization occurs slowly at room temperature. This reversible polymorphic transition is accompanied by a remarkable rearrangement of the molecular conformation and reorganization of the noncovalent intermolecular interactions.

In a single crystal of the chiral polymorph (right), only one enantiomer is present, with a chiral conformation defined by the torsion angle values ($\Phi 1 = -11.7(3)$; $\Phi 2 = -50.7(3)°$). On the contrary, the achiral low-temperature polymorph is a racemic mixture of two enantiomers defined by $\Phi 1 = \pm 18.8(2)$ and $\Phi 2 = \pm 23.1(2)°$.

Another eye-catching example is provided by the case of the MDPI. Figure 36 shows the structure of MDPI ((4Z)-4-(4-methoxybenzylidene)-1-phenyl-2-(4-phenylbuta-(1E)-(3E)-dienyl)-1,4-dihydro-5H-imidazolin-5-one) which is an achiral molecule analogue of the green fluorescent protein (GFP) luminophore.[423]

When crystallized from a methanol solution impregnated with dichloromethane, it segregates into two different crystal forms by concomitant polymorphism (Figure 36b). The major product (form B; red, space groups $P4_1$) is thermodynamically more stable than form A (orange, space groups $P4_3$). Each polymorph is likely to be enantiomerically pure. Their
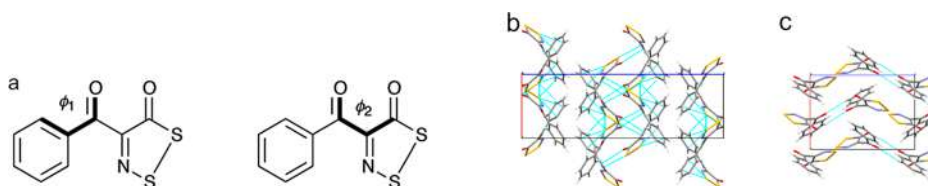
Figure 35. (a) Structure of the 4-benzoyl-1,2,3-dithiazol-5-one. Its conformational chirality is achieved by rotation about σ bonds in accordance with torsion angle values. (b and c) Stick representation of the unit cell viewed normal to (010) for achiral (b) and chiral (c) polymorphs; cyan lines represent contacts within the sum of van der Waals radii at 150 K. Multiple S⋯O contacts are a major source of supramolecular stabilization in the low temperature achiral form. Reproduced with permission from ref 422. Copyright 2017 The Royal Society of Chemistry.
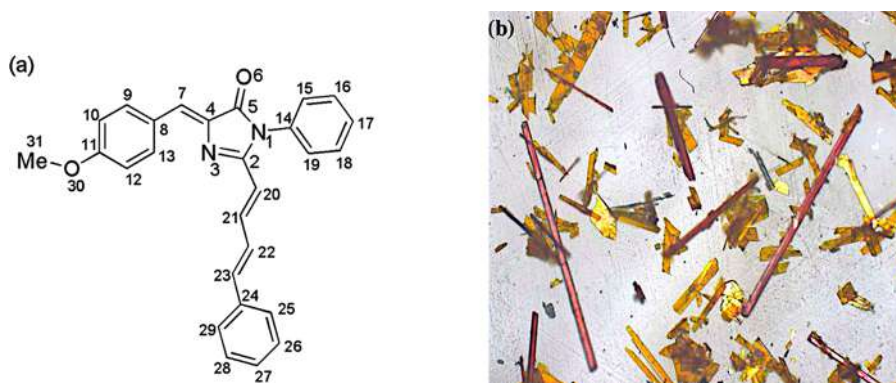
Figure 36. (a) Structure of the substituted imidazolinone; (b) concomitant polymorphic crystallization. Adapted from ref 423. Copyright 2012 American Chemical Society.

enantiomorphic space groups (i.e., $P4_3$ for the red and $P4_1$ for the yellow) are not mentioned by the authors. The color difference has been ascribed to a difference in the packing of the two crystal forms. In form B, molecules pack slightly more tightly than in form A. The difference in melting points of the two polymorphs is small, but the difference in the latent heat of fusion and solid-state fluorescence spectra is substantial. Crystal structure studies along with temperature-dependent ^{1}H NMR studies and theoretical calculations suggest that concomitant polymorphism arises from the presence of two rotamers along the N(1)−C(14) bond.

5.7.2. Temperature, Solvent, and pH Driven Polymorphism. 2-Chlorobenzamide[375] also provides an example of temperature and solvent driven polymorphism. It appears as long white needles (or cotton-wool-like) under either a monoclinic achiral α-form (space group $P2_1/n$) or an orthorhombic chiral β-form (space group $P2_12_12_1$) depending on commercial samples (see Table 9, structure **41**). At approximately 135 °C, the chiral β-form undergoes a solid−solid phase transformation to the α-form prior to melting at 150 °C. At room temperature, the achiral α-form easily converts to the chiral β-form on milling. Although a computational investigation suggested a complex crystal-energy landscape, no new polymorphs of 2-chlorobenzamide were found despite systematic milling studies carried out in a search for supplementary polymorphic forms.

Molecular crystals often show polymorphs that can form several stable and metastable packing structures by containing external guest molecules into the cavity of the crystals. 4-Hydroxyquinoline-2-carboxylic acid (kynurenic acid, a neuroactive inhibitor shown on Figure 37) is an interesting simple compound to expose how tautomerization and guest solvent affect its crystal packing in the solid state.[424] This wealth of behavior gives rise to a rich variety of tautomeric solid-state polymorphic forms.

Figure 38 shows two achiral hydrates (one monoclinic, space group $P2_1/n$, the second orthorhombic, space group $Pccn$), and a chiral DMSO solvate (space group $P2_12_12_1$). In this last case, the kynurenic acid occurs as the keto tautomer, i.e., as 4-oxo-1,4-dihydroquinoline-2-carboxylic acid.

The appearance of concomitant polymorphs in solution is due to the interplay of kinetic and thermodynamic factors, with the kinetic factor playing a dominant role. For instance, reaction of the antibiotic 4-aminosalicylic acid with ammonia in acetone or ethanol yields three polymorphic forms (I, II, and III) of the ammonium 4-aminosalicylate salt (see Table 8 structure **32**).[368]
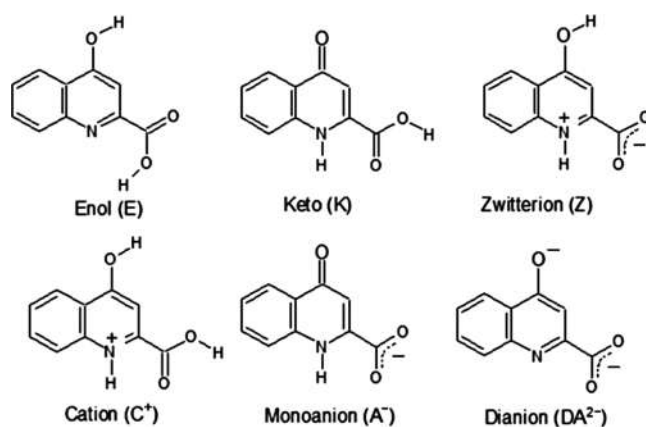
Figure 37. Depending on the proton migration and the pH, kynurenic acid displays enol and keto tautomers, zwitterions, and three ionic forms (cation, monoanion, and dianion). Reproduced from ref 424. Copyright 2019 International Union of Crystallography under Creative Commons Attribution 4.0 International License https://creativecommons.org/licenses/by/4.0/.
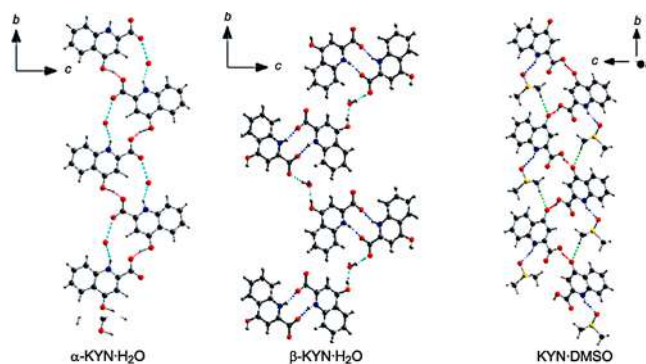
Figure 38. Helical arrangements in various kynurenic acid solvates polymorphs. Note the COH···COO⁻ interaction in the α-hydrate, zwitterionic cycles in the β-hydrate, and the CO···COOH interaction in the DMSO solvate. While exhibiting helical formations, both hydrates do not belong to any Sohncke space group and therefore are not chiral. Reproduced from ref 424. Copyright 2019 International Union of Crystallography under Creative Commons Attribution 4.0 International License https://creativecommons.org/licenses/by/4.0/.

Forms I and II crystallize in the $P2_12_12_1$ orthorhombic space group. Both asymmetric units contain one ammonium cation and one aminosalicylate-anion. On the other hand, form II was obtained as a single phase when the reaction was carried out in

the solid state (solid−gas and liquid-assisted grinding). Monoclinic form III crystallizes in the achiral $P2_1/n$ space group. As shown in Figure 39, the three polymorphs have similar
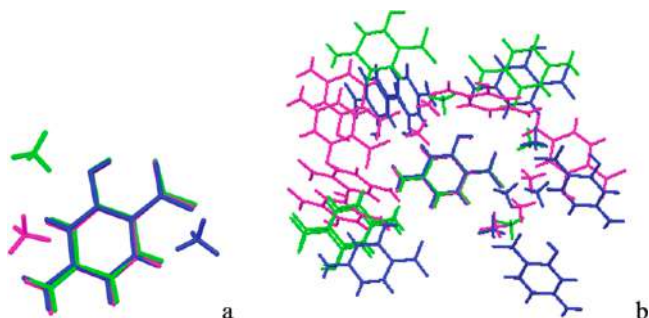
Figure 39. (a) Overlap of the structures of the asymmetric units occurring in the various polymorphic forms of ammonium 4-aminosalicylate salt: I (blue), II (magenta), and III (green). Note the different hydrogen bonding patterns of the ammonium cations and (b) crystal packing. Reproduced from ref 368. Copyright 2012 American Chemical Society.

conformations but are characterized by their distinct supramolecular arrangements due to the very different hydrogen bond patterns between the structurally rigid anions and the ammonium cations.

We cannot bring this list to a close without pointing out an unusual crystal habit of the achiral antihypertensive drug hydrochlorothiazide (HCT), which reveals large polar enantiopure domains (Figure 40).[425] Its subtle conformational chirality
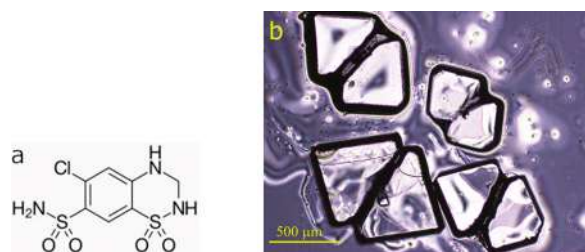
Figure 40. (a) Structure of 6-chloro-1,1-dioxo-3,4-dihydro-2H-1,2,4-benzothiadiazine-7-sulfonamide (hydrochlorothiazide, HCT); (b) conjoined two-winged habit of enantiomorphic pairs of form I of HCT crystals polymorph. Reproduced with permission from ref 425. Copyright 2019 John Wiley and Sons.

arises from the pyramidal nature of the sultam nitrogen atom adjacent to the sulfone group, combined with a low barrier to flipping of the saturated ring. Two polymorphs have been described: form I belonging to the Sohncke group ($P2_1$) which appears to be the most stable, and a centrosymmetric metastable form II (space group $P2_1/c$).

An intriguing feature is the unusual solid-state enantiomorphic growth of conjoined twin crystals that differ structurally from the known cases of racemic twins and lamellar twin crystals (Figure 40b). A closer look at these two crystal structures reveals that the individual wings include large polar enantiopure domains belonging to the form I $P2_1$ space group. The junction is a strong pairwise interaction centrosymmetric $\pi\cdots\pi$ stacking of form II (Figure 41). Such an interaction is a key step in nucleation and cluster growth in solution. Because $P2_1$ is a polar space group, polar crystals formed by strongly dipolar molecules such as HCT can build up significant electric polarity, leading to
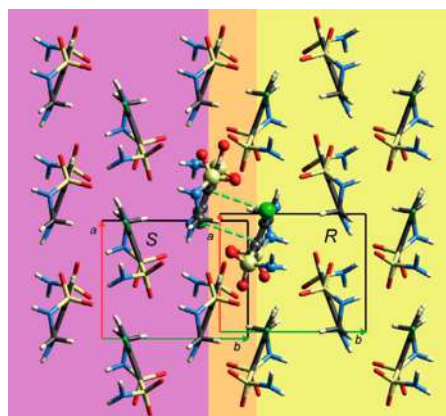
Figure 41. Sketch of the possible centrosymmetric boundary junction between the two enantiomorphic wings of form I HCT crystals. Reproduced with permission from ref 425. Copyright 2019 John Wiley and Sons.

instability during crystal growth. It is therefore likely that the growth of opposite polar domains would be a way to reduce the net electric polarity of the growing crystals.

Finally, it is worth mentioning that polymorphism results in different possible packing arrangements of a given substance under different crystallization conditions. Besides the industrial and commercial importance of polymorphism in pharmaceuticals, dyes, and pigments and the high-energy materials industry, there are many fundamental and academic aspects which deserve to be very closely scrutinized.

For instance, from the fundamental question of the origin of biological homochirality, the role played by glycine polymorphs is particularly remarkable. Glycine is the simplest amino acid with the lowest molecular weight. It is achiral. In the crystalline state, it can exist in several polymorph modifications: α, β, and γ under ambient conditions and more under high pressure.[426] While the α-polymorph is an achiral crystal (space group $P2_1/n$), the β- and γ-polymorphs are chiral crystals, which belong to $P2_1$ and $P3_1$ or $P3_2$, respectively. The selectivity toward these three polymorphs depends on solvent, laser induced nucleation,[427] seeding,[152] temperature cycling,[428] supersaturation, rate of evaporation, pH, and additives. Typically, aqueous solutions afford α-glycine, addition of methanol provides β-glycine, while γ-glycine grows from acetic acid, ammonium hydroxide, or sodium chloride aqueous solutions. Various experimental measurements and computational studies support a stability ranking in the order $\gamma > \alpha > \beta$ for bulk crystals. The metastable β polymorph exhibits a single-crystal-to-single-crystal transformation to either α or γ phase with retention of the crystal habit of the parent β phase.[429] Slow crystallization of the γ-polymorph without stirring gives either (+), i.e., $P3_2$ or (−), i.e., $P3_1$ optically active single crystals.[430] Under mechanical grinding with glass beads, the chiral γ-polymorph undergoes spontaneous mirror symmetry breaking. Several independent crystallizations under stirring, revealed an attrition-induced spontaneous chiral amplification, leading eventually to a homochiral batch. The distribution of the optical activity being roughly bimodal, this behavior is claimed to have a stochastic nature. A precise control of the emergence of homochirality in the γ-glycine crystalline phase has been carried-out by addition of 5% of L- or D-alanine enantiomers and long-stirring experiments.[431]

Another interesting example related to a molecule of biological interest is the generation of chiral cytosine crystals

($P2_12_12_1$) by removal of crystal water from achiral crystals of nucleobase cytosine ($P2_1/c$).[432] The crystal chirality of anhydrous cytosine corresponds to the enantiotopic crystal face of the achiral monohydrate. Dehydration of crystal water by warming from the b1-face of the achiral crystal of cytosine monohydrate gives a chiral crystal of dehydrated cytosine of CD(−), while from the b2-face gives CD(+) dehydrated cytosine crystal. Interestingly, dehydration of crystal water under "reduced pressure" from the b-1 face of the achiral crystal of cytosine monohydrate affords the chiral crystal of cytosine anhydrate of CD(+), opposite to that of warming, while dehydration from the b-2 face affords the CD(−) crystal of cytosine anhydrate.[433]

In any attempt to perform a preferential crystallization strategy from achiral molecules to chiral crystals, one should bear in mind that achiral structures can show somewhat elevated levels of polymorphism.[202] Therefore, it must be ascertained that the most stable polymorph belongs to a Sohncke space group.[434] While polymorph searching could be a time-consuming trial-and-error exercise, the prospect of computationally predicting polymorphism appears therefore highly attractive.[435] While it remains in general difficult to predict the structure of even the simplest crystalline solids from their chemical composition, some progress has been made in the crystal structure prediction of small organic molecules.[436] Deep learning algorithms have been developed, which are now able to solve the problem of energy ranking of molecular crystal structures that is intimately related to polymorphism.[437]

6. CHIRAL SUPRAMOLECULAR ASSEMBLIES FROM ACHIRAL BUILDING BLOCKS

6.1. Metal−Organic Frameworks

Metal−organic frameworks, abbreviated as MOFs, are porous crystalline coordination compounds with repeating coordination entities extending in 1, 2, or 3 dimensions. They are constructed by metal ions/clusters and organic linkers.[438] Because of their considerable variety of architectures and topologies, MOFs have drawn considerable attention as possible functional materials.[439,440] Special efforts have been directed to the design and synthesis of chiral MOFs due to their attracting potential applications in enantioselective catalysis,[441−443] chiral separation,[444,445] chiral recognition,[446,447] nonlinear optics,[448−451] and magnetic materials.[452,453]

Three main strategies are used for preparing homochiral MOFs: (a) the use of an enantiopure organic ligand, which translates chirality to the resultant framework and makes them homochiral in nature;[454] (b) the use of chiral induction reagents such as an enantiopure solvent, additive, catalyst, or template;[455] (c) the use of achiral ligands under spontaneous resolution conditions if the target bulk sample tends to be a conglomerate.[452] Homochiral MOFs from achiral linker ligands can be considered as interesting systems for the study of spontaneous resolution.[456]

As an illustrative example, let us look at a 3D chiral metal phosphonate framework built from achiral precursors in the absence of chiral sources,[457] namely, a cobalt-phosphonate Co(H₂L)(4,4′-bipy)·H₂O [H₄L = thiophene-2-phosphonic acid and 4,4′-bipy = 4,4′-bipyridine], which is synthesized by simply mixing Co(NO₃)₂·H₂O, thiophene-2-phosphonic acid and 4,4′-bipy in a 2:1:2 molar ratio in aqueous solution at 100 °C during 3 days (Figure 42). Single-crystal X-ray diffraction studies showed that this compound crystallizes in the Sohncke space group $P2_1$
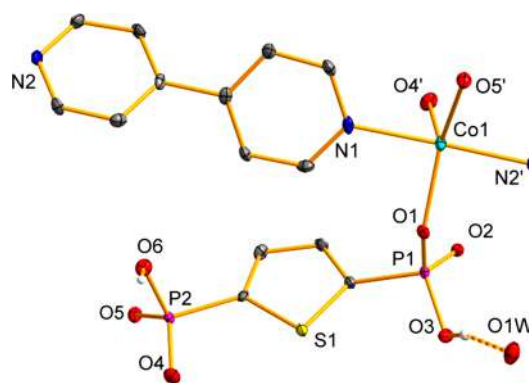
Figure 42. ORTEP representation of the asymmetric unit in the Co-phosphonate framework with thermal ellipsoids set at 50% probability. CH hydrogen atoms are omitted for clarity. Reprinted from ref 457. Copyright 2016 American Chemical Society.

with a Flack parameter near 0, indicating enantiomeric purity of the single crystals despite the use of achiral reagents. Figure 43
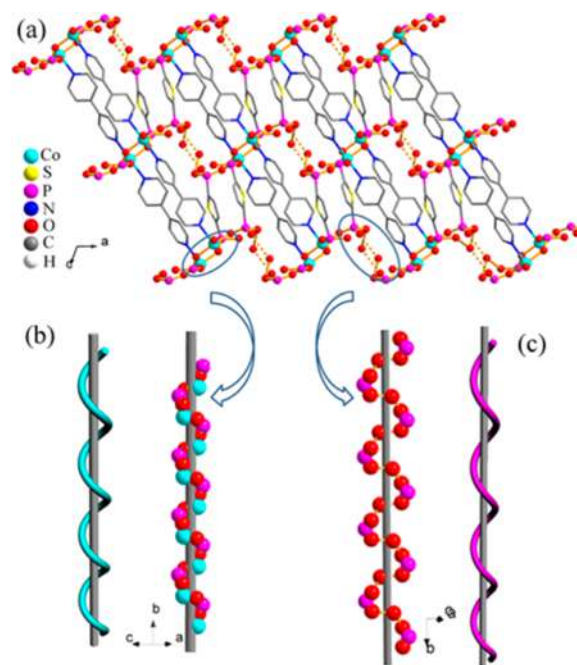
Figure 43. (a) 3D network along the *b* axis; (b) −Co−O−P−O−Co− helical chain with pitch artist's view; (c) ···O−P−O···H−O−H···O−P−O··· helical chain with pitch artist's view. Reprinted from ref 457. Copyright 2016 American Chemical Society.

shows that each asymmetric unit includes one crystallographically independent cobalt(II) cation, one protonated thiophene phosphonate anion, one 4,4′-bipy ligand, and one water molecule. Each cobalt(II) center is five-coordinated in a distorted trigonal-bipyramidal geometry environment, with two nitrogen atoms from two 4,4′-bipy ligands and three oxygen atoms from three different phosphonic ligands in a monodentate fashion. Moreover, in each thiophene phosphonate anion, one phosphonate is attached to two cobalt atoms and the other coordinates to one cobalt, hence the infinite 3D network shown on Figure 43a.

Each cobalt ion, which is ligated by two nonplanar bidentate 4,4′-bipy and three conformationally distorted thiophene phosphonate ligands becomes an asymmetric center. The

interconnection with its neighbors results in a 2_1 −Co−O−P−O−Co− helical chain (Figure 43b). Water molecules are linked through strong hydrogen-bonding to adjacent phosphonate groups from different thiophene phosphonate anions. The arrangement of their lattice creates a ···O−P−O···H−O−H···O−P−O··· helical chain (Figure 43c). Owing to this architecture, this Co-phosphonate compound undergoes a spontaneous resolution.

From a more general point of view, MOF chirality arises by the helical secondary structures. Flexible V-shaped, multidentate organic bridging ligands may be efficient candidates to generate chiral MOFs.[458,456,459] N- or O-donor achiral ligands with diverse flexibility are able to form versatile conformation and coordination modes. Nitrogen-rich organic ligands such as imines, nitriles, pyridines, pyrazines, imidazoles, pyrazoles, triazoles, and tetrazoles derivatives bring various coordination sites toward different metal ions. On the other hand, the introduction of secondary auxiliary ligands, such as carboxylic acids, has also been attempted.[460] Progresses in the synthetic and functional aspects of chiral metal−organic frameworks containing only achiral building blocks have been reviewed recently.[275,439,445,461−465]

6.1.1. Examples of Spontaneous Resolving MOFs. For a spontaneous resolution to occur, it is necessary that the solid form was a racemic conglomerate. In that case, each crystal contains only one enantiomer. Without any chiral induction, the handedness of individual nuclei during crystallization remains uncontrollable and the whole bulk materials tend to be racemic. To demonstrate this situation in no uncertain terms, the best way is to pick-up individual monocrystals as Pasteur did with his tweezers, to record individual CD spectra and to check that a bulk mixture remains CD silent (Figure 44).
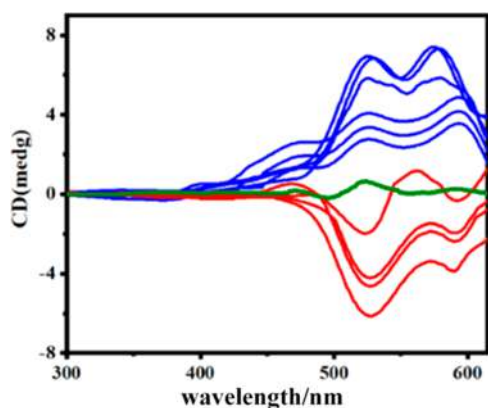
Figure 44. CD spectra of 10 crystals of a Ni(II) metal−organic framework from an achiral 3-(pyridin-3-yl)-1,2,4-triazine-5,6-diol **77**. Four are Λ (red lines) and the others are Δ (blue lines), and a mixture of few randomly picked up crystals exhibit no CD signals (green line). Reprinted from ref 441. Copyright 2019 American Chemical Society.

Figure 45 (see the associated Table 12) shows the structures of some achiral building blocks giving rise to self-resolving chiral MOFs. Table 12 collects some examples of chiral MOFs consisting only of achiral building blocks for which a clear-cut spontaneous resolution has been observed. They are tabulated according to the metal's atomic numbers.

More examples of spontaneously resolving MOFs can be found in refs 477−483.

6.1.2. Examples of Symmetry Breaking MOFs. However, in some cases, the *ee* of the bulk chirality is about 100%, which means that an absolute asymmetric synthesis or symmetry breaking has occurred. A Viedma deracemization effect (see section 2.2.4) is often mentioned to interpret this deracemization process. Here again, in the absence of any chiral influence, it is expected that the mean value of a large number of independent experiments was racemic, owing to the stochastic nature of crystallization.[140,22] We will show that it is not always the case and that some chiral MOFs crystallizations are, in some cases, accompanied by a bias to a preferential enantiomer even if there are only nonchiral precursors.[484] The published mechanisms are unclear and are ascribed to chiral contaminants of either biological or chemical origin, without entering more in the experimental details, thus allowing a source of potentially extremely useful chemical information to be lost. In order to analyze this question in the MOFs specific case, a careful bibliographic investigation including the scrutiny of the Supporting Information parts of the chiral MOFs literature has been carried-out. Figure 46 shows the structures of the achiral building blocks that are involved in some symmetry breaking MOFs. They are gathered in Table 13 according to the metals atomic numbers.

Because there are no driving forces for symmetry breaking crystallization, the spontaneous asymmetric crystallizations presented here are unexpected. Under achiral conditions, the spontaneous resolution process usually results in a mixture of crystals with opposite handedness (i.e., a racemic conglomerate). The main difference between spontaneous resolution and symmetry-breaking does not concern the structures of the MOFs but more likely the crystallization conditions. In general, the static process produces the expected statistically equal number of left-handed and right-handed crystals, and a racemic conglomerate is obtained. On the contrary, if the solution is constantly stirred during crystallization, new crystals are generated by the surface of a crystal in contact with a fluid in motion. The handedness of these secondary crystals is the same as that of the parent crystals. Therefore, as was already demonstrated by Kondepudi, and then by Viedma (see section 2.2.4), there is a chance that almost all the harvested crystals will have the same handedness.

From a statistical point of view, symmetry breaking can be compared to coin flipping. In the case of just one toss, the chance of getting only a head or only a tail is 100%. Thus, the expected equal probability of forming either a left- or a right-handed primary nucleus is significantly skewed toward one particular enantiomeric form when the number of independent crystallizations is very limited. On the other hand, if a coin is flipped a sufficient number of times, it will come to rest on either side with equal probability.

More intriguing are the rarely published selective chiral symmetry breakings, during chiral MOFs crystallization, without any chiral sources. Zhang et al.[493] recently observed, in multiple repeated experiments, a nonstochastic handedness excess of chiral MOF $[(CH_3)_2NH_2]_5[Zn_{1.5}(Zn_3O)(TATAT)_2]·9DMF·17H_2O$ which was synthesized using achiral flexible ligands H_6TATAT **98** and $Zn(NO_3)_2·6H_2O$ (see entry (u) in Table 13). Figure 47 shows the persistent positive CD signals.

The final proposed speculation is that the crystallization of ZnTATAT MOF may be catalyzed selectively by the sporadic presence of chiral impurities (cryptochiral environment) in their laboratory (see section 2.2.3).

A second example was published by Zheng et al.[488] about the chiral coordination polymer $[Cu(DPT)]_n$, which was assembled from achiral precursors (see entry (p) in Table 13). A total of 39

Figure 45. Main achiral ligands corresponding to the self-resolving chiral MOFs collected in Table 12.

Table 12. List of Some Chiral MOFs Built from Achiral Building Blocks But Giving Rise to a Spontaneous Resolution

metal	main ligands	empirical formula	system	Z	space group	comments[a]	ref
Mn(II)	N-(1H-tetrazol-5-yl)benzamide (71)	$C_{16}H_{12}MnN_{10}O_2$	tetragonal	4	$P4_12_12/$ $P4_32_12$	(a)	466
Mn(II)	methylene-diisophthalic acid (72); 1,2-bis(4-pyridyl)ethylene (73)	$C_{92}H_{124}Mn_7N_4O_{67}/$ $C_{92}H_{138}Mn_7N_4O_{74}$	monoclinic		C_2	(b)	467
Fe(II)	3-methyl-2-(5-(4-(pyridin-4-yl)phenyl)-4H-1,2,4-triazol-3-yl)-pyridine (74)	$C_{38}H_{28}FeN_{10}$	trigonal	3	$P3_112/$ $P3_212$	(c)	453
Ni(II)	4,4'-sulfonyldibenzoate (75); 1,4-bis(imidazol-1-ylmethyl) benzene (76)	$C_{28}H_{22}N_4NiO_6S$	orthorhombic	8	F_{222}	(d)	468
Ni(II)	3-(pyridin-3-yl)-1,2,4-triazine-5,6-diol (77)	$C_{48}H_{30}N_{24}Ni_3O_{12}$	tetragonal/ monoclinic	4	I_4/C_2	(e)	441
Cu(II)	succinic acid (78); 4,4'-bipyridine (79)	$C_{14}H_{20}CuN_2O_8$	hexagonal	6	$P6_522/$ $P6_122$	(f)	469
Cu(II)	VO_3^-; ethylenediamine (en); imidazole (80)	$C_8H_{16}CuN_6O_6V_2$	orthorhombic	4	$P2_12_12_1$	(g)	470
Cu(II)	4'-(4-methoxyphenyl)-4,2':6',4''-ter-pyridine 81	$C_{188}H_{172}Cu_4N_{24}O_{14}S_6$	tetragonal	4	$P4_12_12/$ $P4_32_12$	(h)	471
Zn(II)	1,4-benzeneditetrazol-5-yl) (82)	$C_8H_4N_8Zn$	orthorhombic	4	$P2_12_12_1$	(i)	472
Zn(II)	5-sulfoisophthalic acid (83); imidazole (80); 1-ethyl-3-methylimidazolium tetrafluoroborate (84)	$C_{17}H_{18}N_4O_7SZn$	orthorhombic	4	$P2_12_12_1$	(j)	473
Zn(II)	4'-(1H-benzo[d]imidazol-1-yl)biphenyl-4-carboxylic acid (85)	$C_{44}H_{32}N_4O_8Zn_2$	monoclinic	2	$P2_1$	(j)	474
Ag(I)	2-(2'-cyanophenoxy) benzonitrile (86); CF_3SO_3H	$C_{15}H_8AgF_3N_2O_4S$	orthorhombic	4	$C222_1$	(k)	475
Ag(I)	bis(3,5-dimethylpyrazol-1-yl)(pyridine-4-yl) methane (87); HBF_4	$C_{18}H_{23}AgBF_4N_5O_{0.5}$	monoclinic	4	$P2_1$	(l)	476

[a](a) Expected formation of the pair of enantiomeric complexes, no CD bulk; (b) mixed ligands, the "enantiomers" differ by their hydration level but afford approximately mirror-image CD spectra, no CD bulk; (c) the bulk sample is a racemic mixture; (d) mixed ligands, four of nine randomly selected single crystals exhibit positive CD signals, and the remaining five showed negative CD signals, while a mixture of a few crystals did not show dichroic signals; (e) as expected, a mixture of few randomly picked up crystals exhibits no CD signal; unfortunately, the single crystal structure of monoclinic methanol solvate was not obtained after many attempts; (f) every single crystal within a cluster crystallizes in the same enantiomeric form, but the specific handedness of the crystals in any of the clusters cannot be predicted, as there is no systematic bias in favor of one particular enantiomer over the other, nonbiased symmetry breaking; (g) it was found that the probabilities of the two enantiomers was close to 6:4, no bulk CD; (h) each crystal probably contains about 17% of the second enantiomorph. The bulk sample shows no CD signal, which confirmed the nature of the conglomerate state; (i) CD measurements confirm the spontaneous resolution process; (j) confirmation of the spontaneous resolution; (k) either positive (P) or negative (M) Cotton effects were observed for crystals obtained from different crystallization batches suggesting that either P or M enantiopure crystals form in each crystallization batch; (l) both enantiomers were observed from solid-state circular dichroism (CD) spectroscopy applied to bunches of crystals. This reveals that locally, one enantiomer is formed in excess, possibly even exclusively, and suggests that growth of single colonies of homochiral crystals starting from single nucleation points may occur.

individual batches under the same solvothermal reaction conditions were analyzed. For each batch, all the crystal products were ground into powder and mixed evenly, and then 2 mg of sample was randomly taken for VCD testing. The results are shown in Figure 48. As the authors were also interested in the photophysical and photocatalytic properties of

their coordination polymer, there are only few attempts to speculate on the origin of such selective symmetry breaking.

Other examples of a nonstochastic chiral bias in MOFs crystallized from strictly achiral conditions can be found in refs 495–499. Their relative synthetic easiness and fascinating structures make chiral MOFs built from achiral precursors a
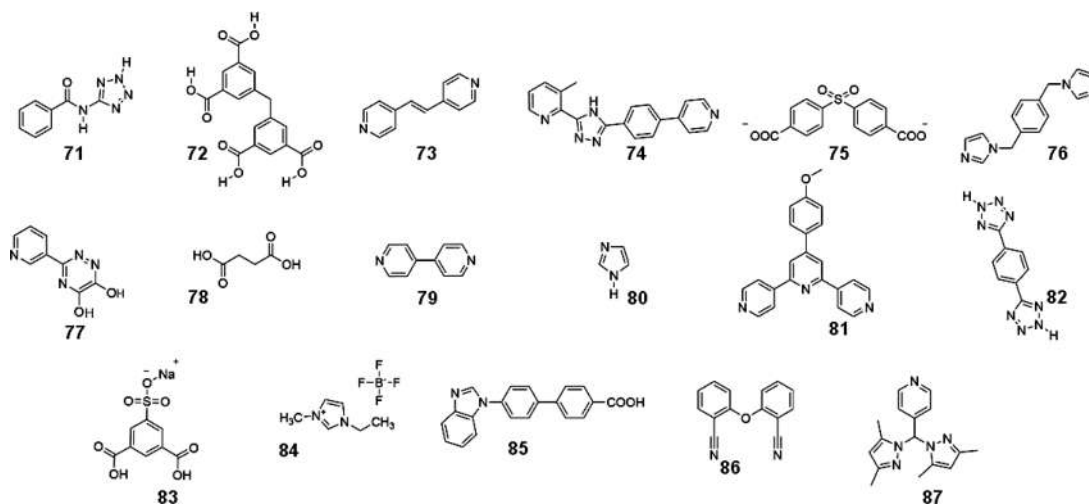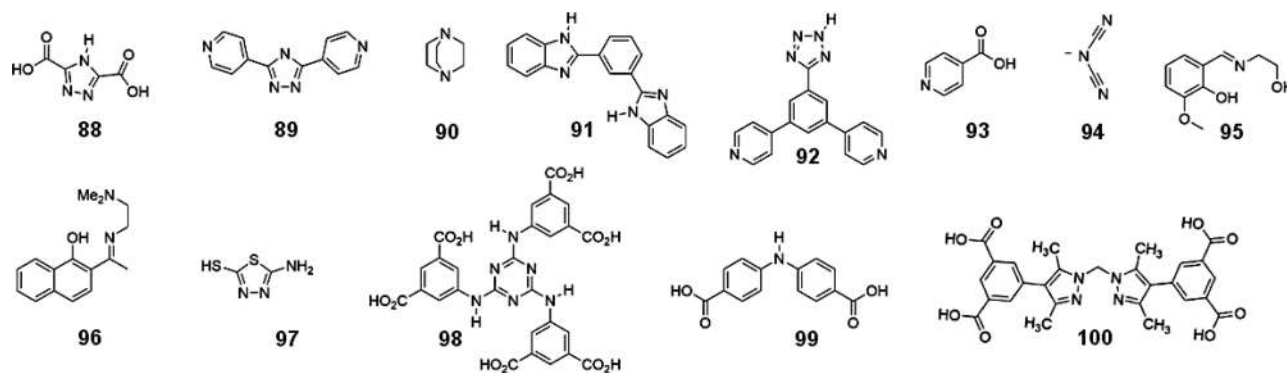
Figure 46. Main achiral ligands corresponding to the symmetry-breaking chiral MOFs gathered in Table 13.

Table 13. List of Some Chiral MOFs Built from Achiral Building Blocks but Giving Rise to a Symmetry Breaking

metal	main ligands	empirical formula	system	Z	space group	comments[a]	ref
Ni(II)	4H-1,2,4-triazole-3,5-dicarboxylic acid (**88**)	$C_4H_{12}N_3O_{10}Ni_{1.5}$	trigonal	6	$P3_121$	(m)	485
Cu(I)	3,5-bis(2-pyridyl)-1,2,4-triazolate anion (**89**)	$C_{73}H_{50}N_{31}OCu_7$	monoclinic	2	$C2$	(n)	486
Cu(I)	dabco (**90**; 1,3-bis(2-benzimidazol)-benzene (**9**)**1**	$C_{41}H_{57}Cu_6I_4N_{11}O_3$	hexagonal	6	$P6_122$	(o)	487
Cu(I)	3,5-di-4-pyridinyl−2H-tetrazole (**92**)	$C_{17}H_{11}CuN_6$	trigonal	3	$P3_221/$ $P3_121$	(p)	488
Cu(I)/Pr(III/ IV)	isonicotinic acid (**93**)	$C_{48}H_{38}Cu_5I_4N_7O_{16}Pr_2$	orthorhombic	4	$P2_12_12_1$	(q)	489
Cu(II)	dicyanamide (**94**); Schiff base (**95**)	$C_{12}H_{12}CuN_4O_3$	orthorhombic	4	$P2_12_12_1$	(r)	490
Cu(II)	(1-(2-(dimethylamino) ethylimino)ethyl) naphthalen-1-ol (**96**)	$C_{17}H_{19}CuN_3O_2$	orthorhombic	4	$P2_12_12_1$	(s)	491
Zn(II)	2-amino-5-mercapto-1,3,4-thiadiazole (**97**)	$C_4H_4N_6S_4Zn$	orthorhombic	4	$P2_12_12_1$	(t)	492
Zn(II)	5,5′,5″-(1,3,5-triazine-2,4,6-triyl)tris(azanediyl)tri-isophthalate (TATAT) (**98**)	$C_{54}H_{24}Zn_{4.5}N_{12}O_{25}$	cubic		$F4_132$	(u)	493
Cd(II)	4,4′-dicarboxy-diphenylamine (**99**); DMF	$C_{37}H_{55}Cd_2N_5O_{19}$	monoclinic	2	$P2_1$	(v)	494
Cd(II)	bis[4-(3,5-dicarboxyphenyl)-1H-3,5-dimethylpyrazolyl] methane (**100**)	$C_{39}H_{54}Cd_2N_8O_{15}$	triclinic	1	$P1$	(w)	442

[a] (m) CD spectra of each whole batch from these 5 parallel products were also measured in the solid-state and exhibit positive signal at about 260 nm; (n) the results demonstrate that the product is enantioenriched; (o) the CD spectra reaffirms that the bulk sample is homochiral, indicating that the resultant crystals are optically active even without the presence of chiral precursors in the original synthesis; (p) only 5 batches (1-B) showed a mirror-symmetric VCD signal compared to the other 34 batches (1-A), indicating a clearly higher probability of generating one of the enantiomers than the other; (q) nine batches of the bulk sample obtained from repetitive syntheses are CD measured, revealing enantiopure bulk sample; (r) solid-state CD measurement confirms that the bulk material is homochiral; (s) in the present case, stirred crystallization favors the propagation of crystals of a particular handedness; (t) both the Cotton effect displayed in the CD spectrum and the structural refinements of the 14 crystals demonstrate that the bulk sample is enantioenriched; (u) interestingly, we observed nonstochastic handedness excess through selective chiral symmetry breaking in multiple repeated experiments; (v) bulk crystals are chosen to determine the solid-state CD spectra in a KCl matrix, a negative CD signal, revealing the formation of enantiomers in crystals. This result confirms spontaneous chiral symmetry breaking in crystallization; (w) the solid-state circular dichroism (CD) spectrum confirmed the chirality of the bulk material, which showed a positive Cotton effect.

promising area for those interested in spontaneous resolution and symmetry breaking.

6.2. Polyoxometalates

Polyoxometalates (abbreviated POMs) are polyatomic transition metal oxyanions linked together by shared oxygen. Typically, the metal atoms are from groups 6 (Mo, W) or 5 (V, Nb, Ta) in high oxidation states. They self-assemble into extended structural motifs to form closed 3-dimensional frameworks. Chiral polyoxometalates exhibit interesting structures and topologies and have also potential applications in nonlinear optics, enantioselective catalysis, chiral separation, and molecular recognition. However, the spontaneous resolution of chiral POMs is still a relatively scarce phenomenon.

A first example of enantiomerically 3D POM-based compounds is based on the achiral ligand 1,1′-(1,4-butanediyl)-bis(imidazole) (bbi), $^{[V_{10}O_{26}]4−}$ polyoxoanion and mixed valence Cu(I/II). The compound $[Cu(bbi)_2V_{10}O_{26}][Cu(bbi)]_2·H_2O$ has been isolated by hydrothermal methods. It gives rise to

spontaneous resolution without any chiral auxiliary. Single-crystal X-ray diffraction analyses reveal that the crystals belong to the orthorhombic system within the $I222$ space group.[500]

The reaction of the silicotungstic acid with KCl in the presence of manganese nitrate or europium nitrate did not give any incorporation of the transition metal ion into the framework but to the spontaneous resolution of $H_{16}K_2O_{47}Si_1W_{12}$ crystals. These crystals belong to the hexagonal system within either the chiral space groups $P6_222$ (if the additive was Mn) or $P6_422$ (if the additive was Eu). The presence of transition metal additives seems necessary for the spontaneous resolution (or symmetry breaking) since in their absence, a racemic CD silent mixture has been obtained.[501]

Another case of possible symmetry breaking has been described by Yang et al.[502] during the crystallization of a new chiral compound, $[LiCu_2[BP_2O_8(OH)_2]$, from achiral inorganic raw materials. This compound was prepared by the boric acid flux reaction of a mixture of H_3BO_3, LiH_2PO_4, and $Cu(OAc)_2·$
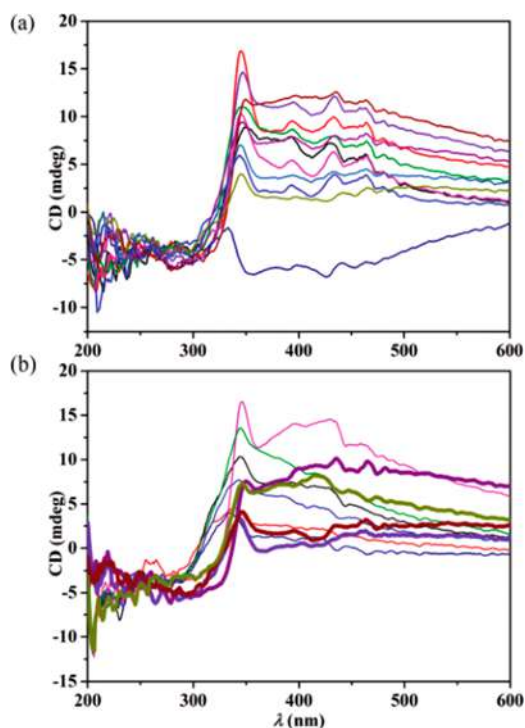
Figure 47. (a) Solid-state CD spectra of 11 randomly selected single crystals of ZnTATAT MOF picked from 11 individual reaction vessels. (b) Solid-state CD spectra of bulk samples picked from one reactor (thin lines). The thick lines represent bulk samples picked from 10 reactors. Reproduced with permission from ref 493. Copyright 2018 The Royal Society of Chemistry.
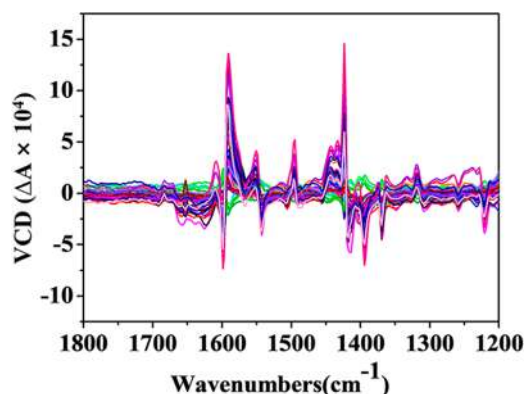
Figure 48. VCD spectra of 39 batch experiments. The green lines are the five batches assigned to mirror-symmetric VCD signal, and the other 34 lines are assigned to enantio-enriched batches. Reprinted from ref 488. Copyright 2019 American Chemical Society.

H_2O in a molar ratio of 8:2:1 at 200 °C for 5 days. Homochirality of the single crystals of this copper borophosphate compound was checked by single-crystal X-ray diffraction analysis revealing a $P2_12_12_1$ space group, with a Flack parameter of 0.010(11). In order to study its optical activity, over seven batches of crystalline powder were randomly taken for solid-state CD analyses from several different syntheses, carried-out from achiral inorganic raw materials without any stirring process or other mechanical power. Each measurement showed a negative Cotton effect, suggesting an enantiometric excess of the bulk sample. It was admitted that, except for the well-known example of $NaClO_3$, the phenomenon was unprecedented in a pure

inorganic synthetic system. Other chiral inorganic polyoxometalates-based frameworks involving helical motifs give rise to spontaneous resolution during crystallization without any chiral auxiliary.[447,503,504]

The sophistication of the MOF and POM structures contrasts with the relative easiness of their synthesis conditions (simple mixing, solvent diffusion, solvothermal conditions...). However, despite an apparent simplicity of synthesis, many parameters such as pH, counterions, ionic strength, solvent, temperature, reaction time, additives, or concentration play important roles in the formation of such coordination structures and therefore have to be controlled carefully. This is a new area for those who like to delve into the intimate secret of these chiral crystallizations.

6.3. Self-Assembly of Achiral Compounds to Chiral Structures Other than Crystals

Supramolecular chirality arising from the self-assembly of chiral and achiral compounds has been the subject of excellent reviews.[463,505−509] The emergence of chirality by deposition of achiral monomers upon ordered surfaces (e.g., ref 283) and the bidimensional self-assembly toward layered structures in solution (e.g., ref 510) have also been the subject of specific reviews.[271,506,511] Here, we review the emergence of chirality and SMSB in these systems.

The study of mesophases constitutes a wide and transversal topic spanning from the molecular self-assemblies to nanoparticles, comprising the huge field of liquid-crystals and reaching even to classical colloid/gel chemistry. All these fields make use of specific notations and are based on different physicochemical models; this does not help to make a comprehensive description of supramolecular chirality using the same terms as those of organic and asymmetric synthesis. The definition of mesophase comprises a wide range of aggregates, from "soft crystals"[512] to thermotropic liquid crystals and also lyotropic liquid crystals whose structure depends on their interactions with the solvent. Furthermore, the term comprises structures that are obtained at different size scales from macroscopic phases to nanoassemblies.

In the same way as in solid crystals, nonideal liquids[508,513,514] and mesophases[515−517] may yield racemic conglomerate phases from achiral compounds.[518,519] The analogies between crystallization and mesophase formation have been used as an approach for the preparation of chiral mesophases starting from achiral compounds yielding racemic conglomerate solid crystals.[520] The preference for homochiral ordering from initially small aggregates of mesogens is called by some authors, "synchronization".[273] This approach is in agreement with well-accepted models for noncovalent supramolecular polymerization[521] and for crystal nucleation and growth.[522] Notice that these models show cooperative effects that generate nonlinear autocatalytic dynamics and, in far from equilibrium conditions, SMSB may occur (see section 9). A difference between solid crystals and liquid mesophases, in the absence of solvent, is that in mesophases, the enantiomorphic domains are in contact while they are separated in conglomerate crystals. There results a specific enantioselective interaction between domains that does not exist in solid crystals. In this respect, the comparison of SMSB in mesophases with SMSB in crystals needs to take into account two issues: in analogy with solid crystals, the self-ordering yielding permanent anisotropies and in analogy with liquids the mobility between components of their supramolecular structure.
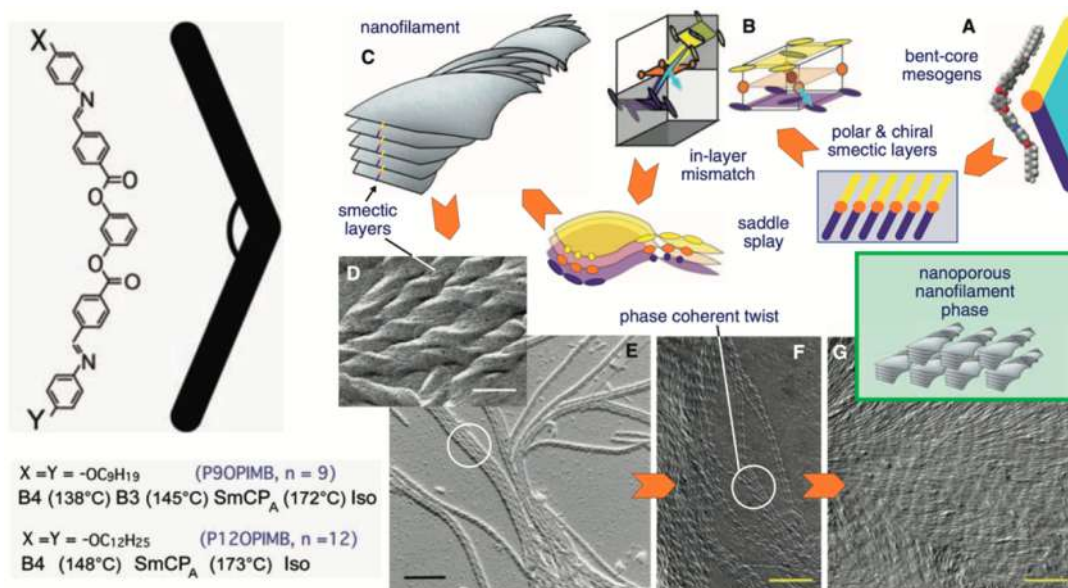
Figure 49. Hierarchical self-assembly of achiral banana-shaped molecules showing SMSB.[537] The chiral helicodal microfibers images were obtained by freeze-fracture transmission electron microscopy. Reproduced with permission from ref 537. Copyright 2009 American Association for the Advancement of Science.

6.3.1. Chirality and Mesophase Anisotropies. Mesophase anisotropies are formed during hierarchical self-assembly processes occurring at different size scales.[102] The mesophase mesogens can be single chemical compounds, for example, banana-like shaped molecules.[523,524] In this respect, the banana-like shape shows a natural tendency to give SMSB.[525] However, it may also originate from already self-assembled single compounds as, for example, in the case of J-aggregates.[526] Mesophase dissymmetric anisotropies may appear at all hierarchical growth stages.[527] Some of the orderings at larger size scales correspond to noninteracting electronic systems. However, optical effects yielding circular polarizations (chiro-optical response) may occur also because of linear anisotropy combinations between noninteracting electronic parts.[528] The resulting circular optical polarizations will be added to and may be much more intense than those originated by the intrinsic chirality of the mesophase (see section 8). The hierarchical aggregation stages of the formation of mesophases[527,529,530] can be roughly described as the following:

(a) The formation of a geometrically well-defined structure obtained from the noncovalent bond interactions between molecular building blocks. The symmetry breaking from achiral compound to chiral aggregate should occur at this stage.

(b) An aggregate of (a)-structures becomes stable after to reach a critical size where further growth is driven by a cooperative noncovalent polymerization/nucleation processes.[521,522]

(c) Compared to solid crystals, the former growth may be frustrated in some of the three space directions, for example, the growth can occur in only one direction, as in the case of noncovalent linear polymers, or in two directions, as in the case of monolayers. It can be also limited in the third direction, such as in bilayers.

(d) Orientation between (c)-structures occurs through new second-order interactions leading to additional anisotropies (e.g., cylindrical anisotropies) that may be chiral or not; even the rare case of spherical isotropic distribution of smaller chiral (c)-units may occur.[513] When solvent is necessary to stabilize the (c)-structures, such as in the case of lyotropic liquid crystals, the mesophase particles are separated by the bulk solvent, but they may evolve toward different morphologies,[99,531] for example, vesicles, micelles, helices, spirals, and nanotubes. The anisotropies originated at this stage belong to different limiting space groups (see section 3.3) than those of stages (a,b).

(e) The last stage of the hierarchical processes depends on the presence or absence of solvent, on the concentrations, and on the presence of additional species such as ions and gelators.[532] At this stage when solvent is present, classical phenomena of colloid chemistry, such as phase segregations, sol/gel formation, and flocculation may occur. At this stage, additional anisotropies may arise, even by the action of external forces, for example, by mechanical stress due to the elastic/plastic properties of the material[99,533] or by dissymmetric orientation in flows.[534]

The symmetry breaking at stages (a,b) transfers chirality toward stages (c) and (d). There are reports showing that the mesophase aggregation may not progress toward higher aggregation stages. The simplest, but dramatic case, is that of fluid nonideal liquids, where homochiral association leads to the spontaneous segregation of enantiomorphic liquid phases.[513,535,536] More complex cases have been reported. For instance, in Figure 49 a banana-shaped molecule self-assembles into a hierarchical fashion toward chiral shaped microfibers. SMSB could be inferred in each self-assembly stage.[537]

At the (c) stage of aggregation, there are different kinetically controlled paths whose selectivity depends on the experimental parameters.[538,530] J-aggregate particles of amphiphilic porphyrins are a paradigm of this situation.[287,539−541] Therefore, the same chiral structure may evolve toward different morphologies.[539,540] This represents an additional difficulty for the comparison between results of different research groups. Notice

that the manifestation of the chemical chirality, as observed in the shape of objects present in the hemihedral faces of the solid crystal (see page 5 in ref 107), is often observed in self-assembled nanoparticles.

The chiral shape at stage (d) very probably cannot arise from achiral (a,b)-structures but represent a chirality transfer from small to larger size levels of the supramolecular structure. However, intrinsically chiral assemblies do not necessarily show chiral shapes.[99,100] The so-called chiral memory effects,[542−546] come from the backward transformation of higher self-assembly stages toward the lower stage (a) that can act as a seed for further self-assemblies.

In the case of thermotropic liquid crystals, although X-ray diffraction techniques have been the usual tool for the identification of phase classes,[547] the resolution of the space group of the (c)-structures so as to verify if they belong or not to one of the 65 Sohncke groups is rarely successful. However, the identification of the cubic $I432$, $I23$ and $I4_132$ (refs 548, 549, and 550, respectively) space point groups has been reported.[551] In the case of particles of lyotropic liquid crystals and soft microcrystals, the X-ray assessment of the space group is hindered by the small mesophase size. In spite of this, a monolayer of a J-aggregate of an amphiphilic porphyrin has been shown to belong to the $P2_1$ space point group (see section 6.3.3).[510] Diffraction techniques, such as small-angle X-ray scattering, are useful in the identification of long distance anisotropies, for example in nanotubes[286,552] but cannot identify the space point group. Notice that X-ray diffraction method-ology requires alignment/orientation of the mesophase particle with respect to the analyzing beam that is, however, possible in the case of fibril-like mesophases.

Microscopy techniques are used to observe the chirality of supramolecular objects. Atomic force microscopy (AFM) and related force microscopies allow for the determination of the topological features. Scanning and transmission electron microscopies (SEM and TEM), and particularly Cryo-TEM[553−556] for frozen solutions, benefit from the progress in the study of biological macromolecules.[557] Figure 50 shows typical chiral supramolecular objects.[102,463]

Circular optical polarizations (CD and CB) in mesophases may result in important spurious interferences (see section 8).[563] CD and CB and differential scattering properties of mesophases arise from

(i) The chiral electronic distribution of the aggregates in the chiral space point group and electronic perturbation between cell units, such as chiral exciton coupling,[564] in the case of circular dichroism in J-aggregates[565] or differential circular scattering[566,567] in nontransparent materials or delocalized chiral electronic bands[568,569] in conducting materials.

(ii) The dissymmetry arising from the relative spatial position in space of electronic noninteracting supramolecular parts of the mesophase, which show linear optical polar-izations.[528,570,571] This effect is similar to that obtained by superposition of linear polarization filters in P or M angular orientations (see Figure 51) and its intensity can be very intense.[294,571−573] Obviously, the circular polar-izations resulting from this ordering cannot be assigned to electronic, i.e., to chemical chirality.

The differentiation between "nonchemical chirality" and intrinsic chemical chirality is difficult. Long shaped nano- or microparticles and ordered mesogens show linear optical
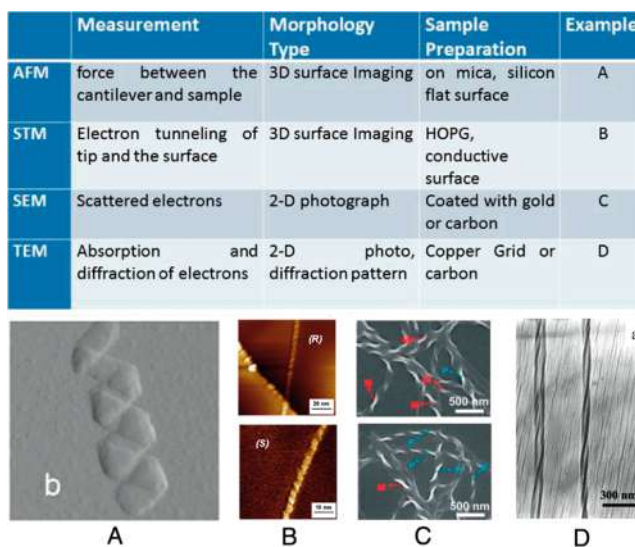
Figure 50. Nanoparticle supramolecular chirality from achiral compounds observed by different microscopies such as discussed by the Liu group:[463] (A) achiral porphyrin,[558] (B) achiral porphyrin,[559] (C) azobenzene supramolecular aggregate,[560] and (D) achiral polydiacetylene film.[561] Reproduced and adapted with permissions from ref 463, Copyright 2015 American Chemical Society; ref 558, Copyright 2003 Royal Society of Chemistry; ref 559, Copyright 2020 Wiley; ref 562, Copyright 2014 Wiley.
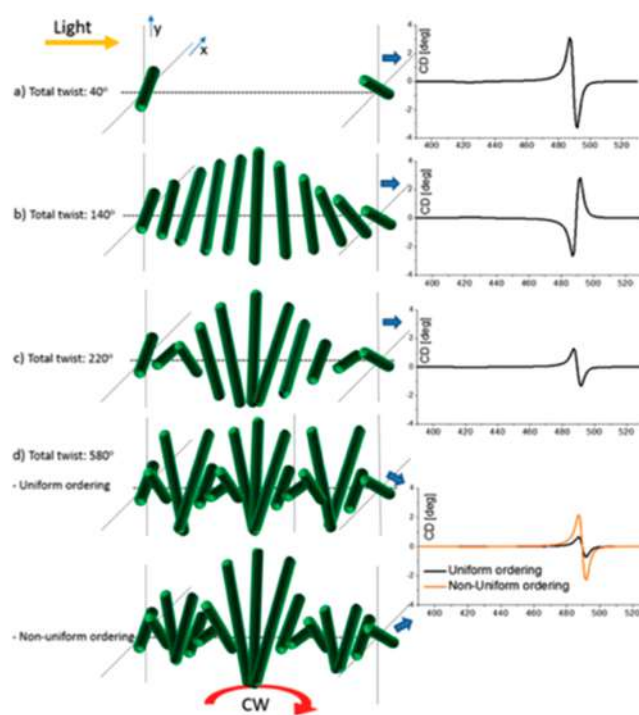
Figure 51. Simulations of chiroptical responses (circular optical polarizations) of macroscopic helical arrangements of achiral nano-tubes showing linear optical polarizations in a vortex (rotation + progression): (a) two layer system in the empty cuvette with wall deposits, (b) continuous helicity through all the cuvette path length (corresponding to CCW stirring), (c) arrangement with opposite chirality for the ascending and descending vortices, and (d) special situations in which only one of the two vortices maintains a chiral ordering while the other becomes chaotic. Reproduced from ref 577. Copyright 2016 The Royal Society of Chemistry.

polarizations (for example, as observed by the classical petrographic microscope), which interfere with the determination of the circular ones. However, new Mueller matrix microscopy (section 8) allows one to overcome the simultaneous observation of linear and circular optical polarizations: see refs 574 and 575 and section 8. In the case of solutions out of the Brownian regime, long-shape nano- and microparticle when they are oriented in laminar flows or simply by gravity may lead to sample dissymmetries expressed by one of the enantiomorphic conical and cylindrical limiting point groups. For example, nematic achiral mesophases, when subjected to a shear force orthogonal to the nematic axis, belongs to enantiomorphic group $\infty \cdot 2$ (see Figure 17 in section 3.3). Achiral long shaped nanoparticles oriented in a vortex belongs to the group ∞. Notice that in the case where the former mesophases are intrinsically chiral, they will show an additional chiral response to that of the intrinsic chirality. There are several reports, for example, refs 294, 570, 572, and 576, whose results may be interpreted by the addition of electronic chirality to supramolecular orientation effects (for a discussion on the specific case of porphyrin J-aggregates, see ref 92). In summary, the chiro-optical response in mesophases arises from two different causes:

(1) the dissymmetry of the chiral space group in the mesophase that cannot be detected in the case of racemates.

(2) the optical effects originated by the dissymmetric spatial ordering between mesophases or parts of the mesophase.

An indirect but ultimate proof of intrinsic chemical chirality of supramolecular structures would be their ability to induce asymmetric induction upon enantioselective reactions. This effect has been recently published in two quite different systems.[578,579]

6.3.2. Positional Mobility Role in SMSB. Mesophases, in contrast with crystal solids, show internal mesogen mobility. In thermotropic liquid crystals, this mobility assures fast phase transitions. Most of the technological applications of these mesophases take advantage of this ability when they are triggered by temperature changes or by the application of external fields.[580,581] The effect of a chiral polarization or the addition of a chiral "dopant" can lead also to biases from the racemic composition.[582] This could be a consequence of the free energy changes of the chiral species exerted by the chiral polarization, converting enantiomorphic domains into diastereomorphic ones (Figure 6, section 2.2.2). This is the case in classical chiral doping which is achieved by relatively high dopant concentrations. However, some reports describe transitions to "homochirality", for such small concentrations of chiral dopant,[583] that it suggests a SMSB process. Furthermore, other reports also point to SMSB processes. In closed systems, the effect of circular polarized light[584] (photostationary state) or of an electric field along an axis of the mesophase[585] may convey the system toward homochirality. Once the external force is suppressed, the system returns to a racemic distribution of chiral domains. In chiral liquid crystals forming racemic conglomerates,[548] each chiral domain is supposed to be formed from a unique seed. However, despite the mesogen mobility inside the mesophase, the racemic distribution of enantiomorphic domains remain in analogy to solid crystals[517,586] (see section 4.2). Furthermore, changes in the experimental conditions in the mesophase formation may also lead to the detection of a unique enantiomorphic phase. Figure 52 (first row) shows the
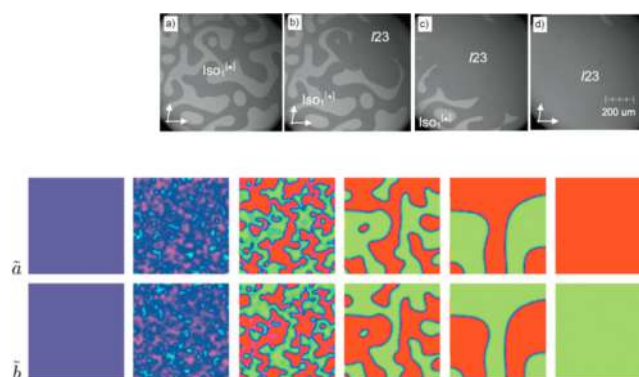
Figure 52. First row: Thermotropic phase transition (deracemization) of a racemic conglomerate of a nonideal liquid phase of an achiral compound (∞/∞) to a homochiral domain of a chiral liquid crystal (*I*23). Second and third rows: 2D simulation of the SMSB of a Frank autocatalytic reaction network showing the transition from perfect racemic composition (left) to enantiomorphic domains and finally to a homochiral final state (right, both rows are examples of the stochastic distribution of chiral signs). Adapted with permission from refs 517 and 586. Copyright 2006 Elsevier; Copyright 2020 MPDI (Basel, Switzerland) under Creative Commons Attribution 4.0 International License https://creativecommons.org/licenses/by/4.0/, respectively.

experimental observation (polarized microscopy) of the SMSB transition from a racemic conglomerate liquid phase (∞/∞) to only one homochiral domain of a chiral liquid crystal (*I*23)[548] (deracemization). Note the analogy with the 2D image of the simulation of the phase transition of a Frank reaction network from racemic to homochiral (Figure 52 (2nd and 3rd row)).

6.3.3. Particles of Chiral Mesophases Showing Only One or Two Directions of Growth. Symmetry breaking during the formation of chiral mesophases from achiral building blocks is often observed in mesophases formed by uni- and bidirectional growth.[511,524,531] Unidirectional growth leads to helices which may evolve to columnar packings. Bidirectional growth leads to initial monolayers which may evolve toward vesicle/micelles, planar surfaces, spirals, and/or nanotubes. Bidirectional growth may show very different rates along both directions. As a consequence of this, the particle dimensions need to be known, for example, by topology measurements using scanning probe microscopies (AFM, PFM) to distinguish between helical structures: unidirectional growth leads to helices (one molecule) and bidirectional growth may lead to spirals (more than one molecule wide).[531]

Structural models for the intrinsic chirality of mesophases, with the lack of available X-ray diffraction data, are mostly based on helical structures (see, e.g., ref 555). X-ray analysis offers a low number of diffraction data compared to monocrystals. Because of this, the assumption of the initial structure in the refinement analysis is decisive: α-helix may be a reasonable hypothesis to start the structure refinement. However, α-helices (e.g., ref 587) and also β-sheets (e.g., ref 588) of chiral amino acids crystallize in similar space groups as those of most chiral organic crystals, i.e., within the enantiomorphic monoclinic and orthorhombic *P* lattices. Therefore, structures other than that of α-helix could be more adequate starting options. For example, the J-aggregates of an amphiphilic porphyrin yielding monolayers showing axial chirality between its building blocks, belong to the space point group *P*2$_1$ and show axial chirality (Figure 53)[510] instead of helicoidal structures, and this could also be the case of other chiral J-aggregates built from planar compounds.[526]
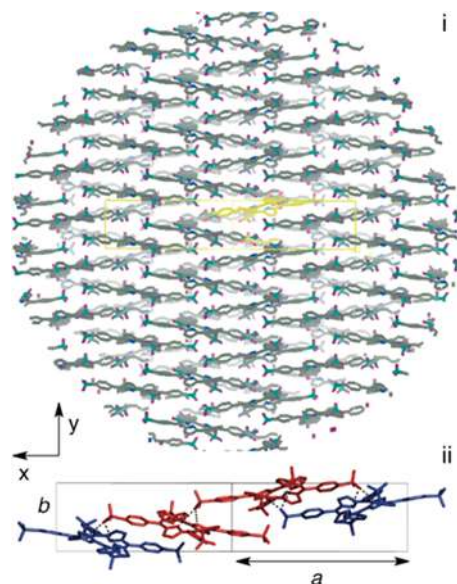
Figure 53. Sheet of J-aggregates of an amphiphilic achiral porphyrin ($P2_1$ space point group). The different colors of the porphyrins in the unit cell represent two frozen conformational enantiomers. The building blocks are racemic dimers. Optimization of the hydrogen bond, van der Waals interactions, and solvent exclusion effects deforms a possible achiral P-2 structure, which would result from a perfect adjustment between monomer dimensions and planar packing, into a chiral axial structure. This basic sheet structure may evolve toward nanotubes along the π-stacking direction (see refs 286 and 571) or to other nanoparticle morphologies. Reproduced and adapted from ref 510. Copyright 2013 Royal Society of Chemistry.

Classical linear amphiphiles, such as nonsubstituted fatty acid salts, are probably unable to show symmetry breaking in the self-assembly toward micelles and vesicles. However, simple bola-amphiphiles and amphiphiles showing two polar or two lipophilic tails may lead to symmetry breaking and to the formation of homochiral micelles and vesicles[589] formed by the curvature of the initial chiral monolayer. This issue is significant with respect to the emergence of chiral membranes in chemical evolution, but the corresponding studies are hindered because of the inaccessibility to the "non-natural" enantiomer,[590] despite the intense research in this topic.[591] Futhermore, there are reports suggesting symmetry breaking in the formation of chiral monolayers from racemic mixtures of 1-glycerol monoesters.[592,593] It is worth noticing that, in biological systems, the chiral sign resulting from glycerol mono and diesters does not seem to be directly related to those of peptides and nucleic acids. For example, in the primitive biological major transition from Archaea to Eukaryote, there is a change of the absolute configuration of 1-glycerol monophosphate in phospholipidic membranes.[594]

As inferred from the many reports in the field, amphiphiles able to lead to mono and bidirectional growth correspond to compounds showing a wide planar surface. They self-assemble through $\pi-\pi$ interactions and/or solvent excluding effects and through several lateral polar groups which may interact with the solvent and/or form internal hydrogen bonds in the supramolecular structure. When adequately substituted by polar and/or lipophilic lateral chains, amphiphilic planar aromatics give rise to bidirectional growth. Among them are the porphyrinoids,[541,595] cyanine dyes,[526] tetrathiofulvalene,[596] perylene,[441,597,598] and phenyl and polyphenyl based amphi-

philes.[550,599,600] Molecules showing C_3 symmetry, e.g., triphenylenes, and similar star-shaped structures are also extensively used for the self-assembly of achiral compounds to chiral mesophases.[463]

Monolayers obtained from amphiphilic compounds may show the same surface composition at both sides or not (see 2D chirality in section 3.2). If the difference between the surfaces is large, the monolayer evolves to spherical micelles or vesicles.[601] If the composition at both surfaces is the same, the monolayer evolves to single- or double-walled nanotubes.[602] In summary, the evolution toward either spherical or cylindrical morphologies is a consequence of the rate growth difference between both plane directions. Growth in the π-stacking direction, which occurs in aromatic crystals, corresponds mostly to the faster growth.[286,571] In some cases, the elasticity of the membrane does not allow the monolayer to close, and the shape of the mesophase particles appears as free-standing monolayers (Figure 54).[287,556,603]
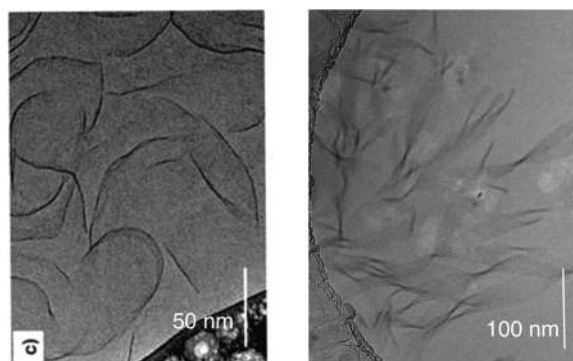
Figure 54. Cryo-TEM image of free-standing chiral monolayers. Left: macrocycles, curved sheets.[603] The sheets show elastic behavior in the solvent flows. Right: porphyrin, spiral-like bends.[287] Reproduced with permission from refs 287 and 603. Copyright 2016 Wiley; Copyright 2019 American Chemical Society.

The consideration of the forces resulting from the double layer potentials at both sides of the monolayer could be the missing link between the self-assembly toward mesophases of defined space point structures and their evolution toward gels and colloids. For example, the symmetry breaking for the bilayered structures of the monolayer mosaic of J-aggregates shown in Figure 54 (right)[287] could be described in the framework of the role of the double layer potentials. First, the monolayer structure is stabilized by the equal electrostatic pressure at both sheet surfaces (Figure 55). Second, and due to an imperfect fit between the dimensions of the building blocks, the hydrogen bonding, and the $\pi-\pi$ interactions, the equal pressure at both sides bends and folds the sheet to the enantiomorphic structure $P2_1$, instead of to the P-2 space group.

The well-demonstrated up-to-down effect of the macroscopic chirality transfer of shear hydrodynamic forces (see section 2.1.2) could also be explained at the molecular level by taking into account the shear hydrodynamic flow induced differential nonstochastic fluctuations between both surfaces of the double layer potentials. We can reasonably speculate that at the nucleation stage, i.e., when autocatalysis acts, differential perturbation by flow fluctuations at both membrane sides would select the chiral sign of the $P2_1$ enantiomorph.
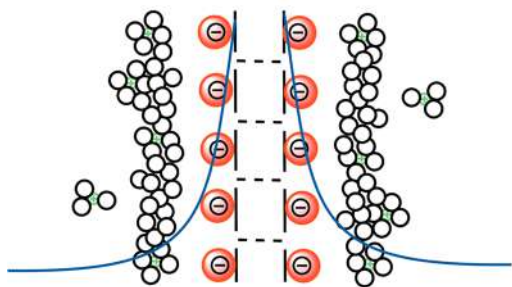
Figure 55. Qualitative description of the double layer electrical potential (blue lines) of a monolayer showing negatively charged surface (red, anions; green, solution counter cations) as a model for the stabilization of chiral monolayers such as those shown in Figure 54. Reproduced and adapted from ref 287. Copyright 2019 American Chemical Society.

7. SPONTANEOUS MIRROR SYMMETRY BREAKING IN MOLECULAR SOLUTIONS

Synthetic chemists had considered it was impossible to achieve, under the so-called conditions of thermodynamic control, final reaction outcomes showing a bias from the racemic composition. Then, after the Soai reaction was shown to be a case of SMSB taking place in solution, the example was considered to be a singular case, probably unique, because of the subsequent lack of new examples. In contrast, the deracemization occurring in chiral conglomerates (Viedma, 2005),[78] in spite of being published later than the Soai reaction (1995),[59] has been extended to many other chemical species which crystallize as racemic conglomerates and is now even being used in applied chemistry. The following reasons explain the lack of further examples and the difficulties to detect SMSB taking place in solution:

(a) Enantioselective autocatalysis is an uncommon feature in synthetic chemistry, in contrast to the usual homochiral autocatalysis in the crystallization of racemic conglomerates.

(b) Reaction networks that may potentially exhibit SMSB require specific experimental conditions regarding how the systems interact and exchange matter with their surroundings. In crystallizations, these requirements may be easily fulfilled giving rise to permanent supersaturation conditions concomitant to the crystal growth. Performing organic synthesis in open systems is an uncommon synthetic methodology that nowadays, thanks to the availability of microliter precision pumps and microfluidic open flow reactors, may change the synthetic chemistry scenario. Notice that the SMSB character of the Soai reaction, expressed through the stochastic distribution of chiral signs among different experiments, was only achieved after very substantial experimental work, relatively uncommon in today's synthetic practice, first described in a patent,[604] and only years later published as a research article.[605]

(c) Racemization in solution is generally unavoidable in low exergonic transformations. By contrast, in crystals, when the system is returned to conditions of saturated solution, racemization does not occur. Therefore, in solution, after the reaction is stopped, and only in the case of high exergonic reactions, as is the case of the Soai reaction, racemization is not a problem that hinders the detection of biases from the racemic composition. Obviously, the search for networks, of low exergonic reactions able to show SMSB, should be performed on a real-time basis during the reaction evolution while it is kept under open system conditions.

(d) Last but not least, there are two psychological barriers concerning chirality that should be overcome:

(i) Chirality, in pure chemistry, is understood as the description of molecular structure, i.e., by virtue of belonging to one of the point groups that break parity. By contrast, materials chemistry explains chirality as the phenomenon arising from the symmetry relationships between matter, given by the ordering of its molecular units into macroscopic entities and physical forces. This latter description of chemical chirality is more adequate for understanding SMSB, in comparison to the usual way that chirality is understood merely on the basis of the structure of individual molecules. This is obvious in the case of crystals but often overlooked in the case of molecular solutions: molecular solutions of achiral compounds or racemates belong to the point group $\infty/\infty \cdot m$, whereas a solution of scalemic or homochiral compositions belongs to the limiting point group ∞/∞ (see section 3.3). Therefore, SMSB, i.e., a spontaneous deracemization in solution, corresponds to the symmetry breaking transformation $\infty/\infty \cdot m \rightarrow \infty/\infty$ of the whole macroscopic sample and not to those of the individual molecules.

(ii) Modern organic chemistry has advanced during the 20th century thanks to the description of chemical species as molecular structures and also thanks to the description of reaction types and reaction mechanisms in terms of the interaction between species and changes in bond orders between molecular structures along the reaction coordinate model represented by a reaction coordinate in a hypersurface of free energy changes. However, a SMSB process belongs to irreversible thermodynamics in the nonlinear regime and must therefore be justified in the scenario of energy dissipative systems, in which the transformation between nonequilibrium stationary states, stability, and the evolution of nonequilibrium states is determined by a physical potential which is not directly related to free energy state functions.[606]

7.1. The Soai Reaction

The autocatalytic Soai reaction[59] represents the exclusive laboratory demonstration of enantioselective autocatalysis able to yield SMSB in a homogeneous reaction system (see refs 60, 118, and 607−612 for recently released reviews and relevant references therein). Soai and co-workers revealed that a chiral product can act as a chiral catalyst for its own formation in the alkylation of certain pyrimidinyl aldehydes with diisopropyl zinc, where the chiral pyrimidine alkanol accelerates its own formation and promotes the prevalence of its own configuration (Scheme 2). The process gives rise to an automultiplication of the chiral compound.

The widespread interest in the Soai reaction is mostly fueled by its plain uniqueness, high sensitivity toward a great variety of chiral and cryptochiral additives, the capability to display SMSB

Scheme 2. Principle of Enantioselective Autocatalysis in the Soai Reaction[a]
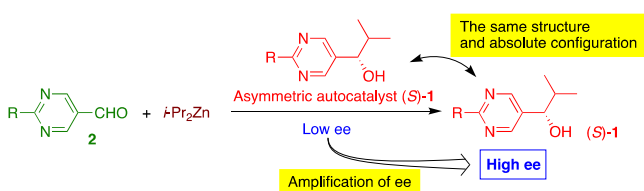
[a]Reproduced with permission from ref 60. Copyright 2018 Elsevier.

when started under achiral conditions, and essentially its relationship to possible pathways for the origin of biological homochirality. Therefore, more recent research has been devoted to the elucidation of the structural, thermodynamic, and kinetic aspects of the reaction mechanism as well as probing and rationalization of the unprecedented chiral additive effects.

Almost all mechanistic rationalizations of the Soai reaction depart from the concept of a Frank-type mechanism,[124] i.e., a bifurcation scenario in which enantioselective autocatalysis and mutual inhibition are provided by the involvement of oligomeric intermediates. This may be considered as an unfamiliar, but also extraordinary, feature compared to a simple kinetic control of the chemical output. In fact, the SMSB as observed in the Soai reaction is not simply a fluctuation followed by habitually termed "asymmetric amplification" but essentially the manifestation of a coupling between nonlinear kinetics and far-from-equilibrium thermodynamics occurring in a system open to the exchange of energy, where the racemic state turns unstable and an enantiomerically enriched outcome becomes the inexorable destiny.

Recent progress has been made by informing the possible structure, oligomericity, and kinetic role of the autocatalytic species. After a prior DFT determination of energetically favored tetramers that could play a prominent role in the autocatalysis and mutual inhibition,[613] Gridnev and Vorobiev[614] proposed a catalytic cycle taking into account that the cavity observed in the homochiral tetramer could form an ideal chiral compartment for the coordination of the aldehyde reactant. Enantioselective alkylation was then supposed to yield the monomeric alcoholate of the same handedness as the tetrameric catalyst.

An important experimental development regarding the catalyst structure was made by the Soai group through single-crystal X-ray diffraction analysis of several zinc alkoxide structures, by which the existence of tetramer and higher oligomer structures was disclosed.[615−617] It is likely that these aggregate structures are the key for providing the highly sensitive autocatalytic amplification and SMSB and represent the starting point to determine a better understanding of the Soai reaction mechanism.

Since the discovery of the Soai reaction, a number of kinetic, stochastic, statistical, and empirical models have been proposed to rationalize the reaction mechanism (see for recent overviews),[612,618] among them also mechanistic principles derived from nonlinear effects (NLE) in asymmetric synthesis.[117,619,620] These models extend over early concepts of monomers or dimers to currently tetramers as the catalytic species.

More recently, Noble-Terán et al.[621] proposed a kinetic model (Scheme 3) based on ordinary differential equations with reference to the experimentally observed tetramer crystal structures by the Soai group. Taking additionally into account data from earlier DFT calculations, it was shown that the autocatalytic amplification from an extremely low *ee*, SMSB and Soai's crystallization conditions could be reproduced by using thermodynamically reasonable rate parameters through tetramer catalysis.

The basic principle of the kinetic model sketched in Scheme 3, i.e., a Frank-type reaction work[124] where homochiral tetramers of the alkoxy reaction product are the termed autocatalytic species and the formation of energetically preferred heterochiral tetramers the inhibition step, was lately supported from an organic chemistry perspective by Denmark and co-workers in an extensive structural and mechanistic study.[622] The starting point was the disclosure that autocatalytic amplification can be achieved with 5-(trimethylsilylethynyl)pyridine-3-carbaldehyde, i.e., a different pyridine substrate as commonly employed in the Soai reaction, showing that one of the nitrogen atoms in the pyrimidine ring is sufficient to yield the enantioenriched alkanol (Scheme 4).

This finding led to the proposal of a different and simplified transition-state structure of the homochiral square-macrocycle-square (SMS) tetramer as the autocatalyst. It was proposed that the catalytic step takes place through an expansion of the cubic tetramer by replacing two Zn−O cube bonds by an aromatic pyridine connection, where subsequently the aldehyde substrate can fit in an enzyme-type manner through a two-point

Scheme 3. Proposed Skeleton Model of the Soai Reaction Representing the Two *S*- and *R*-Autocatalytic Cycles Where Homochiral Tetramers Act as the Autocatalytic Species[a]
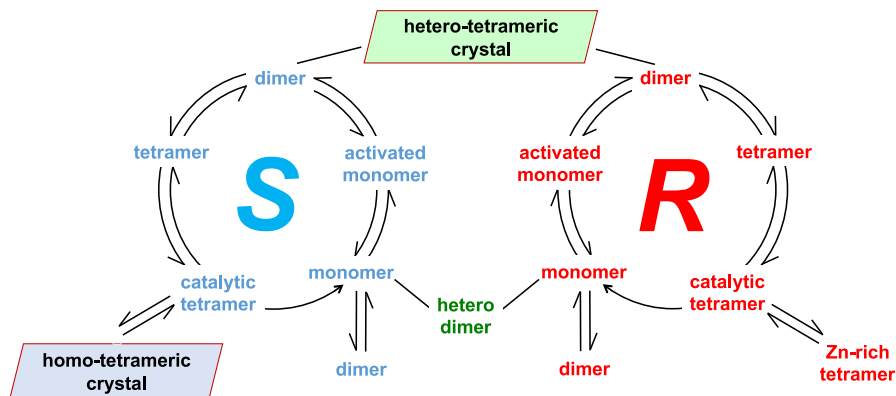
[a]Reproduced with permission from ref 621. Copyright 2018 Wiley-VCH.

Scheme 4. Soai-Like Reaction Using a Pyridine Carbaldehyde
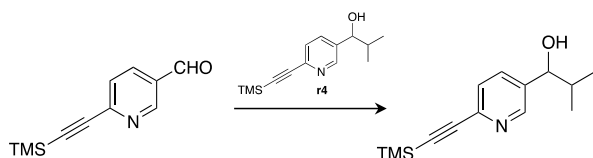
coordination to the unsaturated zinc centers on the catalyst floor (Scheme 5).

Such catalyst floor binding is not possible for the heterochiral tetramers, thus explaining their catalytic inactivity. Hence, with respect to already formerly proposed kinetic models in terms of a Frank-type mechanism,[621,623] the energetically favored heterochiral tetramers play the role of a reservoir representing the essential process of mutual inhibition, while the homochiral tetramers exclusively promote the autocatalytic amplification. Further insight into the Soai reaction mechanism was recently provided by *in situ* high-resolution mass spectrometry, which indicates the transient formation of hemiacetal complexes that are supposed to be involved in the autocatalytic cycle.[624] Recent experimental research was also devoted to the influence of various chiral additives on the Soai reaction (Table 14).

As known for many years, almost every imaginable chiral inductor, including all kinds of functional groups, were able to direct the Soai reaction specifically, either those that are soluble in the reaction mixture giving rise to chiral recognition in solution as well those which are not soluble,[631] bearing chiral surface adsorption. Current research, conducted by the Soai group, was mostly dedicated to heterogeneous systems, among them to the influence of chiral nanoparticles like helical carbon nanotubes,[625] also elsewhere discussed as a possible source of asymmetry in carbonaceous chondrites,[632] mesoporous silica,[626] as well as chiral crystals or enantiotopic surfaces made from achiral precursors such as ethylenediamine,[627] calcium sulfate dihydrate,[280] or glycine.[630] The remarkable response of the Soai reaction toward chiral asymmetries has not been documented only through the presence of known chiral additives but also with respect to acting as an analytical sensing tool.[633,634]

Underlining the extraordinary sensitivity of the Soai reaction toward the smallest chiral asymmetric influences, the response to isotope chirality, as recorded for $^{12}C/^{13}C$,[144] H/D,[635] $^{16}O/^{18}O$,[142] and recently for $^{14}N/^{15}N$ moieties,[628] is definitely the most remarkable feature among all additive effects. In this regard, Hawbaker and Blackmond studied the effect of H/D

chirality using (*R*)-o (*S*)-1-methoxy-(^{2}H)-3-methoxy propanol as the additive.[636] The authors found that the additive, as a function of its concentration, increasingly slows down the overall velocity of the reaction (Figure 56).

To rationalize this unexpected inhibitory effect, Hawbaker and Blackmond conducted kinetic, NMR, and DFT studies that indicated an interaction between the assumed homochiral dimeric zinc alkoxide autocatalyst (R_2 and S_2) and the chiral additive (X) that inhibits the autocatalytic pathway. It is argued that the additive−catalyst interaction can give rise to the formation of the diastereomeric species R_2X and S_2X that differ in their energies and consequently can promote an advantage of one product enantiomer over the other during the autocatalytic stage. Such additive−catalyst interaction has been already anticipated at an earlier time in the framework of kinetic studies on the effect of enantioselectivity reversal in the Soai reaction.[608,637,638]

A subsequent study by the same authors was dedicated to the quantification of the additive effect by variation in the *ee* of the isotopically chiral additive.[41] The idea was to fix the threshold *ee*, at which the system switches from asymmetrically directed to stochastic (racemic) behavior in which, after a series of experiments, a statistical outcome of *R*- or *S*-directed reaction product is expected. This transition was settled for an *ee* of the additive between 0.1 and 1%. Based on theoretical calculations as well as by proposing a kinetic dimer model similar to past approaches,[639,640] the energy difference between the diastereomers R_2X and S_2X was projected to be in the range of 10^{-8}−10^{-7} kJ/mol in order to drive the Soai reaction into a specific direction, unless a fluctuation driven stochastic behavior is anticipated.

Indeed, one of the most salient features of the Soai reaction is the revelation of SMSB or spontaneous absolute asymmetric synthesis, i.e., the formation of enantiomerically enriched pyrimidyl alkanol from the reaction of pyrimidine-5-carbaldehyde and *i*Pr$_2$Zn, without adding a chiral substance. In a recent study, Soai and co-workers reported on apparent SMSB in a heterogeneous reaction system between powder crystals of pyrimidine-5-carbaldehyde and the vapor of *i*Pr$_2$Zn (Scheme 6).[641]

In contrast to earlier attempts under homogeneous conditions,[605,137] here the reaction takes place at the surface of the prochiral reactant powder randomly orientated with its *Re* and *Si* faces in contact with the *i*Pr$_2$Zn vapor. The perceived monomodal shape of the frequency distribution (Figure 57),

Scheme 5. Expansion of the Cubic Zn−O−Zn−O Tetramer to Constitute the Catalytically Active Homochiral SMS Tetramer That Shows High Similarity to the Experimentally Determined Tetrameric Crystal Structure by the Soai Group[615,a]

cubic tetramer   expanded cube   SMS tetramer
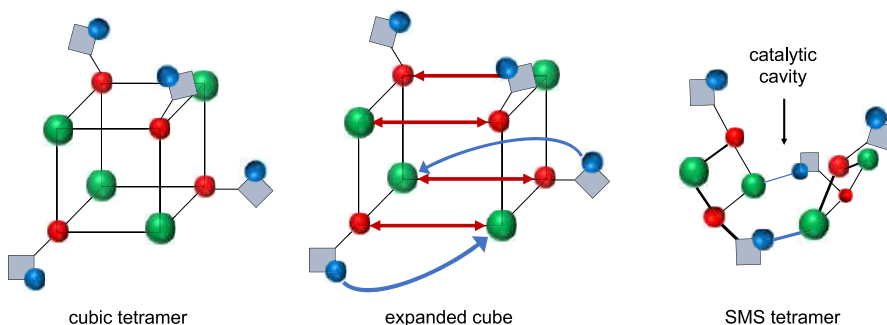
^{a}Zn (green), O (red), nitrogen (blue), TMS aromatic pyridine unit (gray square); blue arrows indicate the concerted attack of heterocyclic nitrogens on Zn. Author drawing inspired by ref 622.

Table 14. List of Recent Soai Reaction Experiments Carried out in the Presence of Chiral Additives[a]

Chiral additive		ee (%)	Reference
P- and M-helical finite single-wall carbon nanotubes		87 – 91*	Reproduced from ref 625. Copyright 2014 American Chemical Society.
P- and M-helical mesoporous silica		80 – 97*	Reproduced from ref 626. Copyright 2015 The Royal Society of Chemistry under Creative Commons Attribution 3.0 Unported License https://creativecommons.org/licenses/by/3.0/.
Chiral crystals of ethylenediamine sulphate		80 – 93*	Reproduced with permission from ref 627. Copyright 2015 The Chemical Society of Japan.
N2,N2,N3-tetramethyl-2,3-butanediamine, (14N/15N isotope chirality)		12 – 54*	Reproduced with permission from ref. 628. Copyright 2016 Wiley-VCH.
1-and 2-aza [6] helicenes (enantioselectivity reversal)		77 – 99*	Reproduced from ref 629. Copyright 2017 The Royal Society of Chemistry under Creative Commons Attribution-NonCommercial 3.0 Unported License. https://creativecommons.org/licenses/by-nc/3.0/.
Calcium sulfate dihydrate, $CaSO_4 \cdot 2 H_2O$		19 – 72*	Reproduced with permission from ref 280. Copyright 2017 Wiley-VCH.

Table 14. continued

Chiral additive		ee (%)	Reference
Chiral γ-glycine crystalline polymorph		35 – 73*	Reproduced from ref 630. Copyright 2019 The Royal Society of Chemistry under Creative Commons Attribution-NonCommercial 3.0 Unported License https://creativecommons.org /licenses/by-nc/3.0/.

*a*The * indicates *ee* > 99.5% after repeated rounds of enantioselective autocatalysis.
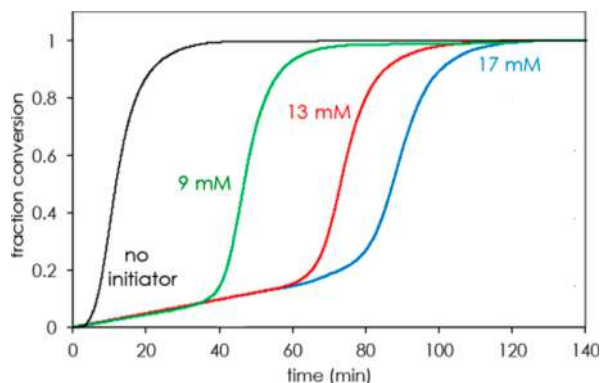
Figure 56. Inhibitory effect on the overall velocity of the Soai reaction by the presence of different concentrations of 1-methoxy-(^{2}H)-3-methoxy propanol as an isotopically chiral additive. Reproduced from ref 636. Copyright 2018 American Chemical Society.

Scheme 6. Heterogeneous Solvent-Vapor Phase Soai Reaction between Powder Crystals of Pyrimidine-Carbaldehyde and *i*Pr$_2$Zn Vapor
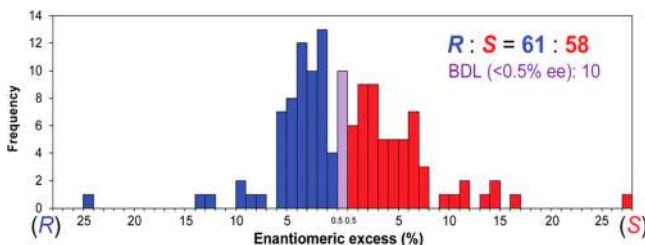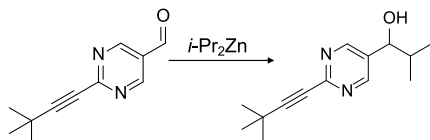
Figure 57. Frequency distribution of the *ee* in the heterogeneously driven Soai reaction under achiral initial conditions after 129 repeated experiments indicating a virtually stochastic behavior; BDL, below detection level. Reproduced from ref 641. Copyright 2019 The Royal Society of Chemistry under Creative Commons Attribution 3.0 Unported License https://creativecommons.org/licenses/by/3.0/.

obtained after 129 repeated experiments under the same conditions, differs notably from the bimodal nature found under the formerly exercised homogeneous reaction conditions (see Figure 8).[137,605]

A similar approach under heterogeneous reaction conditions was also employed by Amedjkouh and co-workers,[642] reporting absolute asymmetric synthesis upon the exposure of solid pyridine-3-carboxaldehyde with diisopropyl zinc vapor (Scheme 7).

Scheme 7. Heterogeneous Soai-Like Reaction between Powder Crystals of Pyridine-Carbaldehyde and *i*Pr$_2$Zn Vapor
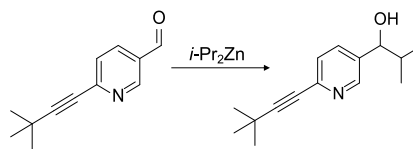
Also in this case, the resulting frequency distribution is of apparent monomodal character; however, it shows a non-stochastic predominance in favor of the *R*-alkanol (Figure 58).
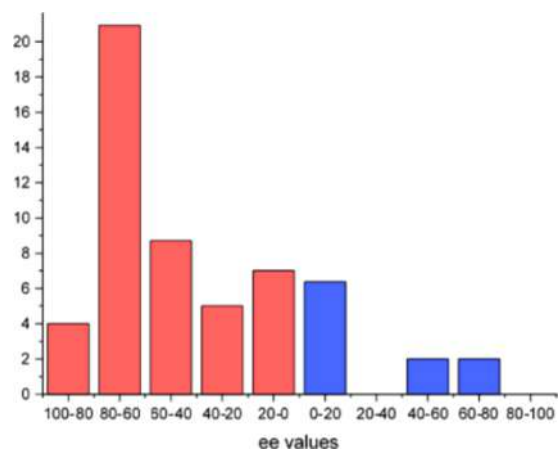
Figure 58. Frequency distribution of the *ee* in the heterogeneously driven Soai reaction with a pyridine-3-carboxaldehyde reactant indicating nonstochastic behavior with an approximate 5:1 predominance of the *R*-product (red) over the *S*-product (blue). Reproduced with permission from ref 642. Copyright 2020 Wiley-VCH.

The *R*-dominance may indicate the influence of unknown chiral impurities, which is perhaps a predictable incident by recalling the extremely high sensitivity of the Soai reaction toward a large variety of asymmetric stimuli. Interestingly, in former analyses[618,643] of the earlier Soai group results[137,605] and other experimental studies[644,645] in the homogeneously driven reaction, an *S*-dominance has been reported. These opposite outcomes, *R* vs *S*, may be due to chiral impurities perhaps associated with the specific laboratory environments or different sources of the reactants but practically exclude a universally present asymmetric influence such as the PVED, in effect recently dismissed,[41] which should give rise to a constant *R*- or *S*-preference, whenever having a possible impact.

In essence, considerable progress has been made in recent years in understanding the uniqueness of the Soai reaction mechanism. At this point, it appears to be much more complex than the simple Frank model, involving numerous oligomeric species and most probably a homochiral tetrameric catalyst at the heart of the autocatalytic processing, which performs with enzyme-like precision. From this point of view, the Soai reaction has a larger outreach than only focusing on enantioselective autocatalysis since it stands also for a prototype of efficient self-replication with highly specific catalytic activity in the whole scope of organocatalysis.

On one hand, the Soai reaction behaves extremely particular "on its own", for instance with respect to the very limited choice of the reactants and reaction conditions, but on the other hand it is susceptible to a great amount of different chiral additives and influences that can drive the outcome into a specific direction. The apparent chimeric, specific vs unspecific, behavior has been puzzling for many years and was informed in a first progress by the Blackmond group, showing that the chiral additive inhibits the autocatalytic kinetics, which points toward an interaction taking place between the autocatalyst and the chiral additive. Such interaction could be understood in terms of enzyme inhibition kinetics. Dynamically speaking, the reaction seemingly proceeds with a slowing-down through the bifurcation scenario, rendering it more susceptible and specific for tiny asymmetric perturbations. The slowing-down could also assist so-called dynamical error correction through the process of kinetic proofreading,[646] as was earlier discussed as a particular feature of the Soai reaction.[647] Nevertheless, further mechanistic studies are required to confirm if this behavior can be generalized, i.e., if it stands also for other types of additives as the isotopomers employed in the Blackmond study.

The emergence of SMSB, or absolute asymmetric synthesis, as a distinctive characteristic of the Soai reaction has also been the subject of recent research related to heterogeneous reaction conditions. Further studies are indicated to better understand the monomodal nature of the frequency distributions, as well as the origin for the repeatedly observed nonstochastic behavior. Especially an interesting approach deserves further research efforts, namely, to define the transition stage and perhaps the threshold value between deterministic and stochastic behavior, driven by directed chiral influences vs reaction noise. Here open-flow techniques screening the bifurcation behavior, as employed in other fields of nonlinear chemical sciences,[648] could perhaps pave the way for a closer insight.

7.2. Behind the Soai Reaction

Asymmetric organo-autocatalysis[649] is a rare type of reaction but not so rare as the Soai reaction suggests.[610] In fact, there have been a few reports pointing to the spontaneous emergence of chirality in organocatalysis.[650−654] Tsogoeva reported the spontaneous emergence of chirality in the aldol and Mannich reactions when using 4-nitro-benzaldehyde as a substrate (Scheme 8).[655,656]

However, these experiments are difficult to reproduce because they depend on specific conditions related both to the reaction and the reactor (e.g., cooling or heating gradients).[182] In spite of this, biases from the racemic composition have been detected and details on the emergence of chirality have been reported for the aldol reaction.[657] The low *ee* values are a consequence of catalysis by a *bis*-aldol occurring at the very beginning of the reaction. The exact pathways of this enantioselective autocatalytic reaction leading to spontaneous emergence of optical

Scheme 8. Aldol and Mannich Reactions[a]
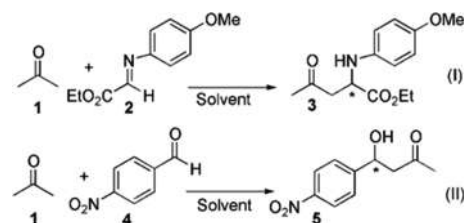
[a]Reproduced with permission from ref 655. Copyright 2007 Wiley.

activity are still unclear. It is likely that the lack of coupling of this enantioselective autocatalysis with other promoting processes makes any SMSB impossible. This is perhaps a consequence of the use of closed systems, which are not able to maintain a nonequilibrium stationary state (NESS) in which a higher *ee* is predicted theoretically.

The difficulty to find new SMSB in organocatalytic reactions is not only a consequence of the fact that autocatalysis is an uncommon reaction, but principally because of:

(i) the fact that most organic reactions are not sufficiently exergonic and the lack of recognized autocatalytic steps.

(ii) the lack of synthetic methodologies currently available to perform experimental organic synthesis in open systems.

With respect to point (i), autocatalysis is commonly defined to be the case when the reaction product acts as a self-replicator catalyzing its own formation. Therefore, the proof for the presence of autocatalysis, simply by testing the changes in the system originating from the addition of the final product under some controlled experimental conditions, may lead to the erroneous conclusion that autocatalysis is absent. This is the case, for instance, of complex reaction networks where the autocatalytic species is a transient intermediate, not present at the end of the reaction.[121] Furthermore, even the presence of bimolecular enantioselective autocatalysis does not suffice to select between enantiomers in the absence of coupling to other enantioselective reactions (section 9).

With respect to point (ii), this implies the requirement to study the open system behavior of the system under well controlled conditions with regard to its matter and energy exchange with the surroundings. Despite the relative unfamiliarity of synthetic chemists with energy-dissipative systems, one must bear in mind that the driving forces in coupled reaction networks cannot be completely described through the classical schemes of organic reaction mechanisms. They are determined by the balance between entropy flows and the entropic heat differences between the reaction medium and its surroundings.[119,120,135]

Nowadays, continuous synthesis, based on mini- and microreaction technologies is a potential methodology for manufacturing high value chemical derivatives and also for the study of open systems at the laboratory bench scale.[658] There are recent reports on this, although not concerned directly with chirality but dealing with complex reaction networks.[659,660] For example, in the case of ref 659, thanks to the possibility to control the open system parameters, autocatalysis amplification and inhibition, bifurcations leading to bistability, and even oscillatory behavior can be soundly studied. These types of bifurcations are, from a fundamental point of view, not different to those expected for SMSB networks: only a reliable spectroscopic detector able to also detect optical polarization
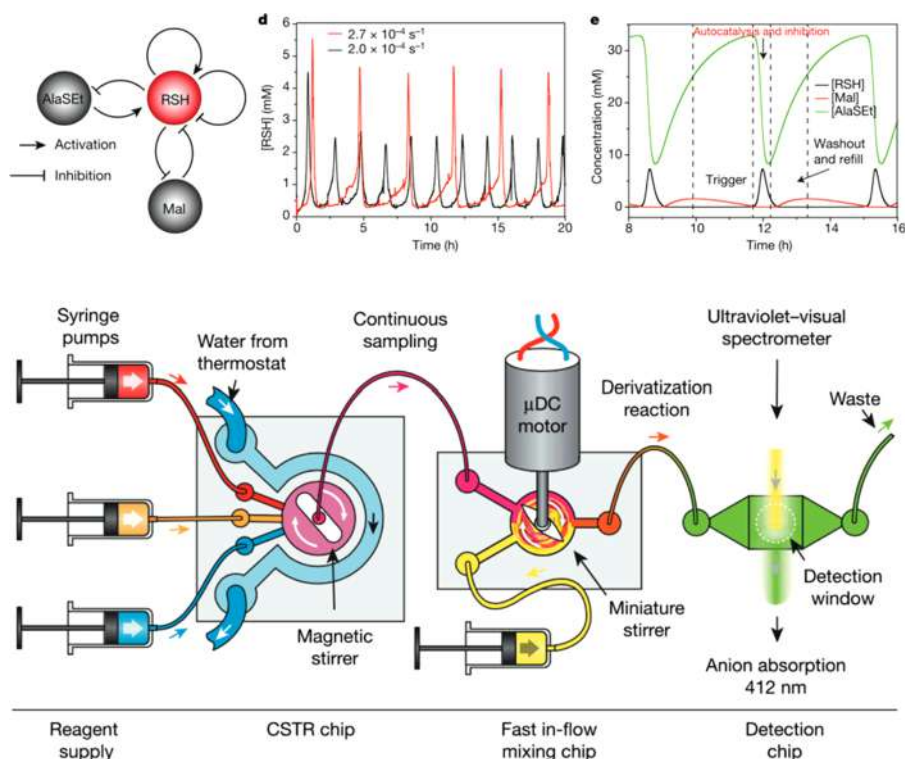
Figure 59. Example of an open system to follow composition changes of the thiol–disulfide transformation ratio in a complex reaction network. Red: reactant cystamine plus buffer solution. Orange: reactant L-alanine ethyl thioester (AlaSEt). Blue: inhibitor maleimide (Mal) or acrylamine. Yellow: reagent to build with thiols a dye for the UV–vis detection. Autocatalysis amplification and inhibition, bistability, and oscillatory transitions between different stationary states could be accurately established for specific pH, compositional, and flow ranges. Reproduced and adapted with permission from ref 659. Copyright 2016 Springer Nature.

properties (see section 8) should substitute the simple UV–vis detector system shown in Figure 59.

The use of open flow microreactors, such as that in Figure 59 and the microfluidic vortices of Figure 5 in section 2.1, shows how necessary the development of experimental synthetic procedures is in energy dissipative arrangements to obtain not only SMSB but also higher chemical selectivity. To the best of our knowledge, the rough approximation of the Soai reaction procedure to an open system, by transferring the reaction output of one batch to the next reaction,[168] has not yet been optimized in an open flow reactor.

Therefore, the experimental quest for SMSB reactions should be directed not only to find enantioselective reactions but to how they can be coupled to other enantioselective processes. SMSB bifurcation scenarios require, as the emergence of stationary states different to those of the thermodynamic branch always do, that the NESS of the thermodynamic branch generates an entropy production above a critical value in such a way that the bifurcation point becomes unstable. This means that not only rate constants of the reaction network but also the chemical mass[661] of the system together with the rates of matter and energy transfer with the surroundings[606,662] play an important role for achieving the critical entropy production. Negative results do not yet signify that any SMSB cannot take place.

With respect to possible relationships between the origins-of-life topic and the present review, the case of the RNA-world[663] is significant. There, the enantioselective reactions, which would be coupled to autocatalysis (by template mechanisms), should not hinder the ability for the Darwinian selection of a nucleic acid self-reproducing system. Therefore, a Frank-like autocata-

lytic scenario is not adequate for the RNA-like-world scenario since it implies a heterochiral inhibition.[664] Old chemical evolution scenarios assuming pools of pure homochiral resources[665] are now considered to be unrealistic (see, e.g., ref 666). Recent proposals, with regard to the emergence of macro and supramolecular complex systems, assume prebiotic mixtures of monomeric and oligomeric species instead of "pure" compounds.[667−669] With respect to chirality, such scenarios imply mixtures of small *ee* values which could have been obtained via previous asymmetric inductions. These small *ee* values determine the handedness of the SMSB (section 9) and are in agreement with the speculation of consecutive enantioselective scenarios leading to biological homochirality.[16,10] On the other hand, *in silico* studies on SMSB[670] remain always possible for RNA-world like scenarios or oligonucleotide replicators, at the stage of emergence of enzymatic abilities,[9] provided that the numerical models can be accurately parametrized.

While experimental approaches are not helped by the lack of the easy availability of the non-natural enantiomers, some reports on the growth of peptides through enantioselective template mechanisms, i.e., leading to sequences of homochiral building blocks (see, e.g., Figure 60),[671−674] justify the speculation about biological SMSB scenarios. The growth, from racemic mixtures of amino acids of isotactic homochiral chains by the template growth mechanism, corresponds to replicator autocatalysis. The coupling of such a synthetic network to an irreversible fragmentation of the final polymer toward intermediate size clusters through a different pathway than that of their growth could lead to a Viedma-like deracemization,[232] i.e., a selection of one of the two
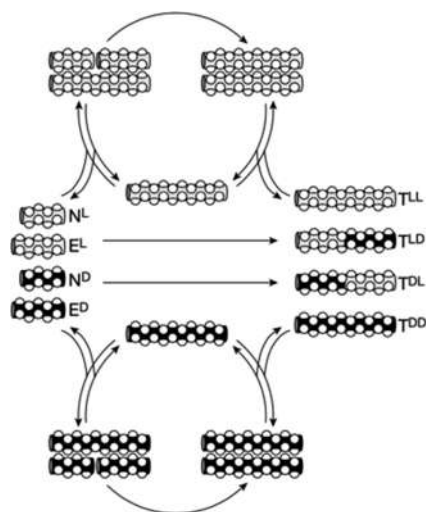
Figure 60. Autocatalytic stereoselective formation of a racemic mixture of homochiral peptides ($T^{LL} + T^{DD}$) by the enantioselective template effect of the final peptide on an initial racemic mixture of oligopeptide ($N^L + E^L + N^D + E^D$). Note that the heterochiral peptides (TLD + TDL) do not participate in the autocatalytic cycle. Reproduced with permission from ref 673. Copyright 2001 Springer Nature.

enantiomeric manifolds. However, in this specific case, it appears that the autocatalytic order is too low to achieve SMSB.[675,676]

Let us now give some other strategies that could be useful to develop examples of experimental systems, which we think might be promising if used either alone or conjugated with any appropriate irreversible process or phase transition. The domains which could be revisited using new experimental approaches are those where important nonlinear effects have been detected. The addition of organozinc on aromatic aldehydes (i.e., to try to extend the field of the Soai reaction)[677] is unavoidable. From this point of view, two recent papers deserve to be analyzed.

As shown in Figure 61, an interesting experimental effect has been unveiled by Geiger et al.[678] while varying the concentration of *N*-methylephedrine as a ligand for the well-known
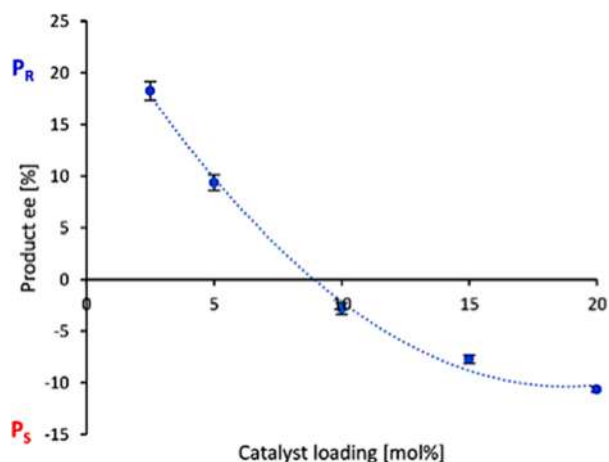
Figure 61. Plot of the product *ee* vs catalyst loading of the (−)-NME-catalyzed enantioselective addition of ZnMe$_2$ to benzaldehyde (0.56 M) in toluene at 0 °C. Note the left part of the curve showing the high enantioselectivity of the monomeric catalyst. Reproduced with permission from ref 678. Copyright 2020 Springer Nature.

enantioselective addition of dimethylzinc to benzaldehyde. Kinetic monitoring[117] and kinetic modeling of such experiments, and changes in the aldehyde and organozinc structures, could provide some clues for the potential presence of autocatalytic effects.

In the second report, provided by the Amedjkouh group,[642] the scope of absolute asymmetric catalysis has been broadened by an unprecedented phase alteration. While there was no absolute asymmetric catalysis of the pyridinic alkanol under homogeneous conditions in solution, the reaction of *i*Pr$_2$Zn vapor on a solid powder of pyridine carbaldehyde induced some autocatalytic amplification. These observations provide new perspectives on the experimental procedures to be implemented to achieve an absolute asymmetric synthesis.

The Kawasaki group[679,680] has reported an imaginative approach by the combination of a biphasic Strecker synthesis with a Viedma-like deracemization of racemic conglomerates. The reaction is the formation of imino derivate in the presence of HCN that forms an α-amino nitrile that crystallizes as a conglomerate. The presence in the solution of the reactants (HCN, amine, and the corresponding aldehyde), thanks to the low exergonic formation of the amino nitrile, plays the role of racemization while thermal cycles ensure the recycling of a Viedma-like deracemization. Finally, the crystals yield scalemic amino acid mixtures by hydrolysis.

Investigations of asymmetric Mannich reactions under biphasic microfluidic conditions[681] have shown that the enantioselectivity of a catalytic reaction can be dramatically amplified in the confined hydrophobic cavities of microdroplets surrounded by a hydration shell. The observed chirality amplification was further enhanced by decreasing the size of the droplets. Hydrophobic hydration effects ensuring high proximity between chiral catalyst and substrates at the transition state have been assumed to explain this effect.

One can imagine that a combination of synthesis leading to racemic conglomerates represent a heterogeneous synthetic approach that could be of a more general use. In this respect, it is important to stress enantioselective autocatalysis where the mechanism occurs by an enantioselective mediation of an additional conglomerate catalyst,[281] for instance, the action of "racemic" mesoporous silica on the Soai reaction.[626] This approach is quite promising because silicas and silicates are well-known conglomerate catalysts, for example, many phyllosilicates[26] have been proposed for the abiotic synthesis of nucleotides and peptides (able to lead to autocatalytic template mechanisms). Moreover, and even more important from the synthetic point of view, are the MOFs' racemic conglomerates. The idea is to develop self-building racemic conglomerate MOFs capable of asymmetric catalysis coupled to synthetic reactions, according to Scheme 9.

In order to get started, any adventurous reader willing to undergo such an extended research could find some interesting information about catalytic MOFs within the following refs 275, 442, and 682.

8. METHODS FOR CHIRALITY DETERMINATION

This section addresses the specific problems found in the analysis of the racemic biases that emerge in SMSB experiments but does not aim to be an in-depth review about the assessment of enantiomeric ratio values because authoritative reviews and monographs have already been published about this point.[683−688] The requirement of a different approach compared to the case of asymmetric synthesis, which is mostly based on the

Scheme 9. Principle of the Autocatalytic Formation of a Catalytic MOF (Chiral Solid)[a]
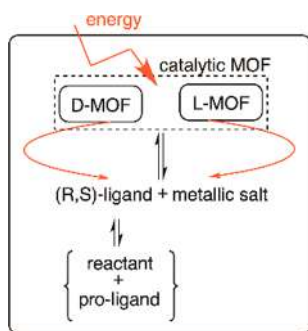
[a]Chiral ligands are produced through the catalytic reaction of appropriate reactants and prochiral pro-ligands. Metallic salt insures the formation of structurally specific MOFs from the ligand major enantiomer. The red lines represent the return-back to the solutions by a different pathway than that of the solid formation, for example, by crystal attrition.

chromatographic separation of enantiomers, is obvious in the case of chiral crystals or chiral aggregates which are achiral in solution. Furthermore, the future research of SMSB processes in molecular solutions will imply reaction conditions under which racemization can occur when the conditions that keep the system open no longer operate, and this limitation would require real time measurements of the emerging optical activity.

8.1. Molecular Solutions of Chiral Compounds

All reports on experimental SMSB, those related with the Soai reaction, as well as other reports discussed in section 7.2 deal with systems in which the final compound, most often an alcohol, does not racemize and, therefore, can be separated by achiral chromatographic techniques, generally TLC or flash chromatography, so that the enantiomer ratio can then be straightforwardly determined by HPLC using chiral columns. This is also the typical procedure used in asymmetric synthesis: both the selection of the chiral column[689] and the control that there has not been enantiomer segregation in the previous achiral chromatographic separation[690] are well solved points in asymmetric synthesis. Notice that the well-established Bull−Jones NMR analytical method, based on the NMR analysis of diastereoisomers[691] derivatives of the final chiral compounds, has not been reported for SMSB experiments. This is a consequence of the fact that the NMR method lacks sufficient precision to reliably measure differences between similar *ee* values. In this respect, the methodology based on chiral HPLC is more accurate from an analytical point of view but requires the use of internal standards and the availability of precise methods for peak area measurement.[657] The search of new reaction networks able to show SMSB, such as pointed out in section 7.2, will require the *in situ* detection of enantiomeric ratios in order to follow changes in the optical polarization properties. This approach has not been reported, to the best of our knowledge, because of the lack of interest of the synthetic chemist in kinetically controlled reactions outputs that easily racemize. However, as a consequence of regulations of the FDA on the chiral purity of some drugs, HPLC analysis using circular dichroism (CD) sensors is now a common method,[692−694] and the technique could be adapted for synthetic methodologies, taking into account the points discussed, in what follows.

The CD signal occurs at an electronic transition, and this requires the use of monochromator systems instead of simple

filter arrangements. Liquid-crystal based polarization modulators, the cheapest option in spectroscopic CD instruments, are suitable in the visible range but offer only a partial coverage of the UV−vis absorption of organic compounds and, hence, quartz photoelastic modulators are necessary to expand the range of measurements into the UV region. Nevertheless, the sensitivity decreases significantly with the wavelength, and the rotational strength of the molecular CD is low, and thus the measurement in the visible range, when possible, is the best option. CD measurements on the secondary and tertiary structures of proteins are studied at the low intensity $n \rightarrow \pi^*$ (or Rydberg) absorption of the carboxamide group (≈ 230 nm) since the intense absorption of the $\sigma \rightarrow \pi^*$ band occurs within the far-UV region. Chirality studies at this absorption band can only be performed using light sources obtained from synchrotron radiation.[695,696] Furthermore, the analysis fails when the absorption is high, for example, determinations at absorbance values ≥ 1 are mostly useless: cuvettes of short optical paths and the selection of CD bands showing high polarization strengths are necessary to follow the reaction progress. However, in the case of suspensions and mesophases, thin path-light can lead to the particle orientation and, as a consequence, to alignments yielding systematic CD errors (see below). Therefore, it seems that the derivation of the chiral reaction products into compounds/dyes showing absorptions in the visible range will be necessary.

The determination of circular birefringence (CB) instead of CD poses similar drawbacks as well. Although far from the transition wavelength in contrast to CD, CB shows limited values far from the electronic absorption, the corresponding rotational strength is very low, but it shows an enormous increase when approaching the electronic transitions (Cotton effect). Therefore, the optimal wavelength for CB measurements is near the same as for CD detection. In fact, Mueller matrix polarimeters may measure simultaneously CD, CB, and absorption, as discussed below for chiral solids, and this type of instruments could be the option of choice for the optical detection of chemical chirality.

8.2. Chiral Solids

In the case of chiral solid phases of chiral compounds which do not racemize the assessment of racemic biases in the crystal mixture is done by dissolution of the sample and analysis of the corresponding solutions.[265,697] Notice that this approach can be also followed in the case of Viedma-like procedures in which additional reagents need to be added in order to achieve the racemization in solution (section 2.2.4), because the final workup previous to the analysis includes the elimination of these reagents and the chiral compounds do not racemize. However, in the case of enantiomorphic phases of achiral compounds, the evaluation of *ee*s must be performed on the solid mixture and this, at best, will only give an approximate result. At the beginning of chirality studies it was even difficult to distinguish between racemate crystals and racemic conglomerates of chiral nonracemizing compounds. Here, the so-called Meyerhoffer rule (1904),[698] that is obvious nowadays, was applied because, assuming ideal behavior, the solubility of a racemic conglomerate should be double compared to that of the pure enantiomer crystal in contrast to the racemic crystal that shows the same solubility than that of the enantiopure crystals. However, in the case of racemic conglomerates of compounds that are racemizing in solution, the rule does not apply because the solubility of the racemate mixture of chiral crystals or that of an

enantiomeric pure crystal mixture at ideal conditions must be the same. In this respect, the paradoxical nature of chirality, i.e., that chirality only exists when there is a chiral recognition process either with a chiral physical force or through the interaction with other chiral entities, was already discussed in the early application of the phase rule in solution equilibria when comparing chiral crystals of achiral and chiral compounds.[110,111] In the case of racemic conglomerates, the two solid enantiomorphs are thermodynamically identical; therefore, in the case of one compound (achiral or chiral racemizing in the solution), the phase rule must count both enantiomorphs as the same phase;[112] this in agreement with the experimental behavior of the system.

The qualitative determination of chirality in crystals, regardless of whether they are present as a racemate, as a scalemic mixture, or in enantiopure composition, is certain when X-ray crystallographic analysis determines that they belong to one of the 65 Sohncke chiral space groups (section 3.1.4). The search of compounds yielding chiral crystals to be used in heterophase asymmetric inductions[26,430,699] or as potential substrates for Viedma-like deracemizations (section 2.2.4) requires X-ray diffraction facilities, which today is affordable instrumentation even for individual research groups.[616] The search in the Cambridge Structural Database (CSD) is necessary, but considering that the crystallization conditions (temperature, solvent, etc., see, e.g., refs 112 and 167 and section 5.7) are determinant to obtain crystals belonging to different crystal groups, a test for the presence of chirality is necessary prior to any experimental attempt.

Optical assessment of molecular chirality in transmission mode is easy for isotropic solutions, but it is difficult when the sample shows optical anisotropies. Furthermore, large aggregates show important scattering contributions in which the chiral signature lies in the differential scattering of circular polarized light.[700] This matter was studied years ago in relationship to biopolymers, but nowadays, this question is also present in material science and photonics research involving chiral nanostructures.[701−703] The available instrumentation for materials science can be adapted for its use in chemical chirality studies.

Chemical Reviews published 43 years ago a highly detailed review on the question of how to interpret dichroic and birefringent signals when the chemical structure is oriented with respect to the analyzing beam, such as occurs in the case of crystals.[528] Despite the fact that this review was addressed to the chemical audience, it has had little influence, probably because its theoretical basis was useless owing to the absence of reliable optical-instrumentation. Spectrometers based on one Pockels effect cell in old dichrographs or on one photoelastic modulator (PEM) in modern instruments are able to determine CD spectra and CB (optical activity), when the sample is isotropic, i.e., in the case of molecular solutions. In liquid crystals or solutions containing oriented nano- or microparticles, the sample shows optical linear polarization properties that tend to be much larger than their circular counterparts. Their combinations may give rise to an output light beam that, in addition to the CD signal generated by the chemical chiral structure, contains dichroic contributions resulting from these linear anisotropies. In addition, linear dichroic and birefringent signals can be also contaminated by the circular polarization contributions.

In summary, depending on the relative weight of circular and linear signals, the one-PEM common instruments cannot give reliable optical polarization values, neither of circular nor of linear polarizations.[704] In order to differentiate between these contributions, several optical measurements changing the polarization characteristics of the input and output beams must be used with the objective to excite and analyze the sample with a full set of Stokes vectors, thus measuring the Mueller matrix that represents all the optical properties of the sample.[705,730] Algebraic decompositions of the Mueller matrix elements may yield the real CD, CB, linear dichroism, and linear birefringence of the sample.[706] Instruments with two PEM can measure 7 of the 4×4 Mueller matrix elements in one scan and by reorienting some optical elements have access to the full Mueller matrix.[707] Commercial instrumentation using this approach is available today (Figure 62).
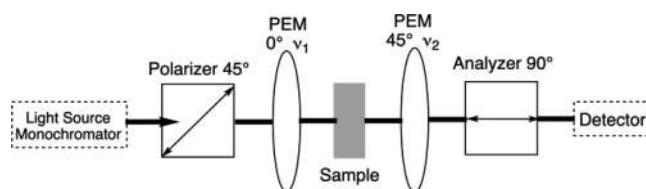
Figure 62. Scheme of a Mueller matrix commercial polarimeter based on two photoelastic modulators (PEM; ν_1 and ν_2 are the different modulating frequencies) (see for example https://www.hindsinstruments.com/techniques/mueller-polarimetry/), mostly used in material science for the characterization of the dielectric constant through optical measurements.[708]

A significant progress has been the advent of four-PEM total Mueller spectroscopy that allows the simultaneous determination of all components of the Mueller matrix.[265] Despite that this approach is still based on homemade instruments, a common practice in physics but uncommon in chemistry, this is the best suited type of spectrometer that should be used when the research objective deals with the study of the emergence of chirality in anisotropic systems. It is important to stress that, for high anisotropies, the spurious CD and CB contributions are often much more intense than those determined by the rotational strengths of the molecular transitions. Therefore, sensitivity questions may hinder the optical evaluation of chirality.

The potential or even the necessity to use Mueller matrix chiroptical methods in the study of anisotropic materials is shown in the Kahr reports,[574,575] which visualize microscopic heterochiral domains in the formation of dissipative crystallite precipitate structures and spherulite aggregates (see Figure 63).

The depolarization exerted by the sample to the analyzing beam can be inferred from the Mueller matrix analysis,[697] and it can be quantified with a depolarization index.[709] At depolarization index values smaller than 0.8 (1 for no depolarization and 0 for total depolarization), the measurement of optical polarization properties may be impossible. This obstacle depends on sample irregularities and particle sizes. Perfect crystals that show high photoelastic coefficients,[245] high birefringence values, or strong absorbance also make the measurement of optical polarization properties impossible.

Optical properties are dependent on the crystal symmetry axis. One of the points that justify the large number of experiments performed on $NaClO_3$ (cubic) is that it belongs to the space group $P2_13$ in which the optical properties are the same for its three symmetry/optical axes.[324] This simplifies the detection of the crystal chirality because a simple polarizing microscope suffices to distinguish between sodium chlorate
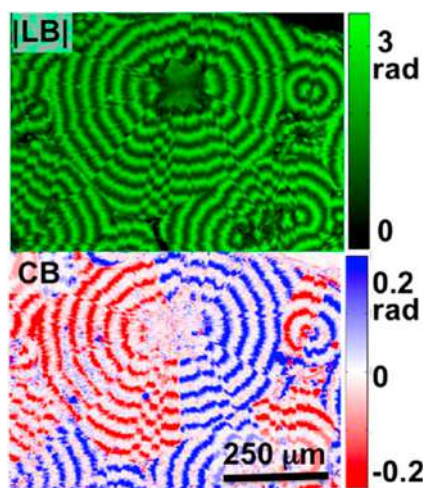
Figure 63. Micrograph obtained by Mueller matrix polarimetry at 532 nm of the crystallization of an aspirin salicylic acid sample that form spherulite aggregates of twisted crystals.[575] The ability to determine the circular birefringence (CB) differentiate the heterochiral domains in domains showing the same linear anisotropic ordering (LB image, such as those obtained in petrographic microscopy but free of CB interferences). Reproduced from ref 575. Copyright 2013 American Chemical Society.

crystals of different chiral signs. A common source of confusion lies in the assignment of its absolute configuration,[710] according to the observed right and left deviations of the polarization plane. Chemists refer to the deviation and optical rotating coefficients by observation of the beam coming out of the sample, while some physicists describe the deviation along the progression of the light beam. The subject for chemists is the sample, but for physicists it is the wave.

In the case of microcrystalline materials, optical samples may be prepared (pellets, films, etc.)[711] such as is done in IR spectroscopy, where it is assumed that the many crystallite orientations average over the anisotropies. In this case, CD and CB measurements using common instruments can be performed, which however, can only give a qualitative or a semiquantitative description of the bias from the racemic composition (see, e.g., refs 182 and 712). Such solid samples may show important scattering contributions which increase the difficulties of the measurement, because this is mostly bound to scattering effects and high depolarization ratios. However, through the measurement of changes in the dichroic signal when the sample is rotated, the presence of nonaveraged anisotropies in the material and homogeneous distribution of anisotropies are detected, and the real CD signal may be inferred.[704] CD spectrometers for solid samples[264,713−715] following this principle and being also able to differentiate between absorption and scattering contributions by using integration spheres give sound results in the chirality study of solid materials, e.g., ref 716 and 717 (Figure 64).

A point to be taken into account is the vertical, microscopy-like, or horizontal, spectroscopy-like configuration of all this instrumentation. The configuration is not a problem for solid samples, but in all samples in which the force of gravity can induce orientational changes (liquid crystals, particle suspensions, etc.), vertical and horizontal determinations may lead to different results, especially concerning long-shaped ordered structures.
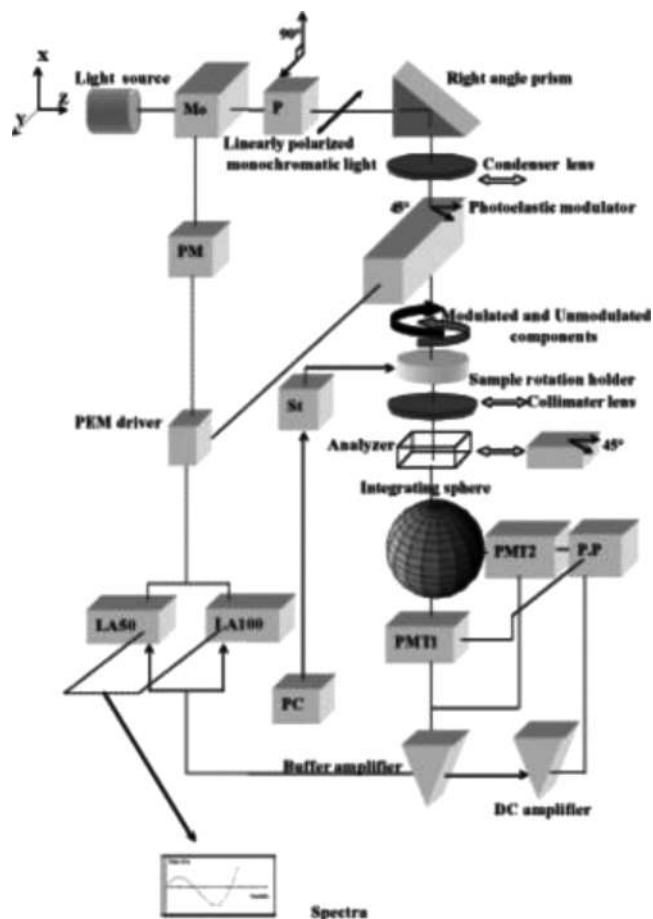
Figure 64. Vertical-type chiroptical spectrophotometer described in ref 715. Mo, monochromator; P, polarizer; PM, pulse motor; St, stage controller; LA, lock-in amplifier; PMT1 and 2, photomultiplier for transmission and DR; P.P, photomultiplier power supply; and PC, personal computer. Reproduced with permission from ref 715. Copyright 2008 AIP Publishing.

In the case of suspensions of nano- and microparticles as stable suspensions in solution, the common option is a horizontal spectrometer using common spectroscopic cuvettes. For round particles, their orientation in solution is averaged and this allows for the interpretation of the spectroscopic results assuming an isotropic distribution. The determination of particle shapes and sizes (e.g., by atomic force microscopy) and the confirmation of the absence of linear polarizations, allows one to perform sample measurements in common CD/CB spectrometers. Thin-layer cuvettes lead easily to orientations in the case of fluid mesophases.[718] Suspensions of long- shaped particles show, as well as in the Brownian regime, an averaged vertical orientation. Solid samples showing linear anisotropies may be studied by the changes originating from the rotation of the sample. However, gravity alignment in solution can only be detected by total Mueller matrix spectroscopy.[571] Furthermore, in the case of nanoparticle suspensions, liquid crystals, and gels of low viscosity, the condition of stagnant solution is not easily obtained. For example, solutions in not very well thermo-stabilized cuvettes show convection flows that may orient the particles of the solution: the symmetry relationship of the convection flows in specific parts of the cuvette lead to chiral macroscopic orientations of the particles transported in the flows, so that CD signals result from the *P* and *M* linear
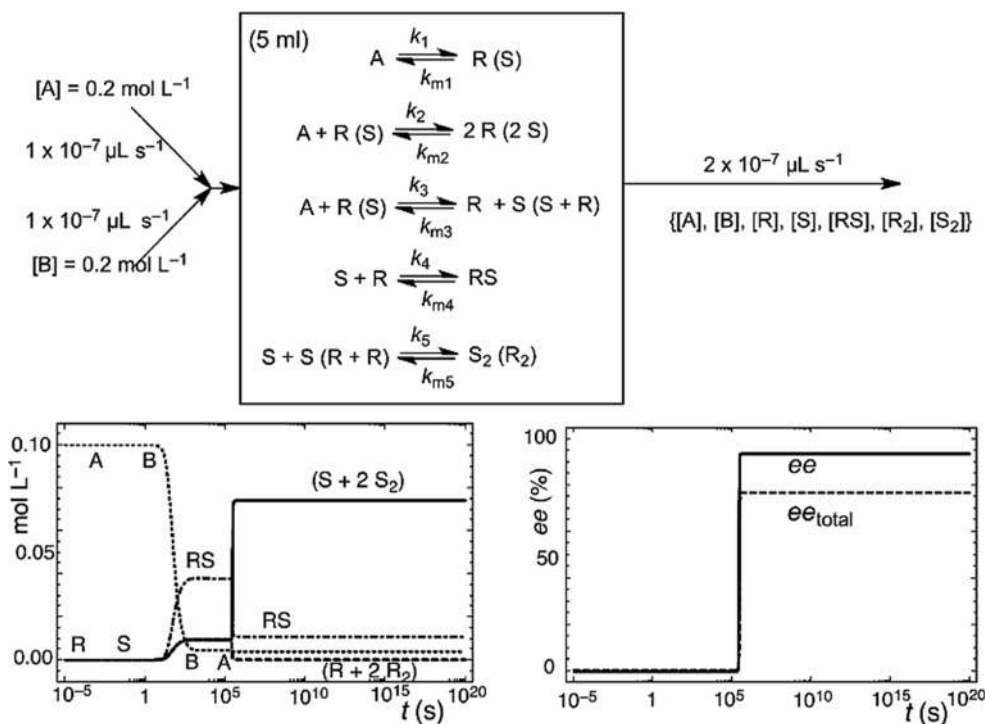
Figure 65. Dynamic simulation in an open flow reactor of a possible network for the Soai reaction. The system leads to SMSB despite significant contributions from the nonenantioselective autocatalysis and from the homochiral dimerization reactions. Yield and total *ee* are calculated by assuming that in the separation method the oligomers of products/catalysts revert back to the monomeric species (R and S), such as occurs in the Soai reaction. Reaction parameters are $k_1 = 1 \times 10^{-5}$, $k_{m1} = 1 \times 10^{-10}$, $k_2 = 10$, $k_{m2} = 1 \times 10^{-4}$, $k_3 = 0.1$, $k_{m3} = 1 \times 10^{-6}$, $k_4 = 1 \times 10^6$, $k_{m4} = 1 \times 10^{-3}$, $k_5 = 1 \times 10^6$, $k_{m5} = 1 \times 10^{-2}$. Initial conditions in the reactor: $[A]_0 = [B]_0 = 0.1$ mol L^{-1}, $[R]_0 = 1 \times 10^{-10}$; $[S]_0 = [R]_0 + 1 \times 10^{-22}$. Reproduced with permission from ref 116. Copyright 2014 Wiley-VCH.

polarization combinations. There are dramatic reports on this: vortex stirred solutions show CD signals of contrary sign depending on the vortex direction that disappear when stirring is stopped.[294,572,576,719] Some other reports describing CD reversible signals probably correspond to this type of macroscopic chiral alignment originated by flows[46,48,49,720−723] or even by *P* and *M* orientations at the opposite cuvette walls, depending on the direction of stirring exerted during the deposition.[724] Thanks to the progress in Mueller matrix methods, the detection of chemical chirality in suspensions showing the simultaneous presence of real CD and macroscopic spurious CD has been possible,[94,570,577] even the differences in CD vertical and transversal to the aggregate nanotubes.[571] In the case of the J-aggregates of achiral amphiphilic porphyrins, Mueller matrix spectroscopy has allowed one to distinguish between SMSB in which the chiral sign was selected by the direction of the stirring vortex[90,93] and those reversible effects that were first attributed, incorrectly, to the elasticity of the material instead of to the orientation in the cuvette flows of long shaped particles. A review of this topic can be found in ref 92 and is also discussed in section 6.2.

A technique that has surely not yet developed all its potential is vibrational circular dichroism (VCD).[725,726] This is a technique offering interesting possibilities as the theoretical modeling of the experimental spectra is simpler than for UV−vis spectra. New instrumentation is being developed to increase the instrument sensitivity for weak dichroic signals, but it is mostly optimized for specific problems, for example, for chiral studies on biopolymers.[727] Figure 27 (see section 5.5) is an example of the potential application of FT-VCD instruments.[728] The achiral propyl benzimidazole compound (in nonpolar solvents) that crystallizes as racemic conglomerates shows SMSB: the experiment shows how very weak chiral unidentified contaminations lead, as it has been found in many other cases, to a bias from the racemic of the same chiral sign. There are not fundamental obstacles to build Mueller matrix FT-VCD instruments[67,68,729] in the mid-IR range 2000 cm^{-1}−800 cm^{-1}, and these will be an important tool in the assignment of biases from the racemic composition, even to assign absolute configurations[731] of chiral organic materials. As a part of the vibrational optical activity methods, there is also Raman scattering optical activity.[732,733] It is useful for the study of chiral structural aspects of biopolymers in water solutions[734] because of feasible correlation between experimental results and theoretical calculations.[735] The Raman scattering method is used too for the study of liquid crystal structures.[736−738]

9. MODELS AND SIMULATIONS

In this section, we give a survey of recent modeling efforts aimed at rationalizing the Soai reaction (see section 7.1) and the Viedma deracemization experiments (see section 2.2.4). Both these experiments have generated an intense debate on the underlying mechanisms and processes involved. A common aspect which must be included in all the modeling efforts are the fundamental constraints imposed by thermodynamics, which if ignored, can lead to artifacts and misinterpretations of the simulations. Such constraints are important for a proper understanding of emergent phenomena and complex behavior in open systems generally.[739] Earlier efforts devoted to the theoretical modeling of the Soai reaction and the Viedma experiment, and distinct from those discussed below, can be found in an excellent review by Saito and Hyuga.[740]

9.1. Mirror Symmetry Breaking and Enantioselective Autocatalysis in the Soai Reaction

The Soai reaction[59,144,605,741−743] (see section 7.1, Scheme 2) corresponds to a kinetically controlled absolute asymmetric synthesis that can be rationalized within the framework of a Frank-like model.[612,638,640,647,744,745] Here, we discuss the basic reactions that make up the Soai reaction network, that is, a reductionist model without consideration of the more specific details of the reaction mechanism that are undoubtedly more complex.[613,677,741,746−748] The analysis of this type of model in coupled reaction networks is needed to establish the relative contributions of the possible reactions in the system dynamics. Several authors have summarized the principal experimental trends of the Soai reaction (see, for example, ref 748). On the other hand, the first kinetic understanding of the mirror-symmetry breaking in the Soai reaction was made by Rivera Islas et al.[640] This paper has served as inspiration for the later models, such as the one defined in Figure 65. Here we highlight those characteristics that suggest that the Soai reaction can be described as a Frank-like reaction network (see section 2.2.2) taking place in a closed system giving rise to a kinetically controlled absolute asymmetric synthesis.

(a) The relatively low *ee* values obtained in a single batch operation indicate that the efficiency of the system is decreased by the significant contribution of several reactions such as the nonenantioselective autocatalysis:

$$A + R \rightleftarrows R + S, \quad A + S \rightleftarrows R + S \qquad (4)$$
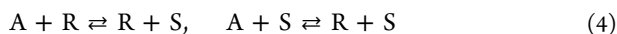
and the homochiral dimerization:

$$2R \rightleftarrows R_2, \quad 2S \rightleftarrows S_2 \qquad (5)$$

(b) The addition of a dialkylzinc species to a carbonyl group to give the zinc alkoxide is a highly exergonic transformation, that is, it must lead to kinetically controlled outcomes. This occurs for most nucleophilic additions of organometallic compounds to the carbon−heteroatom double bond. On the other hand, the rate of the uncatalyzed addition of dialkylzinc is very low, and it is assumed to be reversible:

$$A \rightleftarrows R, \quad A \rightleftarrows S \qquad (6)$$

The enantioselective autocatalytic reaction:

$$A + R \rightleftarrows 2R, \quad A + S \rightleftarrows 2S \qquad (7)$$

can overcome the deleterious contribution of the background reaction.

(c) The nonenantioselective autocatalysis is slower than the enantioselective one, but it plays a significant contribution in the formation of the final products, that is, it decreases the ability of the system to amplify chirality.

(d) The catalytic species is a chiral oligomer of the Zn alkoxide, and the enantioselective autocatalysis is more complex than that of a quadratic asymmetric autocatalytic reaction. The heterochiral dimerization of the catalysts could constitute the mutual inhibition stage. However, several experimental and theoretical reports point toward the similar stability of the homochiral and the heterochiral oligomer catalysts, which, in turn, implies an inefficient mutual inhibition stage.

The Soai reaction requires an experimental procedure of successive batches starting at the same initial concentrations of reactants but using the final reaction mixture obtained in the previous batch.[59,144,741−743] This implies successive increases of volume and chemical mass. As pointed out by Plasson and co-workers,[168] such a procedure is in fact an approximation to

running the reaction in an open system. Therefore, the Soai reaction is a first candidate for absolute asymmetric synthesis in flow chemistry. Figure 65 shows an open flow simulation of the Soai reaction, which in addition to the reactions necessary for SMSB (enantioselective autocatalytic reaction order *m* = 1 and mutual inhibition) shows a much slower noncatalyzed background reaction and significant contributions of nonenantioselective autocatalysis and homochiral dimerization. The same network simulated in a closed system, following the successive batch procedure, yields a kinetically controlled absolute asymmetric synthesis of similar *ee* after 4−5 successive batch additions (see ref 744). These results show that nothing beyond a Frank-like mechanism (see section 2.2.2) is required for being able to capture all the main dynamic features of the Soai reaction, even if nothing is said about the real structure of the catalytic species and their reaction cycles.

9.2. Mirror Symmetry Breaking and Enantioselective Autocatalysis in Viedma Deracemization

An interesting experimental scenario of absolute asymmetric synthesis is that first reported by Viedma on the deracemization of racemic enantiopure crystal mixtures, the so-called racemic conglomerates[107] of achiral or fast racemizing compounds (see section 2.2.4). The experimental setup involves the continuous wet mechanical grinding of a racemic conglomerate mixture of enantiomorphic crystals.[77,78,80,146,211,237,279,699,749−755]

The theoretical understanding of Viedma's experiment is currently open to debate.[111,172,175,182,183,234,236,237,751,756−768] Nevertheless, the unquestionable nexus of agreement between all reports to date is that the higher solubility of the smaller crystals, the Gibbs−Thomson effect,[174,769] obtained through grinding, creates a supersaturated media for the larger crystals and that a steady state continuous distribution of visible crystal sizes and small crystal clusters down to the monomer must be obtained. This is most likely due to the fact that the mechanisms of crystal growth are modeled as reaction networks. They are discussed as a thermodynamic system, while grinding and permanent temperature gradients maintain the system in nonequilibrium stationary states. Therefore, these mechanisms can be subject to some misinterpretation. A Viedma reaction-type network model includes the following three elements,[178] all the three based on the characteristics of nucleation and crystal growth: (i) A growth process that is endergonic during its initial stages, but from a critical size onward of the aggregates (clusters in crystallization), becomes exergonic by virtue of cooperative effects (see Figure 73). (ii) In addition to isodesmic "polymerization" (see the list of transformations depicted in the boxes denoted by "monomer-to-cluster aggregation" in Figure 73), homochiral cluster-to-cluster growth must be present. Only the latter gives nonlinear kinetic dependences, reminiscent of autocatalysis, capable of yielding SMSB. These mechanisms are represented in Figure 73 in the boxes denoted by "cluster-to-cluster aggregation". (iii) The cluster-to-cluster growth mechanism involves a range of sizes. Therefore, the product of a cluster-to-cluster aggregation contributes as well to the formation of other homochiral clusters. Most likely, this mutualistic effect creates an exponential growth greater than that of the quadratic dependence of a single cluster-to-cluster step. This is an important point that merits further detailed study, principally because it bears some analogies with the role of cross-catalysis in hypercyclic replicators.[9]

In saturated solutions there are only fluctuations between the crystal and the monomeric species that occur through the
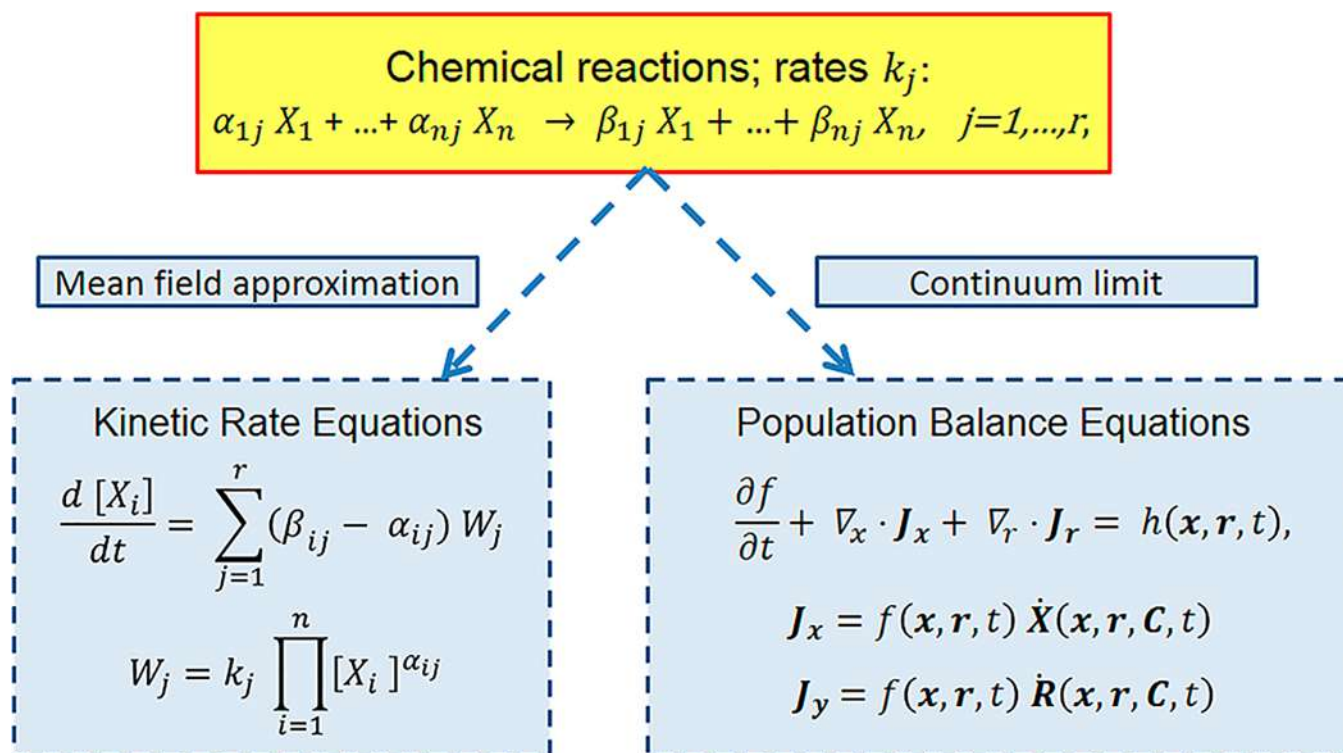
Figure 66. Distinction between kinetic rate equations (left lower panel), based on mass-action reaction rates W_j and population balance equations PBE (right lower panel). See text for further explanation of PBEs. The former are obtained from the underlying chemical transformations (upper panel) involving n chemical species X that participate in r reactions and assuming the mean-field approximation (see also Figure 77). The PBEs can be obtained taking a *continuum limit* of the transformation rules in the upper box. This continuum limit has been carried out explicitly for the microreversible kinetic reaction scheme in Figure 73 for Viedma deracemization[771] and leads to the general class of PBEs that have been used in modeling of this experiment (the results are reviewed below). Even when starting from *microreversible* reactions (upper box), the microreversibility is lost, or washed out, in taking the continuum limit, thus limiting the scope of the PBE approach to strict kinetic control.

isodesmic growth mechanism, i.e., the *ee* of any crystal mixture showing similar crystal sizes (same solubility for all crystals) cannot change. This provides an additional remarkable feature to Viedma deracemization: the stabilization of the final crystal outcome, once the grinding ceases or a homogeneous temperature distribution is achieved.

9.2.1. Population Balance Models. The Viedma deracemization experiment provides a fertile ground on which to test and compare modeling by kinetic rate versus population balance equations. There have been many variations on a theme involving kinetic reaction-rate models proposed for explaining Viedma deracemization.[2,5,31,34,770] By contrast, population balance equations (PBE) have been applied only relatively recently and for the first time by Iggland and Mazzotti, followed by Blackmond and collaborators.[231,239−241,771] Prior to this, population balance methods have been used for modeling crystallization processes.[772] The PBEs applied to achiral crystallizations are based on a description of crystal growth processes from the first nucleating subcritical clusters up to the large crystals. They generally deal with the crystal growth of single species or to selective crystallization of different compounds. Specific attempts to use PBEs for describing the Viedma deracemization phenomenon are reported using profiles of the energy differences between clusters/crystals by the description of the critical size cluster through the supersaturation value given by the classical primary nucleation theory.[231] We emphasize however that, in population balance modeling, only net crystal growth and dissolution flows, according to whether the cluster/crystal size is above or below

the critical size cluster, are considered. The conclusion drawn from these studies is that small initial differences between enantiomorphs, for example, in crystal size distributions, are the origin of the final chiral outcome, and PBEs can capture only kinetically controlled processes[231] (see section 2.2.2). This limitation of PBES to kinetic controlled processes (see also Figure 66) will become clear below.

Briefly, the ultimate goal in population balance modeling (PBM) is to obtain the particle distribution or density function $f(x,r,t)$, where the vector x denotes a collection of different internal quantities (e.g., size, mass, internal composition, age, etc.) associated with the solid phase particles and r the particle position vector in physical space. This distribution function is obtained as a solution of the general population balance equation:[68]

$$\frac{\partial f}{\partial t} + \nabla_x \cdot J_x + \nabla_r \cdot J_r = h(x, r, t) \tag{8}$$

where

$$J_x = f(x, r, t)\dot{X}(x, r, C, t)$$

$$J_r = f(x, r, t)\dot{R}(x, r, C, t) \tag{9}$$

are the bulk advective *particle fluxes* (Diffusive fluxes can also be accommodated in the PBE framework, and these arise when $\dot{X}$ and $\dot{R}$ include stochastic processes.[68]) through an internal attribute space (x) and through physical space (r), respectively, that is, the number of particles flowing per unit time per unit area normal to the direction of the velocity vectors $\dot{X}$ and $\dot{R}$. These
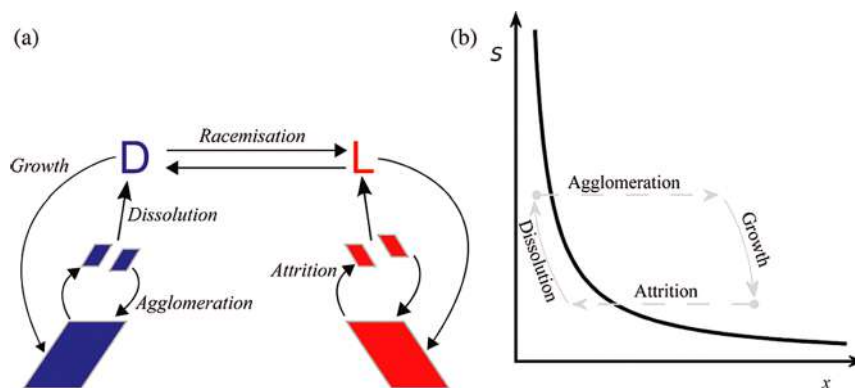
Figure 67. (Left panel) Basic processes considered in the population balance model of ref 231 agglomeration, growth and dissolution, attrition, and racemization. (Right panel) Solubility *S* as a function of crystal size *x* where the gray lines show the effects of the various mechanisms. Reprinted from ref 231. Copyright 2011 American Chemical Society.
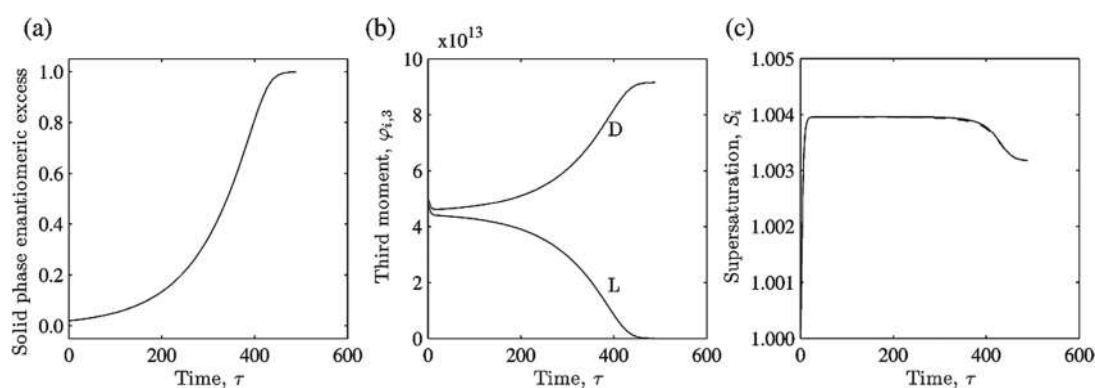
Figure 68. Temporal evolution of the (a) solid phase *ee*, (b) third moments of both crystal populations, and (c) solution concentration. Reprinted from ref 231. Copyright 2011 American Chemical Society.

velocities or rates of change may also depend on the continuous phase vector *C*, including all the continuous background quantities that might affect the behavior of the particles (e.g., chemical concentrations, supersaturation, background fluid flow, etc.). *C* satisfies its own standard transport equation.[773] The term $h(x,r,t)$ represents all birth and death processes in the solid phase, such as particle agglomeration and particle fragmentation. Models must be provided for these rates of change $\dot{X}$ and $\dot{R}$ as well as for h, if agglomeration and or fragmentation are to be included. Equation 8 can then be solved for $f(x,r,t)$, when the initial and boundary conditions are provided.[773]

The specific mechanisms considered by Iggland and Mazzotti in formulating their version of eq 8 include (i) solution phase racemization of the L and D enantiomers, (ii) growth and dissolution of clusters and crystals due to size-dependent solubility (the Gibbs–Thomson rule), (iii) agglomeration, and (iv) mechanical attrition[231] depicted schematically in Figure 67. The simulation results of their corresponding PBE subject to boundary conditions leads to the solid phase *ee* (a), third moments of the distribution function of the crystal populations (b), and solution concentration (c) and are shown in Figure 68.

Iggland and Mazzotti also remark that attrition is not necessary but that it that does increase the rate of deracemization: they claim that Viedma deracemization occurs when the breakage of crystals is suppressed, in which case the process is slow. We will come back to the importance of attrition below when we consider kinetic rate equation models.

In related work, Iggland and Mazzotti[239] considered two populations of crystals f_L and f_D, one for each enantiomer, and write a PBE eq 8 for each. They let *y* denote linear crystal size, then the PBEs (in dimensionless variables) for crystal growth and dissolution alone (no fragmentation nor aggregation: so $h \equiv 0$) and for spatially homogeneous distributions reduce to (i = D,L)

$$\frac{\partial f_i}{\partial \tau} + \frac{\partial (G_i^* f_i)}{\partial y} = 0 \tag{10}$$

for $f_i(\tau, y)$, where the reaction-limited crystal growth rate is

$$G_i^*(y, \tau) = (S_i(\tau) - S^*(y)),$$
$$S^*(y) = e\left(\frac{\alpha^*}{y}\right) \approx 1 + \frac{\alpha^*}{y} \tag{11}$$

Here α^* is a dimensionless capillary length. The size dependent solubility (to accommodate the Gibbs–Thomson effect) is $S^*(y)$, and $G_{R,P}^*$ refers to whether full exponential dependence or linear approximation is used, eq 11, and see Figure 69. S_i is the relative supersaturation of each enantiomer and obeys mass-balance equations (see eqs 3 and 4 in ref 239), which couple back to the PBEs in eq 10. The corresponding absolute particle fluxes J_y in crystal linear size *y* implied by eq 11 are given by

$$J_y = G^*(y)f(\tau, y) \tag{12}$$

The growth rates are represented in Figure 69 as the two opposing black arrows, along with a typical curve illustrating the
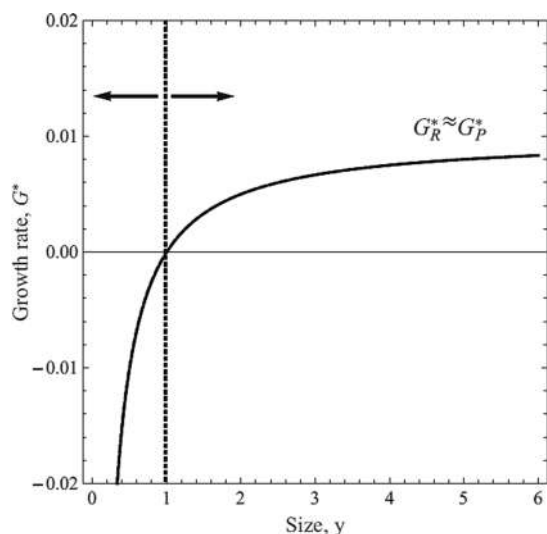
Figure 69. Dimensionless crystal growth rates G versus particle size y eq 4 used in ref 239 for a given supersaturation $S > 1.01$ and dimensionless capillary length $\alpha^* = 10^{-2}$. The large arrows denote direction of the net particle fluxes $J_y = G^*(y) f(\tau, y)$: for y greater than a critical length (at $y = 2$), the crystal growth rate is positive (to the right) and negative if less than the critical length (arrow to the left), indicating dissolution of the critical nucleus back to monomers. However, the inverse processes or counterfluxes, i.e., (i) primary nucleation up to the critical size and (ii) partial deaggregation for crystal sizes greater than the critical size are absent from G^* This growth rate function reflects the Gibbs−Thomson rule. Reprinted with permission from ref 771. Copyright 2015 The American Physical Society.

explicit growth rate function G employed. When solution phase racemization is included with the PBE, an apparent permanent solid phase ee is seen in their simulations, see Figure 70, which display the temporal evolution of the (a) supersaturation S_i, (b) the average crystal size, and (c) the solid phase ee, and with the additional proviso that "*sufficient difference between initial particle populations are required*".

The main conclusions drawn from their simulations[239] is that the processes of only growth, dissolution, and solution phase racemization (excluding both breakage and agglomeration) can lead to complete dissolution of one population of crystals and thus to a solid phase consisting of crystals having the same chirality. The authors claim that, given enough time, any *closed*

system (!) of chiral crystals in contact with a solution in which the enantiomers can interconvert will deracemize.

This latter conclusion stands in bold defiance of the dictates of thermodynamics, which state that the ultimate fate of any *closed system* of enantiomers subject to racemization will inextricably be the mirror symmetric racemic configuration, provided the underlying reactions are microreversible. In this light, we point out that in the PBE approaches taken thus far, the *reverse processes*: that is, (i) primary nucleation up to the critical cluster size and (ii) partial dissolution for crystal sizes greater than the critical size are not included in the growth rate function G, eq 4. A derivation of PBE growth rates starting from microreversible transformations proves that the absent reverse steps are actually lost in taking the continuum limit.[771] Thus, chemical equilibrium is an unattainable physicochemical state in these PBE models: simulations can only reveal kinetic controlled phenomena (see section 2.2.2), for which the system remains kinetically trapped in a scalemic configuration, see also Figure 66, distinguishing the main features between kinetic rate equations and PBEs.

Blackmond and co-workers[241] have used a PBE approach to model a net crystal growth rate term for chiral crystals, based on the Gibbs−Thomson rule and which depends additionally on a certain "frequency" factor proportional to the total area of crystals of given radius R. Their specific PBEs, one for each enantiomer, are expressed as

$$\frac{\partial f_i}{\partial t} + \frac{\partial (f_i \cdot G_i)}{\partial R} = S_i(R, R') + Q_i(R, R'), \quad i = D, L$$

(13)

where S_i, Q_i denote the breakage and agglomeration terms (compare to h in eq 8). Their proposed net growth term is

$$G_i = k'(1 + k'' f_i(R, t) R^2)(C_{i,0} - C_R^{sol})$$

(14)

where C_i, C_R^{sol} denote the solution concentration and solubility of the crystal of radius R, respectively, and depends explicitly on the particle distribution function f_i. Hence, the product of their growth rate eq 14 times the particle distribution function (f_i, G_i), as written in eq 13, is both of first and of *second order* in this distribution function f_i and in consequence cannot be interpreted as a true particle flux within the mathematical framework of population balance equations. Textbook derivations of the most general PBEs (see Ramkrishna, ref 773) demonstrate that growth rate terms are independent of the particle distributions. The product of any growth rate by the

(a)   (b)   (c)
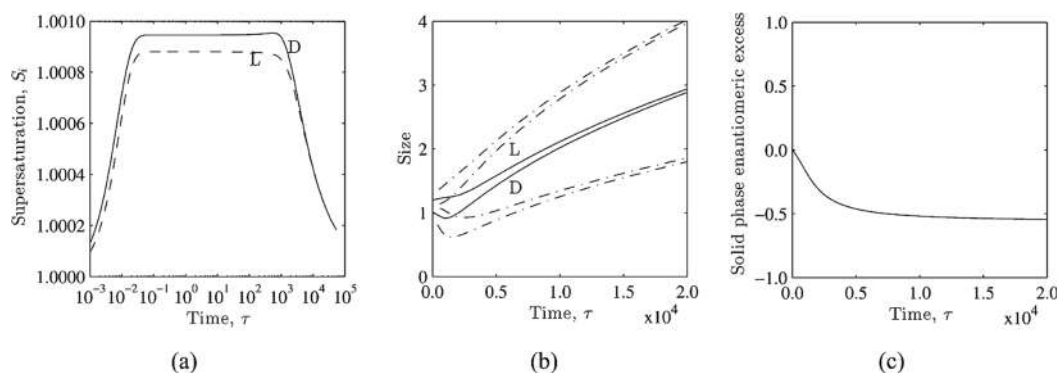
Figure 70. Temporal evolution of the (a) supersaturation S_i, (b) average crystal size (solid lines) with one standard deviation above and below marked by the dashed lines, and (c) solid phase ee. For simulation parameters, see Table 2 of ref 239. Reproduced with permission from ref 239. Copyright 2013 The Royal Society of Chemistry.

particle distribution must have the form of a particle flux (a density times a velocity: see eq 8 and eq 9), and the flux is always *first-order* in the particle distribution function. This must be so that, in the absence of sources and sinks and system boundary terms, the PBE reduces, as it must, to a continuity equation for the particle distribution. This is a fundamental tenet of transport and balance equations and is the basis for continuum mechanics.

Blackmond et al. use their nonstandard PBE model to explain experimental studies presented in the earlier part of their paper, in which they claim that particle agglomeration is not needed to account for their experimental findings. The role of agglomeration was examined by including an explicit agglomeration term Q_i on the right-hand side of their PBE. Figure 71 shows that the
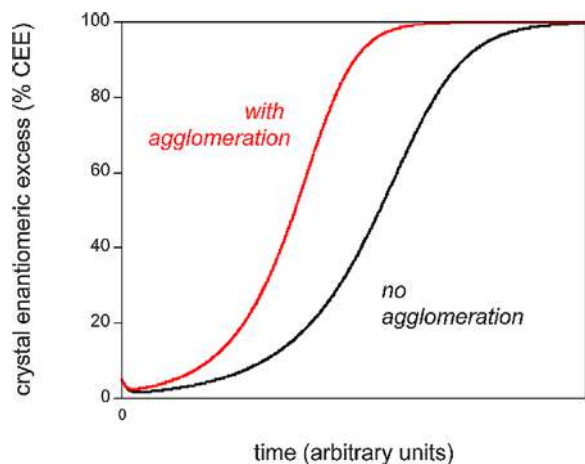
Figure 71. Evolution of solid phase *ee* for the case where an explicit agglomeration term Q_i is included in the model compared to the case where only the implicit agglomeration, which comes in through their unconventional growth term eq 14, is operative. Reprinted from ref 241. Copyright 2014 American Chemical Society.

temporal evolution of solid phase *ee* is accelerated when crystals add to crystals. Most notably, however, because this exponential behavior is demonstrated even in the absence of an *explicit* agglomeration term Q_i in the model, the authors conclude that the action of clusters is not a necessary condition for observation of the autocatalytic profile for solid phase *ee*. We hasten to point out, however, that the unconventional growth term eq 14 they introduced into their PBE contains a two-particle agglomeration kernel and shows that their PBE actually does include crystal−crystal agglomeration, even when the explicit agglomeration term is set to zero $Q_i = 0$, and this results from an implementation that falls outside the PBE framework[240] (for the demonstration of this important point, see ref 771).

9.2.2. Kinetic Reaction-Rate Models. In contrast to the PBEs surveyed above, which are transport equations governing the evolution of continuous-valued populations, kinetic reaction-rate equations deal with the microscopic reactions and transformations involving the individual chemical species themselves (see Figure 66). The transformations are discrete, typically indicating the outcome of the inelastic *collisions* of one or more species. Kinetic schemes lead to sets of coupled nonlinear ordinary differential equations, one equation corresponding to each one of the species. These are solved specifying the initial conditions.

Classical nucleation theory,[178,774] in its definition of a critical size nucleus, gives estimates of the free energy relationships for the addition/loss of monomer units to/from the growing or
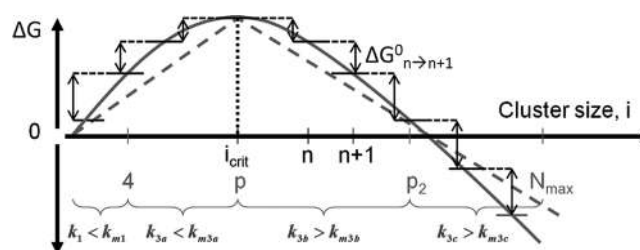
Figure 72. Solid curve: typical profile of the Gibbs free energy of nucleation and growth by monomer addition to clusters as a function of cluster size i according to the classical nucleation theory[774] and for a given value of the supersaturation $S > 1$. The energy levels indicate the free energy differences ΔG^0 in going from n to $n + 1$ monomer units. The difference between adjacent levels $\Delta G^0_{n \to n+1}$ yields the ratio of forward and reverse rates at each step of monomer-to-cluster aggregation/deaggregation. The underbraces indicate a convenient isodesmic approximation employed in the simulations: within each indicated cluster size subrange i, the ratio of the forward to reverse rates is a constant. Compare with Figure 73, which lists the monomer-cluster reactions for each isodesmic range. Reprinted with permission from ref 771. Copyright 2015 The American Physical Society.

dissolving cluster, see Figure 72. The solid curve represents the difference in the bulk and surface free energies of a growing cluster of p monomer units. The maximum corresponds to the critical size nucleus (critical cluster radius), which in turn corresponds to a critical number of monomer units p_{crit}, indicating the transition between endergonic to exergonic reactions. This critical size, or corresponding critical number of monomer units $p_{crit}(S)$, depends on the supersaturation value $S > 1$ and on a capillary length which combines all the physical parameters of the particles such as surface tension, molar volume, area, and volume shape factors, etc.[775]

Blanco et al. carried out numerical simulations with this microreversible kinetic scheme and their results indicate that the Viedma deracemization phenomenon corresponds to a true SMSB scenario.[178] Selected examples of these simulations highlight the effects of reversible versus irreversible transformations on pure growth and dissolution and the role of microreversible agglomeration and irreversible mechanical grinding or attrition.

Details of the complete kinetic network parameters, rate constants, isodesmic approximations used for the free energy profile, and the sizes of clusters involved in both the aggregation and in the fragmentation processes have been published previously, as has an in-depth discussion of the numerical methodology employed.[178] Here we highlight the role of agglomerations and attrition to compare and contrast with the above population balance models. We underscore the fact that only homochiral cluster−cluster agglomeration was operative, and no heterochiral cluster−cluster agglomeration was implemented.

We first address the presence or absence of reversible agglomeration. A characteristic and illustrative example of the different final states achieved in the presence or in the absence of cluster-to-cluster agglomeration is shown in Figure 74. This is a nonequilibrium steady state (NESS) as the attrition is maintained. In the presence of cluster-to-cluster agglomeration a final chiral state is obtained but in its absence, even when starting from a significant large initial *ee*, of 33% the final outcome is a racemic stationary state: after an initial chirality
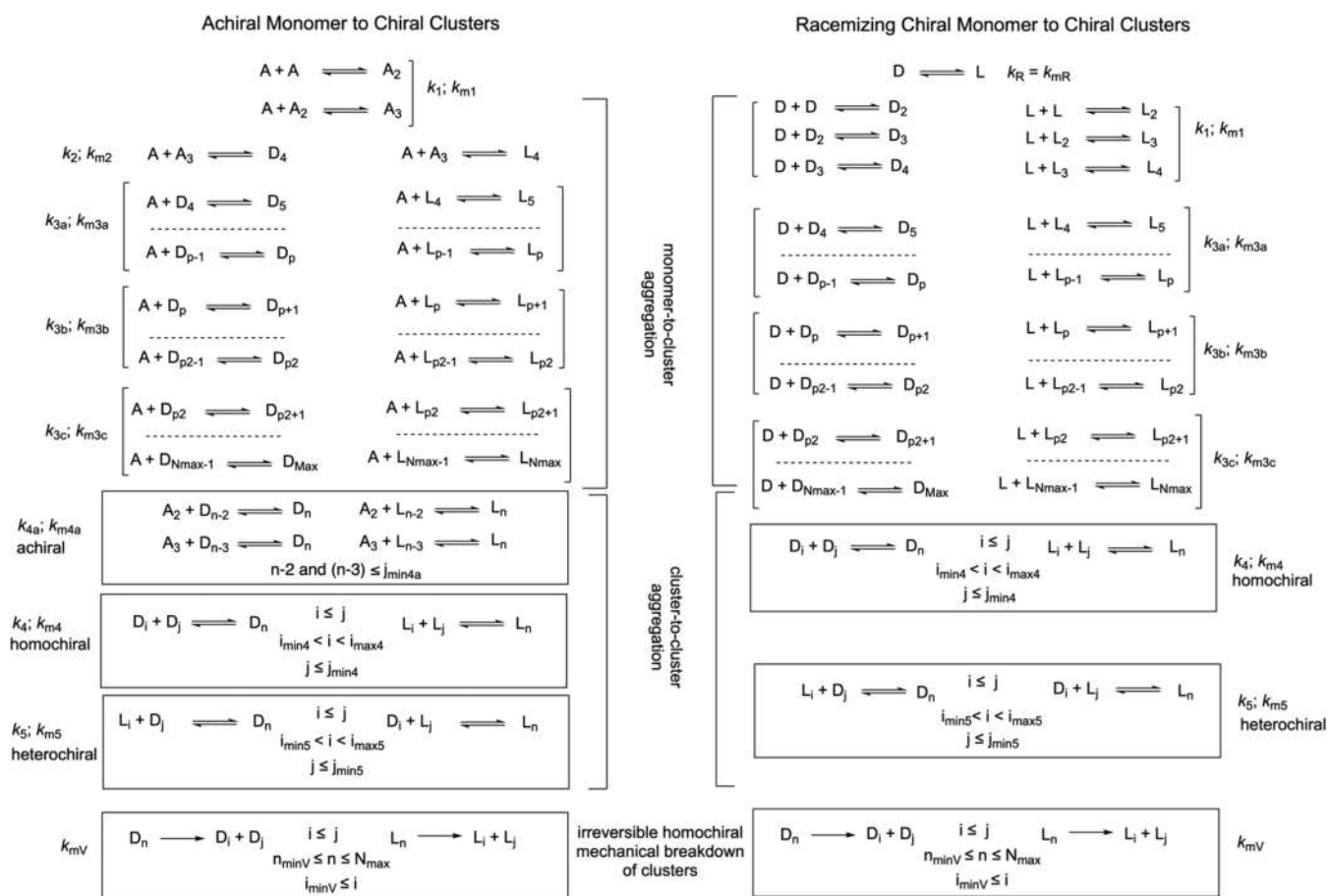
Figure 73. Kinetic scheme based on free energy diagram for classical theory of primary nucleation. Left hand side: for achiral monomer to chiral clusters. Right hand side: racemizing chiral monomers to chiral clusters. A racemizing monomer pair (L_1, L_1) in solution (rate, $k_R = k_{mR}$) and monomer-cluster aggregation yielding chiral aggregates of a maximum size (L_{Nmax}, D_{Nmax}). The network approximates the free energy curve in Figure 72 by four isodesmic regions (indicated by the reaction steps grouped within the vertical brackets): whose end points are (1) a precritical cluster size fixed to be 4 monomer units, (2) the critical cluster size denoted $p = i_{crit}$, (3) a postcritical cluster of $p_2 > p$ units, and (4) chiral clusters of maximum size N_{max} (2 → 4): rates k_1, k_{m1}, (4 → p): rates k_{3a}, k_{m3a}, (p → $p2$): rates k_{3b}, k_{m3b}, and (p_2 → N_{max}): rates k_{3c}, k_{m3c}. Note: the heterochiral cluster−cluster aggregation terms are *not* used in these simulations and are only included here for completeness in order to indicate how they can be implemented. Reproduced with permission from ref 178. Copyright 2013 Wiley-VCH.

transfer to the rest of clusters, the system cannot retain the initial *ee* and eventually racemizes: see Figure 75.

To contrast to Figure 74, which shows reversible agglomeration in the presence of grinding, we consider agglomeration without grinding. The system eventually racemizes, even when starting from a large initial *ee* of 33% and for the same rates used in the simulation (see Figure 74 and Figure 76). This underscores the importance of grinding, which on the basis of the approximation leading to net flows in PBEs has been claimed to be unnecessary for obtaining a final chiral state in a system with a homogeneous temperature distribution.[239] In the kinetic rate equation approach, agglomeration is a necessary process in order to achieve a final homochiral configuration.

We next turn to attrition. Most importantly, the simulations of kinetic rate equations demonstrate that (i) in the absence of agglomeration but even with irreversible grinding present the final outcome will be racemic (Figure 75); (ii) with agglomeration operative but no grinding the outcome will be racemic (Figure 76). Only for the case (iii) when *both* agglomeration and irreversible grinding are operative simultaneously can the system lead to a final chiral outcome and with large *ees* close to 100% for the largest chiral clusters (see Figure 74).

We mention some recent work devoted to the chirality of metal nanoclusters. A longstanding challenge has been to construct highly connected chiral 3D MOFs (see section 6.1.1) through spontaneous resolution. A remarkable example of a chiral (3,12)-connected **ttt**3D MOF was realized by spontaneous resolution upon crystallization in the absence of any chiral source.[482] Vibrational circular dichroism (VCD) (see section 8.2) has also been used to study the conformation of chiral thiolate-protected gold nanoclusters.[776] This method demonstrated that such a cluster can transfer its chirality to achiral thiolate ligands. Another recent study has confirmed that chalcogenide can enlarge the nuclearity of silver core−shell nanoclusters. The enlarged tetrahedral core leads to homochiral crystallization[777] affording a new strategy to synthesize chiral core−shell silver nanoclusters in a higher-order and controlled manner.

9.3. Deterministic vs Stochastic Models

Theoretical proposals for the emergence of homochirality in abiotic chemical evolution are based either on deterministic or on chance events, which may involve chemical reactions or physical rate processes.[778,779] Reaction rate equations are customarily employed to cast chemical reaction schemes in
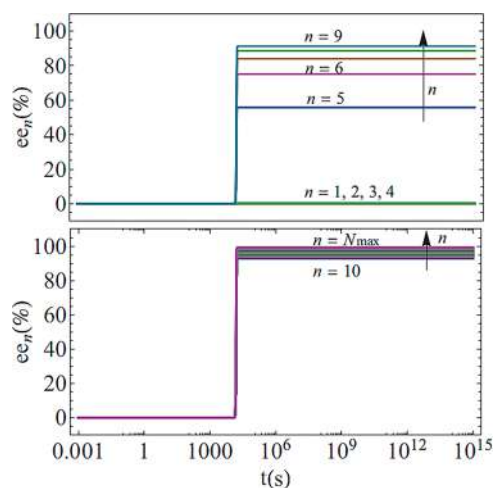
Figure 74. Full kinetic model[178] with reversible agglomeration and mechanical grinding. Initial conditions: tiny initial *ee*. The ee_n depends on the cluster and crystal size *n*. The top panel shows the ee_n for the monomer $n = 1$ and the smallest clusters of size $n = 2, 3, 4$ up to $n = 9$; the lower panel shows the ee_n for clusters ranging in sizes from $n = 10$ up to $n = Nmax = 70$. Reprinted with permission from ref 178. Copyright 2015 The American Physical Society.
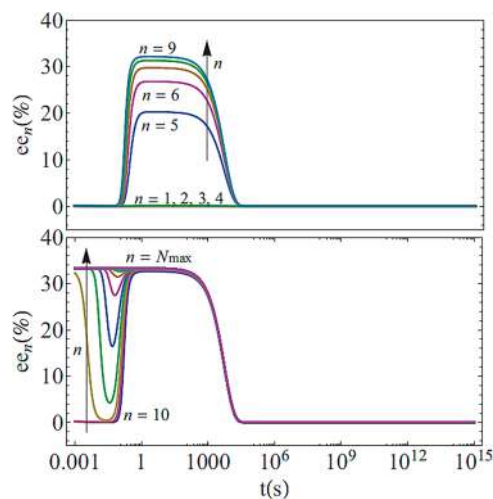
Figure 75. Full kinetic model[178] with mechanical grinding but without agglomeration. Initial conditions large initial *ee* of 33%. The resultant percent *ee* depends on the cluster and crystal size. The upper panel shows the percent *ee* for the monomer and small cluster sizes up to $n = 9$, and the lower panel from cluster sizes $n = 10$ to $n = Nmax = 70$. The latter curves collapse onto to a common curve (purple). Note the brief chiral excursion, after which the system racemizes. There is no final stable scalemic state in the absence of agglomeration, even with mechanical attrition operative. Reprinted with permission from ref 771. Copyright 2015 The American Physical Society.

terms of coupled ordinary differential equations (ODE) for the evolution of the concentrations of the species involved. In this deterministic approach, initial conditions must be taken to simulate the inherent statistical fluctuations about the ideal racemic composition.[24,109] In contrast, chemical reactions are inherently stochastic in nature: the reagents in solution (or attached on surfaces) must encounter each other via an inelastic collision before they can react, and the probability per unit time for the reaction to occur is related to the corresponding reaction rate constant. The discrete molecular nature of chemical reagents and reactions gives rise to the concept of intrinsic
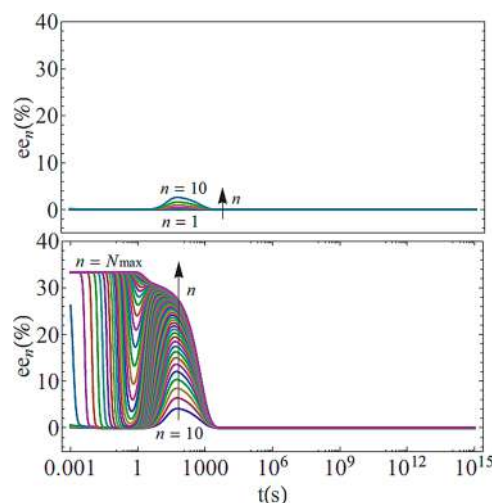
Figure 76. Full model without grinding but with agglomeration: Initial conditions large initial *ee* of 33%. Initial conditions large initial *ee*. The percent ee_n depends on the cluster and crystal size *n*. Note the brief chiral excursion, after which the system completely racemizes. There is no final stable scalemic state in the absence of the mechanical attrition mechanism, even when the agglomeration is operative. Reprinted with permission from ref 771. Copyright 2015 The American Physical Society.

reaction noise.[780] Although stochastic and deterministic kinetics must coincide in the thermodynamic limit (i.e., for large numbers of molecules and large volumes while keeping the species concentrations constant), stochastic methods can be used to explore the issue of whether noise affects the final outcome of the underlying reaction, for finite size systems and small populations of molecules.

Chemical reactions are inherently stochastic in nature: molecules are discrete entities that come in positive integer numbers and exhibit some degree of randomness in their dynamical behavior.[781] There are three major aspects that contribute to this randomness. First, the dynamical evolution does not evolve deterministically with respect to the species populations: reactions leading to change of species are due solely to the inelastic collisions, whereas the elastic collisions are nonreactive. Yet the latter types are in the majority. Second, quantum indeterminacy plays a role, especially in the unimolecular transformations such that we cannot know with certainty when a molecule will transform into a different isomeric form. Lastly, chemical systems are usually in contact with the external environment, coupling to which introduces random perturbations, thermal as well as other kinds, into the system.

9.3.1. Principles of Stochastic Modeling. We consider well-stirred systems for *r* chemical reactions involving *n* reacting species obeying mass-action kinetics:

$$\alpha_{1j}S_1 + ... + \alpha_{nj}S_n \rightarrow \beta_{1j}S_1 + ... + \beta_{nj}S_n, \quad j = 1, ..., r \quad (15)$$
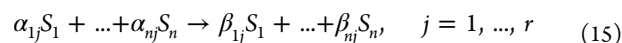
where the S_i, $1 \leq i \leq n$, are the chemical species and k_j the reaction rate constant for the *j*th reaction. Let $X_i(t)$ denote the number of molecules of species S_i at time *t*. We are interested in calculating the state vector $X(t) = (X_1(t), X_2(t), ..., X_n(t))$ given that the system was in the initial state $X(t_0) = x_0$ at time t_0. From eq 15 we obtain the entries of the $n \times r$ stoichiometric matrix $\boldsymbol{\nu}$:

$$\nu_{ij} = \beta_{ij} - \alpha_{ij} \quad (16)$$
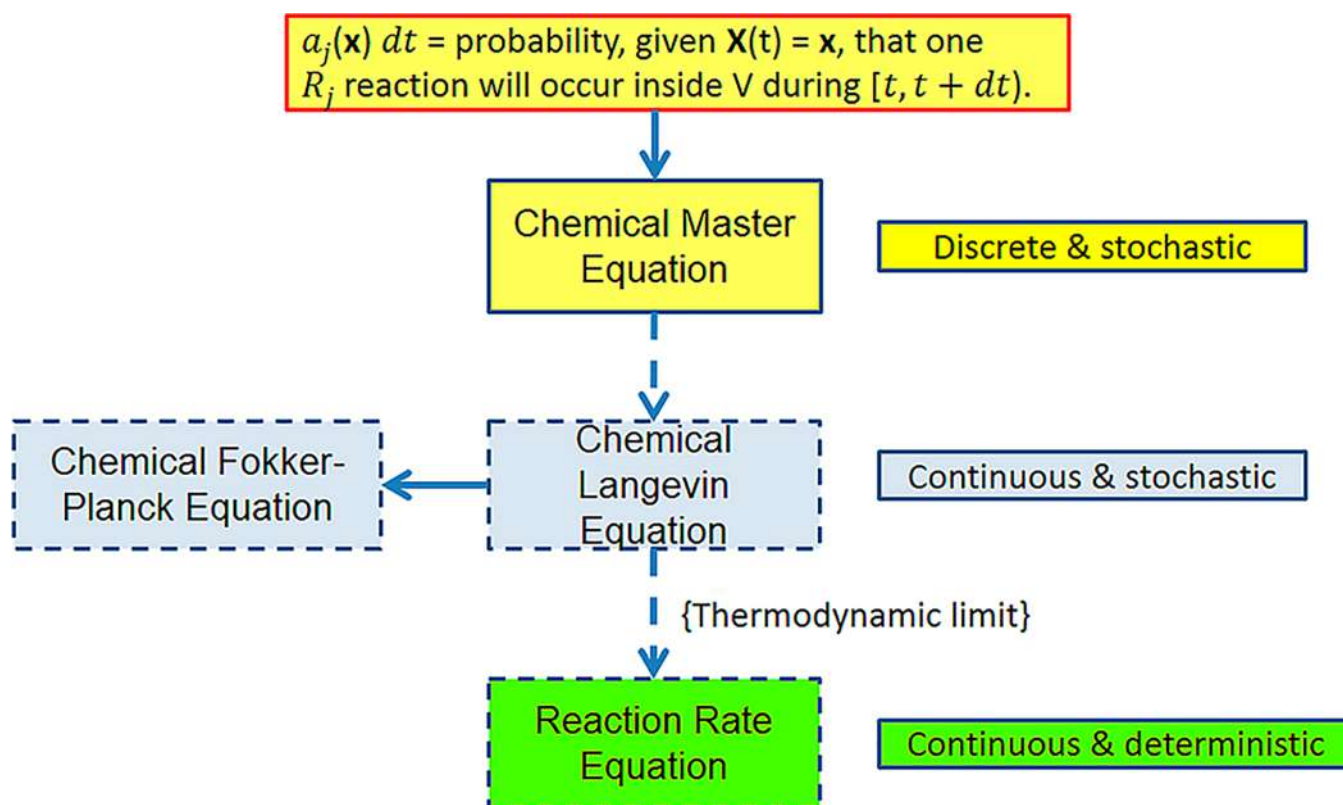
Figure 77. Logical structure of stochastic chemical kinetics and relationships among exact and approximate results and the thermodynamic limit which leads to deterministic reaction rate equations. The fundamental premise based on the propensity function is indicated at the top. Scheme modified and adapted from ref 781. Note the important distinction between the deterministic reaction rate equation and the population balance equation (PBE) approaches is outlined in Figure 66.

thus the state-change vector for the jth reaction channel is $\boldsymbol{\nu}_j = (\nu_{1j},...,\nu_{nj})$: if the system is in state $\boldsymbol{x}$ and one j-reaction occurs, the system jumps to the new state $\boldsymbol{x} + \boldsymbol{\nu}_j$. Then the fundamental premise of stochastic chemical kinetics is founded on the so-called propensity function $a_j(\boldsymbol{x})$,[782] whose product with dt gives the probability that one j-reaction will take place within the next time interval dt. Then an evolution equation for the probability

$$P(\boldsymbol{x}, t|\boldsymbol{x}_0, t_0) = Prob[\boldsymbol{X}(t) = \boldsymbol{x}, \quad \text{given } \boldsymbol{X}(t_0) = x_0] \tag{17}$$

can be derived from the fundamental premise and leads to the chemical master equation (CME):[783,784]

$$\frac{\partial P(\boldsymbol{x}, t|\boldsymbol{x}_0, t_0)}{\partial t} = \sum_{j=1}^{r} [a_j(\boldsymbol{x} - \boldsymbol{\nu}_j)P(\boldsymbol{x} - \boldsymbol{\nu}_j, t|\boldsymbol{x}_0, t_0) - a_j(\boldsymbol{x})P(\boldsymbol{x}, t|\boldsymbol{x}_0, t_0)] \tag{18}$$

While this completely determines the probability function $P(\boldsymbol{x}, t|\boldsymbol{x}_0, t_0)$, it leads to a set of coupled ODEs, one differential equation for every possible combination of reacting molecules and can be solved analytically only for a few simple cases.[785] An analytic study of stochastic enantioselective autocatalysis, starting from the CME,[127] is reviewed briefly below (see section 9.3.2).

In the absence of fluctuations, the chemical master equation implies the standard deterministic reaction rate equations. Multiplying eq 18 through by $\boldsymbol{x}$ and summing over all $\boldsymbol{x}$ leads to[781]

$$\frac{d\boldsymbol{X}(t)}{dt} = \sum_{j=1}^{r} \boldsymbol{\nu}_j a_j(\boldsymbol{X}(t)) \tag{19}$$

For systems of test tube size or larger, the deterministic reaction rate equation approach (eq 19) works extremely well. However, if the system is sufficiently small, and if the population of at least some of the reactant species is within a few orders of magnitude of unity, the discreteness and randomness may play important roles. Fluctuations can be important in systems with small molecular populations in small volumes, notably in compartmentalized cellular systems in biology.[786−790] Then approximations to the master equation may be required which retain some information about the underlying randomness, such as the chemical Langevin equation (CLE) or stochastic differential equation:[791]

$$\frac{d\boldsymbol{X}(t)}{dt} = \sum_{j=1}^{r} \boldsymbol{\nu}_j a_j(\boldsymbol{X}(t)) + \sum_{j=1}^{r} \boldsymbol{\nu}_j \sqrt{a_j(\boldsymbol{X}(t))} \, \Gamma_j(t) \tag{20}$$

where the $\Gamma_j(t)$ are Gaussian white noise processes obeying $\langle \Gamma_j(t) \Gamma_k(t') \rangle = \delta_{jk}(t - t')$. Then the state function $\boldsymbol{X}(t)$ is a random variable whose probability density function obeys the chemical Fokker−Planck equation (CFPE). The relation between the CLE and the CFPE is exact. For a derivation and discussion of these points see, refs 791 and 792.

9.3.2. Chiral Autocatalysis: Stochastic Models. Key issues of stochastic vs deterministic chemical evolution can be revealed through the analysis of a simple first-order enantioselective autocatalytic scheme (see section 2.2.2) subject to various approximations and assumptions, while also

illustrating the direct application of many of the equations comprising the above scheme in Figure 77.

Lente[127] used the continuous time discrete state chemical master equation to study a simple chiral autocatalytic model defined by the following three irreversible reactions (i.e., a Frank-like model but without mutual-inhibition):

$$A \rightarrow \frac{1}{2}(L + D), \quad A + L \rightarrow 2L, \quad A + D \rightarrow 2D \tag{21}$$
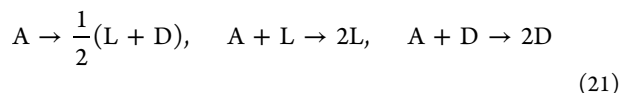
In this model, the two enantiomers L and D are produced either directly (with rate constant k_n) or autocatalytically (with rate constant k_a) and each enantiomer catalyzes its own production. Note that all these processes are irreversible. The exact analytic solution of the deterministic reaction rate equations implies a racemic outcome for strictly racemic initial conditions, whereas any small initial *ee* does not get amplified. Starting from the master equation, Lente derived a normalized stationary probability distribution function $P(x)$ for the mole fraction of enantiomers x valid in the limit of a large number of molecules:

$$P(x) = \frac{\Gamma\left(\frac{1}{\alpha}\right)}{\Gamma\left(\frac{1}{2\alpha}\right)\Gamma\left(\frac{1}{2\alpha}\right)}(x)^{1/2\alpha - 1}(1 - x)^{1/2\alpha - 1} \tag{22}$$

where Γ is the Gamma function[793] and $\alpha = \frac{k_a}{k_n N_A V}$, $N_A = 6.022 \times 10^{23}$ mol^{-1} is Avogadro's number and V is the system volume. The stationary normalized probability distribution for different values of x is shown in Figure 78. This distribution has a
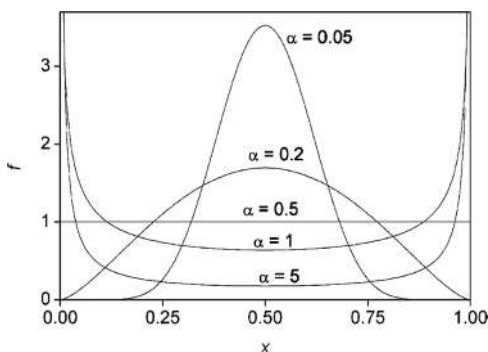
Figure 78. Stationary probability distribution function $f = P(x)$ eq 22 for the molar fraction x of enantiomers, for five different values of $\alpha = \frac{k_a}{k_n N_A V}$. Reprinted from ref 127. Copyright 2004 American Chemical Society.

maximum at $x = 0.5$ (the racemic state) for $\alpha < 0.5$ and a minimum at $x = 0.5$ for all $\alpha > 0.5$. A flat distribution results for $\alpha = 0.5$, indicating equal probability for every final state.

Thus, the trend is that large values of $\alpha > 0.5$ favor scalemic compositions, and to achieve this requires that, for fixed $N_A V$, the rate of the enantioselective autocatalysis be sufficiently greater than the rate of direct production: $k_a \gg k_n$. At the same time, the extensive factor $N_A V$ must be sufficiently small, that is, small system volumes V. Since the reverse reactions are completely ignored, Lente's scheme is seen to be under kinetic control. Once a bias away from the pure racemic is generated, the system has no way of returning to the racemic, and it becomes kinetically trapped in scalemic configurations. The equilibrium constants (the ratio of the forward to reverse rate constants) for the catalysis and the direct production steps in eq

21 are both formally divergent: this is because the inverse rates are both vanishing: $k_{-a} = k_{-n} = 0$, thus $\frac{k_a}{k_{-a}} = \frac{k_n}{k_{-n}} \rightarrow \infty$

Recently, a modeling study by Goldenfeld and co-workers[794] developed a simple modification of Lente's model aiming to show that the Frank model's inhibition criterion is unnecessary. They reported that in a nonequilibrium steady-state system, homochirality may emerge from the racemic state by a noise-induced mechanism.

The model of ref 794 depicts enantiomers D or L forming from substrate A, as in eq 23 for the reaction autocatalyzed by D (or L) and in eq 24 for the reaction for the uncatalyzed reactions. These authors modified Lente's[127] in that the uncatalyzed background reaction is allowed to proceed in both the forward and backward directions. Moreover, the computations in ref 794 are carried out in a closed system, meaning that the total number of molecules (comprising the sum of A, D, and L) remains constant over time.

$$A + D \rightarrow 2D, \quad A + L \rightarrow 2L \tag{23}$$

$$A \rightleftarrows D, \quad A \rightleftarrows L \tag{24}$$
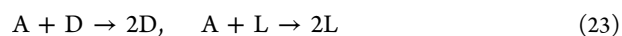
The enantioselective autocatalysis (eq 23) proceeds with forward rate constant k_a but has no finite inverse rate. Here, the direct production step (eq 24) is now allowed to be reversible, with forward rate k_n and reverse rate k_d. Values for the constants were chosen in ref 794 as $k_a = k_n = k_d = 1$ (with appropriate units, not given). Instead of the chemical master equation (CME), these authors derive the chemical Langevin equation (CLE) corresponding to the transformations eqs 23 and 24) and then use the well-known transformation to obtain the associated chemical Fokker−Planck equation. They solve this CFPE for the stationary probability distribution for the chiral order parameter $\omega = (d - l)/(d + l)$, see Figure 79:

$$P(\omega) = \frac{\Gamma\left(\alpha + \frac{1}{2}\right)}{\sqrt{\pi}\,\Gamma(\alpha)}(1 - \omega^2)^{\alpha - 1}, \quad \text{with } \alpha = \frac{V k_n}{k_a} \tag{25}$$

This distribution is of course qualitatively similar to that obtained by Lente: note that Goldenfeld's definition of α is essentially the inverse of Lente's parameter (Figure 79). The distribution will be strongly peaked at $|\theta| = 1$ if and only if $\alpha < 1$. Now consider the thermodynamic limit in which the total
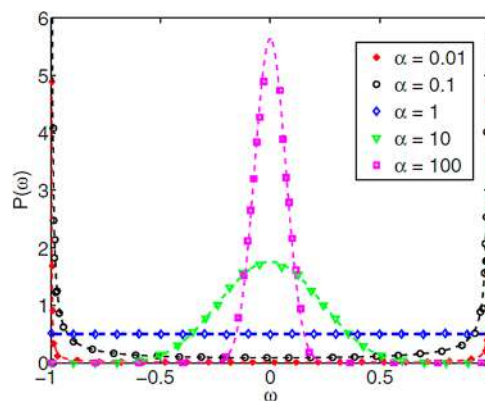
Figure 79. Stationary probability distribution function $P(\omega)$ eq 25 for the *ee* ω of enantiomers, for five different values of $\alpha = \frac{k_a}{k_n N_A V}$. Reprinted with permission from ref 794. Copyright 2015 The American Physical Society.

species population $N = A + L + D$ and the system volume V each approach infinity, while the concentration $N/V = \rho$ remains constant.[781] Then, regardless of what values are chosen for the individual rate constants $k_n$, k_a, the exponent $\alpha \gg 1$ will exceed unity, and the distribution function eq 25 will be strictly zero for $|\theta| = 1$ and strongly peaked about the racemic state $|\theta| = 0$. From this we conclude that the noise induced homochiral states implied by eq 25 for $\alpha < 1$ are kinetically-controlled (the autocatalysis is irreversible) finite-size effects.

Equation 24 is written as a reversible reaction, which critically sets the theoretical equilibrium position as the ratio of the forward and backward rate constants, k_n and k_d. The equilibrium constant, K_{eq}, is given by eq 26:

$$K_{eq} = \frac{k_n}{k_d} = \frac{[D]_{eq}}{[A]_{eq}} = \frac{[L]_{eq}}{[A]_{eq}} \tag{26}$$

The reactants and products in eq 24 using $k_n = k_d = 1$ exhibit equal stability, as shown by the Gibbs free energy, $\Delta G^0 = 0$:

$$-\frac{\Delta G^\circ}{RT} = \ln(K_{eq}) = \ln\left(\frac{k_n}{k_d}\right) = \ln\left(\frac{1}{1}\right) = 0 \tag{27}$$

A catalyst can only change the kinetics but not the thermodynamics of a reaction, thus a catalytic reaction possesses the same ΔG° as its uncatalyzed version. Thus, eqs 26 and 27 apply equally to the reactions in eqs 23 and 24. Once the values for the three rate constants shown in eqs 23 and 24 are set, the fourth, the missing rate constant describing the reverse of eq 23, is fixed. The value of this rate constant, denoted k_{-a} is dictated by eq 28:

$$k_{-a} = k_a \frac{k_d}{k_n} \tag{28}$$

Equation 28 shows that, given the values chosen for the other three rate constants, k_{-a} cannot be set equal to zero.

With this constraint in mind, Stich et al.[795] carried out an in depth study of the stochastic behavior of a fully reversible scheme:

$$A + D \rightleftharpoons 2D, \quad A + L \rightleftharpoons 2L \tag{29}$$

$$A \rightleftharpoons D, \quad A \rightleftharpoons L \tag{30}$$
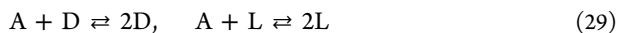
Here the enantioselective autocatalysis (eq 29) proceeds with forward rate constant k_a and is now furnished with an inverse rate constant k_{-a}. The direct production step (eq 30) is also allowed to be reversible, with forward rate k_n and reverse rate k_d. Stich et al.[795] derive the chemical Langevin equation (CLE) corresponding to the fully reversible transformations on eqs 29 and 30 in accordance with the thermodynamic constraint and obtain the associated chemical Fokker−Planck equation (see Figure 77). They solve this CFPE for the stationary probability distribution for the chiral order parameter $\omega = (d - l)/(d + l)$, see Figure 80:

The normalized stationary distribution obtained is given by

$$P_s(\theta) = \frac{2^{1+b}\Gamma\left(b + \frac{1}{2}\right)}{\sqrt{\pi}\,\Gamma(b)F\left(\frac{1}{2}, 1+b, \frac{1}{2}+b; \frac{1}{2}\right)} \frac{(1-\theta^2)^{b-1}}{(2-\theta^2)^{b+1}},$$

$$\text{with } b = \frac{N}{1 + \frac{k_{-a}}{2k_a}} \tag{31}$$
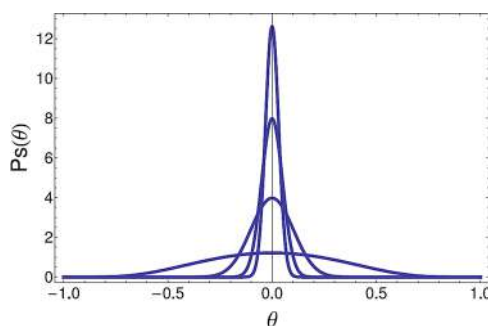
Figure 80. Stationary probability distribution for the chiral order parameter, eq 31. Different values of $b = 10, 100, 400, 1000$ correspond going from the broadest to the narrowest distribution. $P_s\ (|\theta| = 1) = 0$ is strictly zero for homochiral states. Reproduced with permission from ref 795. Copyright 2016 AIP Publishing.

where F is the hypergeometric function, see ref 793. This $P_s(\theta)$ is plotted for various values of b in Figure 80. The distribution $P_s(\theta)$ is always peaked around the racemic state $\theta = 0$ since the parameter b is greater than unity: $b = 0\ (N) \gg 1$. As the total number of molecules N increases, so does b and the distribution becomes ever more sharply peaked around $\theta = 0$. In particular, the probability for homochiral states $|\theta| = 1$ is strictly zero for all values of b.

The study by Goldenfeld and co-workers[794] was aimed at showing that the Frank model mutual inhibition step (see section 2.2.2) is unnecessary for achieving homochirality in the presence of intrinsic reaction noise. This specific feature was already demonstrated by Lente's earlier stochastic model and is seen there to be a consequence of the joint irreversibility of both the catalytic and direct production transformations. In Lente's case, both equilibrium constants are divergent, and so there is no overt mathematical nor thermodynamic inconsistency with this model. It is under kinetic control (see section 2.2.2). By contrast, the model proposed by Goldenfeld implies an equilibrium constant which is simultaneously finite and divergent and so is mathematically and thermodynamically inconsistent. Further pedagogical issues concerning autocatalysis and reversibility are discussed by Blackmond.[612,796] Spontaneous mirror symmetry breaking, which dispenses with Frank-like mutual inhibition, can be achieved in heterocatalytically coupled enantioselective replicators.[9]

10. CONCLUSION

This review describes the analogies between a wide variety of physicochemical transformations able to generate chiral molecular architectures from achiral compounds and the spontaneous formation of strong racemic biases (deracemizations) in such transformations, from an interdisciplinary point of view. The examples of spontaneous deracemization processes reported here can be understood within the framework of coupled reaction networks functioning in systems that exchange matter with their surroundings or which have an input of energy that acts selectively on some of the species.

In order to promote all avenues of investigation in solid−liquid systems, a survey of easily accessible achiral organic, inorganic, organometallic, and MOF compounds is provided from the databases. All of these give rise to conglomerate crystals that could be used to realize spontaneous deracemization experiments. Moreover, the reader is advised to be aware of the possible polymorphisms resulting in different possible packing

arrangements of a given substance, under different crystallization conditions.

The so-called Viedma ripening, which is actually a deracemization occurring in conglomerate crystallizations, has been extended to many chemical species and is now being used in applied chemistry. This deracemization may occur either under mechanical crystal attrition, ultrasound irradiation, or cycles of temperature variation. Grinding, fragmentation, or attrition of the larger crystals dispersed in the supersaturated solution cause their partial recycling owing to the higher solubility of the newborn smaller crystals. This is a selective energy input leading to a final nonequilibrium stationary state than may be nonracemic. The Viedma deracemization is limited to compounds that crystallize as a conglomerate (belonging to one of the 65 Sohncke space groups) and which either racemize in the solution phase or are achiral.

There are analogies between crystallization and mesophase formation. However, in distinction to conglomerate crystallization, the mesophase growth can occur in only one or two space directions toward noncovalent linear polymers or monolayers, respectively. The formation of a geometrically well-defined structure from noncovalent bond interactions between molecular building blocks can give rise to symmetry breaking from an achiral compound to a chiral aggregate. Energy flows are required as the driving force for the supramolecular self-assembly, where chiral dissipative structures can be formed. If one of these structures catalyzes its own formation and is coupled to other enantioselective aggregations or to a nonlinear process (e.g., the so-called sergeant-and-soldier, majority-rule or chiral memory principles), then spontaneous deracemization could occur. Due to their elastic and plastic properties, these mesophases are sensitive to chiral polarizations or chiral physical forces, such as electric fields through oriented phases, or hydrodynamic shear forces, which do not have detectable effects when acting on solid crystals or in mesophases or in solutions under the Brownian regime. Most of the numerous examples reported on the formation of racemic biases in liquid crystals could probably be explained within the framework of a Viedma-like deracemization mechanism.

The Soai reaction (alkylation of pyrimidine or pyridine aldehydes by diisopropylzinc) is a unique laboratory demonstration of absolute asymmetric synthesis, i.e., the spontaneous formation of an enantiomerically enriched product, even in the absence of any chiral inductors or physical forces. The Soai reaction is autocatalytic, where the product is a chiral carbinol that acts as a highly enantioselective catalyst for its own formation. Owing to the high exergonicity of the reaction, the *ees* can be easily detected, and the reaction products isolated, before any significant racemization takes place. Despite the fact that the Soai reaction can be rationalized within the framework of a theoretical Frank-like model, the real mechanisms involve numerous oligomeric species and most likely an homochiral tetrameric autocatalyst. Soai reaction models and experimental reports confirm the Soai reaction as a synonym for "absolute asymmetric synthesis", which is a longstanding ambition for many synthetic chemists[23] as well as a challenge for theoreticians[746] to decipher its complex dynamics. Furthermore, the chiral sign selection effects achieved in the Soai reaction by cryptochiral species definitively adscribe the Soai reaction to a bifurcation scenario of an energy dissipative system. The lack of new independent experimental demonstrations makes the Soai reaction a leading representative of such kinds of SMSB in solutions.

Modeling studies on spontaneous deracemizations, have been reported. A common aspect which must be included in all the modeling efforts are the fundamental constraints imposed by thermodynamics, which if ignored, can lead to artifacts and misinterpretations of the simulations. All these systems involve microreversible steps but are driven into a nonequilibrium state by selective chemical, photochemical, thermal, or mechanical energy. Spontaneous mirror symmetry breaking is the consequence of a bifurcation scenario where systems are highly sensitive to any chiral polarization. As demonstrated in this review, although stochastic and deterministic kinetics must coincide in the thermodynamic limit, stochastic methods can be used also to explore finite size systems and small populations of molecules.

In spite of the abundance of examples of spontaneous deracemization processes in crystals and mesophases, we believe that the future developments of the field will be in the search for new and more elaborate "absolute" asymmetric transformations and autocatalytic cycles occurring in fluid solutions. This search should be directed to the study of complex autocatalytic networks and aimed at the control of the interactions of the internal reaction networks with the surroundings. For that purpose, open flow reactors, photo- and mechano- stationary states, closed systems with temperature cycles or fixed temperature gradients, or inhomogenoeus matter distributions, etc., are advocated. For liquid systems, microfluidic reactors could allow one to analyze the behavior of extremely minute amounts of reacting material in nonequilibrium conditions. Finally, besides their fundamental and academic aspects, spontaneous deracemizations deserve to be very closely scrutinized because they also inspire research of practical importance, such as the deeper understanding of reaction mechanisms, and the application of this expertise for the elaboration of novel synthetic methods in pharmacology and materials sciences.

AUTHOR INFORMATION

Corresponding Author

Thomas Buhse — *Centro de Investigaciones Químicas–IICBA, Universidad Autónoma del Estado de Morelos, 62209 Cuernavaca, Morelos, Mexico;* orcid.org/0000-0001-5082-0873; Email: buhse@uaem.mx

Authors

José-Manuel Cruz — *Facultad de Ciencias en Física y Matemáticas, Universidad Autónoma de Chiapas, Tuxtla Gutiérrez, Chiapas 29050, Mexico*

María E. Noble-Terán — *Centro de Investigaciones Químicas–IICBA, Universidad Autónoma del Estado de Morelos, 62209 Cuernavaca, Morelos, Mexico*

David Hochberg — *Department of Molecular Evolution, Centro de Astrobiología (CSIC-INTA), 28850 Torrejón de Ardoz, Madrid, Spain;* orcid.org/0000-0002-0411-019X

Josep M. Ribó — *Institut de Ciències del Cosmos (IEEC-ICC), Universitat de Barcelona, 08028 Barcelona, Catalunya, Spain;* orcid.org/0000-0001-6258-1726

Joaquim Crusats — *Institut de Ciències del Cosmos (IEEC-ICC), Universitat de Barcelona, 08028 Barcelona, Catalunya, Spain;* orcid.org/0000-0003-3511-4676

Jean-Claude Micheau — *Laboratoire des IMRCP, UMR au CNRS No. 5623, Université Paul Sabatier, F-31062 Toulouse, France;* orcid.org/0000-0002-1193-4306

Complete contact information is available at:
https://pubs.acs.org/10.1021/acs.chemrev.0c00819

Notes

The authors declare no competing financial interest.

Biographies

Thomas Buhse studied chemistry at the University of Bremen and graduated as Diplom-Chemiker. After his Ph.D. (Dr. rer. nat.) in Bremen with Prof. Dr. Wolfram H. P. Thiemann in 1995, he joined the group of Dr. Jean-Claude Micheau in Toulouse as a postdoctoral fellow (poste rouge CNRS). In 1997 he spent 2 years at Wake Forest University in the group of Prof. Dilip K. Kondepudi, where he was appointed as a Visiting Assisting Professor in the Chemistry Department. In 2008, he received The American Institute of Chemists Student Award for Outstanding Post-Doctoral Student. He is currently a Full Research-Professor at Morelos State University and a Member of the Mexican National System of Researchers (Level III). His research interests are focused on complex systems, chirality research, and kinetic modeling. He is an active member of the French-Mexican International Associated Laboratory of Molecular Chemistry for Catalysis and Materials.

José-Manuel Cruz studied at the Faculty of Sciences at the Universidad Autónoma del Estado de Morelos, in México. He did his Ph.D. with Dr. Punit Parmananda and has held postdoctoral positions at the Universidade de São Paulo, Universidad Autónoma del Estado de Morelos, and the Indian Institute of Technology Bombay. His research interests are nonlinear dynamics, chemical kinetics, and chirality, mainly focusing on performing experiments, both from the physical and chemical points of view. Currently he is a faculty member at the Universidad Autónoma de Chiapas, in México.

María E. Noble-Terán is a Ph.D. student at Morelos State University. In 2017, she obtained her master's degree in Chemistry at the Center of Chemical Research on kinetic and structural aspects of the Soai Reaction supervised by Dr. Thomas Buhse and in collaboration with Dr. Jean-Claude Micheau, including an academic stay at the University Paul Sabatier in 2017. Her current research in the group of Dr. Thomas Buhse is centered on the emergence of homochirality via autocatalytic processes in crystallization informed by numerical simulations.

David Hochberg earned a B.A. in Physics in 1979 from the University of California, Berkeley, and a Ph.D in Physics from the University of Chicago (1984). After holding postdoctoral positions in physics in England, USA, and Spain, he joined the Centro de Astrobiología (CSIC-INTA; Madrid) as a founding member, where he is a permanent research scientist. His current research interests include symmetry breaking processes in the physics of complex systems and spontaneous mirror symmetry breaking in chemical systems.

Josep M. Ribó was born in Barcelona in 1940. His academic career has taken place entirely at the University of Barcelona, where he has been a Full Professor of Organic Chemistry since 1989 and has been Emeritus since 2011. His research interests in chronological order from 1970 have been natural products, oligopyrrole chemistry (reactivity and structure), polypyrroles as organic conducting polymers, self-assembly of amphiphilic porphyrins, supramolecular chirality, and spontaneous mirror symmetry breaking in chemical processes.

Jean-Claude Micheau graduated from the Toulouse School of Chemistry in 1967. He did his Ph.D. in Toulouse in organic photochemistry. As a postdoctoral fellow, he spent 1 year in Brussels with Ilya Prigogine. His major research interests are in systems chemistry, photochromism, nonlinear chemical dynamics, reaction mechanisms, and chirality. Dr. J. C. Micheau is the author of more than

160 articles and book chapters. He has been awarded with the CNRS Bronze Medal, and in 2014, he received the title of Doctor Honoris Causa in Rostov-on-Don (Russia). He is now an Emeritus Senior Scientist at the Université de Toulouse, Paul Sabatier. He is involved in several international collaborations.

Joaquim Crusats studied Chemistry at the University of Barcelona, graduating in 1989, where he also obtained his Ph.D. degree in Organic Chemistry in 1996 under the guidance of Prof. Josep M. Ribó. He subsequently spent 18 months conducting postdoctoral work in Japan as a joint EU/JSPS postdoctoral fellow at Kyoto University in the group of Prof. Hisanobu Ogoshi (1996−1997) working on porphyrin reactivity. He moved back to the University of Barcelona as an Assistant Professor in the Department of Physical Chemistry (2002−2004) where he conducted research in the field of self-organizing systems. After rejoining the Department of Organic Chemistry under the Spanish Ramón y Cajal Program (2004−2006), since 2007 he has been an Associate Professor in the same department.

REFERENCES

(1) Pavlov, V. A.; Shushenachev, Y. V.; Zlotin, S. G. Chiral and Racemic Fields Concept for Understanding of the Homochirality Origin, Asymmetric Catalysis, Chiral Superstructure Formation from Achiral Molecules, and B-Z DNA Conformational Transition. *Symmetry* **2019**, *11*, 649.

(2) Takahashi, J.; Kobayashi, K. Origin of Terrestrial Bioorganic Homochirality and Symmetry Breaking in the Universe. *Symmetry* **2019**, *11*, 919.

(3) Nguyen, L. A.; He, H.; Pham-Huy, C. Chiral Drugs: An Overview. *Int. J. Biomed. Sci.* **2006**, 85−100.

(4) Ruiz-Mirazo, K.; Briones, C.; De La Escosura, A. Prebiotic Systems Chemistry: New Perspectives for the Origins of Life. *Chem. Rev.* **2014**, *114*, 285−366.

(5) Lazcano, A.; Miller, S. L. The Origin and Early Evolution of Life: Prebiotic Chemistry, the Pre-RNA World, and Time. *Cell* **1996**, *85*, 793−798.

(6) Kondepudi, D. K.; Nelson, G. W. Chiral Symmetry Breaking in Non-Equilibrium Systems. *Phys. Rev. Lett.* **1983**, *50*, 1023−1026.

(7) Kondepudi, D. K.; Nelson, G. W. Weak Neutral Currents and the Origin of Biomolecular Chirality. *Nature* **1985**, *314*, 438−441.

(8) Ribó, J. M.; Hochberg, D. Spontaneous Mirror Symmetry Breaking: An Entropy Production Survey of the Racemate Instability and the Emergence of Stable Scalemic Stationary States. *Phys. Chem. Chem. Phys.* **2020**, *22*, 14013−14025.

(9) Ribó, J. M.; Crusats, J.; El-Hachemi, Z.; Moyano, A.; Hochberg, D. Spontaneous Mirror Symmetry Breaking in Heterocatalytically Coupled Enantioselective Replicators. *Chem. Sci.* **2017**, *8*, 763−769.

(10) Ribó, J. M.; Hochberg, D.; Crusats, J.; El-Hachemi, Z.; Moyano, A. Spontaneous Mirror Symmetry Breaking and Origin of Biological Homochirality. *J. R. Soc., Interface* **2017**, *14*, 20170699.

(11) Ávalos, M.; Babiano, R.; Cintas, P.; Jiménez, J. L.; Palacios, J. C. Homochirality and Chemical Evolution: New Vistas and Reflections on Recent Models. *Tetrahedron: Asymmetry* **2010**, *21*, 1030−1040.

(12) Walker, S. I. Origins of Life: A Problem for Physics, a Key Issues Review. *Rep. Prog. Phys.* **2017**, *80*, 092601.

(13) Bada, J. L.; Lazcano, A. The Origin of Life. In *Evolution: The First Four Billions Years*; Ruse, M., Travis, J., Eds.; Harvard University Press, 2009; pp 49−79.

(14) Luisi, P. L. *The Emergence of Life: From Chemical Origins to Synthetic Biology*; Cambridge University Press, 2016.

(15) Avetisov, V. V.; Goldanskii, V. I. Homochirality and Stereo-specific Activity: Evolutionary Aspects. *BioSystems* **1991**, *25*, 141−149.

(16) Avetisov, V.; Goldanskii, V. Mirror Symmetry Breaking at the Molecular Level. *Proc. Natl. Acad. Sci. U. S. A.* **1996**, *93*, 11435−11442.

(17) Joyce, G. F.; Szostak, J. W. Protocells and RNA Self-Replication. *Cold Spring Harbor Perspect. Biol.* **2018**, *10*, No. a034801.

(18) Wu, M.; Walker, S. I.; Higgs, P. G. Autocatalytic Replication and Homochirality in Biopolymers: Is Homochirality a Requirement of Life or a Result of It? *Astrobiology* **2012**, *12*, 818−829.

(19) Lee, D. H.; Severin, K.; Ghadiri, M. R. Autocatalytic Networks: The Transition from Molecular Self-Replication to Molecular Ecosystems. *Curr. Opin. Chem. Biol.* **1997**, *1*, 491−496.

(20) Pérez-García, L.; Amabilino, D. B. Spontaneous Resolution under Supramolecular Control. *Chem. Soc. Rev.* **2002**, *31*, 342−356.

(21) Gol'danskii, V. I.; Kuz'min, V. V. Spontaneous Breaking of Mirror Symmetry in Nature and the Origin of Life. *Sov. Phys. - Uspekhi* **1989**, *32*, 1−29.

(22) Amabilino, D. B.; Kellogg, R. M. Spontaneous Deracemization. *Isr. J. Chem.* **2011**, *51*, 1034−1040.

(23) Feringa, B. L.; van Delden, R. A. Absolute Asymmetric Synthesis. *Angew. Chem., Int. Ed.* **1999**, *38*, 3418−3438.

(24) Mislow, K. Absolute Asymmetric Synthesis: A Commentary. *Collect. Czech. Chem. Commun.* **2003**, *68*, 849−864.

(25) Avalos, M.; Babiano, R.; Cintas, P.; Jiménez, J. L.; Palacios, J. C.; Barron, L. D. Absolute Asymmetric Synthesis under Physical Fields: Facts and Fictions. *Chem. Rev.* **1998**, *98*, 2391−2404.

(26) Guijarro, A.; Yus, M. *The Origin of Chirality in the Molecules of Life: A Revision from Awareness to the Current Theories and Prespectives of This Unsolved Problem*; Royal Society Publishing: Cambridge, U.K., 2009.

(27) Barron, L. D. True and False Chirality and Absolute Asymmetric Synthesis. *J. Am. Chem. Soc.* **1986**, *108*, 5539−5542.

(28) Barron, L. D. Chirality and Life. *Space Sci. Rev.* **2008**, *135*, 187−201.

(29) Barron, L. D. True and False Chirality and Absolute Enantioselection. *Rend. Lincei* **2013**, *24*, 179−189.

(30) Barron, L. D. False Chirality, Absolute Enantioselection and CP Violation: Pierre Curie's Legacy. *Magnetochemistry* **2020**, *6*, 5.

(31) Barron, L. D. Chirality, Magnetism and Light. *Nature* **2000**, *405*, 895−896.

(32) Rikken, G. L. J. A.; Raupach, E. Enantioselective Magnetochiral Photochemistry. *Nature* **2000**, *405*, 932−935.

(33) Breitmaier, E. No Enantioselective Reactions in a Static Magnetic Field. *Angew. Chem. Int. Ed.* **1994**, *33*, 1207.

(34) Barron, L. D. Can a Magnetic Field Induce Absolute Asymmetric Synthesis? *Science* **1994**, *266*, 1491−1492.

(35) Stevenson, C. D.; Davis, J. P. Magnetars and Magnetic Separation of Chiral Radicals in Interstellar Space: Homochirality. *J. Phys. Chem. A* **2019**, *123*, 9587−9593.

(36) Micali, N.; Engelkamp, H.; van Rhee, P. G.; Christianen, P. C. M.; Scolaro, L. M.; Maan, J. C. Selection of Supramolecular Chirality by Application of Rotational and Magnetic Forces. *Nat. Chem.* **2012**, *4*, 201−207.

(37) Banerjee-Ghosh, K.; Ben Dor, O.; Tassinari, F.; Capua, E.; Yochelis, S.; Capua, A.; Yang, S.-H.; Parkin, S. S. P.; Sarkar, S.; Kronik, L.; Baczewski, L. T.; Naaman, R.; Paltiel, Y. Separation of Enantiomers by Their Enantiospecific Interaction with Achiral Magnetic Substrates. *Science* **2018**, *360*, 1331−1334.

(38) Tassinari, F.; Steidel, J.; Paltiel, S.; Fontanesi, C.; Lahav, M.; Paltiel, Y.; Naaman, R. Enantioseparation by Crystallization Using Magnetic Substrates. *Chem. Sci.* **2019**, *10*, 5246−5250.

(39) Wu, C. S.; Ambler, E.; Hayward, R. W.; Hoppes, D. D.; Hudson, R. P. Experimental Test of Parity Conservation in Beta Decay. *Phys. Rev.* **1957**, *105*, 1413−1415.

(40) Quack, M. How Important Is Parity Violation for Molecular and Biomolecular Chirality? *Angew. Chem., Int. Ed.* **2002**, *41*, 4618−4630.

(41) Hawbaker, N. A.; Blackmond, D. G. Energy Threshold for Chiral Symmetry Breaking in Molecular Self-Replication. *Nat. Chem.* **2019**, *11*, 957−962.

(42) Macdermott, A. J. Chiroptical Signatures of Life and Fundamental Physics. *Chirality* **2012**, *24*, 764−769.

(43) Mason, S. F.; Tranter, G. E. The Parity-Violating Energy Difference between Enantiomeric Molecules. *Chem. Phys. Lett.* **1983**, *94*, 34−37.

(44) Ulbricht, T. L. V.; Vester, F. Attempts to Induce Optical Activity with Polarized β-Radiation. *Tetrahedron* **1962**, *18*, 629−637.

(45) Bonner, W. A. The Origin and Amplification of Biomolecular Chirality. *Origins Life Evol. Biospheres* **1991**, *21*, 59−111.

(46) Bonner, W. A. Chirality and Life. *Origins Life Evol. Biospheres* **1995**, *25*, 175−190.

(47) Bonner, W. A. Parity Violation and the Evolution of Biomolecular Homochirality. *Chirality* **2000**, *12*, 114−126.

(48) Mahurin, S.; Mcginnis, M.; Bogard, J. S.; Hulett, L. D.; Pagni, R. M.; Compton, R. N. Effect of Beta Radiation on the Crystallization of Sodium Chlorate from Water: A New Type of Asymmetric Synthesis. *Chirality* **2001**, *13*, 636−640.

(49) Pagni, R. M.; Compton, R. N. Asymmetric Synthesis of Optically Active Sodium Chlorate and Bromate Crystals. *Cryst. Growth Des.* **2002**, *2*, 249−253.

(50) Bonner, W. A.; Dort, M. A. V. A. N.; Yearian, M. R. Asymmetric Degradation of DL-Leucine with Longitudinally Polarised Electrons. *Nature* **1975**, *258*, 419−421.

(51) Dreiling, J. M.; Gay, T. J. Chirally Sensitive Electron-Induced Molecular Breakup and the Vester-Ulbricht Hypothesis. *Phys. Rev. Lett.* **2014**, *113*, 118103.

(52) Rosenberg, R. A. Electrochirogenesis: The Possible Role of Low-Energy Spin-Polarized Electrons in Creating Homochirality. *Symmetry* **2019**, *11*, 528.

(53) Naaman, R.; Waldeck, D. H. Spintronics and Chirality: Spin Selectivity in Electron Transport Through Chiral Molecules. *Annu. Rev. Phys. Chem.* **2015**, *66*, 263−281.

(54) Aragonès, A. C.; Medina, E.; Ferrer-Huerta, M.; Gimeno, N.; Teixidó, M.; Palma, J. L.; Tao, N.; Ugalde, J. M.; Giralt, E.; Díez-Pérez, I.; Mujica, V. Measuring the Spin-Polarization Power of a Single Chiral Molecule. *Small* **2017**, *13*, 1602519.

(55) Naaman, R.; Paltiel, Y.; Waldeck, D. H. Chiral Molecules and the Spin Selectivity Effect. *J. Phys. Chem. Lett.* **2020**, *11*, 3660−3666.

(56) Darquié, B.; Stoeffler, C.; Shelkovnikov, A.; Daussy, C.; Amy-Klein, A.; Chardonnet, C.; Zrig, S.; Guy, L.; Crassous, J.; Soulard, P.; Asselin, P.; Huet, T. R.; Schwerdtfeger, P.; Bast, R.; Saue, T. Progress toward the First Observation of Parity Violation in Chiral Molecules by High-Resolution Laser Spectroscopy. *Chirality* **2010**, *22*, 870−884.

(57) Lahamer, A. S.; Mahurin, S. M.; Compton, R. N.; House, D.; Laerdahl, J. K.; Lein, M.; Schwerdtfeger, P. Search for a Parity-Violating Energy Difference between Enantiomers of a Chiral Iron Complex. *Phys. Rev. Lett.* **2000**, *85*, 4470−4473.

(58) Quack, M.; Stohner, J. Parity Violation in Chiral Molecules. *Chimia* **2005**, *59*, 530−538.

(59) Soai, K.; Shibata, T.; Morioka, H.; Choji, K. Asymmetric Autocatalysis and Amplification of Enantiomeric Excess of a Chiral Molecule. *Nature* **1995**, *378*, 767−768.

(60) Soai, K.; Kawasaki, T.; Matsumoto, A. Asymmetric Autocatalysis of Pyrimidyl Alkanol and Related Compounds. Self-Replication, Amplification of Chirality and Implication for the Origin of Biological Enantioenriched Chirality. *Tetrahedron* **2018**, *74*, 1973−1990.

(61) Meinert, C.; Filippi, J. J.; Nahon, L.; Hoffmann, S. V.; d'Hendecourt, L.; de Marcellus, P.; Bredehöft, J. H.; Thiemann, W. H. P.; Meierhenrich, U. J. Photochirogenesis: Photochemical Models on the Origin of Biomolecular Homochirality. *Symmetry* **2010**, *2*, 1055−1080.

(62) Evans, A. C.; Meinert, C.; Giri, C.; Goesmann, F.; Meierhenrich, U. J. Chirality, Photochemistry and the Detection of Amino Acids in

Interstellar Ice Analogues and Comets. *Chem. Soc. Rev.* **2012**, *41*, 5447–5458.

(63) Bailey, J.; Chrysostomou, A.; Hough, J. H.; Gledhill, T. M.; McCall, A.; Clark, S.; Ménard, F.; Tamura, M. Circular Polarization in Star-Formation Regions: Implications for Biomolecular Homochirality. *Science* **1998**, *281*, 672–674.

(64) Meierhenrich, U. J. *Amino Acids and the Asymmetry of Life*; Springer-Verlag: Berlin Heidelberg, Germany, 2008.

(65) Meierhenrich, U. J. *Comets and Their Origin*; Wiley-VCH: Weinheim, Germany, 2014.

(66) Rau, H. Asymmetric Photochemistry in Solution. *Chem. Rev.* **1983**, *83*, 535–547.

(67) Inoue, Y. Asymmetric Photochemical Reactions in Solution. *Chem. Rev.* **1992**, *92*, 741–770.

(68) Muñoz Caro, G. M.; Meierhenrich, U. J.; Schutte, W. A.; Barbier, B.; Arcones Segovia, A.; Rosenbauer, H.; Thiemann, W. H. P.; Brack, A.; Greenberg, J. M. Amino Acids from Ultraviolet Irradiation of Interstellar Ice Analogues. *Nature* **2002**, *416*, 403–406.

(69) de Marcellus, P.; Meinert, C.; Nuevo, M.; Filippi, J.-J.; Danger, G.; Deboffle, D.; Nahon, L.; Le Sergeant d'Hendecourt, L.; Meierhenrich, U. J. Non-Racemic Amino Acid Production by Ultraviolet Irradiation of Achiral Interstellar Ice Analogs with Circulary Polarized Light. *Astrophys. J., Lett.* **2011**, *727*, L27.

(70) Cronin, J. R.; Pizzarello, S. Enantiomeric Excesses in Meteoritic Amino Acids. *Science* **1997**, *275*, 951–955.

(71) Cronin, J.; Pizzarello, S. Amino Acid Enantiomer Excesses in Meteorites: Origin and Significance. *Adv. Space Res.* **1999**, *23*, 293–299.

(72) Sharma, A. Magnetic Circular Dichroism in Archean Atmosphere and Asymmetric Photolysis of Biomolecules: Enantiomeric Excess of Prebiotic Sugar. *J. Biol. Phys.* **2020**, *46*, 283–295.

(73) de Marcellus, P.; Meinert, C.; Myrgorodska, I.; Nahon, L.; Buhse, T.; D'Hendecourt, L. L. S.; Meierhenrich, U. J. Aldehydes and Sugars from Evolved Precometary Ice Analogs: Importance of Ices in Astrochemical and Prebiotic Evolution. *Proc. Natl. Acad. Sci. U. S. A.* **2015**, *112*, 965–970.

(74) Meinert, C.; Myrgorodska, I.; de Marcellus, P.; Buhse, T.; Nahon, L.; Hoffmann, S. V.; Dhendecourt, L. L. S.; Meierhenrich, U. J. Ribose and Related Sugars from Ultraviolet Irradiation of Interstellar Ice Analogs. *Science* **2016**, *352*, 208–212.

(75) Cruz-Castañeda, J.; Aguilar-Ovando, E.; Buhse, T.; Ramos-Bernal, S.; Meléndez-López, A.; Camargo-Raya, C.; Fuentes-Carreón, C.; Negrón-Mendoza, A. The Importance of Glyceraldehyde Radiolysis in Chemical Evolution. *J. Radioanal. Nucl. Chem.* **2017**, *311*, 1135–1141.

(76) Kawasaki, T.; Sato, M.; Ishiguro, S.; Saito, T.; Morishita, Y.; Sato, I.; Nishino, H.; Inoue, Y.; Soai, K. Enantioselective Synthesis of Near Enantiopure Compound by Asymmetric Autocatalysis Triggered by Asymmetric Photolysis with Circularly Polarized Light. *J. Am. Chem. Soc.* **2005**, *127*, 3274–3275.

(77) Noorduin, W. L.; Bode, A. A. C.; Van Der Meijden, M.; Meekes, H.; Van Etteger, A. F.; Van Enckevort, W. J. P.; Christianen, P. C. M.; Kaptein, B.; Kellogg, R. M.; Rasing, T.; Vlieg, E. Complete Chiral Symmetry Breaking of an Amino Acid Derivative Directed by Circularly Polarized Light. *Nat. Chem.* **2009**, *1*, 729–732.

(78) Viedma, C. Chiral Symmetry Breaking during Crystallization: Complete Chiral Purity Induced by Nonlinear Autocatalysis and Recycling. *Phys. Rev. Lett.* **2005**, *94*, 065504.

(79) Noorduin, W. L.; Vlieg, E.; Kellogg, R. M.; Kaptein, B. From Ostwald Ripening to Single Chirality. *Angew. Chem., Int. Ed.* **2009**, *48*, 9600–9606.

(80) Noorduin, W. L.; Izumi, T.; Millemaggi, A.; Leeman, M.; Meekes, H.; Van Enckevort, W. J. P.; Kellogg, R. M.; Kaptein, B.; Vlieg, E.; Blackmond, D. G. Emergence of a Single Solid Chiral State from a Nearly Racemic Amino Acid Derivative. *J. Am. Chem. Soc.* **2008**, *130*, 1158–1159.

(81) Yeom, J.; Yeom, B.; Chan, H.; Smith, K. W.; Dominguez-Medina, S.; Bahng, J. H.; Zhao, G.; Chang, W.-S.; Chang, S.-J.; Chuvilin, A.; Melnikau, D.; Rogach, A. L.; Zhang, P.; Link, S.; Král, P.; Kotov, N. A.

(82) Yang, G.; Zhang, S.; Hu, J.; Fujiki, M.; Zou, G. The Chirality Induction and Modulation of Polymers by Circularly Polarized Light. *Symmetry* **2019**, *11*, 474.

(83) Park, C.; Lee, J.; Kim, T.; Lim, J.; Park, J.; Kim, W. Y.; Kim, S. Y. Homochiral Supramolecular Thin Film from Self-Assembly of Achiral Triarylamine Molecules by Circularly Polarized Light. *Molecules* **2020**, *25*, 402.

(84) Hu, J.; Xie, Y.; Zhang, H.; He, C.; Zhang, Q.; Zou, G. Chiral Induction, Modulation and Locking in Porphyrin Based Supramolecular Assemblies with Circularly Polarized Light. *Chem. Commun.* **2019**, *55*, 4953–4956.

(85) Kim, J.-Y.; Yeom, J.; Zhao, G.; Calcaterra, H.; Munn, J.; Zhang, P.; Kotov, N. Assembly of Gold Nanoparticles into Chiral Superstructures Driven by Circularly Polarized Light. *J. Am. Chem. Soc.* **2019**, *141*, 11739–11744.

(86) Niinomi, H.; Sugiyama, T.; Tagawa, M.; Murayama, K.; Harada, S.; Ujihara, T. Enantioselective Amplification on Circularly Polarized Laser-Induced Chiral Nucleation from a NaClO3 Solution Containing Ag Nanoparticles. *CrystEngComm* **2016**, *18*, 7441–7448.

(87) Le Barbu, K.; Brenner, V.; Millié, P.; Lahmani, F.; Zehnacker-Rentien, A. An Experimental and Theoretical Study of Jet-Cooled Complexes of Chiral Molecules: The Role of Dispersive Forces in Chiral Discrimination. *J. Phys. Chem. A* **1998**, *102*, 128–137.

(88) Aquilanti, V.; Grossi, G.; Lombardi, A.; Maciel, G. S.; Palazzetti, F. The Origin of Chiral Discrimination: Supersonic Molecular Beam Experiments and Molecular Dynamics Simulations of Collisional Mechanisms. *Phys. Scr.* **2008**, *78*, 058119.

(89) Su, T.-M.; Palazzetti, F.; Lombardi, A.; Grossi, G.; Aquilanti, V. Molecular Alignment and Chirality in Gaseous Streams and Vortices. *Rend. Lincei* **2013**, *24*, 291–297.

(90) Ribó, J. M.; Crusats, J.; Sagués, F.; Claret, J.; Rubires, R. Chiral Sign Induction by Vortices during the Formation of Mesophases in Stirred Solutions. *Science* **2001**, *292*, 2063–2066.

(91) Crusats, J.; El-Hachemi, Z.; Ribó, J. M. Hydrodynamic Effects on Chiral Induction. *Chem. Soc. Rev.* **2010**, *39*, 569–577.

(92) Ribó, J. M.; El-Hachemi, Z.; Arteaga, O.; Canillas, A.; Crusats, J. Hydrodynamic Effects in Soft-Matter Self-Assembly: The Case of J-Aggregates of Amphiphilic Porphyrins. *Chem. Rec.* **2017**, *17*, 713–724.

(93) Escudero, C.; Crusats, J.; Díez-Pérez, I.; El-Hachemi, Z.; Ribó, J. M. Folding and Hydrodynamic Forces in J-Aggregates of 5-Phenyl-10,15,20-Tris- (4-Sulfophenyl)Porphyrin. *Angew. Chem., Int. Ed.* **2006**, *45*, 8032–8035.

(94) Arteaga, O.; Canillas, A.; Purrello, R.; Ribó, J. M. Evidence of Induced Chirality in Stirred Solutions of Supramolecular Nanofibers. *Opt. Lett.* **2009**, *34*, 2177–2179.

(95) Li, Y.; Liu, C.; Bai, X.; Tian, F.; Hu, G.; Sun, J. Enantiomorphic Microvortex-Enabled Supramolecular Sensing of Racemic Amino Acids by Using Achiral Building Blocks. *Angew. Chem., Int. Ed.* **2020**, *59*, 3486–3490.

(96) Sun, J.; Li, Y.; Yan, F.; Liu, C.; Sang, Y.; Tian, F.; Feng, Q.; Duan, P.; Zhang, L.; Shi, X.; Ding, B.; Liu, M. Control over the Emerging Chirality in Supramolecular Gels and Solutions by Chiral Microvortices in Milliseconds. *Nat. Commun.* **2018**, *9*, 2599.

(97) Chen, P.; Ma, X.; Hu, K.; Rong, Y.; Liu, M. Left or Right? The Direction of Compression-Generated Vortex-Like Flow Selects the Macroscopic Chirality of Interfacial Molecular Assemblies. *Chem. - Eur. J.* **2011**, *17*, 12108–12114.

(98) Hamba, F.; Niimura, K.; Kitagawa, Y.; Ishii, K. Helicity Transfer in Rotary Evaporator Flow. *Phys. Fluids* **2014**, *26*, 017101.

(99) Sorrenti, A.; El-Hachemi, Z.; Arteaga, O.; Canillas, A.; Crusats, J.; Ribó, J. M. Kinetic Control of the Supramolecular Chirality of Porphyrin J-Aggregates. *Chem. - Eur. J.* **2012**, *18*, 8820–8826.

(100) Sorrenti, A.; El-Hachemi, Z.; Crusats, J.; Ribó, J. M. Effects of Flow-Selectivity on Self-Assembly and Auto-Organization Processes: An Example. *Chem. Commun.* **2011**, *47*, 8551–8553.

(101) Sang, Y.; Yang, D.; Duan, P.; Liu, M. Towards Homochiral Supramolecular Entities from Achiral Molecules by Vortex Mixing-Accompanied Self-Assembly. *Chem. Sci.* **2019**, *10*, 2718−2724.

(102) Sang, Y.; Liu, M. Symmetry Breaking in Self-Assembled Nanoassemblies. *Symmetry* **2019**, *11*, 950.

(103) Sang, Y.; Yang, D.; Shen, Z.; Duan, P.; Liu, M. Mechanically Controlled and Consecutively Boosted Circularly Polarized Luminescence of Nanoassemblies from Achiral Molecules. *J. Phys. Chem. C* **2020**, *124*, 17274−17281.

(104) Kuhn, W.; Braun, E. Photochemische Erzeugung Optisch Aktiver Stoffe. *Naturwissenschaften* **1929**, *17*, 227−228.

(105) Eliel, E. L., Wilen, S. H. *Stereochemistry of Organic Compounds*; Wiley: New York, 1994.

(106) *Basic Terminology of Stereochemistry (IUPAC Recommendations 1996)*, Blackell, S., McNaught, A. D., Wilkinson, A., Eds.; Oxford, U.K., 1997.

(107) Jacques, J.; Collet, A.; Wilen, S. *Enantiomers, Racemates and Resolutions*; Wiley-Interscience: New York, 1981.

(108) Ben-Naim, A. *Information, Entropy, Life and the Universe*; World Scientific, 2015.

(109) Mills, W. H. Some Aspects of Stereochemistry. *J. Soc. Chem. Ind., London* **1932**, *51*, 750−759.

(110) van't Hoff, J. H. Die Phasenlehre. *Ber. Dtsch. Chem. Ges.* **1902**, *35*, 4252−4264.

(111) Crusats, J.; Veintemillas-Verdaguer, S.; Ribó, J. M. Homochirality as a Consequence of Thermodynamic Equilibrium? *Chem. - Eur. J.* **2006**, *12*, 7776−7781.

(112) El-Hachemi, Z.; Arteaga, O.; Canillas, A.; Crusats, J.; Sorrenti, A.; Veintemillas-Verdaguer, S.; Ribó, J. M. Achiral-to-Chiral Transition in Benzil Solidification: Analogies with Racemic Conglomerates Systems Showing Deracemization. *Chirality* **2013**, *25*, 393−399.

(113) *The Philosophy of Right and Left*; Cleve, J., Frederik, R. F., Eds.; Kluwer Academic Publishers: Dordrecht, The Netherlands, 1991.

(114) Kagan, H. B.; Gopalaiah, K. Early History of Asymmetric Synthesis: Who Are the Scientists Who Set up the Basic Principles and the First Experiments? *New J. Chem.* **2011**, *35*, 1933−1937.

(115) Wynberg, H.; Feringa, B. Enantiomeric Recognition and Interactions. *Tetrahedron* **1976**, *32*, 2831−2834.

(116) Ribó, J. M.; Blanco, C.; Crusats, J.; El-Hachemi, Z.; Hochberg, D.; Moyano, A. Absolute Asymmetric Synthesis in Enantioselective Autocatalytic Reaction Networks: Theoretical Games, Speculations on Chemical Evolution and Perhaps a Synthetic Option. *Chem. - Eur. J.* **2014**, *20*, 17250−17271.

(117) Noble-Terán, M. E.; Buhse, T.; Cruz, J.-M.; Coudret, C.; Micheau, J.-C. Nonlinear Effects in Asymmetric Synthesis: A Practical Tool for the Discrimination between Monomer and Dimer Catalysis. *ChemCatChem* **2016**, *8*, 1836−1845.

(118) Soai, K.; Kawasaki, T.; Matsumoto, A. Asymmetric Autocatalysis of Pyrimidyl Alkanol and Its Application to the Study on the Origin of Homochirality. *Acc. Chem. Res.* **2014**, *47*, 3643−3654.

(119) Glansdorf, P.; Prigogine, I. *Thermodynamic Theory of Structure, Stbility and Fluctuations*; Wiley-Interscience: London, 1971.

(120) Nicolis, G.; Prigogine, I. *Self-Organization in Non-Equlibrium Systems*; Wiley-Interscience: New York, 1977.

(121) Plasson, R.; Brandenburg, A.; Jullien, L.; Bersini, H. Autocatalyses. *J. Phys. Chem. A* **2011**, *115*, 8073−8085.

(122) Plasson, R.; Brandenburg, A. Homochirality and the Need for Energy. *Origins Life Evol. Biospheres* **2010**, *40*, 93−110.

(123) Girard, C.; Kagan, H. B. Nonlinear Effects in Asymmetric Synthesis and Stereoselective Reactions: Ten Years of Investigation. *Angew. Chem., Int. Ed.* **1998**, *37*, 2922−2959.

(124) Frank, F. C. On Spontaneous Asymmetric Synthesis. *Biochim. Biophys. Acta* **1953**, *11*, 459−463.

(125) de Min, M.; Levy, G.; Micheau, J.C. Review Chiral Resolutions, Asymmetric Synthesis and Amplification of Enantiomeric Excess. *J. Chim. Phys. Phys.-Chim. Biol.* **1988**, *85*, 603−619.

(126) Lente, G. Stochastic Kinetic Models of Chiral Autocatalysis: A General Tool for the Quantitative Interpretation of Total Asymmetric Synthesis. *J. Phys. Chem. A* **2005**, *109*, 11058−11063.

(127) Lente, G. Homogeneous Chiral Autocatalysis: A Simple, Purely Stochastic Kinetic Model. *J. Phys. Chem. A* **2004**, *108*, 9475−9478.

(128) Gellman, A. J.; Ernst, K. H. Chiral Autocatalysis and Mirror Symmetry Breaking. *Catal. Lett.* **2018**, *148*, 1610−1621.

(129) Havinga, E. Spontaneous Formation of Optically Active Substances. *Biochim. Biophys. Acta* **1954**, *13*, 171−174.

(130) Addadi, L.; van Mil, J.; Lahav, M. Useful Impurities for Optical Resolutions. 2. Generality and Mechanism of the Rule of Reversal. *J. Am. Chem. Soc.* **1981**, *103*, 1249−1251.

(131) Addadi, L.; Mil, J.; Gati, E.; Lahav, M. Amplification of Optical Activity by Crystallization in the Presence of Tailor-Made Additives. The "Inversion Rule. *Origins Life* **1981**, *11*, 107−118.

(132) Gentili, P. L.; Micheau, J.-C. Light and Chemical Oscillations: Review and Perspectives. *J. Photochem. Photobiol., C* **2020**, *43*, 100321.

(133) Kondepudi, D.; Kapcha, L. Entropy Production in Chiral Symmetry Breaking Transitions. *Chirality* **2008**, *20*, 524−528.

(134) Kondepudi, D.; Prigogine, I. *Modern Thermodynamics*; Wiley, 2014.

(135) Wehrt, H. Über Irreversibilität, Naturprozesse Und Zeitstruktur. In *Offene Systeme I*; von Weizsäcker, E. U., Ed.; Klett-Cotta: Stuttgart, Germany, 1974; pp 114−199.

(136) Pross, A.; Khodorkovsky, V. Extending the Concept of Kinetic Stability: Toward a Paradigm for Life. *J. Phys. Org. Chem.* **2004**, *17*, 312−316.

(137) Kawasaki, T.; Suzuki, K.; Shimizu, M.; Ishikawa, K.; Soai, K. Spontaneous Absolute Asymmetric Synthesis in the Presence of Achiral Silica Gel in Conjunction with Asymmetric Autocatal. *Chirality* **2006**, *18*, 479−482.

(138) Dykman, M. I.; Mori, E.; Ross, J.; Hunt, P. M. Large Fluctuations and Optimal Paths in Chemical Kinetics. *J. Chem. Phys.* **1994**, *100*, 5735−5750.

(139) Kondepudi, D. K.; Nelson, G. W. Chiral-Symmetry-Breaking States and Their Sensitivity in Nonequilibrium Chemical Systems. *Phys. A* **1984**, *125*, 465−496.

(140) Mislow, K.; Bickart, P. An Epistemological Note on Chirality. *Isr. J. Chem.* **1976**, *15*, 1−6.

(141) Sato, I.; Omiya, D.; Saito, T.; Soai, K. Highly Enantioselective Synthesis Induced by Chiral Primary Alcohols Due to Deuterium Substitution. *J. Am. Chem. Soc.* **2000**, *122*, 11739−11740.

(142) Kawasaki, T.; Okano, Y.; Suzuki, E.; Takano, S.; Oji, S.; Soai, K. Asymmetric Autocatalysis: Triggered by Chiral Isotopomer Arising from Oxygen Isotope Substitution. *Angew. Chem., Int. Ed.* **2011**, *50*, 8131−8133.

(143) Kawasaki, T.; Tanaka, H.; Tsutsumi, T.; Kasahara, T.; Sato, I.; Soai, K. Chiral Discrimination of Cryptochiral Saturated Quaternary and Tertiary Hydrocarbons by Asymmetric Autocatalysis. *J. Am. Chem. Soc.* **2006**, *128*, 6032−6033.

(144) Kawasaki, T.; Matsumura, Y.; Tsutsumi, T.; Suzuki, K.; Ito, M.; Soai, K. Asymmetric Autocatalysis Triggered by Carbon Isotope (12C/13C) Chirality. *Science* **2009**, *324*, 492−495.

(145) Vestergren, M.; Johansson, A.; Lennartson, A.; Håkansson, M. Non-Stochastic Homochiral Helix Crystallization: Cryptochirality in Control? *Mendeleev Commun.* **2004**, *14*, 258−260.

(146) Viedma, C. Selective Chiral Symmetry Breaking during Crystallization: Parity Violation or Cryptochiral Environment in Control? *Cryst. Growth Des.* **2007**, *7*, 553−556.

(147) Shan Monica Cheung, P.; Gagnon, J.; Surprenant, J.; Tao, Y.; Xu, H.; Cuccia, L. A. Complete Asymmetric Amplification of Ethylenediammonium Sulfate Using an Abrasion/Grinding Technique. *Chem. Commun.* **2008**, 987−989.

(148) Azeroual, S.; Surprenant, J.; Lazzara, T. D.; Kocun, M.; Tao, Y.; Cuccia, L. A.; Lehn, J. M. Mirror Symmetry Breaking and Chiral Amplification in Foldamer-Based Supramolecular Helical Aggregates. *Chem. Commun.* **2012**, *48*, 2292−2294.

(149) Armstrong, D. W.; Kullman, J. P.; Chen, X.; Rowe, M. Composition and Chirality of Amino Acids in Aerosol/Dust from Laboratory and Residential Enclosures. *Chirality* **2001**, *13*, 153−158.

(150) El-Hachemi, Z.; Escudero, C.; Arteaga, O.; Canillas, A.; Crusats, J.; Mancini, G.; Purrello, R.; Sorrenti, A.; D'Urso, A.; Ribó, J. M. Chiral

Sign Selection on the J-Aggregates of Diprotonated Tetrakis-(4-Sulfonatophenyl)Porphyrin by Traces of Unidentified Chiral Contaminants Present in the Ultra-Pure Water Used as Solvent. *Chirality* **2009**, *21*, 408−412.

(151) Kovács, K. L. Stereoselective Crystallization Induced by Traces of Dissolved Optically Active Impurities. *J. Mol. Evol.* **1977**, *10*, 161−166.

(152) Lahav, M.; Weissbuch, I.; Shavit, E.; Reiner, C.; Nicholson, G. J.; Schurig, V. Parity Violating Energetic Difference and Enantiomorphous Crystals-Caveats; Reinvestigation of Tyrosine Crystallization. *Origins Life Evol. Biospheres* **2006**, *36*, 151−170.

(153) Osuna-Esteban, S.; Zorzano, M.-P.; Menor-Salván, C.; Ruiz-Bermejo, M.; Veintemillas-Verdaguer, S. Asymmetric Chiral Growth of Micron-Size NaClO3 Crystals in Water Aerosols. *Phys. Rev. Lett.* **2008**, *100*, 146102.

(154) Steendam, R. R. E.; Harmsen, B.; Meekes, H.; Van Enckevort, W. J. P.; Kaptein, B.; Kellogg, R. M.; Raap, J.; Rutjes, F. P. J. T.; Vlieg, E. Controlling the Effect of Chiral Impurities on Viedma Ripening. *Cryst. Growth Des.* **2013**, *13*, 4776−4780.

(155) Siegel, J. S. Homochiral Imperative of Molecular Evolution. *Chirality* **1998**, *10*, 24−27.

(156) Murray, J. I.; Sanders, J. N.; Richardson, P. F.; Houk, K. N.; Blackmond, D. G. Isotopically Directed Symmetry Breaking and Enantioenrichment in Attrition-Enhanced Deracemization. *J. Am. Chem. Soc.* **2020**, *142*, 3873−3879.

(157) Steendam, R. R. E.; Dickhout, J.; van Enckevort, W. J. P.; Meekes, H.; Raap, J.; Rutjes, F. P. J. T.; Vlieg, E. Linear Deracemization Kinetics during Viedma Ripening: Autocatalysis Overruled by Chiral Additives. *Cryst. Growth Des.* **2015**, *15*, 1975−1982.

(158) Szurgot, M.; Szurgot, J. Chiral Symmetry Breaking in Sodium Chlorate Crystallization from Unstirred Solution. *Cryst. Res. Technol.* **1995**, *30*, 949−956.

(159) Szurgot, M. Chiral Symmetry Breaking in Unstirred Crystallization. *Cryst. Res. Technol.* **2012**, *47*, 109−114.

(160) Wyrouboff, M. G. Recherches Sur Les Silicotungstates. *Bull. Soc. Franc. Miner.* **1896**, 219−354.

(161) Soret, C. Causes Qui Donnent Lieu a La Production Des Cristaux Gauches et Droites. *Arch. d. Sc. Phys. Nat. Genève* **1899**, *7*, 80−82.

(162) Thiemann, W. Disproportionation of Enantiomers by Precipitation. *J. Mol. Evol.* **1974**, *4*, 85−97.

(163) McLaughlin, D. T.; Nguyen, T. P. T.; Mengnjo, L.; Bian, C.; Leung, Y. H.; Goodfellow, E.; Ramrup, P.; Woo, S.; Cuccia, L. A. Viedma Ripening of Conglomerate Crystals of Achiral Molecules Monitored Using Solid-State Circular Dichroism. *Cryst. Growth Des.* **2014**, *14*, 1067−1076.

(164) Kawasaki, T.; Takamatsu, N.; Aiba, S.; Tokunaga, Y. Spontaneous Formation and Amplification of an Enantioenriched α-Amino Nitrile: A Chiral Precursor for Strecker Amino Acid Synthesis. *Chem. Commun.* **2015**, *51*, 14377−14380.

(165) Kondepudi, D. K.; Kaufman, R. J.; Singh, N. Chiral Symmetry Breaking in Sodium Chlorate Crystallizaton. *Science* **1990**, *250*, 975−976.

(166) Kondepudi, D. K.; Bullock, K. L.; Digits, J. A.; Yarborough, P. D. Stirring Rate as a Critical Parameter in Chiral Symmetry Breaking Crystallization. *J. Am. Chem. Soc.* **1995**, *117*, 401−404.

(167) Kondepudi, D. K.; Laudadio, J.; Asakura, K. Chiral Symmetry Breaking in Stirred Crystallization of 1,1'-Binaphthyl Melt. *J. Am. Chem. Soc.* **1999**, *121*, 1448−1451.

(168) Plasson, R.; Kondepudi, D. K.; Bersini, H.; Commeyras, A.; Asakura, K. Emergence of Homochirality in Far-from-Equilibrium Systems: Mechanisms and Role in Prebiotic Chemistry. *Chirality* **2007**, *19*, 589−600.

(169) McBride, J. M.; Carter, R. L. Spontaneous Resolution by Stirred Crystallization. *Angew. Chem., Int. Ed. Engl.* **1991**, *30*, 293−295.

(170) Cartwright, J. H. E.; García-Ruiz, J. M.; Piro, O.; Sainz-Díaz, C. I.; Tuval, I. Chiral Symmetry Breaking during Crystallization: An Advection-Mediated Nonlinear Autocatalytic Process. *Phys. Rev. Lett.* **2004**, *93*, 035502.

(171) Buhse, T.; Durand, D.; Kondepudi, D.; Laudadio, J.; Spilker, S. Chiral Symmetry Breaking in Crystallization: The Role of Convection. *Phys. Rev. Lett.* **2000**, *84*, 4405−4408.

(172) Skrdla, P. J. Kinetics and Thermodynamics of Efficient Chiral Symmetry Breaking in Nearly Racemic Mixtures of Conglomerate Crystals. *Cryst. Growth Des.* **2011**, *11*, 1957−1965.

(173) Blackmond, D. G. "Chiral Amnesia" as a Driving Force for Solid-Phase Homochirality. *Chem. - Eur. J.* **2007**, *13*, 3290−3295.

(174) Perez, M. Gibbs-Thomson Effects in Phase Transformations. *Scr. Mater.* **2005**, *52*, 709−712.

(175) Cartwright, J. H. E.; Piro, O.; Tuval, I. Ostwald Ripening, Chiral Crystallization, and the Common-Ancestor Effect. *Phys. Rev. Lett.* **2007**, *98*, 165501.

(176) Xiouras, C.; Fytopoulos, A. A.; Ter Horst, J. H.; Boudouvis, A. G.; Van Gerven, T.; Stefanidis, G. D. Particle Breakage Kinetics and Mechanisms in Attrition-Enhanced Deracemization. *Cryst. Growth Des.* **2018**, *18*, 3051−3061.

(177) Viedma, C. Solvay Workshop, Chiral Symmetry Breaking at Molecular Level (with Author Authorization).

(178) Blanco, C.; Crusats, J.; El-Hachemi, Z.; Moyano, A.; Veintemillas-Verdaguer, S.; Hochberg, D.; Ribó, J. M. The Viedma Deracemization of Racemic Conglomerate Mixtures as a Paradigm of Spontaneous Mirror Symmetry Breaking in Aggregation and Polymerization. *ChemPhysChem* **2013**, *14*, 3982−3993.

(179) Niinomi, H.; Yamazaki, T.; Harada, S.; Ujihara, T.; Miura, H.; Kimura, Y.; Kuribayashi, T.; Uwaha, M.; Tsukamoto, K. Achiral Metastable Crystals of Sodium Chlorate Forming Prior to Chiral Crystals in Solution Growth. *Cryst. Growth Des.* **2013**, *13*, 5188−5192.

(180) Liu, G.; Liu, J.; Sun, H.; Zheng, X.; Liu, Y.; Li, X.; Qi, H.; Bai, X.; Jackson, K. A.; Tao, X. In Situ Imaging of On-Surface, Solvent-Free Molecular Single-Crystal Growth. *J. Am. Chem. Soc.* **2015**, *137*, 4972−4975.

(181) He, K.; Nie, A.; Yuan, Y.; Ghodsi, S. M.; Song, B.; Firlar, E.; Lu, J.; Lu, Y.; Shokuhfar, T.; Megaridis, C. M.; Shahbazian-Yassar, R. In Situ Transmission Electron Microscopy Explores a New Nanoscale Pathway for Direct Gypsum Formation in Aqueous Solution. *ACS Appl. Nano Mater.* **2018**, *1*, 5430−5440.

(182) El-Hachemi, Z.; Crusats, J.; Ribo, J. M.; Veintemillas-Verdaguer, S. Spontaneous Transition toward Chirality in the NaClO3 Crystallization in Boiling Solutions. *Cryst. Growth Des.* **2009**, *9*, 4802−4806.

(183) El-Hachemi, Z.; Crusats, J.; Ribó, J. M.; McBride, J. M.; Veintemillas-Verdaguer, S. Metastability in Supersaturated Solution and Transition towards Chirality in the Crystallization of NaClO3. *Angew. Chem., Int. Ed.* **2011**, *50*, 2359−2363.

(184) Sögütoglu, L.-C.; Steendam, R. R. E.; Meekes, H.; Vlieg, E.; Rutjes, F. P. J. T. Viedma Ripening: A Reliable Crystallisation Method to Reach Single Chirality. *Chem. Soc. Rev.* **2015**, *44*, 6723−6732.

(185) Steendam, R. R. E.; Ter Horst, J. H. Scaling Up Temperature Cycling-Induced Deracemization by Suppressing Nonstereoselective Processes. *Cryst. Growth Des.* **2018**, *18*, 3008−3015.

(186) Nguyen, T. P. T.; Cheung, P. S. M.; Werber, L.; Gagnon, J.; Sivakumar, R.; Lennox, C.; Sossin, A.; Mastai, Y.; Cuccia, L. A. Directing the Viedma Ripening of Ethylenediammonium Sulfate Using "Tailor-Made" Chiral Additives. *Chem. Commun.* **2016**, *52*, 12626−12629.

(187) Björemark, P. M.; Olsson, S.; Kokoli, T.; Håkansson, M. Absolute Asymmetric Synthesis of a Tetrahedral Silver Complex. *Chem. - Eur. J.* **2015**, *21*, 8750−8753.

(188) Björemark, P. M.; Jönsson, J.; Håkansson, M. Absolute Asymmetric Synthesis: Viedma Ripening of [Co(Bpy)3]2+ and Solvent-Free Oxidation to [Co(Bpy)3]3+. *Chem. - Eur. J.* **2015**, *21*, 10630−10633.

(189) Wu, S.-T.; Zhang, Y.-S.; Zhang, B.; Hu, X.-L.; Huang, X.-H.; Huang, C.-C.; Zhuang, N.-F. Viedma Ripening of Chiral Coordination Polymers Based on Achiral Molecules. *Cryst. Growth Des.* **2019**, *19*, 2537−2541.

(190) Noorduin, W. L. *Single Chirality through Crystal Grinding.* Dissertation, Radbound Universiteit, Nijmegen, The Netherlands, 2010.

(191) Van Der Meijden, M. W.; Leeman, M.; Gelens, E.; Noorduin, W. L.; Meekes, H.; Van Enckevort, W. J. P.; Kaptein, B.; Vlieg, E.; Kellogg, R. M. Attrition-Enhanced Deracemization in the Synthesis of Clopidogrel - A Practical Application of a New Discovery. *Org. Process Res. Dev.* **2009**, *13*, 1195−1198.

(192) Steendam, R. R. E.; Brouwer, M. C. T.; Huijs, E. M. E.; Kulka, M. W.; Meekes, H.; van Enckevort, W. J. P.; Raap, J.; Rutjes, F. P. J. T.; Vlieg, E. Enantiopure Isoindolinones through Viedma Ripening. *Chem. - Eur. J.* **2014**, *20*, 13527−13530.

(193) Engwerda, A. H. J.; Maassen, R.; Tinnemans, P.; Meekes, H.; Rutjes, F. P. J. T.; Vlieg, E. Attrition-Enhanced Deracemization of the Antimalaria Drug Mefloquine. *Angew. Chem., Int. Ed.* **2019**, *58*, 1670−1673.

(194) Noorduin, W. L.; Kaptein, B.; Meekes, H.; Van Enckevort, W. J. P.; Kellogg, R. M.; Vlieg, E. Fast Attrition-Enhanced Deracemization of Naproxen by a Gradual in Situ Feed. *Angew. Chem., Int. Ed.* **2009**, *48*, 4581−4583.

(195) Baglai, I.; Leeman, M.; Kellogg, R. M.; Noorduin, W. L. A Viedma Ripening Route to an Enantiopure Building Block for Levetiracetam and Brivaracetam. *Org. Biomol. Chem.* **2019**, *17*, 35−38.

(196) Belletti, G.; Tortora, C.; Mellema, I. D.; Tinnemans, P.; Meekes, H.; Rutjes, F. P. J. T.; Tsogoeva, S. B.; Vlieg, E. Photoracemization-Based Viedma Ripening of a BINOL Derivative. *Chem. - Eur. J.* **2020**, *26*, 839−844.

(197) Engwerda, A. H. J.; Meekes, H.; Kaptein, B.; Rutjes, F. P. J. T.; Vlieg, E. Speeding up Viedma Ripening. *Chem. Commun. (Cambridge, U. K.)* **2016**, *52*, 12048−12051.

(198) Noorduin, W. L.; van der Asdonk, P.; Bode, A. A. C.; Meekes, H.; van Enckevort, W. J. P.; Vlieg, E.; Kaptein, B.; van der Meijden, M. W.; Kellogg, R. M.; Deroover, G. Scaling Up Attrition-Enhanced Deracemization by Use of an Industrial Bead Mill in a Route to Clopidogrel (Plavix). *Org. Process Res. Dev.* **2010**, *14*, 908−911.

(199) Spix, L.; Alfring, A.; Meekes, H.; van Enckevort, W. J. P.; Vlieg, E. Formation of a Salt Enables Complete Deracemization of a Racemic Compound through Viedma Ripening. *Cryst. Growth Des.* **2014**, *14*, 1744−1748.

(200) Yoshioka, R.; Sakai, K.; Hirayama, N.; Tamura, R. Racemization, Optical Resolution and Crystallization-Induced Asymmetric Transformation of Amino Acids and Pharmaceutical Intermediates. *Top. Curr. Chem.* **2007**, *269*, 83−132.

(201) Xiouras, C.; Ter Horst, J. H.; Van Gerven, T.; Stefanidis, G. D. Coupling Viedma Ripening with Racemic Crystal Transformations: Mechanism of Deracemization. *Cryst. Growth Des.* **2017**, *17*, 4965−4976.

(202) Taylor, R.; Wood, P. A. A Million Crystal Structures: The Whole Is Greater than the Sum of Its Parts. *Chem. Rev.* **2019**, *119*, 9427−9477.

(203) Oketani, R.; Marin, F.; Tinnemans, P.; Hoquante, M.; Laurent, A.; Brandel, C.; Cardinael, P.; Meekes, H.; Vlieg, E.; Geerts, Y.; Coquerel, G. Deracemization in a Complex Quaternary System with a Second-Order Asymmetric Transformation by Using Phase Diagram Studies. *Chem. - Eur. J.* **2019**, *25*, 13890−13898.

(204) Spix, L.; Meekes, H.; Blaauw, R. H.; van Enckevort, W. J. P.; Vlieg, E. Complete Deracemization of Proteinogenic Glutamic Acid Using Viedma Ripening on a Metastable Conglomerate. *Cryst. Growth Des.* **2012**, *12*, 5796−5799.

(205) Engwerda, A. H. J.; Meekes, H.; Bickelhaupt, F. M.; Rutjes, F. P. J. T.; Vlieg, E. Racemization and Deracemization through Intermolecular Redox Behaviour. *Chem. - Eur. J.* **2019**, *25*, 9639−9642.

(206) Engwerda, A. H. J.; Koning, N.; Tinnemans, P.; Meekes, H.; Bickelhaupt, F. M.; Rutjes, F. P. J. T.; Vlieg, E. Deracemization of a Racemic Allylic Sulfoxide Using Viedma Ripening. *Cryst. Growth Des.* **2017**, *17*, 4454−4457.

(207) Engwerda, A. H. J.; van Schayik, P.; Jagtenberg, H.; Meekes, H.; Rutjes, F. P. J. T.; Vlieg, E. Solid Phase Deracemization of an Atropisomer. *Cryst. Growth Des.* **2017**, *17*, 5583−5585.

(208) Ishikawa, H.; Uemura, N.; Saito, R.; Yoshida, Y.; Mino, T.; Kasashima, Y.; Sakamoto, M. Chiral Symmetry Breaking of Spiropyrans and Spirooxazines by Dynamic Enantioselective Crystallization. *Chem. - Eur. J.* **2019**, *25*, 9758−9763.

(209) Sakamoto, M.; Shiratsuki, K.; Uemura, N.; Ishikawa, H.; Yoshida, Y.; Kasashima, Y.; Mino, T. Asymmetric Synthesis by Using Natural Sunlight under Absolute Achiral Conditions. *Chem. - Eur. J.* **2017**, *23*, 1717−1721.

(210) Baglai, I.; Leeman, M.; Wurst, K.; Kaptein, B.; Kellogg, R. M.; Noorduin, W. L. The Strecker Reaction Coupled to Viedma Ripening: A Simple Route to Highly Hindered Enantiomerically Pure Amino Acids. *Chem. Commun.* **2018**, *54*, 10832−10834.

(211) Flock, A. M.; Reucher, C. M. M.; Bolm, C. Enantioenrichment by Iterative Retro-Aldol/Aldol Reaction Catalyzed by an Achiral or Racemic Base. *Chem. - Eur. J.* **2010**, *16*, 3918−3921.

(212) Uemura, N.; Sano, K.; Matsumoto, A.; Yoshida, Y.; Mino, T.; Sakamoto, M. Absolute Asymmetric Synthesis of an Aspartic Acid Derivative from Prochiral Maleic Acid and Pyridine under Achiral Conditions. *Chem. - Asian J.* **2019**, *14*, 4150−4153.

(213) Uemura, N.; Toyoda, S.; Shimizu, W.; Yoshida, Y.; Mino, T.; Sakamoto, M. Absolute Asymmetric Synthesis Involving Chiral Symmetry Breaking in Diels-Alder Reaction. *Symmetry* **2020**, *12*, 910.

(214) Cintas, P. On Cavitation and Chirality: A Further Assessment. *Cryst. Growth Des.* **2008**, *8*, 2626−2627.

(215) Iggland, M.; Fernández-Ronco, M. P.; Senn, R.; Kluge, J.; Mazzotti, M. Complete Solid State Deracemization by High Pressure Homogenization. *Chem. Eng. Sci.* **2014**, *111*, 106−111.

(216) Xiouras, C.; Van Aeken, J.; Panis, J.; Ter Horst, J. H.; Van Gerven, T.; Stefanidis, G. D. Attrition-Enhanced Deracemization of NaClO3: Comparison between Ultrasonic and Abrasive Grinding. *Cryst. Growth Des.* **2015**, *15*, 5476−5484.

(217) Ahn, J.; Kim, D. H.; Coquerel, G.; Kim, W. S. Chiral Symmetry Breaking and Deracemization of Sodium Chlorate in Turbulent Flow. *Cryst. Growth Des.* **2018**, *18*, 297−306.

(218) Song, Y.; Chen, W.; Chen, X. Ultrasonic Field Induced Chiral Symmetry Breaking of NaClO3 Crystallization. *Cryst. Growth Des.* **2008**, *8*, 1448−1450.

(219) Ward, M. R.; Copeland, G. W.; Alexander, A. J. Enantiomorphic Symmetry Breaking in Crystallization of Molten Sodium Chloride. *Chem. Commun.* **2010**, *46*, 7634−7636.

(220) Song, Y.; Chen, W.; Chen, X. Crystal Chiral Symmetry Breaking: A Self-Seed Inducing Effect Controlled by Kinetics. *Cryst. Growth Des.* **2012**, *12*, 8−11.

(221) Viedma, C.; Cintas, P. Homochirality beyond Grinding: Deracemizing Chiral Crystals by Temperature Gradient under Boiling. *Chem. Commun.* **2011**, *47*, 12786−12788.

(222) Suwannasang, K.; Flood, A. E.; Coquerel, G. A Novel Design Approach To Scale Up the Temperature Cycle Enhanced Deracemization Process: Coupled Mixed-Suspension Vessels. *Cryst. Growth Des.* **2016**, *16*, 6461−6467.

(223) Suwannasang, K.; Flood, A. E.; Rougeot, C.; Coquerel, G. Use of Programmed Damped Temperature Cycles for the Deracemization of a Racemic Suspension of a Conglomerate Forming System. *Org. Process Res. Dev.* **2017**, *21*, 623−630.

(224) Breveglieri, F.; Maggioni, G. M.; Mazzotti, M. Deracemization of NMPA via Temperature Cycles. *Cryst. Growth Des.* **2018**, *18*, 1873−1881.

(225) Rougeot, C.; Guillen, F.; Plaquevent, J. C.; Coquerel, G. Ultrasound-Enhanced Deracemization: Toward the Existence of Agonist Effects in the Interpretation of Spontaneous Symmetry Breaking. *Cryst. Growth Des.* **2015**, *15*, 2151−2155.

(226) Plaza, M.; Jandl, C.; Bach, T. Photochemical Deracemization of Allenes and Subsequent Chirality Transfer. *Angew. Chem., Int. Ed.* **2020**, *59*, 12785−12788.

(227) van't Hoff, J. H. Die Phasenlehre. *Ber. Dtsch. Chem. Ges.* **1902**, *35*, 4252−4264.

(228) Voorhees, P. W. The Theory of Ostwald Ripening. *J. Stat. Phys.* **1985**, *38*, 231−252.

(229) Enüstün, B. V.; Turkevich, J. Solubility of Fine Particles of Strontium Sulfate. *J. Am. Chem. Soc.* **1960**, *82*, 4502−4509.

(230) Wu, W.; Nancollas, G. H. A New Understanding of the Relationship Between Solubility and Particle Size. *J. Solution Chem.* **1998**, *27*, 521−531.

(231) Iggland, M.; Mazzotti, M. A Population Balance Model for Chiral Resolution via Viedma Ripening. *Cryst. Growth Des.* **2011**, *11*, 4611−4622.

(232) Blanco, C. A.; Chen, I. Connections Between Mathematical Models of Prebiotic Evolution and Homochirality. In *Prebiotic Chemistry and Chemical Evolution of Nucleic Acids*; Nucleic Acids and Molecular Biology, Vol. 35; Springer International Publishing; 2018; pp 245−261,.

(233) Bodák, B.; Maggioni, G. M.; Mazzotti, M. Population-Based Mathematical Model of Solid-State Deracemization via Temperature Cycles. *Cryst. Growth Des.* **2018**, *18*, 7122−7131.

(234) Wattis, J. A. D. Mathematical Models of the Homochiralisation of Crystals by Grinding. *Origins Life Evol. Biospheres* **2011**, *41*, 133−173.

(235) Suwannasang, K.; Coquerel, G.; Rougeot, C.; Flood, A. E. Mathematical Modeling of Chiral Symmetry Breaking Due to Differences in Crystal Growth Kinetics. *Chem. Eng. Technol.* **2014**, *37*, 1329−1339.

(236) Noorduin, W. L.; Meekes, H.; Bode, A. A. C.; Van Enckevort, W. J. P.; Kaptein, B.; Kellogg, R. M.; Vlieg, E. Explanation for the Emergence of a Single Chiral Solid State during Attrition-Enhanced Ostwald Ripening: Survival of the Fittest. *Cryst. Growth Des.* **2008**, *8*, 1675−1681.

(237) Noorduin, W. L.; Meekes, H.; Van Enckevort, W. J. P.; Millemaggi, A.; Leeman, M.; Kaptein, B.; Kellogg, R. M.; Vlieg, E. Complete Deracemization by Attrition-Enhanced Ostwald Ripening Elucidated. *Angew. Chem., Int. Ed.* **2008**, *47*, 6445−6447.

(238) Noorduin, W. L.; Meekes, H.; van Enckevort, W. J. P.; Kaptein, B.; Kellogg, R. M.; Vlieg, E. Enantioselective Symmetry Breaking Directed by the Order of Process Steps. *Angew. Chem., Int. Ed.* **2010**, *49*, 2539−2541.

(239) Iggland, M.; Mazzotti, M. Solid State Deracemisation through Growth, Dissolution and Solution-Phase Racemisation. *CrystEngComm* **2013**, *15*, 2319−2328.

(240) Iggland, M.; Müller, R.; Mazzotti, M. On the Effect of Initial Conditions in Viedma Ripening. *Cryst. Growth Des.* **2014**, *14*, 2488−2493.

(241) Gherase, D.; Conroy, D.; Matar, O. K.; Blackmond, D. G. Experimental and Theoretical Study of the Emergence of Single Chirality in Attrition-Enhanced Deracemization. *Cryst. Growth Des.* **2014**, *14*, 928−937.

(242) Blanco, C.; Stich, M.; Hochberg, D. Mechanically Induced Homochirality in Nucleated Enantioselective Polymerization. *J. Phys. Chem. B* **2017**, *121*, 942−955.

(243) Joyce, G. F.; Schwartz, A. W.; Miller, S. L.; Orgel, L. E. The Case for an Ancestral Genetic System Involving Simple Analogues of the Nucleotides. *Proc. Natl. Acad. Sci. U. S. A.* **1987**, *84*, 4398−4402.

(244) Eigen, M.; Schuster, P. Stages of Emerging Life —Five Principles of Early Organization. *J. Mol. Evol.* **1982**, *19*, 47−61.

(245) Newnham, R. E. *Properties of Materials: Anisotropy, Symmetry, Structure*; Oxford University Press: Oxford, U.K., 2005.

(246) Shubnikov, A. V. On the Works of Pierre Curie on Symmetry. *Comput. Math. with Appl.* **1988**, *16*, 357−364.

(247) Gal, J. Louis Pasteur, Language, and Molecular Chirality. I. Background and Dissymmetry. *Chirality* **2011**, *23*, 1−16.

(248) Zhang, J.; Chen, S.; Nieto, R. A.; Wu, T.; Feng, P.; Bu, X. A Tale of Three Carboxy Lates: Cooperative Asymmetric Crystallization of a Three-Dimensional Microporous Framework from Achiral Precursors. *Angew. Chem., Int. Ed.* **2010**, *49*, 1267−1270.

(249) Nespolo, M.; Aroyo, M. I.; Souvignier, B. Crystallographic Shelves: Space-Group Hierarchy Explained. *J. Appl. Crystallogr.* **2018**, *51*, 1481−1491.

(250) Flack, H. D. Chiral and Achiral Crystal Structures. *Helv. Chim. Acta* **2003**, *86*, 905−921.

(251) De Graef, M.; McHenry, M. E. *Structure of Materials: An Introduction to Crystallography, Diffraction and Symmetry*; Cambridge University Press: Cambridge, U.K., 2007.

(252) Addadi, L.; Weinstein, S.; Gati, E.; Weissbuch, I.; Lahav, M. Resolution of Conglomerates with the Assistance of Tailor-Made Impurities. Generality and Mechanistic Aspects of the "Rule of Reversal". A New Method for Assignment of Absolute Configuration. *J. Am. Chem. Soc.* **1982**, *104*, 4610−4617.

(253) Matsuura, T.; Koshima, H. Introduction to Chiral Crystallization of Achiral Organic Compounds: Spontaneous Generation of Chirality. *J. Photochem. Photobiol., C* **2005**, *6*, 7−24.

(254) Pidcock, E. Achiral Molecules in Non-Centrosymmetric Space Groups. *Chem. Commun.* **2005**, No. 27, 3457−3459.

(255) Dryzun, C.; Avnir, D. On the Abundance of Chiral Crystals. *Chem. Commun.* **2012**, *48*, 5874−5876.

(256) Yogev-Einot, D.; Avnir, D. Quantitative Symmetry and Chirality of the Molecular Building Blocks of Quartz. *Chem. Mater.* **2003**, *15*, 464−472.

(257) Ramachandran, G. N.; Chandrasekaran, K. S. The Absolute Configuration of Sodium Chlorate. *Acta Crystallogr.* **1957**, *10*, 671−675.

(258) Matsumoto, A.; Tsuchiya, S.; Hagiwara, Y.; Ishikawa, K.; Koshima, H.; Asahi, T.; Soai, K. Absolute Structure Determination of Chiral Crystals Consisting of Achiral Benzophenone with Single-Crystal X-Ray Diffraction and Its Correlation with Solid-State Circular Dichroism. *Chem. Lett.* **2016**, *45*, 526−528.

(259) Kaminskii, A. A.; Bagayev, S. N.; Hulliger, J.; Eichler, H.; Findeisen, J.; Macdonald, R. Acentric Cubic NaClO3 - A New Crystal for Raman Lasers. *Appl. Phys. B: Lasers Opt.* **1998**, *67*, 157−162.

(260) Lennartson, A.; Vestergren, M.; Håkansson, M. *Chem. - Eur. J.* **2005**, *11*, 1757−1762.

(261) Bijvoet, J. M.; Peerdeman, A. F.; van Bommel, A. J. Determination of the Absolute Configuration of Optically Active Compounds by Means of X-Rays. *Nature* **1951**, *168*, 271−272.

(262) Parsons, S. Determination of Absolute Configuration Using X-Ray Diffraction. *Tetrahedron: Asymmetry* **2017**, *28*, 1304−1313.

(263) Flack, H. D.; Bernardinelli, G. The Use of X-Ray Crystallography to Determine Absolute Configuration. *Chirality* **2008**, *20*, 681−690.

(264) Kuroda, R.; Honma, T. CD Spectra of Solid-State Samples. *Chirality* **2000**, *12*, 269−277.

(265) Arteaga, O.; Freudenthal, J.; Wang, B.; Kahr, B. Mueller Matrix Polarimetry with Four Photoelastic Modulators: Theory and Calibration. *Appl. Opt.* **2012**, *51*, 6805−6817.

(266) Kaminsky, W.; Claborn, K.; Kahr, B. Polarimetric Imaging of Crystals. *Chem. Soc. Rev.* **2004**, *33*, 514−525.

(267) Claborn, K.; Isborn, C.; Kaminsky, W.; Kahr, B. Optical Rotation of Achiral Compounds. *Angew. Chem., Int. Ed.* **2008**, *47*, 5706−5717.

(268) Thalal, A.; Aboufadil, Y.; Elidrissi Raghni, M. A.; Jali, A.; Oueriagli, A.; Ait Rai, K. Symmetry in Art and Architecture of the Western Islamic World. *Crystallogr. Rev.* **2018**, *24*, 102−130.

(269) Albert, F.; Gómis, J. M.; Blasco, J.; Valiente, J. M.; Aleixos, N. A New Method to Analyse Mosaics Based on Symmetry Group Theory Applied to Islamic Geometric Patterns. *Comput. Vis. Image Underst.* **2015**, *130*, 54−70.

(270) Pérez-Gómez, R. The Four Regular Mosaics Missing in the Alhambra. *Comput. Math Applic* **1987**, *14*, 133−137.

(271) Ernst, K.-H. Molecular Chirality in Surface Science. *Surf. Sci.* **2013**, *613*, 1−5.

(272) Kulkarni, C.; Balasubramanian, S.; George, S. J. What Molecular Features Govern the Mechanism of Supramolecular Polymerization? *ChemPhysChem* **2013**, *14*, 661−673.

(273) Tschierske, C.; Ungar, G. Mirror Symmetry Breaking by Chirality Synchronisation in Liquids and Liquid Crystals of Achiral Molecules. *ChemPhysChem* **2016**, *17*, 9−26.

(274) Mislow, K. A Commentary on the Topological Chirality and Achirality of Molecules. *Croat. Chem. Acta* **1996**, *69*, 485−511.

(275) Yoon, M.; Srirambalaji, R.; Kim, K. Homochiral Metal-Organic Frameworks for Asymmetric Heterogeneous Catalysis. *Chem. Rev.* **2012**, *112*, 1196−1231.

(276) Attard, G. A.; Clavilier, J.; Feliu, J. M. Chirality at Well-Defined Metal Surfaces. In *Chirality: Physical Chemistry*; ACS Symposium Series, Vol. *810*; American Chemical Society, 2002; pp 18−254.

(277) Hazen, R. M.; Sholl, D. S. Chiral Selection on Inorganic Crystalline Surfaces. *Nat. Mater.* **2003**, *2*, 367−374.

(278) Ahmadi, A.; Attard, G.; Feliu, J.; Rodes, A. Surface Reactivity at "Chiral" Platinum Surfaces. *Langmuir* **1999**, *15*, 2420−2424.

(279) Tsogoeva, S. B.; Wei, S.; Freund, M.; Mauksch, M. Generation of Highly Enantioenriched Crystalline Products in Reversible Asymmetric Reactions with Racemic or Achiral Catalysts. *Angew. Chem., Int. Ed.* **2009**, *48*, 590−594.

(280) Matsumoto, A.; Kaimori, Y.; Uchida, M.; Omori, H.; Kawasaki, T.; Soai, K. Achiral Inorganic Gypsum Acts as an Origin of Chirality through Its Enantiotopic Surface in Conjunction with Asymmetric Autocatalysis. *Angew. Chem., Int. Ed.* **2017**, *56*, 545−548.

(281) Blanco, C.; Crusats, J.; El-Hachemi, Z.; Moyano, A.; Hochberg, D.; Ribó, J. M. Spontaneous Emergence of Chirality in the Limited Enantioselectivity Model: Autocatalytic Cycle Driven by an External Reagent. *ChemPhysChem* **2013**, *14*, 2432−2440.

(282) Gomar-Nadal, E.; Puigmartí-Luis, J.; Amabilino, D. B. Assembly of Functional Molecular Nanostructures on Surfaces. *Chem. Soc. Rev.* **2008**, *37*, 490−504.

(283) Mark, A. G.; Forster, M.; Raval, R. Recognition and Ordering at Surfaces: The Importance of Handedness and Footedness. *ChemPhysChem* **2011**, *12*, 1474−1480.

(284) Abbasi-Pérez, D.; Sang, H.; Pérez-García, L.; Floris, A.; Amabilino, D. B.; Raval, R.; Recio, J. M.; Kantorovich, L. Controlling the Preferential Motion of Chiral Molecular Walkers on a Surface. *Chem. Sci.* **2019**, *10*, 5864−5874.

(285) Voskuhl, J.; Ravoo, B. J. Molecular Recognition of Bilayer Vesicles. *Chem. Soc. Rev.* **2009**, *38*, 495−505.

(286) El-Hachemi, Z.; Balaban, T. S.; Campos, J. L.; Cespedes, S.; Crusats, J.; Escudero, C.; Kamma-Lorger, C. S.; Llorens, J.; Malfois, M.; Mitchell, G. R.; Tojeira, A. P.; Ribó, J. M. Effect of Hydrodynamic Forces on Meso-(4-Sulfonatophenyl)-Substituted Porphyrin J-Aggregate Nanoparticles: Elasticity, Plasticity and Breaking. *Chem. - Eur. J.* **2016**, *22*, 9740−9749.

(287) El-Hachemi, Z.; Crusats, J.; Troyano, C.; Ribó, J. M. Diastereoisomerism, Stability, and Morphology of Substituted Meso-4-Sulfonatophenylporphyrin J-Aggregates. *ACS Omega* **2019**, *4*, 4804−4813.

(288) Berfeld, M.; Zbaida, D.; Leiserowitz, L.; Lahav, M. 'Tailor-Made' Polymers for the Removal of Lamellar Twinning: Resolution of α-Amino Acids by Entrainment. *Adv. Mater.* **1999**, *11*, 328−331.

(289) Kuzmenko, I.; Rapaport, H.; Kjaer, K.; Als-Nielsen, J.; Weissbuch, I.; Lahav, M.; Leiserowitz, L. Design and Characterization of Crystalline Thin Film Architectures at the Air-Liquid Interface: Simplicity to Complexity. *Chem. Rev.* **2001**, *101*, 1659−1696.

(290) Weissbuch, I.; Bolbach, G.; Leiserowitz, L.; Lahav, M. Chiral Amplification of Oligopeptides via Polymerization in Two-Dimensional Crystallites on Water. *Origins Life Evol. Biospheres* **2004**, *34*, 79−92.

(291) Weissbuch, I.; Lahav, M. Crystalline Architectures as Templates of Relevance to the Origins of Homochirality. *Chem. Rev.* **2011**, *111*, 3236−3267.

(292) Fedotov, V. A.; Schwanecke, A. S.; Zheludev, N. I.; Khardikov, V. V.; Prosvirnin, S. L. Asymmetric Transmission of Light and Enantiomerically Sensitive Plasmon Resonance in Planar Chiral Nanostructures. *Nano Lett.* **2007**, *7*, 1996−1999.

(293) Simpson, G. J. Molecular Origins of the Remarkable Chiral Sensitivity of Second-Order Nonlinear Optics. *ChemPhysChem* **2004**, *5*, 1301−1310.

(294) Wolffs, M.; George, S. J.; Tomović, Ž.; Meskers, S. C. J.; Schenning, A. P. H. J.; Meijer, E. W. Macroscopic Origin of Circular Dichroism Effects by Alignment of Self-Assembled Fibers in Solution. *Angew. Chem., Int. Ed.* **2007**, *46*, 8203−8205.

(295) Honglawan, A.; Beller, D. A.; Cavallaro, M.; Kamien, R. D.; Stebe, K. J.; Yang, S. Topographically Induced Hierarchical Assembly and Geometrical Transformation of Focal Conic Domain Arrays in Smectic Liquid Crystals. *Proc. Natl. Acad. Sci. U. S. A.* **2013**, *110*, 34−39.

(296) Stiewe, A.; Kemnitz, E. Synthesis and Crystal Structure of K2(HSO4)(H2PO4), K4(HSO4)3(H2PO4), and Na(HSO4)-(H3PO4). *Z. Anorg. Allg. Chem.* **2000**, *626*, 2004−2011.

(297) Ferraris, G.; Jones, D. W.; Yerkess, J. Refinement of the Crystal Structure of Magnesium Sulphate Heptahydrate (Epsomite) by Neutron Diffraction. *J. Chem. Soc., Dalton Trans.* **1973**, 816−821.

(298) Calleri, M.; Gavetti, A.; Ivaldi, G.; Rubbo, M. Synthetic Epsomite, MgSO4.7H2O: Absolute Configuration and Surface Features of the Complementary {111} Forms. *Acta Crystallogr., Sect. B: Struct. Sci.* **1984**, *40*, 218−222.

(299) Saha, J. K.; Podder, J. Crystallization of Zinc Sulphate Single Crystals and Its Structural, Thermal and Optical Characterization. *J. Bangladesh Acad. Sci.* **2012**, *35*, 203−210.

(300) Bartl, H.; Catti, M.; Ferraris, G. Hydrogen Bonding in the Crystalline State. The Crystal Structure of NaH2PO4.2H2O by X-Ray and Neutron Diffraction. *Acta Crystallogr., Sect. B: Struct. Crystallogr. Cryst. Chem.* **1976**, *32*, 987−994.

(301) Prieto, A. C.; Gonzalez, A.; Hernandez, E.; Rull, F.; de Saja, J. A. Preparation and Characterization of Strontium Formate Dihydrate. *Cryst. Res. Technol.* **1983**, *18*, 1093−1100.

(302) Galigné, J. L. Affinement de La Structure Cristalline Du Formiate de Strontium Dihydraté, Sr(HCOO)2.2H2O. *Acta Crystallogr., Sect. B: Struct. Crystallogr. Cryst. Chem.* **1971**, *27*, 2429−2431.

(303) Watanabé, T.; Matsui, M. A Redetermination of the Crystal Structures of α-Calcium Formate, α-Strontium Formate and Barium Formate by X-Ray Analyses. *Acta Crystallogr., Sect. B: Struct. Crystallogr. Cryst. Chem.* **1978**, *34*, 2731−2736.

(304) Stadnicka, K.; Glazer, A. M.; Koralewski, M. Structure, Absolute Configuration and Optical Activity of A-nickel Sulfate Hexahydrate. *Acta Crystallogr., Sect. B: Struct. Sci.* **1987**, *43*, 319−325.

(305) Rousseau, B.; Maes, S. T.; Lenstra, A. T. H. Systematic Intensity Errors and Model Imperfection as the Consequence of Spectral Truncation. *Acta Crystallogr., Sect. A: Found. Crystallogr.* **2000**, *56*, 300−307.

(306) Ptasiewicz-Bak, H.; Olovsson, I.; McIntyre, G. J. Bonding Deformation and Superposition in the Electron Density of Tetragonal NiSO4.6H2O at 25 K. *Acta Crystallogr., Sect. B: Struct. Sci.* **1993**, *49*, 192−201.

(307) Choudhury, R. R.; Chitra, R.; Makarova, I. P.; Manomenova, V. L.; Rudneva, E. B.; Voloshin, A. E.; Koldaeva, M. V. α-Nickel Sulfate Hexahydrate Crystals: Relationship of Growth Conditions, Crystal Structure and Properties. *J. Appl. Crystallogr.* **2019**, *52*, 1371−1377.

(308) Pohl, D.; Gross, T. Caesium Nitrate (II) at 296 K. *Acta Crystallogr., Sect. C: Cryst. Struct. Commun.* **1993**, *49*, 316−318.

(309) Pohl, J.; Pohl, D.; Adiwidjaja, G. Phase Transition in Rubidium Nitrate at 346 K and Structure at 296, 372, 413 and 437 K. *Acta Crystallogr., Sect. B: Struct. Sci.* **1992**, *48*, 160−166.

(310) Dean, C.; Hambley, T. W.; Snow, M. R. Structures of Phase IV Rubidium Nitrate, RbNO3, and Phase II Caesium Nitrate, CsNO3. *Acta Crystallogr., Sect. C: Cryst. Struct. Commun.* **1984**, *40*, 1512−1515.

(311) Fábry, J. Structure Redetermination of SrS2O6.4H2O. *Acta Crystallogr., Sect. B: Struct. Sci.* **1995**, *51*, 23−30.

(312) de Matos Gomes, E.; Zúñiga, F. J.; Ortega, J.; Etxebarria, J. The Structure and Optical Activity of SrS2O6.4H2O. *J. Appl. Crystallogr.* **1994**, *27*, 563−566.

(313) Agron, P. A.; Busing, W. R. Calcium and Strontium Dichloride Hexahydrates by Neutron Diffraction. *Acta Crystallogr., Sect. C: Cryst. Struct. Commun.* **1986**, *C42*, 141−143.

(314) de Matos Gomes, E.; Ortega, J.; Etxebarria, J.; Zúñiga, F. J.; Breczewski, T. The Crystal Structure and Optical Activity of Potassium Dithionate, K2S2O6. *J. Phys.: Condens. Matter* **1996**, *8*, 2063−2071.

(315) De Matos Gomes, E. Optical Rotatory Dispersion and Absolute Optical Chirality of Strontium and Calcium Dithionate Tetrahydrate, SrS2O6.4H2O and CaS2O6.4H2O. *Acta Crystallogr., Sect. B: Struct. Sci.* **1991**, *47*, 7−11.

(316) Thomas, P. A.; Gomes, E. Absolute Chirality and Crystal Structure of Barium Nitrite Monohydrate, Ba(NO2)2.H2O. *Acta Crystallogr., Sect. B: Struct. Sci.* **1989**, *45*, 348−355.

(317) Schäfer, G.; Fischer, K. F. Die Struktur von Bariumnitrit-Monohydrat Ba(NO2)2•H2O. *Z. Kristallogr. - Cryst. Mater.* **1981**, *155*, 75−79.

(318) De Boer, J. L.; van Bolhuis, F.; Olthof-Hazekamp, R. V. Re-Investigation of the Crystal Structure of Lithium Iodate. *Acta Crystallogr.* **1966**, *21*, 841−843.

(319) Abrahams, S. C. Structure Relationship to Dielectric, Elastic and Chiral Properties. *Acta Crystallogr., Sect. A: Found. Crystallogr.* **1994**, *50*, 658−685.

(320) Karppinen, M.; Lundgren, J. O.; Liminga, R. Structure of Pyroelectric Lithium Potassium Sulphate, LiKSO4. *Acta Crystallogr., Sect. C: Cryst. Struct. Commun.* **1983**, *39*, 34−38.

(321) Balagurov, A. M.; Savenko, B. N.; Dlouhá, M.; Vratislav, S.; Jirák, Z. A Neutron Diffraction Study of Crystal and Domain Structure in LiKSO4. *Phys. Status Solidi* **1984**, *83*, K117−K121.

(322) Rajagopal, H.; Jaya, V.; Sequeira, A.; Chidambaram, R. Neutron Profile Refinement Study of the Low-Temperature Structural Phases of LiKSO4. *Phys. B* **1991**, *174*, 95−100.

(323) Pinheiro, C. B.; Pimenta, M. A.; Chapuis, G.; Speziali, N. L. Analysis of LiKSO4 Crystals in the Temperature Range from 573 to 943 K. *Acta Crystallogr., Sect. B: Struct. Sci.* **2000**, *56*, 607−617.

(324) Abrahams, S. C.; Bernstein, J. L. Remeasurement of Optically Active NaClO3 and NaBrO3. *Acta Crystallogr., Sect. B: Struct. Crystallogr. Cryst. Chem.* **1977**, *B33*, 3601−3604.

(325) Breidenstein, B.; Follner, H. On Crystal Growth of Ammonium and Potassium Dichromate. A Study of the Shubnikov Effect. *Cryst. Res. Technol.* **1990**, *25*, 1375−1384.

(326) Weissbuch, I.; Popovitz-Biro, R.; Lahav, M.; Leiserowitz, L.; Rehovot. Understanding and Control of Nucleation, Growth, Habit, Dissolution and Structure of Two- and Three-dimensional Crystals Using 'tailor-made' Auxiliaries. *Acta Crystallogr., Sect. B: Struct. Sci.* **1995**, *51*, 115−148.

(327) Glazer, A. M.; Stadnicka, K. On the Origin of Optical Activity in Crystal Structures. *J. Appl. Crystallogr.* **1986**, *19*, 108−122.

(328) Matsumoto, A.; Ozawa, H.; Inumaru, A.; Soai, K. Asymmetric Induction by Retgersite, Nickel Sulfate Hexahydrate, in Conjunction with Asymmetric Autocatalysis. *New J. Chem.* **2015**, *39*, 6742−6745.

(329) Madhava, M. S.; Haussühl, S. Linear Electrooptical Constants of Orthorhombic Strontium Formate, Strontium Formate Dihydrate, and Barium Formate Single Crystals. *Z. Krist. Krist.* **1975**, *141*, 25−30.

(330) Cruz, J. M.; Hernández-Lechuga, K.; Domínguez-Valle, I.; Fuentes-Beltrán, A.; Sánchez-Morales, J. U.; Ocampo-Espindola, J. L.; Polanco, C.; Micheau, J. C.; Buhse, T. Non-Stochastic Behavior in Sodium Chlorate Crystallization. *Chirality* **2020**, *32*, 120−134.

(331) Weissbuch, I.; Lahav, M.; Leiserowitz, L. Toward Stereochemical Control, Monitoring, and Understanding of Crystal Nucleation. *Cryst. Growth Des.* **2003**, *3*, 125−150.

(332) Urusov, V. S.; Nadezhina, T. N. Frequency Distribution and Selection of Space Groups in Inorganic Crystal Chemistry. *J. Struct. Chem.* **2009**, *50*, 22−37.

(333) Fortes, A. From Surrey to the Moons of Jupiter (via Mars): The Story of Epsomite. *Axis* **2005**, *1*, 1−28.

(334) Allen, F. H. The Cambridge Structural Database: A Quarter of a Million Crystal Structures and Rising. *Acta Crystallogr., Sect. B: Struct. Sci.* **2002**, *58*, 380−388.

(335) Ziach, K.; Jurczak, J. Mirror Symmetry Breaking upon Spontaneous Crystallization from a Dynamic Combinatorial Library of Macrocyclic Imines. *Chem. Commun.* **2015**, *51*, 4306−4309.

(336) Groom, C. R.; Bruno, I. J.; Lightfoot, M. P.; Ward, S. C. The Cambridge Structural Database. *Acta Crystallogr., Sect. B: Struct. Sci., Cryst. Eng. Mater.* **2016**, *72*, 171−179.

(337) Sivakumar, R.; Kwiatoszynski, J.; Fouret, A.; Nguyen, T. P. T.; Ramrup, P.; Cheung, P. S. M.; Cintas, P.; Viedma, C.; Cuccia, L. A. Enantiomer-Specific Oriented Attachment of Guanidine Carbonate Crystals. *Cryst. Growth Des.* **2016**, *16*, 3573−3576.

(338) Miyata, M.; Tohnai, N.; Hisaki, I.; Sasaki, T. Generation of Supramolecular Chirality around Twofold Rotational or Helical Axes in Crystalline Assemblies of Achiral Components. *Symmetry* **2015**, *7*, 1914−1928.

(339) Koshima, H.; Hayashi, E.; Matsuura, T.; Tanaka, K.; Toda, F.; Kato, M.; Kiguchi, M. Preparation, Structure and Discrimination of a Chiral Bimolecular Crystal by the Self-Assembly of 3-Indolepropionic Acid and Phenanthridine. *Tetrahedron Lett.* **1997**, *38*, 5009−5012.

(340) Koshima, H.; Miyauchi, M. Polymorphs of a Cocrystal with Achiral and Chiral Structures Prepared by Pseudoseeding: Tryptamine/Hydrocinnamic Acid. *Cryst. Growth Des.* **2001**, *1*, 355−357.

(341) Nayak, A.; Pedireddi, V. R. Rational Analysis of Melting Point Behavior of Co-Crystals of 4-Nitrophenol with Some Aza-Compounds. *Cryst. Growth Des.* **2016**, *16*, 5966−5975.

(342) Sowmya, N. S.; Sampathkrishnan, S.; Sudhahar, S.; Chakkaravarthi, G.; Kumar, R. M. Crystal Structure of Piperidinium 4-Nitrophenolate. *Acta Crystallogr., Sect. E: Struct. Rep. Online* **2014**, *70*, 559−561.

(343) Vembu, N.; Nallu, M.; Spencer, E. C.; Howard, J. A. K. 4-Dimethylaminopyridinium-4-Nitrophenolate-4-Nitrophenol (1/1/1). *Acta Crystallogr., Sect. E: Struct. Reports Online* **2003**, *59*, o1192−o1195.

(344) Xiong, Y.; An, T.; He, C.; Liu, Y.; Chen, J.; Zha, C.; Karlsson, H. T.; Chen, X. Crystal Structures and Supramolecular Assembly of 1:2 Piperazine with o- and p-Nitrophenol. *J. Chem. Crystallogr.* **2002**, *32*, 219−225.

(345) Smith, G.; Lynch, D. E. Cyclic Heterotetrameric and Low-Dimensional Hydrogen-Bonded Polymeric Structures in the Morpholinium Salts of Ring-Substituted Benzoic Acid Analogues. *Acta Crystallogr., Sect. C: Struct. Chem.* **2016**, *72*, 105−111.

(346) Ramon, G.; Davies, K.; Nassimbeni, L. R. Structures of Benzoic Acids with Substituted Pyridines and Quinolines: Salt versus Co-Crystal Formation. *CrystEngComm* **2014**, *16*, 5802−5810.

(347) Shen, H.; Nie, J.-J.; Xu, D.-J. 2-Amino-4-Methylpyridinium 4-Aminobenzoate. *Acta Crystallogr., Sect. E: Struct. Rep. Online* **2008**, *64*, o1129−o1129.

(348) Smith, G.; Wermuth, U. D. Guanidinium 3-Nitrobenzoate. *Acta Crystallogr., Sect. E: Struct. Rep. Online* **2010**, *66*, o1946−o1946.

(349) Thanigaimani, K.; Khalib, N. C.; Arshad, S.; Razak, I. A. 2-Amino-5-Bromopyridinium 5-Chloro-2-Hydroxybenzoate. *Acta Crystallogr., Sect. E: Struct. Rep. Online* **2013**, *69*, o537−o538.

(350) Daisy Rani, T.; Rajkumar, M.; Chandramohan, A. Synthesis, Crystal Structure, Thermal, Mechanical and Laser Damage Threshold Studies of an NLO Active Organic Molecular Adduct: 4-Acetylpyridine:4-Aminobenzoicacid. *Mater. Lett.* **2018**, *222*, 118−121.

(351) Tan, T.-F.; Han, J.; Pang, M.-L.; Song, H.-B.; Ma, Y.-X.; Meng, J.-B. Achiral Benzoic Acid Derivatives as Chiral Cocrystal Building Blocks in Supramolecular Chemistry: Adducts with Organic Amines. *Cryst. Growth Des.* **2006**, *6*, 1186−1193.

(352) Lah, N.; Leban, I. 4-Aminopyridinium Hydrogen Maleate. *Acta Crystallogr., Sect. C: Cryst. Struct. Commun.* **2003**, *59*, o537−o538.

(353) Hemamalini, M.; Fun, H.-K. 2-Amino-5-Methylpyridinium Picolinate 0.63-Hydrate. *Acta Crystallogr., Sect. E: Struct. Rep. Online* **2010**, *66*, o1420−o1421.

(354) Thirumurugan, R.; Babu, B.; Anitha, K.; Chandrasekaran, J. Investigation on Growth, Structure and Characterization of Succinate Salt of 8-Hydroxyquinoline: An Organic NLO Crystal. *Spectrochim. Acta, Part A* **2015**, *140*, 44−53.

(355) Kama, A. B.; Génois, R.; Massuyeau, F.; Sidibé, M.; Diop, C. A. K.; Gautier, R. Cyclohexylammonium Sulfanilate: A Simple Representative of the Chiral Materials Containing Only Achiral Building Units. *Mater. Lett.* **2019**, *241*, 6−9.

(356) Fonari, M. S.; Antal, S.; Castañeda, R.; Ordonez, C.; Timofeeva, T. V. Crystalline Products of CO2 Capture by Piperazine Aqueous Solutions. *CrystEngComm* **2016**, *18*, 6282−6289.

(357) Herler, S.; Mayer, P.; Schulz, A.; Villinger, A. N-Methyl-2-Pyrrolidone Hydrochloride. *Acta Crystallogr., Sect. E: Struct. Rep. Online* **2007**, *63*, o3991−o3991.

(358) Jones, G. P.; Pauling, P. J. Crystal and Molecular Structure of Imidazole-4-Acetic Acid Hydrochloride. *J. Chem. Soc., Perkin Trans. 2* **1976**, 34−36.

(359) Daszkiewicz, M. Elementary Graph-Set Descriptors in Crystal Structure Comparison of 2-Methyl-4-Nitroanilinium Hexachloridostannate(IV), Bromide and Two Noncentrosymmertic Chlorides. X-Ray, Vibrational and Theoretical Studies. *Cryst. Growth Des.* **2013**, *13*, 2277−2285.

(360) Seethalakshmi, T.; Venkatesan, P.; Fronczek, F. R.; Kaliannan, P.; Thamotharan, S. 4-Amino-(1-Carboxymethyl)Pyridinium Chloride. *Acta Crystallogr., Sect. E: Struct. Rep. Online* **2006**, *62*, o3389−o3390.

(361) Pécaut, J.; Lévy, J. P.; Masse, R. Structural Evidence in 2-Amino-5-Nitropyridinium Halides (Cl-, Br-) of Herringbone Motifs Favourable to Efficient Quadratic Non-Linear Optical Properties. *J. Mater. Chem.* **1993**, *3*, 999−1003.

(362) Ibanez, A.; Levy, J. P.; Mouget, C.; Prieur, E. Crystal Growth of a Promising Nonlinear Optical Material: 2-Amino-5-Nitropyridinium Chloride. *J. Solid State Chem.* **1997**, *129*, 22−29.

(363) Chen, T.; Sun, Z.; Liu, X.; Wang, J.; Zhou, Y.; Ji, C.; Zhang, S.; Li, L.; Chen, Z. N.; Luo, J. Strong Enhancement of Second Harmonic Generation in Nonlinear Optical Crystals: 2-Amino-3-Nitropyridinium Halides (Cl, Br, I). *J. Mater. Chem. C* **2014**, *2*, 8723−8728.

(364) Janczak, J.; Perpétuo, G. J. Supramolecular Aggregation in New Crystals with Nonlinear Optical Properties: 2-Aminophenol-HClO4, 3-Aminophenol-HClO4 and 4-Aminophenol-HClO4. *Solid State Sci.* **2009**, *11*, 1576−1581.

(365) Grigoriev, M. S.; German, K. E.; Maruk, A. Y. Morpholinium Perchlorate. *Acta Crystallogr., Sect. E: Struct. Rep. Online* **2008**, *64*, o390−o390.

(366) Głowiak, T.; Debrus, S.; May, M.; Barnes, A. J.; Ratajczak, H. New Molecular Crystals with Nonlinear Optical Properties: 3-Aminophenol-H3PO4 and 4-Aminophenol-H3PO4. *J. Mol. Struct.* **2001**, *596*, 77−82.

(367) Fang, Y.-X.; Huang, H.-R.; Du, Z.-Y.; Huang, B.-H.; Zhang, K. 5-Hydroxy-1-Methyl-3,4-Dihydro-2 H -Pyrrolium Hydrogensulfate. *Acta Crystallogr., Sect. E: Struct. Rep. Online* **2008**, *64*, o1622−o1622.

(368) André, V.; Duarte, M. T.; Braga, D.; Grepioni, F. Polymorphic Ammonium Salts of the Antibiotic 4-Aminosalicylic Acid. *Cryst. Growth Des.* **2012**, *12*, 3082−3090.

(369) Berking, B.; Craven, B. M. The Crystal Structure of Sodium 5,5-Diethylbarbiturate (Sodium Barbital). *Acta Crystallogr., Sect. B: Struct. Crystallogr. Cryst. Chem.* **1971**, *27*, 1107−1115.

(370) Ma, D.-S.; Liu, P.-J.; Zhang, S.; Hou, G.-F. 2-(4-Chlorophenyl)-Acetamide. *Acta Crystallogr., Sect. E: Struct. Rep. Online* **2011**, *67*, o3261−o3261.

(371) Shi, Y.-B.; Xia, S.; He, F.-F.; Wang, H.-B. Methyl 2-Amino-5-Chlorobenzoate. *Acta Crystallogr., Sect. E: Struct. Rep. Online* **2010**, *66*, o3025−o3025.

(372) Latosińska, J. N.; Latosińska, M.; Tomczak, M. A.; Seliger, J.; Žagar, V.; Maurin, J. K. Conformations and Intermolecular Interactions Pattern in Solid Chloroxylenol and Triclosan (API of Anti-Infective Agents and Drugs). A 35Cl NQR, 1H- 14aN NQDR, X-Ray and DFT/QTAIM Study. *Magn. Reson. Chem.* **2012**, *50*, 89−105.

(373) Lennartson, A.; Hedström, A.; Hakansson, M. Spontaneous Generation of Chirality in Simple Diaryl Ethers. *Chirality* **2015**, *27*, 425−429.

(374) Moribe, K.; Tsuchiya, M.; Tozuka, Y.; Yamaguchi, K.; Oguchi, T.; Yamamoto, K. Equimolar Complex Formation of Urea or Thiourea with 2-Alkoxy-Benzamides: Structural Factors Required for the Equimolar Complex Formation. *J. Inclusion Phenom. Mol. Recognit. Chem.* **2006**, *54*, 9−16.

(375) Cockcroft, J. K.; Buanz, A. B. M.; Ntantou, A.; Price, L. S.; Tocher, D. A.; Vickers, M.; Lancaster, R. W. Polymorphism in 2-Chlorobenzamide: Run of the Mill or Not? *Cryst. Growth Des.* **2016**, *16*, 6144−6147.

(376) Ali, S.; Hameed, S.; Luqman, A.; Akhtar, T.; Parvez, M. 4-Methoxybenzenecarbothioamide. *Acta Crystallogr., Sect. E: Struct. Rep. Online* **2010**, *66*, o1272−o1272.

(377) Betz, R.; Britten-Kelly, M.; McCleland, C.; Hosten, E. Refinement of the Crystal Structure of 1-Chloromethyl-Nitrobenzene, C 7H 6ClNO 2, at 200 K. *Z. Kristallogr. - New Cryst. Struct.* **2011**, *226*, 583−584.

(378) Hamzaoui, F.; Baert, F.; Wojcik, G. Electron-Density Study of m-Nitrophenol in the Orthorhombic Structure. *Acta Crystallogr., Sect. B: Struct. Sci.* **1996**, *52*, 159−164.

(379) Wójcik, G.; Holband, J.; Szymczak, J. J.; Roszak, S.; Leszczynski, J. Interactions in Polymorphic Crystals of M-Nitrophenol as Studied by Variable-Temperature X-Ray Diffraction and Quantum Chemical Calculations. *Cryst. Growth Des.* **2006**, *6*, 274−282.

(380) Aranburu Leiva, A. I.; Benjamin, S. L.; Langley, S. K.; Mewis, R. E. Crystal Structure of 2,4-Di-Tert-Butyl-6-(Hydroxymethyl)Phenol. *Acta Crystallogr. Sect. E Crystallogr. Commun.* **2016**, *72*, 1614−1617.

(381) Czapik, A.; Nitka, A.; Gdaniec, M. 5-Amino-1-Naphthol. *Acta Crystallogr., Sect. E: Struct. Rep. Online* **2009**, *65*, o2964−o2964.

(382) Rozycka-Sokolowska, E.; Marciniak, B. 5-Amino-1-Naphthol: Two-Dimensional Sheets Built up from R 4 4 (18) Rings Formed by O—H···N, N—H···O and π-π Interactions. *Acta Crystallogr., Sect. C: Cryst. Struct. Commun.* **2009**, *65*, o565−o568.

(383) Betz, R.; Gerber, T.; Hosten, E. (3-Aminophenyl)Methanol. *Acta Crystallogr., Sect. E: Struct. Rep. Online* **2011**, *67*, o2118−o2118.

(384) Banu, A.; Golzar Hossain, G. M. A New Polymorph of Sulfanilic Acid Monohydrate. *Acta Crystallogr., Sect. E: Struct. Rep. Online* **2006**, *62*, o2252−o2253.

(385) Kumarasamy, E.; Raghunathan, R.; Sibi, M. P.; Sivaguru, J. Nonbiaryl and Heterobiaryl Atropisomers: Molecular Templates with Promise for Atropselective Chemical Transformations. *Chem. Rev.* **2015**, *115*, 11239−11300.

(386) Yathirajan, H. S.; Nagaraj, B.; Gaonkar, S. L.; Narasegowda, R. S.; Prabhuswamy, B.; Bolte, M. 5-Amino-3 H -Isobenzofuran-1-One (5-Aminophthalide). *Acta Crystallogr., Sect. E: Struct. Rep. Online* **2005**, *61*, o343−o344.

(387) Maliha, B.; Hussain, I.; Tahir, M. N.; Tariq, M. I.; Siddiqui, H. L. 1-Oxoisoindoline-2-Carboxamide. *Acta Crystallogr., Sect. E: Struct. Rep. Online* **2008**, *64*, o626−o626.

(388) Qachchachi, F. Z.; Kandri Rodi, Y.; Haoudi, A.; Essassi, E. M.; Capet, F.; Zouihri, H. 1-Propyl-1 H -Indole-2,3-Dione. *IUCrData* **2016**, *1*, No. x160609.

(389) Glidewell, C.; Low, J. N.; Skakle, J. M. S.; Wardell, J. L. Isomeric Nitrophthalimides: Sheets Built from N—H···O and C—H···O Hydrogen Bonds. *Acta Crystallogr., Sect. C: Cryst. Struct. Commun.* **2004**, *60*, o872−o875.

(390) Quesada-Moreno, M. M.; Cruz-Cabeza, A. J.; Avilés-Moreno, J. R.; Cabildo, P.; Claramunt, R. M.; Alkorta, I.; Elguero, J.; Zúñiga, F. J.; López-González, J. J. The Curious Case of 2-Propyl-1H-Benzimidazole in the Solid State: An Experimental and Theoretical Study. *J. Phys. Chem. A* **2017**, *121*, 5665−5674.

(391) Zuniga, F. J.; Cruz-Cabeza, A. J.; Aretxabaleta, X. M.; De La Pinta, N.; Breczewski, T.; Quesada-Moreno, M. M.; Avilés-Moreno, J. R.; López-González, J. J.; Claramunt, R. M.; Elguero, J. Conformational Aspects of Polymorphs and Phases of 2-Propyl-1H-Benzimidazole. *IUCrJ* **2018**, *5*, 706−715.

(392) Cabildo, P.; Claramunt, R. M.; López, C.; García, M. Á.; Pérez-Torralba, M.; Pinilla, E.; Torres, M. R.; Alkorta, I.; Elguero, J. Crystal and Molecular Structure of Three Biologically Active Nitroindazoles. *J. Mol. Struct.* **2011**, *985*, 75−81.

(393) Boulhaoua, M.; El Hafi, M.; Benchidmi, M.; Essassi, E. M.; Mague, J. T. 1-Ethyl-5-Nitro-1 H -Indazole. *IUCrData* **2016**, *1*, No. x160567.

(394) Groth, P.; Josephson, S.; Vallén, S.; Hedman, K.; Leander, K.; Swahn, C.-G. Crystal Structure of Some Benzoxazoline Derivatives. *Acta Chem. Scand.* **1973**, *27*, 945−969.

(395) Wang, X.; Yang, J.-X.; You, C.; Tan, X.; Lin, Q. 2-(3-Oxo-2,3-Dihydro-1,2-Benzothiazol-2-Yl)Acetic Acid. *Acta Crystallogr., Sect. E: Struct. Rep. Online* **2011**, *67*, o3295−o3295.

(396) Saha, B. K.; Nangia, A.; Nicoud, J. F. Using Halogen···halogen Interactions to Direct Noncentrosymmetric Crystal Packing in Dipolar Organic Molecules. *Cryst. Growth Des.* **2006**, *6*, 1278−1281.

(397) Gao, S.; Zhang, Z.-Y.; Huo, L.-H.; Zhao, J.-G.; Zain, S. M.; Ng, S. W. (4-Oxo-1,4-Dihydropyridin-1-Yl)Acetic Acid. *Acta Crystallogr., Sect. E: Struct. Rep. Online* **2004**, *60*, o1006–o1008.

(398) Braga, D.; Maini, L.; Fagnano, C.; Taddei, P.; Chierotti, M. R.; Gobetto, R. Polymorphism in Crystalline Cinchomeronic Acid. *Chem. - Eur. J.* **2007**, *13*, 1222–1230.

(399) Sievert, M.; Dienelt, R.; Bock, H. Phenyl 2-Pyridyl Ketone at 150 K. *Acta Crystallogr., Sect. C: Cryst. Struct. Commun.* **1998**, *54*, 674–676.

(400) Dunne, S. J.; von Nagy-Felsobuki, E. I.; MacKay, M. F. 4,4'-Oxybispyridine and 4,4'-Seleno- Bispyridine. *Acta Crystallogr., Sect. C: Cryst. Struct. Commun.* **1996**, *C52*, 2040–2042.

(401) Deflon, V. M.; Bessler, K. E.; Kretschmar, M.; Abram, U. Tris[3-Hydroxy-2(1H)-Pyridinonato]-Komplexe von Al 3+, Cr 3+ Und Fe 3+ - Kristall- Und Molekülstrukturen von 3-Hydroxy-2(1H)-Pyridinon Und Tris[3-Hydroxy-2(1H)-Pyridinonato]Chrom(III). *Z. Anorg. Allg. Chem.* **2000**, *626*, 1545–1549.

(402) Yang, H. W.; Craven, B. M. Charge Density Study of 2-Pyridone. *Acta Crystallogr., Sect. B: Struct. Sci.* **1998**, *54*, 912–920.

(403) Öztürk Yildirim, S.; Butcher, R. J.; Simsek, R.; El-Khouly, A.; Safak, C. 2,2,7,7-Tetramethyl-1,2,3,4,5,6,7,8-Octahydroacridine-1,8-Dione. *Acta Crystallogr., Sect. E: Struct. Rep. Online* **2013**, *69*, o88–o89.

(404) Jones, P. G N -Hydroxysuccinimide. *Acta Crystallogr., Sect. E: Struct. Rep. Online* **2003**, *59*, o1951–o1952.

(405) Bröring, M.; Brégier, F.; Kleeberg, C. 3,4-Diethyl-2,5-Dihydro-1 H -Pyrrole-2,5-Dione. *Acta Crystallogr., Sect. C: Cryst. Struct. Commun.* **2007**, *63*, o225–o227.

(406) Yadav, C. L.; Rajput, G.; Bisht, K. K.; Drew, M. G. B.; Singh, N. Spontaneous Resolution upon Crystallization and Preferential Induction of Chirality in a Discrete Tetrahedral Zinc(II) Complex Comprised of Achiral Precursors. *Inorg. Chem.* **2019**, *58*, 14449–14456.

(407) Lennartson, A.; Håkansson, M. Total Spontaneous Resolution of Five-Coordinate Complexes. *Angew. Chem., Int. Ed.* **2009**, *48*, 5869–5871.

(408) Lennartson, A.; Håkansson, M. Absolute Asymmetric Synthesis of Five-Coordinate Complexes. *New J. Chem.* **2015**, *39*, 5936–5943.

(409) Cheung, E. Y.; Fujii, K.; Guo, F.; Harris, K. D. M.; Hasebe, S.; Kuroda, R. Structural Chemistry of a New Chiral Anhydrous Phase of Ru(Bipy) 3(ClO4)2 Established from Powder X-Ray Diffraction Analysis. *Cryst. Growth Des.* **2011**, *11*, 3313–3317.

(410) Mentes, A.; Singh, K. Tris(2, 2'-Bipyridine-κ 2 N, N ')Cobalt(II) Bis(Hexafluoridophosphate). *Acta Crystallogr., Sect. E: Struct. Rep. Online* **2013**, *69*, m58–m58.

(411) Ou, G. C.; Li, Z. Z.; Yuan, L.; Yuan, X. Y. Hydrogen Bond Induced Chiral Symmetry Breaking in the Crystallization of Nickel(II) Complexes. *Transition Met. Chem.* **2014**, *39*, 393–398.

(412) Saritha, A.; Raju, B.; Ramachary, M.; Raghavaiah, P.; Hussain, K. A. Synthesis, Crystal Structure and Characterization of Chiral, Three-Dimensional Anhydrous Potassium Tris(Oxalato)Ferrate(III). *Phys. B* **2012**, *407*, 4208–4213.

(413) Asakura, K.; Kobayashi, K.; Mizusawa, Y.; Ozawa, T.; Osanai, S.; Yoshikawa, S. Generation of an Optically Active Octahedral Cobalt Complex by a Chiral Autocatalysis. *Phys. D* **1995**, *84*, 72–78.

(414) Asakura, K.; Kondepudi, D. K.; Martin, R. Mechanism of Chiral Asymmetry Generation by Chiral Autocatalysis in the Preparation of Chiral Octahedral Cobalt Complex. *Chirality* **1998**, *10*, 343–348.

(415) Guo, F.; Casadesus, M.; Cheung, E. Y.; Coogan, M. P.; Harris, K. D. M. On the Spontaneous Induction of Chirality in the Preparation of Werner's Complex Cis-[CoBr(NH3)(En)2]Br2. *Chem. Commun.* **2006**, No. 17, 1854–1856.

(416) Bučar, D. K.; Lancaster, R. W.; Bernstein, J. Disappearing Polymorphs Revisited. *Angew. Chem., Int. Ed.* **2015**, *54*, 6972–6993.

(417) Fischer, A.; Pagni, R. M.; Compton, R. N.; Kondepudi, D. Laser Induced Crystallization. In *Nanoclusters: A Bridge across Disciplines*; Science and Technology of Atomic, Molecular, Condensed Matter & Biological Systems, Vol. *1*; Jena, P., Castleman, A. W., Jr., Eds.; Elsevier B.V.: Amsterdam, The Netherlands, 2010; pp 343–364.

(418) Dunitz, J. D.; Bernstein, J. Disappearing Polymorphs. *Acc. Chem. Res.* **1995**, *28*, 193–200.

(419) Cruz-Cabeza, A. J.; Reutzel-Edens, S. M.; Bernstein, J. Facts and Fictions about Polymorphism. *Chem. Soc. Rev.* **2015**, *44*, 8619–8635.

(420) Bond, A. D. Polymorphism in Molecular Crystals. *Curr. Opin. Solid State Mater. Sci.* **2009**, *13*, 91–97.

(421) Quesada-Moreno, M. M.; Avilés-Moreno, J. R.; López-González, J. J.; Zúñiga, F. J.; María, D. S.; Claramunt, R. M.; Reviriego, F.; Alkorta, I.; Elguero, J. The Synergy of Different Solid-State Techniques to Elucidate the Supramolecular Assembly of Two 1: H -Benzotriazole Polymorphs. *Phys. Chem. Chem. Phys.* **2019**, *21*, 19879–19889.

(422) Mayo, R. A.; Sullivan, D. J.; Fillion, T. A. P.; Kycia, S. W.; Soldatov, D. V.; Preuss, K. E. Reversible Crystal-to-Crystal Chiral Resolution: Making/Breaking Non-Bonding SO Interactions. *Chem. Commun.* **2017**, *53*, 3964–3966.

(423) Rajbongshi, B. K.; Nair, N. N.; Nethaji, M.; Ramanathan, G. Segregation into Chiral Enantiomeric Conformations of an Achiral Molecule by Concomitant Polymorphism. *Cryst. Growth Des.* **2012**, *12*, 1823–1829.

(424) Pogoda, D.; Janczak, J.; Pawlak, S.; Zaworotko, M.; Videnova-Adrabinska, V. Tautomeric Polymorphism of the Neuroactive Inhibitor Kynurenic Acid. *Acta Crystallogr., Sect. C: Struct. Chem.* **2019**, *75*, 793–805.

(425) Thomas, S. P.; Grosjean, A.; Flematti, G. R.; Karton, A.; Sobolev, A. N.; Edwards, A. J.; Piltz, R. O.; Iversen, B. B.; Koutsantonis, G. A.; Spackman, M. A. Investigation of an Unusual Crystal Habit of Hydrochlorothiazide Reveals Large Polar Enantiopure Domains and a Possible Crystal Nucleation Mechanism. *Angew. Chem., Int. Ed.* **2019**, *58*, 10255–10259.

(426) Guerra, D.; Gómez, L. A.; Restrepo, A.; David, J. New Stable Phases of Glycine Crystals. *Chem. Phys.* **2020**, *530*, 110645.

(427) Myerson, A. S.; Erdemir, D.; Lee, A. Y. Nucleation of Crystals from Solution: Classical and Two-Step Models. *Acc. Chem. Res.* **2009**, *42*, 621–629.

(428) Wu, Z.; Yang, S.; Wu, W. Application of Temperature Cycling for Crystal Quality Control during Crystallization. *CrystEngComm* **2016**, *18*, 2222–2238.

(429) Jiang, Q.; Shtukenberg, A. G.; Ward, M. D.; Hu, C. Non-Topotactic Phase Transformations in Single Crystals of β-Glycine. *Cryst. Growth Des.* **2015**, *15*, 2568–2573.

(430) Ishikawa, K.; Tanaka, M.; Suzuki, T.; Sekine, A.; Kawasaki, T.; Soai, K.; Shiro, M.; Lahav, M.; Asahi, T. Absolute Chirality of the γ-Polymorph of Glycine: Correlation of the Absolute Structure with the Optical Rotation. *Chem. Commun.* **2012**, *48*, 6031–6033.

(431) Tarasevych, A. V.; Sorochinsky, A. E.; Kukhar, V. P.; Toupet, L.; Crassous, J.; Guillemin, J. C. Attrition-Induced Spontaneous Chiral Amplification of the γ Polymorphic Modification of Glycine. *CrystEngComm* **2015**, *17*, 1513–1517.

(432) Kawasaki, T.; Hakoda, Y.; Mineki, H.; Suzuki, K.; Soai, K. Generation of Absolute Controlled Crystal Chirality by the Removal of Crystal Water from Achiral Crystal of Nucleobase Cytosine. *J. Am. Chem. Soc.* **2010**, *132*, 2874–2875.

(433) Mineki, H.; Kaimori, Y.; Kawasaki, T.; Matsumoto, A.; Soai, K. Enantiodivergent Formation of a Chiral Cytosine Crystal by Removal of Crystal Water from an Achiral Monohydrate Crystal under Reduced Pressure. *Tetrahedron: Asymmetry* **2013**, *24*, 1365–1367.

(434) Otero-De-La-Roza, A.; Hein, J. E.; Johnson, E. R. Reevaluating the Stability and Prevalence of Conglomerates: Implications for Preferential Crystallization. *Cryst. Growth Des.* **2016**, *16*, 6055–6059.

(435) Whittleton, S. R.; Otero-De-La-Roza, A.; Johnson, E. R. Exchange-Hole Dipole Dispersion Model for Accurate Energy Ranking in Molecular Crystal Structure Prediction. *J. Chem. Theory Comput.* **2017**, *13*, 441–450.

(436) Nyman, J.; Yu, L.; Reutzel-Edens, S. M. Accuracy and Reproducibility in Crystal Structure Prediction: The Curious Case of ROY. *CrystEngComm* **2019**, *21*, 2080–2088.

(437) Ryan, K.; Lengyel, J.; Shatruk, M. Crystal Structure Prediction via Deep Learning. *J. Am. Chem. Soc.* **2018**, *140*, 10158–10168.

(438) Öhrström, L. Let's Talk about MOFs—Topology and Terminology of Metal-Organic Frameworks and Why We Need Them. *Crystals* **2015**, *5*, 154−162.

(439) Morris, R. E.; Bu, X. Induction of Chiral Porous Solids Containing Only Achiral Building Blocks. *Nat. Chem.* **2010**, *2*, 353−361.

(440) Li, M.; Li, D.; O'Keeffe, M.; Yaghi, O. M. Topological Analysis of Metal-Organic Frameworks with Polytopic Linkers and/or Multiple Building Units and the Minimal Transitivity Principle. *Chem. Rev.* **2014**, *114*, 1343−1370.

(441) Tao, Y.; Yang, C.; Fang, H.; Bian, H. D.; Xu, X. L.; Huang, F. P. Spontaneous Resolution and Structure Transformation of NiII Metal-Organic Frameworks from an Achiral Precursor. *Cryst. Growth Des.* **2019**, *19*, 3358−3364.

(442) Verma, A.; Tomar, K.; Bharadwaj, P. K. Chiral Cadmium(II) Metal-Organic Framework from an Achiral Ligand by Spontaneous Resolution: An Efficient Heterogeneous Catalyst for the Strecker Reaction of Ketones. *Inorg. Chem.* **2017**, *56*, 13629−13633.

(443) Rao, P. C.; Chaudhary, S. P.; Kuznetsov, D.; Mandal, S. Transformation of One-Dimensional Achiral Structure to Three-Dimensional Chiral Structure: Mechanistic Study and Catalytic Activities of Chiral Structure. *Inorg. Chem.* **2016**, *55*, 12669−12674.

(444) Liu, Y.; Xuan, W.; Cui, Y. Engineering Homochiral Metal-Organic Frameworks for Heterogeneous Asymmetric Catalysis and Enantioselective Separation. *Adv. Mater.* **2010**, *22*, 4112−4135.

(445) Bisht, K. K.; Parmar, B.; Rachuri, Y.; Kathalikattil, A. C.; Suresh, E. Progress in the Synthetic and Functional Aspects of Chiral Metal-Organic Frameworks. *CrystEngComm* **2015**, *17*, 5341−5356.

(446) Park, K. H.; Noh, T. H.; Shim, Y. B.; Jung, O. S. Construction of Right-Handed-, Left-Handed-, and Racemic Helical Coordination Polymers. Enantioselective Recognition Using Chiral Helical Crystals. *Chem. Commun.* **2013**, *49*, 4000−4002.

(447) Yang, M. X.; Zhou, M. J.; Cao, J. P.; Han, Y. M.; Hong, Y. L.; Xu, Y. Application of Temperature-Controlled Chiral Hybrid Structures Constructed from Copper(Ii)-Monosubstituted Keggin Polyoxoanions and Copper(Ii)-Organoamine Complexes in Enantioselective Sensing of Tartaric Acid. *RSC Adv.* **2020**, *10*, 13759−13765.

(448) Qin, L.; Hu, J. S.; Zhang, M. D.; Guo, Z. J.; Zheng, H. G. Structure-Property Relationship of Homochiral and Achiral Supramolecular Isomers Obtained by One-Pot Synthesis. *Chem. Commun.* **2012**, *48*, 10757−10759.

(449) Chen, N.; Li, M. X.; Yang, P.; He, X.; Shao, M.; Zhu, S. R. Chiral Coordination Polymers with SHG-Active and Luminescence: An Unusual Homochiral 3D MOF Constructed from Achiral Components. *Cryst. Growth Des.* **2013**, *13*, 2650−2660.

(450) Liu, Y.; Xuan, W.; Zhang, H.; Cui, Y. Chirality-and Threefold-Symmetry-Directed Assembly of Homochiral Octupolar Metal - Organoboron Frameworks. *Inorg. Chem.* **2009**, *48*, 10018−10023.

(451) Zhang, M. D.; Li, Y. L.; Shi, Z. Z.; Zheng, H. G.; Ma, J. A Pair of 3D Enantiotopic Zinc(II) Complexes Based on Two Asymmetric Achiral Ligands. *Dalt. Trans* **2017**, *46*, 14779−14784.

(452) Yu, Y. D.; Luo, C.; Liu, B. Y.; Huang, X. C.; Li, D. Spontaneous Symmetry Breaking of Co(II) Metal-Organic Frameworks from Achiral Precursors via Asymmetrical Crystallization. *Chem. Commun.* **2015**, *51*, 14489−14492.

(453) Liu, W.; Bao, X.; Mao, L. L.; Tucek, J.; Zboril, R.; Liu, J. L.; Guo, F. S.; Ni, Z. P.; Tong, M. L. A Chiral Spin Crossover Metal-;Organic Framework. *Chem. Commun.* **2014**, *50*, 4059−4061.

(454) Li, Y. W.; Tao, Y.; Wang, L. F.; Hu, T. L.; Bu, X. H. New Chiral Coordination Polymers Constructed from Well Elaborated Achiral and Chiral Ligands. *RSC Adv.* **2012**, *2*, 4348−4352.

(455) Han, Y.-H.; Liu, Y.-C.; Xing, X.-S.; Tian, C.-B.; Lin, P.; Du, S.-W. Chiral Template Induced Homochiral MOFs Built from Achiral Components: SHG Enhancement and Enantioselective Sensing of Chiral Alkamines by Ion-Exchange. *Chem. Commun.* **2015**, *51*, 14481−14484.

(456) Goswami, A.; Bala, S.; Pachfule, P.; Mondal, R. Comprehensive Study on Mutual Interplay of Multiple V-Shaped Ligands on the Helical Nature of a Series of Coordination Polymers and Their Properties. *Cryst. Growth Des.* **2013**, *13*, 5487−5498.

(457) Gao, C. Y.; Wang, F.; Tian, H. R.; Li, L. J.; Zhang, J.; Sun, Z. M. Particular Handedness Excess through Symmetry-Breaking Crystallization of a 3D Cobalt Phosphonate. *Inorg. Chem.* **2016**, *55*, 537−539.

(458) Gupta, V.; Mandal, S. K. Design and Construction of a Chiral Cd(II)-MOF from Achiral Precursors: Synthesis, Crystal Structure and Catalytic Activity toward C-C and C-N Bond Forming Reactions. *Inorg. Chem.* **2019**, *58*, 3219−3226.

(459) Du, M. X.; Wang, M. S.; Guo, G. C. Solvent-Dependent Chirality Transformation: Construction of a Helical Homochiral Silver(I) MOF Using the V-Shaped Ligand 3-Aminobenzoate. *Inorg. Chem. Commun.* **2018**, *92*, 22−26.

(460) Gong, C.; Guo, H.; Zeng, X.; Xu, H.; Zeng, Q.; Zhang, J.; Xie, J. Flexible and Rigid Dicarboxylic Acids Enable the Assembly of Achiral and Chiral 3D Co(Ii) Metal-Organic Frameworks. *Dalt. Trans.* **2018**, *47*, 6917−6923.

(461) Crassous, J. Chiral Transfer in Coordination Complexes: Towards Molecular Materials. *Chem. Soc. Rev.* **2009**, *38*, 830−845.

(462) An, G.; Yan, P.; Sun, J.; Li, Y.; Yao, X.; Li, G. The Racemate-to-Homochiral Approach to Crystal Engineering via Chiral Symmetry Breaking. *CrystEngComm* **2015**, *17*, 4421−4433.

(463) Liu, M.; Zhang, L.; Wang, T. Supramolecular Chirality in Self-Assembled Systems. *Chem. Rev.* **2015**, *115*, 7304−7397.

(464) Ma, W.; Xu, L.; De Moura, A. F.; Wu, X.; Kuang, H.; Xu, C.; Kotov, N. A. Chiral Inorganic Nanostructures. *Chem. Rev.* **2017**, *117*, 8041−8093.

(465) Wei, Y.-S.; Zhang, M.; Zou, R.; Xu, Q. Metal-Organic Framework-Based Catalysts with Single Metal Sites. *Chem. Rev.* **2020**, *120*, 12089−12174.

(466) Tong, X. L.; Hu, T. L.; Zhao, J. P.; Wang, Y. K.; Zhang, H.; Bu, X. H. Chiral Magnetic Metal-Organic Frameworks of MnII with Achiral Tetrazolate-Based Ligands by Spontaneous Resolution. *Chem. Commun.* **2010**, *46*, 8543−8545.

(467) Duan, X.; Meng, Q.; Su, Y.; Li, Y.; Duan, C.; Ren, X.; Lu, C. Multifunctional Polythreading Coordination Polymers: Spontaneous Resolution, Nonlinear-Optic, and Ferroelectric Properties. *Chem. - Eur. J.* **2011**, *17*, 9936−9943.

(468) Bisht, K. K.; Suresh, E. Spontaneous Resolution of a Mixed-Ligand Nickel(II) Coordination Polymer with Achiral Precursors. *Inorg. Chem.* **2012**, *51*, 9577−9579.

(469) Wu, S.-T.; Wu, Y.-R.; Kang, Q.-Q.; Zhang, H.; Long, L.-S.; Zheng, Z.; Huang, R.-B.; Zheng, L.-S. Chiral Symmetry Breaking by Chemically Manipulating Statistical Fluctuation in Crystallization. *Angew. Chem., Int. Ed.* **2007**, *46*, 8475−8479.

(470) Dong, H.; Hu, H.; Liu, Y.; Zhong, J.; Zhang, G.; Zhao, F.; Sun, X.; Li, Y.; Kang, Z. Obtaining Chiral Metal-Organic Frameworks via a Prochirality Synthetic Strategy with Achiral Ligands Step-by-Step. *Inorg. Chem.* **2014**, *53*, 3434−3440.

(471) Zuo, T.; Luo, D.; Huang, Y. L.; Li, Y. Y.; Zhou, X. P.; Li, D. Chiral 3D Coordination Polymers Consisting of Achiral Terpyridyl Precursors: From Spontaneous Resolution to Enantioenriched Induction. *Chem. - Eur. J.* **2020**, *26*, 1936−1940.

(472) Liu, W. T.; Ou, Y. C.; Lin, Z. J.; Tong, M. L. Spontaneous Resolution of Four-Coordinate Zn(Ii) Complexes in the Formation of Three-Dimensional Metal-Organic Frameworks. *CrystEngComm* **2010**, *12*, 3487−3489.

(473) Liu, Q. Y.; Wang, Y. L.; Zhang, N.; Jiang, Y. L.; Wei, J. J.; Luo, F. Spontaneous Resolution in the Ionothermal Synthesis of Homochiral Zn(II) Metal-Organic Frameworks with (10,3)- a Topology Constructed from Achiral 5-Sulfoisophthalate. *Cryst. Growth Des.* **2011**, *11*, 3717−3720.

(474) Bejan, D.; Bahrin, L. G.; Shova, S.; Sardaru, M.; Clima, L.; Nicolescu, A.; Marangoci, N.; Lozan, V.; Janiak, C. Spontaneous Resolution of Non-Centrosymmetric Coordination Polymers of Zinc(II) with Achiral Imidazole-Biphenyl-Carboxylate Ligands. *Inorg. Chim. Acta* **2018**, *482*, 275−283.

(475) Anthony, S. P.; Wang, L.; Varughese, S.; Draper, S. M. A Structurally Versatile Coordination Polymer: Demonstrating Sponta-

neous Resolution, Conformational Polymorphism and Gel Formation. *CrystEngComm* **2013**, *15*, 6602−6605.

(476) Durá, G.; Carrión, M. C.; Jalón, F. A.; Rodríguez, A. M.; Manzano, B. R. Self-Assembly of Silver(I) and Ditopic Heteroscorpionate Ligands. Spontaneous Chiral Resolution in Helices and Sequence Isomerism in Coordination Polymers. *Cryst. Growth Des.* **2013**, *13*, 3275−3282.

(477) Yao, R. X.; Cui, X.; Wang, J.; Zhang, X. M. A Homochiral Magnet Based on D3 Symmetric [(NaO3)Co3] Clusters: From Spontaneous Resolution to Absolute Chiral Induction. *Chem. Commun.* **2015**, *51*, 5108−5111.

(478) Bisht, K. K.; Suresh, E. Spontaneous Resolution to Absolute Chiral Induction: Pseudo-Kagomé Type Homochiral Zn(II)/Co(II) Coordination Polymers with Achiral Precursors. *J. Am. Chem. Soc.* **2013**, *135*, 15690−15693.

(479) Song, B. Q.; Chen, D. Q.; Ji, Z.; Tang, J.; Wang, X. L.; Zang, H. Y.; Su, Z. M. Control of Bulk Homochirality and Proton Conductivity in Isostructural Chiral Metal-Organic Frameworks. *Chem. Commun.* **2017**, *53*, 1892−1895.

(480) Yu, J.-T.; Shi, Y.-Y.; Sun, J.; Lin, J.; Huang, Z.-T.; Zheng, Q.-Y. Spontaneous Chiral Resolution Directed by Symmetry Restriction and π-π Interaction. *Sci. Rep.* **2013**, *3*, 2947.

(481) Tripathi, S.; Srirambalaji, R.; Singh, N.; Anantharaman, G. Chiral and Achiral Helical Coordination Polymers of Zinc and Cadmium from Achiral 2,6-Bis(Imidazol-1-Yl)Pyridine: Solvent Effect and Spontaneous Resolution. *J. Chem. Sci.* **2014**, *126*, 1423−1431.

(482) Yuan, S.; Deng, Y. K.; Xuan, W. M.; Wang, X. P.; Wang, S. N.; Dou, J. M.; Sun, D. Spontaneous Chiral Resolution of a 3D (3,12)-Connected MOF with an Unprecedented Ttt Topology Consisting of Cubic [Cd4(M3- OH)4] Clusters and Propeller-like Ligands. *CrystEngComm* **2014**, *16*, 3829−3833.

(483) Song, B. Q.; Qin, C.; Zhang, Y. T.; Wu, X. S.; Yang, L.; Shao, K. Z.; Su, Z. M. Spontaneous Chiral Resolution of a Rare 3D Self-Penetration Coordination Polymer for Sensitive Aqueous-Phase Detection of Picric Acid. *Dalt. Trans.* **2015**, *44*, 18386−18394.

(484) Kushida, Y.; Sawato, T.; Shigeno, M.; Saito, N.; Yamaguchi, M. Deterministic and Stochastic Chiral Symmetry Breaking Exhibited by Racemic Aminomethylenehelicene Oligomers. *Chem. - Eur. J.* **2017**, *23*, 327−333.

(485) Zheng, W.; Wei, Y.; Xiao, X.; Wu, K. Spontaneous Asymmetric Crystallization of a Quartz-Type Framework from Achiral Precursors. *Dalt. Trans.* **2012**, *41*, 3138−3140.

(486) He, X.; Fang, K.; Guo, X. H.; Han, J.; Lu, X. P.; Li, M. X. A Homochiral Cu(I) Coordination Polymer Based on Achiral Precursors and Its Photocatalytic Properties. *Dalt. Trans.* **2015**, *44*, 13545−13549.

(487) Luo, X.; Cao, Y.; Wang, T.; Li, G.; Li, J.; Yang, Y.; Xu, Z.; Zhang, J.; Huo, Q.; Liu, Y.; Eddaoudi, M. Host-Guest Chirality Interplay: A Mutually Induced Formation of a Chiral ZMOF and Its Double-Helix Polymer Guests. *J. Am. Chem. Soc.* **2016**, *138*, 786−789.

(488) Deng, S. Q.; Mo, X. J.; Cai, S. L.; Zhang, W. G.; Zheng, S. R. Homochiral Cu(I) Coordination Polymers Based on a Double-Stranded Helical Building Block from Achiral Ligands: Symmetry-Breaking Crystallization, Photophysical and Photocatalytic Properties. *Inorg. Chem.* **2019**, *58*, 14660−14666.

(489) Jin, H. G.; Hong, X. J.; Tan, H. C.; Wei, Q.; Lin, X. M.; Cai, Y. P. Achiral Aromatic Solvent-Induced Assembly of 3-D Homochiral Porous 3d-4f Heterometallic-Organic Frameworks Based on Isonicotinic Acid. *CrystEngComm* **2017**, *19*, 5956−5959.

(490) Ding, S.; Gao, Y.; Ji, Y.; Wang, Y.; Liu, Z. Homochiral Crystallization of Single-Stranded Helical Coordination Polymers: Generated by the Structure of Auxiliary Ligands or Spontaneous Symmetry Breaking. *CrystEngComm* **2013**, *15*, 5598−5601.

(491) Bhattacharyya, A.; Ghosh, B. N.; Herrero, S.; Rissanen, K.; Jimenez-Aparicio, R.; Chattopadhyay, S. Formation of a Novel Ferromagnetic End-to-End Cyanate Bridged Homochiral Helical Copper(II) Schiff Base Complex via Spontaneous Symmetry Breaking. *Dalt. Trans* **2015**, *44*, 493−497.

(492) Chen, S. C.; Zhang, J.; Yu, R. M.; Wu, X. Y.; Xie, Y. M.; Wang, F.; Lu, C. Z. Spontaneous Asymmetrical Crystallization of a Three-Dimensional Diamondoid Framework Material from Achiral Precursors. *Chem. Commun.* **2010**, *46*, 1449−1451.

(493) Cui, Z.; Zhou, L.; Qin, B.; Zhou, B.; Zhang, X.; Li, W.; Zhang, J. Selective Chiral Symmetry Breaking and Luminescence Sensing of a Zn(Ii) Metal-Organic Framework. *Dalt. Trans.* **2018**, *47*, 7934−7940.

(494) Yang, Q.; Chen, Z.; Hu, J.; Hao, Y.; Li, Y.; Lu, Q.; Zheng, H. A Second-Order Nonlinear Optical Material with a Hydrated Homochiral Helix Obtained via Spontaneous Symmetric Breaking Crystallization from an Achiral Ligand. *Chem. Commun.* **2013**, *49*, 3585−3587.

(495) Zhou, T. H.; Zhang, J.; Zhang, H. X.; Feng, R.; Mao, J. G. A Ligand-Conformation Driving Chiral Generation and Symmetry-Breaking Crystallization of a Zinc(II) Organoarsonate. *Chem. Commun.* **2011**, *47*, 8862−8864.

(496) Liu, C.-M.; Zhang, D.-Q.; Xiong, R.-G.; Hao, X.; Zhu, D.-B. A Homochiral Zn-Dy Heterometallic Left-Handed Helical Chain Complex without Chiral Ligands: Anion-Induced Assembly and Multifunctional Integration. *Chem. Commun.* **2018**, *54*, 13379−13382.

(497) Larpent, P.; Jouaiti, A.; Kyritsakas, N.; Hosseini, M. W. Molecular Tectonics: From a Rigid Achiral Organic Tecton to 3D Chiral Co and Fe Coordination Networks. *Chem. Commun.* **2019**, *55*, 91−94.

(498) Xue, H.; Zhou, K.; Liu, L.; Wu, D.; Hong, Z.; Chen, Q.; Jiang, F.; Yuan, D.; Zhang, J.; Hong, M. Chiral Induction in a Pcu-Derived Network from Achiral Precursors. *Chem. Commun.* **2019**, *55*, 4611−4614.

(499) Liao, W. M.; Zeng, Q.; He, Y.; Duan, J.; He, J. Two Homochiral Crystals of Anion-Directed Cu(I) and Zn(II) Helical Coordination Polymers. *J. Solid State Chem.* **2019**, *277*, 448−453.

(500) Lan, Y. Q.; Li, S. L.; Su, Z. M.; Shao, K. Z.; Ma, J. F.; Wang, X. L.; Wang, E. B. Spontaneous Resolution of a 3D Chiral Polyoxometalate-Based Polythreaded Framework Consisting of an Achiral Ligand. *Chem. Commun.* **2008**, 58−60.

(501) Kaur, A.; Hundal, G.; Hundal, M. S. Spontaneous Resolution upon Crystallization of 3D, Chiral Inorganic Networks Assembled from Achiral, Polyoxometallate Units and Metal Ions. *Cryst. Growth Des.* **2013**, *13*, 3996−4001.

(502) Yang, M.; Li, X.; Yu, J.; Zhu, J.; Liu, X.; Chen, G.; Yan, Y. LiCu2[BP2O8(OH)2]: A Chiral Open-Framework Copper Borophosphate via Spontaneous Asymmetrical Crystallization. *Dalt. Trans.* **2013**, *42*, 6298−6301.

(503) Tang, Q.; Liu, S.; Liu, Y.; Li, S.; Ma, F.; Li, J.; Wang, S.; Liu, C. Assembly and Spontaneous Resolution of the Chiral Inorganic Polyoxometalates-Based Frameworks via Helical Chains Association. *Dalt. Trans.* **2013**, *42*, 8512−8518.

(504) Li, N.; Jiang, D.; Pan, Q.; Zhao, J.; Zhang, S.; Xing, B.; Du, Y.; Zhang, Z.; Liu, S. Polyoxometalates-Based Chiral Frameworks Involving Helical Motifs Generated by Spontaneous Resolution. *J. Mol. Struct.* **2018**, *1159*, 79−82.

(505) Mateos-Timoneda, M. A.; Crego-Calama, M.; Reinhoudt, D. N. Supramolecular Chirality of Self-Assembled Systems in Solution. *Chem. Soc. Rev.* **2004**, *33*, 363−372.

(506) Amabilino, D. B. *Supramolecular Chemistry at Surfaces*; The Royal Society of Chemistry: Cambridge, U.K., 2016.

(507) Miyake, H. Supramolecular Chirality in Dynamic Coordination Chemistry. *Symmetry* **2014**, *6*, 880−895.

(508) Tschierske, C. Mirror Symmetry Breaking in Liquids and Liquid Crystals. *Liq. Cryst.* **2018**, *45*, 2221−2252.

(509) Palmans, A. R. A.; Meijer, E. W. Amplification of Chirality in Dynamic Supramolecular Aggregates. *Angew. Chem., Int. Ed.* **2007**, *46*, 8948−8968.

(510) El-Hachemi, Z.; Escudero, C.; Acosta-Reyes, F.; Casas, M. T.; Altoe, V.; Aloni, S.; Oncins, G.; Sorrenti, A.; Crusats, J.; Campos, J. L.; Ribó, J. M. Structure vs. Properties — Chirality, Optics and Shapes — in Amphiphilic Porphyrin J-Aggregates. *J. Mater. Chem. C* **2013**, *1*, 3337−3346.

(511) Shen, B.; Kim, Y.; Lee, M. Supramolecular Chiral 2D Materials and Emerging Functions. *Adv. Mater.* **2020**, *32*, 1905669.

(512) Goodby, J. W.; Mandle, R. J.; Davis, E. J.; Zhong, T.; Cowling, S. J. What Makes a Liquid Crystal? The Effect of Free Volume on Soft Matter. *Liq. Cryst.* **2015**, *42*, 593−622.

(513) Dressel, C.; Reppe, T.; Prehm, M.; Brautzsch, M.; Tschierske, C. Chiral Self-Sorting and Amplification in Isotropic Liquids of Achiral Molecules. *Nat. Chem.* **2014**, *6*, 971−977.

(514) Alaasar, M.; Poppe, S.; Dong, Q.; Liu, F.; Tschierske, C. Isothermal Chirality Switching in Liquid-Crystalline Azobenzene Compounds with Non-Polarized Light. *Angew. Chem., Int. Ed.* **2017**, *56*, 10801−10805.

(515) Fechtenkötter, A.; Tchebotareva, N.; Watson, M.; Müllen, K. Discotic Liquid Crystalline Hexabenzocoronenes Carrying Chiral and Racemic Branched Alkyl Chains: Supramolecular Engineering and Improved Synthetic Methods. *Tetrahedron* **2001**, *57*, 3769−3783.

(516) Rauch, S.; Bault, P.; Sawade, H.; Heppke, G.; Nair, G. G.; Jákli, A. Ferroelectric-Chiral–Antiferroelectric-Racemic Liquid Crystal Phase Transition of Bent-Shape Molecules. *Phys. Rev. E: Stat. Phys., Plasmas, Fluids, Relat. Interdiscip. Top.* **2002**, *66*, 21706.

(517) Tschierske, C.; Dressel, C. Mirror Symmetry Breaking in Liquids and Their Impact on the Development of Homochirality in Abiogenesis: Emerging Proto-RNA as Source of Biochirality? *Symmetry* **2020**, *12*, 1098.

(518) Nagayama, H.; Varshney, S. K.; Goto, M.; Araoka, F.; Ishikawa, K.; Prasad, V.; Takezoe, H. Spontaneous Deracemization of Disc-like Molecules in the Columnar Phase. *Angew. Chem., Int. Ed.* **2010**, *49*, 445−448.

(519) Takezoe, H. Spontaneous Achiral Symmetry Breaking in Liquid Crystalline Phases. In *Liquid Crystals*; Topics in Current Chemistry, Vol. *318*; Thschierske, C., Ed.; Springer Berlin Heidelberg: Berlin Heidelberg, Germany, 2011.

(520) Reppe, T.; Poppe, S.; Cai, X.; Cao, Y.; Liu, F.; Tschierske, C. Spontaneous Mirror Symmetry Breaking in Benzil-Based Soft Crystalline, Cubic Liquid Crystalline and Isotropic Liquid Phases. *Chem. Sci.* **2020**, *11*, 5902−5908.

(521) De Greef, T. F. A.; Smulders, M. M. J.; Wolffs, M.; Schenning, A. P. H. J.; Sijbesma, R. P.; Meijer, E. W. Supramolecular Polymerization. *Chem. Rev.* **2009**, *109*, 5687−5754.

(522) Cölfen, H.; Antonietti, M. Nonclassical Crystallization. In *Mesocrystals and Nonclassical Crystallization*; John Wiley & Sons, Ltd: Chichester, U.K., 2008; pp 73−101.

(523) Ros, M. B.; Serrano, J. L.; de la Fuente, M. R.; Folcia, C. L. Banana-Shaped Liquid Crystals: A New Field to Explore. *J. Mater. Chem.* **2005**, *15*, 5093−5098.

(524) Lehmann, A.; Alaasar, M.; Poppe, M.; Poppe, S.; Prehm, M.; Nagaraj, M.; Sreenilayam, S. P.; Panarin, Y. P.; Vij, J. K.; Tschierske, C. Stereochemical Rules Govern the Soft Self-Assembly of Achiral Compounds: Understanding the Heliconical Liquid-Crystalline Phases of Bent-Core Mesogens. *Chem. - Eur. J.* **2020**, *26*, 4714−4733.

(525) Dozov, I. On the Spontaneous Symmetry Breaking in the Mesophases of Achiral Banana-Shaped Molecules. *Europhys. Lett.* **2001**, *56*, 247−253.

(526) Würthner, F.; Kaiser, T. E.; Saha-Möller, C. R. J-Aggregates: From Serendipitous Discovery to Supramolecular Engineering of Functional Dye Materials. *Angew. Chem., Int. Ed.* **2011**, *50*, 3376−3410.

(527) Salamończyk, M.; Vaupotič, N.; Pociecha, D.; Walker, R.; Storey, J. M. D.; Imrie, C. T.; Wang, C.; Zhu, C.; Gorecka, E. Multi-Level Chirality in Liquid Crystals Formed by Achiral Molecules. *Nat. Commun.* **2019**, *10*, 1922.

(528) Schellman, J.; Jensen, H. P. Optical Spectroscopy of Oriented Molecules. *Chem. Rev.* **1987**, *87*, 1359−1399.

(529) De Napoli, M.; Nardis, S.; Paolesse, R.; Vicente, M. G. H.; Lauceri, R.; Purrello, R. Hierarchical Porphyrin Self-Assembly in Aqueous Solution. *J. Am. Chem. Soc.* **2004**, *126*, 5934−5935.

(530) Jeon, S.-W.; Kim, D.-Y.; Araoka, F.; Jeong, K.-U.; Choi, S.-W. Nanosegregated Chiral Materials with Self-Assembled Hierarchical Mesophases: Effect of Thermotropic and Photoinduced Polymorphism in Rodlike Molecules. *Chem. - Eur. J.* **2017**, *23*, 17794−17799.

(531) Barclay, T. G.; Constantopoulos, K.; Matisons, J. Nanotubes Self-Assembled from Amphiphilic Molecules via Helical Intermediates. *Chem. Rev.* **2014**, *114*, 10217−10291.

(532) Zhao, T.; Duan, P.; Liu, M. Circular Polarized Luminescence from Gelator Molecules: From Isolated Molecules to Assemblies. In *Circular Polarized Luminescence of Isolated Small Molecules*; Mori, T., Ed.; Springer: Singapore, 2020; pp 249−272.

(533) Okano, K.; Arteaga, O.; Ribó, J. M.; Yamashita, T. Emergence of Chiral Environments by Effect of Flows: The Case of an Ionic Oligomer and Congo Red Dye. *Chem. - Eur. J.* **2011**, *17*, 9288−9292.

(534) Takechi, H.; Canillas, A.; Ribó, J. M.; Watarai, H. Alignment and Chirality of Porphyrin J Aggregates Formed at the Liquid-Liquid Interface of a Centrifugal Liquid Membrane Cell. *Langmuir* **2013**, *29*, 7249−7256.

(535) Hough, L. E.; Spannuth, M.; Nakata, M.; Coleman, D. A.; Jones, C. D.; Dantlgraber, G.; Tschierske, C.; Watanabe, J.; Körblova, E.; Walba, D. M.; Maclennan, J. E.; Glaser, M. A.; Clark, N. A. Chiral Isotropic Liquids from Achiral Molecules. *Science* **2009**, *325*, 452−456.

(536) Alaasar, M.; Poppe, S.; Dong, Q.; Liu, F.; Tschierske, C. Isothermal Chirality Switching in Liquid-Crystalline Azobenzene Compounds with Non-Polarized Light. *Angew. Chem., Int. Ed.* **2017**, *56*, 10801−10805.

(537) Hough, L. E.; Jung, H. T.; Krüerke, D.; Heberling, M. S.; Nakata, M.; Jones, C. D.; Chen, D.; Link, D. R.; Zasadzinski, J.; Heppke, G.; Rabe, J. P.; Stocker, W.; Körblova, E.; Walba, D. M.; Glaser, M. A.; Clark, N. A. Helical Nanofilament Phases. *Science* **2009**, *325*, 456−460.

(538) Le, K. V.; Takezoe, H.; Araoka, F. Chiral Superstructure Mesophases of Achiral Bent-Shaped Molecules - Hierarchical Chirality Amplification and Physical Properties. *Adv. Mater.* **2017**, *29*, 1602737.

(539) Micali, N.; Romeo, A.; Lauceri, R.; Purrello, R.; Mallamace, F.; Scolaro, L. M. Fractal Structures in Homo- and Heteroaggregated Water Soluble Porphyrins. *J. Phys. Chem. B* **2000**, *104*, 9416−9420.

(540) Escudero, C.; D'Urso, A.; Lauceri, R.; Bonaccorso, C.; Sciotto, D.; Di Bella, S.; El-Hachemi, Z.; Crusats, J.; Ribó, J. M.; Purrello, R. Hierarchical Dependence of Porphyrin Self-Aggregation: Controlling and Exploiting the Complexity. *J. Porphyrins Phthalocyanines* **2010**, *14*, 708−712.

(541) Magna, G.; Monti, D.; Di Natale, C.; Paolesse, R.; Stefanelli, M. The Assembly of Porphyrin Systems in Well-Defined Nanostructures: An Update. *Molecules* **2019**, *24*, 4307.

(542) Helmich, F.; Lee, C. C.; Schenning, A. P. H. J.; Meijer, E. W. Chiral Memory via Chiral Amplification and Selective Depolymerization of Porphyrin Aggregates. *J. Am. Chem. Soc.* **2010**, *132*, 16753−16755.

(543) Mammana, A.; D'Urso, A.; Lauceri, R.; Purrello, R. Switching Off and On the Supramolecular Chiral Memory in Porphyrin Assemblies. *J. Am. Chem. Soc.* **2007**, *129*, 8062−8063.

(544) Randazzo, R.; Mammana, A.; D'Urso, A.; Lauceri, R.; Purrello, R. Reversible "Chiral Memory" in Ruthenium Tris(Phenanthroline)-Anionic Porphyrin Complexes. *Angew. Chem., Int. Ed.* **2008**, *47*, 9879−9882.

(545) Purrello, R. Lasting Chiral Memory. *Nat. Mater.* **2003**, *2*, 216−217.

(546) Lauceri, R.; Raudino, A.; Scolaro, L. M.; Micali, N.; Purrello, R. From Achiral Porphyrins to Template-Imprinted Chiral Aggregates and Further. Self-Replication of Chiral Memory from Scratch. *J. Am. Chem. Soc.* **2002**, *124*, 894−895.

(547) Azároff, L. V. X-Ray Diffraction by Liquid Crystals. *Mol. Cryst. Liq. Cryst.* **1980**, *60*, 73−97.

(548) Dressel, C.; Liu, F.; Prehm, M.; Zeng, X.; Ungar, G.; Tschierske, C. Dynamic Mirror-Symmetry Breaking in Bicontinuous Cubic Phases. *Angew. Chem., Int. Ed.* **2014**, *53*, 13115−13120.

(549) Zeng, X.; Ungar, G. Spontaneously Chiral Cubic Liquid Crystal: Three Interpenetrating Networks with a Twist. *J. Mater. Chem. C* **2020**, *8*, 5389−5398.

(550) Chen, C.; Kieffer, R.; Ebert, H.; Prehm, M.; Zhang, R.; Zeng, X.; Liu, F.; Ungar, G.; Tschierske, C. Chirality Induction through Nano-Phase Separation: Alternating Network Gyroid Phase by Thermotropic

Self-Assembly of X-Shaped Bolapolyphiles. *Angew. Chem., Int. Ed.* **2020**, *59*, 2725−2729.

(551) Lewandowski, W.; Vaupotič, N.; Pociecha, D.; Górecka, E.; Liz-Marzán, L. M. Chirality of Liquid Crystals Formed from Achiral Molecules Revealed by Resonant X-Ray Scattering. *Adv. Mater.* **2020**, *32*, 1905591.

(552) Gandini, S. C. M.; Yushmanov, V. E.; Borissevitch, I. E.; Tabak, M. Interaction of the Tetra(4-Sulfonatophenyl)Porphyrin with Ionic Surfactants: Aggregation and Location in Micelles. *Langmuir* **1999**, *15*, 6233−6243.

(553) De Yoreo, J. J.; Sommerdijk, N. A. J. M. Investigating Materials Formation with Liquid-Phase and Cryogenic TEM. *Nat. Rev. Mater.* **2016**, *1*, 16035.

(554) Martynowycz, M. W.; Gonen, T. From Electron Crystallography of 2D Crystals to MicroED of 3D Crystals. *Curr. Opin. Colloid Interface Sci.* **2018**, *34*, 9−16.

(555) Short, J. M.; Berriman, J. A.; Kübel, C.; El-Hachemi, Z.; Naubron, J.-V.; Balaban, T. S. Electron Cryo-Microscopy of TPPS4· 2HCl Tubes Reveals a Helical Organisation Explaining the Origin of Their Chirality. *ChemPhysChem* **2013**, *14*, 3209−3214.

(556) Moradi, M.; Opara, N. L.; Tulli, L. G.; Wäckerlin, C.; Dalgarno, S. J.; Teat, S. J.; Baljozovic, M.; Popova, O.; van Genderen, E.; Kleibert, A.; Stahlberg, H.; Abrahams, J. P.; Padeste, C.; Corvini, P. F.-X.; Jung, T. A.; Shahgaldian, P. Supramolecular Architectures of Molecularly Thin yet Robust Free-Standing Layers. *Sci. Adv.* **2019**, *5*, No. eaav4489.

(557) Murata, K.; Wolf, M. Cryo-Electron Microscopy for Structural Analysis of Dynamic Biological Macromolecules. *Biochim. Biophys. Acta, Gen. Subj.* **2018**, *1862*, 324−334.

(558) Crusats, J.; Claret, J.; Díez-Pérez, I.; El-Hachemi, Z.; García-Ortega, H.; Rubires, R.; Sagués, F.; Ribó, J. M. Chiral Shape and Enantioselective Growth of Colloidal Particles of Self-Assembled Meso-Tetra(Phenyl and 4-Sulfonatophenyl)Porphyrins. *Chem. Commun.* **2003**, 1588−1589.

(559) Abd El-Mageed, A. I. A.; Ogawa, T. Single-Walled Carbon Nanotube Absolute-Handedness Chirality Assignment Confirmation Using Metalized Porphyrin's Supramolecular Structures via STM Imaging Technique. *Chirality* **2020**, *32*, 345−352.

(560) Gopal, A.; Hifsudheen, M.; Furumi, S.; Takeuchi, M.; Ajayaghosh, A. Thermally Assisted Photonic Inversion of Supramolecular Handedness. *Angew. Chem., Int. Ed.* **2012**, *51*, 10505−10509.

(561) Huang, X.; Liu, M. Chirality of Photopolymerized Organized Supramolecular Polydiacetylene Films. *Chem. Commun.* **2003**, 66−67.

(562) Gopal, A.; Hifsudheen, M.; Furumi, S.; Takeuchi, M.; Ajayaghosh, A. Thermally Assisted Photonic Inversion of Supramolecular Handedness. *Angew. Chem., Int. Ed.* **2012**, *51*, 10505−10509.

(563) Freudenthal, J. H.; Hollis, E.; Kahr, B. Imaging Chiroptical Artifacts. *Chirality* **2009**, *21*, E20−E27.

(564) *Comprehensive Chiroptical Spectroscopy*, Vol. 2; Berova, N., Polavarapu, P. L., Nakanishi, K., Woody, R. W., Eds.; Wiley: Hoboken, NJ, 2012.

(565) Escudero, C.; El-Hachemi, Z.; Crusats, J.; Ribó, J. M. Zwitterionic vs Porphyrin Free-Base Structures in 4-Phenylsulfonic Acid Meso-Substituted Porphyrins. *J. Porphyrins Phthalocyanines* **2005**, *09*, 852−863.

(566) Sharma, A.; Campbell, A.; Leoni, J.; Cheng, Y. T.; Müllner, M.; Lakhwani, G. Circular Intensity Differential Scattering Reveals the Internal Structure of Polymer Fibrils. *J. Phys. Chem. Lett.* **2019**, *10*, 7547−7553.

(567) McDonald, L. T.; Finlayson, E. D.; Wilts, B. D.; Vukusic, P. Circularly Polarized Reflection from the Scarab Beetle Chalcothea Smaragdina: Light Scattering by a Dual Photonic Structure. *Interface Focus* **2017**, *7*, 20160129.

(568) Funahashi, M.; Tamaoki, N. Organic Semiconductors with Helical Structure Based on Oligothiophene Derivatives Exhibiting Chiral Nematic Phase. *Mol. Cryst. Liq. Cryst.* **2007**, *475*, 123−135.

(569) Wang, L.; Urbas, A. M.; Li, Q. Nature-Inspired Emerging Chiral Liquid Crystal Nanostructures: From Molecular Self-Assembly to DNA Mesophase and Nanocolloids. *Adv. Mater.* **2020**, *32*, 1801335.

(570) Takechi, H.; Arteaga, O.; Ribó, J. M.; Watarai, H. Chiroptical Measurement of Chiral Aggregates at Liquid-Liquid Interface in Centrifugal Liquid Membrane Cell by Mueller Matrix and Conventional Circular Dichroism Methods. *Molecules* **2011**, *16*, 3636−3647.

(571) Arteaga, O.; Canillas, A.; El-Hachemi, Z.; Crusats, J.; Ribó, J. M. Structure vs. Excitonic Transitions in Self-Assembled Porphyrin Nanotubes and Their Effect on Light Absorption and Scattering. *Nanoscale* **2015**, *7*, 20435−20441.

(572) Tsuda, A.; Alam, M. A.; Harada, T.; Yamaguchi, T.; Ishii, N.; Aida, T. Spectroscopic Visualization of Vortex Flows Using Dye-Containing Nanofibers. *Angew. Chem., Int. Ed.* **2007**, *46*, 8198−8202.

(573) Arteaga, O.; Kahr, B. Mueller Matrix Polarimetry of Bianisotropic Materials [Invited]. *J. Opt. Soc. Am. B* **2019**, *36*, F72−F83.

(574) Gunn, E.; Sours, R.; Benedict, J. B.; Kahr, B. Mesoscale Chiroptics of Rhythmic Precipitates. *J. Am. Chem. Soc.* **2006**, *128*, 14234−14235.

(575) Cui, X.; Rohl, A. L.; Shtukenberg, A.; Kahr, B. Twisted Aspirin Crystals. *J. Am. Chem. Soc.* **2013**, *135*, 3395−3398.

(576) Tsujimoto, Y.; Ie, M.; Ando, Y.; Yamamoto, T.; Tsuda, A. Spectroscopic Visualization of Right- and Left-Handed Helical Alignments of DNA in Chiral Vortex Flows. *Bull. Chem. Soc. Jpn.* **2011**, *84*, 1031−1038.

(577) Arteaga, O.; El-Hachemi, Z.; Canillas, A.; Crusats, J.; Rovira, M.; Ribó, J. M. Reversible and Irreversible Emergence of Chiroptical Signals in J-Aggregates of Achiral 4-Sulfonatophenyl Substituted Porphyrins: Intrinsic Chirality: Vs. Chiral Ordering in the Solution. *Chem. Commun.* **2016**, *52*, 10874−10877.

(578) Arlegui, A.; Soler, B.; Galindo, A.; Arteaga, O.; Canillas, A.; Ribó, J. M.; El-Hachemi, Z.; Crusats, J.; Moyano, A. Spontaneous Mirror-Symmetry Breaking Coupled to Top-Bottom Chirality Transfer: From Porphyrin Self-Assembly to Scalemic Diels-Alder Adducts. *Chem. Commun.* **2019**, *55*, 12219−12222.

(579) Shen, Z.; Sang, Y.; Wang, T.; Jiang, J.; Meng, Y.; Jiang, Y.; Okuro, K.; Aida, T.; Liu, M. Asymmetric Catalysis Mediated by a Mirror Symmetry-Broken Helical Nanoribbon. *Nat. Commun.* **2019**, *10*, 3976.

(580) Collings, P. J.; Goodby, J. W. *Introduction to Liquid Crystals: Chemistry and Physics*, 2nd ed.; CRC Press: Boca Raton, FL, 2019.

(581) Cowling, S. J.; Hall, A. W.; Goodby, J. W. A Chiral Electrooptic Response in a Racemic Liquid Crystal. *Chem. Commun.* **2005**, 1546−1548.

(582) Eelkema, R.; Feringa, B. L. Amplification of Chirality in Liquid Crystals. *Org. Biomol. Chem.* **2006**, *4*, 3729−3745.

(583) Peng, C.; Lavrentovich, O. D. Chirality Amplification and Detection by Tactoids of Lyotropic Chromonic Liquid Crystals. *Soft Matter* **2015**, *11*, 7257−7263.

(584) Choi, S.-W.; Izumi, T.; Hoshino, Y.; Takanishi, Y.; Ishikawa, K.; Watanabe, J.; Takezoe, H. Circular-Polarization-Induced Enantiomeric Excess in Liquid Crystals of an Achiral, Bent-Shaped Mesogen. *Angew. Chem., Int. Ed.* **2006**, *45*, 1382−1385.

(585) Sayama, S.; Yoshizawa, A. Achiral H-Shaped Liquid Crystals Exhibiting an Electric-Field-Induced Chiral Nematic Phase. *J. Mater. Chem. C* **2019**, *7*, 6905−6913.

(586) Hochberg, D.; Zorzano, M.-P. Reaction-Noise Induced Homochirality. *Chem. Phys. Lett.* **2006**, *431*, 185−189.

(587) Alemán, C.; Lotz, B.; Puiggali, J. Crystal Structure of the α-Form of Poly(l-Lactide). *Macromolecules* **2001**, *34*, 4795−4801.

(588) Karle, I. L.; Karle, J.; Mastropaolo, D.; Camerman, A.; Camerman, N. [Leu 5]Enkephalin: Four Cocrystallizing Conformers with Extended Backbones That Form an Antiparallel β-Sheet. *Acta Crystallogr., Sect. B: Struct. Sci.* **1983**, *39*, 625−637.

(589) Sorrenti, A.; Illa, O.; Ortuño, R. M. Amphiphiles in Aqueous Solution: Well beyond a Soap Bubble. *Chem. Soc. Rev.* **2013**, *42*, 8200−8219.

(590) Altamura, E.; Comte, A.; D'Onofrio, A.; Roussillon, C.; Fayolle, D.; Buchet, R.; Mavelli, F.; Stano, P.; Fiore, M.; Strazewski, P. Racemic Phospholipids for Origin of Life Studies. *Symmetry* **2020**, *12*, 1108.

(591) Walde, P. Building Artificial Cells and Protocell Models: Experimental Approaches with Lipid Vesicles. *BioEssays* **2010**, *32*, 296−303.

(592) Nandi, N.; Vollhardt, D.; Brezesinski, G. Chiral Discrimination Effects in Langmuir Monolayers of 1-O-Hexadecyl Glycerol. *J. Phys. Chem. B* **2004**, *108*, 327−335.

(593) Escudero, C.; El-Hachemi, Z.; Díez-Pérez, I.; Crusats, J.; Ribó, J. M. Formation of an Epitaxial Monolayer on Graphite upon Short-Time Surface Contact with Highly Diluted Aqueous Solutions of 1-Monostearoylglycerol. *Thin Solid Films* **2007**, *515*, 5391−5394.

(594) Peretó, J.; López-García, P.; Moreira, D. Ancestral Lipid Biosynthesis and Early Membrane Evolution. *Trends Biochem. Sci.* **2004**, *29*, 469−477.

(595) Song, H.; Zhu, H.; Huang, Z.; Zhang, Y.; Zhao, W.; Liu, J.; Chen, Q.; Yin, C.; Xing, L.; Peng, Z.; Liao, P.; Wang, Y.; Wang, Y.; Wu, K. Steering the Achiral into Chiral with a Self-Assembly Strategy. *ACS Nano* **2019**, *13*, 7202−7208.

(596) Liu, Y.; Jia, Y.; Zhu, E.; Liu, L.; Qiao, Y.; Che, G.; Yin, B. Supramolecular Helical Nanofibers Formed by an Achiral Monop-yrrolotetrathiafulvalene Derivative: Water-Triggered Gelation and Chiral Evolution. *New J. Chem.* **2017**, *41*, 11060−11068.

(597) Draper, E. R.; Wilbraham, L.; Adams, D. J.; Wallace, M.; Schweins, R.; Zwijnenburg, M. A. Insight into the Self-Assembly of Water-Soluble Perylene Bisimide Derivatives through a Combined Computational and Experimental Approach. *Nanoscale* **2019**, *11*, 15917−15928.

(598) Dehm, V.; Chen, Z.; Baumeister, U.; Prins, P.; Siebbeles, L. D. A.; Würthner, F. Helical Growth of Semiconducting Columnar Dye Assemblies Based on Chiral Perylene Bisimides. *Org. Lett.* **2007**, *9*, 1085−1088.

(599) Greciano, E. E.; Calbo, J.; Buendía, J.; Cerdá, J.; Aragó, J.; Ortí, E.; Sánchez, L. Decoding the Consequences of Increasing the Size of Self-Assembling Tricarboxamides on Chiral Amplification. *J. Am. Chem. Soc.* **2019**, *141*, 7463−7472.

(600) Zhang, H.; Cheng, J.; Zhou, Q.; Zhang, Q.; Zou, G. Impact of a Chiral Supramolecular Nanostructure on the Mechanical and Electrical Performances of Triphenylene-Based Discotic Physical Gels. *Soft Matter* **2020**, *16*, 5203−5209.

(601) Yang, Y.; Walz, J.; Pintauro, P. Curvature Effects on Electric Double-Layer Forces. Part 1.—Comparisions with Parallel Geometry. *J. Chem. Soc., Faraday Trans.* **1995**, *91*, 2827−2836.

(602) Shimizu, T.; Kameta, N.; Ding, W.; Masuda, M. Supramolecular Self-Assembly into Biofunctional Soft Nanotubes: From Bilayers to Monolayers. *Langmuir* **2016**, *32*, 12242−12264.

(603) Wang, Y.; Kim, Y.; Lee, M. Static and Dynamic Nanosheets from Selective Assembly of Geometric Macrocycle Isomers. *Angew. Chem., Int. Ed.* **2016**, *55*, 13122−13126.

(604) Soai, K.; Shibata, T.; Kowata, Y. Spontaneous Asymmetric Synthesis of Pyrimidyl Alkanol. *Japan Kokai Tokkyo Koho* **1996**, JP1997-268.

(605) Soai, K.; Sato, I.; Shibata, T.; Komiya, S.; Hayashi, M.; Matsueda, Y.; Imamura, H.; Hayase, T.; Morioka, H.; Tabira, H.; Yamamoto, J.; Kowata, Y. Asymmetric Synthesis of Pyrimidyl Alkanol without Adding Chiral Substances by the Addition of Diisopropylzinc to Pyrimidine-5-Carbaldehyde in Conjunction with Asymmetric Autocatalysis. *Tetrahedron: Asymmetry* **2003**, *14*, 185−188.

(606) Hochberg, D.; Ribó, J. M. Stoichiometric Network Analysis of Entropy Production in Chemical Reactions. *Phys. Chem. Chem. Phys.* **2018**, *20*, 23726−23739.

(607) Soai, K.; Kawasaki, T.; Matsumoto, A. The Origins of Homochirality Examined by Using Asymmetric Autocatalysis. *Chem. Rec.* **2014**, *14*, 70−83.

(608) Buhse, T.; Noble-Terán, M. E.; Cruz, J. M.; Micheau, J. C.; Coudret, C. Kinetic and Structural Aspects of Mirror-Image Symmetry Breaking in the Soai Reaction. In *Advances in Asymmetric Autocatalysis and Related Topics*; Pályi, G., Kurdi, R., Zucchi, C., Eds.; Elsevier, Academic Press: London, 2017; pp 71−110.

(609) Soai, K.; Matsumoto, A.; Kawasaki, T. Asymmetric Autocatalysis and the Origins of Homochirality of Organic Com-pounds. An Overview. In *Advances in Asymmetric Autocatalysis and Related Topics*; Pályi, G., Kurdi, R., Zucchi, C., Eds.; Elsevier, Academic Press: London, 2017; pp 1−30.

(610) Soai, K. Asymmetric Autocatalysis. Chiral Symmetry Breaking and the Origins of Homochirality of Organic Molecules. *Proc. Jpn. Acad., Ser. B* **2019**, *95*, 89−110.

(611) Soai, K.; Kawasaki, T.; Matsumoto, A. Role of Asymmetric Autocatalysis in the Elucidation of Origins of Homochirality of Organic Compounds. *Symmetry* **2019**, *11*, 694.

(612) Blackmond, D. G. Autocatalytic Models for the Origin of Biological Homochirality. *Chem. Rev.* **2020**, *120*, 4831−4847.

(613) Gridnev, I. D.; Serafimov, J. M.; Brown, J. M. Solution Structure and Reagent Binding of the Zinc Alkoxide Catalyst in the Soai Asymmetric Autocatalytic Reaction. *Angew. Chem., Int. Ed.* **2004**, *43*, 4884−4887.

(614) Gridnev, I. D.; Vorobiev, A. K. On the Origin and Structure of the Recently Observed Acetal in the Soai Reaction. *Bull. Chem. Soc. Jpn.* **2015**, *88*, 333−340.

(615) Matsumoto, A.; Abe, T.; Hara, A.; Tobita, T.; Sasagawa, T.; Kawasaki, T.; Soai, K. Crystal Structure of the Isopropylzinc Alkoxide of Pyrimidyl Alkanol: Mechanistic Insights for Asymmetric Autocatalysis with Amplification of Enantiomeric Excess. *Angew. Chem., Int. Ed.* **2015**, *54*, 15218−15221.

(616) Matsumoto, A.; Fujiwara, S.; Abe, T.; Hara, A.; Tobita, T.; Sasagawa, T.; Kawasaki, T.; Soai, K. Elucidation of the Structures of Asymmetric Autocatalyst Based on X-Ray Crystallography. *Bull. Chem. Soc. Jpn.* **2016**, *89*, 1170−1177.

(617) Matsumoto, A.; Kawasaki, T.; Soai, K. Structural Study of Asymmetric Autocatalysis by X-Ray Crystallography. In *Advances in Asymmetric Autocatalysis and Related Topics*; Pályi, G., Kurdi, R., Zucchi, C., Eds.; Elsevier, Academic Press: London, 2017; pp 183−202.

(618) Barabás, B.; Zucchi, C.; Maioli, M.; Micskei, K.; Pályi, G. Stochastic and Empirical Models of the Absolute Asymmetric Synthesis by the Soai-Autocatalysis. *J. Mol. Model.* **2015**, *21*, 33.

(619) Ercolani, G. Principles for Designing an Achiral Receptor Promoting Asymmetric Autocatalysis with Amplification of Chirality. *Tetrahedron: Asymmetry* **2014**, *25*, 405−410.

(620) Bryliakov, K. P. Dynamic Nonlinear Effects in Asymmetric Catalysis. *ACS Catal.* **2019**, *9*, 5418−5438.

(621) Noble-Terán, M. E.; Cruz, J. M.; Micheau, J. C.; Buhse, T. A Quantification of the Soai Reaction. *ChemCatChem* **2018**, *10*, 642−648.

(622) Athavale, S. V.; Simon, A.; Houk, K. N.; Denmark, S. E. Demystifying the Asymmetry-Amplifying, Autocatalytic Behaviour of the Soai Reaction through Structural, Mechanistic and Computational Studies. *Nat. Chem.* **2020**, *12*, 412−423.

(623) Micheau, J.-C.; Cruz, J.-M.; Coudret, C.; Buhse, T. An Autocatalytic Cycle Model of Asymmetric Amplification and Mirror-Symmetry Breaking in the Soai Reaction. *ChemPhysChem* **2010**, *11*, 3417−3419.

(624) Trapp, O.; Lamour, S.; Maier, F.; Siegle, A. F.; Zawatzky, K.; Straub, B. F. In Situ Mass Spectrometric and Kinetic Investigations of Soai's Asymmetric Autocatalysis. *Chem. - A Eur. J.* **2020**, *26*, 15871−15880.

(625) Hitosugi, S.; Matsumoto, A.; Kaimori, Y.; Iizuka, R.; Soai, K.; Isobe, H. Asymmetric Autocatalysis Initiated by Finite Single-Wall Carbon Nanotube Molecules with Helical Chirality. *Org. Lett.* **2014**, *16*, 645−647.

(626) Kawasaki, T.; Araki, Y.; Hatase, K.; Suzuki, K.; Matsumoto, A.; Yokoi, T.; Kubota, Y.; Tatsumi, T.; Soai, K. Helical Mesoporous Silica as an Inorganic Heterogeneous Chiral Trigger for Asymmetric Autocatalysis with Amplification of Enantiomeric Excess. *Chem. Commun.* **2015**, *51*, 8742−8744.

(627) Matsumoto, A.; Ide, T.; Kaimori, Y.; Fujiwara, S.; Soai, K. Asymmetric Autocatalysis Triggered by Chiral Crystal of Achiral Ethylenediamine Sulfate. *Chem. Lett.* **2015**, *44*, 688−690.

(628) Matsumoto, A.; Ozaki, H.; Harada, S.; Tada, K.; Ayugase, T.; Ozawa, H.; Kawasaki, T.; Soai, K. Asymmetric Induction by a Nitrogen

14 N/ 15 N Isotopomer in Conjunction with Asymmetric Autocatalysis. *Angew. Chem., Int. Ed.* **2016**, *55*, 15246−15249.

(629) Matsumoto, A.; Yonemitsu, K.; Ozaki, H.; Míšek, J.; Starý, I.; Stará, I. G.; Soai, K. Reversal of the Sense of Enantioselectivity between 1- and 2-Aza[6]Helicenes Used as Chiral Inducers of Asymmetric Autocatalysis. *Org. Biomol. Chem.* **2017**, *15*, 1321−1324.

(630) Matsumoto, A.; Ozaki, H.; Tsuchiya, S.; Asahi, T.; Lahav, M.; Kawasaki, T.; Soai, K. Achiral Amino Acid Glycine Acts as an Origin of Homochirality in Asymmetric Autocatalysis. *Org. Biomol. Chem.* **2019**, *17*, 4200−4203.

(631) Sato, I.; Kadowaki, K.; Ohgo, Y.; Soai, K. Highly Enantioselective Asymmetric Autocatalysis Induced by Chiral Ionic Crystals of Sodium Chlorate and Sodium Bromate. *J. Mol. Catal. A: Chem.* **2004**, *216*, 209−214.

(632) Cruz-Rosas, H. I.; Riquelme, F.; Santiago, P.; Rendón, L.; Buhse, T.; Ortega-Gutiérrez, F.; Borja-Urby, R.; Mendoza, D.; Gaona, C.; Miramontes, P.; Cocho, G. Multiwall and Bamboo-like Carbon Nanotubes from the Allende Chondrite: A Probable Source of Asymmetry. *PLoS One* **2019**, *14*, e0218750.

(633) Kawasaki, T.; Hatase, K.; Fujii, Y.; Jo, K.; Soai, K.; Pizzarello, S. The Distribution of Chiral Asymmetry in Meteorites: An Investigation Using Asymmetric Autocatalytic Chiral Sensors. *Geochim. Cosmochim. Acta* **2006**, *70*, 5395−5402.

(634) Welch, C. J.; Zawatzky, K.; Makarov, A. A.; Fujiwara, S.; Matsumoto, A.; Soai, K. Can the Analyte-Triggered Asymmetric Autocatalytic Soai Reaction Serve as a Universal Analytical Tool for Measuring Enantiopurity and Assigning Absolute Configuration? *Org. Biomol. Chem.* **2017**, *15*, 96−101.

(635) Kawasaki, T.; Shimizu, M.; Nishiyama, D.; Ito, M.; Ozawa, H.; Soai, K. Asymmetric Autocatalysis Induced by Meteoritic Amino Acids with Hydrogen Isotope Chirality. *Chem. Commun.* **2009**, No. 29, 4396−4398.

(636) Hawbaker, N. A.; Blackmond, D. G. Rationalization of Asymmetric Amplification via Autocatalysis Triggered by Isotopically Chiral Molecules. *ACS Cent. Sci.* **2018**, *4*, 776−780.

(637) Lavabre, D.; Micheau, J. C.; Rivera Islas, J.; Buhse, T. Enantioselectivity Reversal by Achiral Additives in the Soai Reaction: A Kinetic Understanding. *J. Phys. Chem. A* **2007**, *111*, 281−286.

(638) Lavabre, D.; Micheau, J.-C.; Rivera Islas, J.; Buhse, T. Kinetic Insight into Specific Features of the Autocatalytic Soai Reaction. In *Amplification of Chirality*; Topics in Current Chemistry, Vol. *284*; Springer Berlin Heidelberg, 2007;67−96,.

(639) Buhse, T. A Tentative Kinetic Model for Chiral Amplification in Autocatalytic Alkylzinc Additions. *Tetrahedron: Asymmetry* **2003**, *14*, 1055−1061.

(640) Islas, J. R.; Lavabre, D.; Grevy, J.-M.; Lamoneda, R. H.; Cabrera, H. R.; Micheau, J.-C.; Buhse, T. Mirror-Symmetry Breaking in the Soai Reaction: A Kinetic Understanding. *Proc. Natl. Acad. Sci. U. S. A.* **2005**, *102*, 13743−13748.

(641) Kaimori, Y.; Hiyoshi, Y.; Kawasaki, T.; Matsumoto, A.; Soai, K. Formation of Enantioenriched Alkanol with Stochastic Distribution of Enantiomers in the Absolute Asymmetric Synthesis under Heterogeneous Solid-Vapor Phase Conditions. *Chem. Commun.* **2019**, *55*, 5223−5226.

(642) Rotunno, G.; Petersen, D.; Amedjkouh, M. Absolute Autocatalytic Amplification under Heterogenous Phase Conditions Involving Subsequent Hydride Transfer and a Hemiacetal Intermediate. *ChemSystemsChem.* **2020**, *2*, 1900060.

(643) Barabas, B.; Caglioti, L.; Zucchi, C.; Maioli, M.; Gál, E.; Micskei, K.; Pályi, G. Violation of Distribution Symmetry in Statistical Evaluation of Absolute Enantioselective Synthesis. *J. Phys. Chem. B* **2007**, *111*, 11506−11510.

(644) Singleton, D. A.; Vo, L. K. Enantioselective Synthesis without Discrete Optically Active Additives. *J. Am. Chem. Soc.* **2002**, *124*, 10010−10011.

(645) Gridnev, I. D.; Serafimov, J. M.; Quiney, H.; Brown, J. M. Reflections on Spontaneous Asymmetric Synthesis by Amplifying Autocatalysis. *Org. Biomol. Chem.* **2003**, *1*, 3811−3819.

(646) Hopfield, J. J. Kinetic Proofreading: A New Mechanism for Reducing Errors in Biosynthetic Processes Requiring High Specifity. *Proc. Natl. Acad. Sci. U. S. A.* **1974**, *71*, 4135−4139.

(647) Micheau, J. C.; Coudret, C.; Cruz, J. M.; Buhse, T. Amplification of Enantiomeric Excess, Mirror-Image Symmetry Breaking and Kinetic Proofreading in Soai Reaction Models with Different Oligomeric Orders. *Phys. Chem. Chem. Phys.* **2012**, *14*, 13239−13248.

(648) Sagués, F.; Epstein, I. R. Nonlinear Chemical Dynamics. *Dalt. Trans.* **2003**, 1201−1217.

(649) Romero-Fernández, M. P.; Babiano, R.; Cintas, P. On the Asymmetric Autocatalysis of Aldol Reactions: The Case of 4-Nitrobenzaldehyde and Acetone. A Critical Appraisal with a Focus on Theory. *Chirality* **2018**, *30*, 445−456.

(650) Mauksch, M.; Tsogoeva, S. B.; Martynova, I. M.; Wei, S. Evidence of Asymmetric Autocatalysis in Organocatalytic Reactions. *Angew. Chem., Int. Ed.* **2007**, *46*, 393−396.

(651) Amedjkouh, M.; Brandberg, M. Asymmetric Autocatalytic Mannich Reaction in the Presence of Water and Its Implication in Prebiotic Chemistry. *Chem. Commun.* **2008**, 3043−3045.

(652) Brandberg, M.; Amedjkouh, M. Autocatalytic Mannich Reaction. *Synfacts* **2008**, *2008*, 0420−0420.

(653) Tsogoeva, S. B. When Chiral Product and Catalyst Are the Same: Discovery of Asymmetric Organoautocatalysis. *Chem. Commun.* **2010**, *46*, 7662.

(654) Wang, X.; Zhang, Y.; Tan, H.; Wang, Y.; Han, P.; Wang, D. Z. Enantioselective Organocatalytic Mannich Reactions with Autocatalysts and Their Mimics. *J. Org. Chem.* **2010**, *75*, 2403−2406.

(655) Mauksch, M.; Tsogoeva, S. B.; Wei, S.; Martynova, I. M. Demonstration of Spontaneous Chiral Symmetry Breaking in Asymmetric Mannich and Aldol Reactions. *Chirality* **2007**, *19*, 816−825.

(656) Mauksch, M.; Wei, S.; Freund, M.; Zamfir, A.; Tsogoeva, S. B. Spontaneous Mirror Symmetry Breaking in the Aldol Reaction and Its Potential Relevance in Prebiotic Chemistry. *Origins Life Evol. Biospheres* **2010**, *40*, 79−91.

(657) Valero, G.; Ribó, J. M.; Moyano, A. A Closer Look at Spontaneous Mirror Symmetry Breaking in Aldol Reactions. *Chem. - Eur. J.* **2014**, *20*, 17395−17408.

(658) Coley, C. W.; Thomas, D. A.; Lummiss, J. A. M.; Jaworski, J. N.; Breen, C. P.; Schultz, V.; Hart, T.; Fishman, J. S.; Rogers, L.; Gao, H.; Hicklin, R. W.; Plehiers, P. P.; Byington, J.; Piotti, J. S.; Green, W. H.; Hart, A. J.; Jamison, T. F.; Jensen, K. F. A Robotic Platform for Flow Synthesis of Organic Compounds Informed by AI Planning. *Science* **2019**, *365*, No. eaax1566.

(659) Semenov, S. N.; Kraft, L. J.; Ainla, A.; Zhao, M.; Baghbanzadeh, M.; Campbell, V. E.; Kang, K.; Fox, J. M.; Whitesides, G. M. Autocatalytic, Bistable, Oscillatory Networks of Biologically Relevant Organic Reactions. *Nature* **2016**, *537*, 656−660.

(660) Maguire, O. R.; Wong, A. S. Y.; Westerdiep, J. H.; Huck, W. T. S. Early Warning Signals in Chemical Reaction Networks. *Chem. Commun.* **2020**, *56*, 3725−3728.

(661) Ribó, J. M.; Hochberg, D. Stability of Racemic and Chiral Steady States in Open and Closed Chemical Systems. *Phys. Lett. A* **2008**, *373*, 111−122.

(662) Hochberg, D.; Ribó, J. Entropic Analysis of Mirror Symmetry Breaking in Chiral Hypercycles. *Life* **2019**, *9*, 28.

(663) Neveu, M.; Kim, H. J.; Benner, S. A. The "Strong" RNA World Hypothesis: Fifty Years Old. *Astrobiology* **2013**, *13*, 391−403.

(664) Orgel, L. E. Prebiotic Chemistry and the Origin of the RNA World. *Crit. Rev. Biochem. Mol. Biol.* **2004**, *39*, 99−123.

(665) Schwartz, A. W. Prebiotic Evolution: Selecting for Homochirality before RNA. *Curr. Biol.* **1997**, *7*, R477−R479.

(666) Bolli, M.; Micura, R.; Eschenmoser, A. Pyranosyl-RNA: Chiroselective Self-Assembly of Base Sequences by Ligative Oligomerization of Tetra Nucleotide-2′,3′-Cyclophosphates (with a Commentary Concerning the Origin of Biomolecular Homochirality). *Chem. Biol.* **1997**, *4*, 309−320.

(667) Krishnamurthy, R. Giving Rise to Life: Transition from Prebiotic Chemistry to Protobiology. *Acc. Chem. Res.* **2017**, *50*, 455−459.

(668) Krishnamurthy, R. Life's Biological Chemistry: A Destiny or Destination Starting from Prebiotic Chemistry? *Chem. - Eur. J.* **2018**, *24*, 16708−16715.

(669) Chen, Y.; Ma, W. The Origin of Biological Homochirality along with the Origin of Life. *PLoS Comput. Biol.* **2020**, *16*, No. e1007592.

(670) Ribó, J. M.; Hochberg, D. Spontaneous Mirror Symmetry Breaking: An Entropy Production Survey of the Racemate Instability and the Emergence of Stable Scalemic Stationary States. *Phys. Chem. Chem. Phys.* **2020**, *22*, 14013−14025.

(671) Hitz, T.; Luisi, P. L. Chiral Amplification of Oligopeptides in the Polymerization of α-Amino Acid N-Carboxyanhydrides in Water. *Helv. Chim. Acta* **2003**, *86*, 1423−1434.

(672) Illos, R. A.; Bisogno, F. R.; Clodic, G.; Bolbach, G.; Weissbuch, I.; Lahav, M. Oligopeptides and Copeptides of Homochiral Sequence, via β-Sheets, from Mixtures of Racemic α-Amino Acids, in a One-Pot Reaction in Water; Relevance to Biochirogenesis. *J. Am. Chem. Soc.* **2008**, *130*, 8651−8659.

(673) Saghatelian, A.; Yokobayashi, Y.; Soltani, K.; Ghadiri, M. R. A Chiroselective Peptide Replicator. *Nature* **2001**, *409*, 797−801.

(674) Frenkel-Pinter, M.; Samanta, M.; Ashkenasy, G.; Leman, L. J. Prebiotic Peptides: Molecular Hubs in the Origin of Life. *Chem. Rev.* **2020**, *120*, 4707−4765.

(675) Rivera Islas, J.; Pimienta, V.; Micheau, J. C.; Buhse, T. Kinetic Analysis of Artificial Peptide Self-Replication. Part II: The Heterochiral Case. *Biophys. Chem.* **2003**, *103*, 201−211.

(676) Rivera Islas, J.; Micheau, J.; Buhse, T. Kinetic Analysis of Self-Replicating Peptides: Possibility of Chiral Amplification in Open Systems. *Origins Life Evol. Biospheres* **2004**, *34*, 497−512.

(677) Gehring, T.; Busch, M.; Schlageter, M.; Weingand, D. A Concise Summary of Experimental Facts about the Soai Reaction. *Chirality* **2010**, *22*, E173−E182.

(678) Geiger, Y.; Achard, T.; Maisse-François, A.; Bellemin-Laponnaz, S. Hyperpositive Nonlinear Effects in Asymmetric Catalysis. *Nat. Catal.* **2020**, *3*, 422−426.

(679) Miyagawa, S.; Yoshimura, K.; Yamazaki, Y.; Takamatsu, N.; Kuraishi, T.; Aiba, S.; Tokunaga, Y.; Kawasaki, T. Asymmetric Strecker Reaction Arising from the Molecular Orientation of an Achiral Imine at the Single-Crystal Face: Enantioenriched l - and d -Amino Acids. *Angew. Chem., Int. Ed.* **2017**, *56*, 1055−1058.

(680) Aiba, S.; Takamatsu, N.; Sasai, T.; Tokunaga, Y.; Kawasaki, T. Replication of α-Amino Acids: Via Strecker Synthesis with Amplification and Multiplication of Chiral Intermediate Aminonitriles. *Chem. Commun.* **2016**, *52*, 10834−10837.

(681) Song, C. E.; Park, S. J.; Hwang, I.-S.; Jung, M. J.; Shim, S. Y.; Bae, H. Y.; Jung, J. Y. Hydrophobic Chirality Amplification in Confined Water Cages. *Nat. Commun.* **2019**, *10*, 851.

(682) Berijani, K.; Morsali, A.; Hupp, J. T. An Effective Strategy for Creating Asymmetric MOFs for Chirality Induction: A Chiral Zr-Based MOF for Enantioselective Epoxidation. *Catal. Sci. Technol.* **2019**, *9*, 3388−3397.

(683) *Chiral Separation Techniques: A Practical Approach*, 3rd ed.; Subramanian, G., Ed.; Wiley-VCH Verlag: Weinheim, Germany, 2007.

(684) Yang, L.; Wenzel, T.; Williamson, R. T.; Christensen, M.; Schafer, W.; Welch, C. J. Expedited Selection of NMR Chiral Solvating Agents for Determination of Enantiopurity. *ACS Cent. Sci.* **2016**, *2*, 332−340.

(685) Yu, X.; Yao, Z.-P. Chiral Recognition and Determination of Enantiomeric Excess by Mass Spectrometry: A Review. *Anal. Chim. Acta* **2017**, *968*, 1−20.

(686) Ward, T. J.; Hamburg, D.-M. Chiral Separations. *Anal. Chem.* **2004**, *76*, 4635−4644.

(687) Silva, M. Recent Advances in Multinuclear NMR Spectroscopy for Chiral Recognition of Organic Compounds. *Molecules* **2017**, *22*, 247.

(688) Pérez-Fuertes, Y.; Kelly, A. M.; Fossey, J. S.; Powell, M. E.; Bull, S. D.; James, T. D. Simple Protocols for NMR Analysis of the Enantiomeric Purity of Chiral Primary Amines. *Nat. Protoc.* **2008**, *3*, 210−214.

(689) Koppenhoefer, B.; Nothdurft, A.; Pierrot-Sanders, J.; Piras, P.; Popescu, C.; Roussel, C.; Stiebler, M.; Trettin, U. CHIRBASE, a Graphical Molecular Database on the Separation of Enantiomers by Liquid-, Supercritical Fluid-, and Gas Chromatography. *Chirality* **1993**, *5*, 213−219.

(690) Soloshonok, V. A. Remarkable Amplification of the Self-Disproportionation of Enantiomers on Achiral-Phase Chromatography Columns. *Angew. Chem., Int. Ed.* **2006**, *45*, 766−769.

(691) Yeste, S. L.; Powell, M. E.; Bull, S. D.; James, T. D. Simple Chiral Derivatization Protocols for 1H NMR and 19F NMR Spectroscopic Analysis of the Enantiopurity of Chiral Diols. *J. Org. Chem.* **2009**, *74*, 427−430.

(692) Bertucci, C.; Andrisano, V.; Cavrini, V.; Castiglioni, E. Reliable Assay of Extreme Enantiomeric Purity Values by a New Circular Dichroism Based HPLC Detection System. *Chirality* **2000**, *12*, 84−92.

(693) Jenkins, A. L.; Hedgepeth, W. A. Analysis of Chiral Pharmaceuticals Using HPLC with CD Detection. *Chirality* **2005**, *17*, S24−S29.

(694) Swartz, M. HPLC Detectors: A Brief Review. *J. Liq. Chromatogr. Relat. Technol.* **2010**, *33*, 1130−1150.

(695) Miles, A. J.; Wallace, B. A. Synchrotron Radiation Circular Dichroism Spectroscopy of Proteins and Applications in Structural and Functional Genomics. *Chem. Soc. Rev.* **2006**, *35*, 39−51.

(696) Meinert, C.; Bredehöft, J. H.; Filippi, J.-J.; Baraud, Y.; Nahon, L.; Wien, F.; Jones, N. C.; Hoffmann, S. V.; Meierhenrich, U. J. Anisotropy Spectra of Amino Acids. *Angew. Chem., Int. Ed.* **2012**, *51*, 4484−4487.

(697) Arteaga, O.; Kahr, B. Characterization of Homogenous Depolarizing Media Based on Mueller Matrix Differential Decomposition. *Opt. Lett.* **2013**, *38*, 1134−1136.

(698) Meyerhoffer, W. Stereochemische Notizen. *Ber. Dtsch. Chem. Ges.* **1904**, *37*, 2604−2610.

(699) Wei, S.; Mauksch, M.; Tsogoeva, S. B. Autocatalytic Enantiomerisation at the Crystal Surface in Deracemisation of Scalemic Conglomerates. *Chem. - Eur. J.* **2009**, *15*, 10255−10262.

(700) Bustamante, C.; Maestre, M. F.; Keller, D.; Tinoco, I. Differential Scattering (CIDS) of Circularly Polarized Light by Dense Particles. *J. Chem. Phys.* **1984**, *80*, 4817−4823.

(701) Ben-Moshe, A.; Maoz, B. M.; Govorov, A. O.; Markovich, G. Chirality and Chiroptical Effects in Inorganic Nanocrystal Systems with Plasmon and Exciton Resonances. *Chem. Soc. Rev.* **2013**, *42*, 7028−7041.

(702) Maoz, B. M.; Chaikin, Y.; Tesler, A. B.; Bar Elli, O.; Fan, Z.; Govorov, A. O.; Markovich, G. Amplification of Chiroptical Activity of Chiral Biomolecules by Surface Plasmons. *Nano Lett.* **2013**, *13*, 1203−1209.

(703) Golaraei, A.; Mirsanaye, K.; Ro, Y.; Krouglov, S.; Akens, M. K.; Wilson, B. C.; Barzda, V. Collagen Chirality and Three-Dimensional Orientation Studied with Polarimetric Second-Harmonic Generation Microscopy. *J. Biophotonics* **2019**, *12*, No. e201800241.

(704) Shindo, Y.; Nishio, M.; Maeda, S. Problems of CD Spectrometers (V): Can We Measure CD and LD Simultaneously? Comments on Differential Polarization Microscopy (CD and Linear Dichroism). *Biopolymers* **1990**, *30*, 405−413.

(705) Savenkov, S. N. *Light Scattering Reviews 4*; Kokhanovsky, A. A., Ed.; Springer: Berlin, Heidelberg, Germany, 2009.

(706) Arteaga, O.; Canillas, A. Analytic Inversion of the Mueller-Jones Polarization Matrices for Homogeneous Media. *Opt. Lett.* **2010**, *35*, 559−561.

(707) Jellison, G. E.; Modine, F. A. Two-Modulator Generalized Ellipsometry: Experiment and Calibration. *Appl. Opt.* **1997**, *36*, 8184−8189.

(708) Jellison, G. E.; Modine, F. A. Parameterization of the Optical Functions of Amorphous Materials in the Interband Region. *Appl. Phys. Lett.* **1996**, *69*, 371−373.

(709) Gil, J. J.; Bernabeu, E. A Depolarization Criterion in Mueller Matrices. *Opt. Acta* **1985**, *32*, 259−261.

(710) Chandrasekaran, K. S.; Mohanlal, S. K. The X-Ray Anomalous Dispersion and Optical Rotation in the Crystalline Solid Solution NaClO3: NaBrO3. *Pramana* **1976**, *7*, 152.

(711) Castiglioni, E.; Biscarini, P.; Abbate, S. Experimental Aspects of Solid State Circular Dichroism. *Chirality* **2009**, *21*, E28–E36.

(712) Forato, L. A.; Bernardes-Filho, R.; Colnago, L. A. Protein Structure in KBr Pellets by Infrared Spectroscopy. *Anal. Biochem.* **1998**, *259*, 136–141.

(713) Kuroda, R.; Harada, T.; Shindo, Y. A Solid-State Dedicated Circular Dichroism Spectrophotometer: Development and Application. *Rev. Sci. Instrum.* **2001**, *72*, 3802–3810.

(714) Kuroda, R. Techniques for Crystal Optical Characterisation. Chiroptical Spectroscopy. In *Engineering Crystallography: From Molecule to Crystal to Functional Form*; NATO Science for peace and security. Series A: Chemistry and Biology; Roberts, K., Docherty, R., Tamura, R., Eds.; Springer, 2017; pp 395–408.

(715) Harada, T.; Hayakawa, H.; Kuroda, R. Vertical-Type Chiroptical Spectrophotometer (I): Instrumentation and Application to Diffuse Reflectance Circular Dichroism Measurement. *Rev. Sci. Instrum.* **2008**, *79*, 073103.

(716) Kuroda, R.; Saito, Y. Solid-State Circular Dichroism Spectra of Tris(Diamine)Cobalt(III) Complexes: Decomposition into E and A2 Components. *Bull. Chem. Soc. Jpn.* **1976**, *49*, 433–436.

(717) Hasuike, E.; Akimoto, A. M.; Kuroda, R.; Matsukawa, K.; Hiruta, Y.; Kanazawa, H.; Yoshida, R. Reversible Conformational Changes in the Parallel Type G-Quadruplex Structure inside a Thermoresponsive Hydrogel. *Chem. Commun.* **2017**, *53*, 3142–3144.

(718) El-Hachemi, Z.; Arteaga, O.; Canillas, A.; Crusats, J.; Llorens, J.; Ribó, J. M. Chirality Generated by Flows in Pseudocyanine Dye J-Aggregates: Revisiting 40 Years Old Reports. *Chirality* **2011**, *23*, 585–592.

(719) Okano, K.; Taguchi, M.; Fujiki, M.; Yamashita, T. Circularly Polarized Luminescence of Rhodamine B in a Supramolecular Chiral Medium Formed by a Vortex Flow. *Angew. Chem., Int. Ed.* **2011**, *50*, 12474–12477.

(720) Yamaguchi, T.; Kimura, T.; Matsuda, H.; Aida, T. Macroscopic Spinning Chirality Memorized in Spin-Coated Films of Spatially Designed Dendritic Zinc Porphyrin J-Aggregates. *Angew. Chem., Int. Ed.* **2004**, *43*, 6350–6355.

(721) Arteaga, O.; Canillas, A.; Crusats, J.; El-Hachemi, Z.; Llorens, J.; Sacristan, E.; Ribó, J. M. Emergence of Supramolecular Chirality by Flows. *ChemPhysChem* **2010**, *11*, 3511–3516.

(722) Mineo, P.; Villari, V.; Scamporrino, E.; Micali, N. Supramolecular Chirality Induced by a Weak Thermal Force. *Soft Matter* **2014**, *10*, 44–47.

(723) Arteaga, O.; Escudero, C.; Oncins, G.; El-Hachemi, Z.; Llorens, J.; Crusats, J.; Canillas, A.; Ribo, J. M. Reversible Mechanical Induction of Optical Activity in Solutions of Soft-Matter Nanophases. *Chem. - Asian J.* **2009**, *4*, 1687–1696.

(724) Ohno, O.; Kaizu, Y.; Kobayashi, H. J-aggregate Formation of a Water-soluble Porphyrin in Acidic Aqueous Media. *J. Chem. Phys.* **1993**, *99*, 4128–4139.

(725) Nafie, L. A.; Diem, M. Optical Activity in Vibrational Transitions: Vibrational Circular Dichroism and Raman Optical Activity. *Acc. Chem. Res.* **1979**, *12*, 296–302.

(726) Keiderling, T. A. Instrumentation for Vibrational Circular Dichroism Spectroscopy: Method Comparison an Newer Development. *Molecules* **2018**, *23*, 2404.

(727) Stephens, P. J.; Devlin, F. J.; Pan, J.-J. The Determination of the Absolute Configurations of Chiral Molecules Using Vibrational Circular Dichroism (VCD) Spectroscopy. *Chirality* **2008**, *20*, 643–663.

(728) Quesada-Moreno, M. M.; Cruz-Cabeza, A. J.; Avilés-Moreno, J. R.; Cabildo, P.; Claramunt, R. M.; Alkorta, I.; Elguero, J.; Zúñiga, F. J.; López-González, J. J. The Curious Case of 2-Propyl-1H-Benzimidazole in the Solid State: An Experimental and Theoretical Study. *J. Phys. Chem. A* **2017**, *121*, 5665–5674.

(729) Buffeteau, T.; Lagugné-Labarthet, F.; Sourisseau, C. Vibrational Circular Dichroism in General Anisotropic Thin Solid Films:

(730) Measurement and Theoretical Approach. *Appl. Spectrosc.* **2005**, *59*, 732–745.

(730) Cross, L. J. K.; Hore, D. K. Dual-Modulator Broadband Infrared Mueller Matrix Ellipsometry. *Appl. Opt.* **2012**, *51*, 5100–5110.

(731) Freedman, T. B.; Cao, X.; Dukor, R. K.; Nafie, L. A. Absolute Configuration Determination of Chiral Molecules in the Solution State Using Vibrational Circular Dichroism. *Chirality* **2003**, *15*, 743–758.

(732) Barron, L. D.; Hecht, L.; McColl, I. H.; Blanch, E. W. Raman Optical Activity Comes of Age. *Mol. Phys.* **2004**, *102*, 731–744.

(733) Barron, L. D.; Zhu, F.; Hecht, L.; Tranter, G. E.; Isaacs, N. W. Raman Optical Activity: An Incisive Probe of Molecular Chirality and Biomolecular Structure. *J. Mol. Struct.* **2007**, *834–836*, 7–16.

(734) Blanch, E. W.; Hecht, L.; Barron, L. D. Vibrational Raman Optical Activity of Proteins, Nucleic Acids, and Viruses. *Methods* **2003**, *29*, 196–209.

(735) Polavarapu, P. L. Ab Initio Vibrational Raman and Raman Optical Activity Spectra. *J. Phys. Chem.* **1990**, *94*, 8106–8112.

(736) Kachynski, A. V.; Kuzmin, A. N.; Prasad, P. N.; Smalyukh, I. I. Realignment-Enhanced Coherent Anti-Stokes Raman Scattering and Three-Dimensional Imaging in Anisotropic Fluids. *Opt. Express* **2008**, *16*, 10617–10632.

(737) Jen, S.; Clark, N. A.; Pershan, P. S.; Priestley, E. B. Raman Scattering from a Nematic Liquid Crystal: Orientational Statistics. *Phys. Rev. Lett.* **1973**, *31*, 1552–1556.

(738) Lee, T.; Trivedi, R. P.; Smalyukh, I. I. Multimodal Nonlinear Optical Polarizing Microscopy of Long-Range Molecular Order in Liquid Crystals. *Opt. Lett.* **2010**, *35*, 3447–3449.

(739) Wagner, N.; Hochberg, D.; Peacock-Lopez, E.; Maity, I.; Ashkenasy, G. Open Prebiotic Environments Drive Emergent Phenomena and Complex Behavior. *Life* **2019**, *9*, 45.

(740) Saito, Y.; Hyuga, H. Colloquium: Homochirality: Symmetry Breaking in Systems Driven Far from Equilibrium. *Rev. Mod. Phys.* **2013**, *85*, 603–621.

(741) Lutz, F.; Igarashi, T.; Kinoshita, T.; Asahina, M.; Tsukiyama, K.; Kawasaki, T.; Soai, K. Mechanistic Insights in the Reversal of Enantioselectivity of Chiral Catalysts by Achiral Catalysts in Asymmetric Autocatalysis. *J. Am. Chem. Soc.* **2008**, *130*, 2956–2958.

(742) Matsumoto, A.; Oji, S.; Takano, S.; Tada, K.; Kawasaki, T.; Soai, K. Asymmetric Autocatalysis Triggered by Oxygen Isotopically Chiral Glycerin. *Org. Biomol. Chem.* **2013**, *11*, 2928–2931.

(743) Singleton, D. A.; Vo, L. K. A Few Molecules Can Control the Enantiomeric Outcome. Evidence Supporting Absolute Asymmetric Synthesis Using the Soai Asymmetric Autocatalysis. *Org. Lett.* **2003**, *5*, 4337–4339.

(744) Crusats, J.; Hochberg, D.; Moyano, A.; Ribó, J. M. Frank Model and Spontaneous Emergence of Chirality in Closed Systems. *ChemPhysChem* **2009**, *10*, 2123–2131.

(745) Blanco, C.; Stich, M.; Hochberg, D. Temporary Mirror Symmetry Breaking and Chiral Excursions in Open and Closed Systems. *Chem. Phys. Lett.* **2011**, *505*, 140–147.

(746) Schiaffino, L.; Ercolani, G. Unraveling the Mechanism of the Soai Asymmetric Autocatalytic Reaction by First-Principles Calculations: Induction and Amplification of Chirality by Self-Assembly of Hexamolecular Complexes. *Angew. Chem., Int. Ed.* **2008**, *47*, 6832–6835.

(747) Quaranta, M.; Gehring, T.; Odell, B.; Brown, J. M.; Blackmond, D. G. Unusual Inverse Temperature Dependence on Reaction Rate in the Asymmetric Autocatalytic Alkylation of Pyrimidyl Aldehydes. *J. Am. Chem. Soc.* **2010**, *132*, 15104–15107.

(748) Gehring, T.; Quaranta, M.; Odell, B.; Blackmond, D. G.; Brown, J. M. Observation of a Transient Intermediate in Soai's Asymmetric Autocatalysis: Insights from 1H NMR Turnover in Real Time. *Angew. Chem., Int. Ed.* **2012**, *51*, 9539–9542.

(749) Cheung, P. S. M.; Cuccia, L. A. Amino Acid Directed Mirror Symmetry Breaking and Chiral Amplification of Ethylenediammonium Sulfate Crystals. *Chem. Commun.* **2009**, 1337–1338.

(750) Levilain, G.; Rougeot, C.; Guillen, F.; Plaquevent, J. C.; Coquerel, G. Attrition-Enhanced Preferential Crystallization Com-

bined with Racemization Leading to Redissolution of the Antipode Nuclei. *Tetrahedron: Asymmetry* **2009**, *20*, 2769−2771.

(751) Noorduin, W. L.; Van-Enckevort, W. J. P.; Meekes, H.; Kaptein, B.; Kellogg, R. M.; Tully, J. C.; McBride, J. M.; Vlieg, E. The Driving Mechanism behind Attrition-Enhanced Deracemization. *Angew. Chem., Int. Ed.* **2010**, *49*, 8435−8438.

(752) Kaptein, B.; Noorduin, W. L.; Meekes, H.; van Enckevort, W. J. P.; Kellogg, R. M.; Vlieg, E. Attrition-Enhanced Deracemization of an Amino Acid Derivative That Forms an Epitaxial Racemic Conglomerate. *Angew. Chem., Int. Ed.* **2008**, *47*, 7226−7229.

(753) Viedma, C.; Ortiz, J. E.; De Torres, T.; Izumi, T.; Blackmond, D. G. Evolution of Solid Phase Homochirality for a Proteinogenic Amino Acid. *J. Am. Chem. Soc.* **2008**, *130*, 15274−15275.

(754) Rybak, W. K. Asymmetric Autocatalysis: Crystallization-Induced Highly Enantioselective Synthesis of a Conglomerating Oxo-Rhenium(V) Complex. *Tetrahedron: Asymmetry* **2008**, *19*, 2234−2239.

(755) Noorduin, W. L.; Van Der Asdonk, P.; Meekes, H.; Van Enckevort, W. J. P.; Kaptein, B.; Leeman, M.; Kellogg, R. M.; Vlieg, E. Complete Chiral Resolution Using Additive-Induced Crystal Size Bifurcation during Grinding. *Angew. Chem., Int. Ed.* **2009**, *48*, 3278−3280.

(756) Uwaha, M. A Model for Complete Chiral Crystallization. *J. Phys. Soc. Jpn.* **2004**, *73*, 2601−2603.

(757) Viedma, C. Chiral Symmetry Breaking and Complete Chiral Purity by Thermodynamic-Kinetic Feedback near Equilibrium: Implications for the Origin of Biochirality. *Astrobiology* **2007**, *7*, 312−319.

(758) McBride, J. M.; Tully, J. C. Did Life Grind to a Start? *Nature* **2008**, *452*, 161−162.

(759) Uwaha, M. Simple Models for Chirality Conversion of Crystals and Molecules by Grinding. *J. Phys. Soc. Jpn.* **2008**, *77*, 083802.

(760) Saito, Y.; Hyuga, H. Chiral Crystal Growth under Grinding. *J. Phys. Soc. Jpn.* **2008**, *77*, 113001.

(761) Katsuno, H.; Uwaha, M. Monte Carlo Simulation of a Cluster Model for the Chirality Conversion of Crystals with Grinding. *J. Cryst. Growth* **2009**, *311*, 4265−4269.

(762) Uwaha, M.; Katsuno, H. Mechanism of Chirality Conversion by Grinding Crystals: Ostwald Ripening vs Crystallization of Chiral Clusters. *J. Phys. Soc. Jpn.* **2009**, *78*, 023601.

(763) Saito, Y.; Hyuga, H. Selection of Crystal Chirality: Equilibrium or Nonequilibrium? *J. Phys. Soc. Jpn.* **2009**, *78*, 104001.

(764) Saito, Y.; Hyuga, H. Crystal Chirality Selected by Mutual Antagonism. *J. Phys. Soc. Jpn.* **2010**, *79*, 083002.

(765) Hatch, H. W.; Stillinger, F. H.; Debenedetti, P. G. Chiral Symmetry Breaking in a Microscopic Model with Asymmetric Autocatalysis and Inhibition. *J. Chem. Phys.* **2010**, *133*, 224502.

(766) Uwaha, M. Steady Chirality Conversion by Grinding Crystals—Supercritical and Subcritical Bifurcations. *J. Cryst. Growth* **2011**, *318*, 89−92.

(767) Saito, Y.; Hyuga, H. Grinding-Induced Homochirality in Crystal Growth. *J. Cryst. Growth* **2011**, *318*, 93−98.

(768) Katsuno, H.; Uwaha, M. Appearance of a Homochiral State of Crystals Induced by Random Fluctuation in Grinding. *Phys. Rev. E - Stat. Nonlinear, Soft Matter Phys.* **2012**, *86*, 051608.

(769) Andrews, D. H. The Collected Works of J. Willard Gibbs. Two Volumes. *J. Chem. Educ.* **1929**, *6*, 591.

(770) Gibbs, J. W. *Thermodynamics, Collected Works*, Vol. *1*; Yale University Press: New Haven, CT, 1948.

(771) Blanco, C.; Ribó, J. M.; Hochberg, D. Modeling Spontaneous Chiral Symmetry Breaking and Deracemization Phenomena: Discrete versus Continuum Approaches. *Phys. Rev. E - Stat. Nonlinear, Soft Matter Phys.* **2015**, *91*, 022801.

(772) Hounslow, M. J.; Ryall, R. L.; Marshall, V. R. A Discretized Population Balance for Nucleation, Growth, and Aggregation. *AIChE J.* **1988**, *34*, 1821−1832.

(773) Ramkrishna, D. *Population Balances: Theory and Applications to Particulate Systems in Engineering*; Academic Press: San Diego, CA, 2000.

(774) Polak, W.; Sangwal, K. Modelling the Formation of Solute Clusters in Aqueous Solutions of Ionic Salts. *J. Cryst. Growth* **1995**, *152*, 182−190.

(775) Mullin, J. W. *Crystallization*, 4th ed.; Butterworths: Oxford, U.K., 2000.

(776) Nieto-Ortega, B.; Bürgi, T. Vibrational Properties of Thiolate-Protected Gold Nanoclusters. *Acc. Chem. Res.* **2018**, *51*, 2811−2819.

(777) Wang, Z.; Liu, J. W.; Su, H. F.; Zhao, Q. Q.; Kurmoo, M.; Wang, X. P.; Tung, C. H.; Sun, D.; Zheng, L. S. Chalcogens-Induced Ag6Z4@ Ag36 (Z = S or Se) Core-Shell Nanoclusters: Enlarged Tetrahedral Core and Homochiral Crystallization. *J. Am. Chem. Soc.* **2019**, *141*, 17884−17890.

(778) Blackmond, D. G. The Origin of Biological Homochirality. *Cold Spring Harbor Perspect. Biol.* **2010**, *2*, a002147−a002147.

(779) *Biochirality*; Topics in Current Chemistry, Vol. *333*; Cintas, P., Ed.; Springer: Berlin, Heidelberg, Germany, 2013.

(780) van Kampen, N. G. *Stochastic Processes in Physics and Chemistry*; Elsevier: Amsterdam, The Netherlands, 2007.

(781) Gillespie, D. T. Stochastic Simulation of Chemical Kinetics. *Annu. Rev. Phys. Chem.* **2007**, *58*, 35−55.

(782) Gillespie, D. T. Exact Stochastic Simulation of Coupled Chemical Reactions. *J. Phys. Chem.* **1977**, *81*, 2340−2361.

(783) McQuarrie, D. A. Stochastic Approach to Chemical Kinetics. *J. Appl. Probab.* **1967**, *4*, 413−478.

(784) Gillespie, D. T. A Rigorous Derivation of the Chemical Master Equation. *Phys. A* **1992**, *188*, 404−425.

(785) Gardiner, C. W. *Handbook of Stochastic Methods*, 2nd ed.; Springer: Berlin, Heidelberg, Germany.

(786) Mcadams, H. H.; Arkin, A. Stochastic Mechanisms in Gene Expression. *Proc. Natl. Acad. Sci. U. S. A.* **1997**, *94*, 814−819.

(787) Arkin, A.; Ross, J.; McAdams, H. H. Stochastic Kinetic Analysis of Developmental Pathway Bifurcation in Phage-Infected Escherichia Coli Cells. *Genetics* **1998**, *149*, 1633−1648.

(788) Elowitz, M. B.; Levine, A. J.; Siggia, E. D.; Swain, P. S. Stochastic Gene Expression in a Single Cell. *Science* **2002**, *297*, 1183−1186.

(789) Raser, J. M.; O'Shea, E. K. Control of Stochasticity in Eukaryotic Gene Expression. *Science* **2004**, *304*, 1811−1814.

(790) Blake, W. J.; Kærn, M.; Cantor, C. R.; Collins, J. J. Noise in Eukaryotic Gene Expression. *Nature* **2003**, *422*, 633−637.

(791) Gillespie, D. T. Chemical Langevin Equation. *J. Chem. Phys.* **2000**, *113*, 297−306.

(792) Risken, H. *The Fokker-Planck Equation*; Springer Series in Synergetics, Vol. *18*; Springer Berlin Heidelberg: Berlin, Heidelberg, Germany, 1989.

(793) Hochstadt, H. *The Functions of Mathematical Physics*; Dover: New York, 1986.

(794) Jafarpour, F.; Biancalani, T.; Goldenfeld, N. Noise-Induced Mechanism for Biological Homochirality of Early Life Self-Replicators. *Phys. Rev. Lett.* **2015**, *115*, 158101.

(795) Stich, M.; Ribó, J. M.; Blackmond, D. G.; Hochberg, D. Necessary Conditions for the Emergence of Homochirality via Autocatalytic Self-Replication. *J. Chem. Phys.* **2016**, *145*, 074111.

(796) Blackmond, D. G. "If Pigs Could Fly" Chemistry: A Tutorial on the Principle of Microscopic Reversibility. *Angew. Chem., Int. Ed.* **2009**, *48*, 2648−2654.

Apéndice C

A Complex Reaction Network Model for Spontaneous Mirror Symmetry Breaking in Viedma Deracemizations

ChemPhysChem

A Complex Reaction Network Model for Spontaneous Mirror Symmetry Breaking in Viedma Deracemizations

María E. Noble-Terán,[a] José-Manuel Cruz,[b] Hugo I. Cruz-Rosas,[a] Thomas Buhse,*[a] and Jean-Claude Micheau*[c]

Attrition-enhanced chiral symmetry breaking in crystals, known as Viedma deracemization, is a promising method for converting racemic solid phases into enantiomerically pure ones under non-equilibrium conditions. However, many aspects of this process remain unclear. In this study, we present a new investigation into Viedma deracemization using a comprehensive kinetic rate equation continuous model based on classical primary nucleation theory, crystal growth, and Ostwald ripening. Our approach employs a fully microreversible kinetic scheme with a size-dependent solubility following the Gibbs–Thomson rule. To validate our model, we use data from a real NaClO$_3$ deracemization experiment. After parametrization, the model shows spontaneous mirror symmetry breaking (SMSB) under grinding. Additionally, we identify a bifurcation scenario with a lower and upper limit of the grinding intensity that leads to deracemization, including a minimum deracemization time within this window. Furthermore, this model uncovers that SMSB is caused by multiple instances of concealed high-order autocatalysis. Our findings provide new insights into attrition-enhanced deracemization and its potential applications in chiral molecule synthesis and understanding biological homochirality.

Introduction

Attrition-enhanced deracemization,[1] or Viedma ripening,[2] has become a milestone in current chirality research to achieve spontaneous racemic-to-homochiral transitions in solid/liquid mixtures of racemic conglomerate crystals that are submitted to attrition.[3–7] In 2005, Viedma reported for the first time that total symmetry breaking and complete chiral purity can be achieved from a saturated and racemic NaClO$_3$ crystal slurry that was subjected for several hours to continuous stirred-grinding in the presence of glass beads.[8,9] The large and symmetric population of D and L crystals moved into complete chiral purity, with one of the enantiomorphous crystal forms completely disappearing. Repeated experiments show in theory, however not always in practice,[10,11] a stochastic distribution between the 100% L or 100% D results. Therefore, it appears that the Viedma deracemization stands for rarely observed spontaneous mirror symmetry breaking (SMSB).[12–16] SMSB denotes the appearance of optically active states starting from achiral, racemic, or nearly racemic initial conditions without the influence of any applied

asymmetric forces or additives.[14] The achievement of a final chiral state more stable than the racemic one is an inescapable outcome in the Viedma deracemization or, in other words, it can be compared to a special case of absolute asymmetric synthesis.[13]

NaClO$_3$ is a particularly interesting compound, for which spontaneous deracemization has been already observed during stirred crystallization in the pioneering work by Kondepudi.[17–20] It crystallizes in the chiral space group $P2_13$, which can easily be analysed by optical rotation.[21,22] It turns into an achiral solute upon dissolution,[23] i.e. it shows intrinsically the effect of "chiral amnesia".[24] According to the crystal Gibbs free energy,[25] the surface dominates at small sizes, while the volume dominates at large sizes, therefore it exists a critical size for their formation. Beyond this size, crystals grow, whereas below they dissolve (Gibbs-Thomson rule).[8,26–28] Supersaturation promotes primary nucleation,[29,30] supplying equal amounts of both enantiomeric crystals. Small crystals can also agglomerate with larger crystals of the same chirality, thus contributing to their growth via Ostwald ripening. During Viedma deracemization, the bigger NaClO$_3$ crystals are crushed into smaller clusters.[31] Under these conditions, small chiral nuclei can preferentially dissolve or favour secondary nucleation of crystals with the same handedness. Such a non-equilibrium situation is unstable from the chirality point of view. If there is a difference in average size between the two enantiomorphous crystals, a concentration gradient may be established, because the reincorporation of these smaller clusters into larger crystals takes place more often for the enantiomorphous crystals that are in excess.[32] This continuous process of dissolution–recrystallization[12] results in the autocatalytic emergence of a single chiral phase by the conversion of one solid enantiomorph into the other.[30,33] In terms of the crystal enantiomeric excess (Cee), the system performs a transition from Cee ≈ 0 to almost 100% even in the

[a] M. E. Noble-Terán, Dr. H. I. Cruz-Rosas, Dr. T. Buhse
Centro de Investigaciones Químicas – IICBA
Universidad Autónoma del Estado de Morelos
Avenida Universidad 1001, 62209 Cuernavaca, Morelos, Mexico
E-mail: buhse@uaem.mx
[b] Dr. J.-M. Cruz
Facultad de Ciencias en Física y Matemáticas
Universidad Autónoma de Chiapas
29050 Tuxtla Gutiérrez, Chiapas, Mexico
[c] Dr. J.-C. Micheau
Laboratoire des IMRCP, UMR au CNRS No. 5623
Université Paul Sabatier
31062 Toulouse Cedex, France
E-mail: jean-claude.micheau@univ-tlse3.fr

ChemPhysChem

Research Article
doi.org/10.1002/cphc.202300318

**Chemistry
Europe**
European Chemical
Societies Publishing

absence of any applied chiral asymmetric influence. In this last case, the chirality sign varies randomly between the dominance of either L- or D-NaClO₃ crystals in repeated experiments.

The signature of autocatalytic kinetics[8,34–36] in Viedma type systems has been evidenced as sigmoidal time-evolutions of the experimentally observed C*ee*.[37–39] Various theoretical models have been proposed attempting to explain the Viedma deracemization with the aim to rationalize the core of the process and to bring into accord with the experimental observations:

(i) Among them an original approach, using dispersive kinetic algebraic sigmoidal equations, has been examined by Skrdla.[40] However, it is evident that such an empirical equation is not able to capture the essence of SMSB, *i.e.*, the occurrence of optically activity from achiral conditions.

(ii) Monte-Carlo[41–45] or agent-based models[46] describe the changes in the crystal size distribution in a discrete manner. For instance, each Monte Carlo move represents a time interval during which a randomly chosen crystal either grows at the cost of smaller ones or is split into smaller pieces with a given random probability.

(iii) Population balance models have been proposed,[27,28,47–49] which all are based on the Gibbs thermodynamics and describe the change in the particle characteristic lengths as a function of the particle size, the temperature and supersaturation, according to primary nucleation theory. They treat entire populations by considering that birth and death of a large number of particles of different sizes are due to nucleation, growth, dissolution, solution-phase racemization, agglomeration, and mechanical breakage and obey the mass balance to account for the phase continuity.[50] It is expected that population balance models exhibit some ability to describe size-dependent effects. However, when taking the continuum limit, these models lose the microreversibility principle and as a consequence, they cannot mimic equilibrium situations.[16]

(iv) On the other side, chemical kinetics models have been developed in the framework of the mean field assumption.[11,32,40,49,51–59] As in the population balance models, they consider whether the crystal size is above or below a critical value by including the Gibbs-Thomson effect,[25] *i.e.*, smaller crystals dissolve faster than the larger ones. Then they translate the corresponding free energy relationships into reversible (or irreversible) differential rate equations in order to respect (or not) the principle of microreversibility.[60,61] Simulations are carried out by numerical integration of the differential equation system, describing the assumed kinetic network. Among the various kinetic rate equation approaches, the most complete and certainly the most sophisticated one has been proposed by Blanco *et al.*[12] It is concluded that the Viedma deracemization belongs to a true SMSB scenario, invalidating definitively the argument that homochirality arises only from the principle that bigger crystals are thermodynamically more stable than the smaller ones. Their model is based on a step-by-step polymerization-like monomer to cluster aggregation mechanism truncated to a maximum size of 100 monomeric units. While the maximum size is relatively high from the point of view of the model dimension, it is markedly small from a crystal size point of view, since more than 10^{10} monomeric units are in a 1 micron-sized chlorate crystal. Moreover, it is shown that the resulting C*ee* depends strongly on the size of the oligomers but does not increase very much for sizes higher than 6, thus confirming previous results from Saito and Hyuga[62] and Wattis[57] that a maximum size of 6 monomeric units is sufficient to reach SMSB in such step-by-step polymerization-like models.

In this study, we consider an original kinetic rate equation approach where all transformations are microreversible except for crystal breakage. The model includes primary nucleation giving rise to equal amounts of NaClO₃ D- and L-crystals, selective step-by-step aggregation, grinding producing daughter crystals of the same handedness as the parent crystals and non-discriminative dissolution of the L and D crystals. We show that these four elements, imbedded in several coupled aggregation equilibria, are sufficient to describe the C*ee* time-evolution, as observed in experimental settings,[63] as well as to reproduce either the equilibrium state or the non-equilibrium SMSB phenomenon.

Model Presentation

To provide new insight into the NaClO₃ deracemization,[8–10] our purpose is to mimic the different reversible and irreversible mechanisms present in a crystallization process; namely: primary nucleation, selective step-by-step aggregation, dissolution and grinding. Our kinetic rate equation model is based on a Becker-Döring inspired approach, which describes nucleation and ripening based on the enantiospecific adsorption and desorption of monomer units on chiral clusters of various size.[50,56,57,64–68] The model is left–right symmetric, *i.e.*, all left steps have their right counterparts with the same rate constants (Figure 1). Unlike several previously published models,[54,56,62,69] all steps involved in the present model are reversible and obey the detailed balance (microreversibility). Under these conditions, the thermodynamic equilibrium is the unescapable consequence of the reversibility. Moreover, we use the simpler Becker-Döring monomer to cluster aggregation step, thus avoiding to assume some involvement of cluster-to-cluster aggregations.[12,52,70,71]

From the Figure 1 diagram, the main steps occurring at equilibrium and under grinding can be described more in detail.

Primary Nucleation

According to the results of the plasmonic manipulation of NaClO₃ chiral crystallization,[72] a two-step nucleation mechanism has been suggested. First, the formation of a disordered local region of higher concentration, and second the development of a crystal nucleus in this region. It has been assumed
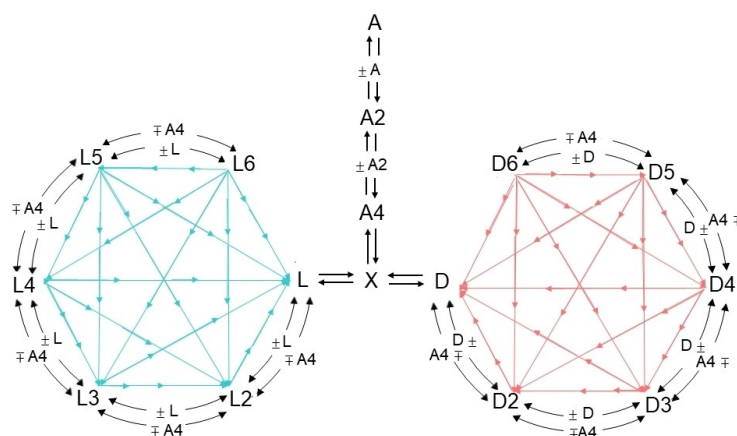
ChemPhysChem

Research Article
doi.org/10.1002/cphc.202300318

Chemistry
Europe
European Chemical
Societies Publishing

Figure 1. Proposed kinetic rate equation model for the numerical simulation of the NaClO$_3$ attrition-induced deracemization. A corresponds to the free solute and A2, A4 to the dense liquid formation; X represents the achiral phase which deracemizes towards chiral L or D according to a martensitic transformation;[72] L to L6 multiple equilibria are assumed to mimic the crystal growth and dissolution processes from crystals to dense liquid; for instance, reversible crystal growth is shown as Ln + L $\rightleftharpoons$ Ln + 1 (or Ln + 1 − L $\rightleftharpoons$ Ln), while reversible secondary nucleation/dissolution is schematized by Ln + A4 $\rightleftharpoons$ Ln + 1 (or Ln + 1 − A4 $\rightleftharpoons$ Ln); a series of irreversible steps (thin arrows in the centre of the two cycles) denote the crystal fragmentation under grinding. Note the perfect symmetry between the L and D side. The solvent molecules are not shown since they are inert.[73]

that in a supersaturated solution the solute (molecules or ion-pairs) is forming transitorily short-lived embryos through bimolecular additions,[62] as displayed in the K_{A2} and K_{A4} processes on Table 1. The species A represents the solvated ionic species, A2 being a partially desolvated dimer and A4 denotes the dense liquid phase, as it has been observed by

Niinomi et al.[72] during NaClO$_3$ crystallization. The dimerization steps have been truncated at K_{A4} to emphasize that that there are four NaClO$_3$ entities in the cubic chiral crystal unit cell.[74] The dense liquid A4 plays the role of a precursor of the achiral metastable monoclinic crystal phase X.[75] This process has been modelled by the step K_X in Table 1.

Table 1. List of processes and constants that describe the proposed model for the nucleation, growth, and dissolution of sodium chlorate in water at equilibrium. To simplify, only the L-side is shown. A is a schematic representation of the NaClO$_3$ element. Each reversible process has been unfolded: the forward rate constant has been written as the product of the reverse rate constant by the equilibrium constant, for instance in A + A $\rightleftharpoons$ A2, $K_{A2} = (k_a \cdot K_{A2})/k_a$ where $(k_a \cdot K_{A2})$ is a first-order forward rate constant describing the primary nucleation process. K_{A2} and K_{A4} are two semi-empirical equilibrium constants for the formation of the fragile aggregates A2 and A4. In A4 $\rightleftharpoons$ X, the equilibrium constant K_X translates the strengthening of the ionic bonds giving rise to the metastable achiral phase X. In X $\rightleftharpoons$ L, the martensitic transformation (chiralization of X to L or D) has been described by a rate constant k_c and an equilibrium constant K_C. For the sake of simplicity, all step-by-step aggregation processes from L2 to L6 have been described by only one encounter frequency (k) while the various equilibrium constants (K_2 to K_6) obey the free enthalpy variation according to the Gibbs-Thomson rule. The rate constant k_d has been used to describe the dissolution kinetics, while the corresponding equilibrium constants have been calculated according to the detailed balance requirements.

species and processes	forward rate constants	equilibrium constants	rates	comments
A + A $\rightleftharpoons$ A2	$k_a \cdot K_{A2}$	K_{A2}	$k_a(K_{A2}[A]^2 - [A2])$	dense liquid dimerization
A2 + A2 $\rightleftharpoons$ A4	$k_a \cdot K_{A4}$	K_{A4}	$k_a(K_{A4}[A2]^2 - [A4])$	dense liquid tetramerization
A4 $\rightleftharpoons$ X	$k_a \cdot K_X$	K_X	$k_a(K_X[A4] - [X])$	achiral phase nucleation
X $\rightleftharpoons$ L	$k_c \cdot K_C$	K_C	$k_c(K_C[X] - [L])$	martensitic transformation
L + L $\rightleftharpoons$ L2	$k \cdot K_2$	K_2	$k(K_2[L]^2 - [L2])$	chiral unit dimerization
L2 + L $\rightleftharpoons$ L3	$k \cdot K_3$	K_3	$k(K_3[L][L2] - [L3])$	chiral unit trimerization
L3 + L $\rightleftharpoons$ L4	$k \cdot K_4$	K_4	$k(K_4[L][L3] - [L4])$	chiral unit tetramerization
L4 + L $\rightleftharpoons$ L5	$k \cdot K_5$	K_5	$k(K_5[L][L4] - [L5])$	chiral unit pentamerization
L5 + L $\rightleftharpoons$ L6	$k \cdot K_6$	K_6	$k(K_6[L][L5] - [L6])$	chiral unit hexamerization
L6 $\rightleftharpoons$ L5 + A4	k_d	$1/(K_X.K_C.K_6)$	$k_d([L6] - (K_X.K_C.K_6)\ [L5][A4])$	hexamer dissolution
L5 $\rightleftharpoons$ L4 + A4	k_d	$1/(K_X.K_C.K_5)$	$k_d([L5] - (K_X.K_C.K_5)\ [L4][A4])$	pentamer dissolution
L4 $\rightleftharpoons$ L3 + A4	k_d	$1/(K_X.K_C.K_4)$	$k_d([L4] - (K_X.K_C.K_4)\ [L3][A4])$	tetramer dissolution
L3 $\rightleftharpoons$ L2 + A4	k_d	$1/(K_X.K_C.K_3)$	$k_d([L3] - (K_X.K_C.K_3)\ [L2][A4])$	trimer dissolution
L2 $\rightleftharpoons$ L + A4	k_d	$1/(K_X.K_C.K_2)$	$k_d([L2] - (K_X.K_C.K_2)\ [L][A4])$	dimer dissolution

ChemPhysChem

Research Article
doi.org/10.1002/cphc.202300318

Chemistry Europe
European Chemical
Societies Publishing

The chiral cubic form ($P2_13$) is generated during a martensitic transformation of the achiral one.[76] The two enantiomeric crystals L or D have the same probability to emerge.[76,77] This polymorphic evolution has been modelled by step K_C in Table 1 where L (or D, not shown) represents the minimal chiral nucleus. All four K_{A2}, K_{A4}, K_X and K_C processes mimic the sensitive dependence of the primary nucleation to the solute concentration.[78] At low supersaturation, the model predicts that nucleation is negligible, while at high supersaturation nucleation occurs.[28,69] Moreover, as all the steps are fully reversible, chiral monomers (L or D) can lose their chirality.[29]

Crystal Growth

Crystal growth becomes significant as soon as crystals are present and proceeds by the incorporation of elementary units from the solute into the already existing crystals. The crystals in excess catalyse their own production, they grow by capturing elements of the same chirality. They deplete the supersaturation thus favouring the dissolution of the minor enantiomorphous crystals (Ostwald ripening). We use a Becker-Döring approach[64] (a series of $L+Ln \rightleftharpoons Ln+1$ processes (the same for D)) to describe the enantiospecific addition/splitting of a chiral elementary unit into a bigger unit of the same chirality as it is shown in the processes K_2 to K_6 on Table 1. The successive units (L to L6 and D to D6) are assumed to be representative of the various crystal sizes. Therefore, crystals can grow or split by the gain or loss of a single unit at a time, mimicking the change of the crystal size distribution and the mass flow between crystals.[67] However, to maintain an acceptable tractability, the system has been truncated by not allowing clusters larger than 6. Such value appears minuscule regarding the macroscopic size that a $NaClO_3$ crystal can reach ($\approx 10^{22}$ units), but it has been shown that an hexamer model is already sufficient to exhibit the SMSB phenomenon.[57,62] Moreover, the model maintains the mass balance and it also has a unique equilibrium state by taking into account the detailed balance condition for all elementary reversible processes.[67] Finally, it is assumed that the cluster distribution is representative for a simplified crystal size distribution by considering only six classes as a depiction of the smaller, medium-sized and larger crystals in the experimental system.[2] We show that this streamlined distribution carries enough information about the crystal number and size to disclose that either larger crystal size or greater crystal number can determine the final handedness.[32]

Dissolution

Continuous dissolution and recrystallization take place on the crystal surfaces at solid-liquid equilibrium.[79] It is assumed that smaller crystals are more subjected to dissolution than the bigger ones.[23,80] As shown on Table 1, these dissolution processes are non-discriminative in respect to the crystal handedness and the chirality of the $NaClO_3$ solid phase is not preserved during this process. As a result, the achiral species generated from dissolution are recyclable and can recrystallize into either chiral form.[8] Worth to be pointed out is the full reversibility of these processes.[30,34] The entire list of species and processes for building our nucleation, growth and dissolution model are gathered on Table 1.

Grinding

During grinding in the presence of glass beads, crystals are fragmented by collisions and shear-forces into smaller crystals of the same handedness.[2,20,54,77,81,82] The system is driven out of equilibrium by an influx of mechanical energy; there is a continuous circulating flux in the reaction loop. The smaller crystals quickly dissolve,[80] while collisions generate secondary nuclei playing the role of seed crystals.[34,83,84] As a consequence, grinding promotes both the dissolution steps and the recrystallization rate.[26] However, attrition is size-dependent where bigger clusters are more prone to be broken than the smaller ones.[85,86]

The fragmentation and redistribution effects are described in our model by a series of irreversible steps where all possible combinatorial fragmentations of each aggregate from L2 to L6 or D2 to D6 (not shown) are considered,[85,87] dividing them into pieces of large+fine or medium+medium sizes as displayed on Table 2. The grinding intensity is related to the stirring rate and the number of glass beads. When grinding is stopped, the system returns to an achiral equilibrium state after substantial delay.

Considering the combined processes displayed on both Table 1 and 2, we compiled a symmetric kinetic rate equation model (see Supporting Information). Each of the reversible processes displayed on Table 1 (nucleation, aggregation, and dissolution) is defined by an equilibrium constant and a relaxation constant that describe the rate at which equilibrium is reached and strictly obey the detailed balance. On the other side, Table 2 describes the irreversible attrition processes occurring under non-equilibrium conditions. To analyse the equilibrium and non-equilibrium aspects of our system, the model has been converted into a set of 16 ordinary differential

Table 2. List of processes and rate constants that describe the proposed model for the attrition of sodium chlorate crystals under grinding. To simplify, only the L-side is shown. k_g represents the grinding intensity; h_6 to h_2 denote the sensitivity of each crystal sizes (L6 to L2) to grinding while j_1 and j_2 characterize the crystal splitting by abrasion or fracture.

species and processes	forward rate constants	rates	comments
$L6 \rightarrow L5+L$	k_g, h_6, j_1	$k_g, h_6, j_1[L6]$	fine grinding
$L6 \rightarrow L4+L2$	k_g, h_6, j_2	$k_g, h_6, j_2[L6]$	medium grinding
$L6 \rightarrow L3+L3$	k_g, h_6, j_2	$k_g, h_6, j_2[L6]$	medium grinding
$L5 \rightarrow L4+L$	k_g, h_5, j_1	$k_g, h_5, j_1[L5]$	fine grinding
$L5 \rightarrow L3+L2$	k_g, h_5, j_2	$k_g, h_5, j_2[L5]$	medium grinding
$L4 \rightarrow L3+L$	k_g, h_4, j_1	$k_g, h_4, j_1[L4]$	fine grinding
$L4 \rightarrow L2+L2$	k_g, h_4, j_2	$k_g, h_4, j_2[L4]$	medium grinding
$L3 \rightarrow L2+L$	k_g, h_3, j_1	$k_g, h_3, j_1[L3]$	fine grinding
$L2 \rightarrow L+L$	k_g, h_2, j_1	$k_g, h_2, j_1[L3]$	fine grinding

ChemPhysChem

Research Article
doi.org/10.1002/cphc.202300318

Chemistry Europe
European Chemical
Societies Publishing

equations (ODEs). Representative parameters values have been obtained from a curve fitting procedure based on a real experiment.

Model Parametrization

We have selected experimental data reported by Xiouras et al.,[63] showing the time evolution of the NaClO$_3$ C*ee* at different initial values of 20%, 30%, 40% and 50% in a Viedma-type system. The four kinetic curves were fitted simultaneously, i.e., with the same set of parameters (multi-experiment parameter fitting). To avoid over-parametrization (to escape the "horse description") and to fulfil the thermodynamic requirements of crystal growth and solubility, a free energy pattern satisfying the Gibbs–Thomson effect[25] has been used to establish the values of the equilibrium constants K_X to K_6. Since smaller crystals have a higher interfacial energy because their surface is more strongly curved,[49,88–90] they dissolve more readily than the larger ones.[74] Thus, there exists a critical nucleus size[88] corresponding to the critical number of units where the transition between endergonic to exergonic aggregation takes place.[12,50] In our truncated model, this feature occurs at L2 (or D2 not shown) as it can be seen on Figure 2, showing a parabolic-like free energy curve vs the cluster size. Therefore, only crystals bigger than the critical size can grow, while the smaller ones have the tendency to dissolve (Ostwald ripening).[37,46,55,78,84]

Likewise, the equilibrium constants K_{A2}, K_{A4} and K_C were also fixed to fulfil the temperature dependency on the NaClO$_3$ water solubility and the metastability of the dense liquid phase (A4) with respect to the dilute solution.[91] The initial amount of L6 and D6 crystals was calculated based on the Xiouras experimental protocol. Solubilized sodium chlorate (A$_0$) and a mixture of big L6 and D6 crystals with the corresponding crystal enantiomeric excess were considered as the only matter present at the beginning of our simulations. Out of the 7 parameters allowed to vary freely, multiple repetitive fitting runs, initiated from random initial values, consistently returned results within a range of $\pm 30\%$. The outcome of the simultaneous numerical fitting of the Xiouras experiment is depicted in Figure 3.
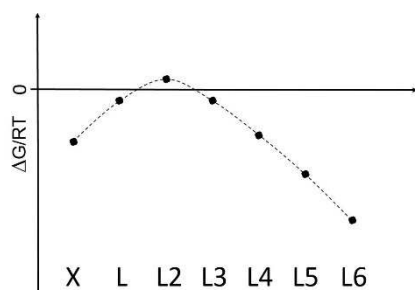

Figure 2. Classical nucleation curve showing the variation of the free energy difference between the bulk and the surface vs. the size of a growing cluster where $K_{(X \text{ to } 6)} = \exp(-\Delta G_{(X \text{ to } 6)}/RT)$. L2 represents the critical size unit.
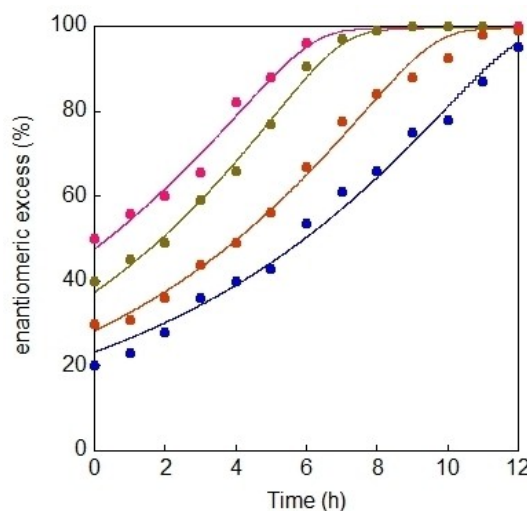

Figure 3. Kinetic modelling of the evolution of the crystal enantiomeric excess in a series of NaClO$_3$ deracemization experiments starting from different initial crystal enantiomeric excess (solid lines). Data points are taken from ref. [63] Solid lines: numerically integrated model using $k_a = 8.6e-2$; $k_c = 25.8$; $k = 0.24$; $k_d = 1.24e-3$; $k_g = 1.54e-2$; $h_n = \exp(n)$ with n = 2 to 6; $j_1 = 0.96$; $j_2 = 0.78$; $K_{A2} = 0.87$; $K_{A4} = 1.35$; $K_X = 2.46$; $K_C = 1.40$; $K_2 = 0.87$; $K_3 = 21$; $K_4 = 400$; $K_5 = 1.7e+7$; $K_6 = 1.2e+10$; $[A]_0 = 13$; all other initial concentrations at 0 excepted for L6 and D6; curve blue $ee_0 = 20\%$, L6 = 7.62e-2; D6 = 1.16e-1; curve purple $ee_0 = 30\%$, L6 = 6.77e-2; D6 = 1.23e-1; curve green $ee_0 = 40\%$, L6 = 5.98e-2; D6 = 1.49e-1; curve red $ee_0 = 50\%$, L6 = 4.95e-2; D6 = 1.52e-1.

Since some parameters are empirical, none of the extracted ones can be discussed independently. To explore the main features of our model and particularly its ability to mimic the global behaviour of aqueous sodium chlorate suspensions at rest and under deracemization conditions, we have carried out a dynamic analysis both in equilibrium and in non-equilibrium (with grinding) conditions. At this point, it must be borne in mind that the 6 clusters classes (L to L6 or D to D6) will be assumed to represent real crystal size distributions.[92]

Dynamic Analysis of the Model

Simulation of the Equilibrium Conditions

For that purpose, the set of the 16 ODEs has been integrated by setting the grinding intensity at 0. The numerical integration has been continued until the system has reached its equilibrium state. A saturation phenomenon has been mimicked by varying the initial amounts of the bigger clusters ([L6]$_0$ and [D6]$_0$) that were added in pure water. Figure 4a shows that all clusters dissolve provided that their initial amount was sufficiently small. On the contrary, when [L6]$_0$ and [D6]$_0$ increase, there is a turning point from which the amount of [A] in solution starts to saturate. This is the manifestation of the solute maximum solubility. However, this turning point is not sharp, and the saturation part slightly increases. It is likely that this is the result of the truncation at hexamers. This assumption is confirmed by the analysis of the nucleation-growth coupled equilibria (see Supporting Information), which shows that such a curve
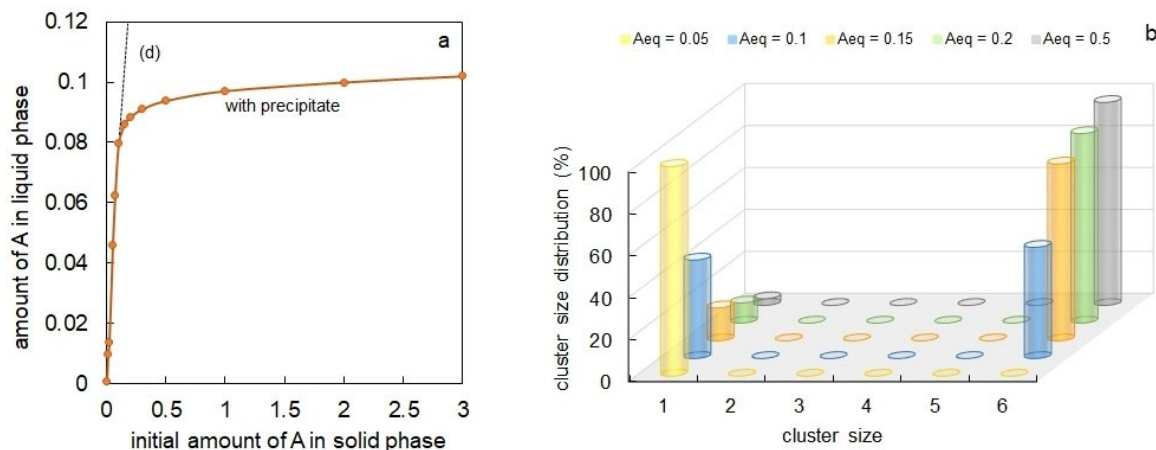
ChemPhysChem

Research Article
doi.org/10.1002/cphc.202300318

**Chemistry
Europe**
European Chemical
Societies Publishing

Figure 4. a) Variation in the amount of A in the liquid phase *vs* the initial amount of A in the solid phase. Note the first diagonal (d) showing the region where all the solid phase is exactly solubilized; the solute "solubility" is between 0.05 and 5 in arbitrary units. Beyond this point, the solid phase accumulates as a precipitate. b) Relative cluster size distribution around the turning point showing the exchange between subcritical (L or D) and supercritical (L6 or D6) clusters as the initial amount of A in solid phase increases. Parameter values are those of Figure 3 excepted $k_g = 0$.

corresponds to a 23rd degree polynomial equation. Figure 4b shows that as the supersaturation increases, subcritical clusters (size = 1, L or D) are progressively transformed into supercritical clusters (size = 6, L6 or D6).

The model mimics a liquid-solid equilibrium. The amount of solute in solution does not depend on the history of the system provided the same temperature and initial conditions. In Figure 5 (solid lines), a given volume of hot saturated fluid solution of $NaClO_3$ is rapidly cooled down to 30 °C until a precipitation occurs. During this process, nucleation (N), growth of the smaller crystals L and D (CG), dissolution of the smaller

crystals at the expense of the growth of the bigger L6 and D6 (Ostwald ripening (OR)), and equilibrium (EQ) can be recognized. A reverse situation is displayed by the dashed lines; this is the partial dissolution in the same volume of pure water at 30 °C of the same amount of $NaClO_3$, but initially under the form of big crystals (L6 and D6). As expected, the two situations reach the same equilibrium values.

Worth to be noted in Figure 5 (solid blue line) is the sigmoidal shape of the total crystal mass (TCM) evolution, which is reminiscent to the autocatalytic evolution encountered in many crystal growths situations.[93,94] These results show that crystallization and dissolution behaviour of a solute in solution are satisfactorily mimicked by our model.

Simulation of the Viedma Deracemization

The model shows SMSB, a situation that was initially described in the Viedma seminal paper,[8] namely that "symmetric" proportion of both enantiomeric crystals gives rise to total symmetry breaking and crystal purity by the random disappearance of one of the two enantiomers. In other words, chiral purity and total symmetry breaking occur even in the absence of any external chiral polarization. In the Viedma deracemization, the racemic state is unstable and evolves towards a pair of energetically identical stable chiral states. The final handedness is triggered by a very slight imbalance stochastically created by statistical fluctuations. This symmetry breaking is clearly a particular manifestation of general bifurcation theory. Figure 6 shows the evolution of the Cee of a suspension of $NaClO_3$ under grinding for various tiny Cee_0. The larger the Cee_0, the faster the deracemization.[49] For instance, an exponential increase of Cee_0 (from 1e-5 to 1e-2) leads to a linear decrease of the deracemization time.[48] On the other side, a stochastic behaviour at the entirely racemic initial situation ($Cee_0 = 0$) is unveiled by the numerical noise coming from rounding in our semi-
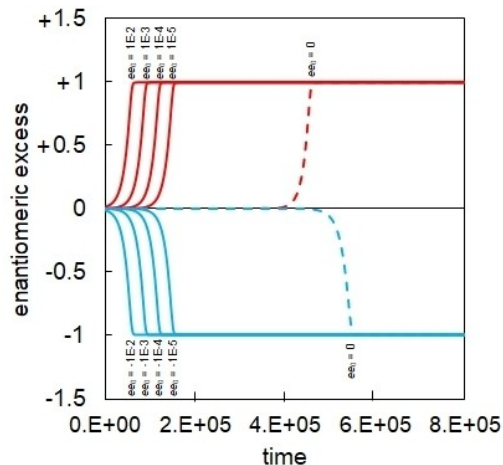

Figure 5. Evolution towards a solid-liquid equilibrium. Solid lines: simulation of the precipitation after cooling to 30 °C of a hot fluid solution, $[A]_0 = 1$ (solid green curve); total crystal mass, $TCM_0 = 0$, (solid blue curve); note the various phases of the process, N: nucleation, CG: crystal growth, OR: Ostwald ripening, EQ: equilibrium. Dashed lines: simulation of the crystal dissolution in pure water at 30 °C, $[A]_0 = 0$, (dashed green curve); $TCM_0 = 1$, *i.e.* $[L6]_0 = [D6]_0 = 1/48$ (in A units); all other $Ln = Dn = 0$), (dashed blue curve); note the same equilibrium values at 30 °C for the same amount of initial matter, either in fluid solution or in solid phase.

ChemPhysChem

Research Article
doi.org/10.1002/cphc.202300318

Chemistry Europe
European Chemical
Societies Publishing

Figure 6. Effect of the initial crystal enantiomeric excess (Cee_0) on the evolution of the Cee in a series of numerical simulations of the $NaClO_3$ deracemization. Note for $Cee_0=0$ the spontaneous symmetry breaking and the stochastic behaviour of the system regarding both the deracemization time and the final handedness. Parameter values are those of Figure 3 excepted [L6]$=$7e-2$-\varepsilon$ and [D6]$=$7e-2$+\varepsilon$ with $\varepsilon=\pm6.86$e-2 for $ee_0=\pm1$e-2, $\varepsilon=\pm6.986$e-2 for $ee_0=\pm1$e-3, $\varepsilon=\pm6.999$e-2 for $ee_0=\pm1$e-4, $\varepsilon=\pm6.99986$e-2 for $ee_0=\pm1$e-5 and $\varepsilon=0$ for $Cee_0=0$.

implicit 4^{th-}order Runge-Kutta integrator for stiff differential equations. Such a numerical simulation result is reminiscent to the high sensitivity to initial conditions that has been often reported.[95,96]

It should be noted that SMSB arises with the same parameters values that reproduce the real experiment (Section 3). Such situation is completely different from previously published models, which use purposely selected parameters values. If $Cee_0=0$, deracemization occurs systematically, but the final crystal handedness cannot be predicted (dashed curves in Figure 6). Moreover, we have shown that the intensity of

abrasive crystal grinding is crucial for a successful deracemization.

As claimed by Saito et al.,[97] Ostwald ripening without grinding is extremely slow to select chirality, if it is possible at all. In our model, racemization in solution prevents any deracemization. Such a situation is illustrated in the left part of the diagram shown in Figure 7a. No deracemization takes place if the grinding intensity is too low. On the contrary, deracemization occurs if the grinding intensity is sufficient. In the Viedma-like glass bead grinding, the formation of small, highly soluble particles is slow, which results in long deracemization times. However, as shown in Figure 7b, the deracemization time decreases by increasing the grinding intensity:[98] there is an optimum value of the grinding intensity after which there is no more gain. When applying very intense grinding, there is a very fast crystal breakage leading to a significant average crystal size reduction as attrition destroys large crystals. While the crystal size distribution becomes narrow, the size induced solubility gradients vanish in such a way that the system remains racemic. These results should be interpreted in light of the experiments conducted on ultrasound grinding, which demonstrated that the increase in enantiomeric excess was impeded with prolonged ultrasonication.[63,81,86] These are also in accordance with the Mazzotti et al. population balance equations, predicting from the observed trends that the application of a strong attrition can be disadvantageous regarding the process performance.[99] Lastly, we predict the existence of a bifurcation scenario with two critical grinding intensities within deracemization occurs.

Despite the crystal size distribution was simplified to merely six sizes, our simulation shows the effect of attrition on the relative amount of larger and smaller clusters during deracemization. At low grinding intensity, the system is close to equilibrium, it remains racemic and both enantiomorphs are in the L6/D6 form (Figure 8a and b, rows 1e-6 and 1.2e-5). But as the grinding intensity is increased, deracemization occurs through SMSB. As shown in the Figure 8a and b (row 7e-3), the
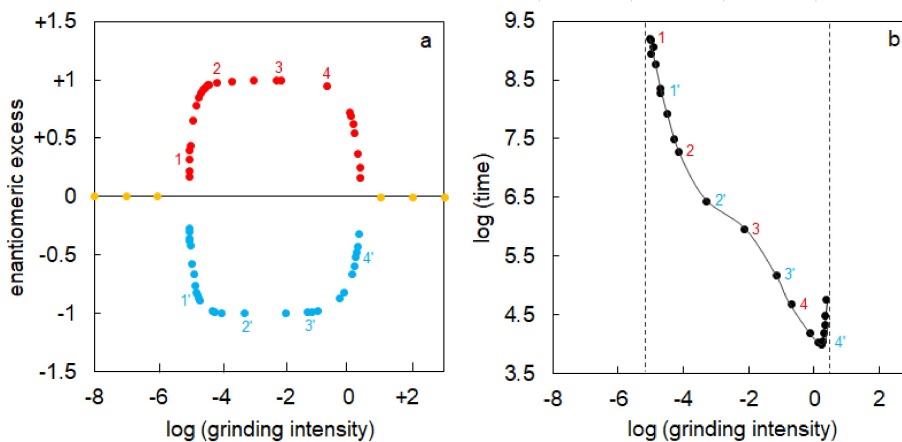

Figure 7. a) Numerical simulation of SMSB during the deracemization of $NaClO_3$ crystals under various grinding intensities ($Cee_0=0$). b) Time needed to reach a Cee of 90% as a function of the grinding intensity. The parameter values are those of Figure 3 excepted $A_0=10$, L6$=$D6$=$7e-2.

ChemPhysChem

Research Article
doi.org/10.1002/cphc.202300318

Chemistry Europe
European Chemical
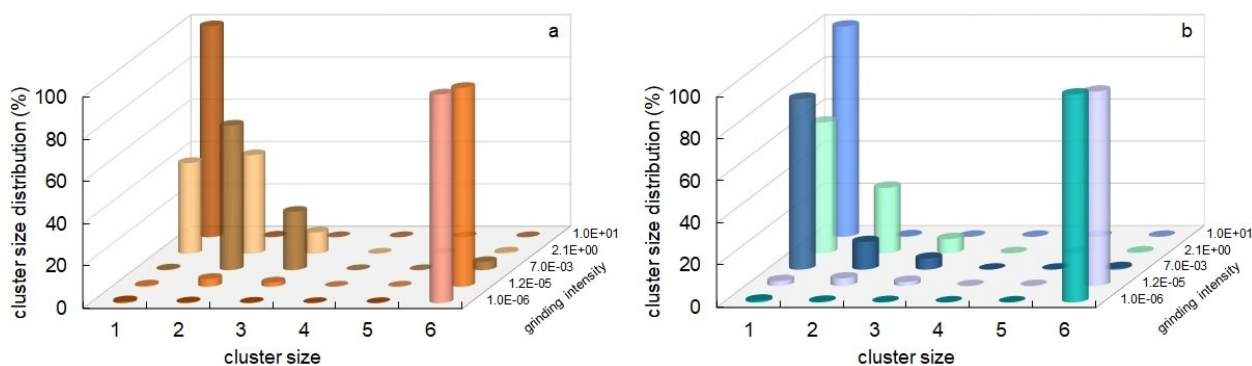Societies Publishing

Figure 8. Effect of the grinding intensity on the cluster size distribution: a) major enantiomer, b) minor enantiomer. Note that for the extreme rows (*i.e.* 1.0e-6 and 1.2e-5 on one side and 1.0e+1 on the other side), the mixture remains racemic: same distribution in both diagrams. Chiral symmetry breaking is seen for the intermediate rows: 7.0e-3 and 2.1e+0 where the two diagrams display different cluster size distributions.

major enantiomer is trapped under sizes 6, 3 and 2 (mainly L2 or D2), while the smaller sized cluster L (or D) dominates within the minor enantiomer. Increasing again the grinding intensity, the bigger sized cluster is also broken into small pieces, giving rise to a broadening of the distribution of the major enantiomer[95] (Figure 8a, row 2.1). Increasing again, there is a point where the two populations become identical as they are both trapped into the small sized L (or D) clusters. At this point the deracemization is lost and the system returns to a racemic state (Figure 8a and b, row 10). The loss of deracemization at high grinding intensities is likely to originate from the presence of small crystals of similar sizes giving rise to too small solubility gradients. These results are also in accordance with Ahn *et al.* who have found that the crystal size of the minor enantiomer decreases under sufficiently turbulent flow.[100]

Another important bifurcation parameter is the quantity of the initial matter. The larger clusters often impose the direction of evolution.

Figure 9 shows a competition between L2 and D4 clusters. On curves c and d, the effect of the larger D4 *vs* the smaller L2 is so strong that the evolution goes towards the D-side even if the amount of D4 is 10 times less than the amount of L2. (curves c and d). To counterbalance the bigger cluster D4 effect, *i.e.*, to reach the L-side, it is necessary to increase the amount of the smaller cluster L2 until a ratio nearby 20 times of the amount of D4 (curves a and b). This effect results from two antagonist processes: the solubility and the fracture. This is the combination of the two processes that determines the final handedness. While this simulation has been performed with monodisperse L2 and D4 clusters, these numerical results are reminiscent to the deracemization of an imine derivative carried out using mixtures of R- and S-samples of different crystal size distributions.[32,89] The minor enantiomer wins if it is bigger in size. In the same way, the smaller crystal size wins if it corresponds to the major enantiomer. Our simulation sends the same message: the minor enantiomer D4 wins because it has the larger crystal size (curves c and d). In the same way, the smaller crystal size L2 wins when its amount is sufficiently high (curves a and b).
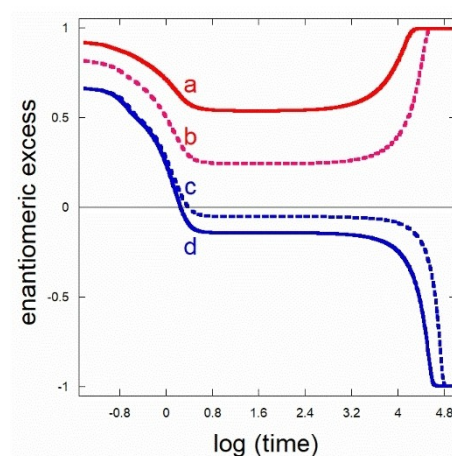

Figure 9. Simulation of the competition between larger and smaller clusters as initial additives. Parameter values are those of Figure 3 excepted $[A]_0 = 10$ and a: $[L2] = 0.5$, $[D4] = 0.01$; b: $[L2] = 0.4$, $[D4] = 0.02$; c: $[L2] = 0.3$, $[D4] = 0.03$; d: $[L2] = 0.2$, $[D4] = 0.04$; all other clusters at 0. Note the log(time) scale helping to visualize the $Cee = 0$ crossing point on curves c and d.

How Microreversibility Violation Unveils Hidden Autocatalysis

During crystal grinding, microreversibility is violated,[12,50,67] *i.e.*, a net flux exists within the cycles. These unidirectional fluxes are triggering the emergence of efficient high-order autocatalytic effects that are concealed within the kinetic network. The high-order autocatalytic processes can be understood in the following manner. When attrition occurs, the smaller clusters L are produced in many cases, together with higher clusters form L2 to L5. This high amount of small cluster L displaces all the reversible aggregation processes towards aggregation. For instance, considering the first line on Figure 10, the following unidirectional processes are occurring: L+L5 → L6 with L+L → L2, then L+L2 → L3, then L+L3 → L4, then L+L4 → L5, then L+L5 → L6 whose global mass balance including attrition and aggregation can be written as L6+6 L → 2 L6 resulting in a formal high-order autocatalysis in L.[101] All these effects are derived from the coupling between attrition and aggregations
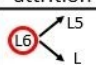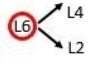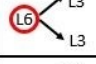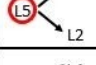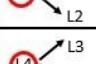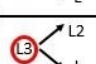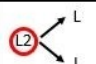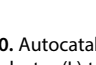
attrition	aggregation from L addition (net flux)	global balance
L6 → L5, L	then L + L5 → L6 then L + L → L2, then L + L2 → L3, then L + L3 → L4, then L + L4 → L5, then L + L5 → L6	L6 + 6L → 2L6
L6 → L4, L2	then L + L4 → L5, then L + L5 → L6 then L + L2 → L3, then L + L3 → L4, then L + L4 → L5, then L + L5 → L6	L6 + 6L → 2L6
L6 → L3, L3	then L + L3 → L4, then L + L4 → L5, then L + L5 → L6 then L + L3 → L4, then L + L4 → L5, then L + L5 → L6	L6 + 6L → 2L6
L5 → L3, L2	then L + L3 → L4, then L + L4 → L5 then L + L2 → L3, then L + L3 → L4, then L + L4 → L5	L5 + 5L → 2L5
L5 → L4, L	then L + L4 → L5 then L + L → L2, then L + L2 → L3, then L + L3 → L4, then L + L4 → L5	L5 + 5L → 2L5
L4 → L2, L2	then L + L2 → L3, then L + L3 → L4 then L + L2 → L3, then L + L3 → L4	L4 + 4L → 2L4
L4 → L3, L	then L + L3 → L4 then L + L → L2, then L + L2 → L3, then L + L3 → L4	L4 + 4L → 2L4
L3 → L2, L	then L + L2 → L3 then L + L → L2, then L + L2 → L3	L3 + 3L → 2L3
L2 → L, L	then L + L → L2 then L + L → L2	L2 + 2L → 2L2

Figure 10. Autocatalytic effects from the coupling between attrition and agglomeration. Crystal fragmentation by attrition. Net flux of aggregation of the smallest cluster (L) to the other ones (L to L5) under non-equilibrium conditions unveils several global balance high-order autocatalysis. Same for D side (not shown).

resulting in high-order autocatalysis, such as $LN + NL \rightarrow 2\,LN$ (N = 2 to 6) that sustain asymmetric amplification without the requisite of heterochiral interactions. The complete deracemization[2,86] is ensured by the continuous growth of the major enantiomer (here L) at the expense of the minor one (here D) through the essential racemization communication bridge,[102] $L \rightleftharpoons X \rightleftharpoons D$, which occurs within the solution phase (Figure 1). The enantiomer, which is able to produce the higher amount of the smallest clusters under grinding, will be more efficient and will win at the end. If the size distributions are comparable, the winner will be that of the higher initial amount. But if the size distributions are different, the winner will be that able to produce the higher amount of the smallest clusters. It could be the minor enantiomer if its size distribution is larger, *i.e.*, more sensitive to the grinding as it shown on Figure 9. Of course, all these net fluxes, which are responsible of the autocatalytic effects, do not exist at equilibrium when the microreversibility principle is respected without any unidirectional flux. These explanations apply also to other non-equilibrium situations such as thermal cycling.[103]

Conclusions

This study presents a novel multipurpose reaction-type model to elucidate the attrition-enhanced deracemization of sodium chlorate crystals using a truncated Becker-Döring microreversible approach. The model describes nucleation, growth, and Ostwald ripening using the same kinetic rate equations and accounts for the size dependence of solubility based on the Gibbs–Thomson rule. Secondary nucleation has been incorporated by assuming that amorphous clusters of the dense liquid (A4) are crystallized by crystal contact. Furthermore, the model considers the achiral phase of $NaClO_3$, which deracemizes towards chiral L- or D-crystals according to a martensitic transformation. Under grinding, crystal breakage into various smaller pieces is the only irreversible process.

For the first time, an accurate fitting of the evolution of the Cee in a series of $NaClO_3$ deracemization experiments under grinding when starting from different initial Cee has been accomplished. The delivered semi-empirical parameters allow for the identification of characteristic times for nucleation, crystal growth, Ostwald ripening, and equilibrium. The influence of the supersaturation value on the crystal size distribution is also illustrated. Using the same set of semi-empirical parameters extracted from our curve fitting process, we find numerical evidence for SMSB. Moreover, an unprecedented finding is the presence of a grinding intensity window. There is no deracemization if the grinding intensity is too small, but if the attrition is too strong, the difference in the shape of the particle size distribution vanishes and the symmetry breaking is no longer sustained. Since the Viedma deracemization is a true bifurcation scenario, a stochastic character of the deracemization process is expected when performed without any initial Cee nor any chiral impurity. By starting from different Cee_0, a threshold has been found that separates conditions where deracemization evolves towards either L or D crystals depending on their respective amount and size distribution.

ChemPhysChem

Research Article
doi.org/10.1002/cphc.202300318

Chemistry Europe
European Chemical
Societies Publishing

Our model, exhibiting a limited number of independent species, can serve as a useful guide for laboratory chemists, because it helps to understand that SMSB is the result of hidden high-order autocatalysis that is unveiled under non-equilibrium conditions. Considering that over 1800 chiral species capable of conglomerate crystallization have been curated and can be found in the Cambridge Structural Data Base,[104] it can be concluded that there are plenty of situations where Viedma deracemization will be the easy way towards new chiral auxiliaries. This study provides an important step towards this goal by presenting a multipurpose model that is an easier, more manageable theoretical basis than previously published models, since it features the same familiar chemical kinetic approach for mimicking both equilibrium and non-equilibrium situations.

Acknowledgements

Conflict of Interests

The authors declare no conflict of interest.

Data Availability Statement

The data that support the findings of this study are available in the supplementary material of this article.

[1] Deracemization is a classical organic chemistry concept where interconversion of the enantiomers is requisite. It primarily occurs in the presence of a chiral auxiliary (P. S. Portoghese, D. L. Larson, *J. Pharm. Sci.* **1964**, *53*, 302–305) or spontaneously in the case of chiral crystals (D. B. Amabilino, R. M. Kellogg, *Isr. J. Chem.* **2011**, *51*, 1034–1040).

[2] W. L. Noorduin, W. J. P. Van Enckevort, H. Meekes, B. Kaptein, R. M. Kellogg, J. C. Tully, J. M. McBride, E. Vlieg, *Angew. Chem. Int. Ed.* **2010**, *49*, 8435–8438.

[3] R. R. E. Steendam, M. C. T. Brouwer, E. M. E. Huijs, M. W. Kulka, H. Meekes, W. J. P. van Enckevort, J. Raap, F. P. J. T. Rutjes, E. Vlieg, *Chem. Eur. J.* **2014**, *20*, 13527–13530.

[4] T. P. T. Nguyen, P. S. M. Cheung, L. Werber, J. Gagnon, R. Sivakumar, C. Lennox, A. Sossin, Y. Mastai, L. A. Cuccia, *Chem. Commun.* **2016**, *52*, 12626–12629.

[5] A. H. J. Engwerda, N. Koning, P. Tinnemans, H. Meekes, F. M. Bickelhaupt, F. P. J. T. Rutjes, E. Vlieg, *Cryst. Growth Des.* **2017**, *17*, 4454–4457.

[6] S.-T. Wu, Y.-S. Zhang, B. Zhang, X.-L. Hu, X.-H. Huang, C.-C. Huang, N.-F. Zhuang, *Cryst. Growth Des.* **2019**, *19*, 2537–2541.

[7] I. Baglai, M. Leeman, R. M. Kellogg, W. L. Noorduin, *Org. Biomol. Chem.* **2019**, *17*, 35–38.

[8] C. Viedma, *Phys. Rev. Lett.* **2005**, *94*, 065504.

[9] C. Viedma, *Astrobiology* **2007**, *7*, 312–319.

[10] C. Viedma, *Cryst. Growth Des.* **2007**, *7*, 553–556.

[11] J. M. Cruz, K. Hernández-Lechuga, I. Domínguez-Valle, A. Fuentes-Beltrán, J. U. Sánchez-Morales, J. L. Ocampo-Espindola, C. Polanco, J. C. Micheau, T. Buhse, *Chirality* **2020**, *32*, 120–134.

[12] C. Blanco, J. Crusats, Z. El-Hachemi, A. Moyano, S. Veintemillas-Verdaguer, D. Hochberg, J. M. Ribó, *ChemPhysChem* **2013**, *14*, 3982–3993.

[13] J. M. Ribó, C. Blanco, J. Crusats, Z. El-Hachemi, D. Hochberg, A. Moyano, *Chem. Eur. J.* **2014**, *20*, 17250–17271.

[14] J. M. Ribó, D. Hochberg, J. Crusats, Z. El-Hachemi, A. Moyano, *J. R. Soc. Interface* **2017**, *14*, 20170699.

[15] D. Hochberg, C. Blanco, M. Stich, *SEMA SIMAI Springer Ser.* **2019**, *20*, 39–57.

[16] T. Buhse, J.-M. Cruz, M. E. Noble-Terán, D. Hochberg, J. M. Ribó, J. Crusats, J.-C. Micheau, *Chem. Rev.* **2021**, *121*, 2147–2229.

[17] D. K. Kondepudi, R. J. Kaufman, N. Singh, *Science* **1990**, *250*, 975–976.

[18] D. K. Kondepudi, J. K. Hall, *Phys. A: Stat. Mech.* **1992**, *188*, 113–119.

[19] D. K. Kondepudi, K. L. Bullock, J. A. Digits, J. K. Hall, J. M. Miller, *J. Am. Chem. Soc.* **1993**, *115*, 10211–10216.

[20] D. K. Kondepudi, C. Sabanayagam, *Chem. Phys. Lett.* **1994**, *217*, 364–368.

[21] G. N. Ramachandran, K. S. Chandrasekaran, *Acta Crystallogr.* **1957**, *10*, 671–675.

[22] S. C. Abrahams, J. L. Bernstein, *Acta Crystallogr. Sect. B* **1977**, *33*, 3601–3604.

[23] R. Y. Qian, G. D. Botsaris, *Chem. Eng. Sci.* **1998**, *53*, 1745–1756.

[24] D. G. Blackmond, *Chem. Eur. J.* **2007**, *13*, 3290–3295.

[25] M. Perez, *Scr. Mater.* **2005**, *52*, 709–712.

[26] G. Levilain, C. Rougeot, F. Guillen, J.-C. Plaquevent, G. Coquerel, *Tetrahedron: Asymmetry* **2009**, *20*, 2769–2771.

[27] M. Iggland, M. Mazzotti, *Cryst. Growth Des.* **2011**, *11*, 4611–4622.

[28] M. Iggland, M. Mazzotti, *Cryst. Growth Des.* **2012**, *12*, 1489–1500.

[29] Y. Saito, H. Hyuga, *Rev. Mod. Phys.* **2013**, *85*, 603–621.

[30] L.-C. Sögütoglu, R. R. E. Steendam, H. Meekes, E. Vlieg, F. P. J. T. Rutjes, *Chem. Soc. Rev.* **2015**, *44*, 6723–6732.

[31] J. M. McBride, R. L. Carter, *Angew. Chem. Int. Ed.* **1991**, *30*, 293–295.

[32] J. E. Hein, D. Gherase, D. G. Blackmond, *Top. Curr. Chem.* **2012**, *333*, 83–108.

[33] C. Viedma, P. Cintas, *Chem. Commun.* **2011**, *47*, 12786–12788.

[34] J. H. E. Cartwright, J. M. García-Ruiz, O. Piro, C. I. Sainz-Díaz, I. Tuval, *Phys. Rev. Lett.* **2004**, *93*, 035502.

[35] W. L. Noorduin, B. Kaptein, H. Meekes, W. J. P. Van Enckevort, R. M. Kellogg, E. Vlieg, *Angew. Chem. Int. Ed.* **2009**, *48*, 4581–4583.

[36] R. R. E. Steendam, J. Dickhout, W. J. P. Van Enckevort, H. Meekes, J. Raap, F. P. J. T. Rutjes, E. Vlieg, *Cryst. Growth Des.* **2015**, *15*, 1975–1982.

[37] W. L. Noorduin, H. Meekes, W. J. P. Van Enckevort, A. Millemaggi, M. Leeman, B. Kaptein, R. M. Kellogg, E. Vlieg, *Angew. Chem. Int. Ed.* **2008**, *47*, 6445–6447.

[38] W. W. Li, L. Spix, S. C. A. de Reus, H. Meekes, H. J. M. Kramer, E. Vlieg, J. H. Ter Horst, *Cryst. Growth Des.* **2016**, *16*, 5563–5570.

[39] G. Belletti, J. Schuurman, H. Stinesen, H. Meekes, F. P. J. T. Rutjes, E. Vlieg, *Cryst. Growth Des.* **2022**, *22*, 1874–1881.

[40] P. J. Skrdla, *Cryst. Growth Des.* **2011**, *11*, 1957–1965.

[41] H. Katsuno, M. Uwaha, *J. Cryst. Growth* **2009**, *311*, 4265–4269.

[42] Y. Saito, H. Hyuga, *J. Phys. Soc. Jpn.* **2010**, *79*, 083002.

[43] F. Ricci, F. H. Stillinger, P. G. Debenedetti, *J. Chem. Phys.* **2013**, *139*, 174503.

[44] H. Katsuno, M. Uwaha, *Phys. Rev. E* **2017**, *95*, 062804.

[45] Y. Saito, H. Hyuga, *J. Cryst. Growth* **2011**, *318*, 93–98.

[46] J. H. E. Cartwright, O. Piro, I. Tuval, *Phys. Rev. Lett.* **2007**, *98*, 165501.

[47] K. Suwannasang, G. Coquerel, C. Rougeot, A. E. Flood, *Chem. Eng. Technol.* **2014**, *37*, 1329–1339.

[48] M. Iggland, R. Müller, M. Mazzotti, *Cryst. Growth Des.* **2014**, *14*, 2488–2493.

[49] B. Bodák, G. M. Maggioni, M. Mazzotti, *Cryst. Growth Des.* **2018**, *18*, 7122–7131.

[50] C. Blanco, J. M. Ribó, D. Hochberg, *Phys. Rev. E* **2015**, *91*, 022801.

[51] H. Katsuno, M. Uwaha, *Phys. Rev. E* **2012**, *86*, 051608.

[52] H. Katsuno, M. Uwaha, *J. Cryst. Growth* **2014**, *401*, 59–62.

[53] W. L. Noorduin, W. J. P. Van Enckevort, H. Meekes, B. Kaptein, R. M. Kellogg, J. C. Tully, J. M. McBride, E. Vlieg, *Angew. Chem. Int. Ed.* **2010**, *122*, 8613–8616.

[54] M. Uwaha, *J. Phys. Soc. Jpn.* **2008**, *77*, 083802.

[55] M. Uwaha, H. Katsuno, *J. Phys. Soc. Jpn.* **2009**, *78*, 023601.

[56] M. Uwaha, *J. Cryst. Growth* **2011**, *318*, 89–92.

[57] J. A. D. Wattis, *Origins Life Evol. Biospheres* **2011**, *41*, 133–173.

[58] C. Xiouras, J. H. Ter Horst, T. Van Gerven, G. D. Stefanidis, *Cryst. Growth Des.* **2017**, *17*, 4965–4976.

[59] M. Uwaha, *J. Phys. Soc. Jpn.* **2004**, *73*, 2601–2603.

[60] R. Wegscheider, *Monatsh. Chem.* **1911**, *32*, 849–906.

[61] D. G. Blackmond, *Angew. Chem. Int. Ed.* **2009**, *48*, 2648–2654.

[62] Y. Saito, H. Hyuga, *J. Phys. Soc. Jpn.* **2005**, *74*, 535–537.

[63] C. Xiouras, J. Van Aeken, J. Panis, J. H. Ter Horst, T. Van Gerven, G. D. Stefanidis, *Cryst. Growth Des.* **2015**, *15*, 5476–5484.

[64] J. A. D. Wattis, *J. Phys. A. Math.* **1999**, *32*, 8755–8784.

[65] P. G. H. Sandars, *Origins Life Evol. Biospheres* **2003**, *33*, 575–587.

[66] J. A. D. Wattis, P. V. Coveney, *Origins Life Evol. Biospheres* **2005**, *35*, 243–273.

[67] H. Katsuno, M. Uwaha, *Phys. Rev. E* **2016**, *93*, 013002.

[68] H. Katsuno, M. Uwaha, *Cryst. Growth Des.* **2019**, *19*, 2428–2433.

[69] M. Iggland, M. Mazzotti, *CrystEngComm* **2013**, *15*, 2319–2328.

[70] Z. El-Hachemi, J. Crusats, J. M. Ribó, S. Veintemillas-Verdaguer, *Cryst. Growth Des.* **2009**, *9*, 4802–4806.

[71] Z. El-Hachemi, J. Crusats, J. M. Ribó, J. M. McBride, S. Veintemillas-Verdaguer, *Angew. Chem. Int. Ed.* **2011**, *50*, 2359–2363.

[72] H. Niinomi, T. Sugiyama, M. Tagawa, T. Ujihara, T. Omatsu, K. Miyamoto, H. Y. Yoshikawa, R. Kawamura, J. Nozawa, J. T. Okada, S. Uda, *Cryst. Growth Des.* **2020**, *20*, 5493–5507.

[73] Crystallization is mimicked by successive monomer additions. Since the liquid/solid partition is not explicit, our model also applies to the catalysed racemization of a chiral molecule in solution in the presence of a racemization catalyst C. In this latter case, it can be assumed that: $D + C \rightleftharpoons DC \rightleftharpoons LC \rightleftharpoons L + C$, which is equivalent to $D \rightleftharpoons X \rightleftharpoons L$ in the present model.

[74] J. Crusats, S. Veintemillas-Verdaguer, J. M. Ribó, *Chem. Eur. J.* **2006**, *12*, 7776–7781.

[75] Y. Kimura, H. Niinomi, K. Tsukamoto, J. M. García-Ruiz, *J. Am. Chem. Soc.* **2014**, *136*, 1762–1765.

[76] H. Niinomi, H. Miura, Y. Kimura, M. Uwaha, H. Katsuno, S. Harada, T. Ujihara, K. Tsukamoto, *Cryst. Growth Des.* **2014**, *14*, 3596–3602.

[77] H. Niinomi, T. Yamazaki, S. Harada, T. Ujihara, H. Miura, Y. Kimura, T. Kuribayashi, M. Uwaha, K. Tsukamoto, *Cryst. Growth Des.* **2013**, *13*, 5188–5192.

[78] T. Vetter, M. Iggland, D. R. Ochsenbein, F. S. Hänseler, M. Mazzotti, *Cryst. Growth Des.* **2013**, *13*, 4890–4905.

[79] D. A. Malivuk, A. A. Žekić, M. M. Mitrović, B. M. Misailović, *J. Cryst. Growth* **2013**, *377*, 164–169.

[80] K. Suwannasang, A. E. Flood, C. Rougeot, G. Coquerel, *Cryst. Growth Des.* **2013**, *13*, 3498–3504.

[81] W. L. Noorduin, P. Van Der Asdonk, A. A. C. Bode, H. Meekes, W. J. P. Van Enckevort, E. Vlieg, B. Kaptein, M. W. Van Der Meijden, R. M. Kellogg, G. Deroover, *Org. Process Res. Dev.* **2010**, *14*, 908–911.

[82] R. R. E. Steendam, P. J. Frawley, *Cryst. Growth Des.* **2019**, *19*, 3453–3460.

[83] T. Buhse, D. Durand, D. Kondepudi, J. Laudadio, S. Spilker, *Phys. Rev. Lett.* **2000**, *84*, 4405–4408.

[84] W. L. Noorduin, E. Vlieg, R. M. Kellogg, B. Kaptein, *Angew. Chem. Int. Ed.* **2009**, *48*, 9600–9606.

[85] W. L. Noorduin, H. Meekes, A. A. C. Bode, W. J. P. Van Enckevort, B. Kaptein, R. M. Kellogg, E. Vlieg, *Cryst. Growth Des.* **2008**, *8*, 1675–1681.

[86] C. Xiouras, A. A. Fytopoulos, J. H. Ter Horst, A. G. Boudouvis, T. Van Gerven, G. D. Stefanidis, *Cryst. Growth Des.* **2018**, *18*, 3051–3061.

[87] M. W. Van Der Meijden, M. Leeman, E. Gelens, W. L. Noorduin, H. Meekes, W. J. P. Van Enckevort, B. Kaptein, E. Vlieg, R. M. Kellogg, *Org. Process Res. Dev.* **2009**, *13*, 1195–1198.

[88] W. Polak, K. Sangwal, *J. Cryst. Growth* **1995**, *152*, 182–190.

[89] D. Gherase, D. Conroy, O. K. Matar, D. G. Blackmond, *Cryst. Growth Des.* **2014**, *14*, 928–937.

[90] R. R. E. Steendam, J. H. Ter Horst, *Cryst. Growth Des.* **2018**, *18*, 3008–3015.

[91] P. G. Vekilov, *Cryst. Growth Des.* **2004**, *4*, 671–685.

[92] B. Zhang, G. Coquerel, W. S. Kim, *Cryst. Growth Des.* **2023**, *23*, 741–750.

[93] L. Bentea, M. A. Watzky, R. G. Finke, *J. Phys. Chem. C* **2017**, *121*, 5302–5312.

[94] G. Schwartz, U. Hananel, L. Avram, A. Goldbourt, G. Markovich, *J. Am. Chem. Soc.* **2022**, *144*, 9451–9457.

[95] J. E. Hein, B. Huynh Cao, C. Viedma, R. M. Kellogg, D. G. Blackmond, *J. Am. Chem. Soc.* **2012**, *134*, 12629–12636.

[96] C. Rougeot, F. Guillen, J. C. Plaquevent, G. Coquerel, *Cryst. Growth Des.* **2015**, *15*, 2151–2155.

[97] Y. Saito, H. Hyuga, *J. Phys. Soc. Jpn.* **2008**, *77*, 113001.

[98] W. L. Noorduin, H. Meekes, W. J. P. van Enckevort, A. Millemaggi, M. Leeman, B. Kaptein, R. M. Kellogg, E. Vlieg, *Angew. Chem. Int. Ed.* **2008**, *120*, 6545–6547.

[99] B. Bodák, G. M. Maggioni, M. Mazzotti, *Cryst. Growth Des.* **2019**, *19*, 6552–6559.

[100] J. Ahn, D. H. Kim, G. Coquerel, W.-S. Kim, *Cryst. Growth Des.* **2018**, *18*, 297–306.

[101] F. C. Frank, *Biochim. Biophys. Acta* **1953**, *11*, 459–463.

[102] C. Viedma, J. E. Ortiz, T. de Torres, T. Izumi, D. G. Blackmond, *J. Am. Chem. Soc.* **2008**, *130*, 15274–15275.

[103] M. Uwaha, H. Katsuno, *J. Cryst. Growth* **2022**, *598*, 126873.

[104] M. P. Walsh, J. A. Barclay, C. S. Begg, J. Xuan, N. T. Johnson, J. C. Cole, M. O. Kitching, *JACS Au* **2022**, *2*, 2235–2250.

Apéndice D

Spontaneous Emergence of Chirality in Autocatalytic Cycle Models of the Soai Reaction

Asymmetric Autocatalysis: The Soai Reaction

The Royal Society of Chemistry

Buhse, T., Noble-Terán, M.E., Hochberg, D., Ribó, J.M., Micheau, J.-C. Spontaneous Emergence of Chirality in Autocatalytic Cycle Models of the Soai Reaction. In: *Asymmetric Autocatalysis: The Soai Reaction*. T. Kawasaki, A. Matsumoto, K. Soai (Eds.); The Royal Society of Chemistry, 2023, p. 129-155.

Spontaneous Emergence of Chirality in Autocatalytic Cycle Models of the Soai Reaction

THOMAS BUHSE,*[a] MARÍA E. NOBLE-TERÁN,[a]
DAVID HOCHBERG,[b] JOSEP M. RIBÓ[c] AND
JEAN-CLAUDE MICHEAU[d]

[a] Centro de Investigaciones Químicas-IICBA, Universidad Autónoma del Estado de Morelos, 62209 Cuernavaca, Morelos, Mexico; [b] Department of Molecular Evolution, Centro de Astrobiología (CSIC-INTA), 28850 Torrejón de Ardoz, Madrid, Spain; [c] Department of Organic and Inorganic Chemistry, Institute of Cosmos Science (IEEC-UB), University of Barcelona, 08028 Barcelona, Catalonia, Spain; [d] Laboratoire des IMRCP, UMR au CNRS No. 5623, Université Paul Sabatier, F-31062 Toulouse, France
*Email: buhse@uaem.mx

7.1 Introduction

The long-standing objective of organic chemists has been to achieve total asymmetric synthesis in a homogeneous reaction system,[1–3] and in the absence of an external chiral induction. This dream came true after Soai's discovery.[4] The Soai reaction, the addition of diisopropylzinc to prochiral pyrimidine carbaldehydes (see Scheme 7.1), yields unprecedented biases from the racemate (see ref. 5–9 and references therein). The chiral induction is exerted by the same final chiral product acting as an enantioselective catalyst, and this means that the Soai reaction is an autocatalytic enantioselective reaction.
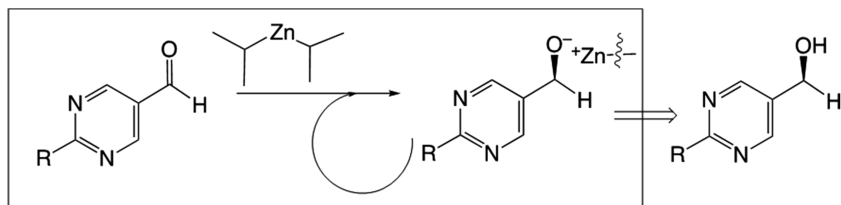
Scheme 7.1   Principle of the enantioselective autocatalysis of the Soai reaction. Initial carbaldehyde and final alkoxide form a diversity of oligomeric complexes with diisopropylzinc. These complexes may be chiral and nowadays it is widely accepted that some of them act as enantioselective catalysts and that additional heterochiral coupling reactions between oligomers, containing the final chiral alkoxides, form a Frank-like reaction network (ref. 10) yielding spontaneous mirror-symmetry breaking (SMSB).

The first efforts to study the Soai reaction were aimed at inferring the mechanisms showing autocatalysis (see Box 7.1). It was realized that this is not a simple direct autocatalysis,[11] but rather one implying a complex reaction network of intermediates (see Section 7.3). The high exergonicity of the alkyl Zn(II) addition to the carbaldehyde points to kinetic control of the reaction before the reverse reaction has had time to racemize the alkoxides. Therefore, the reaction outputs should correspond to transient stationary states.

Several characteristics of the Soai reaction point to a quite different thermodynamic scenario than that of the common asymmetric inductions of organic synthesis. This is an energy dissipative chemical system (see Box 7.2), where the final non-equilibrium stationary state (NESS) does not have the racemic composition: the expected racemate is an unstable NESS, and there is an energetically degenerate enantiomeric pair of scalemic NESS's, which have high enantiomeric excess (ee) values (see Section 7.2). This is an unfamiliar feature compared to the common enantioselective kinetic control of classical asymmetric synthesis. The experimental example of the Soai reaction agrees with a scenario of irreversible non-equilibrium thermodynamics, where a reaction network showing higher order nonlinear enantioselective autocatalysis (Box 7.1) operates at far from equilibrium conditions (Box 7.2). Then, beyond a critical value, an increase in the entropy production converts the racemic NESS into an unstable stationary (saddle) point, from which, by the effect of a chiral fluctuation (Box 7.3), the system evolves towards the corresponding stable scalemic NESS.

In summary, nowadays all rationalizations of the Soai reaction consider a reaction network similar to that of the Frank mechanism[10] (first-order autocatalysis coupled to a heterochiral reaction coupling, called the mutual inhibition step) in which enantioselective autocatalysis and mutual inhibition are provided by the involvement of oligomeric intermediates

Box 7.1   Reaction mechanisms which potentially may yield SMSB

Reaction with linear kinetic dependences on the enantiomers. A common transformation from achiral to chiral products, reversible or irreversible, as for example:

$$A + B \leftrightarrows D(L) \quad \text{or} \quad A + B \rightarrow D(L),$$
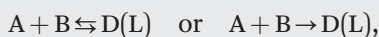
can only lead to the racemate in the deterministic limit and in the absence of any chiral polarization.

Reaction showing enantioselective autocatalysis (enantioselective non-linear dependences). When the transformation from achiral to chiral is autocatalytic, the growth dynamics follows[12] either reversibly (left) or irreversibly (right):

$$A + B + nD \leftrightarrows (n+1)D(L) \quad \text{or} \quad A + B + nD \rightarrow (n+1)D(L).$$

The outcome of this reaction depends on the nature of the system and on the autocatalytic order.

If the autocatalytic order is sufficiently high $(n > 1)$,

In closed systems in equilibrium with their surroundings, the reversible reaction (left) yields the racemate, while the irreversible one (right) may show racemic biases even if the initial conditions start from extremely low enantiomeric excesses:[13,14] unavoidable initial stochastic fluctuations from the racemate are more efficiently transferred in the deterministic limit of the transformation. For the case of a reversible reaction, but sufficiently exergonic, some transient chiral excursions may be detected.

In open far from equilibrium systems, even the reversible transformation may lead to scalemic non-equilibrium stationary states (NESS's) (see Box 7.2).[12]

If the autocatalytic order is too low $(n \leq 1)$ scalemic NESS's cannot be obtained. This is the case, for instance, of first-order autocatalysis $(n = 1)$ which requires coupling with other enantioselective reactions[11] in order to yield SMSB and to achieve the enantiomer growth dynamics up to observable levels.

(Section 7.3). Furthermore, the thermodynamic scenario for SMSB is that far from equilibrium thermodynamics. Figure 7.1 attempts to describe the confluence of these two topics in the discussion of the Soai reaction. This, in open systems, should lead to final stable NESS, but in closed systems to transient stationary scalemic states of similar composition. On the basis of all these considerations and on the basis of previously reported reductionist models (Section 7.2), the design of realistic models (Section 7.4) should be possible.

Box 7.2   Soai reaction as a bifurcation in a dissipative system

Open system. The characteristic methodology of the Soai reaction of successive additions of reagents to the exhausted reaction outcome, in order to achieve the amplification to higher ee values, is an approximation to an open flow reactor, such as previously reported.[15,16] Therefore, the understanding of the reaction is more suited to the framework of systems open to matter exchange.

  Dependence on the boundary conditions. The reaction exhibits high sensitivity to the reaction parameters, the total chemical mass being an important one, and to the boundary conditions. This means for the same reaction mechanisms, that the final reaction outcome may be a racemic or a scalemic mixture depending on whether the system parameters achieve or not the value of the critical entropy production for the bifurcation.[12]

  Stochastic distribution of chiral sign between experiments. In the absence of any external chiral polarization, the spontaneous mirror-symmetry breaking (SMSB) in the Soai reaction must lead to a stochastic distribution of chiral signs between experiments, due to the stochastic distribution of chiral signs of the fluctuations (see Box 7.3). On the contrary, under chiral polarization, acting at the bifurcation point,[17] the SMSB leads to a deterministic chiral sign.

Box 7.3   Effect of fluctuations in the bifurcation scenario

Chiral compositional fluctuations take the system away from its saddle point and the unstable racemic NESS. By their nature they are stochastic, and therefore must lead to a stochastic distribution of chiral signs between experiments. Early reports on the Soai reaction showed biases from the expected 50%/50% bimodal distribution of opposite chiral signs between experiments. However, later reports had shown how the stochastic distribution of chiral signs between experiments may be obtained by optimizing and controlling the experimental conditions.[18]

  Sensitivity of cryptochiral inductions. The Soai reaction shows unprecedented sensitivities to very weak chiral inductions. For example, those of asymmetric centres arising from isotopic substitution ($^1H/^2H$, but also $^{12}C/^{13}C$, $^{16}O/^{18}O$, and $^{14}N/^{15}N$).[19–22] This is the confirmation of previous theoretical reports indicating that a very small chiral polarization may convert a perfect bifurcation into an imperfect one,[17] *i.e.*, different experiments would lead always to the NESS of the same chiral sign. From a factual point of view, such evolution appears as a chiral amplification, but it is a consequence of the instability of the racemic NESS of the

evolution towards a stable NESS. Note that such an effect of a cryptochiral polarization is a selection of the chiral sign but not an asymmetric induction, because with or without the chiral polarization the final NESS is always chiral and practically of the same absolute ee value. It is only the *distribution* of the final chiral signs that differs.

The effect of cryptochirality in the Soai reaction would be also manifested, not only by a cryptochiral substance, but also by the presence of chiral compounds at very low concentrations. In our opinion, the first Soai reaction reports show a divergence from the stochastic bimodal distribution of chiral signs that is probably due to traces of chiral contaminants.[6]
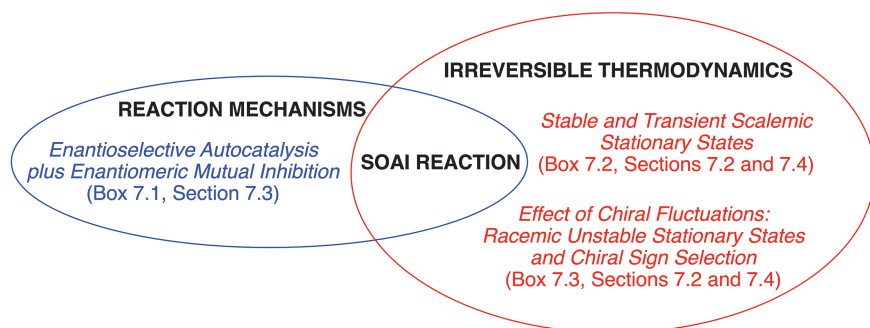

Figure 7.1   Main elements to be considered for the understanding of the Soai reaction.

7.2   Reductionist Frank Models of the Soai Reaction

The main features of the Soai reaction can be summarized in three points: (i) the Soai reaction leads to random outcomes of the chiral sign[18,23–25] starting from the tiny statistical chiral fluctuations about the ideal racemic composition,[26,27] (ii) extremely small chiral polarizations, such as those furnished by isotopic enantiomers[20,28–31] are sufficient to determine the chiral sign of the final reaction outcome, and (iii) the experimental procedure, based on sequential reactions where the reaction product is used in the next reaction stage, leads to amplification of chirality from initial experimentally undetectable ee's to final ee values close to homochirality.[18,24] These features (see Boxes 7.2 and 7.3) have inspired kinetic modeling efforts, based on the Frank reaction network[10] with enantioselective autocatalysis (see Box 7.1) and mutual inhibition, and which have successfully reproduced the variety of the striking phenomena observed in the Soai reaction.[32,33] We discuss briefly selected results from two reductionist approaches.

7.2.1 Models of Rivera Islas *et al.*

The kinetic models defined by Rivera Islas *et al.*[32] are summarized in Table 7.1. Model 1 represents the minimal set of processes that can reproduce qualitatively the main features of the Soai reaction. Reactions 3–5 coincide with Frank's original model, whereas 1 and 2 allow for the direct production of the enantiomers. Model 2 aims at more chemical realism by including the organozinc reactant Z in steps 1′–4′ as well as the reversible formation of the heterochiral (6) and homochiral dimers, 7–8. Lastly, Model 3 allows for the possibility of replacing the monomer-catalyzed steps 3′ and 4′ by dimer catalysis in 9 and 10. Model 3 includes the steps 1′, 2′, and 5–11.

The minimal Model 1 leads to a large racemic bias in a bifurcation scenario (see Figure 7.2) under batch conditions in which any kinetic parameter or achiral substrate concentration can drive the system into either a racemic or scalemic state from achiral initial conditions. The amplification strength depends on the ratio of heterodimerization to enantioselective autocatalysis: (k_2/k_1). The enantiomeric excess is defined as $ee = ([R]_{tot} - [S]_{tot})/([R]_{tot} + [S]_{tot})$, where $[S]_{tot} = [S] + [RS] + 2[SS]$, and similarly for $[R]_{tot}$. As shown in Figure 7.2 the bifurcation threshold depends on the mutual inhibition rate constant (k_2) and the value of the initial ee_0. For curve A no chiral catalyst was added, for curve B, $ee_0 = 1\%$, curve C, $ee_0 = 10\%$ and curve D, $ee_0 = -1\%$. Note, for strictly racemic initial conditions, the expected final outcome must also be racemic, so that the results in curve A are a consequence of the numerical round-off error. Hence, beyond the bifurcation threshold the final outcome of a positive or negative ee is random (curve A). Simulations for which this numerical noise is suppressed are presented in Section 7.2.2.

Model 2 behaves almost identically to Model 1 in so far as reproducing the mirror-symmetry breaking and the amplification of ee are concerned. By contrast, regarding parameter fits, the monomeric model requires a homodimer *vs.* heterodimer energy difference of 6.3 kcal mol^{-1} while for the dimeric model the requisite is only 2.7 kcal mol^{-1}, with the heterodimer being more stable. Figure 7.3 shows a fit to the aldehyde concentration during a one-step Soai reaction.[23]

Table 7.1 The kinetic models proposed by Rivera-Islas *et al.*[32] based on Frank's scheme.[10] Forward and reverse reaction rate constants are indicated by the ordered pairs: (k_{for}, k_{rev}).

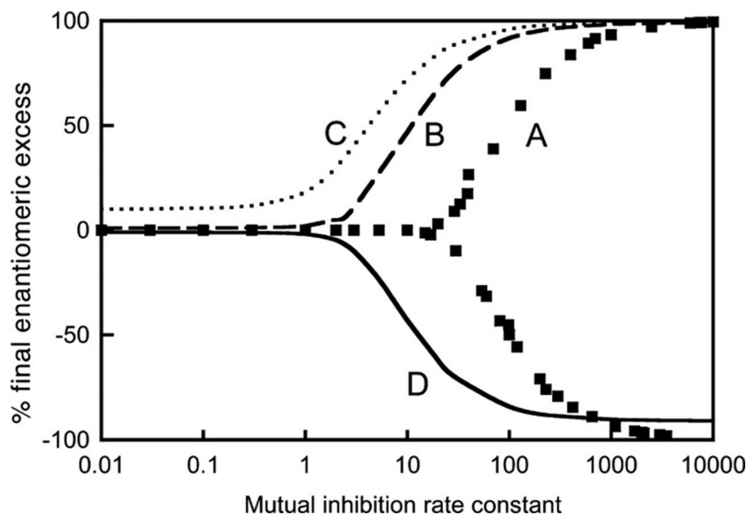| Model 1	Model 2	Model 3
A → R (k_0) [1]	A + Z → R (k'_0) [1′]	A + Z + RR → R + RR (k_6) [9]
A → S (k_0) [2]	A + Z → S (k'_0) [2′]	A + Z + SS → S + SS (k_6) [10]
A + R → 2R (k_1) [3]	A + Z + R → 2R (k'_1) [3′]	A + Z + RS → 0.5 S + 0.5 R + RS (k_7) [11]
A + S → 2S (k_1) [4]	A + Z + S → 2S (k'_1) [4′]	
R + S → RS (k_2) [5]	RS → R + S (k_3) [6]	Model 3 includes steps 1′, 2′ and 5–11.
	R + R ↔ RR (k_4, k_5) [7]	
	S + S ↔ SS (k_4, k_5) [8]	

Figure 7.2 Mirror-symmetry breaking and amplification of ee in Model 1. $[A]_0 = 1$ M, $k_0 = 10^{-6}$ M^{-1}s^{-1}, $k_1 = 1$ M^{-1}s^{-1}. Curve A, racemic initial conditions: $[R]_0 = [S]_0 = 0$; curve B, $[R]_0 = 5.05 \times 10^{-3}$ M, & $[S]_0 = 4.95 \times 10^{-3}$ M (1% catalyst, ee = 10%); curve C, $[R]_0 = 5.50 \times 10^{-3}$ M & $[S]_0 = 4.50 \times 10^{-3}$ M (1% catalyst, ee = −10%); curve D, $[R]_0 = 4.95 \times 10^{-2}$ M & $[S]_0 = 5.05 \times 10^{-2}$ M (10% catalyst, ee = −1%). Reproduced from ref. 32 with permission from the National Academy of Sciences.
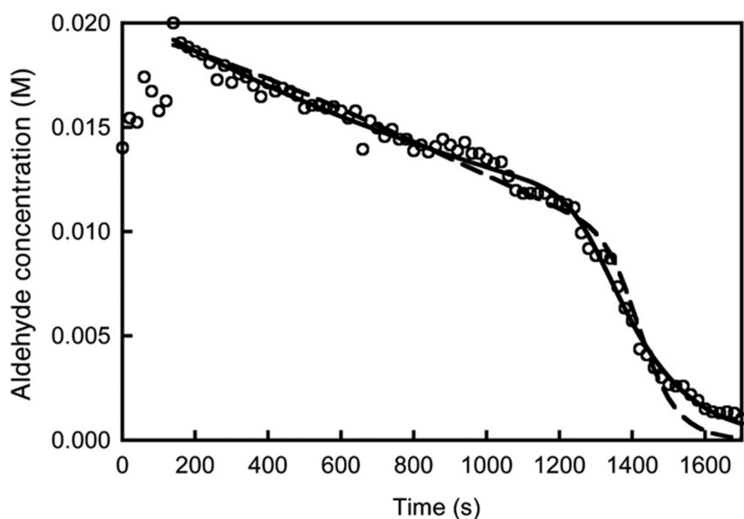

Figure 7.3 Evolution of the aldehyde concentration during a typical Soai reaction (open circles). Fit by Model 2 (continuous line) and by Model 3 (broken line). Initial concentrations (M): $[A] = 1.92 \times 10^{-2}$ & $[Z] = 0.04$; rate parameters Model 2 (Model 3): $k_0 = 5.2 \times 10^{-3}$ (3.7×10^{-3}) M^{-1}s^{-1}; $k_1 = 69$ M^{-2}s^{-1} $(k_6 = 154$ M^{-2}s$^{-1})$, $k_7 = 2.1 \times 10^{-4}$ M^{-2}s^{-1}, $k_2 = 4.5 \times 10^5$ (9.2×10^5) M^{-1}s^{-1}; $k_3 = 5.2 \times 10^{-2}$ (6.4×10^{-4}) s^{-1}; $k_4 = 4.8 \times 10^3$ (1.1×10^4) M^{-1}s^{-1}; $k_5 = 21$ (6.4×10^{-4}) s^{-1}. Reproduced from ref. 32 with permission from the National Academy of Sciences.

We remark that more detailed dynamical perspectives show that the simplified reductionist direct autocatalysis, such as, *e.g.* A + B → 2B, actually derives from a more involved autocatalytic cycle in which dimers, trimers, and tetramers are implicated (see Section 7.4). In this approach, the hetero-oligomers provide the self-inhibition.[34] Comprehensive kinetic analyses of autocatalytic cycle models based on the various oligomeric orders of the assumed catalytic species have been carried out in ref. 35.

7.2.2   Models of Crusats *et al.*

Fully reversible reaction networks in closed systems, based on the Frank model,[10] and in the absence of any chiral polarization, have been considered in detail, see Table 7.2 for the reaction scheme and the corresponding thermodynamic constraint.[33] First, we point out that the network (I) + (II) by itself cannot explain SMSB of the Soai reaction, because it is unable to amplify chirality from an initial enantiomeric excess[33] (see also Box 7.1). The case of limited enantioselectivity (I) + (II) + (III) does no better. In either open or closed systems, this network can only lead to stable final racemic states, and as a consequence of the thermodynamic constraint. By contrast, the network (I) + (II) + (V) (Frank model) may lead to a kinetically controlled SMSB. The amplification by (II) of the initially low non-linear effect of (V) is greater when the initial total concentration of catalysts is low. This implies that the sequential reaction procedure of the Soai reaction works well when it is carried out not only for constant initial concentrations of A and B, but also when the dilution of the previous outcome is performed.[18,24] Soai's repetitive sequential reaction procedure uses the outcome from one reaction as a catalyst for the next reaction. Indeed, in order to increase the ee value of the reaction to significant values, the Soai reaction uses a sequential reaction procedure: the exhausted final reaction mixture is used for a new reaction batch at the same initial conditions. However, this works well only under dilution of the previous batch of the reaction: either by using a larger reaction volume (generally 1 : 10) or by using only a small aliquote of the previous reaction product.[24,36] The point is not intuitive, but it is a simple

Table 7.2   A and B are two achiral reactants. The reversible reactions are (I): direct production of enantiomers L or D, (II) enantioselective autocatalysis, (III) non-enantioselective catalysis, (IV) homodimerization, and (V) heterodimerization. Inset: Thermodynamic constraints that relate (I), (II), and (III) through their corresponding (forward, reverse) reaction rate constants (k_f, k_r).

Reactions	Thermodynamic constraint
A + B ↔ L, A + B ↔ D (k_1, k_{-1}) **(I)**	$\dfrac{k_1}{k_{-1}} = \dfrac{k_2}{k_{-2}} = \dfrac{k_3}{k_{-3}}$
A + B + L ↔ 2L, A + B + D ↔ 2D (k_2, k_{-2}) **(II)**	
A + B + L ↔ L + D, A + B + D ↔ D + L (k_3, k_{-3}) **(III)**	
L + L ↔ LL, D + D ↔ DD (k_4, k_{-4}) **(IV)**	
L + D ↔ LD (k_5, k_{-5}) **(V)**	

consequence of the non-linearity of the autocatalysis. Such as that noted by other authors,[15] this behavior is a consequence of the fact the typical sequential methodology of the Soai reaction is an approximation to an open flow reactor system.[16]

Figure 7.4 indicates how a significant ee_t would be obtained following the dilution procedure after 6 sequential reactions, but not for a repetitive procedure involving only the addition of new reagents A and B. In the latter case, the value of ee_t remains below the limits of experimental detection. This behavior is in agreement with the experimental reports that have led to the optimization of the work-up of the Soai reaction.[18,24,28]

The role of the limited enantioselectivity and homodimerization reactions, (III) and (IV), respectively, when included in the Frank model, (I) + (II) + (V), can be appreciated in Figure 7.5. The formation of the homodimers LL and DD, (IV), does not change the maximum value of ee_t value are lower than for the basic network: compare the curves (b) and (d). The purpose of the formation of the heterodimer LD, (V), is to increase the ee by racemate elimination.
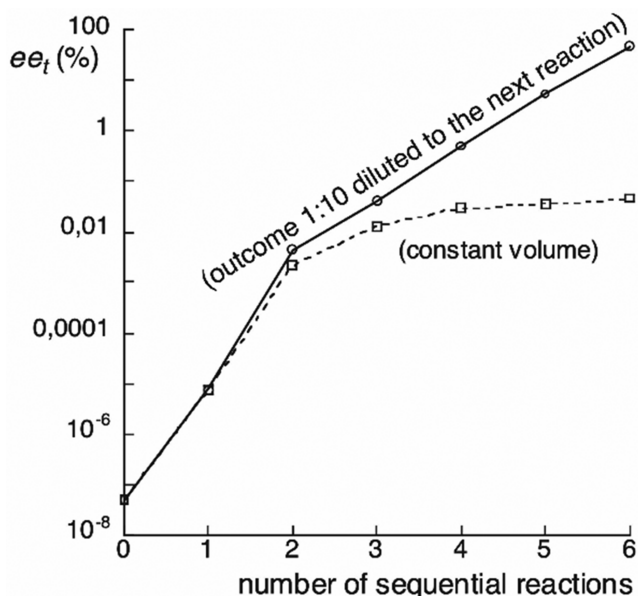

Figure 7.4   Evolution of ee_t by a sequential repetitive asymmetric amplification in a system (I) + (II) + (V) (see Table 7.2) with a low exergonic formation of LD $(K_V = 10)$; $[A]_0 = 1$ M, $[B]_0 = 1$ M, $k_1 = 1 \times 10^{-5}$, $k_{-1} = 1 \times 10^{-10}$, $k_2 = 1$, $k_{-2} = 1 \times 10^{-5}$, $k_5 = 1 \times 10^6$, $k_{-5} = 1 \times 10^5$. The first reaction starts with an initial ee_t below that corresponding to the inherent statistical deviation of the racemic composition (log scale). The dashed line corresponds to a procedure without dilution of the previous reaction outcome and the solid line to a procedure where the reaction volume is increased by a factor of ten in each new reaction (see the text for an explanation). Reproduced from ref. 33 with permission from John Wiley & Sons, Copyright © 2009 Wiley-VCH Verlag GmbH & Co. KGaA, Weinheim.
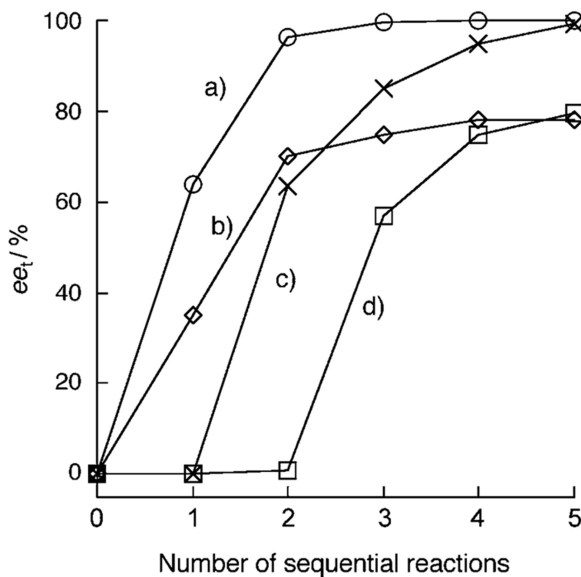
Figure 7.5 The change in ee_t (defined in Table 7.1) *versus* the sequential reaction work-up (1 : 10 volume increase in each stage); $[A]_0 = [B]_0 = 1$ M and in the first reaction $[L]_0 = (1 \times 10^{-7} + 1 \times 10^{-16})$ M, $[D]_0 = 1 \times 10^{-7}$ M. Other parameters are: $k_1 = 1 \times 10^{-5}$, $k_2 = 1$, $k_3 = 0.1$, and $\dfrac{k_i}{k_{-i}} = 1 \times 10^5$; $k_4 = 10^6$, $k_{-4} = 3.33 \times 10^4$, $k_5 = 1 \times 10^6$, $k_{-5} = 3.33 \times 10^3$. (a) (I) + (II) + (V), (b) (I) + (II) + (III) + (V), (c) (I) + (II) + (IV) + (V), (d) (I) + (II) + (III) + (IV) + (V); see Table 7.2 and the text for explanation of the curves in (a), (b), (c), and (d). Reproduced from ref. 33 with permission from John Wiley & Sons, Copyright © 2009 Wiley-VCH Verlag GmbH & Co. KGaA, Weinheim.

The formation of the homodimers LL and DD, (IV), competes with this process, thus limiting its effect. Limited enantioselectivity, (III), tends to racemize the system and so lowers the final enantiomeric excess.

7.3   Mechanistic Investigations of the Soai Reaction

7.3.1   Hemiacetal and Aldehyde Involvement Within the Autocatalytic Scaffold

From the experimental/structural point of view, the biggest actual question refers to the nature of the autocatalyst.[37–40] To address this problem, the Trapp group[39,40] has carried-out detailed kinetic analyses including the record of more than 20 kinetic evolutions of both the starting aldehyde and the produced carbinols. By the clever use of an unprecedented combination of flow-injection enantioselective HPLC and *in situ* high-resolution mass spectrometric measurements, a transient formation of hemiacetal complexes has been unveiled and it has been assumed that they can establish an

autocatalytic cycle. This result is a confirmation of the previous NMR analysis of a hemiacetal formation by Gehring *et al.*[41] However, if the transient has been scaled by NMR at less than 2% of the initial aldehyde (at 0 °C with an adamantly substituted pyrimidinic aldehyde), mass spectrometry does not allow such quantitation although the bell-shaped kinetic was very similar. Fortunately, thanks to a kinetic modeling approach giving rise to the forward and reverse rate constants of acetalization, it is possible to estimate the maximum amount of hemiacetal in a typical Trapp experiment (run at 20 °C with a *tert*-butylacetylenyl substituted aldehyde). Figure 7.6 displays the numerical simulation of the establishment of the hemiacetalization equilibrium between aldehyde and added carbinol before the addition of the alkylzinc. Note that the equilibrium is shifted towards the reactant side and that the amount of hemiacetal is about 0.3% of the minor reactant (the added carbinol).

This value is compatible with the transient hemiacetal bell-shaped kinetic curve, but the involvement of a so-small amount in the catalytic cycle has been already questioned by Gridnev *et al.*[42] Trapp *et al.* recognize themselves that the process is apparently inefficient, but thanks to a well-performed experiment they confirm the autocatalytic properties of the Soai reaction mixture. The experiment consisted of matching a reference Soai reaction with a doped one, *i.e.* the same reaction, but which has received at its starting point, a small injection of a currently running Soai reaction mixture. The results are gathered in Table 7.3.

While these results confirm the catalytic role of the Soai reaction mixture, they don't give any information about the catalyst structure. The claimed sentence: "*It has to be pointed out, that adding 60 μL of a completed Soai reaction does not influence the induction period*", might suggest that both aldehyde and carbinol are needed to build the catalyst. However, as it is well known that the carbinol alone is catalytic,[5] such an assumption requires complementary experiments. Their proposed mechanism has been then translated into a reaction network which was subsequently analyzed by using 26 differential equations allowing the authors to calculate the concentration profiles and the ee in various conditions. Unfortunately, no direct comparison between the experiments and the model were provided. The question about the involvement of the aldehyde within the catalytic cycle is still open.

The key question about the possible involvement of the aldehyde within the catalytic scaffold in the Soai reaction is related to the apparent second kinetic order of the aldehyde. First discovered by Blackmond *et al.*,[43,44] then confirmed by Trapp,[39] this result must be considered carefully. If the kinetic order appears as useful in simple linear kinetic systems, it can be misleading in the case of nonlinear systems such as the Soai autocatalytic reaction. For instance, this second-order story guided Ercolani *et al.* to compute several catalytic scaffolds involving one or two aldehyde moieties, but without acetalization.[45,46] Examples of such calculations are displayed in Scheme 7.2.
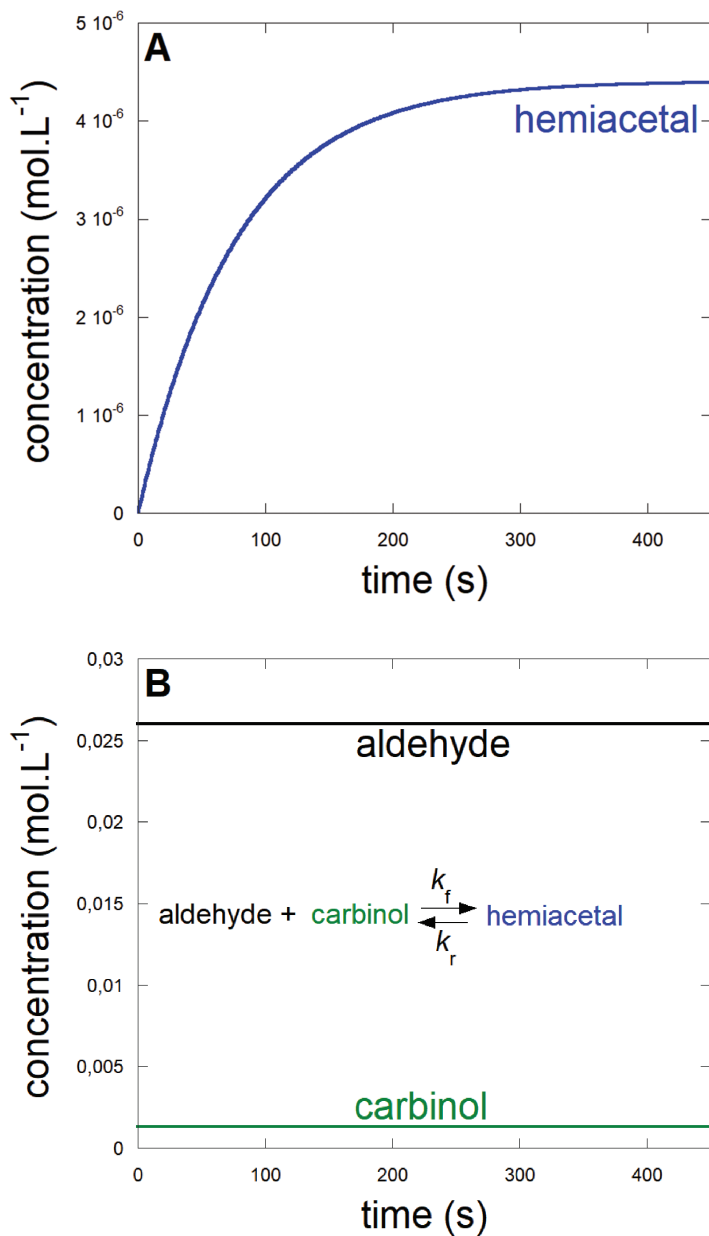
Figure 7.6 (A) Numerical simulation of the establishment of the hemiacetalization equilibrium using the Trapp's published[39] forward and reverse rate constants and initial concentrations: $k_f = 1.7 \times 10^{-3}$ $M^{-1} s^{-1}$; $k_r = 1.3 \times 10^{-2}$ s^{-1}; (B) initial concentrations of the aldehyde (26 mM) and the alcohol (1.3 mM) are not significantly affected by the establishment of this equilibrium.

Table 7.3   Analysis of the reference and doped experiments.

	Reference	Doped	Comment
Initial rate (mol s^{-1})	4.2×10^{-3}	1.4×10^{-2}	From S.I.[39]
Inflexion time (s)	254.9	199.5	From S.I.[39]
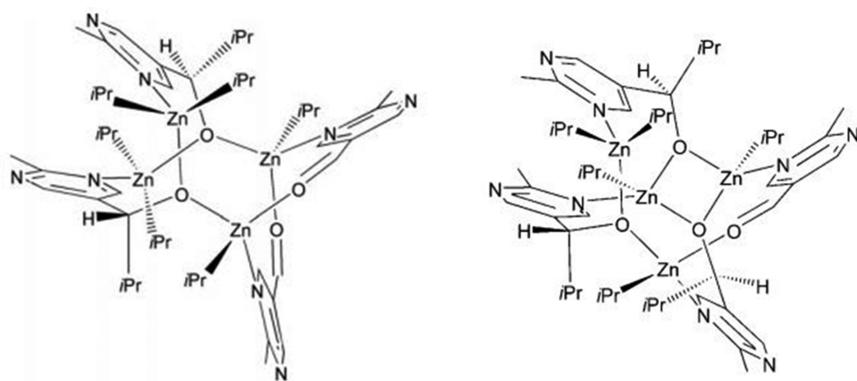
Scheme 7.2   Self-assembled tetramolecular complexes including two or one alde-
hyde as they were computed by Schiaffino and Ercolani Reproduced
from ref. 45 with permission from John Wiley & Sons, Copyright
© 2008 Wiley-VCH Verlag GmbH & Co. KGaA, Weinheim.

To conclude this kinetic second-order diversion, we invite the reader to
look at the supplementary information part of the ref. 34 (see Table S5 and
Figures S6 and S7) where an aldehyde second-order has been demonstrated
in a model in which there is only one involvement of the aldehyde with the
autocatalytic cycle.

7.3.2   Background Uncatalyzed Racemic Alkylation

Among all the kinetic runs, those with a smaller amount of added carbinol
are of particular interest because the added carbinol could mask any auto-
catalytic effect. In fact, it has been known since 2003, that the Soai reaction
can be run without the addition of any chiral catalyst.[18] This property is due
to a slow uncatalyzed racemic alkylation. This process has been unveiled by
Rivera Islas *et al.*[32] at around $4.5 \pm 1 \times 10^{-3}$ M^{-1} s^{-1} for the trimethysilyl-
ethynyl pyrimidinic aldehyde[23] in C$_7$D$_8$ at 273 K and subsequently confirmed
by Noble-Terán *et al.*[47] at 1.3×10^{-3} for the *tert*-butyl-ethynyl pyrimidinic al-
dehyde[48] at 248 K and 3.8×10^{-4} M^{-1} s^{-1} for the adamantly-ethynyl pyr-
imidinic aldehyde[49] at 298 K. The presence of such racemic background
alkylation has also been recognized recently by Hawbaker and Blackmond.[50]

7.3.3   Varying Zinc Alkoxides and Aldehydes Structures

Denmark and co-workers conducted extensive structural and mechanistic
study by combining various zinc alkoxides and aldehyde substrates.[37] *In situ*

IR monitoring at 1710 cm^{-1} of the residual aldehyde allowed them to sample the reaction mixture for the simultaneous determination of the ee. The reactions were started according to the Soai procedure, *i.e.* the aldehyde was added as the final component, such that it was never contacted to the free carbinol as in Trapp's experiment. Figure 7.7 shows that a very nice sigmoidal aldehyde evolution has been recorded by mixing a bulky pyrimidinic aldehyde with di-isopropyl zinc in the absence of any added catalyst. The final ee ($\approx 2\%$) is a sign that spontaneous mirror-symmetry breaking is on the doorstep. On the other hand, the addition of 20% of carbinol gives rise to fast consumption of the initial aldehyde. This catalyst produces a rate about 4 times faster than the rate at inflexion in the sigmoidal run. Such comparison could provide an estimation of the amount of autocatalyst, which has been produced spontaneously in the absence of added carbinol. Interestingly, these results also provide a talented confirmation of the previous Klankermayer *et al.* results that the amplifying asymmetric autocatalysis is dependent on the unique steric properties of the isopropyl group.[51]

Another series of experiments has been carried out in order to compare the classical alkylating agent (di-isopropyl zinc) with the simpler one, diethyl zinc using a trimethylsilyl-ethynyl pyrimidinic di-isopropyl carbinol additive. The observed enantiomeric ratio amplifications are gathered in Table 7.4. However, in the absence of any recorded kinetic evolution showing a characteristic sigmoidal shape, any enantiomeric amplification does not allow us to conclude that chiral autocatalysis is operating. It can be just a simple catalyst association, the so-called "nonlinear effect in asymmetric synthesis".[52]

Nevertheless, the Denmark *et al.* approach is very complete and original, and a lot of interesting DFT calculations have been carried out. Two competing tetrameric SMS Klankermayer-like[51] transition states have been computed, the favored one delivers the isopropyl group from the side which produces the homomorphic alkoxide, while the higher energy other gives rise to the heteromorphic product *via* the delivery of the isopropyl group from the enantiomeric side. Depending on the structure of the carbaldehyde (pyridinic or trimethylsilyl-ethynyl pyridinic), an energy difference lying between 2.2 to 4.4 kcal mol^{-1} is compatible with the observed final high enantiomeric ratio at 99 : 1 (see Section 7.4).

A simplified reaction model for autocatalysis has been developed and used to fit semi-quantitatively several kinetic runs. Unfortunately, neither the chirality, the reversibility of the aggregation steps, nor the contribution of an uncatalyzed background alkylation has yet been taken into account in this model.

The question of the number of nitrogen atoms within the aromatic cycle of the aldehyde has been debated by Denmark,[37,38] and also by Amedjkouh.[55] Azaaryl aldehydes (pyridine-like) represent only a limited-version of the Soai aldehyde; in homogeneous solution, their amplification power is weak. It is likely that they are not able to build an autocatalytic scaffold as is expected with the pyrimidinic Soai aldehyde.
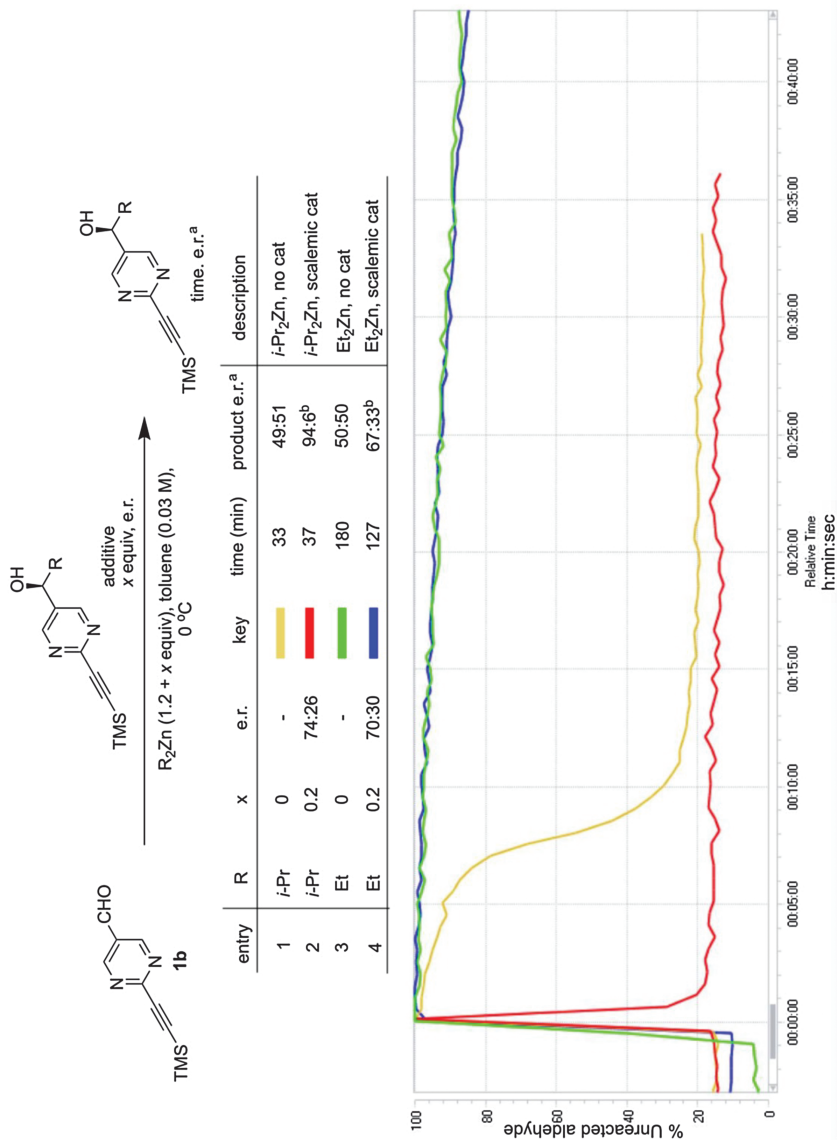
Figure 7.7 Non-catalytic and catalytic alkylation of the trimethylsilyl-ethynyl pyrimidinic carbaldehyde with di-isopropyl zinc (**1**, **2**) and di-ethyl zinc (**3**, **4**). Reproduced from ref. 38 with permission from American Chemical Society, Copyright 2020.

Table 7.4 Enantiomeric ratio (e.r.) amplification during the alkylation of several carbaldehydes by di-isopropyl and di-ethyl zinc in the presence of 20% trimethylsilyl–ethynyl pyrimidinic di-isopropyl carbinol additive. Note the nonlinear character of the amplification gain (e.r.$_{pdt}$/e.r.$_{cat}$). Higher gain is witnessed for higher catalyst enantiomeric ratios.

| Carbaldehydes	Trimethylsilyl-ethynyl-pyridinic	Pyridinic	Triisopropylsilyl-ethynyl-pyrimidinic	t-Butyl-ethynyl-pyrimidinic
Di-isopropyl zinc	1.18 to 6.75[53] 3 to 49[23]	3 to 10.1[38]	1.188 to 1.193[53] 2.57 to 11.5[38]	1.12 to 5.58[53] 1.0000005 to 3.65[54]
Di-ethyl zinc	3 to 5.66[38]	3 to 1.22[38]	2.85 to 3.17[38]	

However, the Amedjkouh group has described two specific situations where the Soai-like character of such limited-version aldehydes can be revealed. The first one is a chemical system combining asymmetric amplification of Soai's autocatalyst (pyrimidinic) alongside a catalytic addition of $Zn(iPr)_2$ to azaaryl (pyridinic) aldehydes.[56,57] The idea was to use the Soai's autocatalyst as a catalyst in an ensuing enantioselective alkylation (or alkynylation[55,57]) of azaaryl aldehydes with moderate to good levels of asymmetric induction. This work demonstrates that the Soai autocatalytic scaffold can play the role of a 'classical' chiral catalyst beyond the traditional chiral pool and indicates a potentially novel approach to access enantiomerically pure molecules. Moreover, the ee increase of the azaarylcarbinol over time suggests some autocatalytic effect, *i.e.* the slow building of a powerful reactive species, the structure of which has yet to be established. The second one is to work in heterogeneous conditions, *i.e.* when aldehyde crystals are contacted by $Zn(iPr)_2$ vapor, a mirror-symmetry breaking has been witnessed.[58] This effect is the signature of chiral autocatalysis. The mechanism is complex since several side products were identified. Moreover, the autocatalytic character is confirmed by monitoring the progress of ee over time. It is likely that the confined reactive layer was favorable to the building-up of some autocatalytic scaffold which does not occur in fluid solution.

7.3.4 Influence of the Isotopic Chirality

The sensitive response of the Soai reaction to the minute isotope chirality, as recorded for $^{12}C/^{13}C,$[20] H/D,[19] $^{16}O/^{18}O,$[21] and recently for $^{14}N/^{15}N$ moieties,[22] is definitely the most remarkable feature among all other additive effects.[59,60] In this regard, Hawbaker and Blackmond studied the effect of H/D chirality using (*R*)- or (*S*)-1-methoxy-(^{2}H)-3-methoxy propanol as the additive (Scheme 7.3).[61]

The authors found that the additive, as a function of its concentration, increasingly slows down the overall velocity of the reaction (Figure 7.8).

To rationalize this inhibitory effect, they conducted kinetic, NMR, and DFT studies that indicated a selective interaction between the assumed
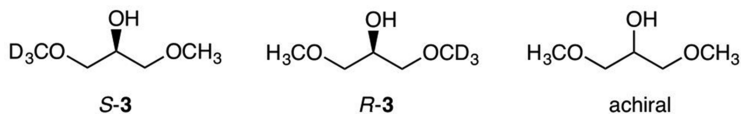
Scheme 7.3 Structures of the ^{2}H-labeled chiral dimethoxy propanol and achiral parent.
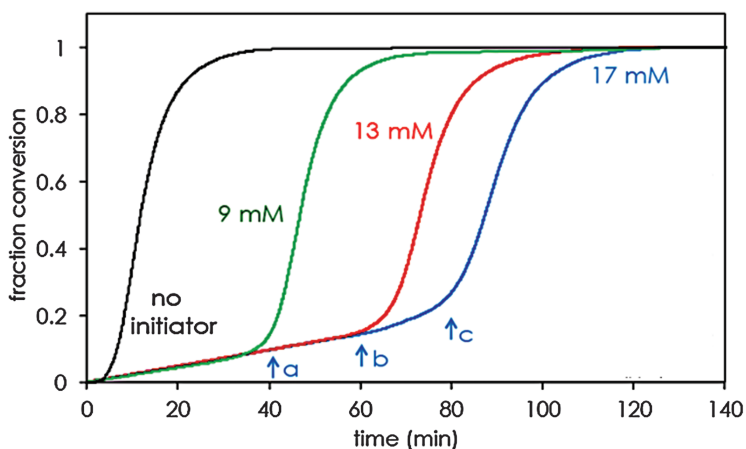

Figure 7.8 Inhibitory effect on the overall velocity of the Soai reaction by the presence of different concentrations of 1-methoxy-(^{2}H)-3-methoxy propanol as an isotopically chiral additive. Reproduced from ref. 61 with permission from American Chemical Society, Copyright 2018.

homochiral dimeric zinc alkoxide autocatalyst (R_2 and S_2) and the chiral additive (X) that inhibits the autocatalytic pathway. It is argued that the additive–catalyst interaction can trap the autocatalyst through the stereo-selective formation of inactive diastereomeric species R_2X and S_2X thus promoting one enantiomer over the other during the autocatalytic stage. Such chiral additive–catalyst inhibition was already anticipated in 2007 in the framework of kinetic understanding of the enantioselectivity reversal by achiral additives in the Soai reaction.[62,63]

Taking into account the similitude of the isotopically-labeled enantio-mers, it is likely that the energy difference between the two diastereoisomers is tiny. This is the reason why a subsequent study by the same authors was carried-out in order to identify the magnitude of the energy imbalance that gives rise to directed symmetry breaking and asymmetric amplification in the Soai reaction.[50] The idea was to perform a long series of Soai reactions in the presence of the same amount of the ^{2}H-labeled chiral dimethoxy pro-panol by decreasing gradually its ee. These experiments demonstrated that when the ee of the initiator was $\geq 1.0\%$, it directed the chiral outcome of the reaction. On the other hand, when the ee of the initiator was less than 1.0%,

fluctuations overtook its influence and gave a stochastic outcome. In order to interpret this result, a Kondepudi–Nelson-like stochastic model[50,64] was programmed to simulate the experiments run at initiator ee = 1.0% and 0.1%. Repeated simulations were useful to estimate whether the outcome would be stochastic or directed. The value of the tiny energy difference between the two diastereoisomers was tuned until all of the ee = 1.0% simulations showed a directed outcome and the 0.1% ones, a stochastic result. The authors estimated this value to be in the range of 10^{-8}–10^{-7} kJ mol^{-1}.

7.4   Critical Analysis of Two Specific Realistic Models: Noble-Terán *vs.* Trapp Cycles

7.4.1   The Noble-Terán Cycle

The Noble-Terán cycle is a kinetic and thermodynamic model of the Soai reaction which integrates the results of the most recently published XRD structural data and DFT calculations and selected experimental kinetic data. The cycle includes the aldehyde: A, the alkyl Zn: Z: ((iPr)$_2$Zn), and the carbinol: R.[23,41,65] The carbinol appears under the form of alcoholates: RZ,[66] square-dimer: R2,[67] alcoholate dimer: R2Z2,[68] alcoholate tetramer: R4Z4[46,65] and the activated tetramer: R4Z5 (catalytic scaffold).[68] A doubly-activated tetramer (R4Z6) has been crystallized and isolated under its enantiomeric form: S4Z6. Among the heterochiral pool, there are the hetero-square dimer RS and the hetero tetramer R2S2Z4 which has been crystallized and isolated. Figure 7.9 displays the structures of all the recognized intermediates that are involved in the cycle.

For the sake of chemical realism, homo- and heterochiral configurations of all oligomeric species were taken into account. All reversible processes were defined by their equilibrium constants and by their relaxation time constants that describe the rate by which the equilibrium is established. The unique irreversible process is the highly exergonic alkylation (Figure 7.10).

The Noble-Terán scaffold (R4Z5) is made of carbinol only. Such structures are reminiscent to previous transition states proposed by Gridnev and Vorobiev[68] as well as by Denmark and co-workers[38] (see Figure 7.11).

The 3D homochiral tetramer cavity displays a suitable shape complementarity for the aldehyde to be positioned. The electrophilicity of the aldehyde group is increased upon Zn coordination, whereas its orientation is insured by the bulky ethynyl substituent. Under these conditions, the two prochiral planes of the aldehyde are discriminated in order to form the carbinol with the same configuration as the tetrameric catalyst. After the alkyl transfer, the catalyst can split reversibly into dimeric[69] and monomeric alcoholates.

Finally, the Noble-Terán cycle model reproduces the simultaneous evolution of the ee and conversion of two independent experiments. The model is also able to mimic strong amplification from extremely low initial ee and
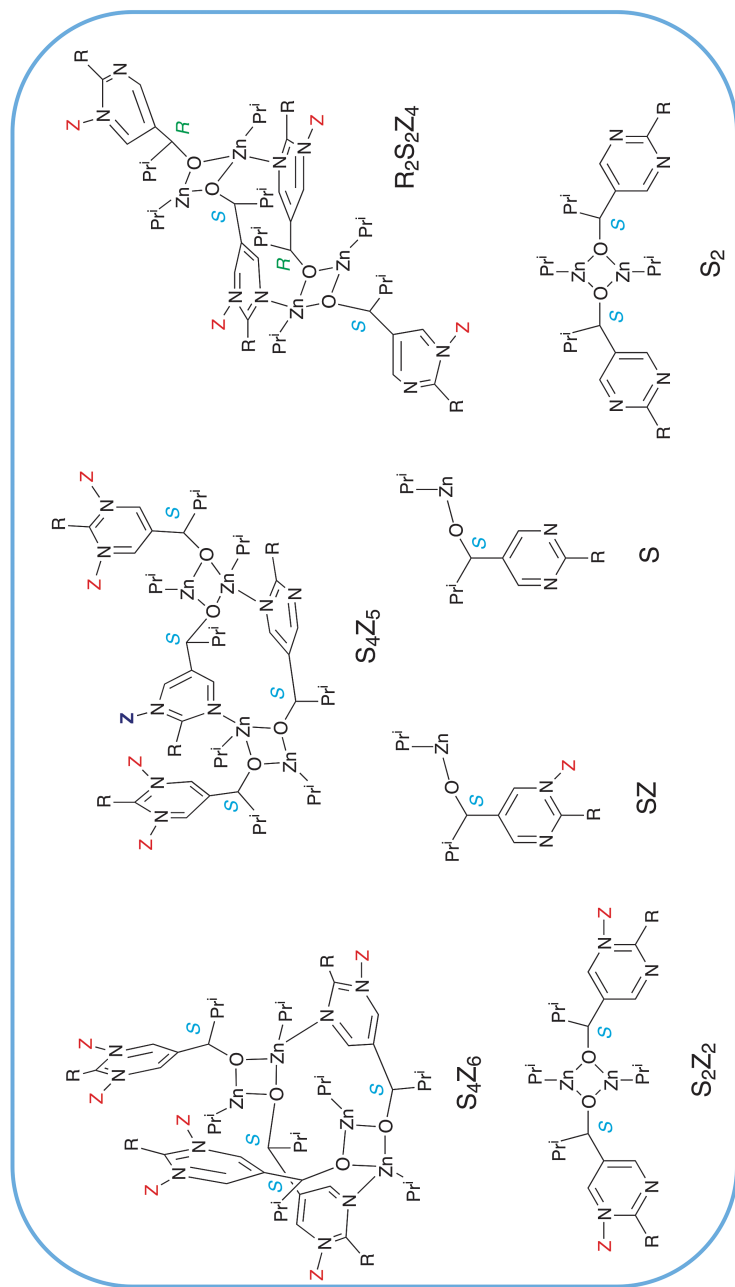
Figure 7.9 The structures of the various intermediates were either determined by using XRD or NMR spectroscopy or were computed by DFT. Reproduced from ref. 47 with permission from John Wiley & Sons, Copyright © 2018 Wiley-VCH Verlag GmbH & Co. KGaA, Weinheim.
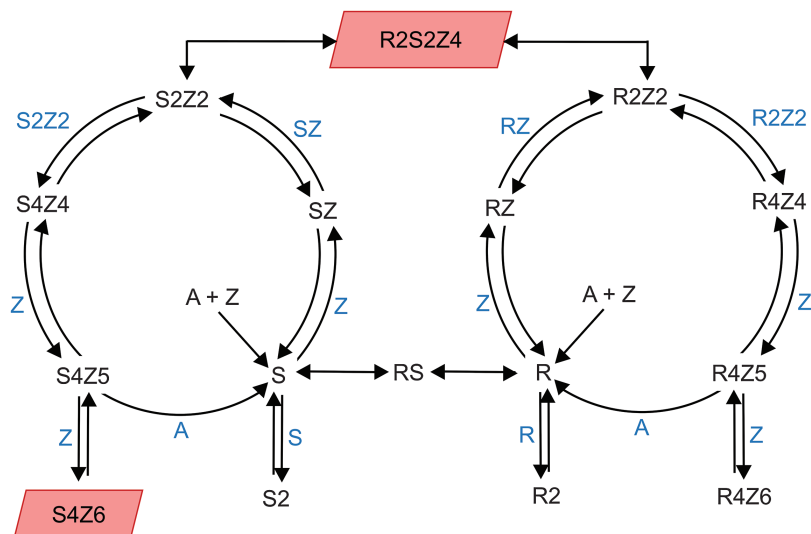
Figure 7.10   Noble-Terán mechanism:[47] A: aldehyde; Z: (*i*-Pr)$_2$Zn; R carbinol; RZ
                   alcoholates; R2: square-dimer; R2Z2: alcoholate dimer; R4Z4: alcoho-
                   late tetramer; R4Z5: activated tetramer (ready for alkylation); R4Z6:
                   doubly-activated tetramer, has been crystallized and isolated under its
                   enantiomeric form: S4Z6 (rhombohedra). Among the heterochiral pool,
                   there are the hetero-square dimer RS and the hetero tetramer R2S2Z4
                   which has been crystallized and isolated (rhombohedra). Reproduced
                   from ref. 47 with permission from John Wiley & Sons, Copyright © 2018
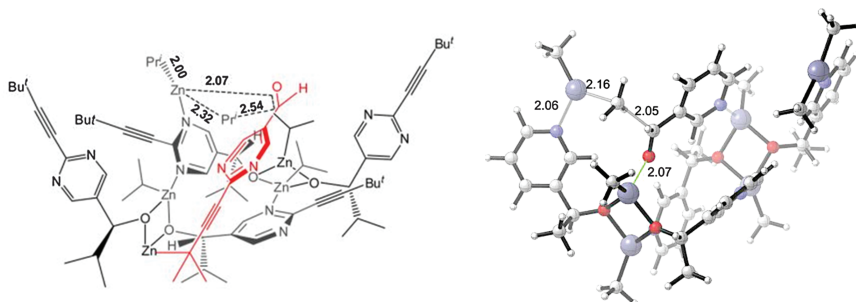   Wiley-VCH Verlag GmbH & Co. KGaA, Weinheim.

Figure 7.11   Gridnev's (left) and Denmark's (right) schedules of supposed tetrameric
                   transition states. The main difference lies in the number of aromatic
                   nitrogens involved in the oligomerization process. In the case of Denmark,
                   the aromatic cycles are pyridinic. Reproduced from ref. 68 (left) and ref. 38
                   (right) with permission from American Chemical Society, Copyright 2012
                   and 2020.

spontaneous mirror-symmetry breaking under ''initial zero-catalyst'' con-
ditions. It also reproduces the crystallization conditions by exhibiting the
preferential accumulation of the corresponding oligomeric species in
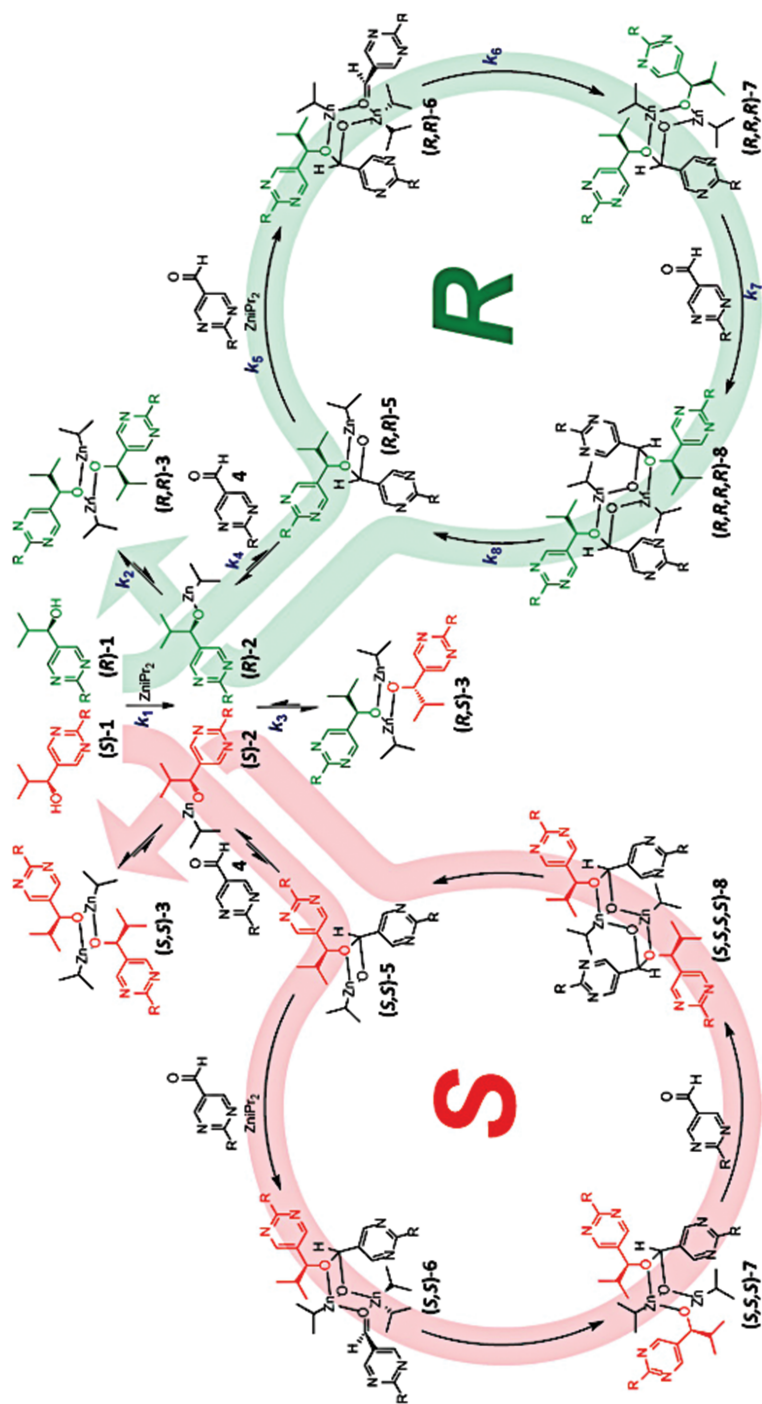solution.

Figure 7.12 Trapp mechanism: involvement of a transient chiral acetal catalyst as a key step intermediate. All the structures proposed have been identified by the *in situ* high-resolution mass spectrometric experiments. Reproduced from ref. 39 with permission from John Wiley & Sons, Copyright © 2020 The Authors. Published by Wiley-VCH GmbH.

7.4.2 The Trapp Cycle

The Trapp cycle mechanism[39,40] has been established from *in situ* high-resolution mass spectrometric measurements, detailed kinetic analyses, and doping with reacting reaction mixtures (see Figure 7.12). It shows some similarities with the Noble-Terán cycle: the aldehyde, carbinols, Zn-alcoholates, and homo- and hetero-square dimers appear as common elements of both mechanisms. Another point of similarity is the building of a catalytic scaffold including the carbinols or the Zn-alcoholates which is in both cases at the origin of the autocatalysis. But the similarity ends here, since it includes the transient formation of hemiacetal complexes which can establish the autocatalytic cycle.

Let us examine the four main intermediates of the Trapp's cycle.

A: SS-5 is the so-called hemiacetal (Scheme 7.4):

In SS-5, the 2 ''S'' do not have the same meaning: one is from carbinol (in red), the other is from acetal (in black). The formation of the acetal results from the reaction of the CO of the aldehyde on the Zn–O bond of the alcoholate: C bonds with the O and O bonds Zn. Only the acetal can be readily racemized by returning back to the aldehyde.

B: SS-6 (Scheme 7.5):

SS-6 includes the SS-5 structure. An aldehyde is now complexed, and it is ready to be alkylated by a di-isopropylzinc also complexed in an appropriate position.
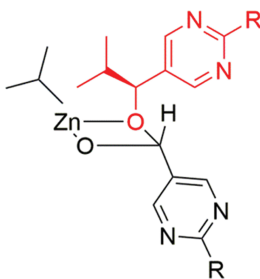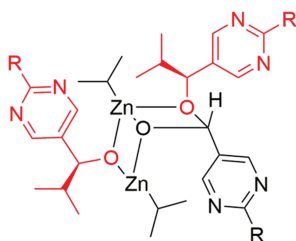

Scheme 7.4
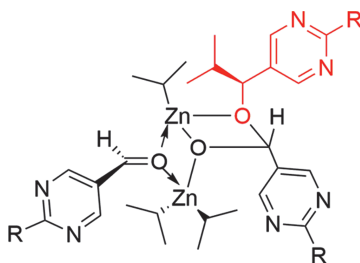
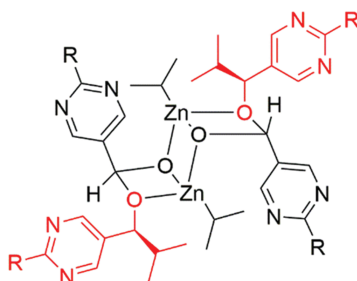**Scheme 7.5**

C: SSS-7 (Scheme 7.6):

SSS-7 is the key structure, the aldehyde has been alkylated, and a new stable chiral carbon has been formed; this alkylation step is highly exergonic, the reverse which is expected to be very slow is a racemizing one.

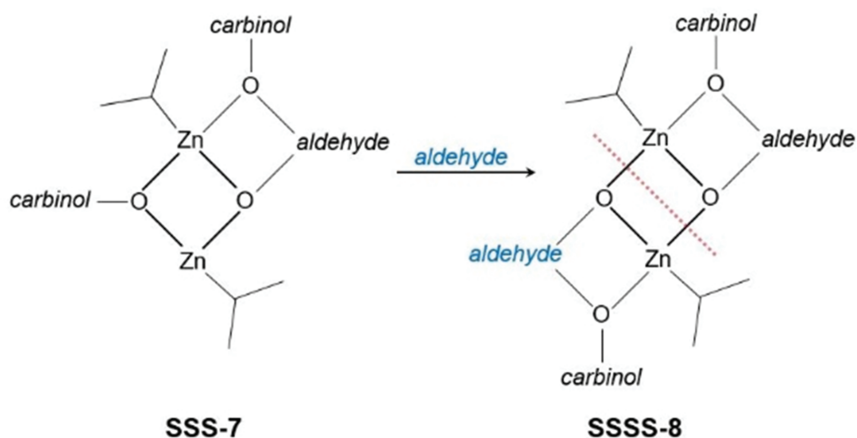D: SSSS-8 (Scheme 7.7):

This intermediate is the result of a second hemiacetalization according to Scheme 7.8.

Scheme 7.6

Scheme 7.7

Scheme 7.8   Attack of a second aldehyde on SSS-7 after breaking the newly formed carbinol Zn bond. A subsequent split of SSSS-8 along the dashed red line gives rise to SS-5 hemiacetal, thus closing the Trapp cycle.

While many transient intermediates have been identified from mass spectrometry, none of these mechanistic assumptions have been really validated. First principles DFT calculations help to define some structures and confirm spectroscopic investigations, but it should be remembered that the structure of the catalytic step can be rather difficult to discern. The Trapp cycle mechanism has been modeled to calculate the concentration profiles and the ee in various conditions. Unfortunately, no direct comparison between the experiments and the model were provided.

7.5   Conclusion

The Soai reaction represents a unique example of total asymmetric synthesis in a homogeneous reaction system. Nowadays it is widely accepted that it forms a Frank-like reaction network where enantioselective autocatalysis and mutual inhibition are provided by the involvement of oligomeric intermediates. The typical sequential methodology of the Soai reaction is an approximation to an open flow reactor system. The high exergonicity of the alkyl Zn(II) addition to the carbaldehyde points to a kinetic control of the reaction. This is an energy dissipative chemical system, where the final non-equilibrium stationary state (NESS) does not have the racemic composition: the expected racemate is an unstable NESS, and there is an energetically degenerate enantiomeric pair of scalemic NESS's, which have high ee values. This is an unfamiliar feature compared to the common enantioselective kinetic control of classical asymmetric synthesis.

In the absence of any external chiral polarization, spontaneous mirror-symmetry breaking (SMSB) must lead to a stochastic distribution of chiral signs between experiments, due to the stochastic distribution of chiral signs of the fluctuations. On the contrary, under a chiral polarization, acting at the bifurcation point, the SMSB leads to a deterministic chiral sign. For example, those of asymmetric centers arising from isotopic substitution are sufficient to direct the chiral sign of the Soai reaction.

Several more or less realistic models inspired by a Frank-like reaction network have been provided. They differ by the structure of the catalyst and by the involvement of reversible steps. More often, these models include a slow uncatalyzed racemic alkylation. It is likely that the true autocatalyst is in equilibrium with a lot of inactive oligomers and that these equilibria are displaced towards the autocatalyst one, once the exergonic alkylation is occurring. These models reproduce the main features of the Soai reaction including the ee amplification through the repetitive sequential reaction procedure which uses the outcome from one reaction as the catalyst for the next reaction. A realistic model based on isolated XRD structures and DFT calculations results has been established including an all-alcoholate tetrameric catalytic scaffold. This scaffold has been confirmed from recent DFT calculation and *in situ* IR monitoring. However, the possible involvement of the aldehyde within the catalytic scaffold is still questioned.

   It appears now that several independent teams are involved in Soai's reaction experimental investigations. All of them confirm the necessary specific structures of the reactants involved, namely di-isopropyl Zn and pyrimidinic bulky aldehydes. This feature makes the Soai's reaction very unique. However, this uniqueness should not be a barrier for the development of new experimental situations and multidimensional monitoring techniques. Much more than varying the structures, this is the concept of a catalytic oligomeric supramolecular scaffold which deserves to be exploited.

Acknowledgements

References

1. B. L. Feringa and R. A. van Delden, *Angew. Chem., Int. Ed.*, 1999, **38**, 3418.
2. J. M. Ribó, C. Blanco, J. Crusats, Z. El-Hachemi, D. Hochberg and A. Moyano, *Chem. - Eur. J.*, 2014, **20**, 17250.
3. J. Crusats and A. Moyano, *Synlett*, 2021, **32**, A.
4. T. Shibata, H. Morioka, T. Hayase, K. Choji and K. Soai, *J. Am. Chem. Soc.*, 1996, **118**, 471.
5. K. Soai, A. Matsumoto and T. Kawasaki, in *Advances in Asymmetric Autocatalysis and Related Topics*, ed. G. Pályi, R. Kurdi and C. Zucchi, Academic Press, London, 2017, ch. 1, pp. 1–30.
6. T. Buhse, J.-M. Cruz, M. E. Noble-Teran, D. Hochberg, J. M. Ribó, J. Crusats and J. C. Micheau, *Chem. Rev.*, 2021, **121**, 2147.
7. K. Soai, *Proc. Japan Acad. Ser. B Phys. Biol. Sci.*, 2019, **95**, 89.
8. K. Soai, T. Kawasaki and A. Matsumoto, *Tetrahedron*, 2018, **74**, 1973.
9. K. Soai, T. Kawasaki and A. Matsumoto, *Symmetry*, 2019, 694.
10. F. C. Frank, *Biochim. Biophys. Acta*, 1953, **11**, 459.
11. R. Plasson, A. Brandenburg, L. Jullien and H. Bersini, *J. Phys. Chem. A*, 2011, **115**, 8073.
12. J. M. Ribó and D. Hochberg, *Phys. Chem. Chem. Phys.*, 2020, **22**, 14013.
13. G. Lente, *J. Phys. Chem. A*, 2004, **108**, 9475.
14. G. Lente, *J. Phys. Chem. A*, 2005, **109**, 11058.
15. R. Plasson, D. K. Kondepudi, H. Bersini, A. Commeyras and K. Asakura, *Chirality*, 2007, **19**, 589.
16. A. Blokhuis, D. Lacoste and P. Gaspard, *J. Chem. Phys.*, 2018, **148**, 144902.
17. D. K. Kondepudi and G. W. Nelson, *Phys. Rev. Lett.*, 1983, **50**, 1023.

18. K. Soai, I. Sato, T. Shibata, S. Komiya, M. Hayashi, Y. Matsueda, H. Imamura, T. Hayase, H. Morioka, H. Tabira, J. Yamamoto and Y. Kowata, *Tetrahedron: Asymmetry*, 2003, **14**, 185.

19. T. Kawasaki, M. Shimizu, D. Nishiyama, M. Ito, H. Ozawa and K. Soai, *Chem. Commun.*, 2009, 4396.

20. T. Kawasaki, Y. Matsumura, T. Tsutumi, K. Suzuki, M. Ito and K. Soai, *Science*, 2009, **324**, 492.

21. T. Kawasaki, Y. Okano, E. Suzuki, S. Takano, S. Oji and K. Soai, *Angew. Chem., Int. Ed.*, 2011, **50**, 8131.

22. A. Matsumoto, H. Ozaki, S. Harada, K. Tada, T. Ayugase, H. Ozawa, T. Kawasaki and K. Soai, *Angew. Chem., Int. Ed.*, 2016, **55**, 15246.

23. I. D. Gridnev, J. M. Serafimov, H. Quiney and J. M. Brown, *Org. Biomol. Chem.*, 2003, **1**, 3811.

24. D. A. Singleton and L. K. Vo, *Org. Lett.*, 2003, **5**, 4337.

25. Y. Kaimori, Y. Hiyoshi, T. Kawasaki, A. Matsumoto and K. Soai, *Chem. Commun.*, 2019, **55**, 5223.

26. W. H. Mills, *J. Soc. Chem. Ind.*, 1932, **51**, 750.

27. K. Mislow, *Collect. Czech. Chem. Commun.*, 2003, **68**, 849.

28. K. Soai, T. Shibata and I. Sato, *Acc. Chem. Res.*, 2000, **33**, 382.

29. I. Sato, D. Omiya, T. Saito and K. Soai, *J. Am. Chem. Soc.*, 2000, **122**, 11739.

30. I. Sato, K. Kadowaki, H. Urabe, J. H. Jung, Y. Ono, S. Shinkai and K. Soai, *Tetrahedron Lett.*, 2003, **44**, 721.

31. T. Kawasaki, H. Tanaka, T. Tsutsumi, T. Kasahara, I. Sato and K. Soai, *J. Am. Chem. Soc.*, 2006, **128**, 6032.

32. J. Rivera Islas, D. Lavabre, J.-M. Grevy, R. H. Lamoneda, H. R. Cabrera, J.-C. Micheau and T. Buhse, *Proc. Natl. Acad. Sci. U. S. A.*, 2005, **102**, 13743.

33. J. Crusats, D. Hochberg, A. Moyano and J. M. Ribó, *Chem. Phys. Chem.*, 2009, **10**, 2123.

34. J. C. Micheau, J. M. Cruz, C. Coudret and T. Buhse, *Chem. Phys. Chem.*, 2010, **11**, 3417.

35. J. C. Micheau, C. Coudret, J. M. Cruz and T. Buhse, *Phys. Chem. Chem. Phys.*, 2012, **14**, 13239.

36. D. A. Singleton and L. K. Vo, *J. Am. Chem. Soc.*, 2002, **124**, 10010.

37. S. V. Athavale, A. Simon, K. N. Houk and S. E. Denmark, *Nat. Chem.*, 2020, **12**, 412.

38. S. V. Athavale, A. Simon, K. N. Houk and S. E. Denmark, *J. Am. Chem. Soc.*, 2020, **142**, 18387.

39. O. Trapp, S. Lamour, F. Maier, A. F. Siegle, K. Zawatzky and B. F. Straub, *Chem. – Eur. J.*, 2020, **26**, 15871.

40. O. Trapp, *Front. Chem.*, 2020, **8**, 615800.

41. T. Gehring, M. Quaranta, B. Odell, D. G. Blackmond and J. M. Brown, *Angew. Chem., Int. Ed.*, 2012, **51**, 9539.

42. I. D. Gridnev and A. K. Vorobiev, *Bull. Chem. Soc. Jpn.*, 2015, **88**, 333.

43. F. G. Buono and D. G. Blackmond, *J. Am. Chem. Soc.*, 2003, **125**, 8978.

44. D. G. Blackmond, *Tetrahedron: Asymmetry*, 2006, **17**, 584.

45. L. Schiaffino and G. Ercolani, *Angew. Chem., Int. Ed.*, 2008, **47**, 6832.
46. L. Schiaffino and G. Ercolani, *Chem. – Eur. J.*, 2010, **16**, 3147.
47. M. E. Noble-Terán, J. M. Cruz, J. C. Micheau and T. Buhse, *ChemCatChem*, 2018, **10**, 642.
48. I. Sato, D. Omiya, H. Igarashi, K. Kato, Y. Ogi, K. Tsukiyama and K. Soai, *Tetrahedron: Asymmetry*, 2003, **14**, 975.
49. M. Quaranta, T. Gehring, B. Odell, J. M. Brown and D. G. Blackmond, *J. Am. Chem. Soc.*, 2010, **132**, 15104.
50. N. A. Hawbaker and D. G. Blackmond, *Nat. Chem.*, 2019, **11**, 957.
51. J. Klankermayer, I. D. Gridnev and J. M. Brown, *Chem. Commun.*, 2007, 3151.
52. M. E. Noble-Terán, T. Buhse, J. M. Cruz, C. Coudret and J. C. Micheau, *ChemCatChem*, 2016, **8**, 1836.
53. T. Shibata, S. Yonekubo and K. Soai, *Angew. Chem., Int. Ed.*, 1999, **38**, 659.
54. I. Sato, H. Urabe, S. Ishiguro, T. Shibata and K. Soai, *Angew. Chem., Int. Ed.*, 2003, **42**, 315.
55. C. Romagnoli, B. Sieng and M. Amedjkouh, *Chirality*, 2020, **32**, 1143.
56. C. Romagnoli, B. Sieng and M. Amedjkouh, *Eur. J. Org. Chem.*, 2015, 4087.
57. M. Funes-Maldonado, B. Sieng and M. Amedjkouh, *Eur. J. Org. Chem.*, 2015, 4081.
58. G. Rotunno, D. Petersen and M. Amedjkouh, *ChemSystemsChem*, 2020, **2**, e1900060.
59. T. Kawasaki, Y. Kaimori, S. Shimada, N. Hara, S. Sato, K. Suzuki, T. Asahi, A. Matsumoto and K. Soai, *Chem. Commun.*, 2021, **57**, 5999.
60. G. Rotunno, G. Kaur, A. Lazzarini, C. Buono and M. Amedjkouh, *Chem. - Asian J.*, 2021, **16**, 2361.
61. N. A. Hawbaker and D. G. Blackmond, *ACS Cent. Sci.*, 2018, **4**, 776.
62. D. Lavabre, J. C. Micheau, J. Rivera Islas and T. Buhse, *J. Phys. Chem. A*, 2007, **111**, 281.
63. D. Lavabre, J.-C. Micheau, J. Rivera Islas and T. Buhse, *Top. Curr. Chem.*, 2008, **284**, 67.
64. D. K. Kondepudi and G. W. Nelson, *Nature*, 1985, **314**, 438.
65. A. Matsumoto, T. Abe, A. Hara, T. Tobita, T. Sasagawa, T. Kawasaki and K. Soai, *Angew. Chem., Int. Ed.*, 2015, **54**, 15218.
66. J. M. Brown, I. Gridnev and J. Klankermayer, *Top. Curr. Chem.*, 2008, **284**, 35.
67. I. D. Gridnev, J. M. Serafimov and J. M. Brown, *Angew. Chem., Int. Ed.*, 2004, **43**, 4884.
68. I. D. Gridnev and A. K. Vorobiev, *ACS Catal.*, 2012, **2**, 2137.
69. A. Matsumoto, A. Tanaka, Y. Kaimori, N. Hara, Y. Mikata and K. Soai, *Chem. Commun.*, 2021, **57**, 11209.

DRA. LINA ANDREA RIVILLAS ACEVEDO
COORDINADORA DEL POSGRADO EN CIENCIAS
PRESENTE

Atendiendo a la solicitud para emitir DICTAMEN sobre la revisión de la tesis titulada: **Desracemización de Viedma: Un Modelo Integral de la Ruptura Espontánea de la Simetría Quiral en un Sistema de Clorato de Sodio**, que presenta la alumna María Eugenia Noble Terán (10012790) para obtener el título de **Doctor en Ciencias.**

Director de tesis: Dr. Thomas Werner Buhse
Unidad Académica: Instituto de Investigación en Ciencias Básicas y Aplicadas (IICBA)

Nos permitimos informarle que nuestro voto es:

NOMBRE	DICTAMEN	FIRMA
Dr. Marco Antonio Rivera Islas CInC - UAEM	APROBADO	
Dr. Hugo Morales Rojas CIQ - UAEM	APROBADO	
Dra. Alicia Negrón Mendoza ICN - UNAM	APROBADO	
Dr. José Manuel Cruz Martínez FC en Física y Matemáticas - UNACH	APROBADO	
Dr. Jaime Escalante García CIQ - UAEM	APROBADO	
Dr. Raúl Salgado García CInC - UAEM	APROBADO	
Dr. Thomas Werner Buhse CIQ - UAEM	APROBADO	

Av. Universidad 1001 Col. Chamilpa, Cuernavaca Morelos, México, 62209.
Tel. (777) 329 70 00, Ext. 6011 posgradoenciencias@uaem.mx

Una universidad de excelencia

RECTORÍA
2017-2023

Se expide el presente documento firmado electrónicamente de conformidad con el ACUERDO GENERAL PARA LA CONTINUIDAD DEL FUNCIONAMIENTO DE LA UNIVERSIDAD AUTÓNOMA DEL ESTADO DE MORELOS DURANTE LA EMERGENCIA SANITARIA PROVOCADA POR EL VIRUS SARS-COV2 (COVID-19) emitido el 27 de abril del 2020.

El presente documento cuenta con la firma electrónica UAEM del funcionario universitario competente, amparada por un certificado vigente a la fecha de su elaboración y es válido de conformidad con los LINEAMIENTOS EN MATERIA DE FIRMA ELECTRÓNICA PARA LA UNIVERSIDAD AUTÓNOMA DE ESTADO DE MORELOS emitidos el 13 de noviembre del 2019 mediante circular No. 32.

Sello electrónico

THOMAS WERNER BUHSE | Fecha:2023-08-07 16:59:20 | Firmante
MLIF6NC8PK8fyG//pEbMCGCnxPvB857ZuzA5iEv+0QnbGvp+nxq3KxwJQ5qkUInVnw/G0ijPIRSGwshByblk2EG6CppYZB1eADEwZ351oncjz43iGuUDpOxihvc0hJNmHfCDkUr3 bF7ykOq7CffRU6U0/4QIfbLbfGJlz7RGLAane8vLbMLas1FoKtbO/bDuPDjhjv0rHDXNjUopxXu5ZECAQgHBlg275t3FzB+mvFTJ1DUOXYE2YljWnr3vxX6ZhbIvjvMDLmXGnIHdnz Q5Nwl3YgpRmKaAfr+uHS2931sQYzCgU5NtkpAdkK+Vbu59hmgsIfMaV4oE8SAYY1lZ8Q==

JAIME ESCALANTE GARCIA | Fecha:2023-08-07 17:23:46 | Firmante
lVYjnlHEAiEot9ArX2ha2ubhUEOk/df8r1s1CI3QRhuGAY2v4gMTKxVem71VWUWUCDiGin6VcENzfXhpoUGSurlQi3vuBseGyJSMbau2sGV7bi5+Iz8l+ULqD6lxuIolt2pm1gqwXRN DRTTnL0cP7T33e4S5zJC6pD+DxuPoRa+BilTE+xZP8ZyxJR0EUi0T0WQPbflFY3SfyzTGeqmJkOWpEvWLgNNq1r+F0i0CpseYWHBph7Hjscya621KuRABvecUemIq81DuiHjzY/ pYJusZU320aulCrVJqjEMOaMu3ssDNWVvTQulcBNyrUWWsPswLYeze7WwbljoGVqB+nA==

JOSÉ MANUEL CRUZ MARTÍNEZ | Fecha:2023-08-07 22:28:30 | Firmante
sGNln0R0C5nPyMlzROzeoxj6Ngp42e16ahVwNx2LzRp60MI+OeyShp8DUIxGUrb5HXaRYSi4HKqgCJLbxguNgg7Uo6h+sMQXEIqCpWUYQh7AcrhL1Sp7o4mhvE3KG2rs4HR6 ZUjac1fJiueDfgwBBVAW7iGMB4j8VOkBa3bAKKyEmCqUanpk9nat9Br6M31by2GnkYcjpWviUsSCBQ1r26w8+4ytmXkjeARK7ZE6V5Xni8TLCF5jHJO34ekktwEED+K7Sk5N7RZ Y5q41NtvxmA1WdhXF0MhnKQMZ0Wi8q7GBDDAKGyc9OvaqRXueSsP82sJli+CjwCe+U4tjTOd9gg==

ALICIA NEGRON MENDOZA | Fecha:2023-08-07 22:55:02 | Firmante
BOMhP4uq9HmyRoabK+y1dqKdqaEM2H25y3axwwFr3GonqfEo9gCItkE27xfSQJybKxxyR5XHI2yNkcEe838HNlznyOt8fMJA7FzZMVEu++k2617dIE5/JVb7M1+S8CHZr+g1V4icy lPFAaPtgxdsFISpkbALMUJwr9Ut/FcgVqVXPikVeJ1fuezjBHtwQ6fOlnHqDfRjmso1EaNrIW73utC/hVy3654TGsW3Wc9xRC2Jmf7Fbrrobc4+zLa75AZ1WzdRU0XG8kpg+WASppj DzmOMI2UN4OTq8DlIj/l+FgnKacKn3JQBiHgFiWlUrw4MJxX278a9VUaD0jn7yEAKC8w==

MARCO ANTONIO RIVERA ISLAS | Fecha:2023-08-08 18:15:06 | Firmante
qjll3or3hmqOyI7qO3FCMfFq2JfV9S0ByakxZUkhmNxAEZBmwy1uYL9QmJnjOnnL15QiA4tCFo1NXTI4KVGqaJz0dI2lLAeN3wIpoyZUVgpXwuH+eF7Qg37rJlfTkG59vc3w4bQrclD TXr/KrjLVXncsQYtnmtggA2OMdOrD6yPSJRmneqURHTK6j+HxRHO1BYg+A0emRvN59RhrcWaI7o6j/WVIA4IvFkL3vPb0yAJ0i2Kkw64ln+DElpqCPS9U7neyvzrw+RnVC8G6ddjc XRcxA5+aMukAqBB11M8wgN/G0dnzdbJutj41CsPLr+sDAdJ7LPIaW3b82UKYAy7uLQ==

RAUL SALGADO GARCIA | Fecha:2023-08-11 08:38:28 | Firmante
KZTSJgZdDNmh6RpX6Q6bMhjEWQYuMeJdX4RPrBH926B3MD6hJWYhVK1EwiOkEB8xV0sp9juW8YnW/xanLnEY9nw4cnAcIMlp4z0GQvHl5oA4DeXeIwb8/cRUi5RGy0E48Bx myu4oqAi2D6INk4wDU0Z+7OcplxduzgQBqekZlsfWLEg6WmhPXyTXjiBH0gd3LM3M+cuX0zPg4vKFpy0TlDqkvMYQLOePypLXPGt4Vjahz11W3VPeQWS6gtsnbC/kvmD4now3r 8wxC9i0y2LPiQHlNtXpK2ob6EyI5mXHjKM1JzxT9DnS5oAmVWaFVi9OglGCAV0//2gEIWWjELe7+g==

HUGO MORALES ROJAS | Fecha:2023-08-15 09:31:25 | Firmante
Iuf3dBaApmA07Fm/CFYYboSvJtKv7tYiH8ixpf75AhTkfM7kyKgk6L1JWKZGYjm0upnDSVn5ZNQ4ljR5J+fwRkg2LAqPZPcC+DrX9oIYqow31MCSzQnxevx0CO/Fjja2aO9OMYuks u0wOkOJcIwujGOpdP6BRLpGfvnCWxt/diCjoN78isa6RhK8QC1M28v5ictsOMCnDd1B4Qjvh2i9wHlXZYa5VjxUUePF44H/iGU+V0EFNRt03OgWxUY6pAw0zdfHpaaU8oHt5+TG4 o7CyaEwyNCJY9xy4/bjAEmzVWxPSr6YqVAKzvU3zVqqKh4sdB94GvO6PGj3IyJG/jG08g==

Puede verificar la autenticidad del documento en la siguiente dirección electrónica o escaneando el código QR ingresando la siguiente clave:

Mfg5bD0qd

https://efirma.uaem.mx/noRepudio/TGWNK3A6f6fJQyKpRpTUeTskWLbbkeB3